AD-A279 368

‖‖‖‖‖‖‖‖‖‖‖‖‖ 5

WHOI-93-24
1992

①

GEOPHYSICAL FLUID DYNAMICS

Great Seal

$H = X\beta\,\Omega + \overline{WT}$

WHOI

94-15145

‖‖‖‖‖‖‖‖‖‖‖

DTIC

**Course Lectures
Abstracts of Participants
Fellows Project Reports**

WHOI-93-24

Dynamics of the Outer Planets

1992 Summer Study Program
in
Geophysical Fluid Dynamics

by

Glenn Flierl, Director
Andrew Ingersoll, Principal Lecturer
Jun-Ichi Yano, Principal Lecturer
Barbara Ewing-DeRemer, Staff Assistant

Woods Hole Oceanographic Institution
Woods Hole, Massachusetts 02543

Summer 1992

Technical Report

Approved for Distribution:

John W. Farrington
Associate Director for Education
Dean of Graduate Studies

Geophysical Fluid Dynamics Program

Summer of 1992

Preface

The topic this summer was "The Dynamics of the Outer Planets." Andrew Ingersoll gave an excellent review of the current understanding of the structure of the atmospheres of Jupiter, Neptune, Saturn, and Uranus. He presented the flow structures inferred from the information gathered by the Voyager probes and other observations. The models of the circulations of the interior and of the weather layer — the jets and vortices that we see in the images — were discussed. Jun–Ichi Yano gave further discussions on vortex dynamics in the lab, analytical, and numerical models as applied to the outer planets. Finally, Andy returned with a discussion of thin atmospheres (some so thin that they disappear at night) and new approaches to the dynamics of the interiors. These lectures provided a thorough background in both the data and the theory.

As usual, we had talks (or what are sometimes called interactive seminars!) from many visitors during the summer, some directly related to the main topic and others covering other new research in geophysical fluid dynamics. From these, the fellows and staff found new areas for collaborative research and new ideas which they may explore after the summer.

Finally, the summer was completed with talks from the fellows on their individual research during the summer. These reports reflect the thought and energy that went into learning new topics and formulating new problems. We look forward to seeing fuller versions of these in journal articles.

We gratefully acknowledge the support of the National Science Foundation and the Office of Naval Research. The assistance of Jake Peirson and Barbara Ewing–DeRemer, made the summer, once again, pleasant and easy for all.

Fellows

Name	Affiliation
Rupert Ford	DAMTP, Univ. of Cambridge
Richard Holme	Harvard
Petros Ioannou	MIT
Ray LeBeau	MIT
Doug Parker	Univ. of Reading
Andrew Stamp	The Australian National Univ.
Louis Tao	University of Chicago
Phil Yecko	Columbia
Qingping Zou	Scripps Institute of Oceanography

Staff and Visitors

Name	Affiliation
Tadashi Asada	Cornell University
Neil Balmforth	Columbia University
Edward Bolton	Yale University
Eric Chaussignet	U. Miami, RSMAS
Bill Dewar	Florida State University
Tim Dowling	MIT
Brian Farrell	Harvard
Glenn Flierl	MIT
John Hart	U. Colorado
Herbert Huppert	DAMTP
Louis Howard	Florida State University
Andy Ingersoll	Caltech
Joe Keller	Stanford
Willem Malkus	MIT
Phil Marcus	Berkeley
Steve Meacham	Florida State University
Phil Morrison	U. Texas, Austin
Kirill Pankratov	WHOI
Lorenzo Polvani	Columbia
Larry Pratt	WHOI
Claes Rooth	U. Miami, RSMAS
Rick Salmon	Scripps Institution of Oceanography
Ted Shepherd	U. Toronto
Tom Solomon	U. Texas, Austin
Ed Spiegel	Columbia
Melvin Stern	Florida State University
George Sutryin	P.P. Shirsov Inst.
Charles Tresser	IBM
Geoff Vallis	Scripps Institution of Oceanography
George Veronis	Yale University
Andrew Woods	DAMTP
Jun-Ichi Yano	NCAR
Eliot Young	MIT

GFD Schedule — 1992

Mon. June 22, 10 AM
   Introduction and Planetary Slide Show
   Andrew Ingersoll

Tues. June 23, 10 AM
   Zonal Jets on the Giant Planets
   Andrew Ingersoll

Tues. June 23, 1:30 PM
   Tutorial on Geostrophic Dynamics

PO Seminar, Tues. June 23, 3 PM Clark Lab
   Geostrophic Turbulence in the California Current
   Goeff Vallis

Wed. June 24, 10 AM
   Interiors of the Giant Planets
   Andrew Ingersoll

Wed. June 24, 1:30 PM
   Intro to computing facilities

Thurs. June 25, 10 AM
   Vortices on the Giant Planets
   Andrew Ingersoll

Thurs. June 25, 1:30 PM
   Initial Development of Eddies in High-Speed Zonal Flow
   Tadashi Asada

Fri. June 26, 10 AM
   continued ...
   Andrew Ingersoll

Fri. June 26, 1:30 PM
   Large Scale Waves and Vortices
   George Sutyrin

Mon. June 29, 10 AM
   Dynamics of Vortices
   Jun-Ichi Yano

Mon. June 29, 1:30 PM
   The Dynamics of Barotropically Dominated Vortices
   William Dewar

Tues. June 30, 10 AM
   continued ...
   Jun-Ichi Yano

iv

Wed. July 15, 10 AM
    Discussion: Dynamical Systems

Fri. July 17, 10 AM
    Vapor Flow in a Hot Rock
    Andrew Woods

Tues. July 21, 10 AM
    Linear Thermal Convection in a Model Jupiter
    Jun-Ichi Yano

Wed. July 22, 10 AM
    Timing Maps for Pulsitile Chaos
    Neil Balmforth

Thurs. July 23, 10 AM
    Chaos and Turbulence in the Solar Cycle
    Ed Spiegel

Mon. July 27, 10 AM
    Tidal Friction in the Outer Planets
    Petros Ioannou

Tues. July 28, 10 AM
    Particle–driven Fluid Flows
    Herbert Huppert

Wed. July 29, 10 AM
    Kida Vortices in Stratified Flows
    Steve Meacham

Thurs. July 30, 10 AM
    Interaction between Eddies and Jets
    Larry Pratt

Fri. July 31, 10 AM
    Instability of Shear Flows
    Joe Keller

Mon. Aug. 3, 10 AM
    What is Potential Vorticity?
    Rick Salmon

Tues. Aug. 4, 10 AM
    Hamiltonian Contour Dynamics
    Phil Morrison

Wed. Aug. 5, 10 AM
    The Limitations of Balance Models
    Rupert Ford

Thurs. Aug. 6, 10 AM
  Discussion Session: Dynamics of Disks

Tues. Aug. 11, 10 AM
  Aspects of Renormalization
  Charles Tresser

Wed. Aug. 12, 10 AM
  Generalized Stability Analysis: Application to Turbulent Transition
  Brian Farrell

Thurs. Aug. 13, 10 AM
  Topographic Contour Dynamics for a Continuously Stratified Ocean
  Kirill Pankratov

Mon. Aug. 17, 10 AM
  Vortex Dynamics in Zonal Flows
  Phil Marcus

Mon. Aug. 17, 1 PM
  Pizza Lunch with a discussion of chaos and transistors
  Lou Howard

Tues. Aug. 18, 10 AM
  Rotating Fluids: Theory vs. Experiments
  Lou Howard

Tues. Aug. 18, 1:30 PM
  Jovian Vortices: Calculations, Conclusions, and Controversies
  Phil Marcus

Thurs. Aug. 20, 10 AM
  Elliptical [Tidal] Instabilities and Planetary Dynamos
  Willem Malkus

Fri. Aug. 21, 10 AM
  Dynamic Signatures of Ocean Climate Transients
  Claes Rooth

Mon. Aug. 24, 1:30 PM
  Discussion session: Convection with Differential Horizontal Heating
  George Veronis

Tues. Aug. 25, 10 AM
  Discussion session: Deep Jets and Shallow Spots?
  Glenn Flierl

Fellows talks: Wed. Aug. 26, 10 AM
  Quasigeostrophy in a Baroclinic Planetary Interior
  Richard Holme

viii

Front row: P. Yecko, E. Bolton, G. Flierl, J. Yano, T. Dowling, R. Ford, T. Shepard.
Middle row: B. Ewing-DeRemer, D. Parker, A. Stamp, A. Ingersoll, Q. Zou, L. Tao, G. Veronis, R. Holme, J. Keller, M. Stern, G. Sutyrin, E. Chassignet, L. Polvani.

Top row: E. Spiegel, P. Iannou, R. Salmon, J. Hart, R. LeBeau, G. Vallis, G. Ierly, N. Balmforth.
Missing: J. Anderson, T. Asada, W. Dewar, B. Farrell, J. Harrington, L. Howard, H. Huppert, R. Jarvis, K. Julien, W. Malkus, P. Marcus, S. Meacham. P. Morrison, M. Proctor, C. Rooth, R. Rosner, T. Soloman, C. Tresser, J. Whitehead, A. Woods, E. Young

Table of Contents

2

Lecture 1 – An Overview of the Outer Planets

Andrew Ingersoll

Introduction

The data obtained from the Voyager spacecraft exploration program has revolutionized the study of the atmospheres of the giant planets. The two probes were launched in 1977, and remain operational to this day. Voyager I successfully completed encounters with Jupiter and Saturn, including a close flypast of Saturn's largest moon, Triton (Stone and Miner, 1981). Voyager II also collected information from Jupiter and Saturn, and, with careful reprogramming to account for slower data retrieval rates and lower light levels, continued on to successful encounters with Uranus and Neptune (Stone and Miner, 1991).

Voyager data has allowed detailed study of atmospheric features over a wide range of time scales. Rapid changes in features may be observed in real time. In addition, "movies" of each planet have been constructed by connecting frames from different times during each encounter with the same view of the surface. These allow the study of the variation of long lived features, such as Jupiter's famous Great Red Spot, over time scales of a rotation period or greater.

The Voyager spacecraft also obtained data on other aspects of the nature of the outer planets of importance in the study of the atmospheres. We shall consider this first, so as to provide a suitable framework for our inquiries.

The Physics and Chemistry of the Outer Planets

Density and composition

Table 1 lists some bulk properties of the outer planets which are relevant to consideration of their atmospheric dynamics.

Parameter	Jupiter	Saturn	Uranus	Neptune
Mass (Earth masses)	318	95	14.5	17
Radius (10^3 km)	71.5	60.3	25.6	24.8
Density (Mg m^{-3})	1.33	0.69	1.29	1.64
Emitted/absorbed power (f_e)	1.7	1.8	1.0	2.7

Table 1: Physical properties of the outer planets

The mass (and also higher gravitational moments) can be determined from careful study of the motions of natural satellites and spacecraft close to the planets. This enables calculation of the mean density, which provides a significant constraint on internal composition. In particular, the low overall density of Jupiter and Saturn requires that they are made almost entirely of hydrogen and helium. While Uranus and Neptune are of similar density, they are much less massive, and so have a much lower central pressure. Thus their principal constituents by mass must be more dense, and, based on cosmic abundances, are thought to be methane (CH_4), ammonia (NH_3), and water vapor (H_2O). All four planets are truly fluid (with the exception of possible small rocky cores of order 10 earth masses,

4

0.1 planetary radii in diameter). Thus any surface "topography" must arise entirely from long lived stresses generated by the internal fluid flow.

At the high pressures characteristic of the interiors of Jupiter and Saturn, hydrogen will exist in other phases than the simple molecular form H_2, with significant changes in physical properties. It is thought that there is no gas-liquid phase change, as the transition occurs at temperatures and pressures much greater than those of the critical point. However, theory predicts a phase change to a metallic structure at about 3 Mbar for the temperatures characteristic of the deep interiors of Jupiter and Saturn. This occurs at a depth of greater than $0.7R_J$ in Jupiter, and $0.5R_S$ in Saturn. The interiors of Uranus and Neptune do not reach sufficiently high pressures for this to occur.

Magnetic fields

Each of the outer planets has an intrinsic magnetic field of some strength. Jupiter has a dipole tilt very similar to that of the Earth (around 10 degrees), but the field of Saturn is entirely axisymmetric to within the precision of the measurements. Uranus and Neptune have highly inclined dipole fields, with evidence of considerable complexity at higher harmonics. The interaction of charged particles with these magnetic fields produces periodic radio emissions from the planets, which are used to determine the rotation period of the magnetic field. This is inferred to be the period of bulk internal rotation, with which atmospheric motions may be compared. Surprisingly, this procedure is possible to high precision even in the case of Saturn, demonstrating that its magnetic field cannot be entirely axisymmetric.

Energy balance

There are gross similarities in bulk thermal structure of the giant planets. Total heat budget can be defined in terms of the ratio of emitted to absorbed power,

$$f_e = \frac{\text{emitted power}}{\text{absorbed power}} \geq 1. \tag{1.1}$$

Values for each of the planets are given in Table 1. The excess of emitted to absorbed power is provided by internal heat sources, a combination of the remanent primordial heat of formation, and energy of gravitational unmixing, in particular the fallout of helium "raindrops" from a predominantly hydrogen atmosphere. With the exception of Uranus, the outer planets have significant internal heat sources.

Energy balance as a function of latitude is given in Figure 1. Jupiter and Saturn have a measured temperature difference between equator and pole of less than 4%, despite an absorbed spectrum characteristic of variation with latitude. Two possible explanations for this are either that the atmospheric circulation is so efficient as to redistribute all the energy in the weather layer, or that the deep circulation is such as to preferentially drive heat towards the poles.

The rotation axis of Uranus is highly inclined to the ecliptic, at 98 degrees. Currently the planet has one pole directed towards the sun, and in fact when averaged over a full orbital period, more energy is incident at the poles than at the equator, exactly opposite to all the other planets.

Atmospheric Chemistry

Bulk planetary chemistry can only be determined by inference from mass and observed cosmic abundances. However, the atmospheric composition has been determined more accurately by spectroscopy. This is given in Table 2, with values for the sun also included for comparison.

	Sun	Jupiter	Saturn	Uranus/Neptune
H_2	85	90	97	83
He	15	10	3	15
H_2O	0.11	0.0001	-	-
CH_4	0.06	0.2	0.2	2
NH_3	0.016	0.03	0.03	-
H_2S	0.003	-	-	-

Table 2: Planetary composition (component % by number)

To summarize, hydrogen and helium are dominant, with the rest of the components making up of order 1 part in 1000 by number (1% by mass). Less volatile substances such as H_2S and H_2O are frozen out at cloud level, forming (in general) white crystals. These cannot be accurately detected using spectroscopy as they are no longer gases. Bright colors such as the reddish color of Jupiter are due to disequilibrium species such as phosphorus and sulfur compounds and hydrocarbons such as C_2H_6 and C_2H_2. Jupiter has a highly reducing atmosphere, with plenty of energy available to drive reactions from uv light and observed lightning, forming additional, more exotic, compounds.

Atmospheric Dynamics

Thermal structure

The thermal structure of the planets has been measured down to the 1 bar level for Jupiter and Saturn, and the 2 bar level for Uranus and Neptune. Below this level it is assumed that the structure is of a moist adiabat to the base of water vapor clouds and a dry adiabat below that. The inferred structure is shown in Figure 2.

The observable atmospheric dynamics can be considered as confined to a weather layer. This is defined in terms of the Brunt-Vaisala frequency, which may be written

$$N^2 = \frac{g}{T}\left(\frac{dT}{dz} + \frac{g}{C_p}\right). \qquad (1.2)$$

Here g is accelation due to gravity and C_p is the specific heat at constant pressure. Of the two terms in brackets, the first is due to the moist adiabat and the second due to the dry adiabat. The weather layer is defined to end at a depth where $N^2 = 0$, at which the fluid is neutrally stratified (the temperature profile is adiabatic) and bulk convection can occur. This is estimated to be the depth of the deepest cloud, about 100 km below the surface for Jupiter. This should be compared with the equatorial radius of the planet, which is

71400 km. Thus the weather layer makes up a very small fraction of the total planetary volume. The Brunt-Vaisala frequency also defines the Rossby radius of deformation

$$L_D = \frac{NH}{f},$$

(1.3)

where f is the coriolis parameter, and H is a scale height.

As noted earlier, and shown in Figure 3, variations in the surface temperature of the planets with latitude are small. This suggests that, to first order,

$$\left(\frac{\partial T}{\partial \phi}\right)_p \approx 0,$$

(1.4)

where ϕ is latitude, at depth within the planet. This would imply that the structure of adiabat is the same at all latitudes.

Zonal winds

The dominant atmospheric structure on all four planets is a pattern of strong zonal winds, concentric on the rotation axis. The detailed velocity structures of the planets show significantly varying rich structure, which for Jupiter and Saturn at least is constant over decades. These patterns are shown in Figure 4. The equatorial jet is prograde on Jupiter and Saturn, and retrograde on Uranus and Neptune. There is clearly no straightforward connection between the radiated energy $F = \sigma T^4$ and the wind speed, as Saturn (500 ms^{-1}) and Neptune (400 ms^{-1}) have the highest observed wind speeds, despite the fact that $F_N \sim \frac{1}{20} F_J \sim \frac{1}{400} F_E$. (Speeds are zonally averaged, and measured at cloud top level (1 bar).) It should be remembered, however, that in the case of Saturn, there may be some uncertainty in the bulk rotation period inferred, due to the axisymmetric magnetic field. All four planets have measured zonal winds considerably stronger than those observed on Earth, which are no faster than 50 ms^{-1}. A possible explanation for this is that as the energy sources (both external and internal) are reduced, so also is the dissipation in the flow, leading more and more to inviscid behavior, of which steady zonal flow is an example. Thus the atmospheres of the outer planets could be said to be coasting, without significant dissipation. This is also suggested by the behavior of Neptune's vortices, and the fact that Uranus shows the same zonal wind structure, despite the north pole being pointed directly towards the sun at the time of the Voyager 2 encounter.

Particular features

Jupiter

Jupiter displays surface features varying in scale from the Great Red Spot, which has a radius of 25,000 km and, being first observed by Robert Hooke in the 17th century, a lifespan of at least 300 years, through 3 white ovals. with scale 5,000km which were formed in 1938, down to small scale features with lifespan less than one Jovian day (10 hours) and of the scale of the radius of deformation. 90% of the long-lived features observed are anticyclonic. There are approximately 10 major longitudinal jets over the body of the planet.

Saturn

In comparison with Jupiter, Saturn is rather bland looking, but it does show some small scale features. One unique such is a hexagonal vortex centered over the North Pole. Also every 30 years, Saturn "burps": a large disturbance of white clouds is observed centered between latitude 10° and 15° north. This was first seen in 1870 and most recently by the Hubble Space telescope in 1990. The feature lasts for about 4 months.

Saturn's satellite, Titan, also has a significant atmosphere, measured by Voyager 1 using a radio occultation technique. It is inferred to have a surface pressure of about 1.1 Earth atmospheres.

Uranus

Uranus is colder on the end facing towards the sun than in regions shielded from solar radiation. This could be due to seasonal heat storage or preferential convectional overturning. It is even more featureless than Saturn.

Neptune

Neptune has a number of significant features. The largest is the Great Dark Spot (GDS), located between 18° and 26° south latitude. This periodically changes size, first by expunging a streamer, and then expanding back to its original dimensions. Despite this streamer, it is remarkably well modeled by the the equations for an elliptical vortex in shear, first given by Kida (1981). The vortex is barotropic, with an infinite deformation radius. Depending on the vorticities of the ellipse and the background shear, and the initial orientation and aspect ratio of the ellipse, it can be steady, rotating, oscillating, or it can be sheared out. The equations governing its motion are

$$\frac{d\lambda}{dt} = -s\lambda \sin 2\varphi; \quad \frac{d\varphi}{dt} = \Omega_k + \frac{s}{2}(-1 + \Lambda \cos 2\varphi), \tag{1.5}$$

where $1/\lambda$ is the aspect ratio of the ellipse, φ is its orientation, s is the background shear vorticity, $\Omega_k = q_v\lambda/(1 + \lambda^2)$ is the angular velocity of the vortex in the absence of shear, q_v is the vorticity of the vortex, and $\Lambda = (1 + \lambda^2)/(1 - \lambda^2)$.

One should note that simply choosing the ratio s/q_v to make the evolution of the vortex match the maximum and minimum aspect ratio of the GDS gives the amplitude of the oscillation in orientation, and the complete evolution for λ and φ once an initial orientation is set. Polvani *et al.* (1990) have shown that the predictions from even this simple model are in very good agreement with observation of the GDS obtained from Voyager, and one may infer from this that the deformation radius on Neptune is large, consistent with it having a moist atmosphere.

There is a second large vortex in Neptune's atmosphere, a white oval located at 50° south, and another two spots traceable over a period of months. There are also some latitudes in which features are observed to move at different speeds, which is interpreted to be different layers of motion.

Conclusion

In this introduction, we have described the principal source of our information on the atmospheres of the outer planets, outlined in very general terms their overall physical and chemical properties, and provided a rapid overview of some of the features observed. We are now in a position to begin properly our investigation of the atmospheric dynamics of the outer planets.

References

Ingersoll, A. P., 1990a: Atmospheric dynamics of the outer planets. *Science*, **248**. 308-315.

Ingersoll, A. P., 1990b: Atmospheres of the Giant Planets, in "The New Solar System", 3rd ed., Ed. J. Kelly Beatty and A. Chaikin, Sky Publishing Corporation.

Kida, S. 1981: Motion of an elliptic vortex in a uniform shear flow. *J. Phys. Soc. Japan*, **50** 3517

Polvani, L. M., J. Wisdom, E. DeJong, and A. P. Ingersoll, 1990: Simple dynamical models of Neptune's Great Dark Spot. *Science*, **249** 1393-1398.

Stone, E. C. and E. D. Miner, 1981: Voyager 1 encounter with the Saturnian system. *Science*, **212** 159-162.

Stone, E. C. and E. D. Miner, 1991: The Voyager encounter with Neptune. *J. Geophys. Res.*, **96** 18903-18906

Figure Captions

Fig. 1: A comparison of absorbed solar energy and emitted infrared radiation for Jupiter, Saturn and Uranus, averaged with respect to longitude, season and time of day. (From Ingersoll, 1990b).

Fig. 2: Pressure-temperature profiles for the upper atmospheres of Jupiter, Saturn and Uranus. (From Ingersoll, 1990b).

Fig. 3: Emitted infrared flux and equivalent brightness temperatures verses latitude for the four outer planets. (From Ingersoll, 1990a).

Fig. 4: Zonal wind velocity verses latitude for the four outer planets. (From Ingersoll, 1990a).

Notes compiled by Rupert Ford and Richard Holme
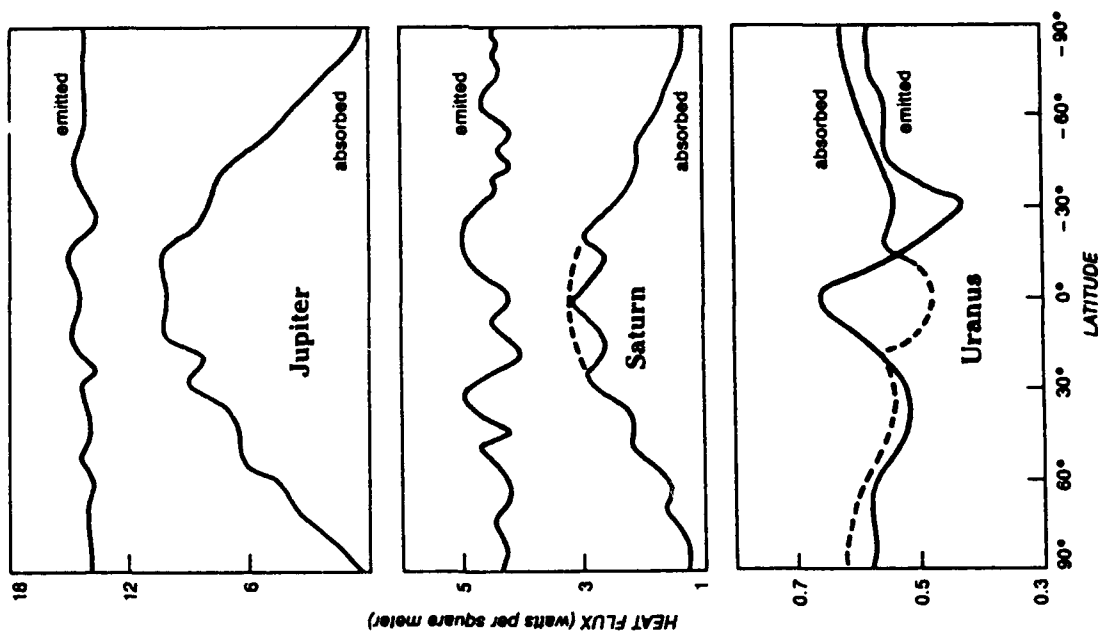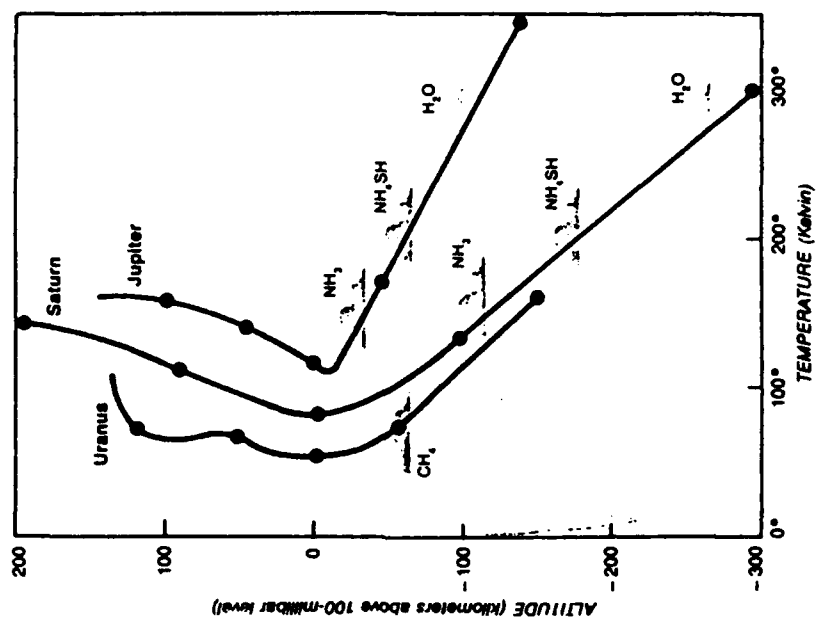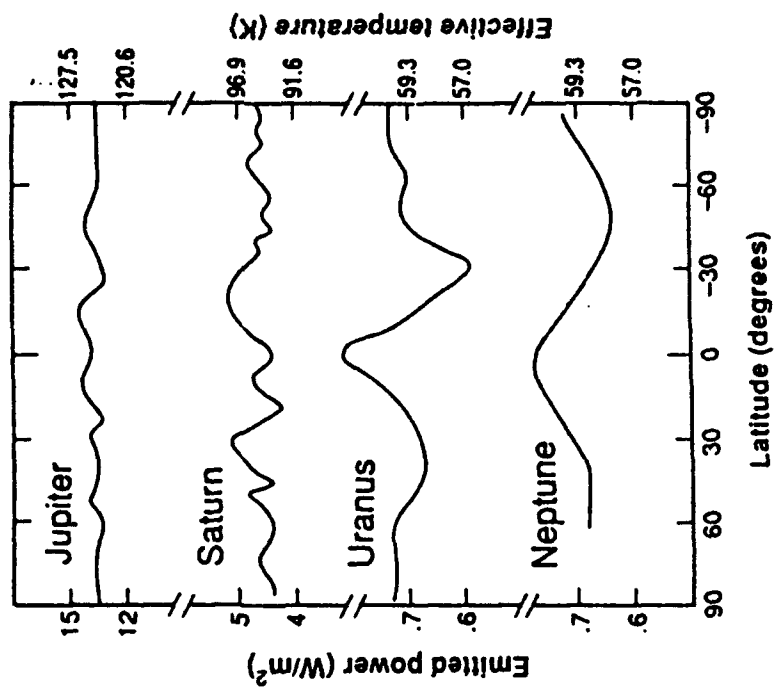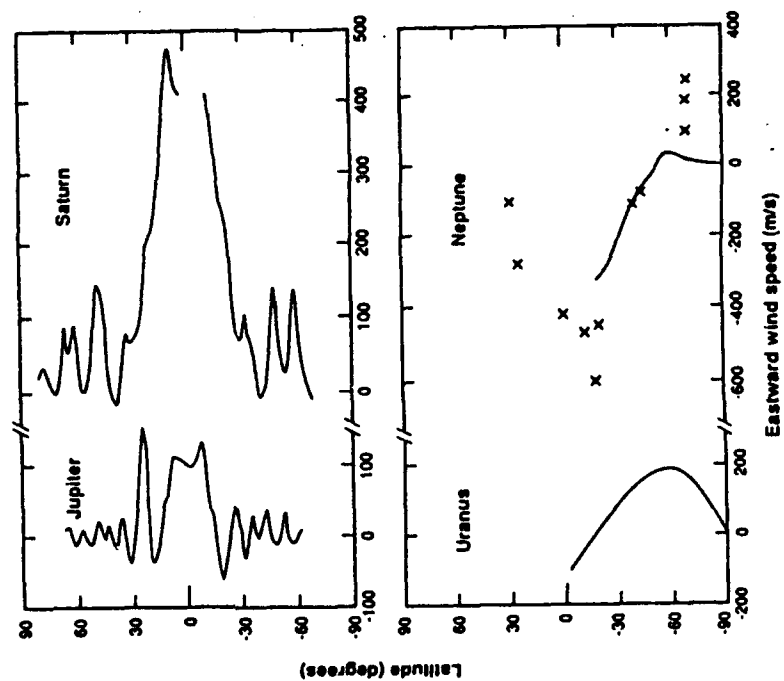
Lecture 2 – The Depth and Decay of Zonal Jets on Jovian Planets

Observations of the cloud layers on the Jovian planets have revealed persistent zonal wind profiles in the upper atmosphere. However, the depths to which these winds persist cannot be determined by direct observation. An estimate of the thickness of the zonal wind layer may be made using the thermal wind equation. The derivation of this equation begins with the assumption of geostrophic flow:

$$fu = -(\frac{\partial \Phi}{\partial y})_p \tag{2.1.1}$$

where

$$\frac{1}{\rho} = -(\frac{\partial \Phi}{\partial p})_y \tag{2.1.2}$$

A derivative with respect to pressure and the assumption of hydrostatic equilibrium to convert pressure to depth (z) yields the thermal wind equation:

$$f(\frac{\partial u}{\partial z})_y = -\alpha g(\frac{\partial T}{\partial y})_p \tag{2.1.3}$$

where α, the thermal coefficient of expansion, is:

$$\alpha = -\frac{1}{\rho}(\frac{\partial \rho}{\partial T})_p \tag{2.1.4}$$

Since the variation of temperature with respect to latitude above the cloud tops is known (figure 1), this equation can be used to calculate the approximate depth of the zero wind velocity layer (where $u = 0$) with a reasonable assumption of the variation of temperature with depth.

Global Estimates

On all four of the giant planets, the relative variation of temperature ($\Delta T/T = \epsilon$) between the equator and the poles is small (less than 10%). In conjuction with the thermal wind equation, this implies that the depth of the zonal wind layer must be large in order to reduce cloud top velocities of a few 100 m/s (up to 500 m/s on Saturn) to no motion. In order to get a quantitative estimate, treat the atmosphere as an ideal gas ($\alpha = 1/T$) and assume that the relative variation in temperature is constant with respect to depth. (This second assumption should yield results on the low end of the potential depth scale, because the temperature would be expected to become more homogeneous with increasing depth.) Further, assume a polytropic relationship between temperature (T) and pressure (p), where:

$$T \propto p^\kappa \tag{2.1.5}$$

By intergrating the thermal wind equation both in z and "y" (or $rd\phi$ for a sphere), an equation for the pressure of the zero motion level can be determined:

$$\frac{p_{u=0}}{p_{cloud}} = \left(\frac{\kappa \int_0^{\pi/2} furd\phi}{\epsilon RT_{cloud}} \right)^{\frac{1}{\kappa}} \tag{2.1.6}$$

where $p_{u=0}$ and p_{cloud} are the pressures at the zero motion level and the cloud tops respectively, T_{cloud} is similarly the temperature at the cloud tops, and ϵ is the relative variation of temperature with respect to latitude.

Using data for Saturn (figure 1,2), with $\epsilon = 0.04$ and $\kappa = 1/3.5$, yields a $p_{u=0}$ of about 10,000 bars. This result is sensitive to the least certain quantity, ϵ, so $p_{u=0}$ could reasonably be on the order of 1,000 bars, but in either case the zonal wind layer consists of a large amount of mass that is unaffected by sunlight (which only penetrates down to pressures of a few bars). However, while this is a sizeable layer, it is still a small fraction of the overall mass of Saturn.

In this calculation u decreases with increasing depth because the equator is warmer than the poles; if this were inverted, then the velocity would increase with depth. The Rossby number for these flows, using the length scale of a jet "wavelength" or width, are 0.1 to 0.5, so the geostrophic approximation is reasonable. It is also reasonable for the cyclostrophic effects to be ignored in this calculation, since that term is dependent on the planetary radius and $fR_{planet}/u >> 1$ for the gas giants.

The Decay of Jets with Height (in the Upper Troposphere)

While the global scale calculation indicates that the variation of zonal wind velocity (u) with increasing depth is slow (since the variation of temperature with latitude is small), there are also local variations in temperature, leading to variations in the gradient of u with respect to altitude (figure 3,4). These variations are correlated with changes in the mean flow at the cloud tops (beneath where the atmospheric temperatures are measured) such that $\partial u/\partial z \propto -u$ above the cloud layer. Applying the thermal wind equation to these local variations yields:

$$|\frac{1}{u}\frac{\partial u}{\partial z}| \approx 3H \tag{2.1.7}$$

where the scale height H is defined by RT/mg, which is approximately 20 km for Jupiter. Therefore, the zonal velocities decay far more rapidly upward than downward, as the local temperature variations are expected to become more uniform with increasing depth.

Interaction of the eddies with the mean zonal flow on Jupiter

Consider the zonal momentum equation in a rotating Boussinesq fluid:

$$\frac{\partial}{\partial t}u + \vec{\nabla} \cdot (\vec{u}u) - fv = \frac{1}{\rho_o}\frac{\partial}{\partial x}p, \tag{2.2.1}$$

Taking the zonal average of the zonal momentum equation we obtain:

$$\frac{\partial}{\partial t}\bar{u} + \bar{v}\frac{\partial}{\partial y}\bar{u} + \bar{w}\frac{\partial}{\partial z}\bar{u} - f\bar{v} = -\frac{\partial}{\partial y}\overline{u'v'} - \frac{\partial}{\partial z}\overline{u'w'}, \tag{2.2.2}$$

where the bar denotes a zonally averaged function and $u' = u - \bar{u}$, etc.. The terms on the r.h.s. of (2.2.2) are called Reynolds stresses and represent momentum exchange between the zonal mean flow and the eddies. For example, the Reynolds stress $\overline{\rho u'v'}$ is the eddy northward transport of eastward momentum. Let us first study the effect of the

Reynolds stress $\overline{u'v'}$ on the energetics of the zonal mean flow. Multiplying (2.2.2) by $\overline{u}$ and integrating over the fluid volume we obtain an equation for the total kinetic energy density of the mean flow. After an integration by parts we obtain:

$$\frac{d}{dt}\left\langle \frac{\overline{u}^2}{2} \right\rangle + \cdots = \left\langle \overline{u'v'}\frac{d}{dy}\overline{u} \right\rangle + \cdots , \qquad (2.2.3)$$

where $\langle \rangle$ denotes integration over the fluid volume. When $\overline{u'v'}\frac{d}{dy}\overline{u} > 0$ the eddies tend to reinforce the mean flow.

Analysis of the Voyager I and II data for Jupiter provide information on the eddy-mean flow exchange of (2.2.3). Observations of the zonal wind on Jupiter at cloud level ($\sim 0.5bar$) have been already discussed. It was possible from the same data-set to infer the tendency of the Reynolds stress forcing in (2.2.3). Towards this purpose the wind observations were separated in latitudinal bins $1°$ wide. There were about 100 observations available per latitudinal bin. For each latitude the mean zonal velocity, $\overline{u}$, and meridional velocity, $\overline{v}$ was calculated. From the mean zonal velocity the latitudinal shear, $\frac{d}{dy}\overline{u}$, was also calculated. Departures from the zonal mean gave, at each latitudinal bin, the eddy zonal velocity u' and eddy meridional velocity v'. The estimated Reynolds stress $\overline{u'v'}$ was subsequently normalized by the variance of the eddy field:

$$r(u,v) = \frac{\overline{u'v'}}{(\overline{u'^2})^{1/2}(\overline{v'^2})^{1/2}} . \qquad (2.2.4)$$

The results of such analysis of the Voyager I and Voyager II data are presented in Fig. 2.2.1. Note that at most latitudes the Reynolds stress is of the same sign as the meridional shear of the zonal wind, indicating forcing of the mean zonal flow by the eddies. Such an eddy transport although characteristic of many geophysical systems, i.e. the Earth's jet stream, runs against our intuition gained from the commonly observed transport processes. According to kinetic theory departures from the mean tend to be homogenized leading to fluxes that are down the mean gradient. For example in thermal convection, the heat flow $\overline{v'T'} = -k\frac{d}{dy}\overline{T}$, with $k > 0$. The Reynolds stress can be similarly related to $\frac{d}{dy}\overline{u}$ through an equivalent eddy viscosity coefficient of exchange ν_e:

$$\overline{u'v'} = -\nu_e\frac{d}{dy}\overline{u} . \qquad (2.2.5)$$

If the process of momentum exchange was diffusive it would associate an eddy viscosity $\nu_e > 0$. Analysis of the data presented in Fig. 2.2.1 shows that for Jupiter $\nu_e < 0$.

Although our knowledge of the energetics of the Jovian atmosphere are partial we will attempt to compare them to the energetics of the terrestrial atmosphere. The exchange between the eddies and the mean are profitably described in terms of the Lorenz energy cycle which is shown for the Earth in Fig. 2.2.2. The equation for the zonal mean kinetic energy and the eddy kinetic energy are concisely written as:

$$\frac{d}{dt}\overline{K} = \{\overline{PK}\} - \{\overline{K}K'\} - \overline{\epsilon},$$

$$\frac{d}{dt}K' = \{P'K'\} + \{\overline{K}K'\} - \epsilon' , \qquad (2.2.6)$$

where

$$\overline{K} = \left\langle \rho \frac{\overline{u}^2}{2} \right\rangle , \qquad (2.2.7a)$$

$$K' = \left\langle \rho \frac{(u'^2 + v'^2)}{2} \right\rangle , \qquad (2.2.7b)$$

$$\{\overline{K}K'\} = -\left\langle \rho \overline{u'v'} \frac{d}{dy}\overline{u} \right\rangle , \qquad (2.2.7c)$$

$$\{\overline{PK}\} \propto \overline{w}\overline{T} , \qquad (2.2.7d)$$

$$\{P'K'\} \propto \overline{w'T'} , \qquad (2.2.7e)$$

and ϵ is the kinetic energy dissipation.

For the Earth $\{\overline{K}K'\} = -0.3 Wm^{-2}$. The estimates of the Reynolds stress, $\overline{u'v'}$, from the Voyager data indicate an energy transfer from the eddies to zonal velocity field which, if left unimpeded, could double the zonal kinetic energy in 75 days. If such a transfer of energy were to take place in a layer of 2.5 bars the transfer rate would lead to $\{\overline{K}K'\} \approx -2 Wm^{-2}$. This estimate is, remarkably, 15% of the total thermal power emitted from the planet ($14 Wm^{-2}$), implying a very high efficiency (for the Earth the corresponding eddy transfer is just 0.1% of the $240 Wm^{-2}$ emitted by the planet). Such efficient eddy interactions suggest that the zonal jets are formed by the eddies which are in turn fuelled by the convective heat flux.

Theoretically our understanding of the processes responsible for the formation of the multiple jets of Jupiter is still at an early stage. However, it is worth noting an idealized model of the Jovian atmospheric circulation that produces jets maintained by upgradient Reynolds stress. Gareth Williams (1979) randomly forced a barotropic thin spherical shell, which upon becoming turbulent, produced a multiple jet structure. The situation is presented in Fig. 2.2.3.

Stability of the zonal winds of Jupiter

We assume that large scale motions on the atmospheric envelope of Jupiter are quasi-geostrophic. In log-pressure coordinates the conserved potential vorticity, q, takes the form:

$$q = \nabla^2 \psi + \frac{1}{\rho} \frac{\partial}{\partial z} \left(\rho \frac{f_o^2}{N^2} \frac{\partial}{\partial z} \psi \right) , \qquad (2.3.1)$$

where $z \equiv -H_s \ln\left(\frac{p}{p_s}\right)$, p_s is a standard reference pressure, $H \equiv \frac{RT_s}{g}$ is the standard scaleheight corresponding to a global average temperature T_s, and $N^2 = \frac{g}{T_s}\left(\frac{\partial}{\partial z}T + \frac{g}{c_p}\frac{T}{T_s}\right)$ is the Brunt-Väisälä frequency. The streamfunction ψ is related to the zonal and meridional velocity by: $u = -\psi_y$, $v = \psi_x$. The density is given by: $\rho = \rho_s \exp\left(-\frac{z}{H}\right)$ where ρ_s is the density at $z = 0$ (Holton, 1992, p.254). We can neglect the vertical contribution to the potential vorticity as long as the radius of deformation which is given by $L_D = \frac{NH_s}{f_o}$ is larger than the characteristic scale of variation in the meridional and zonal direction, L. For Jupiter taking the characteristic values $N \sim 10^{-2}s^{-1}$, $f_o \sim 22 \times 10^{-4}s^{-1}$, and

$H_s \sim 20km$ we obtain $L_D \approx 1000km$, the same value as the Earth. The conservation of potential vorticity reduces to the barotropic vorticity equation:

$$\frac{d}{dt}(\zeta + f) = 0 , \qquad (2.3.2)$$

where $\zeta = \nabla^2 \psi$, and $f = f_o + \beta y$.

To determine the stability of a mean zonal flow $\bar{u}$, it is customary to impose a wavelike disturbance $\psi' e^{ik(x-ct)}$ and determine the dispersion relation $c(k)$ from the linearized form of the field equations. If for certain zonal wavenumber, k, $Im(c) > 0$ then the flow is liable to be disrupted by exponential normal modes and is characterized as unstable. The linearized form of (2.3.2), after substituting a wavelike perturbation, is:

$$(\bar{u} - c)\left[\frac{d^2}{dy^2}\psi' - k^2\psi'\right] + \left(\beta - \frac{d^2}{dy^2}\bar{u}\right)\psi' = 0 , \qquad (2.3.3a)$$

with the boundary conditions

$$\psi' = 0 \qquad y = \pm y_o . \qquad (2.3.3b)$$

Note that $\beta - \frac{d^2}{dy^2}\bar{u} \equiv \frac{d}{dy}\bar{q}$. Suppose that the mean flow $\bar{u}$ is unstable, so that $c_i = Im(c)$ is nonzero (it is not necessary to require $c_i > 0$ because if c is an eigenvalue of (2.3.3a) so is its conjugate c^*).

A necessary condition for instability can be derived by multiplying (2.3.3a) by the complex conjugate of ψ', integrating by parts, using the boundary condition (2.3.3b). The imaginary part of the equation that results is:

$$kc_i \int_{-y_o}^{y_o} \frac{d}{dy}\bar{q} \, \frac{|\psi'|^2}{|\bar{u} - c|^2} = 0 , \qquad (2.3.4)$$

which consequently requires that if there exists an unstable mode with $c_i > 0$ then by necessity $\frac{d}{dy}\bar{q}$ must change sign to satisfy integral constraint (2.3.4). For jets of the form: $\bar{u} \propto \cos\frac{y}{L}$ with $L << y_o$, it has been shown that change of sign of $\frac{d}{dy}\bar{q}$ does indeed imply instability.

The variation of $\frac{d^2}{dy^2}\bar{u}$ for Jupiter's mean winds is shown in Fig. 2.3.1 (Ingersoll et al., 1981; Limaye, 1986). The variation of $\frac{d^2}{dy^2}\bar{u}$ is bounded by $\pm 2\beta$. The necessary condition for instability is satisfied. The mean observed zonal wind are to a fair degree sinusoidal and consequently the flow must be unstable. Note that inclusion of the baroclinic term can not stabilize the flow. The gradient of the mean potential vorticity

$$\frac{d}{dy}\bar{q} \equiv \beta - \frac{\partial^2\bar{u}}{\partial y^2} - \frac{1}{\rho}\frac{\partial}{\partial z}\left(\rho\frac{f_o^2}{N^2}\frac{\partial}{\partial z}\bar{u}\right) \approx \beta - \frac{\partial^2\bar{u}}{\partial y^2} + \frac{\bar{u}}{L_D^2} . \qquad (2.3.5)$$

For a sinusoidal mean wind field $\frac{d^2}{dy^2}\bar{u} \propto -\bar{u}$ and consequently (2.3.5) implies that inclusion of the baroclinic terms reinforce the violation of the necessary condition for instability. Note the $\frac{d}{dy}\bar{q}$ changes sign in regions with westward zonal flow.

16

References

Gierasch, P. J., B. J. Conrath, and J. A. Magalhaes (1986). Zonal Mean Properties of Jupiter's Upper Troposphere from Voyager Infrared Observations. *Icarus* **67**, 456-483.

Ingersoll, A. P. and D. Pollard (1982). Motions in the Interiors and Atmospheres of Jupiter and Saturn: Scale Analysis, Anelastic Equations, Barotropic Stability Criterion. *Icarus* **52**, 62-80.

Notes compiled by Petros Ioannou and Ray LeBeau
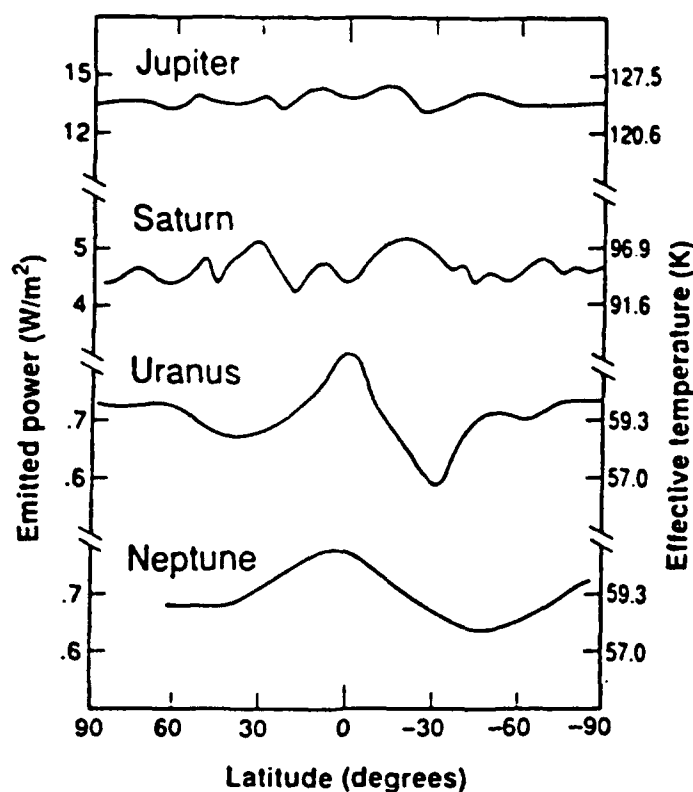
Figure 1. Effective Temperature Profiles of the Giant Planets

Emitted infrared flux and equivalent temperature versus latitude for the giant planets.
The radiation is on average emitted from the 0.3 to 0.5 bar pressure levels.

$$-\int_0^\phi furd\phi = gz$$

NORMALIZED HEIGHT: gz/RT_0, $T_0 = 140K$
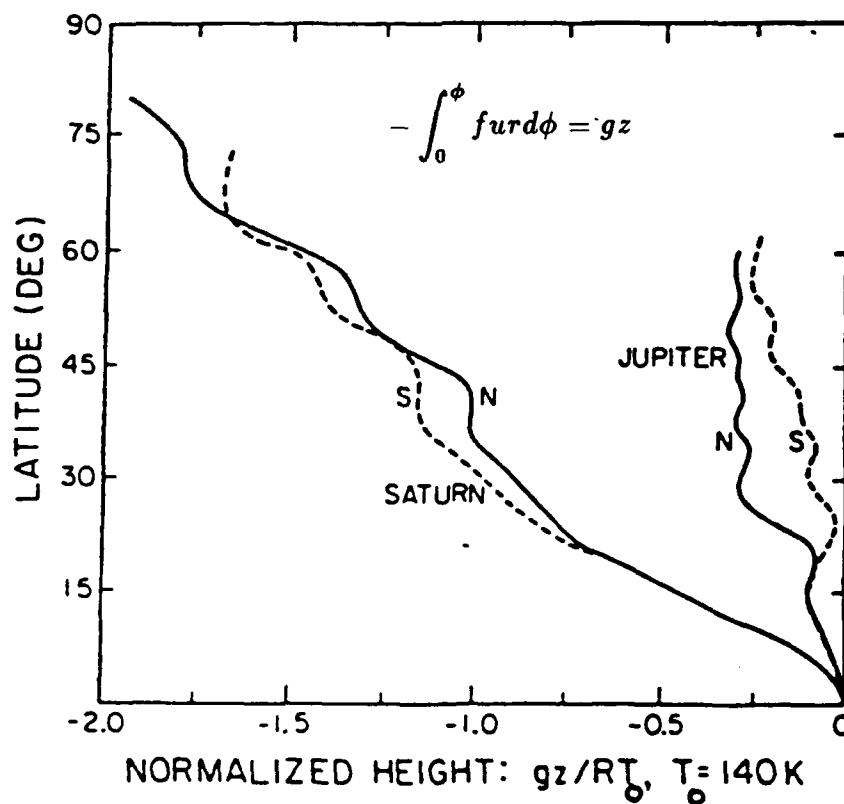
Figure 2 Integrated Zonal Wind Profiles of Jupiter, Saturn

Height of constant pressure surfaces calculated from observed zonal wind profiles and
the geostrophic relation. The units are the pressure scale height RT/g at cloud top level
($T_o = 140$ K). *from Ingersoll and Pollard (1982)*
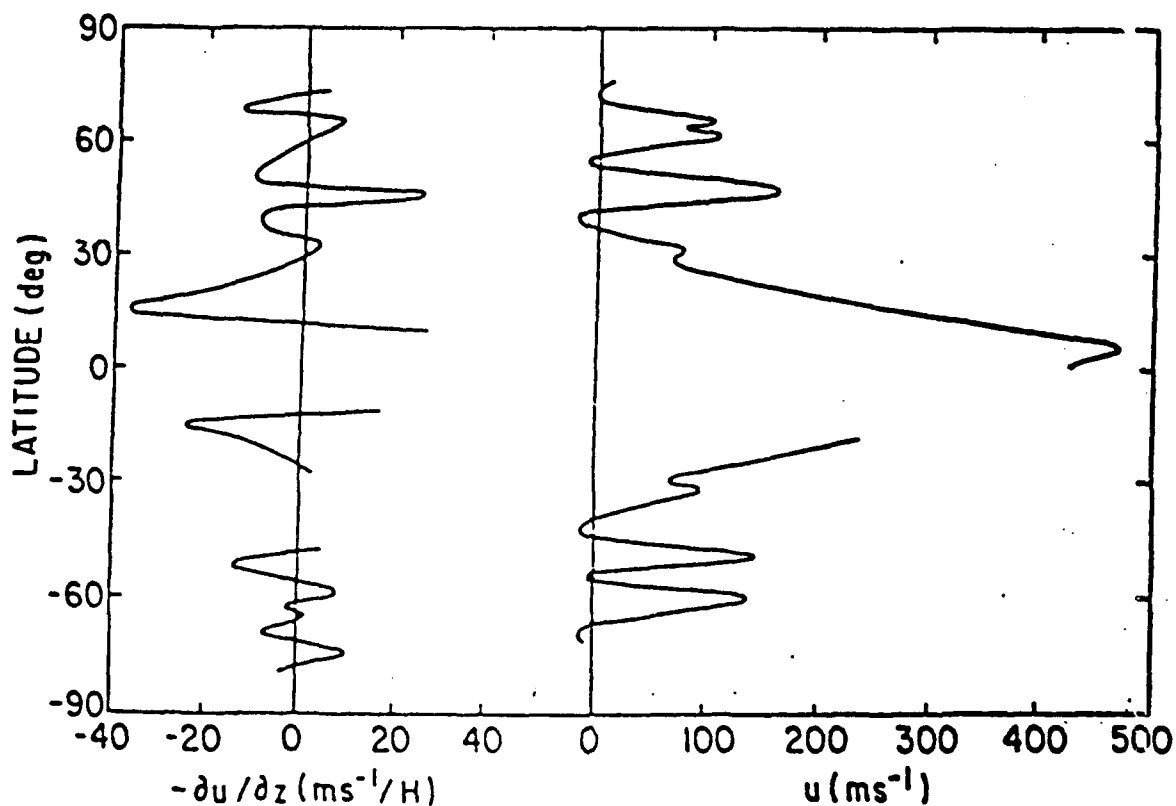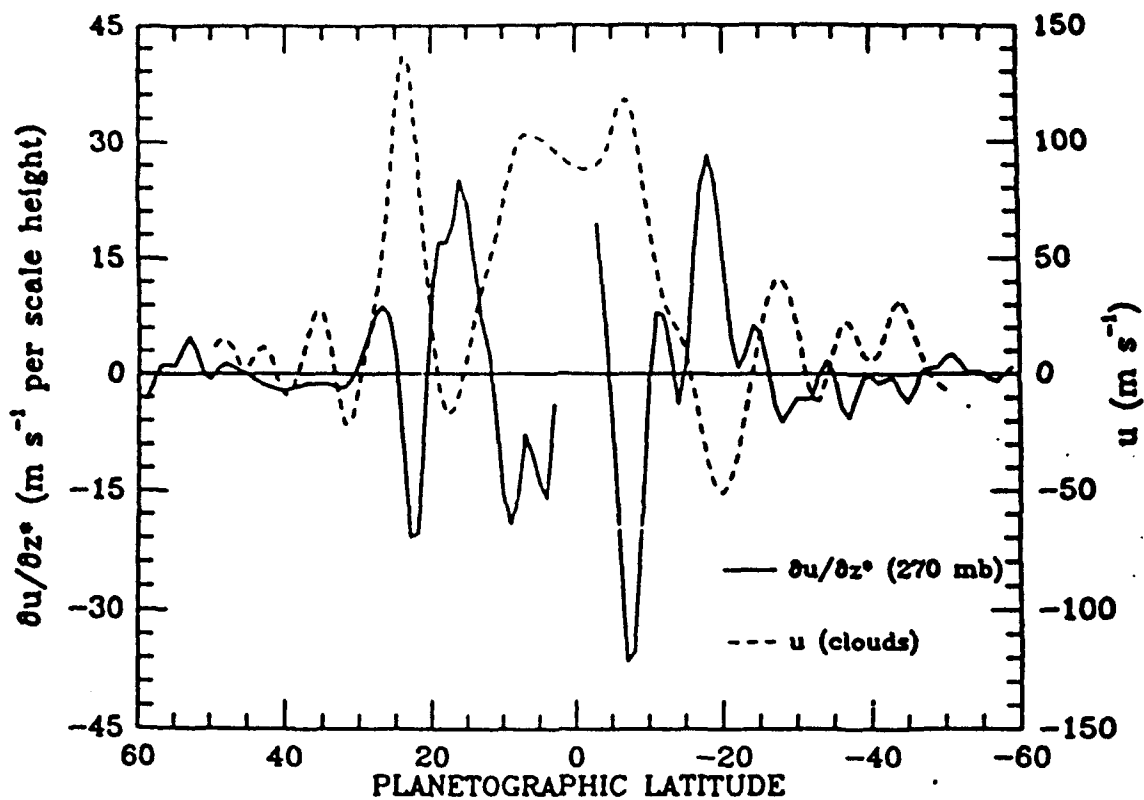
Figures 3, 4 Zonal Wind Shear and Velocity Profiles, Jupiter

The vertical shears are determined from the local temperature profiles, while the velocity profiles are generally from cloud tracers. Upper figure shows Jupiter, lower one Saturn. *Fig ? from Gierasch, et al. (1986)*

Ingersoll JGR 86, 8733 (1981).
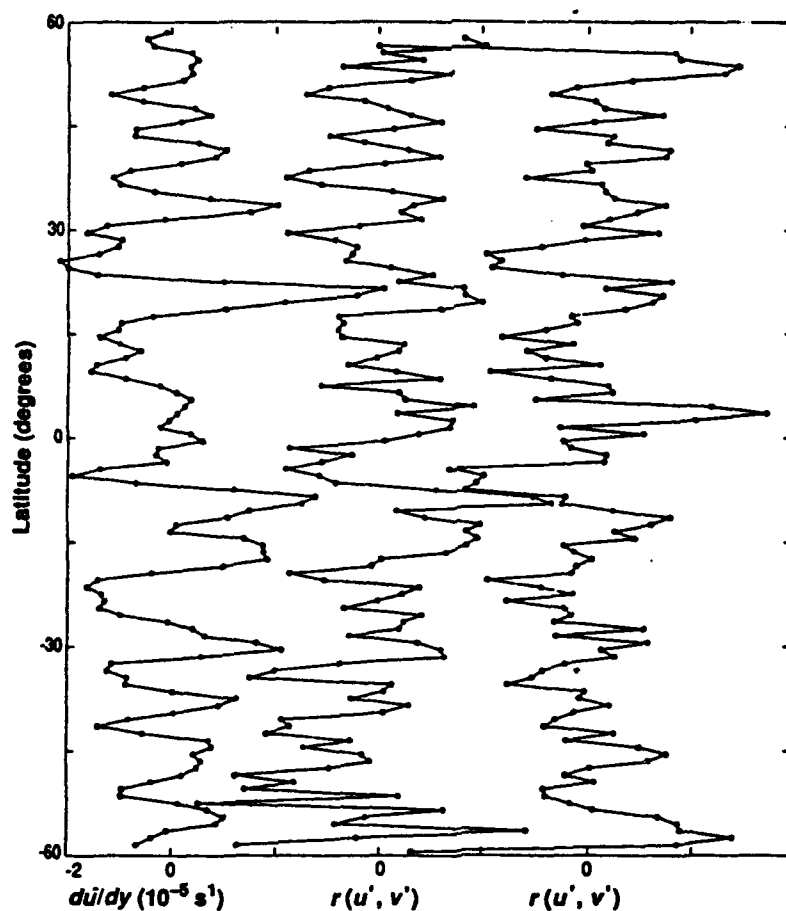
Fig 2.2.1

Fig 2.2 Comparison of the zonal velocity gradient $d\bar{u}/dy$ (left) with the eddy correlation coefficient $r(u',v')$. The center and right curves are from Voyager 1 and Voyager 2, respectively (7). At most latitudes $r(u',v')$ and $d\bar{u}/dy$ have the same sign, indicating that kinetic energy is being transferred from the eddies to the zonal flow through the Reynolds stress term. [Reprinted from (7) with permission from the American Geophysical Union].
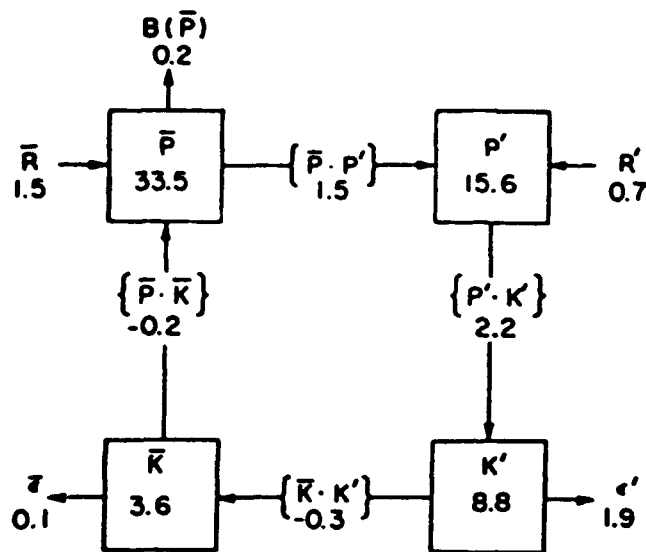
Fig. 2.2.2

Arrows show actual flow, i.e., $\{\bar{K} \cdot K'\} < 0$ means transfer from K' to $\bar{K}$.

The observed mean energy cycle for the Northern Hemisphere. Numbers in the squares are energy amounts in units of 10^5 J m^{-2}. Numbers next to the arrows are energy transformation rates in units of W m^{-2}. $B(\bar{P})$ represents a net energy flux into the Southern Hemisphere. Other symbols are defined in the text. (Adapted from Oort and Peixoto, 1974.)

Fis
2.2.3
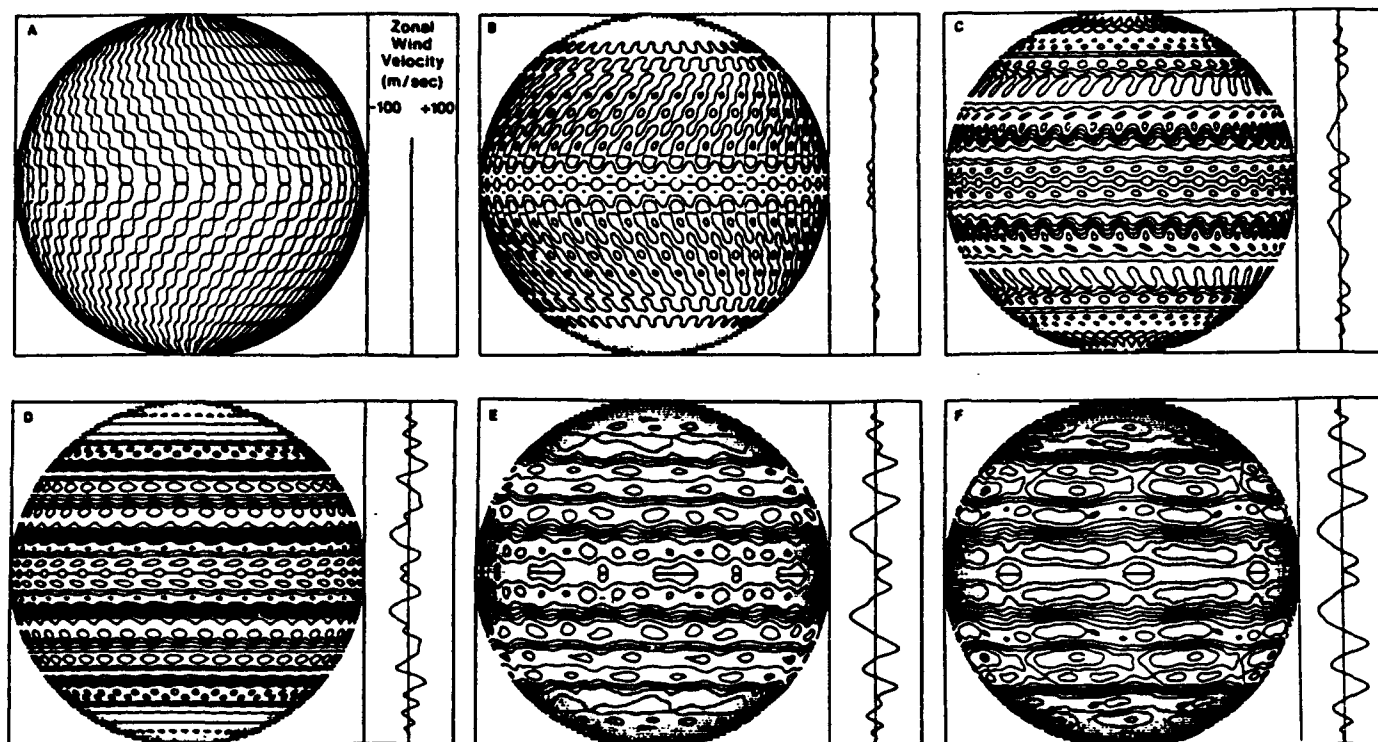
Figure 13. A computer model of Jovian atmospheric circulation made in 1978 by Gareth Williams. He assumes that all of the clouds' energy exchanges occur within a narrow layer of the atmosphere (as is the case on Earth); the eddies get their energy from sunlight, not from the interior. Williams' model first produces small-scale eddies *(a)*, which become unstable *(b)* and give up their energy to zonal jets *(c,d)* that eventually dominate the flow *(e,f)*. Eddies driven by internal heat demonstrate the same behavior, so remaining questions center on the depths of both the eddies and the zonal flow.

Fig. 2.3.1
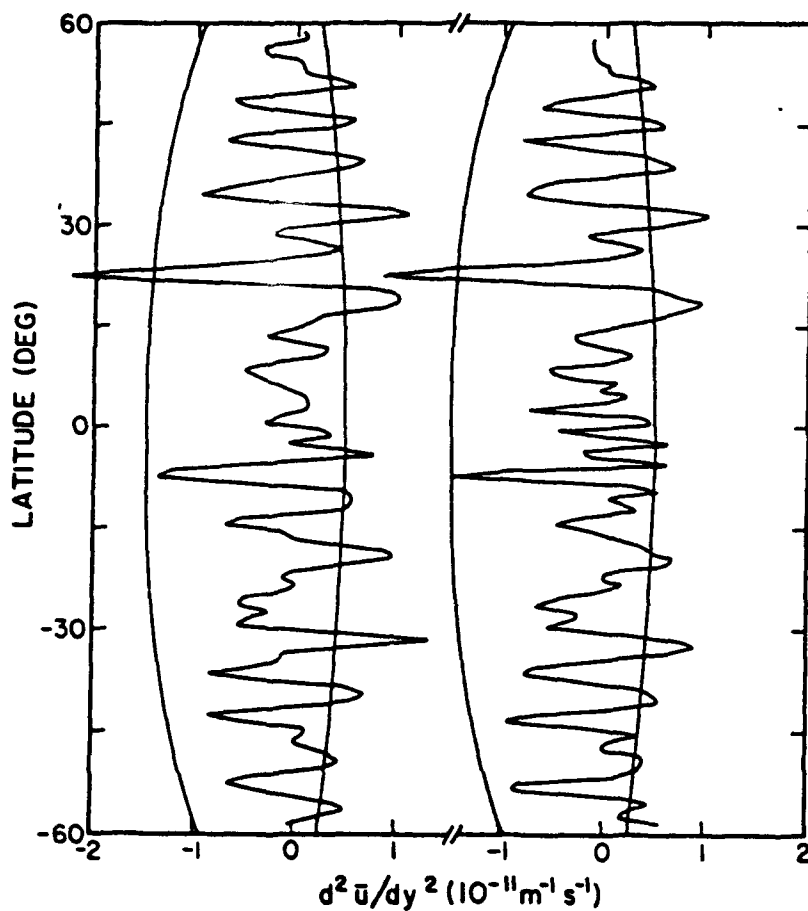
FIG. 4. Curvature or second derivative of Jupiter's zonal velocity profile for the solid curves of Fig. 3. Voyager 1 is on the left and Voyager 2 is on the right. The smooth curve on the right of each profile is β, the planetary vorticity gradient for thin spherical shells. The smooth curve to the left of each profile is $B \sin^2\lambda$, derived in the text for deep fluid spheres. The $B \sin^2\lambda$ curve is relevant up to a latitude of about 40 to 45°, where effects of the metallic core become important. The limiting curve (not shown) for deep flow at higher latitudes is infinite at the critical latitude and lies to the right of each profile. Notice that the observed profiles rarely cross the left curve, but often cross the right curve, suggesting that a deep interior flow with the observed curvature might be marginally stable.

Lecture 3 – Interior Circulations of the Giant Planets

The Voyager spacecraft missions have provided detailed observations and measurements of Jupiter, Saturn, Uranus and Neptune. Unfortunately, however, observations have been limited to the outer or weather layer and consequently relatively little is known about the interior of these planets. The planetary interiors are important because they determine such "bulk" properties as the magnetic field and may couple with the weather layer thus affecting the observed behaviour. In this lecture the interior dynamics of Jupiter are discussed, and it is shown that weather layer observations may be used to infer information about the interior.

Explaining Jupiter's heat flux measurements

In lecture 1 it was shown that despite strong latitudinal variation in solar radiation the surface temperature on Jupiter was essentially uniform. Two extreme views of the Jupiter circulation may be used to explain this result. The first states that interior dynamics profoundly effect the behaviour of the weather layer while the second assumes that the weather layer alone dominates the latitudinal transport of heat.

The assumption of strong interior circulation may be modelled by taking an adiabatic (barotropic), inviscid, steady interior for the planet so that

$$\frac{\partial u}{\partial z} = 0 \qquad (3.1)$$

where z is the axial coordinate and u a zonal velocity. This system may be used to explain the ring-like structure of the observed velocity (Figure 1), recalling that from lecture 2 the weather layer winds appear to increase with depth via the thermal wind relation. Small departures of the system from adiabaticity (e.g. surface radiation and interior heating) may result in columnar convection, axial convection cells, if rotation effects are important. The interaction of the columnar convection cells and the cylindrical zonal flows has been investigated by Busse (1976) and the convection motion shown to produce Reynolds stresses which maintain the strength of $\partial u/\partial r$ and consequently the zonal flows. The interior flow must transport heat poleward in response to the great net radiative cooling discussed above. The simplicity of this model may be interrupted if large departures from the barotropic state (such as hydromagnetic effects or interaction with the solid planetary core) disrupt the convection columns.

The second model suggests, by analogy with the Earth's circulation, that internal heating is distributed evenly and the bulk of latitudinal heat flux occurs within the weather layer via baroclinic instability. The instabilities again induce Reynolds stresses which may maintain the zonal jets in the weather layer. The stable stratification of the weather layer decouples it from the deep interior. A criticism of this second argument is that the baroclinic instability requires a significant poleward temperature gradient, which is not present globally on Jupiter. This model will not be pursued here.

Interior Thermal Balance

To provide a conceptual model of how the radiation budget may be balanced by interior diffusive processes it is useful to evaluate the radiative and conductive timescales for a body.

Consider a highly conducting sphere in space. The equations governing its temperature are

$$\rho c \frac{\partial T}{\partial t} = k \nabla^2 T \tag{3.2a}$$

$$-k \frac{\partial T}{\partial r} = \sigma T^4 - \frac{F}{\pi} \cos \phi \tag{3.2b}$$

where ϕ is the latitude. If we estimate

$$\frac{\partial}{\partial r} \sim \frac{1}{r_1}, \quad \nabla^2 \sim \frac{1}{r_1^2} \quad \text{and} \quad T \sim T_0 \tag{3.3}$$

then the conduction and radiation time scales are

$$\tau_c \sim \frac{\rho c r_1^2}{k} \quad \text{and} \quad \tau_r \sim \frac{\rho c r_1 T_0}{\sigma T_0^4} \tag{3.4}$$

Assuming that the conduction is much more rapid than radiation ($\tau_c \ll \tau_r$) the sphere adjusts to the internal heat distribution quickly compared to the external cooling time. Consequently the sphere is almost isothermal (inside to outside and equator to pole) when the conduction constant k is large. This situation is a model of the giant planets when the convective eddy diffusivity of heat is large.

A Cautionary Tale

The model of Busse (1976), combining inviscid, adiabatic, interior zonal flows with axial convection columns to describe Jupiter's heat transport must be treated with caution, as the following example illustrates. The sun's outer mantle layer appears from observations to be near adiabatic. Consequently, steady zonal flows may be modelled by the inviscid equations,

$$2\Omega \wedge v = -\frac{1}{\rho} \nabla p - \nabla \Phi, \tag{3.5}$$

where $\Phi = \Phi_N - \frac{1}{2}\Omega^2 r^2$, Φ_N is a Newtonian geopotential, r is the cylindrical coordinate and z is the axial coordinate. In this system,

$$2\Omega \frac{\partial u}{\partial z} = \frac{1}{\rho^2} \left(\frac{\partial \rho}{\partial r} \frac{\partial P}{\partial z} - \frac{\partial \rho}{\partial z} \frac{\partial P}{\partial r} \right) \tag{3.6}$$

yielding,

$$\frac{\partial u}{\partial z} = 0 \tag{3.7}$$

as before, if $\rho = \rho(P)$, that is, the layer is barotropic, which includes the case of $\rho = \rho(P, S)$ with constant S, just as has been postulated for the Jupiter interior. However, helioseismological measurements imply that $\partial u / \partial z \neq 0$ (Figure 2), from which it must be deduced that one or more of the assumptions must be violated. This suggests that small deviations from the adiabatic state may have significant effects on the flow field. Thus the assumption of adiabaticity must be applied with caution.

A Mixing Theory

In order to quantify the dynamics of the mixing within giant planets, the mixing length theory of turbulent convection may be invoked. Several assumptions are made, the limiting one being that of no rotation. In addition it is assumed,

1. parcels rise one scale height, $H = \frac{RT}{g} = l$,
2. rising parcels have a typical temperature excess δT,
3. kinetic energy approximately balances work done by buoyancy for a parcel,

$$v^2 \sim gl\frac{\delta\rho}{\rho} \sim gl\frac{\delta T}{T},\qquad(3.8)$$

4. heat flux, $F \sim \rho c_p v \delta T$,
5. the temperature gradient gives $\delta T \sim \frac{d\theta}{dz}l$, where θ is the potential temperature.
These yield,

$$v \sim (\frac{\kappa F}{\rho})^{1/3}\qquad(3.9)$$

which is a measure of typical turbulent velocities at the top of the mixed layer. Here $\kappa = \frac{R}{c_p}$. Combining these assumptions, the departure of the overall temperature gradient from the adiabatic is found by,

$$\frac{\Delta\Gamma}{\Gamma_a} = \frac{1}{\Gamma_a}\frac{d\theta}{dz} \sim \frac{v^2}{\kappa RT}.\qquad(3.10)$$

For Jupiter and Saturn,

$$\frac{\Delta\Gamma}{\Gamma_a} \sim 10^{-5},\qquad(3.11)$$

which suggests that the interiors are very close to adiabatic. Of course rotation is not likely to be insignificant and should be accomodated in these calculations. The Rossby number of this convection will be,

$$R_o = \frac{v}{l\Omega} \sim 0.2\qquad(3.12)$$

The effects of rotation will increase with depth.

Stability of Interior Zonal Flows

Having illustrated that the interior, near adiabatic zonal flows may be essential to the understanding of the dynamics of the giant planets, it is necessary to consider the stability of these flows. This field is largely unexplored except in simplest terms. Writing the momentum equations,

$$-2\Omega\overline{u} = -\frac{\partial\overline{\Phi}}{\partial r} - \delta\overline{S}\frac{\partial T}{\partial r} \tag{13a}$$

$$0 = -\frac{\partial\overline{\Phi}}{\partial z} - \delta\overline{S}\frac{\partial T}{\partial z} \tag{13b}$$

in cylindrical polar coordinates, they combine to give

$$2\Omega\frac{\partial\overline{u}}{\partial z} = \frac{\partial\overline{S}}{\partial z}\frac{\partial T}{\partial r} - \frac{\partial\overline{S}}{\partial r}\frac{\partial T}{\partial z}, \tag{3.14}$$

for the zonal flow.

A first step is to scale for quasi-cylindrical, quasi-geostrophic flow (Ingersoll and Pollard, 1982): let the coordinate length scales behave as,

$$L_z \sim r, L_\theta \sim r, L_r \ll r, \tag{3.15}$$

with $L_r = L \ll r$ and $\epsilon = \frac{U}{2\Omega L} \sim \frac{L}{r} \ll 1$. Now consider a barotropic basic state $\overline{u}(r)$ with $\frac{\partial\overline{u}}{\partial z} = 0$. Here it is possible to obtain an analogue of the barotropic vorticity equation:

$$(\overline{u} - c)\frac{d^2\Psi}{dr^2} + (B - \frac{d^2\overline{u}}{dr^2})\Psi = 0, \tag{3.17}$$

where $B = \frac{2\Omega}{M}\frac{dM}{dr}$ and $M = \int\rho dz$, inegrating axially through the planet from surface to surface. $B\sin^2\phi$ plays the same role as β but is numerically around three times larger for Jupiter. This could provide an explanation for the observation that the maxima of u_{yy} for Jupiter are approximately equal to 3β.

References.

Busse, F. H., 1976 Generation of planetary magnetism by convection. *Phys. Earth Planet. Inter.* **12**, 350.

Ingersoll, A. P. & Pollard, D., 1982 Motion in the interiors and atmospheres of Jupiter and Saturn: Scale analysis, anelastic equations, barotropic stability criterion. *Icarus* **52**, 62.

Libbrecht, K. G., 1988 Proc. Symp. Seismology of the Sun and Sun-like Stars, Tenerife, Spain, 26-30 September

Notes compiled by Douglas Parker and Andrew Stamp
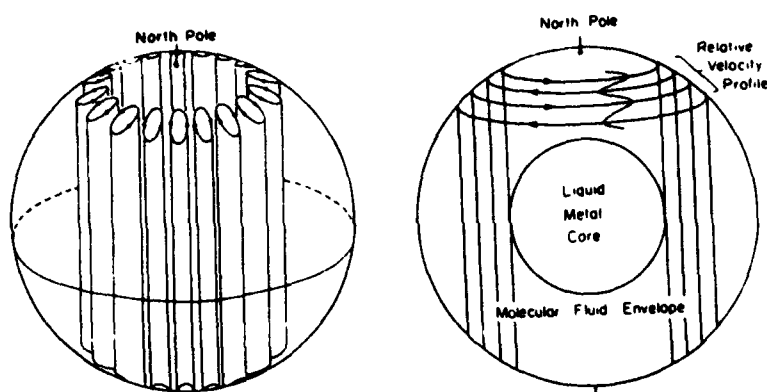
Figure 1: Columnar convection cells (left) and cylindrical zonal flow (right) from Ingersoll & Pollard (1982). Busse (1976) found that the columnar mode is the preferred form of convection in a uniformly rotating, viscous, conducting fluid. The cylindrical mode is the most general form of steady zonal motion in an inviscid, adiabatic fluid.
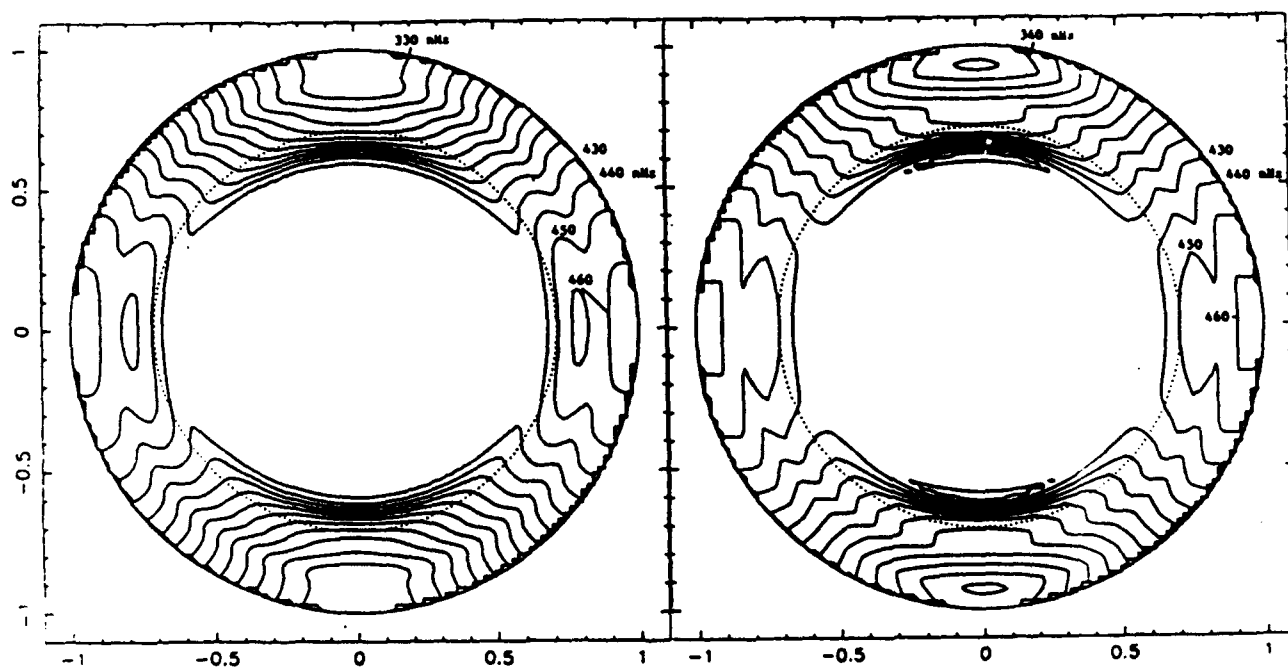
Figure 2: Contour plots showing variations of the solar interior rotation rate from Libbrecht (1988).

28

Lecture 4 – Jovian Vortices

Some of the large scale characteristics of the Jovian atmospheres have been well known for years, observed easily from Earth telescopes. Jupiter is nearby and has a strong visual contrast related somehow to its atmospheric composition, so observers have been familiar with its latitudinal bands and its single large anti-cyclonic vortex at $10°S$ latitude (The Great Red Spot) for over 300 years. It was the arrival of the Voyager spacecrafts that connected the banded structure with the alternating zonal jets that characterize the global circulation of Jupiter's atmosphere. These close up observations also revealed a plethora of vortices on all scales on all of the Jovian planets; it seems that despite the differences in Solar driving, all the giant planets have similar circulations and vortical phenomena. Through the camera eyes of Voyager, we have been able to observe and try to sort out the behavior of vortices in a geophysical environment.

The analysis of Voyager's data is far from complete, but there are characteristics that we notice immediately: there is a lot of activity occuring on the smallest scales of motion, and this activity evolves very quickly. Vortices on this scale have short lifetimes. There is also a lot of uncertainty about the physical processes that may be taking place at these scales (i.e. convection, precipitation, etc). Still, we can form some "rules of thumb" about the dynamics of vortices. The smallest vortices are nearly circular in shape. Most of the vortices (90 percent) have a circulational sense opposite to that of the planetary rotation (they are anti-cyclonic). Although the sense of rotation is difficult to observe directly for the smaller vortices, we may assume that they have the same sign of vorticity as the shear zone in which they reside. Vortices interact with other vortices: two vortices can form an orbiting pair, and they are also seen to merge, forming a larger (stronger) vortex, and we may safely assume that mergers happen between vortices of the same rotational sense. Mergers like this may be the fundamental process responsible for the formation of the larger vortices, even the "great vortices." Often in the merger process, and also from single vortices, a long filament will be shed, presumably a tendril of vorticity that is either ejected or extracted for some reason. Vortices are also observed to split, becomming two or more smaller vortices. Vortices also move: we can see some drifting, some oscillating in their positions or drift velocities; presumably they are interacting with the background flow in which they sit. Larger vortices seem to be more stable, but even they will oscillate in size and position and (if the vortex is oval-shaped) in their orientation and shape.

In the vicinity of the GRS, we see that the small spots that live to the east are advected by the mean flow toward the spot and merge with it. It is difficult to determine the sense of rotation of the smallest vortices, but again we assume that, since they merge, they are anti-cyclonic. Just west of the large ovals (including the GRS) there is a cyclonic chaotic wake, slightly equatorward of the central latitude of the spot. Vortices appear spontaneously inside these wakes, which are reminiscent of the appearance of convective turbulence.

Despite the chaotic behavior and rapid evolution of the small scale structures in the vicinity of the GRS, the spot itself has persisted since it was first observed 300 years ago, and it may be an unknown number of orders of magnitude older than that. Such staying power is even more surprising in light of the small fluid circulation timescales on Jupiter, ; the GRS itself has a circulational frequency on the order of a day. Jupiter's three large

white ovals have also persisted since they formed in 1938 out of the segmentation of a white band at that latitude. The white ovals are 2-3 times smaller than the GRS, but the strongest of the ovals has nearly the same mean vorticity as the GRS. The comparison is made in figure 1, where observed tangential velocities (v_t) are plotted versus distance along the vortex semi-major axis (a) for the white oval BC on the left and for the GRS on the right. We see that the Red Spot has smaller mean vorticity despite its larger size as a consequence of its relatively quiet interior. The GRS is more like a ring of vorticity circulating around a static core as shown in figure 2. The GRS remains fixed in latitude, orientation and size, but is observed to oscillate in longitude (with respect to its mean westward drift) with a period of about 90 days.

Neptune's Great Dark Spot is the same size relative to Neptune that the GRS is relative to Jupiter. The GDS, however, is observed to oscillate in shape and orientation. Figure 3 shows the time evolution of the aspect ratio λ and the ellipse orientation ϕ. Notice that $\phi(t)$ leads $\lambda(t)$ by 90° of phase.

The behavior that we observe through these cloud top motions of the Jovian planets is familiar from laboratory and numerical experiments on two-dimensional and nearly two-dimensional geostrophic flows, and from the limited conclusions that can be drawn from geostrophic and quasi-geostrophic theory. But there is no getting around the fundamental uncertainties related to the inability to observe the Jovian fluid motions at all depths below the cloud tops. We know very little about the vertical structure of the Jovian planets, so there is no way to know to what extent three-dimensional processes are part of or are responsible for producing what we see at the planets' surfaces.

Modelling the Vortices: Vertical Structure

Despite the wealth of cloud-top observations, there is very little data about the vertical structure of the Jovian atmospheres. Ideally, we could consider the vertical structure as an unknown, exploring the possibilities with a full spectrum of models. We would hope that the most realistic model would produce the results that most resemble what is observed.

Normal Mode Decomposition

Since rotational effects are important, we may consider beginning with the geostrophic or quasi-geostrophic equations of motion on a β-plane:

$$\frac{dq}{dt} = 0$$

where the total time derivative is

$$\frac{d}{dt} = \frac{\partial}{\partial t} + \frac{\partial \Psi}{\partial x} - \frac{\partial \Psi}{\partial y} \frac{\partial}{\partial x}$$

and

$$q = \nabla^2 \Psi + f + \frac{1}{\rho} \frac{\partial}{\partial z} \left(\rho \frac{f^2}{N^2} \frac{\partial \Psi}{\partial z} \right)$$

is the quasi-geostrophic potential vorticity, ρ is the density, Ψ is the streamfunction, f is the Coriolis parameter, and N is the Brunt-Vaisala frequency.

We can separate the solutions into the product of a horizontal streamfunction and a vertical structure function:

$$\Psi(x,y,z,t) = \sum_{n=0}^{\mathcal{N}} \Psi_n(x,y,t)\Phi_n(z)$$

from which we see that Φ_n is the solution to the eigenvalue relation:

$$\frac{1}{\rho}\frac{\partial}{\partial z}\left(\rho\frac{f^2}{N^2}\frac{\partial\Phi_n}{\partial z}\right) + \lambda_n^2\Phi_n = 0.$$

and the horizontal structure is now described by a set of coupled equations for the Ψ_n.

In this way, the complete vertical structure of motions is resolved as a superposition of normal modes. This has several advantages over layer models. First, the derivation of the normal mode equations shows the straightforward connection between vertical structure (contained in the vertical variation of N) and the model parameters; and second, it more accurately models the nonlinear interactions among baroclinic modes. The model is founded on the construction of a complete vertical profile of the static stability from Voyager data (which reaches to a depth of about 5 bars) and the assumption of a deep adiabat at great depth. The Voyager temperature profiles that are used to compute N^2 are shown in figure 4. Below this level we assume that the lapse rates, and therfore N^2 may be greatly affected by the presence of condensibles. The true N^2 will depend on the difference between the wet and dry lapse rates, so below the Voyager data, we assume the presence of an ammonia cloud overlying a water cloud in which:

$$N^2 = \frac{g}{T}\left(\left[\frac{dT}{dz}\right]_{wet} + \frac{g}{c_p}\right) > 0$$

and that $N^2 = 0$ below the water cloud (in the interior), yielding the model static stability profile shown in figure 5.

We look for resonant modes now by applying a radiative boundary condition and evaluating a (non-physical) response function for all values of λ. Because of the radiation condition, the modes are near-resonant approximate eigenfunctions; for more details refer to Achterberg and Ingersoll 1989 (*JAS*, **46**, 2448-2462). The peaks in this response function and the associated eigenvalues are shown in figure 6. We note that the zeroth mode Φ_0, with $\lambda_0 = 0$ is hieght independent; it can therefore be identified with the barotropic mode. It includes motion in the interior, which is unaffected by the other modes, but which has a strong influence on all of them. The Φ_n with $n > 0$ have no amplitude in the interior; these are therefore the *weather layer* modes. Indeed, we see that when only one mode beyond the barotropic mode is retained in the model, the standard $1\frac{1}{2}$ layer model equations of quasi-geostrophy are recovered, where:

$$\lambda_1 = \frac{1}{L_D} = (radius \ of \ deformation)^{-1} = \frac{1}{735km} \ .$$

and Ψ_0 plays the role of bottom topography (as we shall see) for the weather layer. For the Jovian models, we can use Ψ_0 to account for the zonal flow $(\overline{u})$ in the interior using:

$$\overline{u}_0 = -\frac{\partial\Psi_0}{\partial y}.$$

Single-Layer Quasi-Geostrophic Models with Topography

The two-mode single-layer equations can be written:

$$\frac{dq}{dt} = 0$$

where

$$q = \nabla^2 \Psi + \beta y - \lambda^2 (\Psi - \Psi_0).$$

We can see that the barotropic mode (Ψ_0) can be thought of as the topography upon deriving potential vorticity conservation directly from the shallow water equations:

$$\frac{d\mathbf{v}}{dt} + f\,\mathbf{k}\,\times\,\mathbf{v} = -g\nabla h_s$$

and

$$\frac{dh}{dt} + h\,\nabla\cdot\mathbf{v} = 0$$

where $h := h_s - h_b$ is the layer thickness, h_s is the free surface height, and h_b is the topographic height, as shown in figure 7. It is straightforward to show then:

$$\frac{d}{dt}\left(\frac{\zeta + f}{h}\right) = 0$$

where ζ is the vorticity and:

$$q = \frac{\zeta + f}{h} \approx \frac{\nabla^2 \Psi + f_0 + \beta y}{h_0 + \delta h_s + \delta h_b}$$

is the potential vorticity; so

$$\Psi = \frac{g\delta h_s}{f_0} \quad , \quad \Psi_0 = \frac{g\delta h_b}{f_0} \, ,$$

therefore associating the barotropic mode with the topographic height.

Single-Layer Models With No Topography

The simplest models do allow some exact solutions of vortex problems. The Kida vortex is an excellent example, and was employed by Polvani et al (1990 *Science*, **249**) to interpret the motion of Neptune's Great Dark Spot (GDS). In two dimensions, we have:

$$\frac{dq}{dt} = 0 \ , \quad q = \nabla^2 \Psi$$

and look at the solution of a uniform vorticity (β is therefore zero) regions demarcated by simple geometric boundaries: in this case an ellipse of constant (potential) vorticity q_1 surrounded by a region of constant potential) vorticity q_2 (see figure 8). The aspect ratio λ and inclination angle ϕ of the elliptical boundary can then be shown to oscillate as:

$$\frac{d\lambda}{dt} = -s\lambda \sin 2\phi$$

$$\frac{d\phi}{dt} = \Omega + \frac{s}{2}[-1 + \Lambda \cos 2\phi]$$

where

$$\Omega := q_1 \frac{\lambda}{(1+\lambda)_2} \ , \quad s := q_2 \ , \quad \Lambda := \frac{1+\lambda^2}{1-\lambda^2} \ .$$

If the three parameters $(q_1, q_2, \lambda(t = 0))$ are matched to the data representing the aspect-ratio and inclination oscillations of Neptune's GDS, we find that the period, mean, and amplitude of $\lambda(t)$ and $\phi(t)$ can be simultaneously fit. Polvani et al have also shown that this model gives rise to a zone just outside the GDS where particle trajectories are chaotic (figure 9).

Unfortunately, no knowledge about the vertical structure is gained from a two dimensional study. Polvani et al have also developed a Kida-like model from the single layer equations (with β and L_D). Contour dynamics is used to follow the evolution of the elliptical boundary that best fits the GDS data. The best fit in this case indicates an unexpectedly large deformation scale: $L_D > 7000km$.

There are some problems with this ellipse-fitting technique. Among them is the fact the the area of the GDS varies. The variations seem to be correlated with the ejection of "streamers" of vorticity filaments, a phenomenon of viscosity, that cannot be accounted for in these inviscid treatments. There is some confidence to be gained by noting that the lost area is always regained, but we cannot take this too far since it is not known what is responsible for the recovery: my guess is that the streamers are somehow eventually recovered.

Notes compiled by Louis Tao and Phil Yecko

34

Observed tangential velocities (V_T) as a function of a within Oval BC.

Observed tangential velocities (V_T) as a function of a within the GRS.

both
lines
show

$\Delta V = 25 \, ^m/_s$

$\frac{1}{2} \Delta a = \frac{1}{2} \times 10^6 \, m$

$\zeta \approx \frac{\Delta V}{\Delta a/2}\Big|_{OVAL\ BC} = 5 \times 10^{-5} \, s^{-1}$

Figure 1

Dowling + Ingersoll   longitude   JAS 45, 1380
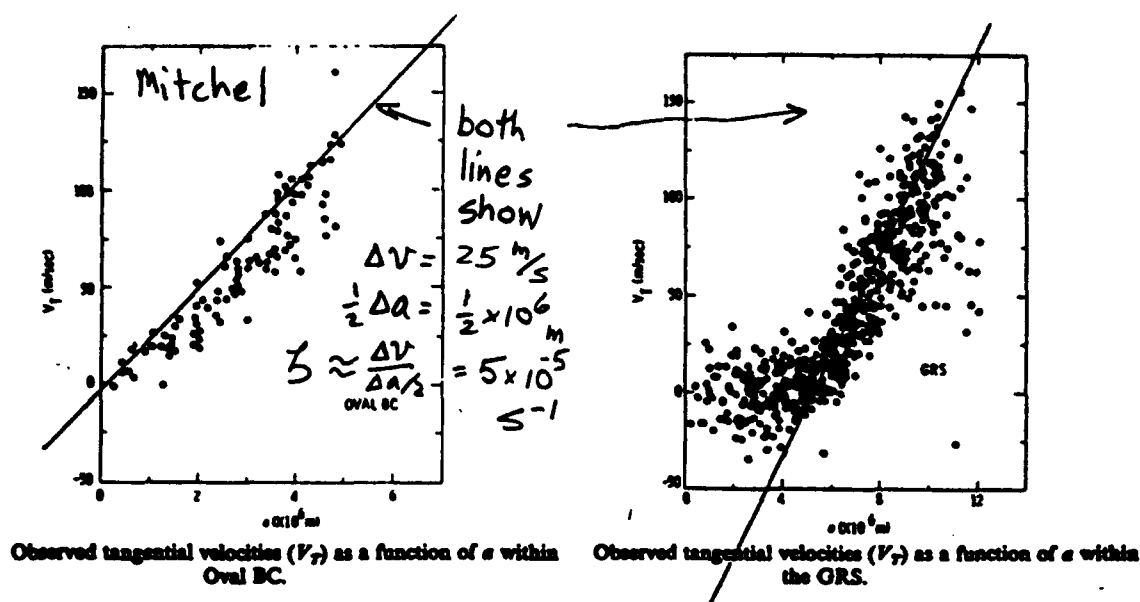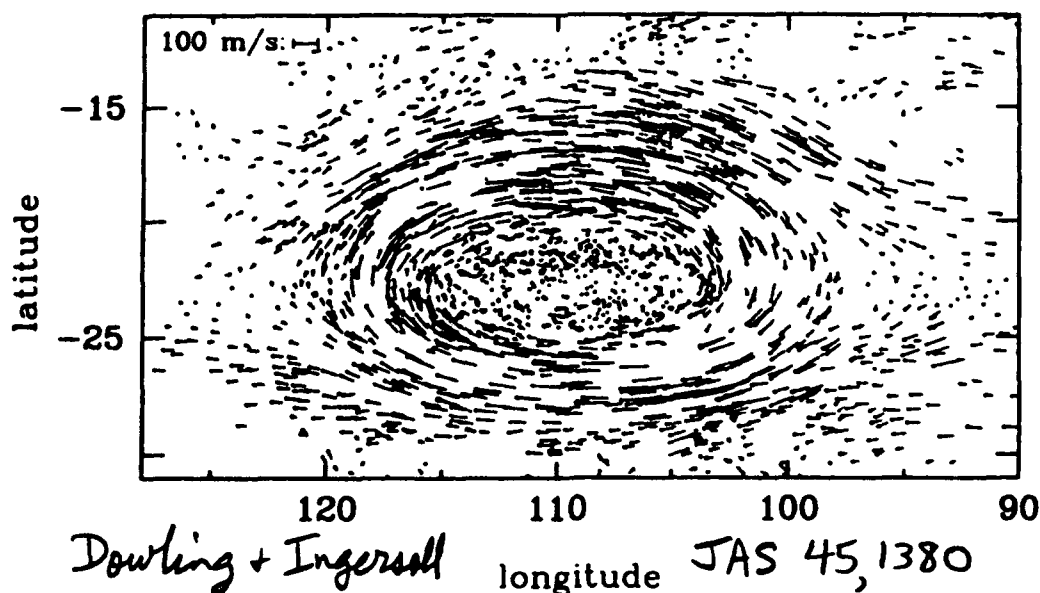
FIG. 2. Velocity data for the GRS. The location of each vector is marked with a dot, and the lines point downwind. The northward and eastward components of velocity are scaled equally in m s^{-1}, with 100 m s^{-1} indicated at the top left of the figure. Longitude and planetographic latitude are labeled in degrees and scaled equally, with the zero of longitude corresponding to System III on 5 July 1979.

Figure 2

Fig. 5. The same as Fig. 4 but for the orientation angle φ.

Fig. 4. The inverse of the aspect ratio versus time. The data points from our fits to the images are superimposed on the fits to the dynamical models. The solid line is the best fit of model 1. The fit for model 2 is indistinguishable from that of model 1. The dashed curve is the fit of model 3, with γ = 0.00025 km⁻¹.

Figure 3
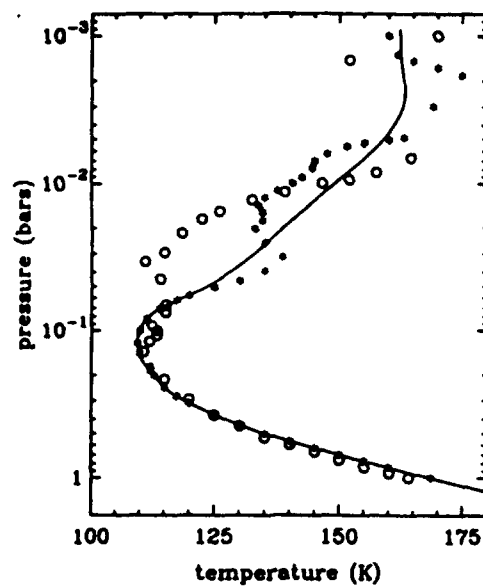
FIG. 1. Temperature profiles for Jupiter's atmosphere. The open circles are from the *Voyager 2* radio occultation egress data, the asterisks are from the *Voyager 2* radio occultation ingress data, and the solid line is the profile used in our models.
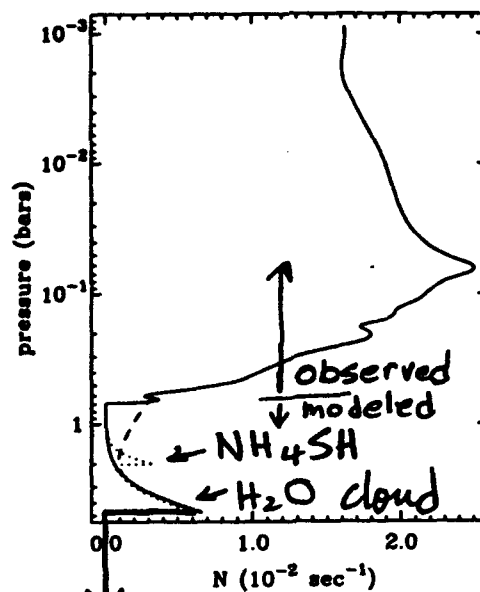
FIG. 2. Model static stability profile. The solid line is for the standard model. The dotted line is for the standard model with an NH₄SH cloud. The dashed line is for equilibrium hydrogen.
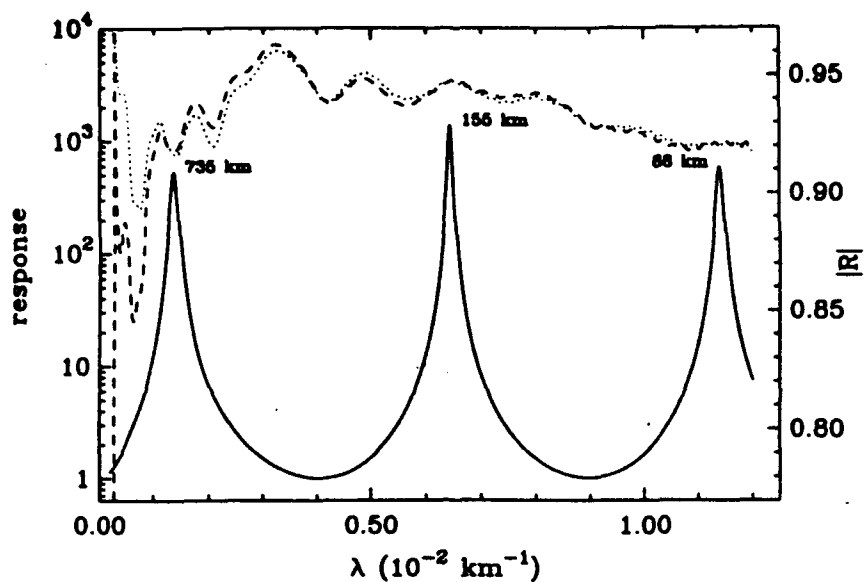
FIG. 3. Reflection coefficients and response function for the standard model. The solid line is the response function. The dashed line is the reflection coefficient with L_D $(z < z_1) = L_D(z_1)$. The dotted line is the reflection coefficient with L_D $(z < z_1) = L_D(z_1) \exp(z_1 - z)$. Numeric labels are the deformation radii (λ^{-1}) corresponding to peaks in the response function.
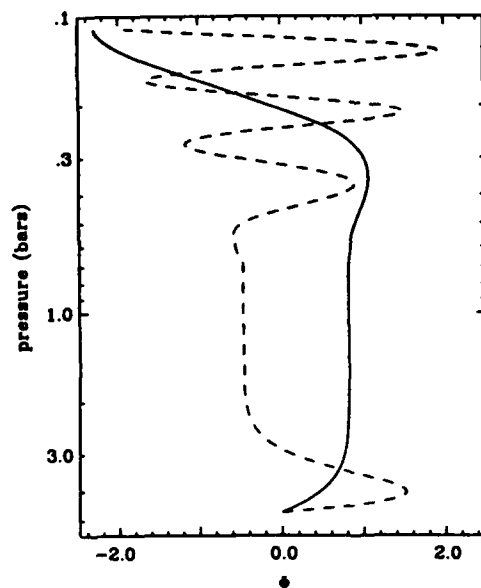
FIG. 4. Vertical structure Φ_I for the first two peaks in the response function in the standard model, shown at the phase when $\partial \Phi_I / \partial z|_{z=z_1}$ is a maximum. The solid line is for $\lambda^{-1} = 735$ km. The dashed line is for $\lambda^{-1} = 155$ km.

Figure 7

h

h_s

h_b

Solid topography

q_2

q_1
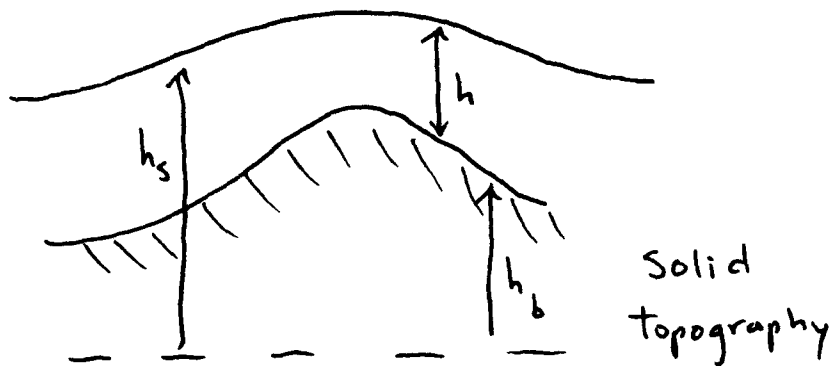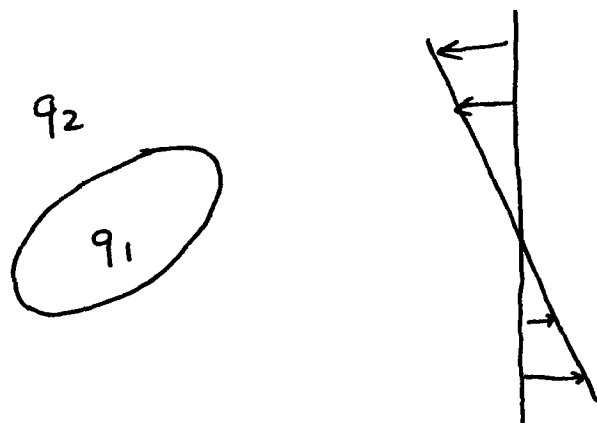
Figure 8
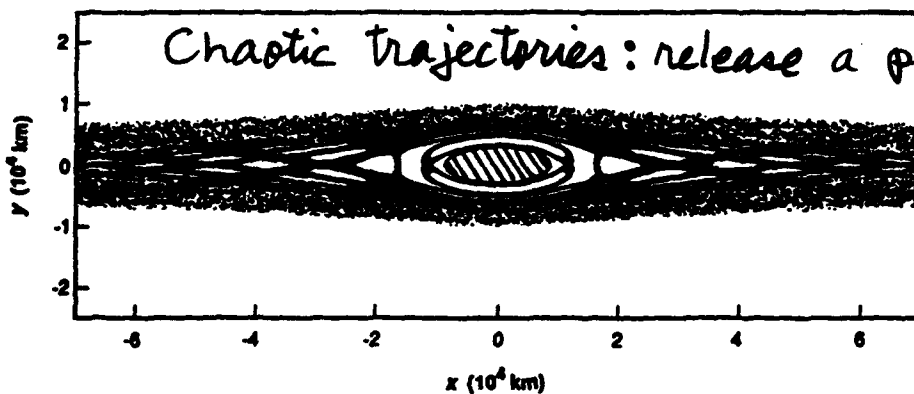
Chaotic trajectories: release a particle, plot its location once per cycle — chaos. Sensitive to initial conditions.

Fig. 7. A Poincaré surface of section for fluid motion near the Great Dark Spot on Neptune. The hatched region is the Great Dark Spot. The chaotic zone, represented by the scattered points, is much larger than the vortex.

y (10^4 km)

2

1

0

-1

-2

-6   -4   -2   0   2   4   6

x (10^4 km)

Figure 9

Lecture 5 – Determining the Deep Flow

In the last lecture, we argued that one may consider the deep zonal flow below the weather layer to be represented by an effective bottom topography in a one layer shallow water system. We performed a vertical mode decomposition, in which only the barotropic mode, with streamfunction ψ_0, has non-zero amplitude in the interior of the planet. For the next mode ($n = 1$), ψ_0 appears as an effective topographic forcing term.

Various authors have adopted stratgies of differing complexity and rationality in selecting an effective deep zonal flow $u_0 = -d\psi_0/dy$ for Jovian numerics.

Ingersoll & Cuong (1981) (hereinafter IC81) took the zonal flow measured in the weather layer as an estimate for u_0, so the weather layer is assumed to have the same basic zonal flow as the deep interior. Taking another view, Williams & Yamagata (1984) (hereinafter WY84) and Williams & Wilson (1988) took $u_0 = 0$ for their simulations. The coherence of the Great Red Spot (GRS) suggested to Marcus (1988) (hereinafter M88) that Rossby wave radiation should be weak in the latitude band of the GRS, so he took $q = $ constant for his simulations.

Subsequently, Dowling & Ingersoll (1988) devised a method of inferring the deep zonal flow from the Voyager data in latitude bands where coherent vortices are present, and used their inferred bottom topography for shallow water simulations of the GRS (Dowling & Ingersoll, 1989 - hereinafter DI89).

We shall now outline the procedure for inferring ψ_0, and discuss the results of the simulations.

Inferring the Deep Zonal Flow

Let us consider the closed streamlines a-d in the GRS (fig.1). We recall that ψ is constant on streamlines, and that, since q is advected with particles, it must also be constant on closed streamlines.

To fix ideas, we consider a quasigeostrophic model, where

$$q = f + \zeta - \lambda^2(\psi - \psi_0)$$

where ψ is the streamfunction in the weather layer, $\zeta \equiv \nabla^2\psi$ is the relative vorticity, f is the planetary vorticity, and λ is the inverse deformation radius.

Rearranging for ψ_0, we have

$$-\psi_0 = -\psi + \lambda^{-2}(-q + \zeta + f) \equiv A_i + B(\zeta + f)$$

where now the A_i depend on the contour, since each contour may have a different potential vorticity, and B is determined by the deformation radius chosen.

Now, ζ is obtained from the wind speeds in the data, and f is known, so we can now proceed to fit this to the data. To do this, we assume $\psi_0(y)$ of the form $\psi_0(y) = Dy + Ey^2$, and fit

$$A_i + B(\zeta + f) + Dy + Ey^2 = 0$$

to the data using a least squares method. The generalization of this method to the shallow water system is presented in Dowling & Ingersoll (1989).

Figure 2 shows the variation with latitude of the absolute vorticity $\zeta + f$ round each of the curves a-h in fig. 1. The smooth lines represent the quadratic least squares fit obtained by the above procedure. The dashed lines show f as a function of latitude. We can see that the foregoing procedure has obtained good agreement with the data.

Figure 3 shows the equivalent bottom topography and deep zonal wind for the shallow water analysis in DI89. The dashed line in figure 3b shows the cloud top zonal wind profile. Notice the significant difference between the cloud top and deep zonal winds at around $20 - 25°$ South.

Single layer simulations

We now consider the effect of different types of topography on the formation and persistance of large coherent strucures such as the GRS in zonal flows realistic for GRS latitudes. The simulations are performed for single layer shallow water equations with periodic zonal boundary conditions and no normal flow boundary conditions at $5°S$ and $40°S$. For the topographies of DI89 and WY84 the mean zonal flow $\bar{u}_1$ in this latitude band is barotropically unstable and Rayleigh relaxation with a time constant of 400 days was used to maintain the mean state. The physical mechanism by which these apparently unstable zonal jet flows are maintained in the Jovian atmosphere is not clear, but we should bear in mind that the true system is not a shallow layer with a bottom topography, but instead has a deep zonal flow which may have very different combined stability properties.

The results from single layer calculations are shown in figures 4-8. In all cases vortices in shear are remarkably stable. If $\bar{u}_1$ is unstable then instabilities develop and small vortices form which merge in time to form one long-lived vortex. When $\bar{u}_1$ is stable, an initial vortex will last indefinitely. If the flows are perturbed randomly or if additional small vortices are introduced into the flow, one finds that the large coherent structures remain intact.

The lesson of single layer models is that vortices in shear are remarkably stable. However, the fundamental limitation of single layer models is that they do not contain the baroclinic instability mechanism. We shall see that a model with two baroclinic modes admits vortices with a rich structure of instabilities, but that the stable barotropic vortices are recovered in a certain limit, which is presumed relevant for the Jovian atmosphere.

Multi layer vortex models

From Achterberg & Ingersoll (1992), we consider a quasigeostrophic model in which there are two baroclinic modes (ψ_1 and ψ_2), and a deep barotropic mode (ψ_0), giving rise to baroclinic flow and possible baroclinic instability in the weather layer.

We shall consider cases where a baroclinic vortex is implanted into the weather layer at time $t = 0$. We shall assume that initially both ψ_1 and ψ_2 have the same horizontal structure.

We let L be a typical horizontal length scale of the vortex and define two parameters

$$\lambda_1^2 = \frac{L^2}{L_1^2}; \quad \lambda_2^2 = \frac{L^2}{L_2^2}$$

where L_1 and L_2 are the first and second baroclinic deformation radii. For Jupiter, we take $L_1 = 735$km, $L_2 = 155$km.

We define a further parameter

$$s = \frac{\psi_2(t=0)}{\psi_1(t=0)}$$

and note that if $-0.2 < s < 1.8$ then the vortex has the same sign of vorticity at all latitudes.

In the absence of background shear, we find that large vortices, for which $\lambda_1^2 > 0.15; \lambda_2^2 > 3.3$, are stable in the regime $-0.2 < s < 0.2$, but otherwise they split horizontally, leaving two smaller vortices.

For small vortices, with $\lambda_1^2 < 0.15; \lambda_2^2 < 3.3$, we find that when $-0.2 < s < 1.8$ "vertical splitting" occurs, in which the vortex splits up to form two vortices, each at a different level. Otherwise, we have stability (figure 9).

With shear present, a large part of the stable regime for zero shear, corresponding to small baroclinic vortices ($\lambda_1^2 < 0.2$ and $s < 0$) becomes unstable due to the shearing out of vortices with vorticity of opposite sign from that of the background shear vorticity. The remaining "stable" states (figure 10) are not steady, but correspond to oscillations in aspect ratio and orientation, similar to the single layer Kida (1982) vortex in the case $s = 0$.

The result of the instability of small vortices leads to vortices splitting into two — one vortex at each level. The remaining fragments will orbit each other, and from above this looks like an oscillation in latitude and longitude of a *single* vortex. This is believed to have been observed on Neptune, and must be borne in mind when interpreting observational data. In particular, the observed oscillations of Neptune's spot D2 (fig. 11) could quite possibly be explained by a two-layer baroclinic strucure.

A GCM for the outer planets?

Having developed some intuition for the similarities and differences between barotropic and baroclinic models by considering barotropic and two-mode baroclinic vortex structures with and without shear, we might be tempted to try to develop a full scale GCM for the outer planets, similar to those which have been developed for the terrestial atmosphere. A partial list of things to study might be

(1) Relative importance of solar versus internal energy

(2) Maintainance of jets — widths and speeds

(3) Maintainance of vortices — cannibalism versus convection

(4) Decay of jets with height in the upper troposphere

(5) Nature of small scale (< 1000km) chaotic motions

(6) Flow beneath the weather layer (adiabatic interior)

Good models for studying diabatic processes use isentropic vertical coordinates (e.g. Hsu & Arakawa). The advantages of isentropic coordinates are that

(1) The *vertical* motion and the *diabatic* circulation are the same thing, since adiabatic dynamics are confined to isentropic layers.

(2) Stacked shallow water code is used, with heating Q represented by a small transfer of mass between layers proportional to Q.

(3) For giant planets, Q is small (the radiative time constant is long - 10 to 100 years).

(4) For giant planets, the bottom of the weather layer is an adiabat - a coordinate surface in isentropic coordinates.

The strategy is then to model the dynamics of the stably stratified weather layer (pressure < 5bars for Jupiter) with the GCM, and treat the interior flow with a bottom boundary condition. However, this potential approach has yet to yield any substantial results.

Mixing length theory of baroclinic eddies

One of the potentially important processes which the weather layer GCMs would require very high resolution to resolve explicitly is the transport of heat by baroclinic eddies in the weather layer of the planet.

Making some elementary assumptions about the vertical distribution of solar heating in the deep interior of Uranus (see fig. 12), Friedson & Ingersoll (1987) used Stone's (1972) mixing length theory of baroclinic eddies to model the the mean surface temperature as a function of latitude.

To use Stone's parameterization, we must first choose a vertical scale height l_v. Assuming the distribution of potential temperature θ to be given, this defines a radius of deformation l_h by

$$l_h = \left(\frac{g}{T} \frac{\partial \theta}{\partial z} \right)^{1/2} \frac{l_v}{f}. \qquad \cdot$$

We then take the departure of temperature δT from the adiabatic equilibrium T to be given by

$$\delta T \sim \left(\frac{\partial \theta}{\partial y} \right) l_h$$

and assume a horizontal heat flux F_h to be given by

$$F_h = \rho c_p v \delta T.$$

Using the thermal wind relation for the horizontal velocity v gives

$$\frac{fv}{l_v} = \frac{g}{l_h} \frac{\delta T}{T}.$$

We then take the ratio of vertical heat flux F_v to horizontal heat flux F_h to be given by

$$\frac{F_v}{F_h} \sim \frac{w}{v} \sim \frac{(\partial \theta / \partial y)}{(\partial \theta / \partial z)}$$

where w represents a typical vertical velocity. Assuming this parameterization the temperature field can now be time stepped by setting its time derivative equal to the convergence of the heat flux (F_h, F_v). The new θ field can then be derived by assuming some relationship between θ and T, such as a perfect gas law.

In addition to Stone's parameterization, one also requires knowledge of seasonal heat storage and convective adjustment for the appropriate season. To understand the role of convective adjustment, we fix our attention on the Northern Spring and Summer (figure 12).

At the start of the Northern Spring, the surface layer (at the top of figure 12a) is assumed to have been radiating heat, and convection from the warm interior of the planet penetrates to the surface at all latitudes north of the equator (fig. 12a). As the sun starts to fall on the top layer, convection is no longer sustained and is turned off (fig. 12c). Note the almost complete disappearance of thermal structure in Southern latitudes in figure 12d, as the surface layer cools in the southern winter and convection becomes active.

Incorporating both of these effects into a model for Uranus allows us to investigate the relative importance of each one in determining the season and annual surface temperature distribution.

The results of the model seem to agree well with observations of mean surface temperature with latitude for Uranus (figure 13), but do not account for small-scale features, which are presumed to be due to zonal jet decay.

References

Achterberg R.K. and Ingersoll A.P. 1992 ????????????? SUBMITTED to ??????????

Dowling T.E. and Ingersoll A.P. 1988 Potential vorticity and thickness variation in the flow around Jupiter's Great Red Spot and White Oval BC. *J. Atmos. Sci.*, **45**, 1380-1396

Dowling T.E. and Ingersoll A.P. 1989 Jupiter's Great Red Spot as a shallow water system. *J. Atmos. Sci.*, **46**, 3256-3278

Friedson J. and Ingersoll A.P. 1987 Seasonal meridional energy balance and thermal structure of the atmosphere of Uranus: A radiative-convective-dynamical model. *Icarus*, **69**, 135-156

Hsu and Arakawa ??

Ingersoll A.P. and Cuong P.G. 1981 Numerical model of long-lived Jovian vortices. *J. Atmos. Sci.*, **38**, 2067-2076

Marcus P.S. 1988 A numerical simulation of the Great Red Spot of Jupiter. *Nature* **331** 693-696

Stone P.H. 1972 A simplified radiative dynamical model for the static stability of rotating atmospheres. *J. Atmos. Sci.*, **29**, 405-418

Williams G.P. and Yamagata T. 1984 Geostrophic regimes, intermediate solitary vortices and Jovian Eddies. *J. Atmos. Sci.*, **41** 453-478

44

Figure Captions

Figure 1 Streamlines in the region of the Great Red Spot, obtained from Voyager Data.

Figure 2 Plots of $\zeta + f$ along streamlines with latitude. The left panel is for streamline segments West of $109°$ longitude, the right panel for East of $109°$. The heavy dots are computed from the Voyager Data. The solid curves are a quadratic least squares fit to the data. The dashed lines are f.

Figure 3 Bottom topography gh_2 and inferred deep layer velocity u_2. (a) Solid curves are inferred bottom topographies for different values of the free parameter λ^2 - the deformation radius. The dashed line is the effective free surface height. (b) Lower layer zonal wind velocities corresponding the bottom topographies given by (a).

Figure 4 GRS simulation using bottom topography of DI89.

Figure 5 GRS simulation using bottom topography of IC81.

Figure 6 GRS simulation using bottom topography of WY84.

Figure 7 GRS simulation using bottom topography of M88.

Figure 8 Extended GRS simulation, showing merging of two large vortices in shear.

Figure 9 Regime diagram for baroclinic vortex stability computations. f-plane, without shear.

Figure 10 Regime diagram for baroclinic vortex stability computations. f-plane, with shear.

Figure 11 Observed oscillations in longitude and latitude of Neptune's Great Dark Spot.

Figure 12 Contours of potential temperature over a 135 day period for the interior of Uranus from the model with convetion parameterization.

Figure 13 Surface temperature predictions for Uranus using the Friedson & Ingersoll (1987) model.

Notes compiled by Qingping Zou and Rupert Ford

Frg. 1

Fig 2

Fig 3

Fig. 5

Fig 6

Fig 7

no shear, f plane

Horizonatal Fragmentation

Tripole Form.

Stable

Tripole Formation

Horiz. Frag.

Stable

Vertical Fragmentation

λ_1^2

s

Fig 9

with shear, f plane

Adjustment with Vortex Ejection

Stable

Adjustment w/o Vortex Ejection

Shearing of Counter-Rotating Vorticity

Oscillation of Vortex Position

λ_1^2

s

Fig 10

54

Start Northern Spring

$L_s = 0$

$L_s = 45$

2 bar

15 bar

Vertical distribution of solar heating

Start Northern Summer

$L_s = 90$

$L_s = 135$

PRESSURE

LATITUDE

TEMPERATURE (K)

LATITUDE

Lecture 6 –A Formalism for Investigating the Atmospheric Dynamics of Jupiter

J.I. Yano

Introduction

In order to study the dynamics of Jovian atmospheres, we must first develop suitable and usable mathematical tools. We approach this by first examining physics that is relevant to the problem. In particular, we justify consideration of an inviscid formulation (i. e. to neglect the external forcings and the dissipations) as a sensible physical limit, and consider, both qualitatively and with a normal mode analysis (i. e. to define the vertical structure of eigenmodes with a given vertical thermodynamical structure), the possible influence of deep motions upon the observed atmospheric layer. This will define the boundary condition for a large number of quasigeostrophic and shallow water models. We derive a shallow water formulation, and specialize to the quasigeostrophic limit. Finally we apply the techniques of solitons and the KdV equation to the analysis of vortex dynamics.

Jovian free dynamics

Table 1 lists order of magnitude estimates of some relevant quantities to the energy budget and atmospheric dynamics of Jupiter and Saturn, normalized to values for the Earth.

Parameter	Jupiter	Saturn	Earth
Distance to Sun (R_S)	5.2	9.5	1.0
Solar Energy Supply ($F_R \sim R_S^{-2}$)	1/25	1/100	1
Steady wind speeds (U/ms^{-1})	100	400	10
Kinematic Energy ($E_K \sim U^2$)	10^2	10^3	1
Energy Dissipation time scale ($\tau_D \sim \frac{E_K}{F_R}$)	2.5×10^3	10^5	1

This illustrates that characteristic speeds of planetary zonal winds increase with distance from the sun, and thus with decreasing solar insolation. Internal heating is of the same order of magnitude in each case as solar radiation. This is suggestive that dissipation of energy in atmospheric flows is very low on Jupiter and Saturn, and so the dynamics can reasonably be examined with an inviscid formulation and without external forcing.

Models of the Jovian atmosphere

Successively more elaborate models have been applied to understand the the atmospheric dynamics of the giant planets. Williams (1978) used a one-layer barotropic model originally due to Rhines(1975). Williams and Yamagata (1982) extended this to a reduced barotropic model, with a solid bottom boundary and a free-surface upper boundary. This was refined by Ingersoll and Cuong (1981), and Dowling and Ingersoll (1989), to a $1\frac{1}{2}$ layer model, with the bottom boundary defined by a fixed deep flow. Yano and Flierl (*in prep.*) introduced a true 2-layer model, with two layers of different density, and a free upper boundary. This can be extended to a model with 3 or more layers, or inverted in its density structure to allow for an unstably stratified configuration.

Deep convection

Much of the behavior of the models described above is controlled by the applied bottom boundary condition. This is defined by the connection of the dynamics of the weather layer to the dynamics of the deep interior. There have been a number of differing views taken of the nature of the internal circulation of the Giant Planets, of which we briefly describe four. The simplest view of interior motion is one of isotropic small scale motions as would be suggested by a mixing length convection theory. Conversely, Busse (1976) suggested a structure in which rotation was an important element, leading to a large number of Taylor columns, as shown in figure 1.1a. Other possible structures are the formation of radial, sinking plumes at the base of the weather layer (figure 1.1b) (*J. Sommeria, personal communication*), or that such plumes form and are then dominantly influenced by rotation, generating "Taylor plumes" (figure 1.1c) (*J. Marshall, personal communication*).

Vertical structure of normal modes

The influence of deep motions within the planets on the observable motions in the weather layer may be inferred by a normal mode analysis. This has been done by Achterberg and Ingersoll (1988). We begin with the equation of conservation of potential vorticity, and consider a separable solution of the form

$$\psi(x, y, z, t) = \psi_0(x, y, t)\Phi(z),$$ (6.1.1)

where x and y are the coordinates parallel to the surface of the planet, z is the vertical coordinate and t is time. The vertical dependence may then be found by solving the equation

$$\left[\frac{1}{\rho}\frac{\partial}{\partial z}\rho\frac{f^2}{N^2}\frac{\partial}{\partial z} + \lambda_n^2\right]\Phi_n = 0,$$ (6.1.2)

where $\lambda_n = 1/L_D$, and L_D is the Rossby deformation radius for a particular order of solution. Expanding the operator,

$$\left[\frac{d^2}{dz^2} - \frac{1}{H(z)}\frac{d}{dz} + \frac{N^2}{f^2 L_D^2}\right]\Phi_n = 0,$$ (6.1.3)

where $H(z)$ is the local vertical scale, defined

$$\frac{1}{H(z)} = \frac{N^2}{\rho}\frac{\partial}{\partial z}\left(\frac{\rho}{N^2}\right).$$ (6.1.4)

We seek a local harmonic solution of the form $\exp(i \int m(z)dz)$. If $m(z)$ is a slowly varying function such that its derivatives may be ignored to first order, then

$$m^2 + \frac{im}{H} - \frac{N^2}{f^2 L_D^2} = 0,$$ (6.1.5)

which has solutions

$$m = -\frac{i}{2H} \pm \frac{1}{fL_D}\left[-\frac{f^2 L_D^2}{4H^2} + N^2\right]^{\frac{1}{2}} \tag{6.1.6}$$

Thus there is a change in behavior of any given mode at $N = \frac{fL_D}{2H} \equiv N_c$. Above this value, the solution is wavey, while above it $\Re(m) \neq 0$, giving exponential behavior in z. Figure 1.2 shows the structure of the two modes with the highest values of L_D for Jupiter.

The two-layer shallow water approximation

Here we develop the equations for a two layer fluid system with rigid plane base using the shallow water approximation. The full details of the relevant scaling relationships are explored by Pedlosky (1987) §3.3. The two layers are denoted by subscripts $j = 1, 2$, and are of equilibrium height H_j, uniform density ρ_j. Small variations in the level of the interfaces are described by η_j, where the subscript relates to the layer below the interface. Hence the fluid density is given by

$$\rho = \begin{cases} \rho_1 : z > H_2 + \eta_2 \\ \rho_2 : z < H_2 + \eta_2. \end{cases} \tag{6.2.1}$$

Using the beta-plane approximation, we consider a local coordinate system on the surface of a sphere at a latitude ϕ. We define a longitudinal coordinate x, and a latitudinal coordinate y, and expand the Coriolis parameter about a local "reference" value:

$$2\Omega \sin \phi \approx f_0 + \beta y$$
$$2\Omega \cos \phi \approx j_0 + \gamma y \tag{6.2.2}$$

This formulation is applicable for small variations in latitude, $\phi \sim \phi_0$, or equivalently $y \sim 0$. This gives rise to the following system of equations:

$$\begin{aligned}
\frac{Du}{Dt} - (f_0 + \beta y)v + (j_0 + \gamma y)w &= -\frac{1}{\rho}\frac{\partial p}{\partial x} \\
\frac{Dv}{Dt} + (f_0 + \beta y)u &= -\frac{1}{\rho}\frac{\partial p}{\partial y} \\
\frac{Dw}{Dt} - (j_0 + \gamma y)u &= -\frac{1}{\rho}\frac{\partial p}{\partial z} - g,
\end{aligned} \tag{6.2.3}$$

with the convective derivative given as usual by

$$\frac{D}{Dt} = \frac{\partial}{\partial t} + u\frac{\partial}{\partial x} + v\frac{\partial}{\partial y} + w\frac{\partial}{\partial z}. \tag{6.2.4}$$

Assuming incompressible flow, continuity gives

$$\frac{\partial u}{\partial x} + \frac{\partial v}{\partial y} + \frac{\partial w}{\partial z} = 0. \tag{6.2.5}$$

58

We non-dimensionalize as follows

$$u^* = Uu, \quad v^* = Uv, \quad w^* = U\frac{H}{L}w, \quad \frac{\partial}{\partial t^*} = \frac{U}{L}\frac{\partial}{\partial t},$$

$$\frac{\partial}{\partial x^*} = \frac{1}{L}\frac{\partial}{\partial x}, \quad \frac{\partial}{\partial y^*} = \frac{1}{L}\frac{\partial}{\partial y}, \quad \frac{\partial}{\partial z^*} = \frac{1}{H}\frac{\partial}{\partial z}. \tag{6.2.6}$$

Henceforth, starred variables are dimensional and unstarred non-dimensinal. H is a vertical length scale, L is a horizontal length scale, and U is a horizonal velocity scale. Two dimensionless numbers arise naturally from this system: the aspect ratio $\delta = H/L$ and the Rossby number $\hat{\epsilon} = U/f_0 L$. Working in the regime such that $\delta \ll \hat{\epsilon}$, we may ignore horizontal components of the Coriolis force, while the assumption that $\delta \ll \hat{\epsilon}^2$ gives as a consistent balance that vertical pressure gradients are entirely hydrostatic, viz.

$$\frac{1}{\rho}\frac{\partial p}{\partial z} + g = 0.$$

Integrating this last condition gives

$$\begin{aligned} p_1^* &= \rho_1 g(H_1 + \eta_1^* - z^* + H_2) \\ p_2^* &= \rho_1 g(H_1 + \eta_1^* - \eta_2^*) + \rho_2 g(H_2 + \eta_2^* - z), \end{aligned} \tag{6.2.7}$$

which when differentiated horizontally yields

$$\begin{aligned} \nabla_H p_1^* &= \rho_1 g \nabla \eta_1^* \\ \nabla_H p_2^* &= \rho_1 g \nabla \eta_1^* + (\rho_2 - \rho_1) g \nabla \eta_2^*. \end{aligned} \tag{6.2.8}$$

As the horizontal pressure gradients do not depend on z, from reexamining equations (6.2.3), it is consistent to assume that the horizontal velocities u and v are also independent of z. Thus

$$\frac{\partial}{\partial z}u_j = 0, \quad \frac{\partial}{\partial z}v_j = 0. \tag{6.2.9}$$

This gives for the first layer

$$\begin{aligned} \hat{\epsilon}\frac{D_1}{Dt}u_1 - (1 + \hat{\beta}y)v_1 &= -\frac{\partial}{\partial x}\eta_1 \\ \hat{\epsilon}\frac{D_1}{Dt}v_1 + (1 + \hat{\beta}y)u_1 &= -\frac{\partial}{\partial y}\eta_1, \end{aligned} \tag{6.2.10}$$

and for the second layer

$$\begin{aligned} \hat{\epsilon}\frac{D_2}{Dt}u_2 - (1 + \hat{\beta}y)v_2 &= -\frac{\partial}{\partial x}\eta_B \\ \hat{\epsilon}\frac{D_2}{Dt}v_2 + (1 + \hat{\beta}y)u_2 &= -\frac{\partial}{\partial y}\eta_B, \end{aligned} \tag{6.2.11}$$

where

$$\frac{D_j}{Dt} = \frac{\partial}{\partial t} + u_j\frac{\partial}{\partial x} + v_j\frac{\partial}{\partial y},$$ (6.2.12)

$$\eta_B = \eta_2 + \gamma\eta, \quad \eta = \eta_1 - \eta_2, \quad \gamma = \rho_1/\rho_2,$$ (6.2.13)

and we define a non-dimensional beta parameter

$$\hat{\beta} \equiv L\beta/f_0.$$ (6.2.14)

We integrate the continuity equation in the z-direction with boundary conditions

$$w_j = \frac{D_j\eta_j}{Dt}$$

at the top of the jth layer (simply the Lagrangian definition of velocity), and require no normal velocity through the bottom boundary, so $w = 0$ at $z = 0$. Then, for the first layer,

$$\hat{\epsilon}\frac{D_1}{Dt}\eta - (\frac{1}{F_1} + \hat{\epsilon}\eta)(\frac{\partial u_1}{\partial x} + \frac{\partial v_1}{\partial y}) = 0$$ (6.2.15)

and for the second layer

$$\hat{\epsilon}\frac{D_2}{Dt}\eta_2 - (\frac{1}{F_2} + \hat{\epsilon}\eta_2)(\frac{\partial u_2}{\partial x} + \frac{\partial v_2}{\partial y}) = 0$$ (6.2.16)

where the unnormalized Froude numbers, F_j, are defined

$$F_j = f_0^2 L^2/gH_j.$$ (6.2.17)

Note also that

$$\eta_1 = (1 - \gamma)\eta + \eta_B.$$ (6.2.18)

Note, the system of equations of the upper-layer derived here for a two layer system is equivalent to that for a one layer model with bottom topography η_B, upper surface displacement η and gravity $g' = (1 - \gamma)g$.

It is possible to transform the governing equations (primitive equations) into different coordinate systems. Common examples are pressure coordinates (x, y, p), where $p = p(x, y, z, t)$, or θ coordinates (x, y, θ), where $\theta = \theta(x, y, p, t)$ is potential temperature. In the pressure coordinates, we define a Lagrangian pressure velocity

$$\omega = \frac{Dp}{Dt} = \frac{D_H p}{Dt} - \rho g w.$$ (6.2.19)

using the equation of hydrostatic balance. Applying simple scaling arguments, it emerges that the relative importance of the two terms is vastly different for the Earth and Jupiter. On Earth,

$$\omega \simeq -\rho g w$$ (6,2.20)

while on Jupiter

$$\omega \simeq \frac{D_H p}{Dt}.$$ (6.2.21)

Thus ω has a different physical meaning when considered for the two atmospheres.

Note that the two layer shallow water system is formally applicable, even with $\rho_1/\rho_2 > 1$, as long as $\delta \ll \hat{\epsilon}$. Furthermore, we may even consider an unstably stratified two layer system with free lower boundary but rigid upper boundary. While at first this may seem to be unphysical, it may be a good model of the Jovian atmosphere, as the tropopause may act as a rigid upper boundary for atmospheric motions. The governing equations are the same as for the system developed here, with the exception that the layers are inverted and the signs of the Froude numbers reversed.

Quasigeostrophic system

We assume a scaling for the shallow water equations

$$\hat{\epsilon} \sim \hat{\beta} \ll 1, F_1 \sim F_2 \sim 1,$$ (6.2.22)

with expansion of variables in small quantities

$$u_j = u_j + \hat{\epsilon}u_j^{(1)} + \dots$$ (6.2.23)

To $O(1)$, this gives

$$u_j = -\frac{\partial \psi_j}{\partial y}, \quad v_j = \frac{\partial \psi_j}{\partial x},$$ (6.2.24)

where $\psi_1 = \eta_1$ and $\psi_2 = \eta_B$. To order $\hat{\epsilon}$, the equations are

$$\frac{\partial Q_j}{\partial t} + J(\psi_j, Q_j) = 0$$ (6.2.25)

where

$$Q_1 = \Delta_2 \psi_1 + \hat{F}_1(\psi_2 - \psi_1) + \beta y$$
$$Q_2 = \Delta_2 \psi_2 + \hat{F}_2(\gamma \psi_1 - \psi_2) + \beta y.$$ (6.2.26)

The horizontal Laplacian is defined

$$\Delta_2 = \frac{\partial^2}{\partial x^2} + \frac{\partial^2}{\partial y^2},$$ (6.2.27)

J is the Jacobian

$$J(\psi_j, Q) = \frac{\partial \psi}{\partial x}\frac{\partial Q}{\partial y} - \frac{\partial \psi}{\partial y}\frac{\partial Q}{\partial x},$$ (6.2.28)

$\beta = \hat{\beta}/\hat{\epsilon}$, and $\gamma = \rho_1/\rho_2$ as before. $\hat{F}_j = F_j/(1 - \gamma)$ is a normalized Froude number, which is implicitly approximately less than or equal to 1.

We note in passing that as $F_j = f_0^2 L^2/gH_j$, $\hat{F}_j = (L/L_{D_j})^2$, where

$$L_{D_j} = [(1 - \gamma)gH_j]^{\frac{1}{2}}/f_0 \qquad (6.2.29)$$

is the Rossby deformation radius characteristic of layer j, and that

$$\hat{F}_2/\hat{F}_1 = F_2/F_1 = H_1/H_2. \qquad (6.2.30)$$

An energy conservation equation can be derived as follows:

$$\left(\frac{\partial}{\partial t} + \frac{\partial}{\partial x}u_1 + \frac{\partial}{\partial y}v_1\right)\gamma K_1 + \left(\frac{\partial}{\partial t} + \frac{\partial}{\partial x}u_2 + \frac{\partial}{\partial y}v_2\right)(K_2 + P) = 0, \qquad (6.2.31)$$

where

$$K_j = \frac{1}{2F_j}(u_j^2 + v_j^2) \qquad (6.2.32)$$

is the kinetic energy of the fluid in layer j, and

$$P = \frac{1}{2(1 - \gamma)}(\psi_1 - \psi_2)^2. \qquad (6.2.33)$$

is the available potential energy. With unstable stratification, $\gamma > 1$, and so the available potential energy P is less than 0 (Yano, 1987a). This means that the differential heating will decrease the available potential energy under unstable stratification. Note that there is an extra positive 'available' potential energy due to this unstable stratification.

The quasi-geostrophic approximation can also be derived in terms of the pressure coordinates described above. For the Earth, the thermodynamic equation reduces to

$$\frac{D_H}{Dt}\left(\frac{\partial\phi}{\partial p}\right) + \frac{1}{F_p}\omega = 0 \qquad (6.2.34)$$

where F_p is the Froude number in pressure coordinates. Given the preceeding scaling analysis, whether this is an appropriate relation for Jovian (giant planet) atmospheres must be called into question.

QG linear dynamics

If we linearize the QG equations, we obtain

$$\frac{\partial}{\partial t}[\Delta_2\psi_1 + F_1(\psi_2 - \psi_1)] + \beta\frac{\partial\psi_1}{\partial x} = 0$$
$$\frac{\partial}{\partial t}[\Delta_2\psi_2 + F_2(\psi_1 - \psi_2)] + \beta\frac{\partial\psi_2}{\partial x} = 0 \qquad (6.2.35)$$

or, with an ansatz for the functional dependences of $\sim \exp[i(\omega t + kx + ly)]$,

$$\omega[-K^2\psi_1 + \hat{F}_1(\psi_2 - \psi_1)] + k\beta\psi_1 = 0$$
$$\omega[-K^2\psi_2 + \hat{F}_2(\gamma\psi_1 - \psi_2)] + k\beta\psi_2 = 0 \qquad (6.2.36)$$

where $K^2 = k^2 + l^2$. The determinant of the solvability condition of these relations leads to the general dispersion relation for Rossby waves.

There are two instructive limiting cases. Firstly, in the limit $\gamma \to 1$ we recover conventional quasi-geostrophy. The two solutions are the barotropic mode

$$\omega = k\beta/K^2, \quad \psi_1 = \psi_2, \qquad (6.2.37)$$

and the baroclinic mode

$$\omega = k\beta/(K^2 + \hat{F}_1 + \hat{F}_2), \quad F_1\psi_2 + F_2\psi_1 = 0. \qquad (6.2.38)$$

The second useful limit is for a deep lower layer, when $\hat{F}_2 \to 0$. This gives

$$\omega = k\beta/(K^2 + \hat{F}_1), \quad \psi_2 \to 0, \qquad (6.2.39)$$

implying no flow in the lower layer. This is the reduced gravity limit.

Note that, with unstable stratification, because $\gamma > 1$, and $\hat{F}_1 = F_1/(1 - \gamma)$, it follows that $\hat{F}_1 < 0$. Thus the solution for ω is discontinuous. This corresponds to a change in the direction of propagation of Rossby waves.

Solitary Wave Theory

We begin exploring models of the GRS from the **soliton**, because it is a most extensively studied permanent wave solution. Redekopp (1977) was the first to derive a KdV equation from the quasi-geostrophic (QG) equation. For brevity, we consider the equivalent barotropic QG system. The governing equation is given by

$$[\frac{\partial}{\partial t} + J(\eta, \cdot)](\nabla^2 - \hat{F})\eta + \frac{\hat{\beta}}{\hat{\epsilon}}\eta_x = 0. \tag{6.3.1}$$

Here, η is the displacement of the surface from a mean state. We divide the flow into the mean zonal state

$$-\int U dy \tag{6.3.2a}$$

and eddy perturbations about this mean. The perturbations are expressed as an expansion in a small parameter ϵ (note: implicitly $\hat{\epsilon} \ll \epsilon \ll 1$):

$$\epsilon\eta^{(1)} + \epsilon^2\eta^{(2)} + O(\epsilon^3). \tag{6.3.2b}$$

By transforming the derivatives by

$$\frac{\partial}{\partial t} = -c\frac{\partial}{\partial x} + \epsilon^{3/2}\frac{\partial}{\partial \tau}, \tag{6.3.3a}$$

$$\frac{\partial}{\partial x} = \epsilon^{1/2}\frac{\partial}{\partial \xi}, \tag{6.3.3b}$$

we obtain to leading order $O(\epsilon^{1/2})$

$$[\frac{d^2}{dy^2} - \hat{F} + \frac{\hat{\beta}/\hat{\epsilon} + \hat{F}U - U''}{U - c}]\phi = 0, \tag{6.3.4a}$$

where the leading order eddy is assumed to be of the form:

$$\eta^{(1)} = A(\xi, \tau)\phi(y) \tag{6.3.4b}$$

Note that (6.3.4a) with appropriate boundary conditions defines an eigenvalue problem for the phase velocity c. The equation for the wave modulation A is given at $O(\epsilon^{3/2})$ by

$$\frac{\partial}{\partial \tau}(\frac{\partial^2}{\partial y^2} - \hat{F})\eta^{(1)} + (U - c)\frac{\partial^3}{\partial \xi^3}\eta^{(1)}$$

$$+ \frac{\partial \eta^{(1)}}{\partial \xi}\frac{\partial}{\partial y}(\frac{\partial^2}{\partial y^2} - \hat{F})\eta^{(1)} - \frac{\partial \eta^{(1)}}{\partial y}\frac{\partial}{\partial \xi}(\frac{\partial^2}{\partial y^2} - \hat{F})\eta^{(1)} \tag{6.3.4c}$$

$$+ \frac{\partial}{\partial \xi}[(U - c)(\frac{\partial^2}{\partial y^2} - \hat{F}) + (\frac{\hat{\beta}}{\hat{\epsilon}} + \hat{F}U - U'')]\eta^{(2)} = 0.$$

64

A solvability condition for $\eta^{(2)}$ is obtained by multiplying (6.3.4c) with $\eta^{(1)}/(U - c)$, and integrating in the y-direction. Finally, we obtain the KdV equation

$$A_\tau + pAA_\xi + qA_{\xi\xi\xi} = 0 \qquad (6.3.5)$$

for a nonlinear Rossby wave, where

$$p = \frac{< \frac{\phi^3}{U-c} \frac{\partial}{\partial y}\left(\frac{\hat{\beta}/\hat{\epsilon}+\hat{F}U-U''}{U-c}\right) >}{< \left(\frac{\hat{\beta}/\hat{\epsilon}+\hat{F}U-U''}{U-c}\right)\frac{\phi^2}{U-c} >}$$

$$q = \frac{< \phi^2 >}{< \left(\frac{\hat{\beta}/\hat{\epsilon}+\hat{F}U-U''}{U-c}\right)\frac{\phi^2}{U-c} >},$$

and $< \cdot >$ denotes integration in y-direction over the domain.

Examples of the solutions obtained are shown in Fig. 3.1. Here, the anticyclonic zonal flow $U = \mathrm{sn}(y \mid m)$, defined in terms of the Jacobian elliptic function with $m = 0.1$, is assumed. The solutions are classified into two types. The E-soliton: an anticyclonic vortex-wave, containing closed elliptically shaped streamlines, which drifts relatively slowly westward ($-0.437 < c < 0$); and the D-soliton: a depressive wave with reversed flow fore and aft of the wave center. Fig. 3.1 (a) and (b) show the fastest-propagating eigenmodes of (3.4a) with a different beta ($\hat{\beta} = 0.3$ and 0.6, respectively). Each of them corresponds to an E-soliton and a D-soliton. Fig. 3.1 (c) shows the second fastest-propagating mode of (3.4): a modulated E-soliton.

Maxworthy and Redekopp (1976) were the first to seek a description of the GRS as a Rossby wave soliton. The morphological similarity of the GRS to the E-soliton and of the South Tropical Disturbance (ʒ. Peek, 1958; Hirabayashi, 1981) to the D-soliton was noted.

Redekopp and Weidman (1978) considered the interactions of two Rossby solitons. In place of the single vortex solution (6.3.4b), they postulated a two vortex solution

$$\psi = \sum_{n=1}^{2} A_n(x,t)\phi_n(y)p_n(z). \qquad (6.3.6)$$

After similar manipulation as in Redekopp (1977), a pair of KdV equations [1]

$$A_{1,t} + c_1A_{1,x} = \epsilon(2r_1A_1A_{1,x} + \lambda_1A_1A_{2,x} + \nu_1A_2A_{1,x} + s_1A_{1,xxx}) \qquad (6.3.7a)$$

$$A_{2,t} + c_12_{2,x} = \epsilon(2r_2A_2A_{2,x} + \lambda_2A_2A_{1,x} + \nu_2A_1A_{2,x} + s_2A_{2,xxx}) \qquad (6.3.7b)$$

are obtained, where λ_i, ν_i ($i = 1,2$) are the coefficients representing the magnitude of the interactions. By expanding the amplitudes A_1 and A_2 in terms of ϵ, the interactions can be described analytically in full. In particular, to leading order, a single soliton solution is

---

[1] Note that the phase velocities c_1 and c_2 are different by factor of order u. while (6.3.5) can just describe the solitons of the phase velocity c in leading order.

recovered for both of the solutions A_i ($i = 1, 2$) propagating with phase velocities c_i. The process of the interactions is described as a higher order perturbation.

The examples of the interactions of the two E-solitons, calculated from (6.3.7a, b) by a perturbation approach, are represented in Fig. 3.2. In Fig. 3.2(a) a very strong soliton 'meets' a weak soliton: at the colliding stage, the weak soliton is completely overwhelmed by the stronger one. Fig. 3.2(b) is an intermediate case: a medium size soliton 'meets' a large soliton. The medium soliton is absorbed by the larger one, as both of them approach, but at the peak of the colliding stage ($t = 0$), the center of both of the solitons can be distinguished. Fig. 3.2(c) is the case of two nearly equal solitons. At $t = -60$, the smaller of the two 'stretches out an arm' to the larger. However, the arm is not persistent, it soon disappears by $t = -40$. The collision is very weak ($t = 0$), and the former one exchanges into the latter one without much overlapping during the collision. Note the evolution after the collision is reproduced by just turning the figure up-side-down, and reversing the x-direction. Features of the interactions of the Rossby solitons are qualitatively in agreement with those of the usual KdV-solitons described by Eq. (3.5). The main difference is found in the phase shifting: both Rossby solitons can be shifted in the same direction during the interaction, as shown at the bottom of each figures.

Maxworthy et al. (1978) elaborate on their rationale to model the GRS as a Rossby soliton. They speculate that a marginally unstable shear flow maintains the GRS-soliton against its dissipation. They also supplement their arguments with observations of the interaction of the South Tropical Disturbance and the GRS in terms of soliton theory. They particularly remarked that both of them experience positive phase jumps after the interaction.

Generality of KdV Dynamics

The derivation of the KdV equation by Redekopp (1977) was based on the skillful scale transformation (3.3a, b). The physical basis of thi- -aling is not obvious. In this section, we turn to the physics underlying the derivat: ιd address the generality of soliton dynamics in geophysical flows in this section.

The KdV equation describes the balance between nonlinearity of the form $\eta\eta_x$ and dispersion of the form η_{xxx}. Dispersion of this type is allowed in large scale geophysical flows by the dispersion relationship of the Rossby waves. This is obtained by linearizing (3.1), and assuming a plane wave solution $\sim \exp[ikx + ily - i\omega t]$

$$\omega = -\frac{k\hat{\beta}}{\hat{\epsilon}} \frac{1}{k^2 + l^2 + \hat{F}}. \tag{6.3.9}$$

When the inequality

$$k^2 \ll l^2 + \hat{F} \tag{6.3.10a}$$

is satisfied, then the dispersion relation is approximated by

$$\omega \simeq -\frac{k\hat{\beta}/\hat{\epsilon}}{l^2 + \hat{F}}(1 - \frac{k^2}{l^2 + \hat{F}}). \tag{6.3.10b}$$

The second term is proportional to k^3 and corresponds to the term η_{xxx} in the KdV equation.

Inequality (6.3.10a) implies that a weak dispersion is obtained by stretching the scale of the x-coordinate compared to that of the y-coordinate by factor, say, $r^{-1}(\gg 1)$ i.e.

$$\frac{\partial}{\partial x} \to r\frac{\partial}{\partial x}, \qquad k \to rk.$$

Consequently, the magnitude of the weak dispersion is measured by

$$\Delta\omega \sim \frac{r^3 k^3}{(l^2 + \hat{F})^2}\frac{\hat{\beta}}{\hat{\epsilon}} \sim r^3\frac{\hat{\beta}}{\hat{\epsilon}}\hat{s}^2$$

by assuming $(l^2 + F)^2 \sim \hat{s}$, where $\hat{s} \equiv \hat{F}^{-1}$.

On the other hand, the magnitude of the nonlinear advection term is measured by

$$(\mathbf{v} \cdot \nabla)\zeta \sim \left(\frac{\partial\eta}{\partial x}\frac{\partial\nabla^2\eta}{\partial y} - \frac{\partial\eta}{\partial y}\frac{\partial\nabla^2\eta}{\partial x}\right) \sim r\epsilon, \tag{6.3.11}$$

where ϵ has been introduced in Eq. (6.3.2b). Consequently, the balance between the weak dispersion and the nonlinear advection requires

$$r^3\frac{\hat{\beta}}{\hat{\epsilon}}\hat{s}^2 \sim r\epsilon, \quad \text{or} \quad \epsilon \sim r^2\frac{\hat{\beta}}{\hat{\epsilon}}\hat{s}^2.$$

In particular, for the QG regime with $\hat{\beta} \sim \hat{\epsilon} \ll \hat{s} \sim 1$, we obtain

$$\epsilon \sim r^2, \quad \text{or} \quad r \sim \epsilon^{1/2},$$

recovering Redekopp's scaling (6.3.3b). For consistency the slow time scale is scaled by

$$\frac{\partial}{\partial\tau} \sim r^3 \sim \epsilon^{3/2}$$

in accordance with (6.3.3a).

By performing this type of a general systematic scaling analysis, we can define the domain of the validity of the soliton dynamics in the nondimensional parameter space $(\hat{\epsilon}, \hat{\beta}, \hat{s}, r, \epsilon)$ characterizing the geophysical flows. Care should be taken in performing this type of analysis. For example, in turns out that a naive scale estimate of the vorticity advection given by (6.3.11) is not always true. Without the basic zonal flow $U(y)$, this type of nonlinearity identically vanishes in leading order. The point is easily confirmed by setting $U \equiv 0$ in (6.3.4a). In this case, the leading order linear eigenvalue problem (6.3.4a) reduces to a Helmholtz equation for the y-dependence, which allows the replacement of ∇^2 by a constant in the nonlinear advection term. The nonlinear advection term may be recovered by taking into account the β-effect in the expression of the vorticity, namely

$$\zeta = \nabla \cdot \left(\frac{\nabla\eta}{1 + \hat{\beta}y}\right).$$

This correction leads to a nonvanishing vorticity advection term even within a weak basic zonal flow.

The parameter ranges of this general analysis is represented in Fig. 3.3, where the classifications of the KdV-Rossby solitons are made in the $(\hat{\epsilon}, \hat{s})$-plane. The nonlinearities responsible for a KdV-type balance in each domain are depicted along with an appropriate name for the domain. The particular scaling adopted in previous studies is represented by small closed circles with the name of the authors. The three typical dynamical regimes (QG, IG, PG) defined for geophysical flows are indicated by open circles. It is seen that the vorticity advection term is responsible for the primary nonlinearity in the regimes of $\hat{s} \geq \hat{\beta}$. However, it is due to the existence of the basic zonal flow only in $\hat{\epsilon} \geq \hat{\beta}^2$, while the existence of $\hat{\beta}$ is imperative in $\hat{\epsilon} < \hat{\beta}^2$. On the other hand, with a weaker stratification (i.e. $\hat{s} < 1$), another nonlinearity, the wave steepening term, denoted by $\hat{\beta}v\eta$ in Fig. 3.3, becomes a dominant term. The source of this nonlinearity, absent in QG dynamics, can be traced by approximating the potential vorticity:

$$Q \equiv \frac{1 + \hat{\beta}y + \hat{\epsilon}\zeta}{1 + \frac{\hat{\epsilon}}{\hat{s}}\eta} = (1 + \hat{\beta}y + \hat{\epsilon}\zeta)(1 - \frac{\hat{\epsilon}}{\hat{s}}\eta) + O(\frac{\hat{\epsilon}^2}{\hat{s}^2})$$

$$= 1 + \hat{\beta}y + \hat{\epsilon}(\zeta - \frac{1}{\hat{s}}\eta) - \frac{\hat{\epsilon}\hat{\beta}}{\hat{s}}y\eta + O(\frac{\hat{\epsilon}^2}{\hat{s}}).$$

The first four terms correspond to the QG potential vorticity, while the advection of the fifth term leads to the wave-steepening term of the form $\hat{\beta}v\eta$.

The main point of Fig. 3.3 is that KdV-type solitons are possible for every basic state $U(y)$ according to shallow water theory, with their amplitude restricted by higher nonlinearities, as shown in Fig. 3.4 for the case of $\hat{\epsilon} = 0$ (without basic zonal flow). Fig. 3.4 suggests the existence of a unique dynamical regime with an isotropic scaling ($r = 1$) characterized by KdV-dynamics. The primary nonlinearity is the wave steepening effect $\hat{\beta}v\eta$. The balance of the nonlinearity with the dispersion term yields

$$\epsilon\hat{\beta} \sim \frac{\hat{\beta}}{\hat{\epsilon}}\hat{s}^2$$

or $\epsilon\hat{\epsilon} \sim \hat{s}^2$ with an isotropic scaling. This curve is represented by a thick line in Fig. 3.4. It is seen that we obtain KdV-dynamics in the range $\epsilon\hat{\epsilon} \sim \hat{s}^2 < \hat{\beta}^2$ with isotropic scaling. Within this range we can identify a dynamical regime characterized by the balance of the meridional twisting term $\hat{\beta}y\eta_x$ of the β-advection[2] to the dynamics. This condition is

---

[2] The meridional twisting term $\hat{\beta}y\eta_x$ is obtained as a higher order correction to the β-advection term $\hat{\beta}v$, by taking into account a correction of the meridional velocity v:

$$v = \frac{\eta_x}{1 + \hat{\beta}y} \simeq (1 - \hat{\beta}y)\eta_x.$$

The first order correction to $\hat{\beta}$ corresponds to the term in concern.

satisfied for $\hat{\beta} \sim \hat{s}$. This identifies the Intermediate Geostrophic (IG) regime at $\epsilon\hat{\epsilon} \sim \hat{s}^2$, $\hat{\beta} \sim \hat{s} \ll 1$ as a regime uniquely characterized by KdV-dynamics. The IG regime was originally identified by Yamagata (1982) and Flierl (1980).

IG Dynamics

The IG dynamics identified by Yamagata (1982) and Flierl (1980) can be considered as a generalized-version of the KdV-dynamics with isotropic scaling. In this section we derive the governing equation for the IG dynamics, and review the numerical results of Matsuura and Yamagata (1982) and Williams and Yamagata (1984).

The system adopted to derive the equation for the IG system is that of shallow water theory:

$$\hat{\epsilon}\frac{D}{Dt}u - (1 + \hat{\beta}y)v = -\eta_x \qquad (6.3.12a)$$

$$\hat{\epsilon}\frac{D}{Dt}v + (1 + \hat{\beta}y)u = -\eta_y \qquad (6.3.12b)$$

$$\frac{D}{Dt}\eta + (\frac{\hat{s}}{\hat{\epsilon}} + \eta)(u_x + v_y) = 0, \qquad (6.3.12c)$$

where

$$\frac{D}{Dt} \equiv \frac{\partial}{\partial t} + u\frac{\partial}{\partial x} + v\frac{\partial}{\partial y}. \qquad (6.3.12d)$$

(We set $\eta_B \equiv 0$ in (2.18) and consider only the upper layer in the two–layer formulation of Sec. 2)

We assume the scaling $\hat{\epsilon} \sim \hat{\beta}^2$ and $\hat{s} \sim \hat{\beta}$, and reduce the system (6.3.12) ordered by $\hat{\beta}$, e.g.

$$u = u^{(0)} + \hat{\beta}u^{(1)} + \cdots.$$

At $O(1)$ we obtain geostrophic balance:

$$u^{(0)} = -\eta_y^{(0)}, \qquad v^{(0)} = \eta_y^{(0)}. \qquad (6.3.13)$$

At $O(\hat{\beta})$:

$$-yv^{(0)} - v^{(1)} = -\eta_x^{(1)} \qquad (6.3.14a)$$

$$+yu^{(0)} + u^{(1)} = -\eta_y^{(1)} \qquad (6.3.14b)$$

$$(\frac{\partial}{\partial t} + u^{(0)}\frac{\partial}{\partial x} + v^{(0)}\frac{\partial}{\partial y})\eta^{(0)} + \frac{\hat{s}\hat{\beta}}{\hat{\epsilon}}(u_x^{(1)} + v_y^{(1)}) = 0. \qquad (6.3.14c)$$

By substituting the expression for $u_x^{(1)} + v_y^{(1)}$ obtained from (6.3.14a, b) into (6.3.14c), and by taking into account the identity $u^{(0)}\frac{\partial}{\partial x}\eta^{(0)} + v^{(0)}\frac{\partial}{\partial y}\eta^{(0)} = 0$, we obtain the linear Rossby wave equation:

$$(\frac{\partial}{\partial t} - \frac{\hat{s}\hat{\beta}}{\hat{\epsilon}}\frac{\partial}{\partial x})\eta^{(0)} = 0,$$

which implies homogeneous propagation with phase speed $c = \hat{s}\hat{\beta}/\hat{\epsilon}$. This necessitates the introduction of a slow time scale $\partial/\partial t \equiv \hat{\beta}\partial/\partial\tau$.

The $O(\hat{\beta}^2)$-equations are

$$\frac{\hat{\epsilon}}{\hat{\beta}^2}\frac{D^{(0)}}{Dt}u^{(0)} - yv^{(1)} - v^{(2)} = -\eta_x^{(2)} \tag{6.3.15a}$$

$$\frac{\hat{\epsilon}}{\hat{\beta}^2}\frac{D^{(0)}}{Dt}v^{(0)} + yu^{(1)} + u^{(2)} = -\eta_y^{(2)} \tag{6.3.15b}$$

$$\frac{D^{(0)}}{Dt}\eta^{(1)} + (\frac{\partial}{\partial\tau} + u^{(1)}\frac{\partial}{\partial x} + v^{(1)}\frac{\partial}{\partial y})\eta^{(0)} +$$

$$+\frac{\hat{s}\hat{\beta}}{\hat{\epsilon}}(u_x^{(2)} + v_y^{(2)}) + \eta^{(2)}(u_x^{(1)} + v_y^{(1)}) = 0. \tag{6.3.15c}$$

By substituting the expression for $u_x^{(2)}+v_y^{(2)}$ obtained from (6.3.15a, b), and the expressions for $u^{(1)}$ and $v^{(1)}$ obtained from (6.3.14a, b) into Eq. (6.3.15c), we finally obtain

$$\frac{\hat{\beta}}{\hat{s}}\frac{\partial\eta}{\partial\tau} - \frac{\hat{\beta}}{\hat{s}}\eta\eta_x - \frac{\hat{s}\hat{\beta}}{\hat{\epsilon}}\frac{\partial}{\partial x}\nabla^2\eta + \frac{2\hat{\beta}^2}{\hat{\epsilon}}y\eta_x - J(\eta, \nabla^2\eta) = 0, \tag{6.3.16}$$

where the superscript $^{(0)}$ has been removed in the final expression. This we denote the Yamagata-Flierl equation, governing the Intermediate Geostrophic scale dynamics.

The first three terms of (6.3.16) constitute a KdV equation. The fourth term is the meridional twisting term, and the fifth term is the vorticity advection term. Because of the scalar nonlinearity of the wave-steepening term (the second term), the equation represents an asymmetry between positive ($\eta > 0$) and negative ($\eta < 0$) displacements. A single soliton solution is allowed for an elevation (anticyclone) but not for a depression (cyclone). This *cyclone-anticyclone asymmetry* is a special characteristic of IG dynamics.

Numerical computations performed by Matsuura and Yamagata (1982) that demonstrate this asymmetry are shown in Fig. 3.5. Note that the isolated cyclone decays rapidly by radiating waves (Fig. 3.5(a)), while the isolated anticyclone is stable (Fig. 3.5(b)).

This asymmetry of the IG vortices may hold the key in explaining the observed robustness and longevity of anticyclones (spots) compared to the cyclones (barges) in the Jovian atmosphere. For this reason, Williams and Yamagata (1984) performed a series of numerical computations that interpret the Jovian vortices as IG vortices.

Fig. 3.6 shows the collision of two IG vortices. Here, again, another remarkable property of the IG vortices is displayed. Unlike the Rossby solitons, the two IG vortices coalesce together as a consequence of the interactions. They end up a single large vortex, because, despite the KdV-dynamics ensured by the first three terms of the Yamagata-Flierl equation, the vorticity advection terms plays an active role during the collision process. This feature of the theory is reminiscent of the absorption by the GRS of small vortices which were observed during the Voyager encounter (Smith, et al., 1979). [3]

---

[3] The detail of collision results depends sensitively to the vortex size, and the IG vortices can behave both as if like solitary waves and the elastic waves by depending on choice of the parameters (Sutyrin).

Problems with the Weakly Nonlinear Assumption

The weakly nonlinear assumption led to canonical solutions. However, there are difficulties in the interpretation of the GRS in the framework of weakly nonlinear theory. A crucial assumption of the weakly nonlinear theories is that the phase velocity c of the vortex is much faster than the typical swirling velocity u of the vortex itself (i.e. $|c| \gg u$)[4].

Inspection of Table 3.1 gives $c = -3$ ms^{-1} and $u \sim 100$ ms^{-1} for the GRS. Consequently, for the GRS the assumptions of weakly nonlinear theory are formally violated. This necessitates the consideration of strongly nonlinear theory with $|c| \ll u$.

A main physical difference of the strongly nonlinear eddies from the weak theories is that fluid material is trapped within the vortex and is carried along as the vortex propagates. The strongly nonlinear version of IG theory (GG) will be presented in the next lecture.

Appendix: The Jovian regime

In this appendix, we present the appropriate scales required for the specification of the nondimensional parameters $\hat{\epsilon}$, $\hat{\beta}$, $\hat{s}$ for the Jovian atmospheres (Jupiter and Saturn) in comparison with the Earth's atmosphere and oceans. The basic physical values required for the scalings are listed in Table 3.2. Most of the values for Jupiter and Saturn are well established. The only remaining uncertainties are the vertical potential temperature gradient $d\theta_s/dz$ and the vertical scale D. To obtain conservative estimates, we adopt the largest possible value of $d\theta_s/dz$ and the smallest possible value for D. We assume $d\theta_s/dz = 1$ K km^{-1} for both Jupiter and Saturn. This value corresponds to tropospheric values for both atmospheres. A tendency towards neutrality is expected at deeper levels. Hence the value adopted is the maximum possible value. On the other hand, for the vertical scale D, we simply take a temperature scale height RT/g, which is 20 km and 35 km for Jupiter and Saturn, respectively. A larger vertical extent of the motions is likely.

Fig. 3.7 shows the dependence of the nondimensional parameters on the horizontal scale L for the Earth (a), the oceans (b), and Jupiter (c). The case for Saturn is not shown due to its general resemblance to Jupiter. A deformation radius of $L_R = 50$ km is assumed for the terrestrial ocean. The dynamical regimes QG (Quasi-Geostrophic), IG (Intermediate Geostrophic), and PG (Planetary Geostrophic) are labeled at a corresponding scale in Fig. 3.7 (a), (b). The appropriateness of the IG scale of the oceans is noted. On the other hand, this simple scaling does not lead to any conventional dynamical regime for Jupiter. Instead, we find a new dynamical regime denoted TG (Thermo-Geostrophic) at a scale of 3000 km, with a scaling $\hat{s} \leq \hat{\epsilon} \sim \hat{\beta}$. This scaling is characterized by a very weak

---

[4] However, the IG theory is a special case that, though it is a weakly nonlinear theory in nature, it does satisfy the scaling $c \sim u$. Due to a special choice of the horizontal scale in IG, the leading nonlinearity is due to the advection of the pressure anomaly, which turns into a trivial statement $J(\psi, \psi) = 0$ in the shallow water formulation of IG. Note that this brings a complexity to generalizing the IG theory to a multiple–layer system.

stratification $\hat{s} \ll 1$. It is weaker than that required for the validity of IG scaling, and leads to dynamics completely governed by a thermodynamic equation

$$\frac{D}{Dt}\frac{\partial \eta}{\partial z} = 0,$$

where $\partial \eta / \partial z$ is the potential temperature (η is reinterpreted as a geopotential).

The nature of the TG dynamics is considered in Yano (1987b; 1989). This regime does not sustain any shallow isolated vortices within the deep barotropic shearing flows; instead the vortex is stretched out by the shear.

It transpires that the recovery of the QG or IG scale requires a larger vertical scale D, probably least of the order $D \sim 10^2$ km (c. f. Dowling and Ingersoll, 1989).

The major conclusion of this appendix is that the scale–analysis does not work well to define the Jovian dynamical regime and to narrow down a possible choice for the model of the GRS.

Table 3.1: Basic Parameters for Jupiter's Great Red Spot (GRS) and the White Oval BC

	GRS	White Oval
Longitudinal Scale	2.42×10^4 km	9.78×10^3 km
Latitudinal Scale	1.12×10^4 km	5.86×10^3 km
Latitude	21°S	32°S
Wind Speeds (Outer Edges)	100–120 m/s	80–100 m/s
Phase Velocity	−3 m/s	+5 m/s

Table 3.2a: Values of physical quantities

	Ω (s^{-1})	g (m/s^2)	r_0	θ_s	$d\theta_s/dz$ (K/km)	D (km)	U (m/s)
Earth	7.3×10^{-5}	9.8	6400 nm	300 K (ground)	2.1	10	10
Jupiter	1.8×10^{-4}	27	71000 km	140 K (500 mb)	(1)	20	100
Saturn	1.6×10^{-4}	12	58000 km	110 K (500 mb)	(1)	35	100

Table 3.2b: Values of non–dimensional parameters and Rossby radius for $\phi_0 = 30°$

	$L\hat{e}$ (km)	$L^2 \hat{S}$ (km^2)	L_r (km)
Earth	1.4×10^2	1.3×10^6	1100
Jupiter	5.6×10^2	2.4×10^6	1500
Saturn	6.3×10^2	5.2×10^6	2300

References

Achterberg, R. K., and A. P. Ingersoll, 1989: A normal-mode approach to Jovian atmospheric dynamics. *J. Atmos. Sci.*, **46**, 2448-2462.

Busse, F. H., 1976: A simple model of convection in the Jovian atmosphere. *Icarus*, **29**, 155-160.

Dowling, T. E., and A. P. Ingersoll, 1989: Jupiter's Great Red Spot as a shallow water system. *J. Atmos. Sci.*, **46**, 3256-3278.

Flierl, G. R., 1980: Introduction to Coherent Features. *1980 Summer Study Program in Geophysical Fluid Dynamics*, Woods Hole Oceanographic Institution.

Gierasch, P. J., and R. M. Goody, 1969: Radiative time constants in the atmosphere of Jupiter. *J. Atmos. Sci.*, **26**, 445-454.

Hirabayashi, I., 1981: Jupiter and its observations, in "Planetary Guide Book 2", Koubundo-Shiko-sha (in Japanese).

Matsuura, T., and T. Yamagata, 1982: On the evolution of nonlinear planetary eddies larger than the radius of deformation. *J. Phys. Oceanogr.*, **12**, 440-456.

Maxworthy, T., and L. G. Redekopp, 1976: A solitary wave theory of the Great Red Spot and other observed features in the Jovian atmosphere. *Icarus*, **29**, 261-271.

Maxworthy, T., L. G. Redekopp, and P. D. Weidman, 1978: On the production and interaction of planetary solitary waves. *Icarus*, **33**, 388-409.

Pedlosky, J., 1987: *Geophysical Fluid Dynamics*, 2nd. ed., Springer-Verlag.

Peek, B. M., *The Planet Jupiter*, Faber and Faber, England, 1958.

Redekopp, L. G., 1977: On the theory of solitary Rossby waves. J. Fluid Mech. **87**, 725-745.

Redekopp, L. G., and P. D. Weidman, 1978: Solitary Rossby waves in zonal shear flows and their interactions. *J. Atmos. Sci.*, **35**, 790-804.

Rhines, P. B., 1975: Waves and turbulence on a beta plane. J. Fluid Mech. **69**, 417-443.

Smith, B. A., et al., 1979: The Jupiter system through the eyes of Voyager 1. *Science*, **204**, 951-972.

Smith, B. A., et al., 1989: Voyager 2 at Neptune: Imaging science results. *Science*, **246**. 1422-1449;

Williams, G. P., 1978: Planetary circulations: 1. Barotropic representations of Jovian and terrestrial turbulence. *J. Atmos. Sci.*, **35**, 1399-1426.

Williams, G. P., and T. Yamagata, 1982: Geostrophic regimes, intermediate solitary vortices and Jovian eddies. *J. Atmos. Sci.*, **41**, 453-478.

Yamagata, T., 1982: On nonlinear planetary waves: A class of solutions missed by the quasi-geostrophic approximation. *J. Oceanogr. Soc. Japan*, **38**, 236-244.

Yano, J. I., 1987a: Rudimentary considerations of the dynamics of Jovian atmospheres. Part I: The depth of motions and energetics. *J. Meteor. Soc. Japan*, **65**, 313-327.

Yano, J. I., 1987b: Rudimentary considerations of the dynamics of Jovian atmospheres. Part II: Dynamics of the atmospheric layer. *J. Meteor. Soc. Japan*, **65**, 313-327.

Yano, J.-I., and Y. N. Tsujimura, 1987: The domain of validity of the KdV-type solitary Rossby waves in the shallow water β-plane model, Dyn. Atmos. Oceans **11**, 101-129.

Figure Captions

Fig. 1.1: Different views of the internal dynamics of Jovian planets. a) Columnar convection cells (From Busse, 1976). b) Boundary plumes. c) Taylor plumes.

Fig. 1.2: Structure of vertical normal modes for Jupiter for Rossby radius of deformation of 735 km (solid line) and 155 km (dotted line). (From Achterberg and Ingersoll, 1989).

Fig. 3.1: Examples of single Rossby soliton solutions. The channel domain $-\pi/2 < y < \pi/2$ is assumed. (From Redekopp and Weismann, 1978).

Fig. 3.2: Interactions of two Rossby E-solitons. (From Redekopp and Weismann, 1978).

Fig. 3.3: The classifications of the Rossby solitons on the $(\hat{\epsilon}, \hat{s})$-plane. Responsible nonlinearities leading to a KdV-type balance in each domain are depicted along with an appropriate naming of the domain. The particular scalings adopted in the previous studies are represented by small closed circles with the name of the authors. The three typical dynamical regimes (QG, IG, PG) defined for the geophysical flows are indicated by open circles. (From Yano and Tsujimura, 1987).

Fig. 3.4: The domain of the validity of the KdV-type Rossby solitons on the $(\epsilon\hat{\epsilon}, \hat{s})$-cross section. The invalidated domains are shaded with an indication of a reason. The broad curve represents the scalings lead to a KdV-type balance with an isotropic scaling (i.e. $r = 1$). In the upper part to the broad curve, the longitudinal stretching (i.e. $r \ll 1$) is required for the KdV balance, while in the lower part to the broad curve the north-south elongation (i.e. $r \gg 1$) is necessitated. In the shaded ares, some remarks to explain the effects to destroy a complete KdV balance are added. Some scalings adopted in the previous studies are also depicted. (From Yano and Tsujimura, 1987).

Fig. 3.5: The cyclone-anticyclone asymmetry of the IG vortices: the stability of (a) the cyclone, (b) the anticyclone. (From Matsuura and Yamagata, 1982).

Fig. 3.6: Collisions of the IG vortices: anticyclone and anticyclone within an anticyclonic flow. (From Williams and Yamagata, 1984).

Fig. 3.7: The dependence of the non-dimensional parameters on the horizontal scale L. (a) Earth, (b) oceans, (c) Jupiter. (From Yano, 1987b.)

Notes compiled by Richard Holme and Petros Ioannou

74

Fig 1.1

Fig 1.2

Fig 3.1

Fig 3.2

ŝ

β-Soliton

$(\tilde{v}\cdot\tilde{v})_\zeta$ (only by $\hat{\beta}$-term)

Clarke(1971), Yamagata(1962)

Shear Soliton (Strong Stratification)

$(\tilde{v}\cdot\tilde{v})_\zeta$ (due to shear)

Long(1964), Larsen(1965), Benny(1966)

Redekopp(1977)

Q. G.

Divergent Soliton

$(\tilde{v}\cdot\tilde{v})_\zeta$ (only by $\hat{\beta}$-term) $\hat{v}n$

Nogami(1982, 1983)

I. G.

Nogami (1982, 1983)

Divergent Soliton $\hat{v}n$

(North-South Elongated Soliton)

Shear Soliton (Weak Stratification)

$\hat{s}-1$

$\hat{s}-\hat{\beta}$

$\hat{\epsilon}-\hat{\beta}^2$

$\hat{\epsilon}-\hat{\beta}$

$\hat{\epsilon}$

P. G.

Fig 3.3

$\hat{S}$

(a)

Clarke (1971)

Yamagata (1982)

$r << 1$

1

Nogami (1982, 1983)

$\hat{\beta}$

$r = 1$
$(\hat{\epsilon} \sim \hat{\beta}^2)$

$r >> 1$

I.G.

$J(n, n_{xx})$ enters the equation

Basic Flow is essential for Dispersion

$\hat{\beta}^2$

$\hat{\beta}$

1

$Q.G.$

$J(n, n_{xx})$ enters the equation

Basic Flow is essential for Nonlinearity

Dispersion is too Strong

$\hat{\epsilon}\hat{\epsilon}$

P.G.

North-South Elongated Soliton

Fig 3.4

Fig 3.5

Fig 3.6

(a) Earth's Atmosphere

(b) Oceans

(c) Jupiter

Fig 3.7

Lecture 7 — Dynamics of Vortices - Continued

Compacting Conditions of Vortices

To investigate the longevity of the analytical vortices obtained in the previous lecture it will be informative to obtain the compacting conditions for the various flow regimes studied. These are the conditions for wavelike disturbances to be evanescent with distance from the vortex, in which case there may be no radiation of energy to the far field.

For Rossby wave radiation the dispersion relation is,

$$c = -\frac{\beta}{\kappa^2 + F}, \tag{7.1.1}$$

with compacting condition, $\kappa^2 < 0$ as $r \to \infty$ in the case of zero basic flow. Defining similar properties for a sinusoidal basic zonal flow, $u = \sin(ky)$, so that,

$$\bar{c} = -\frac{\beta}{k^2 + \bar{F}}, \tag{7.1.2}$$

for the mean flow "phase speed", $\bar{c}$, and applying a matching condition $c = \bar{c}$, gives,

$$F > k^2 + \bar{F}, \tag{7.1.3}$$

as the compacting condition. From this it is required that $F > k^2 \approx O(1)$ (so that $L > L_R$: the Intermediate Geostrophic regime) and that $F > \bar{F} \approx 0$ (barotropic basic flow as in the model of Ingersoll and Cuong,1981).

Various laboratory analogues have been created to investigate large vortices in rotating systems (figure 1). These are summarised in table 1. Note that the only case satisfying the given compacting condition of a baroclinic vortex in a barotropic basic flow is that of Nezlin et al.

Numerical Investigations.

In a numerical simulation of Read and Hide's experiment (figure 2) it can be seen that the vortex breaks down by radiation of energy to the basic flow. In this case the ratio of upper layer depth to lower layer depth, δ, is greater than zero, implying a baroclinic basic flow, and the froude number, F, is greater than one, implying a baroclinic vortex. Vortex collapse is expected since the system does not obey the compacting conditions stated previously.

Further numerical simulations illustrate the influence of varying F and δ. The analogue of the Ingersoll/Cuong (1981) model is that of figure 3a in which $\delta = 0$ and $F=5$: it can be seen that the vortex and basic flow persist. As F decreases ($F=1$ in figure 3b and $F=0.5$ in figure 3c) at $\delta = 0$, the vortex decays, progressively faster with F. The radiation is asymmetric due to the effect of β.

The implication of these examples is that a persistent vortex such as Jupiter's Great Red Spot must have a high F. It is not sufficient to consider the vortex or the basic flow as being stable in isolation as their interaction may yield instability. It is also essential

to be aware of the lower layer dynamics when this layer is finite. The physical tendency will be for a baroclinic disturbance (isolating and evanescent) to develop into a barotropic standing wave which will then radiate. The timescale for this decay will be δ^{-1}. Energy may be radiated to the far field in the lower layer while the upper layer far field appears undisturbed. In figure 4a ($\delta = 0.2$ and $F=5$) the vortex decays without apparent radiation of energy into the upper layer basic flow. Figure 4b shows the lower layer eddy flow for this example and shows radiation of energy away from the locality of the vortex. Graphs of vortex decay rate with varying δ and F are given in figure 5. The decay time of vortices is $O(\delta^{-1})$. An example is also given of the barotropic breakdown of a flow containing a baroclinic eddy (figures 6a, 6b; $\delta = 0.2$, $F = 5$, $\beta = 0.3$).

The role of the deep dynamics of Jupiter's interior may have a strong bearing on the stability of the Great Red Spot. The value of β for deep cylindrical flow would be different than that for the weather layer. A further numerical simulation illustrates how differing values of β for the two layers may stabilise a system which would otherwise break down (figure 7; $\delta = 0.2$, $F = 5$, $\beta_1 = 0.3, \beta_2 = -2$). It remains an outstanding problem to work out a compacting condition for a deeply rooted Great Red Spot.

The Flierl–Stern–Whitehead Theorem.

For a steadily-propagating "strongly-compacting" vortex in a shallow (ie $H/L << 1$), primitive equation system it is shown that,

$$\beta \int \rho \psi' d^3 r = 0 \tag{7.3.1}$$

where,

$$\psi' \equiv \psi - \overline{\psi} \tag{7.3.2}$$

As an exercise this theorem may be proved for a QG 2 layer system (Hint: multiply by x and integrate over the whole horizontal domain). The theorem becomes,

$$\frac{1}{\hat{F}_1} < \psi'_1 > + \frac{1}{\hat{F}_2} < \psi'_2 >= 0. \tag{7.3.3}$$

Another Look at the Compacting Condition - a Unified View for Weakly and Strongly Nonlinear Theories

The QG theory follows,

$$[\frac{\partial}{\partial t} + J(\psi,.)]Q = 0. \tag{7.4.1}$$

In the weakly nonlinear theory,

$$\psi = \overline{\psi}(y) + \epsilon\phi, Q = \overline{Q}(y) + \epsilon q, \tag{7.4.2}$$

from which, to first order in ϵ (the zero order part being trivial),

$$[\frac{\partial}{\partial t} + J(\overline{\psi},.)]q + J(\phi,\overline{Q}) = 0 \tag{7.4.3}$$

For steady, propagating solutions, write $\frac{\partial}{\partial t} = -c\frac{\partial}{\partial x}$ and obtain,

$$J(\tilde{\overline{\psi}}, q - \Lambda\phi) = 0, \tag{7.4.4}$$

where $\Lambda = \partial\overline{Q}/\partial\tilde{\overline{\psi}}$ and $\tilde{\overline{\psi}} = \overline{\psi} - cy$. From this obtain, using the expression for $q(\phi)$,

$$[\Delta - (F + \Lambda)]\phi + F\phi_2 = 0, \tag{7.4.5}$$

or,

$$(\Delta + k^2)\phi + F\phi_2 = 0, \tag{7.4.6}$$

where $k^2 = -(F + \frac{\partial\overline{Q}}{\partial\overline{\psi}})$ so that,

$$c - \overline{u} = -\frac{\overline{Q}_y}{k^2 + F}. \tag{7.4.7}$$

It is apparent that $\overline{Q}_y$ is an equivalent β. The sign of k^2 will determine the nature of solutions to (7.4.4). A 'potential well' of $k^2 > 0$ bounded by regions of $k^2 < 0$ is of physical interest in describing compacting systems.

For the strongly nonlinear theory, write,

$$J(\tilde{\psi}, Q) = 0, \tilde{\psi} = \psi - cy, \tag{7.4.8}$$

as before, so that $Q = Q(\tilde{\psi})$. Then,

$$Q(\tilde{\psi}) \approx \tilde{\psi}\frac{dQ}{d\tilde{\psi}} + \frac{1}{2}\tilde{\psi}^2\frac{d^2Q}{d\tilde{\psi}^2} + O(\tilde{\psi}^3) \tag{7.4.9}$$

which gives,

$$[\Delta - (F + \Lambda)]\tilde{\psi} - \frac{1}{2}\Lambda'\tilde{\psi}^2 = (Fc - \beta)y - F\psi_2 \tag{7.4.10}$$

where $\Lambda = dQ/d\tilde{\psi}$. A compacting solution requires $F + \Lambda > 0$ in the exterior field while $F + \Lambda$ may be negative locally. Note that a sufficient condition for steady flow, by Arnold's 2nd theorem is now that $F + \Lambda$ be everywhere of the same sign.

The "modon" formulation is that in which it is taken that $Q = \Lambda\tilde{\psi}$ in the above, where Λ is a constant and

$$F + \Lambda = \begin{cases} -k^2, & r < r_0 \\ \mu^2, & r > r_0. \end{cases} \tag{7.4.11}$$

This has n-pole solutions of the form,

$$\psi = \Sigma J_n(kr)\sin(n\theta); r < r_0$$
$$\psi = \Sigma K_n(\mu r)\sin(n\theta); r > r_0. \tag{7.4.12}$$

Other Compacting Conditions.

The Yamagata–Flierl system,

$$\frac{\hat{\beta}}{\hat{s}}\frac{\partial \eta}{\partial \tau} - \frac{\hat{\beta}}{\hat{s}}\eta\eta_x - \frac{\hat{s}\hat{\beta}}{\hat{\epsilon}}\frac{\partial}{\partial x}\nabla^2\eta + \frac{2\hat{\beta}^2}{\hat{\epsilon}}y\eta_x - J(\eta, \nabla^2\eta) = 0, \tag{\; \;}$$

may be shown (take $\frac{\partial}{\partial \tau} = -c\frac{\partial}{\partial x}$ and linearise) to be,

$$[\nabla^2 + (\frac{\hat{\epsilon}}{\hat{s}^2}c - \frac{2\hat{\beta}}{\hat{s}}y)]\psi = 0. \tag{7.5.2}$$

It can be shown that the system is radiating at, say, $y < y_c$ (Nycander and Sutyrin, 1992).

The generalised geostrophic system is a strongly nonlinear form of the intermediate geostrophic equations:

$$\hat{\epsilon}u_t - (1 + \hat{\epsilon}\zeta + \hat{\beta}y)v = -B_x$$
$$\hat{\epsilon}v_t + (1 + \hat{\epsilon}\zeta + \hat{\beta}y)u = -B_y \tag{7.5.3a,b,c}$$
$$\frac{D}{Dt}\psi + (\frac{1}{\hat{\epsilon}\hat{F}} + \psi)(u_x + v_y) = 0,$$

where $\zeta = v_x - u_y, B = \eta + \hat{\epsilon}K$ and $K = \frac{u^2 + v^2}{2}$. From these,

$$u = -\frac{B_y + \hat{\epsilon}v_t}{1 + \hat{\epsilon}\zeta + \hat{\beta}y}$$
$$v = \frac{B_x + \hat{\epsilon}u_t}{1 + \hat{\epsilon}\zeta + \hat{\beta}y}. \tag{7.5.4a,b}$$

These are applied iteratively. The first approximation is,

$$u = -\frac{B_y}{1 + \hat{\beta}y}$$
$$v = \frac{B_x}{1 + \hat{\beta}y} \tag{7.5.5a,b}$$

The next approximation (substitute these back into the previous forms) give an improved expression for u and v which may be rearranged to yield the Sutyrin–Nycander equation. This equation system contains a class of semi-analytical solutions similar to the modons in QG formulation.

Stationary Barotropic Modon Solutions.

The phase speed, c, for the modon formulation already introduced (see Eq. 7.4.11, 7.4.12) and the froude number, F, are both taken to be zero, so that

$$(\Delta - \Lambda)\psi + (\Lambda\overline{u} + \beta)y = 0 \qquad (7.6.1)$$

implying $\Lambda\overline{u} + \beta = 0$. Consequently, a westerly flow will be radiating and an easterly flow compacting. It is left as an exercise to derive the dipole modon solution under this formulation, illustrated in figure 8. Figures 9 and 10 illustrate a possible physical example of modons in the form of an atmospheric "blocking high".

Functional Relationship for the GRS and White Ovals

Analysis of Voyager data by Dowling and Ingersoll (1989) determined the relationship between potential vorticity (Q) and the streamfunction (ψ). This effort indicated that $Q(\psi)$ could be approximately modeled by piecewise, linear functions for four different regions: the interior region (I), the outer ring of the spot (C), and the northern (N) and southern (S) exterior regions (figure 11). In terms of $\delta Q/\delta\psi + F$, this system can be modeled by:

$$\frac{\delta Q}{\delta\psi} + F \approx \begin{cases} \mu^2, & r < r_1(\theta) \text{ interior} \\ 0, & r_1(\theta) < r < r_2(\theta) \text{ ring} \\ -k^2, & r_2(\theta) < r \text{ exterior} \end{cases} \qquad (7.7.1)$$

This simple modelling of the Jovian vortices suggests several interesting analytical problems relating to these spots which could be undertaken. An intriguing point in this observational analysis is that the interior is evanescent and the external region is of the radiating structure.

Exercise

Derive a GRS-modon solution using the above assumptions for the following cases: i) QG case (cf Yano and Flierl) ii) GG case (replace ψ by B, etc.) (cf Nynander and Sutyrin, 1992). Of particular interest is the dynamical role of the 'neutral' ring, the stability of the system (cf Arnol'ds theorem), and the estimate of F_θ obtained from fitting the analytical solution to observational data (c. f. the project report by Doug Parker in this volume).

Exercise

Extend the modon formulation to the unsteady case. The typical situation is for a vortex to radiate energy in the form of Rossby waves, causing the vortex to decay. In trying to apply the modon approach to this situation, useful limits may be the case where b approaches zero, or when $\hat{\beta}$ approaches zero (c.f. Flierl, 1984). An extension of this would be to investigate the Rossby wave decay of the GG vortex, where the vortex is baroclinic while the mean flow is barotropic and quasi-geostrophic. In this case, a suggested approach is to look at the limit where $H_1/H_2 \ll 1$.

Contour Dynamics

For time-dependent 'modon' problems such as those previously suggested, the easiest approach with which to determine the time-evolution is contour dynamics. The 'modon' formulation says:

$$Q = Q_0 + \frac{\delta Q}{\delta \psi} \psi \tag{7.8.1}$$

with both Q_0 and $\delta Q/\delta \psi$ piecewise constant. By setting $\delta Q/\delta \psi$ equal to zero, the formulation reduces to a vortex of constant potential vorticity Q_1 in a constant background Q_0. With the vortex boundary defined by:

$$\mathbf{r}_b = (x_b(t), y_b(t)) \tag{7.8.2}$$

the evolution of the vortex shape is calculable from:

$$\dot{x}_b = -\frac{\partial}{\partial x} \psi(x_b, y_b, t)$$
$$\dot{y}_b = \frac{\partial}{\partial y} \psi(\neg_b, y_b, t) \tag{7.8.3a, b}$$

where

$$Q(\psi) = \begin{cases} Q_1 & |\mathbf{r}| < |\mathbf{r}_b| : \quad \Omega_1 \\ Q_0 & |\mathbf{r}| > |\mathbf{r}_b| : \quad \Omega_0 \end{cases} \tag{7.8.4}$$

Alternatively, this can be expressed by:

$$\psi(\mathbf{r}, t) = \sum_{j=1}^{N} \int\!\!\int_{\Omega_j} Q_j G(\mathbf{r}, \mathbf{r}') d^2\mathbf{r}' \tag{7.8.5}$$

for a N–vortex system (with each vortex area is defined by Ω_j ($j = 1, \cdots, N$)), where the Green function $G(\mathbf{r}, \mathbf{r}')$ is defined by

$$\mathbf{Q}_r[G(\mathbf{r}, \mathbf{r}')] = \delta(\mathbf{r} - \mathbf{r}') \tag{7.8.6}$$

with an operator $\mathbf{Q}_r$ defining the potential vorticity.

Exercise

Derive the explicit form of the Green's function in the two-layer QG system.

Vortex Mergers

The merging of vortices is a common feature on Jupiter, most notably with regard to the Great Red Spot absorbing small storms in its latitude range. It is possible to do a wide variety of numerical simulations of vortex mergers, studying the effects of the relative size of the vortices and whether they are baroclinic or barotropic. A potentially realistic simulation of the process by which the GRS merges with small eddies may be done with a large ($F = 2$ for example), baroclinic vortex and a small barotropic vortex within a barotropic shear flow. With such simulations it may be possible to determine the conditions needed for vortices to merge. Studies of these conditions in the case of no shear flow have been undertaken for equal size vortices by Polvani, et al. (1989) and for different sizes by Yasuda and Flierl (1993).

Exercise

The study of the vortex merging conditions within shearing flows is relevant to a problem with the size distribution of vortices on Jupiter. If the larger vortices are the result of multiple mergers of smaller vortices, it would be expected that the number of vortices of a given size would increase monotonically with decreasing radius. However, the actual distribution of vortices on Jupiter appears to have a peak at some radius, after which the number of vortices of a given size decreases with decreasing radius. If some form of merging function were known, then the following equation would be applicable:

$$\frac{\partial}{\partial t} N(r) = \int_{r'} M(r', r - r'; r) - \int_{r'} M(r, r' - r; r') + S(r) \qquad (7.9.1)$$

where $N(r)$ is the size distribution, M is the merging function, and $S(r)$ is the actual distribution of vortices on Jupiter. Ideally, the difference between the expected distribution and the actual one would be explained by the rapid merging of smaller vortices up to some length scale, leading to a relatively low number of small vortices. Therefore, an analysis of vortex merging in shear flows from the limit of $r_1 >> r_2$ to simulations when $r_1 = r_2$ could lead to a merging function that may be realistically tested by observations of the Jovian atmosphere.

Cloud Dynamics on Jupiter

One of the many basic problems remaining in geophysical fluid dynamics is the motions of clouds in the atmosphere of Jupiter, in particular the vertical motions and structure. This is a highly complex problem, involving radiative cooling, latent heating, precipitation, adiabatic warming and cooling, and various atmospheric layers of different moisture content and temperatures. The various features of this problem are shown in figure 12, and a possible modeling approach in figure 13. This is just one of the many phenomena whose dynamics need to be understood in a basic manner before a detailed, successful Jovian global computational model can be developed.

90

References.

Butchart, N., Haines, K., and Marshall, J. C. (1989). A Theoretical and Diagnostic Study of Solitary Waves and Atmospheric Blocking. *J. Atmos. Sci.* **43**, 2063-2078.

Dowling, T.E. and Ingersoll, A.P. (1989). Jupiter's Great Spot as a shallow water system. *J. Atmos. Sci.* **46**, 3256-3278.

Flierl, G. R. (1984). Rossby wave radiation from a strongly nonlinear warm eddy. *J. Phy. Oceanogr.* **14**, 47-58.

Flierl, G. R., Stern, M. E., and Whitehead, Jr., J. A. (1983). The physical significance of modons: laboratory models and general integral constraints. *Dyn. Atmos. Oceans* **7**, 233-263.

Nycander, J., and Sutyrin, G. G. (1992). Steadily translating anticyclones on the beta plane. it Dyn. Atmos. Ocean **16**, 473-498.

Polvani, L. M., Zabusky, N. J., and Flierl, G. R. (1989). Two-layer geostrophic vortex dynamics. Part I: Upper layer V-states and merger. *J. Fluid Mech.* **205**, 215-242.

Yasuda, I., and Flierl, G. R. (1993). Two dimensional asymmetric vortex merger. *J. Fluid Mech.* submitted.

Notes compiled by Ray leBeau and Douglas Parker
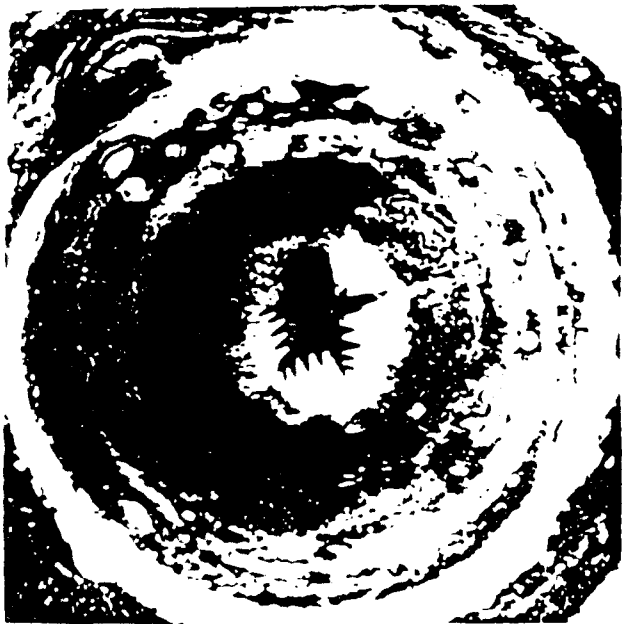
Nezlin, et al., three designs
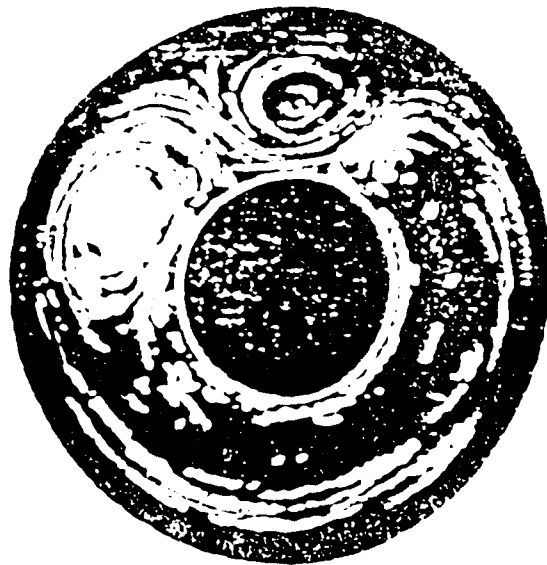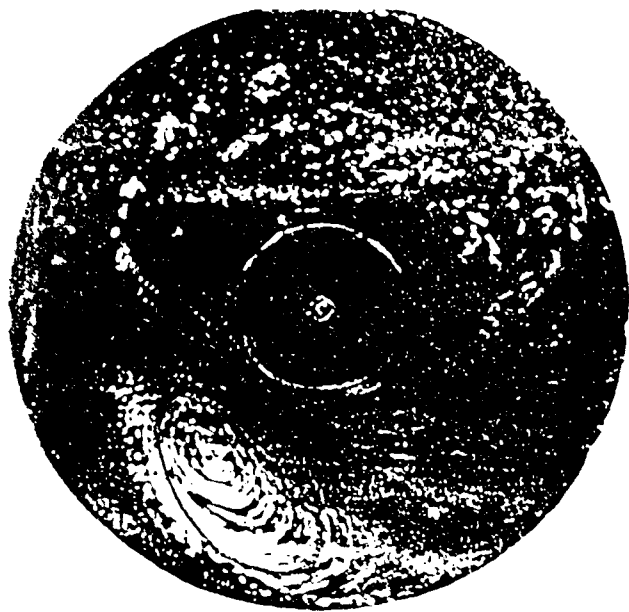
Sommeria, et al.

Nezlin, et al., No. 10
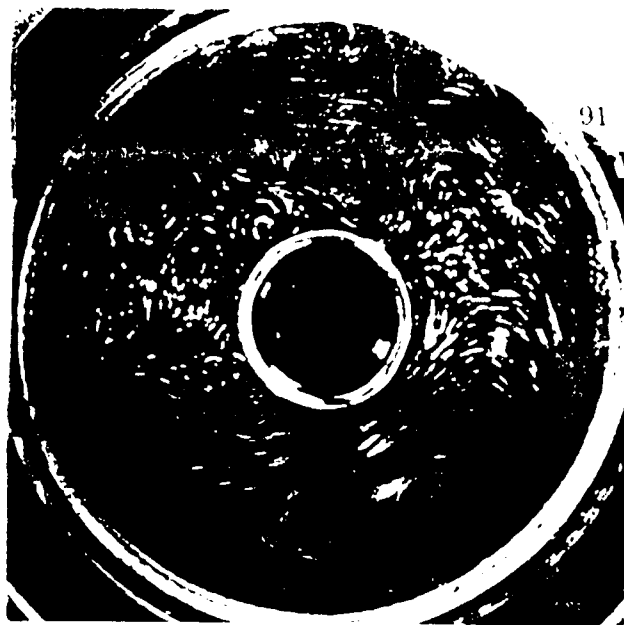
Read & Hide

Jupiter

Figure 1 Laboratory Analogues to the Great Red Spot

Laboratory Experiments

Settings	Read & Hide	Nezlin, et al.		Sommeria, et al.	Actual GRS Jupiter
	Continuously stratified w/heating and cooling	Shallow Water (Free Surface)		Shallow Water Pumping = Decaying	
Scale	QG	IG	(Free Decay)	QG	
Basic Flow	Baroclinic	None	Baroclinic	Barotropic	Barotropic
Vortex	Baroclinic	Baroclinic	Baroclinic	Barotropic	Baroclinic
Compacting	N/A	O.K.	Δ?	N/A	Ingersoll & Cuong (?)

Table 1 Characteristics of Laboratory Analogues
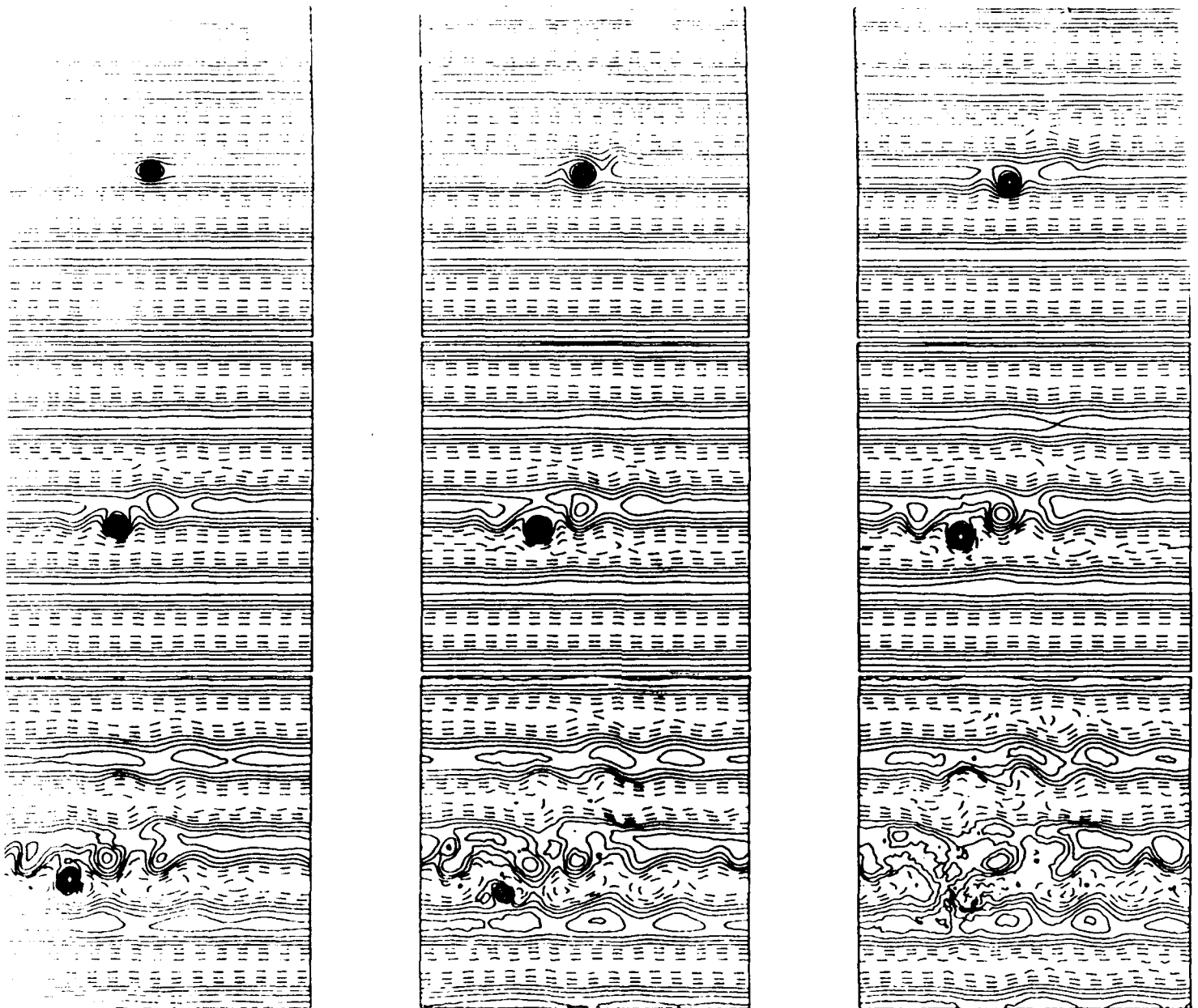
Figure 2 Numerical Simulation of Read & Hide

Baroclinic basic flow with a baroclinic eddy
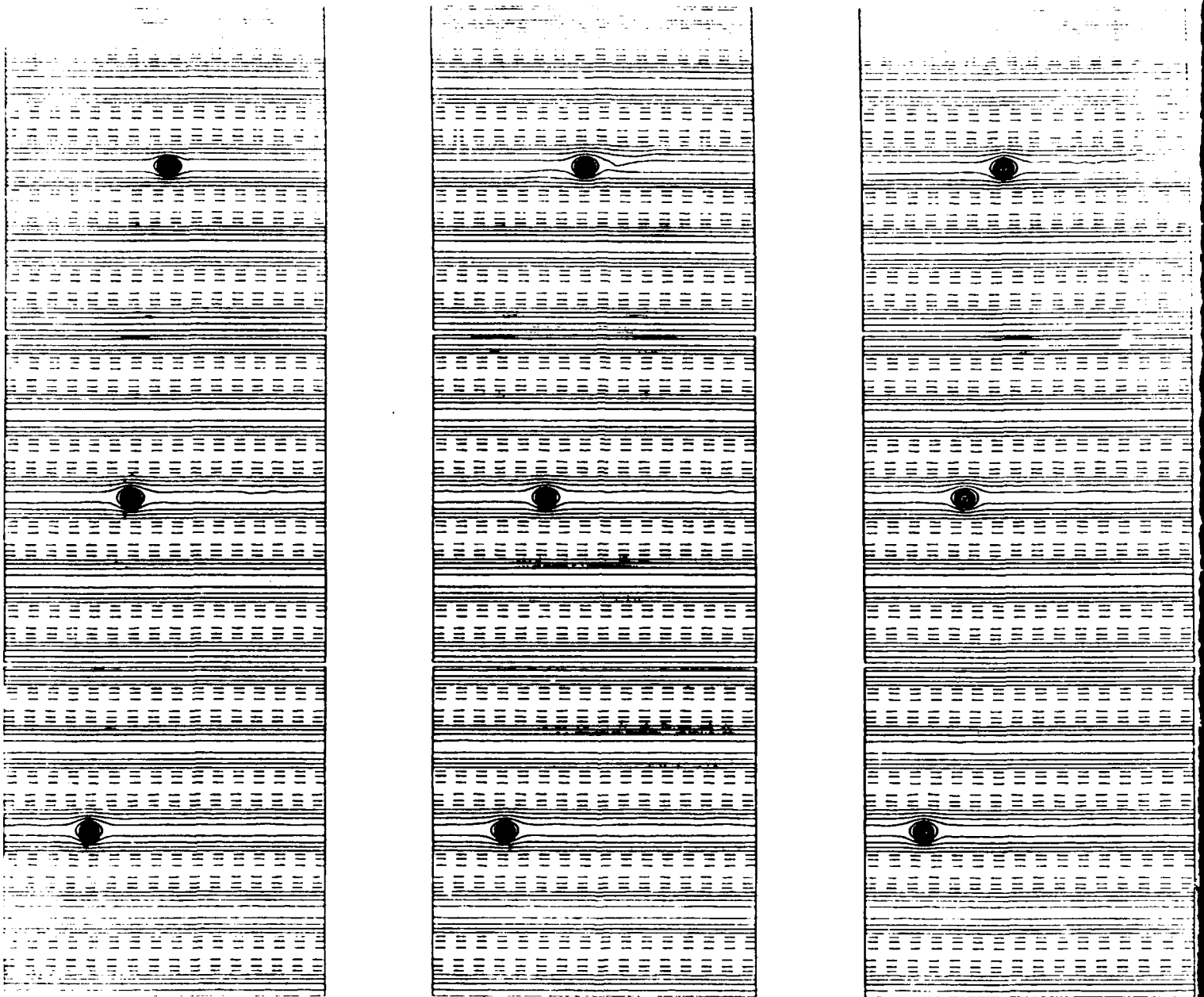
Figure 3a Numerical Simulation of Ingersoll & Cuong

Barotropic basic flow with a baroclinic eddy, $\delta = 0$, $F = 5$
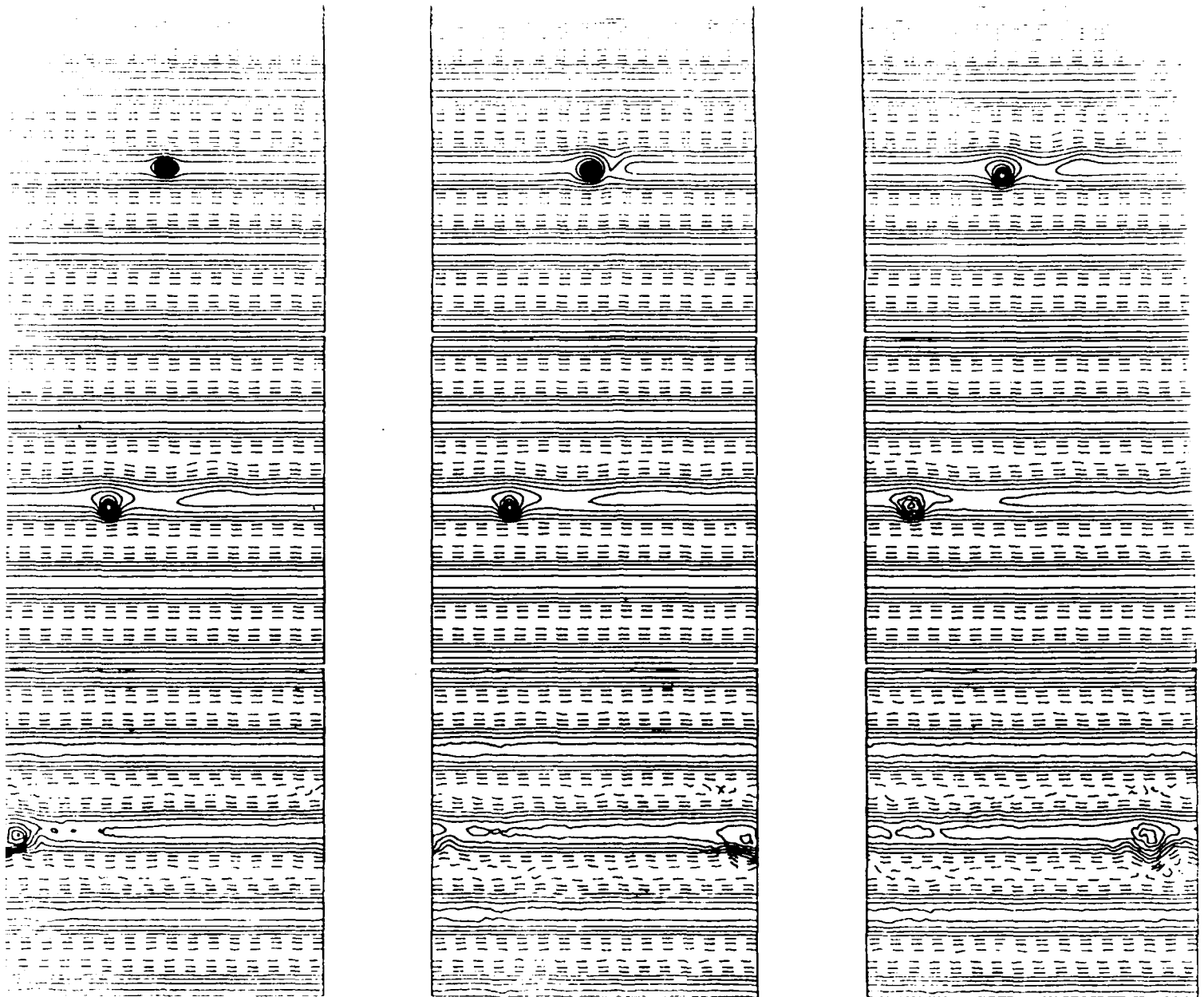
Figure 3b Numerical Simulation of Ingersoll & Cuong

Barotropic basic flow with a baroclinic eddy, $\delta = 0$, $F = 1$
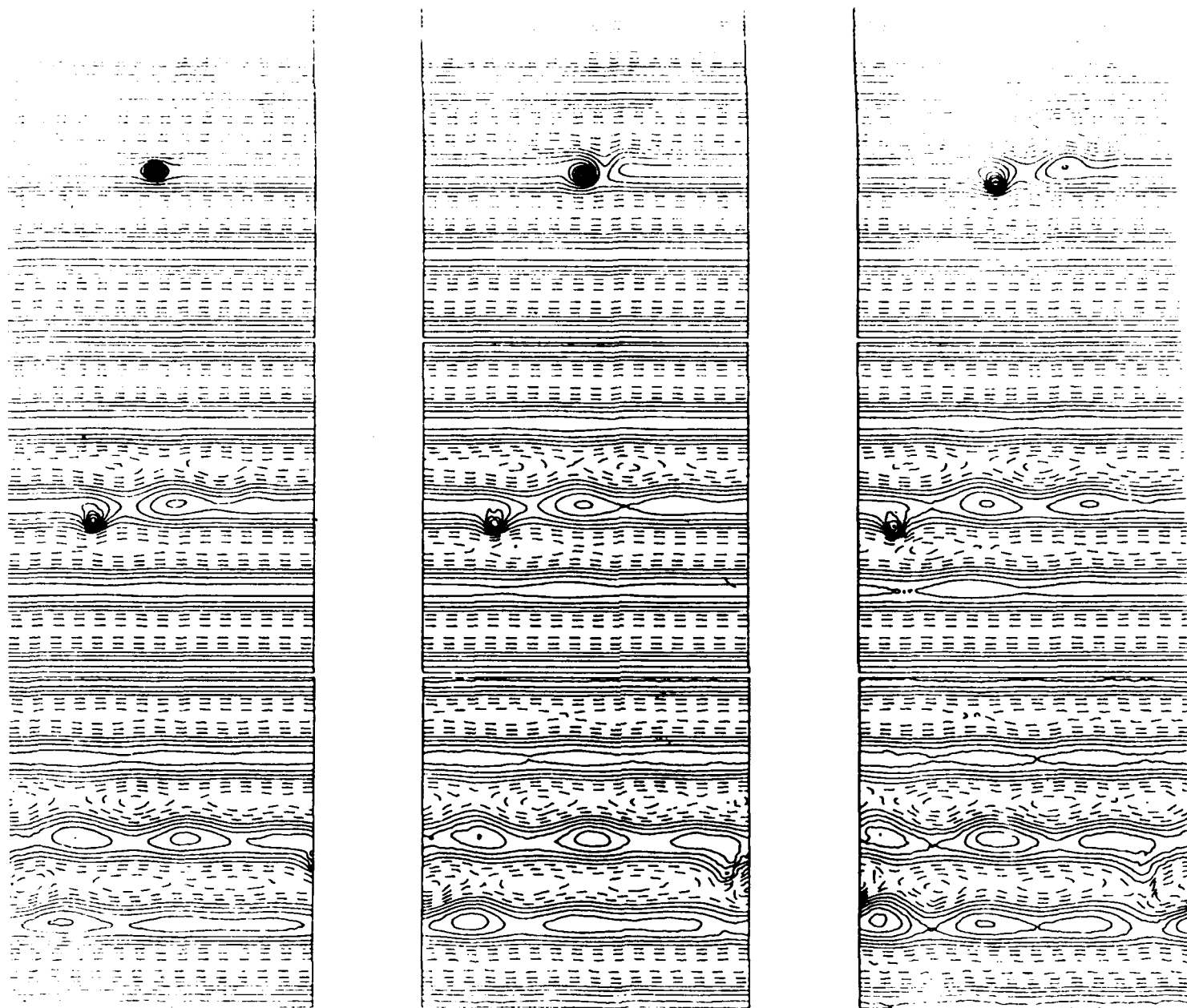
Figure 3c Numerical Simuation of Ingersoll & Cuong

Barotropic basic flow with a baroclinic eddy, $\delta = 0$, $F = 0.5$
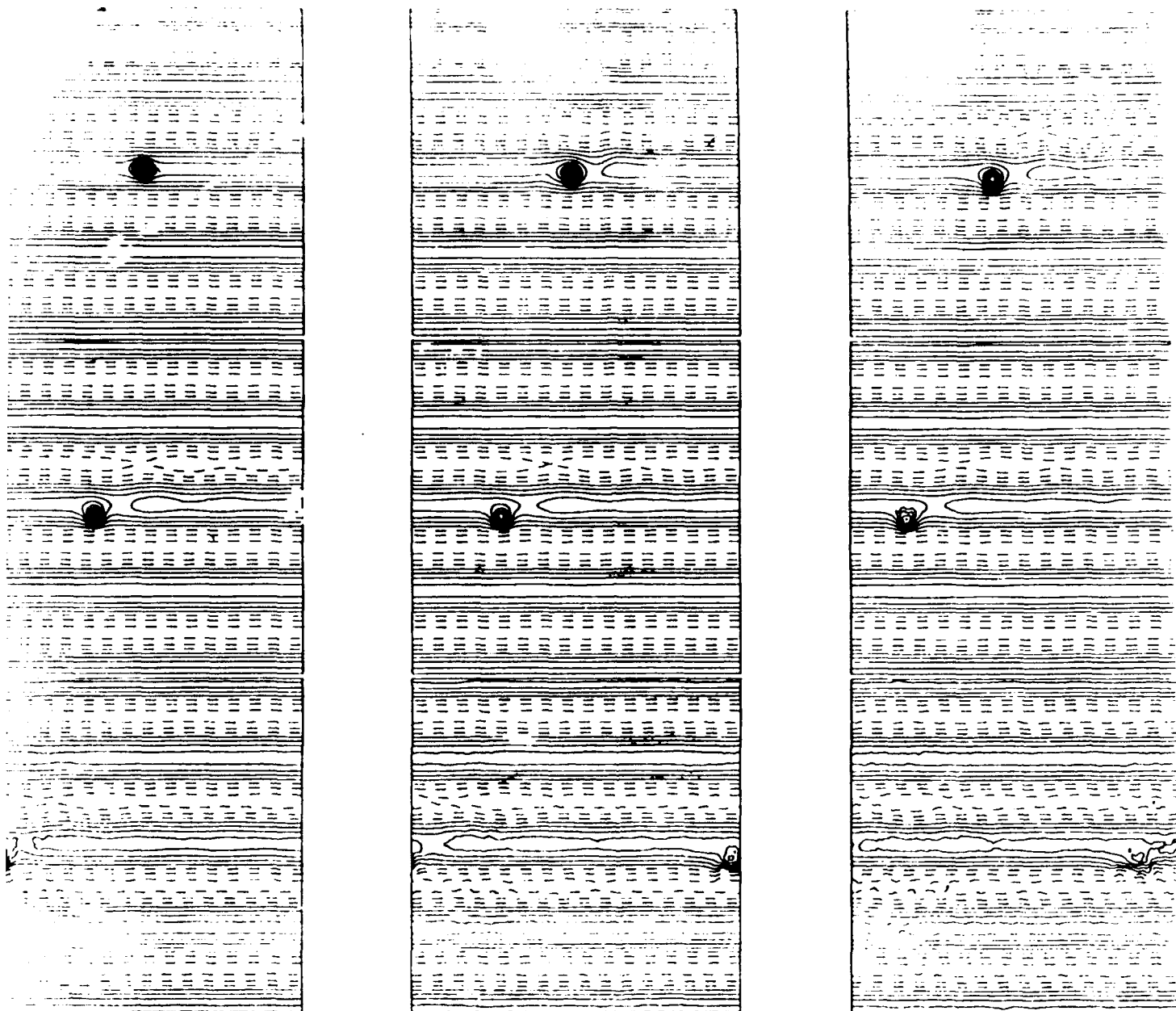
Figure 4a Numerical Simulation, upper layer with finite depth lower layer

Barotropic basic flow with a baroclinic eddy, $\delta = 0.2$, $F = 5$, $\beta = 1$
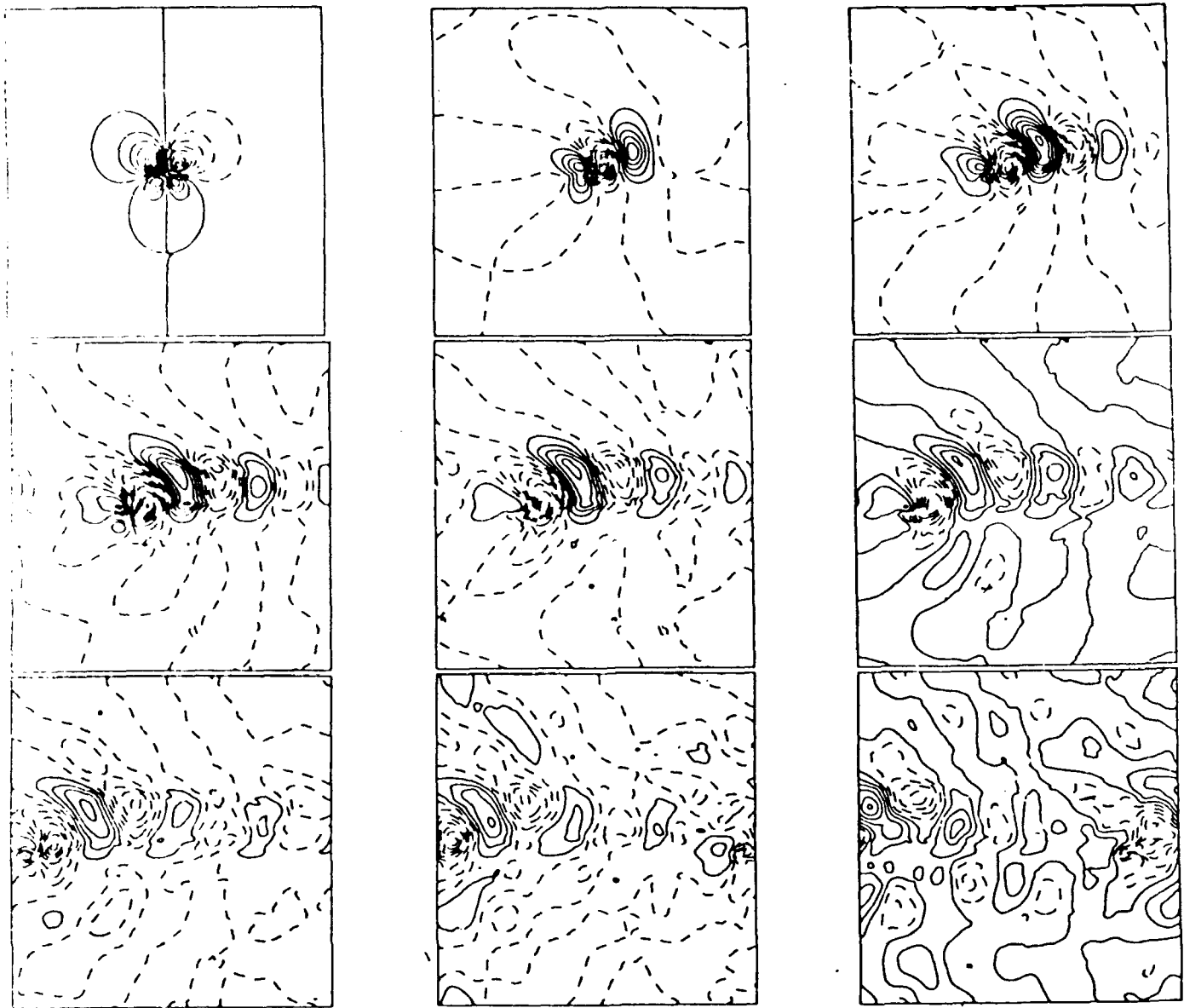
Figure 4b Numerical Simulation, lower layer with finite depth

Barotropic basic flow with a baroclinic eddy, $\delta = 0.2$, $F = 5$, $\beta = 1$
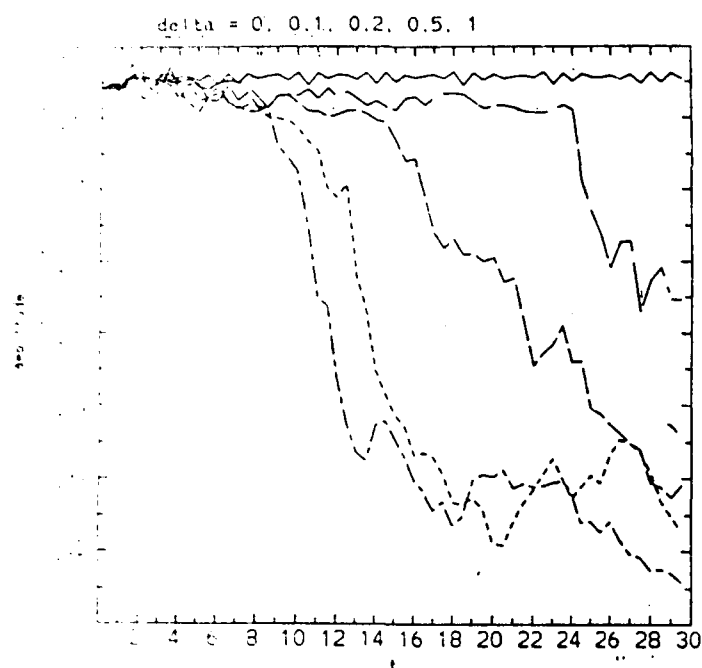
Amplitude vs. Time, varying δ
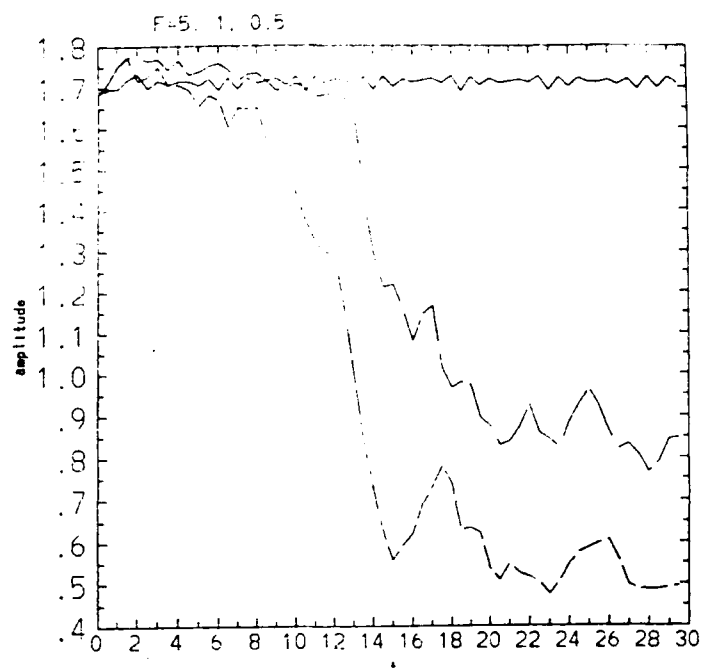
Amplitude vs. Time, varying F
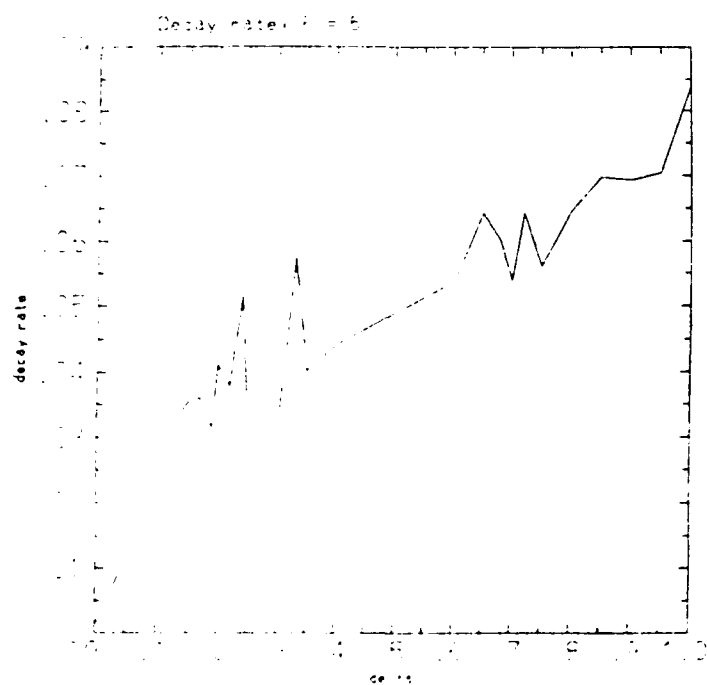
Decay Rate vs. Depth Ratio
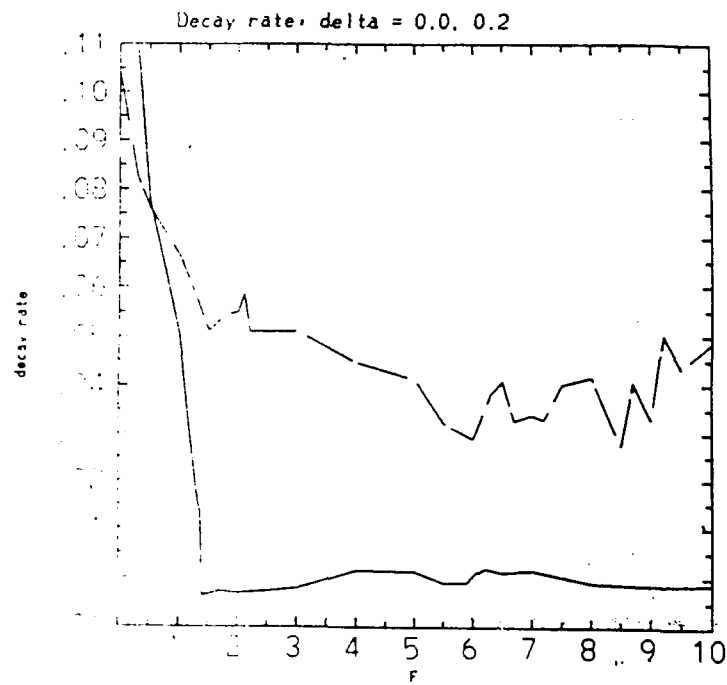
Decay Rate vs. Froude Number

Figure 5 Decay Rates of Various Simulations
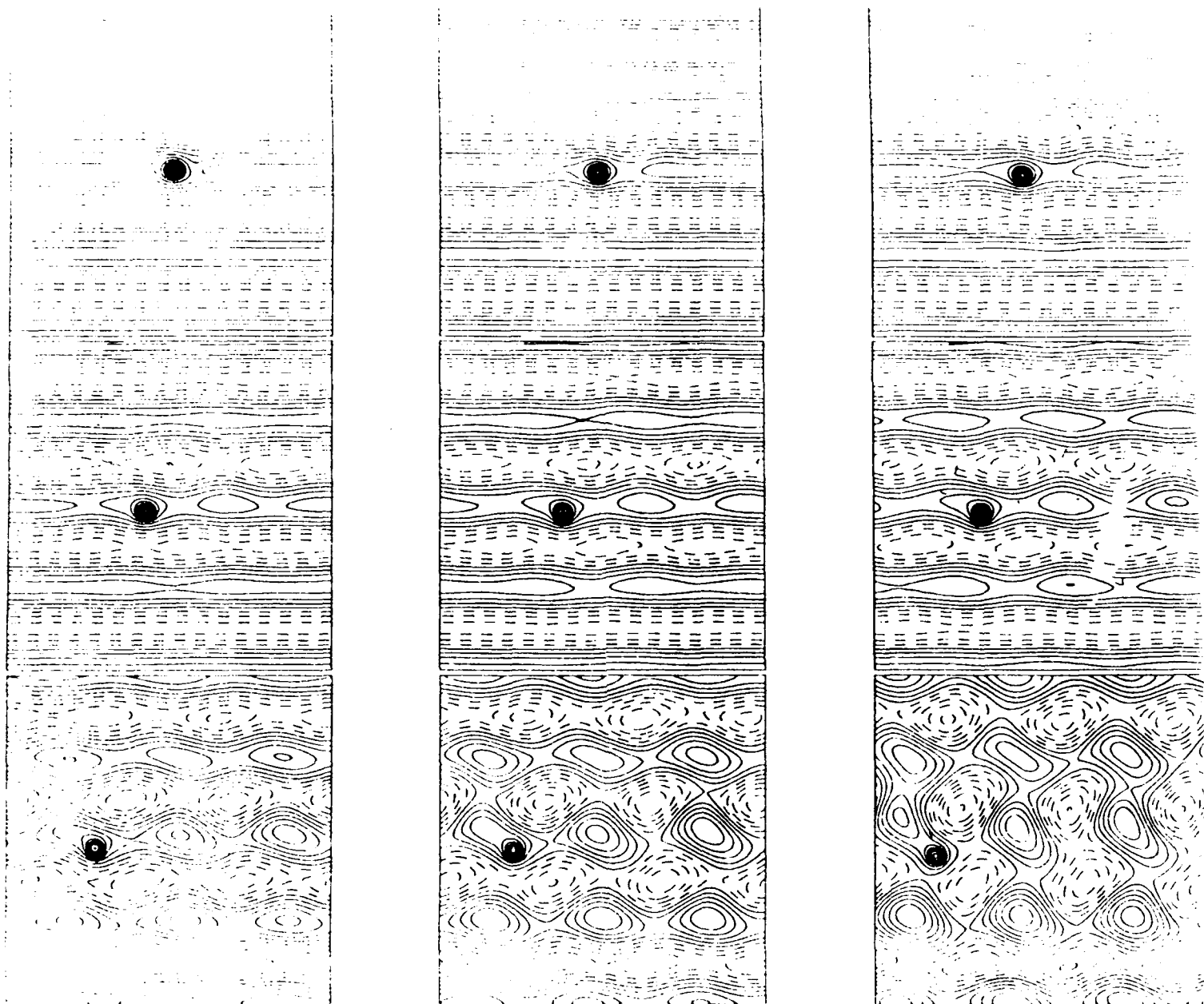
Figure 6a Numerical Simulation, upper layer with finite lower layer

Baroclinic eddy with barotropic instability, $\delta = 0.2$, $F = 5$, $\beta = 0.3$
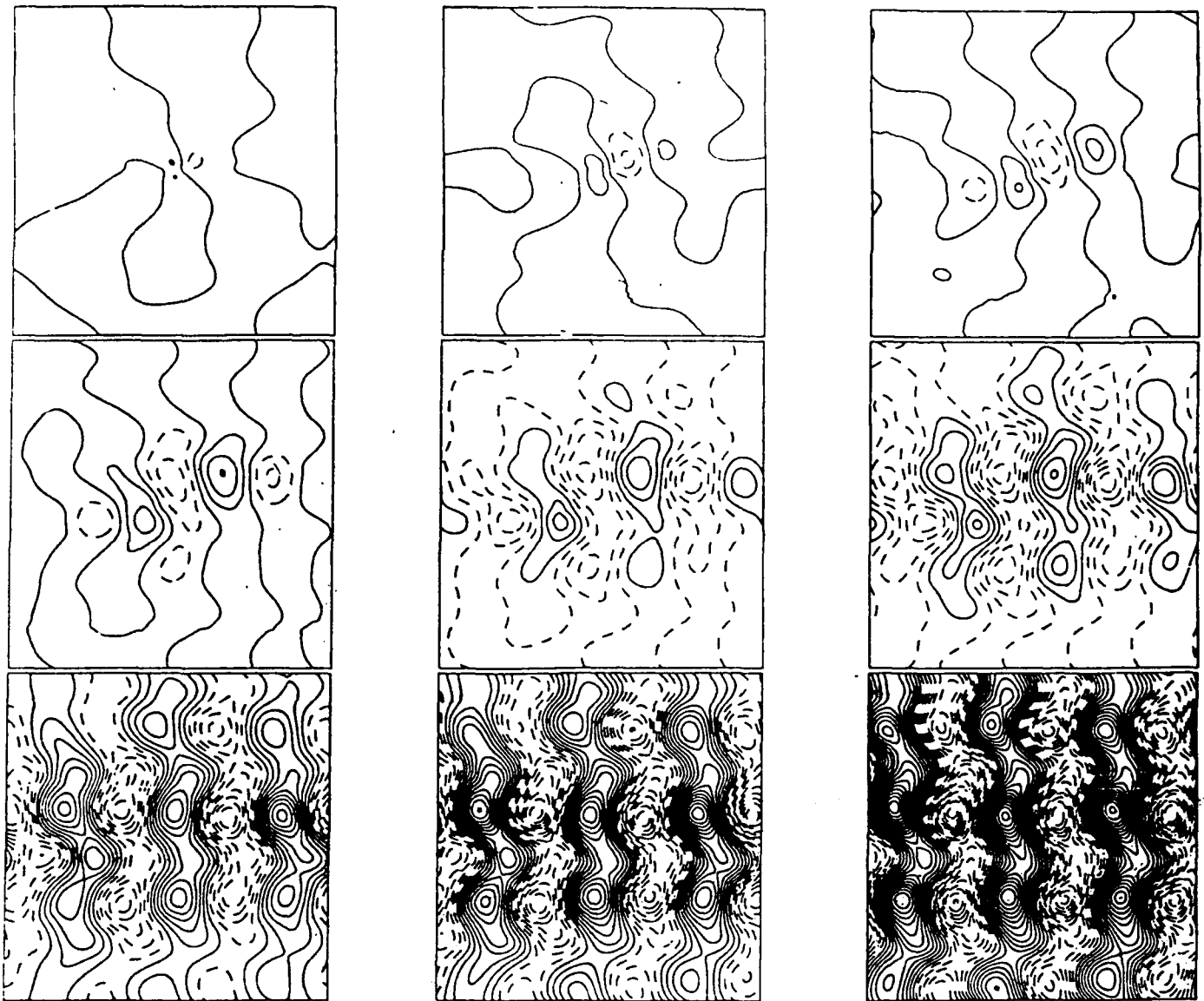
Figure 6b Numerical Simulation, finite lower layer

Baroclinic eddy with barotropic instability, $\delta = 0.2$, $F = 5$, $\beta = 0.3$
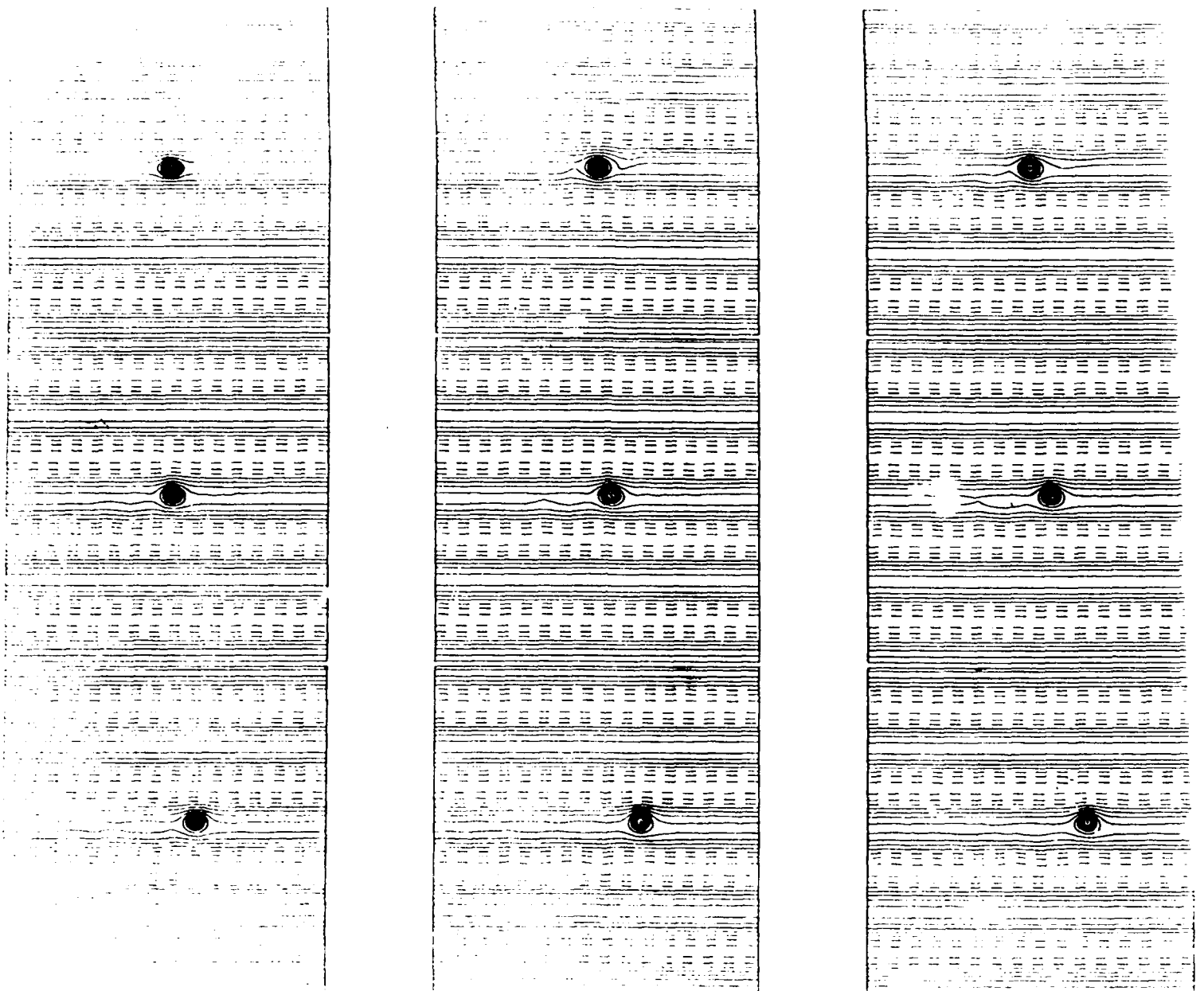
Figure 7 Numerical Simulation with Different Betas

Baroclinic eddy with active deep zonal flow. $\delta = 0.2$, $F = 5$, $\beta_{upper} = 0.3$, $\beta_{lower} = -2$
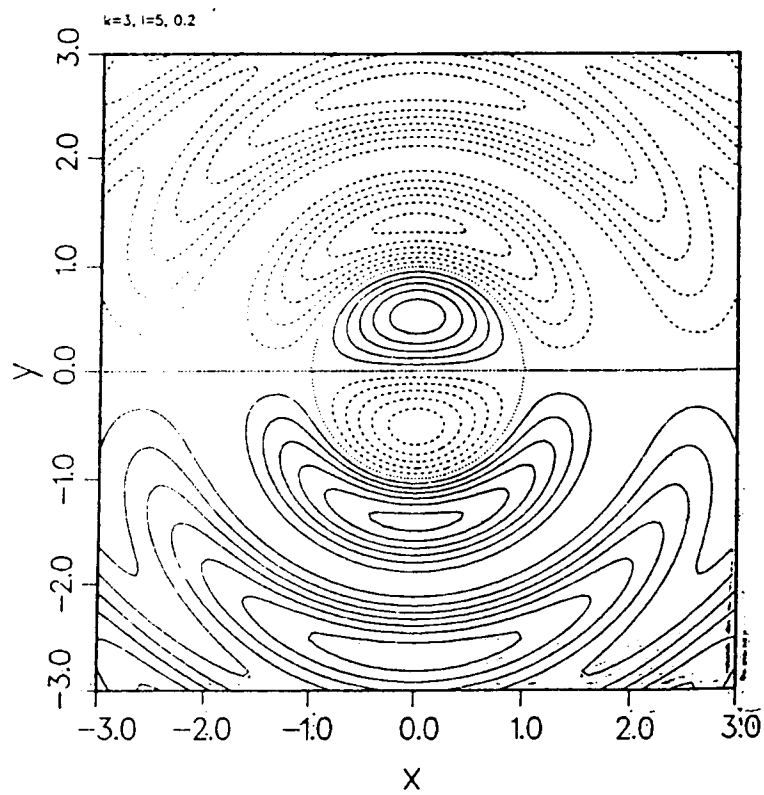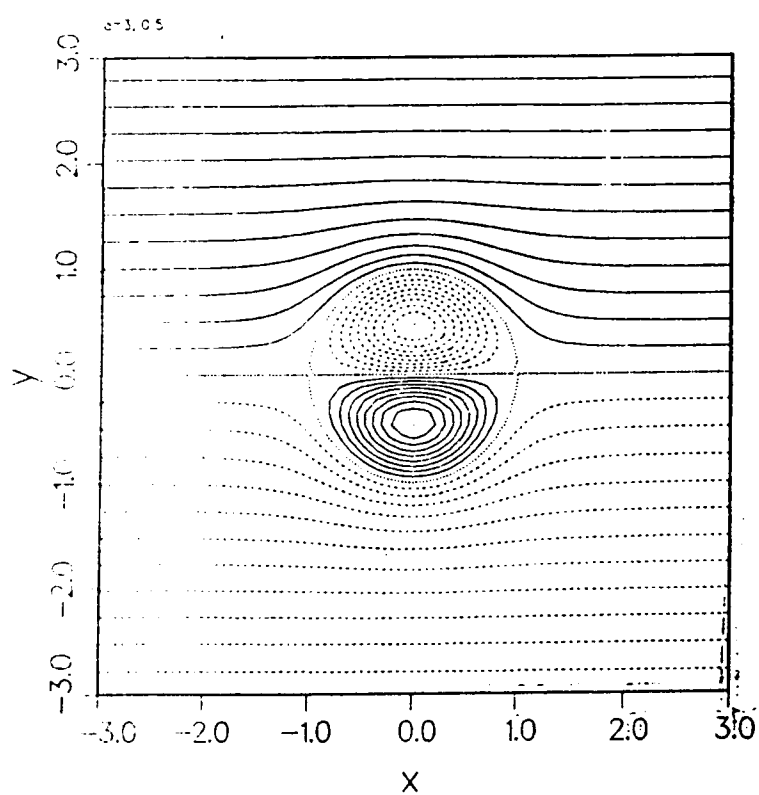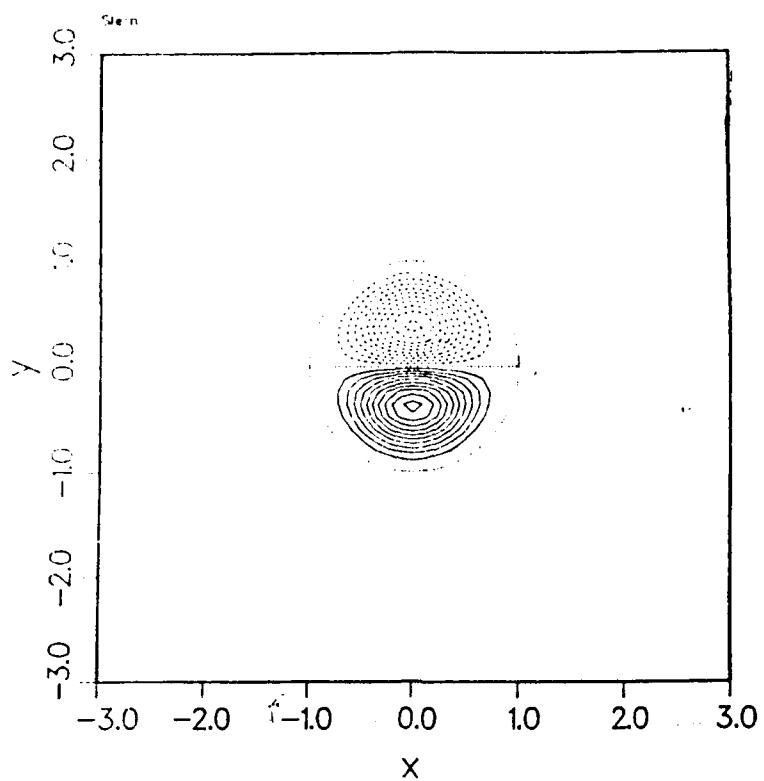
Figure 8 Dipole Modon Formulations

Stream Function

Potential vorticity

19 Oct. 1987
(5-day mean)

19 Oct. 1987
(5-day mean)

20 Oct. 1987
(5-day mean)

20 Oct. 1987
(5-day mean)

21 Oct. 1987
(5-day mean)

21 Oct. 1987
(5-day mean)

22 Oct. 1987
(5-day mean)

22 Oct. 1987
(5-day mean)

23 Oct. 1987
(5-day mean)

23 Oct. 1987
(5-day mean)
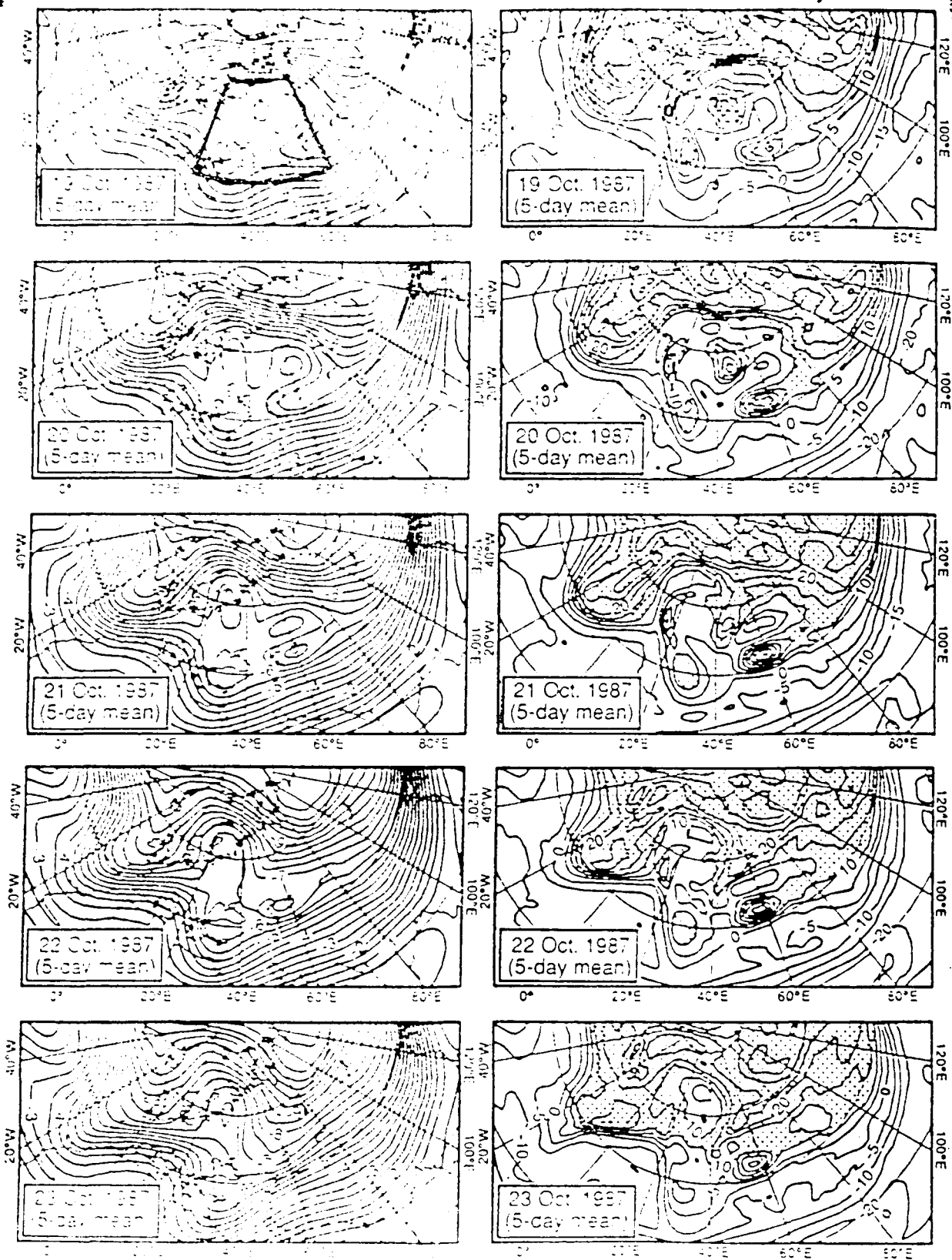
Figure 9 'Blocking High', Stream Function(ψ) and Potential Vorticity (q)

from Butchart et al. (1989)
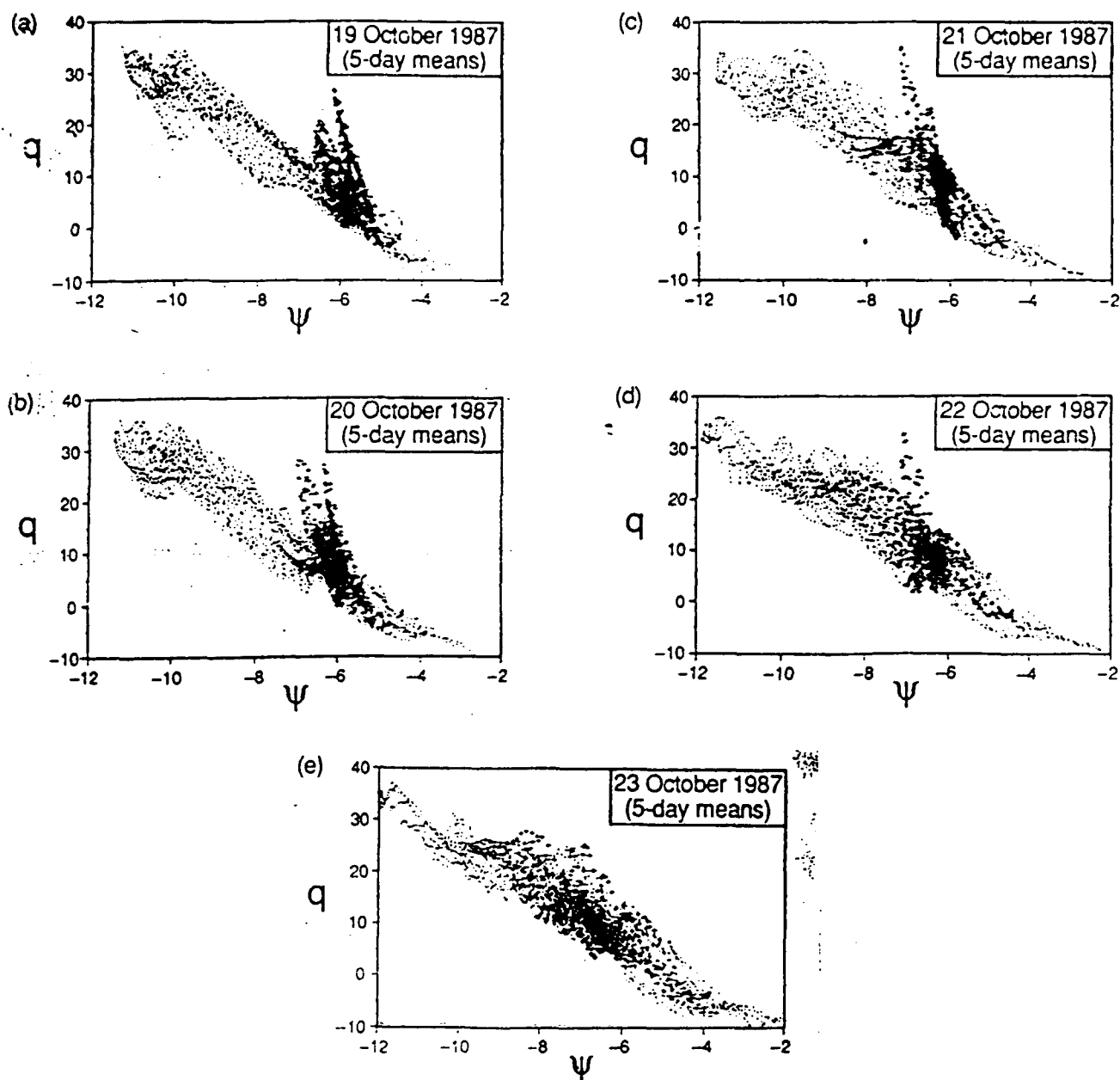
Figure 10 'Blocking High', q vs. ψ

from Butchart, et al. (1989)
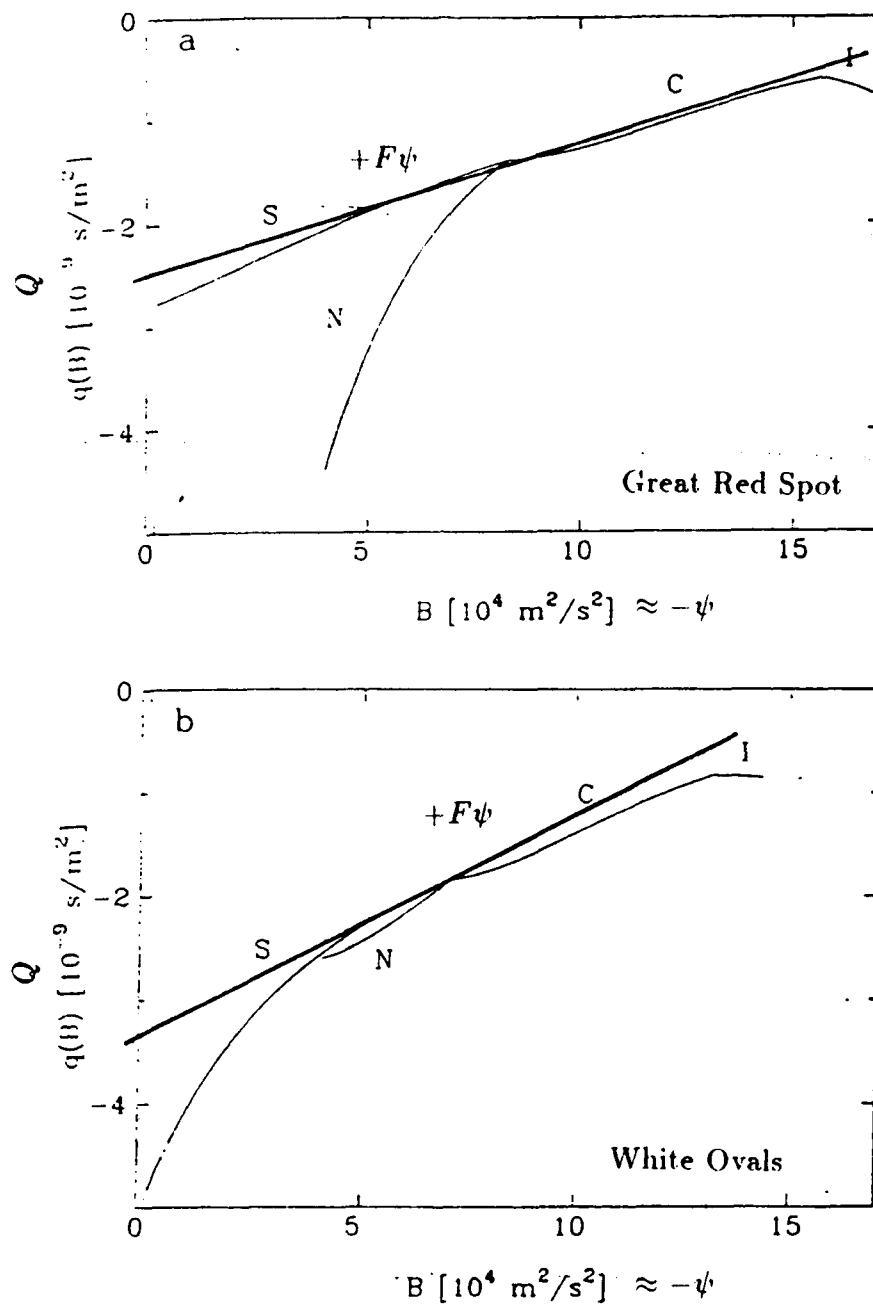
Figure 11 Great Red Spot and White Ovals, q vs. ψ

I is the interior of the vortex, C is the outer ring of the vortex, N is the northern exterior region, and S is the southern exterior region. *from Dowling and Ingersoll (1989)*

Cloud Dynamics on Jupiter

Adiabatic Cooling

Latent Heating

Dry ?

Adiabatic
Warming

Precipitation ?

What are the
basic dynamics?

Parameterization
in JCM

Hot, Moist
Layer

?

Resupply ?
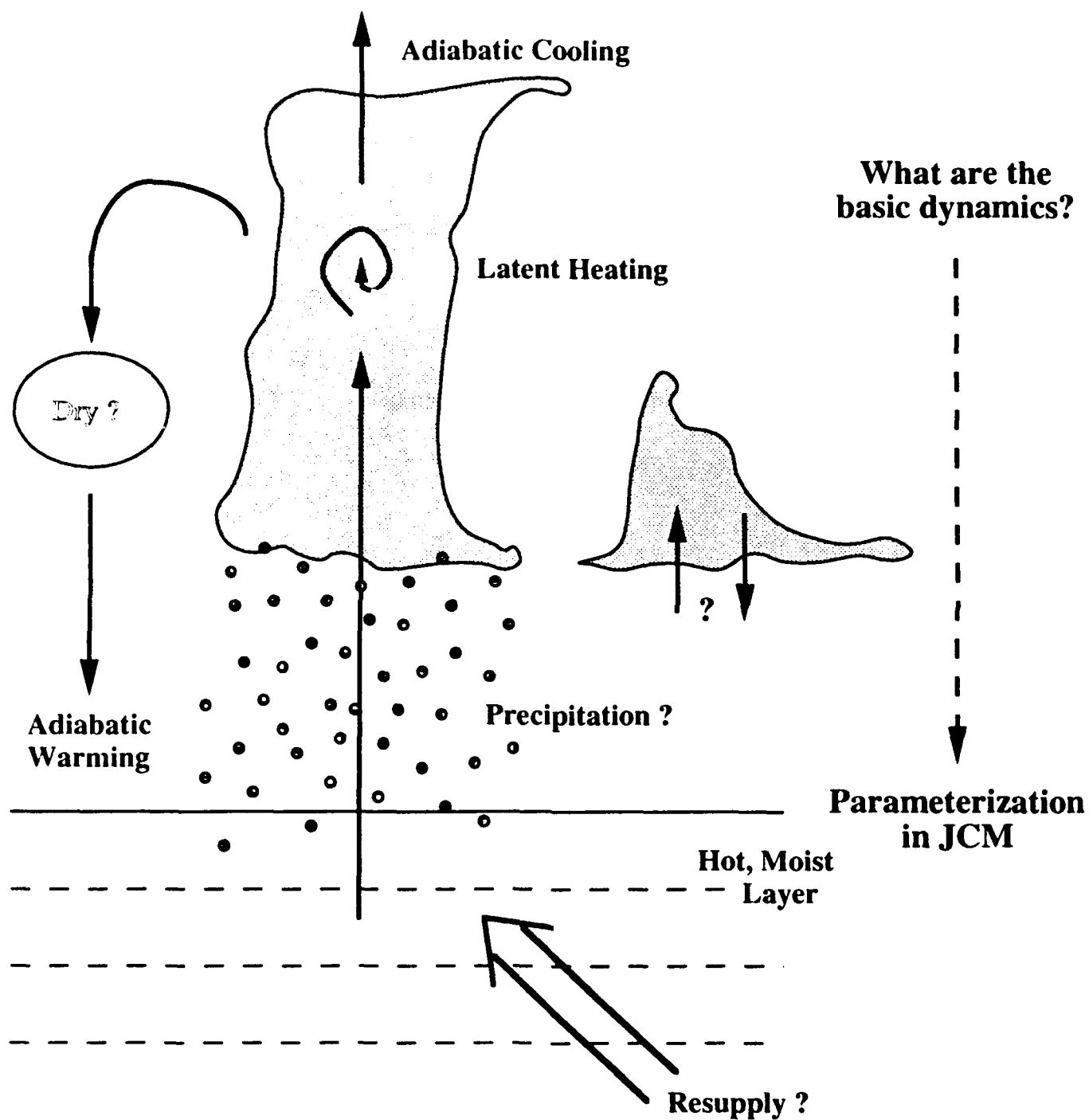
Figure 12 Schematic of the Cloud Dynamics on Jupiter

Vertical Structure

Radiative Decaying
(approx. 1000 days)

Cold

Penetrative Convection

Anticyclonic

Warm

Latent Heating
(Condensation)

Cumulus Convection

Cyclonic

Rainfall

Evaporation   Cooling

D ?

Internal Heat Source / Convection
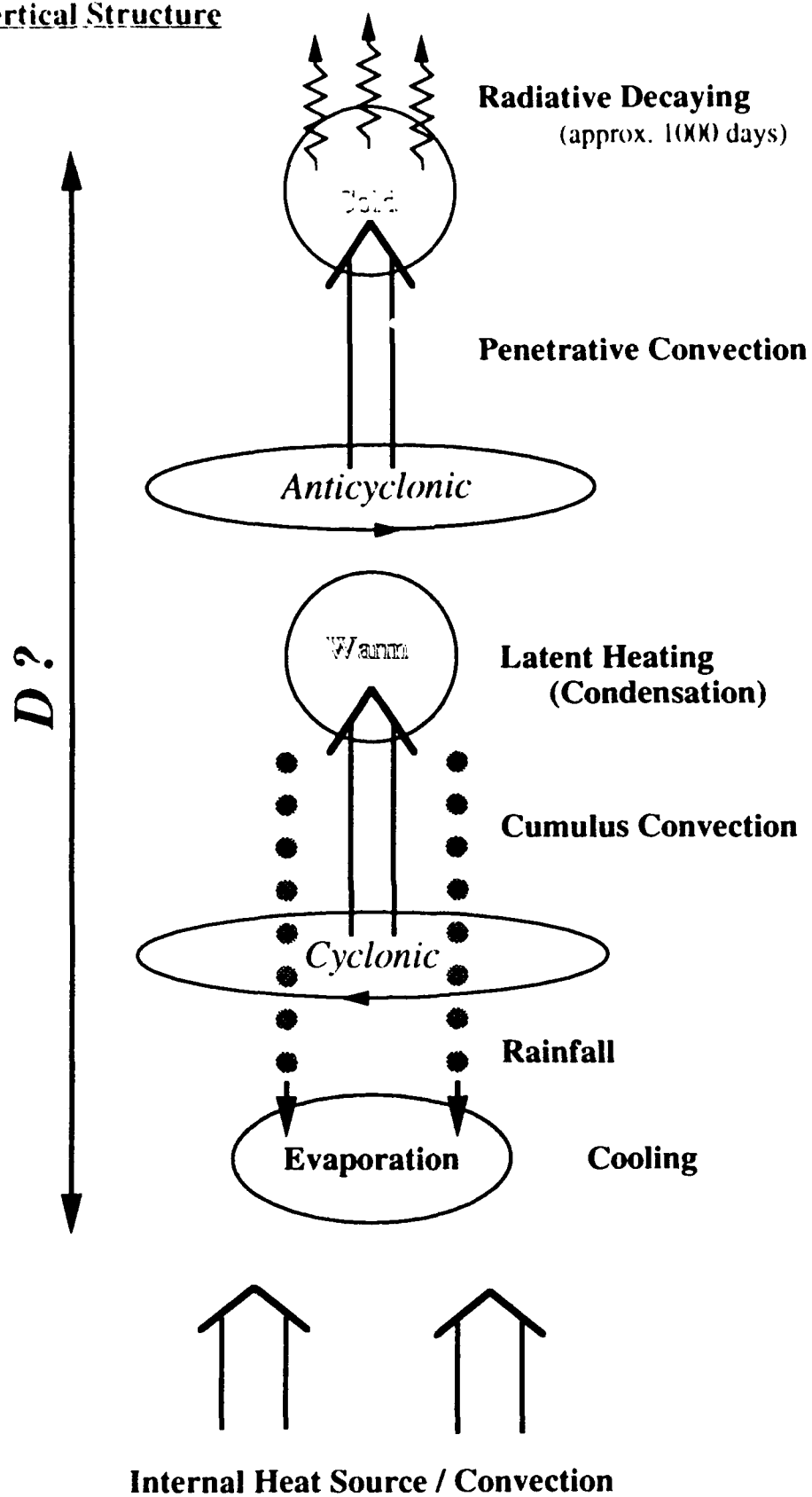
Figure 13 Possible Approach for Modeling Jovian Cloud Dynamics

Lecture 8 — The Atmospheres of Mars, Triton, Io, Mercury, and the Moon

Andrew Ingersoll

Frost-Vapor Equilibrium

The states of these atmospheres are determined by the vapor-frost equilibrium of the main constituents of the atmosphere. The existence of frost regulates the pressure and temperature of the atmospheres as the season changes. In today's lecture, we will describe the qualitative features of various planetary atmospheres as a result of this vapor-frost equilibrium and discuss simple models to gain a better understanding of these atmospheres.

For the planets and major satellites of the solar system that have atmospheres, we list them in the order from thick to thin along with their main chemical constituents:

Jupiter	H_2, He
Saturn	H_2, He
Uranus	H_2, He
Neptune	H_2, He
Venus	CO_2
Titan	N_2
Earth	N_2, O_2
Mars	CO_2
Triton	N_2
Io	SO_2
Mercury	?

For all the objects below Earth in this list, the atmospheric pressure is controlled by the vapor pressure of frost:

$$P = P_V(T), \quad T = T_f$$

and the temperature of the frost is controlled by radiation and sublimation:

$$\sigma T_f^4 = (1 - A)F_\odot \cos\theta + L\dot{m}$$

where m = mass per area of frost, and L = latent heat of vaporization.

Typically, thick atmospheres cover the globe and the atmospheric pressures change little with the seasons. They also have subsonic winds and short mean free paths. Thin atmospheres are a totally different story. It is possible that they only exist on the day side or over volcanoes. In this lecture, we consider the atmospheres of Mars, Mercury, the Moon, Triton and Io. In a increasing order of atmospheric thickness, we have the Moon and Mercury with the thinnest atmospheres, Io and Triton with medium thickness atmospheres, and Mars with the thickest atmosphere.

Thin Atmospheres: Moon and Mercury

The Moon's and Mercury's atmospheres are created primarily by charged particles and by ultraviolet rays from the sun bombarding the surface, and by comets and asteroids crashing on the surface. Consequently, these two atmospheres are extremely transient in nature.

The molecules in the atmosphere hop over the hot surface over tens of kilometeres at a time and eventually stick to cold surface. The mean free path is long and vapor pressure is too small (at $T = 102$ K, the evaporation rate into the vacuum surroundings is $1cm/10^9$ years). The shadowed ice on the Moon and Mercury are eventually destroyed by Ly α radiation from the interstellar medium. (see Morgan and Shemansky, 1991). Na and K are detected (as seen from resonance scattering); however, O is not detected (it is possibly lost from the atmosphere right after being created). We also see polar frost in the shadowed portions of craters where the temperatures are less than 100 K.

Mars

The Martian atmosphere has an atmospheric pressure of 6 mbar and a frost temperature of 148K (at the polar caps). The predominant gas in the atmosphere is CO_2. The seasonal frost thickness is about 1 meter, which makes up about thirty percent of the mass of the atmosphere. The pressure and frost temperatures are almost constant during the years; however, pressure and temperatures do vary with obliquity on a time scale of 10^5 years. Averaging over a year, for which $\dot{m} = 0$, we see that

$$\sigma T_f^4 = (1 - A)F_\odot \frac{\sin \beta}{\pi}$$

where β is the obliquity (currently 25 degrees), but can vary up to 25 ± 10 degrees and A is the visual albedo of the caps. We observe a sensitive dependence on A and β.

(See **Mars** for reference.)

Triton

Triton's atmosphere has a pressure of 15μbars (RSS), a temperature of 38 K (IRIS), and the dominant gas is N_2 (UVS). These values are consistent with solid-vapor equilibrium. Triton has a thick atmosphere (which means that the pressure is approximately constant with respect to both latitude and longitude). And since the frost temperature is a function of pressure only, it is also about constant over a range of latitudes and longitudes. On average,

$$T = T_{frost} = \left[\frac{(1 - A)F_\odot}{4\epsilon\sigma} \right]^{1/4} = 38K$$

for $A = 0.7$, $\epsilon = 1$

In summary, in very thick atmospheres (e.g. Mars), the pressure is almost constant with respect to the seasons. But in very thin atmospheres (e.g. Io) the pressure varies with respect to both latitude and longitude (in the case of Io, up to 5 orders of magnitude).

(See Ingersoll, 1990.)

Io

We see volcanic activities and eruptions up to 200 km high above the surface. (See slides of Io.) The lava lakes formed by volcanic activities are typically about 400 K, and are thought to be molten sulfur. We see no impact craters, leading us to believe that the surface of Io is, geologically speaking, young. The composition of the atmosphere has been measured and Io's atmosphere consists primarily on SO_2. The pressure and temperature vary during the day. Its night side atmosphere is an exosphere (i. e., no collisions). Maximum cooling is achieved via evaporation. The maximum velocity we see is about 300 m/s, which is 2.5 times the speed of sound.

There is no global atmosphere. However, locally, there are atmospheres at the subsolar point and above each volcano. Let's see how these local atmospheres are created.

The maximum flow speed is when all the thermal and gravitational energy is converted into kinetic energy:

$$\frac{v_{max}^2}{2} = \overline{E}_{thermal} + \overline{E}_{grav} = c_P T.$$

So

$$F_{evap} \pi r^2 \le 2\pi r L \rho_{gas} v_{max} H,$$

where F_{evap} is the maximum evaporative cooling rate, L is the latent heat of vaporization, and H is the scale height of the atmosphere.

The frost will heat up if

$$(1 - A) F_{\odot} \cos \theta > F_{evap},$$

and we have a local dayside atmosphere. Similarly for volcanoes, if the rate at which SO_2 is created is greater than $2\pi r \rho_{gas} v_{max} H$, a local atmosphere is created over the volcano.

The internal heat flow of Io has been measured by summing the $400K$ radiation coming from the lava lakes and has a value of $1 - 2$ watts/m^2. It comes mainly from the tidal dissipation with the other satellites. This is one hundred times the Earth's internal heat flow and is probably enough to drive the volcanoes.

Frost Driven Flow

Let's look at the atmosphere of Io in more detail, assuming that the flow we observe is frost driven.

Right away, assuming that the temperature is regulated by solar radiation only, we have

$$(1 - A)F_\odot \cos\theta_\odot = \sigma T_S^4$$

where θ is the co-latitude from the subsolar point and T_S is the surface temperature.

Let us incorporate the effects of frost. We vertically integrate the horizontal flow away from $\theta = 0$, assume the vertical structure satisfies hydrostatic and adiabatic equilibria and that the flow has constant velocity with respect to height above the boundary layer (with a scale height of approximately 10 km).

Then the conservation equations are

$$\frac{1}{r\sin\theta}\frac{\partial}{\partial\theta}\left(\sin\theta\frac{P}{g}v\right) = E = \alpha(P_V - P)\left(\frac{m}{2\pi kT}\right)^{1/2},$$

$$\frac{1}{r\sin\theta}\frac{\partial}{\partial\theta}\left(\sin\theta\frac{P}{g}v^2\right) = -\frac{1}{r}\frac{\partial}{\partial\theta}\int_0^\infty P\,dz + \tau,$$

$$\frac{1}{r\sin\theta}\frac{\partial}{\partial\theta}\left[\sin\theta\frac{P}{g}v\left(\frac{v^2}{2} + c_P T\right)\right] = Q.$$

expressing the conservation of mass, momentum and energy. $P_V(T_S(\theta))$ is the given vapor pressure of frost. Our task is to find $P(\theta)$, $v(\theta)$, $T(\theta)$ subject to $v(0) = 0$ and $T(0) = T_S(0)$. We need a downstream boundary condition to determine $P(0)$ and here we assume that $P \to 0$ downstream. The numerical solutions are shown in Figure 1.

Properties of Numerical Solutions

Flow speed reaches 300 m/s (Mach 4) at $\theta = 75°$ and the flow dies when $P = 10^{-11}$ bar (i. e., when the mean free path is approximately the scale height) at $\theta = 80°$. The hydraulic jump in Fig. 1b comes from a nightside gas (which we currently speculate to be O_2).

Let $\int_0^\infty P\,dz = \frac{c_P T}{g}P\beta$, where $\beta = \frac{R}{R+c_P}$ for adiabatic atmospheres. The maximum flow speed is given by $\frac{v^2}{2} + c_P T = $ constant, so $v \to v_{\max} = [2c_P T(0)]^{1/2}$ as $T \to 0$. The local Mach number is infinite; however, the Mach number calculated using actual value of $T(0)$ is about 2.2. The key to give us high flow speeds, as in rocket nozzles and solar wind, is *expansion* as we can see by rewriting the momentum equation:

$$\frac{1}{r\sin\theta}\frac{\partial}{\partial\theta}\left[\sin\theta\frac{P}{g}\left(\frac{v^2}{2} + \beta c_P T\right)\right] = \frac{\beta c_P TP}{gr\tan\theta} + \tau,$$

where the first term on the right hand side is the force. When $0 < \theta < \frac{\pi}{2}$, the expansion acts as a downstream force—increases the momentum flux.

The hydraulic jump is given by

$$\frac{1}{g}vP = f_{ma}, \quad \frac{P}{g}(v^2 + \beta c_P T) = f_{mo}, \quad \frac{P}{g}v(\frac{1}{2}v^2 + \beta c_P T) = f_e,$$

$$v = \frac{f_{mo} \pm \left[f_{mo}^2 - 2\beta(2 - \beta)f_{ma}f_e\right]^{1/2}}{f_{ma}(2 - \beta)}$$

The positive root gives supercritical flow; the negative root, subcritical flow.

Solar Wind Equation

Let's look at the Solar Wind Equation as applied to this case. Assuming hydrostatic equilibrium,

$$0 = -\frac{1}{\rho}\frac{\partial P}{\partial r} - \frac{GM}{r^2}$$

$$P = RT\rho = c^2\rho,$$

where c is the speed of sound (c^2 is constant if T is constant). This gives us P as a function of r:

$$P(r) = P(\infty)e^{GM/c^2 r}.$$

However, we cannot have pressure at infinity; this is the typical failure of hydrostatic equilibrium descriptions of isothermal atmospheres.

We must add *outflow*. Let us patch our hydrostatic equation with a $v\frac{\partial v}{\partial r}$ term. And let us further assume that we have a constant outflow: $F = \rho v r^2 = $ constant

$$v\frac{\partial v}{\partial r} = -\frac{1}{\rho}\frac{\partial P}{\partial r} - \frac{GM}{r^2}, \quad P = \rho c^2.$$

The radius at which the flow reaches supersonic velocity ($v = c$) is r_0. We can rewrite our equation with rescaled variables: $w = \frac{v}{c}$, $R = \frac{r}{r_0}$, $\frac{P}{P_0} = \frac{1}{wR^2}$, where $w = R = \frac{P}{P_0} = 1$ at $r = r_0$.

$$(w - \frac{1}{w})\frac{\partial w}{\partial R} = \frac{2}{R} - \frac{\mu}{R^2},$$

where $\mu = GM/r_0 c^2$. Right away, we notice that the equation is singular at $R = 1$ (where $w = 1$). The equation is nonsingular only when the right hand side vanishes at $R = 1$, therefore, $\mu = 2$, i. e.,

$$c = \frac{1}{2}\left(\frac{2GM}{r_0}\right)^{1/2} = \frac{1}{2}v_{\text{esc}}, \quad or \quad r_0 = \frac{GM}{2c^2}$$

This is the only solution that satisfies $P \to 0$ as $R \to \infty$. L'Hôpital's rule gives us that $\partial_R w = 1$ at $R = 1$, so integrating we get

$$\frac{1}{2}w^2 = \frac{2}{R} + \ln(wR^2) - \frac{3}{2}$$

with $w = w(R)$ and $w(1) = 1$. This is an implicit equation for $w(R)$, which we can solve. As $R \to \infty$, $w \to \infty$ logarithmically and $\frac{P}{P_0} = \frac{1}{w R^2} \to 0$ faster than $\frac{1}{R^2}$.

However, Io is not exactly the Sun; the solar wind description of the flow on Io is good, except that, for Io, the 'wind' expands *horizontally*, not spherically outwards, and it expands from the subsolar point.

References

Ingersoll, A. *Nature*, **344**, 315, 1990.
Mars. University of Arizona Press.
Morgan and Shemansky, *JGR*, 1991.

Notes compiled by Andrew Stamp and Louis Tao
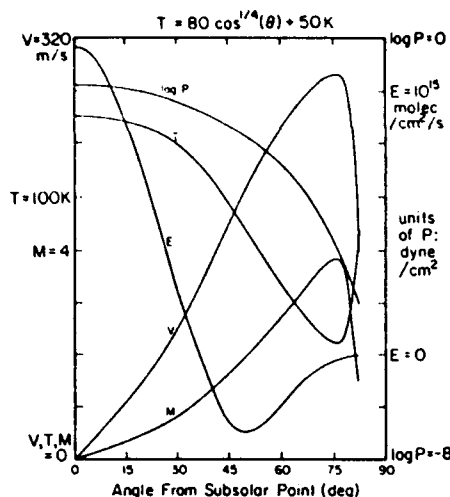
FIG. 2. Solution with subsolar temperature of 130°K. For other parameters, see Table I. The velocity, temperature, and pressure at the top of the boundary layer are V, T, and P, respectively. The Mach number and evaporation rate are M and E. The scales are indicated along the ordinate. Thus, the units of V, T, M, and E are 40 m/sec, 20°K, 1 and 0.2×10^{15} molecules/cm²/ sec, respectively. The logarithm of P is to the base 10, so that log $P = -8$ is a pressure of 10^{-8} dyn/cm².
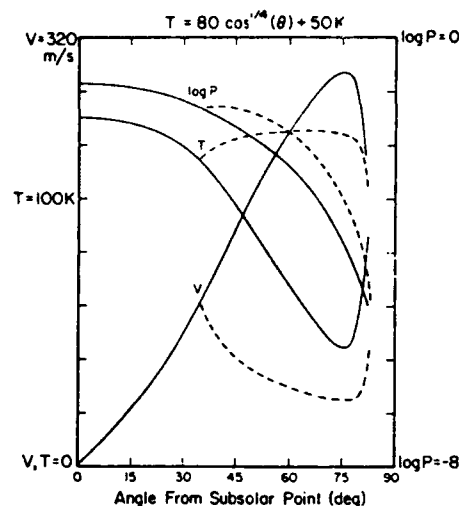
FIG. 10. Change of V, T, and log P across a hydraulic jump. The solid curves are the same as those of Fig. 2, and show the values in the supersonic flow ahead of the jump. The dashed curves show the values immediately behind the jump. The difference between the dashed and solid curves at angle θ indicates the size of the transition for a jump located at that angle.

Figure 1: Plots from Ingersoll *et. al.* (1985) showing numerical solutions to the Io atmospheric model. The velocity, temperature and pressure at the top of the boundary layer are V, T and P. The Mach number and evaporation rate are M and E. In (a) and (b) the solutions are for a subsolar temperature of $130K$ and antisolar temperature of $50K$. In (b) the effects of a hydraulic jump are evident with the dashed lines corresponding to the values of V, T and P that would occur on the subsonic side of a given colatitude.

116

Lecture 9 – Deep Baroclinic Jovian Dynamics

In the case that the dynamics of Jovian circulation may be dominantly that of motion on concentric cylinders, we investigate the necessary momentum and vorticity balances of such a planet, as well as simple instability criteria, comparing all the time to traditional thin weather–layer β-plane systems.

The Anelastic Equations

This system serves as a basis, appropriately, since we intend to account for vertical structure, at the same time being unconcerned with sound waves. The enegry and momentum conservation equations are:

$$-\frac{1}{\rho}\nabla p = -\nabla E + T\nabla S$$

where $E = \frac{enthalpy}{mass}$ and $S = \frac{entropy}{mass}$, and

$$-\frac{1}{\rho}\nabla p - \nabla\Phi_g = -\nabla(E + \Phi_g) + T\nabla s$$

where Φ_g is the gravitational potential energy per unit mass. For our rotating frame, this can be thought of as the ordinary Newtoninan gravitational potential minus the centrifugal potential, so:

$$\Phi_g = \Phi_{NG} - \frac{1}{2}\Omega^2 r^2$$

Now let $\rho_0 + T_0 + \Phi_g$ refer to a uniformly rotating planet with $s = s_0 = constant$. This basic state is hydrostatic:

$$0 = -\frac{1}{\rho_0}\nabla p_0 - \nabla\Phi_g = -\nabla(E_0 + \Phi_g)$$

So $E_0 + \Phi_g = constant$ but $E_0 = E_0(p, S_0)$, so E_0, p_0, ρ_0 are all functions of Φ_g only; i.e. the basic state is adiabatic, hydrostatic and barotropic. Perturb about this state, keeping the leading order balance:

$$\frac{d\mathbf{v}}{dt} + 2\boldsymbol{\Omega} \times \mathbf{v} = -\nabla\Phi - S_1\nabla T_0$$

$$\nabla \cdot (\rho\mathbf{v}) = 0$$

$$\frac{dS_1}{dt} = 0$$

Coordinate System

Now we choose a suitable cylindrical coordinate system in $(\theta, -r, z)$ which forms a right-handed system with velocities (u, v, w). This is like any other right-handed system, in this case:

$$\frac{\partial}{\partial x} \longrightarrow \frac{1}{r}\frac{\partial}{\partial \theta} \quad and \quad \frac{\partial}{\partial y} \longrightarrow -\frac{\partial}{\partial r}$$

So we will have:

$$\hat{\mathbf{z}} \cdot (\nabla x \mathbf{v}) = \zeta = \frac{1}{r}\frac{\partial v}{\partial \theta} + \frac{1}{r}\frac{\partial}{\partial r}(ru)$$

$$\nabla \cdot \mathbf{v_2} = D = \frac{1}{r}\frac{\partial u}{\partial \theta} - \frac{1}{r}\frac{\partial}{\partial r}(rv) \ .$$

The equations of flui acceleration are:

$$\frac{du}{dt} - \frac{uv}{r} - 2\Omega v = -\frac{1}{r}\frac{\partial \Phi}{\partial \theta}$$

$$\frac{dv}{dt} + \frac{u^2}{r} + 2\Omega u = \frac{\partial \Phi}{\partial r} + S_1 \frac{\partial T_0}{\partial r}$$

$$\frac{dw}{dt} = -\frac{\partial \Phi}{\partial z} - S_1 \frac{\partial T_0}{\partial z}$$

$$D - \frac{v}{\rho_0}\frac{\partial \rho_0}{\partial r} + \frac{1}{\rho_0}\frac{\partial}{\partial z}(\rho_0 w) = 0$$

Vorticity

We can extract a vorticity equation from the above; take $\hat{\mathbf{z}} \cdot \left(\nabla \times \frac{d\mathbf{v}}{dt} + 2\Omega \mathbf{v}\right)$ to get:

$$\frac{d\zeta}{dt} + (2\Omega + \zeta)D + \frac{1}{r}\frac{\partial w}{\partial \theta}\frac{\partial v}{\partial z} = \frac{1}{r}\frac{\partial S_1}{\partial \theta}\frac{\partial T_0}{\partial r} \ .$$

Nondimensionalization

So far this analysis has been exact; now we adopt the scaling:

$$\frac{1}{r}\frac{\partial}{\partial \theta} \sim \frac{1}{r}, \quad \frac{\partial}{\partial z} \sim \frac{1}{r}, \quad and \quad \frac{\partial}{\partial r} \sim \frac{1}{L}$$

when $\frac{\partial}{\partial r}$ acts on $(\mathbf{v}, S, \Phi)$ but

$$\frac{\partial}{\partial r} \sim \frac{1}{r}$$

when applied to (ρ, T). Since r represents the planetary radius, it is related to our length-scale: $L << r$. From the continuity equation, we see that the components of velocity are related as:

$$u \sim u, \quad v \sim \frac{L}{r}u \quad and \quad u << 2\Omega L$$

The vertical velocity, w, can be scaled as in quasi-geostrophic theory, assuming:

$$\frac{d\zeta}{dt} \sim 2\Omega D \quad where \quad \zeta \sim \frac{U}{L} \quad and \quad \frac{d}{dt} \sim \frac{U}{r}$$

so $D \sim \frac{U}{2\Omega L}\frac{U}{r} << \frac{U}{r}$ and the two terms in D (each of order $\frac{U}{r}$) nearly cancel. Then

$$D = \frac{v}{\rho}\frac{\partial \rho}{\partial r} - \frac{1}{\rho}\frac{\partial}{\partial z}(\rho w)$$

but the first term scales like:

$$\frac{v}{\rho}\frac{\partial \rho}{\partial r} \sim \frac{L}{r}\frac{U}{r}$$

with the second term having the scale

$$\frac{1}{\rho}\frac{\partial}{\partial z}(\rho w) \sim \frac{w}{r}$$

and therefore the vertical velocity satisfies

$$w \sim \frac{L}{r} \sim v$$

which is also consistent with the boundary condition at the surface of the sphere. This scaling is self-consistent if

$$\frac{U}{2\Omega L} \sim \frac{L}{r} << 1$$

The vorticity equation can be scaled by comparison of ζ and 2Ω.

$$\frac{d\zeta}{dt} + 2\Omega D = -\frac{1}{r}\frac{\partial S_1}{\partial \theta}\frac{\partial T_0}{\partial r}$$

120

If we use this same scaling to examine the momentum equations, we get:

$$-2\Omega v = -\frac{1}{r}\frac{\partial \Phi}{\partial \theta}$$

$$2\Omega u = \frac{\partial \Phi}{\partial r} + S_1 \frac{\partial T_0}{\partial r}$$

Notice that this is nearly geostrophic, but for the last term. So we let $S_1 = \overline{S}(T_0) + S_2(\theta, r, z, t)$ where $\overline{S}$ is the barotropic part. Now

$$\overline{S}(T_0)\frac{\partial T_0}{\partial r} = \frac{\partial}{\partial r}\left[\int^T \overline{S}(t)dt\right]$$

and similarly

$$\overline{S}(T_0)\frac{\partial T_0}{\partial z} = \frac{\partial}{\partial z}\left[\int^T \overline{S}(t)dt\right]$$

in the $\frac{dw}{dt}$ equation. Then

$$-2\Omega v = -\frac{1}{r}\frac{\partial \phi}{\partial \theta}, \quad \phi = \Phi + \int^T \overline{S}(T)dT$$

$$2\Omega u = \frac{\partial \phi}{\partial r} + S_2\frac{\partial T_0}{\partial r} \, and$$

$$\frac{d\zeta}{dt} + 2\Omega D = -\frac{1}{r}\frac{\partial S_2}{\partial \theta}\frac{\partial T_0}{\partial r}$$

Assume the S_2 term in vorticity equation is the same size as other terms, e.g.

$$\frac{d\zeta}{dt} \sim \frac{U}{L}\frac{U}{r} \sim \frac{S_2 T_0}{r^2}$$

then

$$\frac{S_2(\partial T_0/\partial r)}{2\Omega U} \sim \frac{U^2/L}{2\Omega U} \sim \frac{U}{2\Omega L} << 1$$

and we have geostrophic balance:

$$u = \frac{\partial \Psi}{\partial r}, \quad v = \frac{1}{r}\frac{\partial \Psi}{\partial \theta}, \quad \Psi = \frac{\phi}{2\Omega}$$

and

$$\zeta = \nabla^2 \Psi \longrightarrow \frac{\partial^2 \Psi}{\partial r^2}$$

so

$$\frac{d\zeta}{dt} = \frac{\partial \zeta}{\partial t} + \frac{\partial \Psi}{\partial r}\frac{1}{r}\frac{\partial \zeta}{\partial \theta} - \frac{1}{r}\frac{\partial \Psi}{\partial \theta}\frac{\partial \zeta}{\partial r} = \frac{\partial \zeta}{\partial t} + J(\Psi, \zeta).$$

A Potential Vorticity

Is there an interesting potential vorticity in this system? From now on, we replace S_2 by S', T_0 by T and ρ_0 by ρ. So now, we rewrite our equations as:

$$\frac{d\zeta}{dt} + 2\Omega \left[\frac{1}{\rho r} \frac{\partial \Psi}{\partial \theta} \frac{\partial \rho}{\partial r} - \frac{1}{\rho} \frac{\partial}{\partial z}(\rho w) \right] = \frac{1}{r} \frac{\partial S'}{\partial \theta} \frac{\partial T}{\partial r}$$

we need to simplify this by solving for each term explicitly. From the previous section, we know:

$$0 = -2\Omega \frac{\partial \Psi}{\partial z} - S' \frac{\partial T}{\partial z}$$

and:

$$\frac{dS'}{dt} + \frac{d\overline{S}}{dT} \left(-\frac{1}{r} \frac{\partial \Psi}{\partial \theta} \frac{\partial T}{\partial r} + w \frac{\partial T}{\partial z} \right) = 0.$$

from this last equation, we can solve for w, but first we solve for:

$$S' = -2\Omega \frac{\partial \Psi}{\partial z} \frac{\partial z}{\partial T}$$

employing a convenient simplification, referring to figure 1, in that the coordinate variables r and z are related as: $\cot(\phi) = \frac{r}{z}$. So the RHS of the vorticity equation above can be rewritten:

$$\frac{1}{r} \frac{\partial S'}{\partial \theta} \frac{\partial T}{\partial r} = \frac{2\Omega}{r} \frac{\partial^2 \Psi}{\partial \theta \partial z} \left(\frac{\partial z}{\partial r} \right)_T$$

We know from the scaling convention that we followed, that $\overline{S}, \rho, T, etc$ are independent of θ and vary with r and z on the scale of $\frac{1}{r}$. So they commute with:

$$\frac{d}{dt} = \frac{\partial}{\partial t} + \frac{1}{r} \left(\frac{\partial \Psi}{\partial r} \frac{\partial}{\partial \theta} - \frac{\partial \Psi}{\partial \theta} \frac{\partial}{\partial r} \right).$$

So now we find w:

$$w = \frac{1}{r} \frac{\partial \Psi}{\partial \theta} \frac{r}{z} - \frac{1}{d\overline{S}/dT} \frac{\partial z}{\partial T} \frac{dS'}{dt}$$

such that we can find the last term on the LHS of the equation for $\frac{d\zeta}{dt}$:

$$\frac{1}{\rho} \frac{\partial}{\partial z}(\rho w) = \frac{1}{\rho} \frac{\partial}{\partial z} \left(\frac{\rho}{z} \frac{\partial \Psi}{\partial \theta} \right) + \frac{1}{\rho} \frac{\partial}{\partial z} \left[\frac{d}{dt} \left(\frac{\rho}{d\overline{S}/dt} 2\Omega \frac{\partial z}{\partial T} \frac{\partial \Psi}{\partial z} \right) \right]$$

The vorticity equation can now be rewritten:

$$\frac{d}{dt} \left[\zeta - \frac{1}{\rho} \frac{\partial}{\partial z} \left(\frac{\rho 4\Omega^2}{\frac{\partial \overline{S}}{\partial z} \frac{\partial T}{\partial z}} \right) \right] + \frac{2\Omega}{r} \left[\frac{1}{\rho} \frac{\partial \rho}{\partial r} \frac{\partial \Psi}{\partial \theta} + \frac{r}{z} \frac{\partial^2 \Psi}{\partial z \partial \theta} - \frac{1}{\rho} \frac{\partial}{\partial z} \left(\frac{\rho r}{z} \frac{\partial \Psi}{\partial \theta} \right) \right] = 0$$

122

We recognize that $\frac{\partial \overline{S}}{\partial z} > 0$ and $\frac{\partial T}{\partial z} < 0$ in the northern hemisphere, and the opposite inequalities hold in the southern hemsiphere, so the Brunt-Vaisaala frequency is:

$$N = \left[-\frac{\partial \overline{S}}{\partial z} \frac{\partial T}{\partial z} \frac{1}{4\Omega^2} \right]^{\frac{1}{2}}$$

Recalling that our zonal coordinate is captured in θ and the meridional coordinate can be related to r and the latitude: $dr = dy \sin\phi$, we can see that the $\frac{\partial \Psi}{\partial \theta}$ terms are analogous to the βv terms in the well known GFD treatment of potential vorticity. Referring again to figure 1, we use the following relationships:

$$v = \frac{1}{r} \frac{\partial \Psi}{\partial \theta}$$

and

$$\frac{\partial \rho}{\partial r} = 2r\rho' \ , \quad \frac{\partial \rho}{\partial z} = 2z\rho' \quad so \quad \frac{\partial \rho}{\partial r} = \frac{r}{z} \frac{\partial \rho}{\partial z}$$

to express the βv terms as:

$$2\Omega \left[\frac{vr}{\rho z} \frac{\partial \rho}{\partial z} + \frac{r}{z} \frac{\partial v}{\partial z} - \frac{1}{\rho} \frac{\partial}{\partial z} \left(\frac{\rho v r}{z} \right) \right]$$

$$= 2\Omega \left[\frac{r}{z} \frac{\partial v}{\partial z} - \frac{\partial}{\partial z} \left(\frac{rv}{z} \right) \right]$$

$$= 2\Omega v \frac{r}{z^2} = v \frac{\partial}{\partial r} \left(\Omega \frac{r^2}{z^2} \right) \ .$$

So we get the potential vorticity conservation:

$$\frac{dq}{dt} = \frac{\partial q}{\partial t} + J(\Psi, q) = 0$$

where

$$q = \nabla^2 \Psi + \frac{1}{\rho} \frac{\partial}{\partial z} \left(\frac{4\rho\Omega^2}{N^2} \frac{\partial \Psi}{\partial z} \right) + \Omega \frac{r^2}{z^2} \ .$$

From this we could easily recover the meterological limits using the coordinate relationships above.

Boundary Conditions

We require that there be no normal flow out of the planet surface (with outward normal $= \hat{n}$); but $\hat{n}$ is parallel to ∇T, so we have:

$$\mathbf{v} \cdot \nabla T = -\frac{1}{r} \frac{\partial \Psi}{\partial \theta} \frac{\partial T}{\partial r} + w \frac{\partial T}{\partial z} = 0$$

or

$$0 = \frac{dS'}{dt} = \frac{\partial}{\partial t} \frac{\partial \Psi}{\partial z} + J \left(\Psi, \frac{\partial \Psi}{\partial z} \right)$$

as a boundary condition.

Barotropic Case

In this limit, we see that $\frac{\partial \overline{S}}{\partial z} \longrightarrow 0$, but from the vorticity equation, we have:

$$\frac{d\zeta}{dt} + \frac{d}{dt}\left[\frac{1}{\rho}\frac{\partial}{\partial z}\left(\frac{4\rho\Omega^2}{-\frac{\partial \overline{S}}{\partial z}\frac{\partial T}{\partial z}}\frac{\partial \Psi}{\partial z}\right)\right] + 2\Omega v \frac{r}{z^2} = 0$$

so as the denominator approaches zero, so must the numerator, and therefore $\frac{\partial \Psi}{\partial z} = 0$. Again, we commute $\frac{d}{dt}$ and $\frac{\partial}{\partial z}$, multiply by ρ and integrate in z from $-h$ to h; here $\pm h$ describes the top and bottom where a z-collumn intersects the planet surface. If we define M such that:

$$M = \int_{-h}^{h} \rho dz$$

then the previous equation can be integrated with appropriate boundary conditions to get:

$$\frac{d\zeta}{dt} + \frac{2\Omega}{M}\frac{dM}{dr}v = 0$$

where

$$\zeta = \frac{1}{r}\frac{\partial}{\partial r}\left(r\frac{\partial \Psi}{\partial r}\right) \approx \frac{\partial^2 \Psi}{\partial r^2} \; and \; v = \frac{1}{r}\frac{\partial \Psi}{\partial \theta}$$

Baroclinicity

How large are $\overline{S}$ and S'? Recall from our scaling that

$$S'T \sim 2\Omega UL$$

It is a reasonable assumption to make the lengthscale L the same as the deformation lengthscale L_D, so:

$$\overline{S}T \sim (2\Omega L)^2.$$

and we see that the following relation holds:

$$\frac{S'}{\overline{S}} \sim \frac{U}{2\Omega L} \sim \frac{L}{r} << 1.$$

But we also see that:

$$\frac{\partial S'}{\partial r} \sim \frac{\partial \overline{S}}{\partial r} \sim \frac{\partial \overline{S}}{\partial z}$$

so isotherm slopes which are not horizontal are allowed, e.g. figure 2.

Instability Criterion

Following the method of Rayleigh, we perturb some reference streamfunction $\bar{\Psi}$ by adding a small term Ψ', further assuming that the perturbations are normal mode like, so:

$$\Psi' \propto e^{im(\theta - ct)}$$

where c is the angular phase speed of the (possibly unstable) mode. The perturbations are described by the equation:

$$\left[\frac{\partial^2 \Psi'}{\partial r^2} + \frac{1}{\rho} \frac{\partial}{\partial z} \left(\frac{4\rho \Omega^2}{N^2} \frac{\partial \Psi'}{\partial z} \right) \right] + \frac{\partial \bar{q}/\partial r}{(\bar{u} - cr)} \Psi' = 0$$

Now we treat ρ and N^2 as functions of z only, multiply the previous equation by $\rho \Psi'^*$ and integrate, applying suitable perturbation boundary conditions at the surfaces...finally, taking the imaginary part:

$$c_i \int \int r\rho \frac{\partial \bar{q}}{\partial r} \frac{|\Psi'|^2}{|\bar{u} - c|^2} dr \, dz = 0$$

So, for instability, the integral must vanish, and therefore, $\frac{\partial \bar{q}}{\partial r}$ must change sign. This is basically the same as a barotropic stability equation, except that in this case, the *local* (potential) vorticity is not augmented by β effects, but by a term that seems to encompass collumnar depth terms as well as variations in planetary vorticity. Planetary geometric effects can therefore dominate planetary vorticity variation effects, and in this "deep" analysis, it is suggested that instability requires *eastward* jets.

Notes compiled by Phil Yecko and Qingping Zou
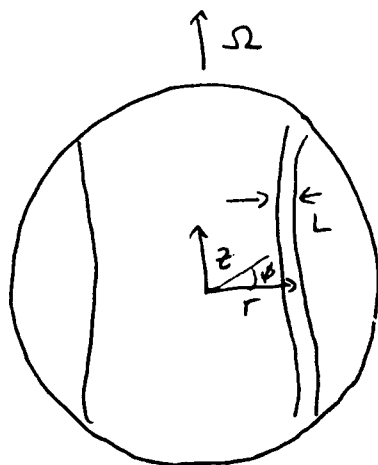
Figure 1

Isolines of $S_0 + S_1$

Stable $\left(\dfrac{\partial S}{\partial R} > 0 \right)$

Figure 2

126

Initial Development of Eddies in High-Speed
Zonal Flow: One Interpretation
for NTB Activity of Jupiter

Tadashi Asada
Kyushu International University

Peter J. Gierasch
Cornell University

and

Toshio Yamagata
Department of Earth and Planetary Physics
Tokyo University

The initial development of an anticyclonic eddy in a high speed jet flow has been examined using a 2-layer rigid-lid model for incompressible fluid governed by the shallow water equations. In the case of large Rossby deformation radius an inertial gravity wave can propagate in all directions, but in the small deformation radius case the gravity wave propagates only in the upstream direction. In the latter case, the phase speed of the internal gravity wave is less than the zonal flow speed, and latitudinal propagation of the wave seems to be prevented by the strong shear region both north and south of the eddy.

This behavior of the inertial wave seems to have some common features with the dark spots of the North Temperate Belt of Jupiter, which is the latitude of the fastest eastward zonal flow in Jupiter. These spots appear only west (upstream side) of the bright spot, and move westward relative to the spot.

If our hypothesis that the dark spots are due to an inertial gravity wave is valid, it suggests small values of the Rossby deformation radius.

Timing Maps and Pulsatile Chaos

N.J. Balmforth

Solitions or pulses can arise from partial differential equations (PDEs) as exact travelling wave solutions. They also describe solutions of ordinary differential equations (ODEs) which model systems that "burst". Recent asymptotic methods have shown how to compose multi-soliton solutions or pulse trains for such equations. These take the original differential equation and represent the pulse train as a superposition of single-pulse solutions. Each of these solitary solutions correspond to homoclinic orbits of an ordinary differential equation (this being either either the original equation itself, or an associated equation derived from the original partial differential equation on introducing a travelling-wave *ansatz*).

On introducing the superposition into a PDE one finds a set of ordinary differential equations governing the temporal evolution of the relative locations of the individual pulses. These centroids are forced to move because each pulse dynamically interacts with its nearest neighbours. When the pulse train is steady, the set of equations reduces to an algebraic map relating the nth pulse spacing to the $(n + 1)^{th}$, which is what one also obtains when substituting the superposition of single-pulse solutions into an ODE.

The map provides a powerful method to analyse pulse-train solutions. This lecture took an example ODE, examined its various homoclinic orbits in parameter space ("the Zoology of Homoclinic Orbits"), applied and assessed the asymptotic multi-pulse method, and explored the different pulse-train solutions.

A New Roll-type Instability in an Oscillating Fluid Plane

Edward W. Bolton
*Department of Geology and Geophysics, Yale University,
KGL, P.O. Box 6666, New Haven, CT 06511-8130, USA*

A new roll-type instability has been discovered experimentally. When fluid between two closely spaced, parallel plates is oscillated about an axis midway between the plates, it exhibits an instability that takes the form of longitudinal rolls aligned perpendicular to the axis of rotation. The basic-state oscillatory shear flow, before the onset of rolls, may be viewed as driven by the $\hat{r} \times \dot{\Omega}$ term of the Navier-Stokes equation in the oscillatory reference frame. Flow regimes are governed by a parameter space defined by the maximum amplitude of angular oscillation, α, and the nondimensional frequency: $\Phi = \omega d^2 / \nu$. The equilibrium wavelength of the rolls scales with d, the gap spacing between the plates, and it increases as Φ increases. Supercritical to a weak-roll onset, an abrupt transition to stronger roll amplitude occurs. Photographs of the cell after an impulsive start show the roll development and initial increase in roll wavelength. A variety of phenomena are observed, including: wavelength selection via defect creation and elimination; front propagation; secondary wavy instabilities; and the transition to turbulence. We also present solutions for the basic-state shear flow in a near-axis approximation, and discuss some issues relating to its stability. The data is compared to a variety of constant Reynolds numbers curves. We also develop a simple resonance model in which the roll turnover time equals the oscillation period. This model shows some promise in understanding the low α, high Φ onset of strong rolls. The roll alignment is parallel to the basic state shear velocity, as is the case for Taylor-Couette flow, and other flows possessing potentially destabilizing body forces. This is in contrast to roll orientation perpendicular to the flow, as is the case for the Kelvin-Helmholtz instability.

References

Bolton, E. W. & Maurer, J., A new roll-type instability in an oscillating fluid plane, submitted to *J. Fluid Mech.* (13 July 1992).

Rings in Numerical Models of Ocean General Circulation:
A Statistical Study

by

Eric P. Chassignet

Because of their importance in the ocean energetics and general circulation, a proper representation of ring generation mechanisms and evolution in numerical models is crucial for an accurate picture of the heat, salt and energy budgets. Ring locus, lifetime, propagation speed, radius and interface displacement statistics are derived for four widely used eddy-resolving numerical models and compared to the 10-year statistical analysis of Gulf Stream rings based on time series of satellite infrared determinations performed by Brown et al. (1986). The ring formation process and behavior in ocean numerical models depends upon the governing equations, the vertical coordinate and the boundary conditions used. It is shown that as more terms are retained in the model equations, the mid-latitude jet becomes more unstable, and its interior penetration as well as the associated number of rings formed are reduced. Rings in the layer model have slower propagation speeds and longer lifetimes than their level counterparts. Such results illustrate the sensitivity of numerical ocean circulation models to the physical and numerical assumptions made.

The Influence of Layer Outcropping on the Separation of
Western Boundary Currents.

by

Eric P. Chassignet

The influence of outcropping layers on the separation of western boundary currents is investigated in a series of purely wind-driven eddy-resolving primitive equation numerical experiments. The outcropping mechanism of Parsons (1969) allows the mid-latitude jet to separate south of the zero wind stress curl line (ZWCL), an important property when one considers that most realistic numerical experiments to date exhibit an overshooting mid-latitude jet.

If the inertial terms are removed from the momentum equations, the Sverdrup relation for the interior flow emerges as the dominant constraint on the placement of the upper layer jet separation latitude. As long as the circulation in the lowest wind forced layer is dynamically inactive, a good agreement is obtained with the analytical theory, namely a separation south of the ZWCL. If dynamically active, the resulting flow pattern then changes drastically by favoring a configuration which satisfies the Sverdrup relation while maintaining a neutral mean state, namely a jet separation at the ZWCL.

As soon as the inertial terms are included, the Sverdrup constraint becomes less dominant, allowing the upper layer mid-latitude jet separation latitude to shift southward whenever the upper layer is chosen sufficiently shallow to cause large-scale outcropping. The degree to which this southward shift depends on the amount of mass in the top layer and on the parameterization of the wind-induced stress profile in the water column was explored in detail.

The Dynamics of Barotropically Dominated Eddies

William K. Dewar and Christine Gailliard
The Florida State University
Tallahassee, FL 32301

Based on observations, the proposition is forwarded that some rings involve an important barotropic component. The work described heiein is directed at understanding the consequences on eddy evolution of such structure. An analysis of the equations of motion is conducted which emphasizes the importance of the evolution of the barotropic mode. The baroclinic component is found to be largely passive.

This theory differs considerably from previous theories which focus on the evolution of surface-intensified rings. The most important practical differences are that the coupled system can be expected to exhibit propagation in any direction (as opposed to predominantly west, as in baroclinic theories), and that the propagation rates can be an order of magnitude greater than those of baroclinic systems. These aspects of the present theory are in accord with many ring observations.

A series of primitive equation numerical experiments are conducted to test the theory, with the result that the experiments support such "barotropically dominated dynamics" as a useful qualitative and quantitative tool for the study of eddies and rings. It is further observed that many initial conditions which are baroclinically unstable in the presence of a resting lower layer are stabilized in the barotropically dominated regime.

The asymptotic theory also suggests that initial conditions with closed regions of potential vorticity should differ significantly from those with no closed potential vorticity zones. This hypothesis is supported by primitive equation runs; approximately compensated lower layer experiments (with no closed potential vorticity contours) exhibit qualitatively and quantitatively different behavior than experiments with initially energetic lower layers (which have closed potential vorticity contours).

Jupiter's Winds and Arnol'd's 2nd Stability Theorem

Timothy E. Dowling

Department of Earth, Atmospheric and Planetary Sciences
Massachusetts Institute of Technology

Stability theorems for zonal (east-west) shear flows typically involve constraints on the potential vorticity gradient with respect to latitude, $\bar{q}_y$, where y is latitude and the overbar denotes a zonal average. Consider $\bar{q}_y$ in the 1-1/2 layer shallow-water model:

$$\bar{q}_y = \frac{1}{g\bar{h}}(\beta - \bar{u}_{yy} + f\bar{q}(\bar{u} - \bar{u}_2)),\tag{1}$$

where f is the Coriolis parameter, β is df/dy, $\bar{u}(y)$ is the upper-layer zonal wind, $\bar{u}_2(y)$ is the deep-layer zonal wind, which is specified in the 1-1/2 layer model, g is the reduced gravity, and $\bar{h}(y)$ is the upper-layer thickness. A vorticity analysis of the Voyager wind data for Jupiter has yielded an empirical relationship between potential vorticity and zonal wind on Jupiter (Dowling 1992):

$$\bar{u} = \bar{q}_y(\bar{q})^{-2},\tag{2}$$

where $\bar{u}$ is measured in the rotating reference frame of the planet's magnetic field (the System III reference frame). Since (2) specifies the basic state of the 1-1/2 layer model as applied to Jupiter, we would like to know its stability properties.

At present, stability theorems are more completely understood in the quasi-geostrophic limit, in which case (1) becomes:

$$\bar{Q}_y = (\beta - \bar{u}_{yy} + L_d^{-2}(\bar{u} - \bar{u}_2)),\tag{3}$$

where $L_d^2 \equiv gh/f^2$ is the square of the (first baroclinic) deformation radius. The empirical relation (2) becomes:

$$\bar{u} = \bar{Q}_y L_d^2.\tag{4}$$

The most widely cited stability criterion is the Rayleigh-Kuo criterion, which states that if:

$$\bar{Q}_y \geq 0,\tag{5}$$

or

$$\bar{Q}_y \leq 0,\tag{6}$$

for all y, then the flow is stable. Since $\bar{u}(y)$ changes sign at many latitudes on Jupiter, (4) implies that the Rayleigh-Kuo stability criterion is strongly violated. This *does not* imply that Jupiter's winds are strongly unstable, however.

There are at least two known ways that a shear flow can violate the Rayleigh-Kuo stability criterion and still be stable. Following results originally obtained by Fjørtoft in 1950 and Arnol'd in 1965-66, and later extended by several workers (see McIntyre and Shepherd 1987), we know that if in some reference frame:

$$-\infty < \frac{\bar{Q}_y}{\bar{u}} < 0,\tag{7}$$

for all y, the 1 the flow is stable. Equation (7) is alternately known as Fjørtoft's theorem or Arnol'd's 1st theorem. The techniques laid out by Arnol'd actually prove nonlinear (large amplitude) stability instead of just linear (small amplitude) stability. Ripa (1983) has extended (7) to the 1-layer shallow-water equations on the beta-plane or the sphere. Unfortunately, (4) implies that Jupiter's winds also violate (7).

However, in addition to his first stability theorem, Arnol'd also proved a second stability theorem, which in our context states that if in some reference frame:

$$0 < \frac{\bar{Q}_y}{\bar{u}} < L_d^{-2} \,, \tag{8}$$

for all y, then the flow is stable. We have assumed in (8) that L_d is much smaller than the radius of the planet; see McIntyre and Shepherd (1987) for the more general cases. By comparing (8) to (4), we see that the zonal winds on Jupiter are apparently neutrally stable with respect to Arnol'd's second stability theorem. Numerical experiments have confirmed this neutrality property for Jupiter's cloud-top zonal-wind profile (Dowling 1992). The linear stability properties of (2) and (4) are the subject of a numerical analysis by A. Stamp in this volume. What is needed now is an extension of Arnol'd's second stability theorem to the primitive case, and a physical explanation for the role of Arnol'd's stability theorems in planetary shear flows.

References

Dowling, T.E. 1992. *J. Atmos. Sci.* **49**, October.
McIntyre, M.E. & T.G. Shepherd 1987. *J. Fluid. Mech.* **181**, 527–565.
Ripa, P. 1983. *J. Fluid. Mech* **126**, 463–489.

Deep Jets and Shallow Spots?

Glenn R. Flierl

We begin with the anelastic model and and simplify to the case where the entropy is uniform below and above the base of the weather layer, with a step discontinuity across the boundary at $R = a + \eta(x, y, t)$. The dynamics then simplifies to

$$\mathbf{u}_t + (\mathbf{u} \cdot \nabla)\mathbf{u} + 2\Omega \hat{\mathbf{k}} \times \mathbf{u} = -\nabla p$$

$$\nabla \cdot \bar{\rho}\mathbf{u} = 0$$

$$[p] = -g'\eta \qquad at \ R = a$$

$$\eta_t + \mathbf{u} \cdot \nabla\eta = \mathbf{u} \cdot \hat{\mathbf{R}} \qquad at \ R = a$$

f we assume small Rossby number, we can follow the standard QG derivation for the shallow layer to find

$$\frac{D}{Dt}[\nabla^2\psi_1 + \beta_1 y + \frac{f}{H_1}\eta] = 0$$

In the deep layer, we follow Ingersoll and Pollard to derive a rather complicated set of equations

$$\frac{D}{Dt}[\tilde{\nabla}^2\psi_2 + \beta(\frac{\partial}{\partial R} \ln \bar{\rho})y] = f\frac{1}{\sin^2\theta}\frac{1}{\bar{\rho}}\frac{\partial}{\partial z}\bar{\rho}w$$

$$\frac{D}{Dt}w = -f\frac{\partial}{\partial z}\psi_2$$

$$\frac{D}{Dt}\eta = -\frac{\partial}{\partial x}\psi_2 \cos\theta \sin\theta + w \sin\theta$$

with $\psi_1 - \psi_2 = -g'\eta/f$ and

$$\tilde{\nabla}^2 = \frac{\partial^2}{\partial x^2} + \frac{1}{\sin^2\theta}\frac{\partial^2}{\partial y^2}$$

If we assume that ψ_2 is nearly depth–independent, multiply the first equation by $\bar{\rho}$ and integrate in the direction parallel to the rotation axis, use the boundary condition (the third equation), we find the approximate statement

$$\frac{D}{Dt}[\tilde{\nabla}^2\psi_2 + \beta_2 y - \frac{f}{H_2}\eta] = 0$$

with β_2 a *negative* constant. H_2 is the mass in the column, divided by the density at the base of the weather layer times $\sin^2\theta$ and is large compared to H_1.

We discussed the stability of barotropic jets (not varying along the rotation axis) in the case where the difference between ∇^2 and $\tilde{\nabla}^2$ was ignored; the upper layer can be stabilized by Arnol'd's second theorem while the deep layer is stabilized because $|\beta_2|$ is larger than $|U_{yy}|$. However, the coupled model still shows a weak instability with growth rates apparently of order $(H_1/H_2)^{1/2}|U_y|$.

If we consider spots embedded in the zonal shear flow, we can show that

1) Isolated spots must have a deep signature such that

$$\int\int \psi_2 = -\frac{\beta_1 H_1}{\beta_2 H_2} \int\int \psi_1$$

2) Spots will be more baroclinic than the jets.
3) Spots can be compact (decaying in the exterior field) if the Froude number is sufficiently large.
4) But this only applies to one mode; the other mode will generally be radiating. Therefore spots will gradually lose energy to Rossby wave radiation. The time scales are long $[(H_2/H1)$ times the characteristic turn-over time for the spot], but not negligible. This suggests that input of energy into at least the Red Spot is required.

We can develop a weakly radiating theory: if we split the fields up into a zonal flow and a spot/wave field

$$\psi_1 = -\int^y U + \phi_1$$

$$\psi_2 = -\int^y U + \delta\phi_2$$

with $\delta = H_1/H_2$, we find the lowest order upper layer equation is

$$[\frac{\partial}{\partial t} + U\frac{\partial}{\partial x} + J(\phi_1,\cdot)](\nabla^2 - F)\phi_1 + (\beta_1 - U_{yy})\frac{\partial}{\partial x}\phi_1 = 0(\delta)$$

as studied by Ingersoll and Cuong and others. The lowest order lower layer equation is linear

$$[\frac{\partial}{\partial t} + U\frac{\partial}{\partial x}]\nabla^2\phi_2 + (\beta_2 - U_{yy})\frac{\partial}{\partial x}\phi_2 = -[\frac{\partial}{\partial t} + U\frac{\partial}{\partial x}]\phi_1$$

This is similar to the problem of flow over topography (especially in the case where the upper layer solution is approximately steady) and therefore will have lee waves in the solution. The energy flux in these lee waves can be shown to cause decay of the upper layer vortex over longer time periods.

The limitations of balance models

Rupert Ford

Department of Applied Mathematics and Theoretical Physics
Silver Street, Cambridge, CB3 9EW, UK.

The degree to which the large scale dynamics of atmospheres and oceans can be described in terms of Potential Vorticity distributions on isentropic or isopycnal surfaces is of both conceptual and practical interest. Conceptually it can lead to simplification of thought and ideas (Hoskins et al, 1985), and practically is of use in areas such as initialization for numerical weather prediction (Baer & Tribbia, 1977).

The ability of time integrations based on inversion of the Potential Vorticity field or Rossby modes to follow closely integrations of the primitive equations starting from the same initial conditions prompted Leith (1980) to postulate the existance of a "slow manifold" for the shallow water equations or truncated versions thereof. Briefly stated:

If there exist (nonlocal) time-independent operators on the Potential Vorticity field giving the velocity and height fields such that

If at $t = 0$ the velocity and height fields are given by these inversion operators then they are given by the same inversion operators for all subsequent times when the system evolves under full (shallow water) evolution

Then this set of inversion operators defines a slow manifold for the system.

Subsequent investigations with severly truncated systems (Warn & Menard 1986; Vautard & Legras, 1986; Lorenz 1986; Lorenz & Krishnamurty 1987) based on the shallow water equations suggested that ultimately freely propagating gravity waves were generated, and in the absence of forcing and dissipation no slow manifold could be found.

In single layer hemispheric simulations, McIntyre & Norton (1992) found that integrations using inversion operators based on eliminating high order time derivatives of the divergence field could follow the equivalent shallow water integrations for up to 25 days, the only coherent difference between the two being a large scale equatorial Kelvin wave, which appeared to be freely propagating, in the sence that its motion was consistent with the Kelvin wave dispersion relation.

The large scale of the generated apparently unbalanced wave prompts one to recall the problem of aerodynamic sound generation (Lighthill, 1952; Crow, 1970), in which the scale of the generated acoustic waves is large compared with the scale of the turbulence which is generating them.

We consider the model problem of a localized potential vorticity anomaly on an f-plane at low Froude number and arbitrary Rossby number. The Froude number is taken as an asymptotic parameter.

The leading order dynamics in the region of the PV anomaly is simply two-dimensional non-divergent vortex dynamics. A matched asymptotic analysis shows that

(1) $O(F^2)$ and $O(F^2 \ln F)$ corrections to the basic vortex dynamics can be written down in terms of the instantaneous PV distribution

(2) at $O(F^4)$ the correction to the basic vortex dynamics involves an integral over the entire past history of the flow, which is not well defined without reference to some arbitrarily chosen initial point in time, unless all frequencies in the vortex dynamical flow lie below the inertial frequency f.

We conclude that it is potentially fruitful to seek high order balanced models, but that no procedure can be entirely rational at all orders of approximation or parameter expansion if it is to deal adequately with the parameter regime $Ro \sim 1$, $F \ll 1$.

In the regime where the Rossby number and the Froude number are both small and of the same order, the asymptotic analysis is not formally valid. To investigate this regime, we consider linearized disturbances to an axisymmetric vortex, imposing the condition that there be no potential vorticity disturbances except those associated with the motion of the boundary of the vortex. Numerical experiments show that for mode 6 disturbances to the vortex boundary the vortex, which has a monotonic PV gradient, and is therefore stable in the absence of gravity waves, is unstable for Rossby numbers greater than 0.3 (if the PV is anticyclonic) or 0.5 (if the PV is cyclonic). Since the exact axisymmetric vortex must lie on the slow manifold, we conclude that the slow manifold is of highly reduced dimension in phase space, consisting only of axisymmetric distributions of potential vorticity, and is unstable, over much, and possibly all, of its domain of existence.

References

Baer, F. and Tribbia, J.J., 1977, On Complete filtering of gravity modes through nonlinear normal mode initialization *Mon. Wea. Rev.* **105** 1536-1539

Crow, S.C., 1970 Aerodynamic sound generation as a singular perturbation problem *Stud. Appl. Math.* **49** 21-44

Hoskins, B.J., McIntyre, M.E., and Robertson, A.W., 1985, On the use and significance of isentropic potential vorticity maps *Q. J. Roy. Met. Soc.* **111** 877-946

Leith, C.E., 1980, Nonlinear normal mode initialization and quasigeostrophic theory. *J. Atmos. Sci.* **37** 958-968

Lighthill, M.J., 1952, On sound generated aerodynamically *Proc. Roy. Soc. Lond.* **A211** 564-587

Lorenz, E.N., 1986 On the existence of a slow manifold *J. Atmos. Sci.* **43** 1547-1557

Lorenz, E.N. and Krishnamurthy, V., 1987 On the nonexistence of a slow manifold *J. Atmos. Sci.* **44** 2940-2950

McIntyre, M.E., and Norton, W.A., 1992, Potential vorticity inversion on a hemisphere *J. Atmos. Sci.* to appear.

Vautard, R. and Legras, B., 1986 Invariant manifolds, quasi-geostrophy and initialization. *J. Atmos. Sci.* **43** 565-584

Warn, T., and Menard, R., 1986, Nonlinear balance and gravity-inertial wave saturation in a sinple atmospheric model *Tellus* **38A** 285-294

138

β - Convection: Chaos, turbulence, and zonal flows.

J.E. Hart

Department of Astrophysical, Planetary and Atmospheric Sciences
University of Colorado

Thermal convection in an equatorial annulus is studied numerically (work done with Nic Brummel). In this zonal channel configuration gravity g is normal to the channel walls, and the zonal direction and the basic rotation Ω are perpendicular to both g and to each other. Sloping endwalls at the top and bottom of the channel lead to a topographic β - effect that acts on convecting columns excited by thermal instability in the presence of an applied temperature gradient opposite to g. Such a system can be realized, for example, in a rapidly rotating cylindrical annular centrifuge where centrifugal buoyancy is radial and naturally perpendicular to the axial rotation vector. A similar model has been proposed by Busse (GAFD, 1983) for the generation of zonal jets on the giant planets by thermal convection.

When the rotation is sufficiently rapid, the motion is invariant along the axis of rotation (by Taylor-Proudman). The dynamics are governed by a barotropic quasi-geostrophic vorticity equation with buoyancy generation, along with a heat conservation equation. The system is constrained to be two-dimensional and is easily integrated numerically. For unit Prandtl number the important parameters are a Rayleigh number $R_a = g\alpha\Delta TD^3/\kappa\nu$ and a differential rotation parameter $\beta = 4 \tan(\eta)D^3/\nu L$, where α is the thermal expansion, ν the kinematic viscosity, κ the thermal diffusivity, D the channel wall separation, L the distance between the endwalls, and η their cross-channel slope. The main results are as follows:

1) When R_a is increased at fixed β a transition to chaos by bifurcation off a two-torus in energy space is observed. The two incommensurate oscillations correspond to an interference vacillation involving two thermal Rossby waves with different cross-channel wavenumbers but the same zonal wavenumber, and an amplitude vacillation where the convection generates a mean zonal flow by a tilted-cell meanflow instability, but later becomes stabilized by the shear when the convection gets too big.

2) When β is increased at fixed and highly supercritical R_a an abrupt transition is made from ordinary convection with weak zonal flows to turbulent β - convection (see figure). Away from the stability boundary $(\beta < R_a^{3/4})$ the zonal wavenumber of the convection is much less than the linear prediction $(k_x \approx \beta^{1/3})$, and the accompanying zonal flows can be very large.

3) Much of the parameter regime of turbulent β - convection is occupied by pulsating states in which bursts of convection accelerate the zonal shear but then are quenched when the shear gets too big. The shear flow relaxes under viscosity until the process repeats itself.

Figure: Eddy streamfunction of convection at $R_a = 10^6$, $P_r = 1$. a) $\beta = 0$ (ordinary convection), b) $\beta = 6000$ (simple travelling wave convection), c) $\beta = 6000$ (chaotic branch with large zonal mean flow), d) $\beta = 8000$, e) $\beta = 20,000$, f) $\beta = 28,000$ (approaching stability boundary). Each set of 4 frames shows the planform of the convection at four successive times. The long side of each box is the zonal direction and the short side is in the direction of gravity. The basic rotation vector is out of the plane of the figure.
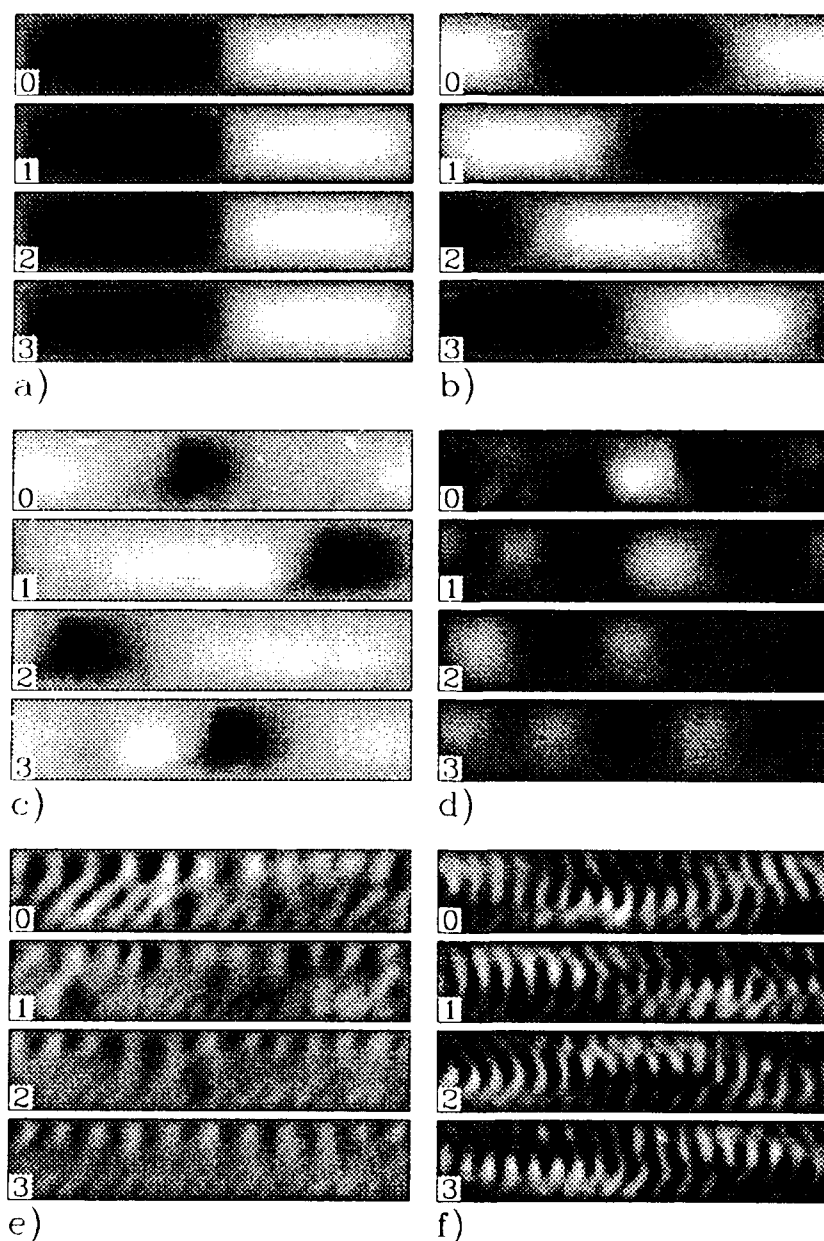
Particle-driven fluid flows

By Herbert E. Huppert

Institute of Theoretical Geophysics,
Department of AppliedMathematics and Theoretical Physics, Silver St.,
Cambridge CB3 9EW England

The motion of particle-laden fluids is of considerable interest to engineers, fluid dynamicists, geophysicists, metallurgists and oceanographers. The seminar presented a series of investigations into fundamental processes in which the fluid flow is a result of a concentration of small, heavy particles in the fluid. In all the cases considered the fluid motion was turbulent at high Reynolds number, while the particles settled with respect to the adjacent fluid motion at low Reynolds number.

1. Sedimentation of particles from a convecting fluid. Consider a fluid seeded with particles which is heated from above. The resultant motion is controlled by the bulk density of the particulate suspension, which is a function of both temperature and particle concentration. The particle distribution initially stabilizes the bulk density gradient while sedimentation proceeds, and convection occurs in an upper, clear layer and a sedimenting lower layer. Eventually the destabilizing thermal gradient can exceed the stablizing effect of the particles, and a sudden overturning of the whole system results. If the fluid is cooled from above, a critical concentration separates a situation of continual overturn from a situation of no overturn, with the sedimentary layer falling unimpeded to the bottom. This system is of relevance to the evolution of magma chambers in the Earth, which will cool from above while crystals grow in the convecting interior. Beyond a critical concentration the crystals will sediment and the process will be re-initiated. A series of sedimentary layers will thus form at the base of the chamber.

2. Polydisperse sedimentation. When a suspension of small particles is overlain by a clear fluid whose density is greater than that of the interstitial fluid, but less than that of the bulk suspension, the settling of the dense suspended particles can lead to vigorous convection in the overlying layer. A sharp interface is observed between the convecting upper layer and a stagnant lower region in which there is unimpeded sedimentation. The interface descends at a constant velocity. Buoyancy arguments based on the calculated density profile are used to evaluate the amount of particle entrainment in the upper layer and the descent rate of the interface. There is good agreement between the theoretical model and experimental results.

3. Particle-laden gravity currents. When a fixed volume of a suspension is quickly released into a less dense ambient fluid, a gravity current can propagate over the rigid horizontal surface at the base of the ambient fluid. We have derived a model for a two-dimensional current using the concepts of shallow water theory augmented by the deposition of particles at the base of the current. The model allows for the interstitial fluid of the current to be less dense than the ambient though the particle concentration is sufficient to make the initial bulk density greater. The resulting equations are solved numerically and the results agree extremely well with data obtained from a series of laboratory experiments using intersitital fluid whose density is either equal to or less than that of the ambient.

There are many industrial and natural applications of the model as well as many possible future extensions of the research.

References

Bonnecaze, R.T., Huppert, H.E. & Lister, J.R. *Particle-driven gravity currents*, J. Fluid Mech. (in press).

Huppert, H.E., Kerr, R.C., Lister, J.R. & Turner, J.S. (1991) *Convection and particle entrainment driven by differential sedimentation*, J. Fluid Mech. 226, 349-369.

Koyaguchi, T., Hallworth, M.A. & Huppert, H.E. *An experimental study on the effects of phenocrysts on convection in magmas*, J. Volcan. & Geotherm. Res. (in press).

Koyaguchi, T., Hallworth, M.A., Huppert, H.E. & Sparks, R.S.J. (1990) *Sedimentation of particles from a convecting fluid*, Nature 343, 447-450.

Sparks, R.S.J., Bonnecaze, R.T., Huppert, H.E., Lister, J.R., Hallworth, M.A., Mader, H. & Phillips, J. *Sediment-laden gravity currents with reversing buoyancy*, Earth & Planet. Sci. Lett. (in press).

Can tidal dissipation account for orbital evolution of the Jovian satellites?

Petros J. Ioannou

M. I. T.

1. Introduction

It has long been recognized that dissipation of ocean tides on the Earth leads to lengthening of the solar day and lunar month, and retreat of the lunar orbit (for a review of the subject refer to Lambeck, 1980). The increase of the radius of the lunar orbit is approximately $4\,cm\,yr^{-1}$, and the retardation of the angular velocity of the earth around its axis is $\dot{\omega} = -(5.5 \pm 0.5) \times 10^{-22} rad\,s^{-2}$. These secular changes have been recorded in the sceletal growth patterns of coral, bivalve, and stromatolite fossils. Analysis of coral and bivalve fossils shows that during the mid-Devonian ($360 \times 10^6 yr\,bp$) the year was longer, $i.e.\,398 - 406\,days$, in accordance with the orbital evolution theory. The same data suggests that the average lunar orbital acceleration $\dot{\omega}$ over the last $400 \times 10^6\,yr$ was about half its present value. Analysis of stromatolite fossils indicate that there were oceanic tides $2 \times 10^9 yr\,bp$, suggesting that the moon was already outside the Roche limit (2.9 earth's radii).

Evolution of the lunar orbit depends on the rate of transfer of angular momentum from the rotating planet to the orbiting satellite. This transfer is proportional to the rate of tidal dissipation. A measure of this dissipation is given by the dissipation factor Q which is defined as:

$$Q = \frac{2\pi E^*}{\oint \frac{d}{dt} E dt},\qquad(1.1)$$

where the line integral over $\frac{d}{dt} E$ is the energy dissipated over a complete cycle, and E^* is the peak energy stored in the system during the cycle (MacDonald, 1964). Note that the dissipation factor Q is inversely proportional to the rate of dissipation. Presently, for the Earth $Q \approx 10$ corresponding to dissipation of $5 \times 10^{12}\,W$, accounted primarily by the dissipation of the ocean tides in shallow seas.

Estimates of Q for the outer planets were obtained by Goldreich and Soter (1966). The existence of close satellites provides a lower bound on Q because if Q were too small the evolution of the orbit would be too rapid for the satellites to occupy their present close orbit if it is assumed that the satellites are as old as the solar system ($4.5 \times 10^9\,yr$). The greatest lower bound on Q for Jupiter obtained by this means is supplied by Io: $Q_J \approx 5 \times 10^5$. For Saturn the present location of its innermost satellite, Mimas, provides the estimate $Q_S \approx 6 \times 10^4$ and for Uranus, Miranda provides $Q_U \approx 7 \times 10^4$. Triton's retrograde orbit around Neptune is shrinking towards the planet and can not provide an estimate of the Q in the manner described. However, a value of Q for Neptune of the order of 7×10^4 is estimated to damp Triton's eccentricity to its present, nearly zero value, in the order of $3.2 \times 10^9\,yr$, even if it were captured in a highly eccentric orbit. The estimates given for the case of Jupiter and Saturn are only approximate because the satellites of

these planets are involved in tight Laplacian resonances. For example Io, Europa and Ganymede are involved in the stable resonance first studied by Laplace. The orbital angular velocities of these satellites are such that: $\omega_{io} \approx 2\omega_{europa}$, $\omega_{europa} \approx 2\omega_{ganymede}$, and $\omega_{io} - 3\omega_{europa} + 2\omega_{ganymede} = \nu$ with $\nu \sim 0.74^o \, day^{-1}$. During their evolution these Jovian satellites distributed angular momentum transferred from Jupiter among themselves so as to remain in resonance. Taking account of angular momentum transfer in the presence of orbital resonances leads to a lower Q value than previously estimated. For example, if we assume that the resonances were formed early, the estimate of Q_J can be reduced by a factor of $5 - 7.5$.

Recently, another line of reasoning has been presented that can provide an estimate of Q_J without appealing to the early history of the solar system. Observations of Io determined a radiated flux from the satellite of the order of $7 \times 10^{13} \, W$ (Mc Ewan *et al.*, 1985). Peale in 1979 suggested that Goldreich and Soter's estimate of the Q could be reduced if the assumption is made that tidal dissipation on Io is strong enough to remove significant orbital energy from the satellite (Peale *et al.*, 1979). If the heat output from Io is due to tidal dissipation the satellite is expected *ceteris paribus* to move in a shrinking orbit at the rate $\frac{d}{dt}\omega_{io} \sim (3 \times 10^{-10}) \, \omega_{io} \, yr^{-1}$ (Greenberg, 1989). This tendency is counteracted by the transfer of angular momentum from Jupiter to Io due to the tidal dissipation in Jupiter. Consequently, determination of the rate of change of Io's orbit can provide an estimate of the rate of tidal dissipation in Jupiter if we have data on the history of Io's orbit. Lieske (1987) analysed a dataset of about 16000 eclipse observations of Io since 1668, when the Paris and the Greenwich Observatories were founded. Lieske was able to deduce that $\frac{d}{dt}\omega_{io} \sim -7.4 \times 10^{-12}\omega_{io} \, yr^{-1}$. The implications of this observation are shown in Fig. 1.1 for various scenarios for the evolution of the Laplacian resonance (ν). Note that Q_J, if it is to account for the observed heat flux from Io of $2.4 \, W \, m^{-2}$, has to be $\sim 5 \times 10^4$.

A major problem facing orbital evolution theory is that we have not been able to identify with confidence an adequate source of energy dissipation despite the fact that Q is very high. Among theoretical attempts to provide an estimate of Q_J, Houben (1978) studied the gravitational tides excited by Io in Jupiter assuming a rigorously neutral interior. He found only $\sim 1.5 \times 10^{10} \, W$ of wave energy radiated from the planet which corresponds to $Q_J = 2.7 \times 10^9$. The only physical mechanism that could give the observed or even lower dissipation has been suggested by Stevenson (1983). According to which the tidal oscillations lead to condensation of helium and the hysteresis of the helium droplet oscillations lead to tidal dissipation in the manner of acoustic waves attenuation in fog. This process depends on the distribution of helium in the planet, the density of nucleation sites, and the size of the helium droplets. Although Stevenson's model is highly speculative, it is remarkable that it can account for Q as low as 10^2.

To account for the astronomically suggested Q we extend the classical theory of tides to planetary bodies. We will investigate the tidal response in the planetary atmospheres of the Jovian planets as a function of the static stability in the interior of the planet. The analysis presented is a summary of Ioannou and Lindzen (1992a; 1992b) which will be referred to as IL1, IL2.

2. Gravitational tides in a fluid planet.

The planet will be modelled as an inviscid adiabatic fluid rotating with constant angular velocity $\vec{\omega}$. We will derive the equations of motion that govern the small adiabatic oscillations about a motionless and spherically symmetric mean state in a frame of reference rotating with the planet. The motion is assumed to be caused by the gravitational tidal potential of a satellite revolving around the planet. Let w, v, u denote the radial (r), zonal (ϕ), and meridional $(\theta$, the colatitude) component of velocity in spherical coordinates. Let the subscript "o" refer to an equilibrium value of any quantity and let a symbol without a subscript represent the perturbed part of that quantity.

The equation of continuity, linearized about a motionless and spherically symmetric basic state in hydrostatic balance, is:

$$\frac{\partial}{\partial t}\rho + w\frac{d}{dr}\rho_o + \rho_o\chi = 0 \; , \tag{2.1}$$

where ρ is the density, and χ the divergence:

$$\chi = \frac{1}{r^2}\frac{\partial}{\partial r}(r^2 w) + \frac{1}{r\sin\theta}\frac{\partial}{\partial \phi}v + \frac{1}{r\sin\theta}\frac{\partial}{\partial \theta}(u\sin\theta) \; . \tag{2.2}$$

The linearized thermodynamic equation for adiabatic motion about the hydrostatic mean state is:

$$\frac{\partial}{\partial t}p = c^2\frac{\partial}{\partial t}\rho - \rho_o\frac{c^2}{g_o}N^2 w \; , \tag{2.3}$$

where p is the pressure, g_o the acceleration of gravity due to the mean distribution of mass, and c the speed of sound:

$$c^2 = \Gamma_1\frac{p_o}{\rho_o} \; . \tag{2.4}$$

The Brunt-Väisälä frequency N, is given by:

$$N^2 = -g_o\left(\frac{d}{dr}\ln\rho_o + \frac{g_o}{c^2}\right) \; . \tag{2.5}$$

The compressibility at constant entropy, $\Gamma_1 = \left(\frac{d\ln p}{d\ln \rho}\right)_S$, reduces, for an ideal gas, to γ, the ratio of specific heat at constant pressure to that at constant volume. In the interior of the planet and in stellar interiors Γ_1 is a variable quantity. However, its variation is relatively small and we assume Γ_1 to be constant. Also, note that thermally driven turbulent eddy exchanges have been ignored in (2.3).

Combining (2.1) and (2.3) we obtain:

$$\frac{\partial}{\partial t}p = \rho_o\left(g_o w - c^2\chi\right) \quad , \tag{2.6}$$

The gravitational potential consists of an equilibrium part, Φ_o, and a perturbed part, Φ. They satisfy, separately, the Poisson equations:

$$\nabla^2 \Phi_o = 4\pi G \rho_o \; , \nabla^2 \Phi = 4\pi G \rho \; , \tag{2.7}$$

with G the universal constant of gravitation.

We ignore the effect of perturbation density on the gravitational potential. This approximation, due to Cowling (1941), is accurate for motions of higher order meridional and azimuthal structure for which the gravitational potential due to the perturbation density at one part of the fluid cancels that from other parts (Unno *et al.*, 1979). Cowling (1941) provided some justification for ignoring Φ, even when the motion is of low meridional and azimuthal order. With the Cowling approximation, the perturbation potential, Φ, is externally determined and equal to the tidal potential, Ω_r , which is related to its surface value, Ω, by:

$$\Omega_r = \Omega(\theta) \, \frac{r^2}{a^2} \, e^{i\sigma t + is\phi} \; , \tag{2.8}$$

in which σ is the frequency of the gravitational forcing, and, s, the zonal wavenumber. The gravitational forcing of Jupiter by Io is primarily semidiurnal with $s = 2$. For the values of the frequency, and the tidal potential at the surface of the jovian planets refer to IL1.

The inviscid momentum equations, neglecting the nonradial component of the rotation vector in the coriolis force (the traditional approximation, Eckart 1960), become:

$$\frac{\partial}{\partial t} u - 2\omega \cos\theta v = -\frac{1}{r} \frac{\partial}{\partial\theta} P \; , \tag{2.9}$$

$$\frac{\partial}{\partial t} v + 2\omega \cos\theta u = -\frac{1}{r\sin\theta} \frac{\partial}{\partial\phi} P \; , \tag{2.10}$$

$$\rho_o \frac{\partial}{\partial t} w = -\frac{\partial}{\partial r} p - \rho_o \frac{\partial}{\partial r} \Omega_r - g_o \rho \; , \tag{2.11}$$

in which $P = p/\rho_o + \Omega_r$ is the reduced pressure. The traditional approximation is accurate for large scale motions in stable thin spherical shells (Phillips 1966). The traditional approximation can be extended deeper into the planet because only the outer layers of the planet are important dynamically. The above approximations: the traditional, the Cowling, and the inviscid, result in major simplification. The equations become separable under these approximations in a manner similar to that in the classical theory of tides (Chapman and Lindzen 1970). The major point of departure from the classical theory is retention of the nonhydrostatic terms in the radial momentum equation (2.11) which become important in the planetary interior when the Brunt-Väisälä frequency is small.

Assume that the tidal response has reached a periodic state under the forcing of the revolving satellite. The dependence of the perturbed quantities on time and azimuthal angle will be the same as that of the forcing which has the form $e^{i\sigma t + is\phi}$. We will continue to denote the perturbed quantities with the same symbol as previously, it being understood that the quantities refer to the (σ, s) mode.

Eliminating the horizontal velocities and substituting into the divergence, χ, we obtain:

$$\chi = \frac{1}{r^2}\frac{\partial}{\partial r}(r^2 w) + \frac{i\sigma}{4\omega^2 r^2}\mathcal{F}[P] , \qquad (2.12)$$

where $\mathcal{F}$ is the Laplace tidal operator, which determines the meridional structure of the tidal fields and which depends only on $f = \sigma/2\omega$. For the gravitational forcing of Jupiter by Io this quantity is $f = 0.766$ (refer to IL1). Expanding the various fields in terms of Hough functions, $\Theta_n(\theta)$, we obtain, i.e. for the tidal potential:

$$\Omega_r = \frac{r^2}{a^2}\sum_1^\infty \Omega_n \Theta_n(\theta)\, e^{i\sigma t + i s\phi} . \qquad (2.13)$$

The divergence (2.12) becomes:

$$\chi_n = \frac{1}{r^2}\frac{\partial}{\partial r}(r^2 w_n) + \frac{i\sigma}{g_s h_n}\frac{a^2}{r^2}P_n , \qquad (2.14)$$

where the subscript, n, denotes the order of the Hough mode, g_s, the gravitational acceleration at the surface of the planet, and h_n the equivalent height of the Hough mode. The values of the equivalent heights for Jupiter due to the gravitational tidal forcing of Io are derived in IL1.

Eliminating the density from (2.11) and (2.3) we obtain:

$$\xi_n = \frac{\frac{d}{dr}P_n - \frac{N^2}{g_o}P_n + \frac{N^2}{g_o}\Omega_n\frac{r^2}{a^2}}{\sigma^2 - N^2} \qquad (2.15)$$

where the radial displacement, $\xi_n = w_n/i\sigma$. Eliminating the divergence, χ_n, from (2.6) and (2.14) gives:

$$\frac{1}{r^2}\frac{d}{dr}(r^2\xi_n) + \left(\frac{1}{c^2} - \frac{1}{g_s h_n}\frac{a^2}{r^2}\right)P_n - \frac{g_o}{c^2}\xi_n = \frac{\Omega_n}{c^2}\frac{r^2}{a^2} . \qquad (2.16)$$

We transform (2.15) and (2.16) into canonical form by defining:

$$\tilde{\xi}_n = r^2\xi_n \exp\left(-\int_0^r \frac{g_o}{c^2}\,dr\right) , \quad \tilde{p}_n = \frac{p_n}{\rho_o}\exp\left(-\int_0^r \frac{N^2}{g_o}\,dr\right) , \qquad (2.17)$$

In terms of the new variables (2.15), (2.16) become:

$$\frac{d}{dr}\tilde{\xi}_n = h(r)\frac{r^2}{c^2}\left(\frac{c^2}{g_s h_n}\frac{a^2}{r^2} - 1\right)\tilde{p}_n + \frac{r^2\Omega_n}{g_s h_n}\exp\left(-\int_0^r \frac{g_o}{c^2}dr\right) , \qquad (2.18)$$

$$\frac{d}{dr}\tilde{p}_n = \frac{1}{r^2 h(r)}(\sigma^2 - N^2)\tilde{\xi}_n - \frac{2r}{a^2}\Omega_n \exp\left(-\int_0^r \frac{N^2}{g_o}\,dr\right) , \qquad (2.19)$$

where

$$h(r) = \exp\left(\int_0^r \left(\frac{N^2}{g_o} - \frac{g_o}{c^2}\right) dr\right) .$$

With the aid of W.K.B. approximation we can classify the possible oscillatory motions of (2.18), (2.19) (refer to IL2). We note that the presence of N in the interior creates ducts for large positive equivalent heights, where propagating inertio-gravity waves can resonate. Remarkably, IL2 find that the resonant configurations can be predicted accurately by W.K.B. methods.

To proceed we must specify the thermodynamic state of the planet. To be specific we will consider the tides excited on Jupiter by Io. Jupiter is taken to be a mixture of hydrogen and helium with a constant abundance of 80% H_2 by mass. The planet's thermodynamic state is taken to be different in the interior of the planet than in the atmospheric envelope. The atmosphere is assumed to be an ideal gas with $\gamma = 1.4$. We assume that the gas in the interior of the planet obeys the polytropic constitutive relation $p_o = \mathcal{K}\rho_o^n$, with $\mathcal{K}$ a constant to be determined by the mass of the planet, M, and the requirement that the density vanish at the planet's surface ($r = a$).

Early theoretical studies of the interior constitution of the Jovian planets together with gravimetric inversions indicated that the distribution of mass is hydrostatic and to a good approximation consistent with the polytropic constitutive relation with $n \approx 2$. On the other hand, work on the high-pressure thermodynamics of hydrogen - helium mixtures indicated that the adiabatic compressibility parameter Γ_1 increases with pressure from the ideal gas value of ≈ 1.4 at the atmospheric envelope to ≈ 3 for pressures of the order of 1 Mbar, and over a substantial range of pressures is ≈ 2, leading to the conclusion that the polytropic equation of state $p_o = \mathcal{K}\rho_o^2$ is a convenient and an appropriate simplification of the constitutive relation in the interior of the planet. The polytropic relation with $n = 2$ has the advantage that the distribution of density is given in closed form:

$$\rho_o(r) = \rho_{oc}\hat{\rho}_o(\eta) = \rho_{oc} \frac{\sin(\pi\eta)}{\pi\eta} , \qquad (2.20)$$

where $\eta = r/a$, $\hat{\rho}_o$ is the normalized density, and the density at the center of the planet is $\rho_{oc} = \pi M/4a^3$. The polytropic constant $\mathcal{K}$ is determined to be $\mathcal{K} = 2Ga^2/\pi$. Having determined the mean density, we obtain the mean mean pressure which is shown in Fig. 2.1. The pressure in Fig. 2.1 is expressed in terms of the number of scaleheights $x = -\ln(p/p_{cloud})$, where p_{cloud} is taken to be the pressure at the top of the visible clouds of the planet ($\approx 300mbar$). Remarkably, there are about 18 scale heights from the visible atmospheric envelope to the center of the planet, while there are only 4 scale heights from $0.9a$ to the center of the planet. The magnitude of the tidal response at the atmospheric envelope depends on the number of scale heights spanning the distance between the atmospheric envelope and the levels of excitation which are concentrated in the interior of the planet. As a consequence the tidal response will depend primarily on the outermost layers of the planet where we can safely make the Eckart approximation.

Although, the interior is taken to obey the polytropic relation with $n = 2$, following Cowling (1941) we also allow for $\Gamma_1 \geq 2$, which leads to stable stratification in the interior. The Brunt-Väisälä frequency is given by:

$$N^2 = \frac{g_s}{a} \frac{\Gamma_1 - 2}{\Gamma_1} \frac{1}{\hat{\rho}_o} \left(\frac{d}{d\eta} \hat{\rho}_o \right)^2 = \frac{\Gamma_1 - 2}{\Gamma_1} \frac{g_o^2}{\hat{\rho}_o a g_s} \cdot \qquad (2.21)$$

When $\Gamma_1 = 2$ the interior is neutral i.e. $N = 0$. When $\Gamma_1 > 2$ the interior is stably stratified.

The distribution of N in the interior of Jupiter is unknown. The observed internal heat source has led to the widely accepted view that the interior is in an average state of neutral stability. However, the processes that maintain the mean static stability are complex and poorly understood. In general, it can be argued that if heat from the interior is supplied to the surface by thin convective plumes the interior must maintain an average positive static stability if the compressional heating in the downwelling regions is to be balanced by loss of heat due to conduction or radiation (Lindzen, 1977). Stable stratification can be also maintained if there is a large meridional circulation in the interior of the planet. Veronis, in the course of this summer's meeting, conducted preliminary numerical experiments in order to determine the mean state maintained by convection in a 2D non-rotating Boussinesq fluid heated uniformly from below and cooled at the top according to the heat flux law: $k \frac{\partial}{\partial z} T = \lambda(T_e - T)$, where k is the thermometric diffusivity, λ a Newtonian cooling coefficient, $T_e = \Delta T \sin(\pi x/2L)$ an imposed externally boundary temperature distribution. He found that the resulting time averaged circulation brings the fluid to a nearly isothermal state, which except from the presence of unstably stratified boundary layers at the top and bottom, the fluid is mildly stably stratified in the interior (refer to Veronis's abstract in this volume).

We find that the inclusion of even small positive static stability in the interior of the planet has a dramatic effect on the tidal response at the atmospheric envelope. Note that low levels of static stability, although dynamically significant, may be difficult to detect by direct measurement of N.

The idealized distribution of N in the interior of the planet (2.21) is shown in Fig. 2.2 for $\Gamma_1 = 2.085$. Note the rapid decrease of N caused by the rapid increase of density with radius and the eventual vanishing of the gravitation acceleration at the center of the planet; for $r/a < 0.75$ we have $N < \sigma$. At the atmospheric envelope N is of the order of $2 \times 10^{-2} \, sec^{-1}$ which is $\approx 65\sigma$ at the 100 mbar level (*cf.* Achterberg and Ingersoll, 1989) and well satisfies the condition $N > \sigma$ which is necessary for oscillations to behave as vertically propagating waves. Note that at the outer parts of the planet, below the atmospheric envelope, $N < 10\sigma$, a value of static stability which may be hard to distinguish observationally from neutrality. To estimate the possible range of values of the compressibility parameter Γ_1, let us first assume that the idealized distribution of N, (2.21), is valid up to the visible region of the atmospheric envelope of Jupiter. In this case, the Γ_1 that matches the observed lapse rate of about $2 \, K \, km^{-1}$ at the atmosphere is 2.56. Assuming that the static stability rapidly decreases under the clouds then a range of values $2.01 < \Gamma_1 < 2.15$, is consistent with continuous transition from the atmosphere to the polytropic interior.

To calculate solutions of (2.18), (2.19) we need to specify the boundary conditions. We will assume a solid boundary at some radius in the interior of the planet for which $N < \sigma$. The specific location of the inner boundary condition was found to be unimportant (refer to IL2). For an outer boundary condition we will assume either decay of energy density or the radiation condition.

For the presentation of the atmospheric response it is informative to define the equilibrium radial displacement of a material surface under the influence of the external tidal potential, Ω_r: $\xi_{equilib} = -\Omega_r/g_o$. For the case of a neutral interior the radial displacement and the equilibrium displacement are shown at the equator as a function of the radius of the planet in Fig. 2.3. The corresponding displacement for the case of a stably stratified interior is shown indicatively in Fig. 2.4. The effectiveness of the forcing in exciting tides in the planetary atmosphere is proportional to the difference between the two displacements, because the tidal fields are forced by this geopotential disequilibrium. For example, if the inner planet were separated by a solid interface from the atmosphere, atmospheric tides would result from the response to the forcing of $13m$ geopotential disequilibrium at the ground (for the Earth the corresponding value is $20cm$, which corresponds to a hydrostatic tidal pressure fluctuation of $20\mu bar$, the observed lunar tidal pressure fluctuation is approximately $60\mu bar$). Instead the neutral interior reduces the geopotential forcing to $30 - 100cm$. This is to be expected because, with the absence of gravitational restoring force, the weak compressional and inertial restoring forces can not oppose the imposed geopotential deformation. Remarkably, a planet with neutral interior has tiny tidal response, while introduction of small stability in the interior leads to greatly enhanced dynamic displacements: $\xi - \xi_{equilib} \approx 20m$. Previous calculations (Houben, 1978) treated a neutral interior, and consequently produced small tidal forcing in the atmosphere and a resulting tidal dissipation factor $Q \approx 10^9$, which is 3-4 orders of magnitudes larger than the values derived from astronomical theory. If we are to account for the astronomically derived tidal Q, it appears to be necessary to assume that the planetary interior has nonzero stability.

Consider now the case of a planetary interior with some static stability. The strength of the tidal fields in the atmosphere is estimated by the resulting radiation energy flux: $\overline{pw}$. This energy flux represents the power radiated from the planet and can provide an estimate for the associated tidal dissipation factor Q through use of (1.1). The peak energy of the tidal fields is calculated as the maximum potential energy of the tide in the planetary interior. Note that the resulting magnitude of Q, although indicative, is certainly an overestimate because neither the dissipation of the trapped modes nor other forms of dissipation have been taken into account. The dependence of the energy flux and the associated Q are plotted in Fig. 2.5 as a function of Γ_1 . The resonant peaks indicate the selective resonance of different Hough modes. As remarked in IL1 and IL2, the tidal forcing, which is proportional to the second spherical harmonic, projects on many Hough modes each of which can separately resonate in the ducts allowed to form in the interior of the planet by the presence of stable stratification. The resonant peaks can be suppressed by introduction of sufficiently large dissipation in the interior. Dissipation can be simulated by allowing the forcing frequency σ to assume complex values. For an interior dissipation of 60 hours, the case shown in Fig. 2.5, the resonances are diffuse.

Disregarding the resonant peaks, the tidal response asymptotes to an energy flux level of $\approx 10^{14}$ W over the whole surface of Jupiter which corresponds to $\approx .005$ Wm^{-2}. The associated Q asymptotes to $\approx 10^5$ in accord with the value expected from astronomical arguments. Note that if the dissipation in the interior is small, so that the resonances are sharp, the energy flux can reach the order of $10^{17} - 10^{18}$ W. These large energy fluxes result in values of Q of the order of 10^3. That such a situation is plausible is indicated by the anomalous heat output of Io (Yoder and Peale 1981). In the case of reduced interior dissipation the tidal fields in the atmosphere may show a discernible episodic signature caused by the time variations of the interior stability. It is then plausible that tidally forced wave fields reach an energy comparable to the thermal emission of Jupiter (14 Wm^{-2} which is $\approx 10^{17}$ W).

3. Conclusions

We have extended the classical theory of tides to study the tidal response of a deep fluid planetary body. We have retained the separation of the meridional and vertical structure equations by neglecting the horizontal components of the rotation vector in the calculation of the coriolis acceleration. We expect this approximation to give accurate results and even prove useful in determining the free modes of a rapidly rotating planet.

The tidal response is found to depend crucially on the distribution of static stability in the interior. The presence of convection in the planetary interior has often been assumed to lead to a state of neutral stability. While absolute neutrality in the interior is a good first approximation to determine the mean thermodynamic state, small departures from neutrality have important implications for the tidal response. The tidal response of the atmospheric envelope is proportional to the departure of the tidal fields from their equilibrium value. In the absence of stability in the interior a neutrally buoyant material surface deforms and becomes nearly an equilibrium equipotential surface leading to small tidal excitation.

We have shown that the presence of small static stability at the outer parts of the planet leads to dramatic enhancement of tidal response in the atmosphere. The tidal fields are then capable of radiating enough energy away from the planet to result in a tidal dissipation factor Q consistent with the bounds set by astronomical considerations. The presence of static stability in the planetary interior creates ducts in which the various Hough modes can resonate. If the viscous dissipation is not very large in the planetary interior we expect that this resonant behavior to result episodically in very large tidal activity as the interior stability is modulated by convection. If we disregard the resonant peaks. the tidal activity asymptotes to a value which is independent of the amount of stabilit and is consistent with the tidal dissipation required by the astronomical arguments.

We have utilized a very simple model for the static stability in which the most stable layers are concentrated in the outer parts of the planet, but are separated by a nine scale height deep neutrally buoyant region below the clouds. We expect our conclusions to apply also to more structured models of interior static stability, as long as the static stability is not concentrated too deep in the interior. Remarkably, the assumption of a rigorously neutral interior is dynamically singular and, encouraged by agreement with astronomically determined tidal dissipation, we are led to the hypothesis that the interior of the planet

should possess some static stability. Verification of this hypothesis must await sufficiently accurate observations of the tidal response of Jupiter.

We have already found that that the tidally forced wave fields may radiate an energy comparable to the thermal emission of Jupiter ($\approx 10^{17}$ W). This energy flux may be a source of momentum that can maintain the puzzling observed cloud level mean zonal circulation of the planet. Using the Eliassen-Palm theorem (Lindzen 1990) we can estimate the expected latitudinally averaged acceleration of the mean flow to be 10^{-2} $ms^{-1}day^{-1}$ assuming that the momentum of the waves is deposited in a layer of one scale height ($25Km$) depth. However the interaction of vertically propagating and vertically trapped modes can lead to a a latitudinal redistribution of zonal angular momentum on the scale of the dominant vertically propagating Hough mode. These alternating local accelerations will be concentrated in restricted latitude bands and will extend as far as the critical latitude of the planet (for Jupiter the critical latitude associated with forcing by Io is 50° N), resembling the visible banding of the planet.

Acknowledgements

References

Achterberg, R. K., and A. P. Ingersoll, 1990: A Normal Mode Approach to Jovian Atmospheric Dynamics. *J. Atmos. Sci.*, **46**, 2448-2462.

Chapman, S. and R. S. Lindzen, 1970:*Atmospheric Tides*. D. Reidel Press, Dordrecht, Holland.

Cowling, G. T., 1941: The Non-Radial Oscillations of Polytropic Stars. *Monthly Notices Roy. Astron. Soc.*,**101**, 367-373.

Eckart, C., 1960: *Hydrodynamics of Oceans and Atmospheres*. Pergamon Press, London.

Goldreich, P., and S. Soter, 1966: Q in the Solar System.*Icarus*, **5**, 375-389.

Greenberg, R., 1989: Time varying orbits and tidal heating of the Galilean satellites. In *Time Varying Phenomena in the Jovian System. Ed. Belton, Weston, Rahe, NASA*, 100-115.

Houben, H. C., 1978:*Tidal Dissipation in the Solar System and the Possibility of Tidally-Driven Planetary Dynamos*. Ph.D. thesis, Cornell University.

Ioannou, P. J., and R. S. Lindzen, 1992a: Gravitational Tides in the Outer Planets. Part I: Implications of Classical Tidal Theory. *J. Ap.*, to appear.

Ioannou, P. J., and R. S. Lindzen, 1992b: Gravitational Tides on Jupiter. Part II: Interior Calculations and estimation of the Tidal Dissipation Factor. *J. Ap.*, to appear.

Lambeck, K., 1980: *The Earth's Variable Rotation*, Cambridge University Press, Cambridge.

Lieske, J., H., 1987: Galilean satellite evolution: Observational evidence for secular change in the mean motion. *Astron. Astrophys.*, **176**, 146-158.

Lindzen, R. S., 1990: *Dynamics in Atmospheric Physics*. Cambridge University Press, Cambridge.

MacDonald, G. J. F., 1964: Tidal Friction. *Rev. of Geophys.*, **2**, 467-541.

McEwen, A. S., D. L. Matson, T. V. Johnson, and L. A. Soderblom, 1985: Volcanic hotspots on Io. Correlation with low albedo calderas. *J. Geophys. Res.*, **90**, 12345-12379.

Peale, S. J., P. Cassen, and R. T. Reynolds, 1979: Melting of Io by tidal dissipation. *Science*, **203**, 892-894.

Phillips, N. A., 1966: The Equations of Motion for a Shallow Rotating Atmosphere and the 'Traditional Approximation'. *J. Atmos. Sci.*. **23**, 626-628.

Stevenson, D. J., 1983: Anomalous Bulk Viscosity of Two-Phase Fluids and Implication for Planetary Interiors. *J. Geophys. Res.*, **88**, 2445-2455.

Unno, W., Osaki, Y., Ando, H., Shibahashi, H., 1979: *Nonradial Oscillations of Stars*. University of Tokyo Press, Tokyo.

Yoder, C. F., and S. J. Peale, 1981: The Tides of Io.*Icarus*, **47**, 1-35.

FIGURE LEGENDS

Fig. 1.1 Relationship between tidal dissipation rates in Io and in Jupiter, Io's orbital acceleration $\dot{\omega}_{io}$, and the rate of evolution of the Laplacian resonance $\dot{\nu}$. Observational determination of the thermal radiation from Io (McEwen *et al*, 1985) is shown. The shaded area is the $\dot{\omega}_{io}$ which consistent with the data analysis of Lieske (1987). If the resonance is in equilibrium (Yoder and Peale, 1981) , the system is constrained to the diagonal line $\dot{\nu} = 0$. Most theoretical models of Jupiter's interior suggest that dissipation is slow that $\dot{\nu} < 0$, except for Stevenson's (1983) speculative model. Lieske's (1987) determination of ν shows that the system lies on the $\dot{\nu} = 0$ line, which requires $Q_J \approx 10^5$. (adapted from Greenberg, 1989).

Fig. 2.1 The mean pressure of Jupiter as a function of the fractional radius of the planet. It is calculated for the polytropic interior: $p_o = \mathcal{K}\rho_o^2$. The pressure is plotted in terms of the log-pressure coordinate, x, which indicates the number of scale heights. At the center of the planet the pressure is around 34 Mbar, at the cloud tops is 0.3 bar. Note that there are around 18 scale heights from the visible clouds to the center of the planet, out of which the 15 are between the clouds and 0.9 of the radius of the planet.

Fig. 2.2 The Brunt-Väisälä frequency , N, in the interior of Jupiter, as a function of the fractional radius of the planet. The interior mean state satisfies the polytropic constitutive relation with $n = 2$ and $\Gamma_1 = 2.05$. The dashed line shows the frequency of the external periodic forcing, σ. For comparison, note that at the visible cloud level $N \approx 65\sigma$.

Fig 2.3 The magnitude of the radial displacement as a function of the fractional radius. Curve 1 is the radial displacement calculated from the dynamic response in Jupiter, the interior is exactly neutral, and the core has been placed at 0.1 of the planetary radius. Curve 2 is the radial displacement of the equilibrium tide.

Fig. 2.4 The magnitude of the difference between the dynamic radial displacement and the equilibrium radial displacement at the equator as a function of the fractional radius of the planet Jupiter. The tidal response of the atmospheric envelope is proportional to the disequilibrium of the dynamic response. Curve 1 represents the response of an interior with some stability ($\Gamma_1 = 2.05$), curve 2 represents the case of an exactly neutral interior.

Fig. 2.5 Total Energy flux $\overline{pw}$ *bar* in Watts, integrated over the surface of the planet at the visible atmosphere, as a function of Γ_1. Only the Hough modes ($n \geq 12$) which propagate in the upper atmosphere contribute to the energy flux. The lower curve shows the corresponding Q. The dotted curves show the corresponding results with an effective dissipation in the planetary interior of 60 hours.

154

Fig. 1.1 Relationship between tidal dissipation rates in Io and in Jupiter, Io's orbital acceleration $\dot{\omega}_{io}$, and the rate of evolution of the Laplacian resonance $\dot{\nu}$. Observational determination of the thermal radiation from Io (McEwen *et al*, 1985) is shown. The shaded area is the $\dot{\omega}_{io}$ which consistent with the data analysis of Lieske (1987). If the resonance is in equilibrium (Yoder and Peale, 1981) , the system is constrained to the diagonal line $\dot{\nu} = 0$. Most theoretical models of Jupiter's interior suggest that dissipation is slow that $\dot{\nu} < 0$, except for Stevenson's (1983) speculative model. Lieske's (1987) determination of ν shows that the system lies on the $\dot{\nu} = 0$ line, which requires $Q_J \approx 10^5$. (adapted from Greenberg, 1989).

155

Fig. 2.1 The mean pressure of Jupiter as a function of the fractional radius of the planet. It is calculated for the polytropic interior: $p_o = K \rho_o^2$. The pressure is plotted in terms of the log-pressure coordinate, x, which indicates the number of scale heights. At the center of the planet the pressure is around 34 Mbar, at the cloud tops is 0.3 bar. Note that there are around 18 scale heights from the visible clouds to the center of the planet, out of which the 15 are between the clouds and 0.9 of the radius of the planet.

Fig. 2.2 The Brunt-Väisälä frequency , N, in the interior of Jupiter, as a function of the fractional radius of the planet. The interior mean state satisfies the polytropic constitutive relation with $n = 2$ and $\Gamma_1 = 2.05$. The dashed line shows the frequency of the external periodic forcing, σ. For comparison, note that at the visible cloud level $N \approx 65\sigma$.

Fig 2.3 The magnitude of the radial displacement as a function of the fractional radius. Curve 1 is the radial displacement calculated from the dynamic response in Jupiter, the interior is exactly neutral, and the core has been placed at 0.1 of the planetary radius. Curve 2 is the radial displacement of the equilibrium tide.

158

Fig. 2.4 The magnitude of the difference between the dynamic radial displacement and the equilibrium radial displacement at the equator as a function of the fractional radius of the planet Jupiter. The tidal response of the atmospheric envelope is proportional to the disequilibrium of the dynamic response. Curve 1 represents the response of an interior with some stability ($\Gamma_1 = 2.05$), curve 2 represents the case of an exactly neutral interior.

Fig. 2.5 Total Energy flux $\overline{pw}$ *bar* in Watts, integrated over the surface of the planet at the visible atmosphere, as a function of Γ_1. Only the Hough modes ($n \geq 12$) which propagate in the upper atmosphere contribute to the energy flux. The lower curve shows the corresponding Q. The dotted curves show the corresponding results with an effective dissipation in the planetary interior of 60 hours.

Stability of Rotating Shear Flows in Shallow Water

Joseph B. Keller and Charles Knessl

Asymptotic methods are used to determine the dispersion equation for disturbances of rotating parallel flows in shallow water. From this equation the unstable modes and their growth rates are determined. The solution involves seven asymptotic expansions which are matched together. The results supplement and extend those which have been obtained previously using numerical methods by Griffiths, Killworth and Stern (1982) and by Hayashi and Young (1987).

Griffiths, R.W., P.D. Killworth, M.E. Stern (1982) A geostrophic instability of ocean currents. *J. Fluid Mech.*, **117**, 343–377.

Hayashi, Y.-Y. and W.R. Young (1987) Stable and unstable shear modes or rotating parallel flows in shallow water. *J. Fluid Mech.*, **184**, 477–504.

C. Knessl and J.B. Keller (1992) Stability of rotating shear flows in shallow water. *J. Fluid Mech.*, **244**, 605–614.

ENERGY SOURCES FOR PLANETARY DYNAMOS
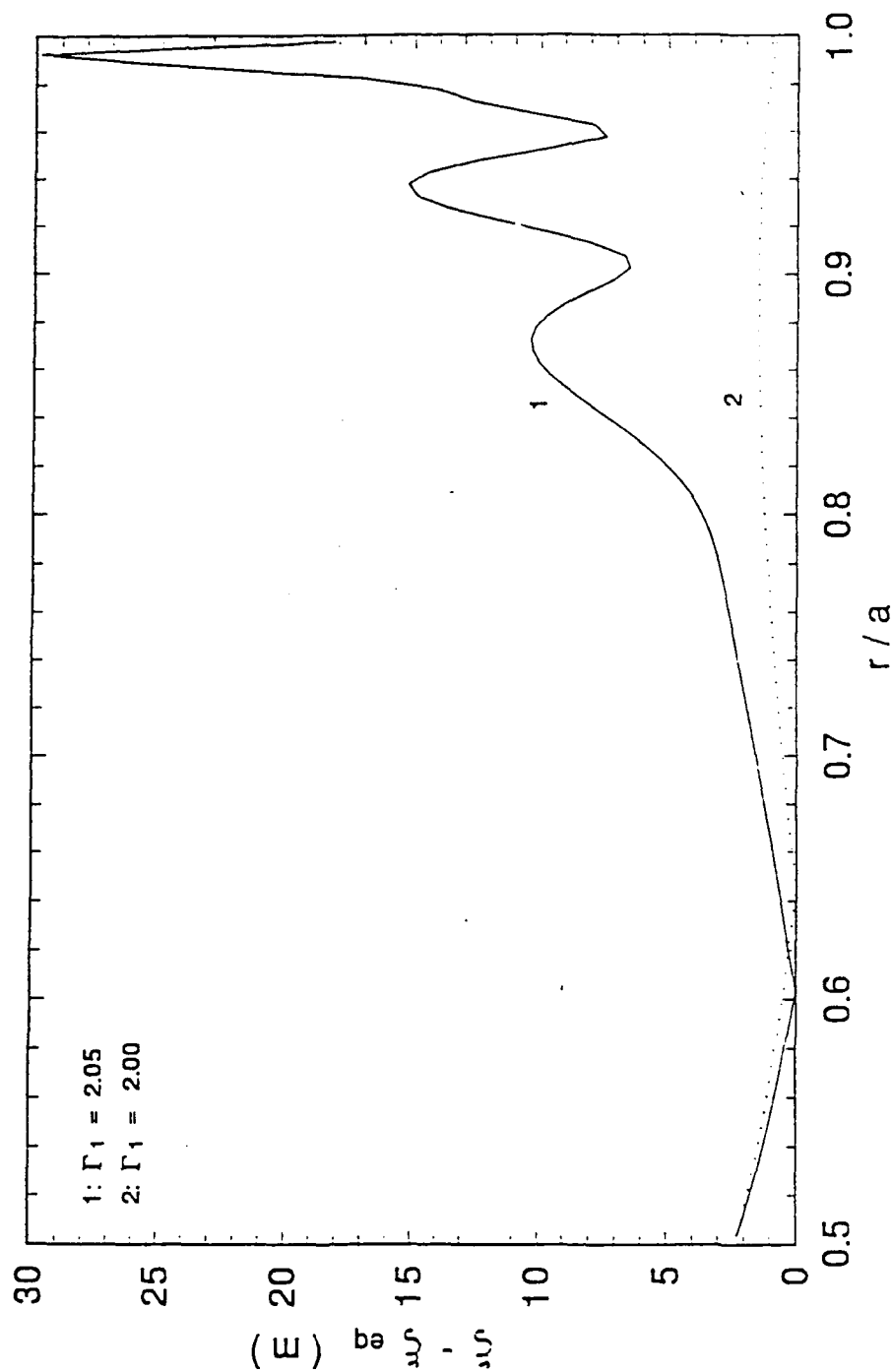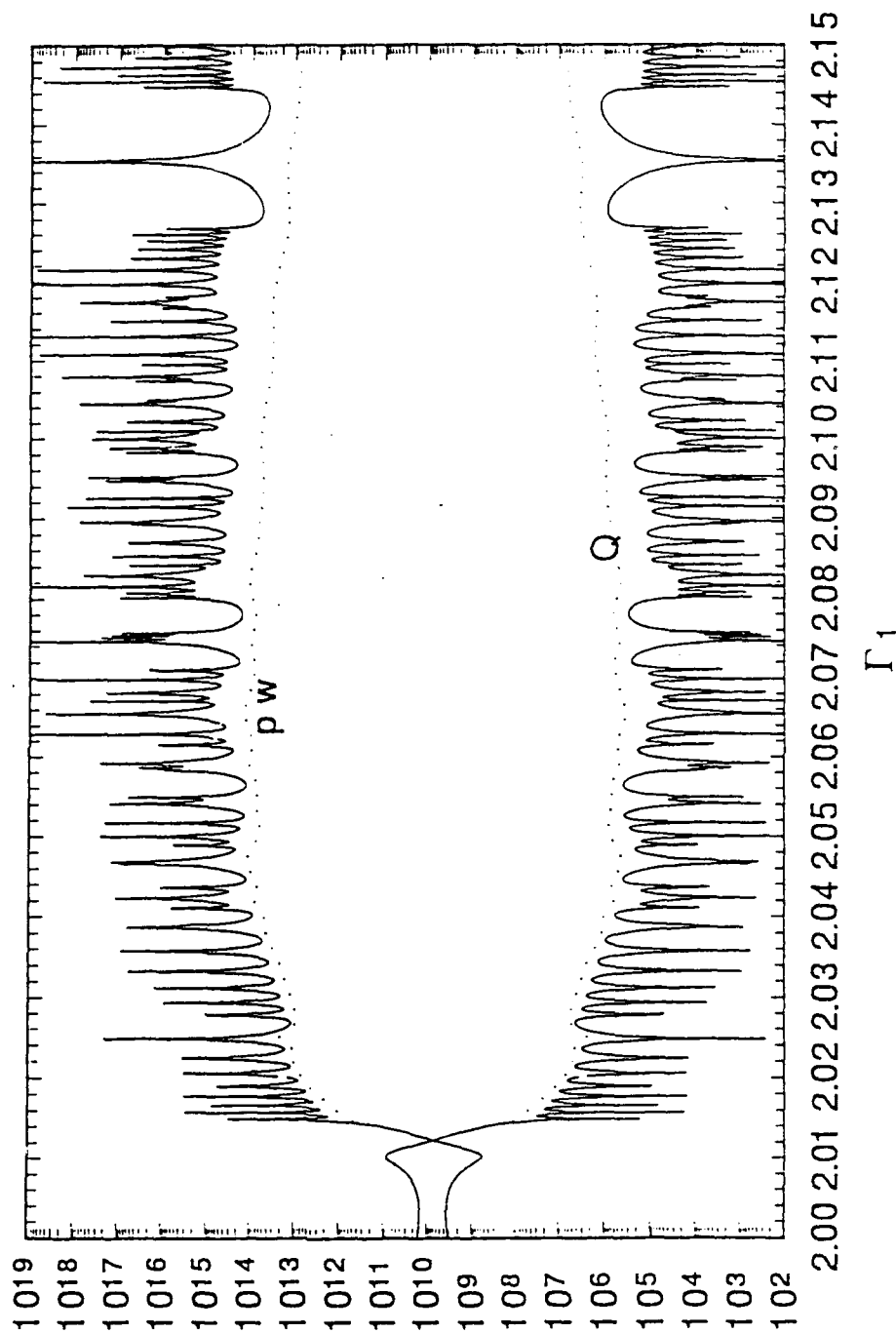
W. V. R. Malkus

In the belief that only unkind gods would arrange two energy sources for planetary dynamos as equally important, this re-exploration of plausible sources seeks to eliminate rotational energy in favor of convection. Recent experiments and theory of the "elliptical" instabilities in a rotating fluid due to precessional and tidal strains provide quantitative results for velocity fields and energy production. The adequacy of these flows to produce a dynamo on both terrestrial and giant planets is assessed in the context of "strong field" scaling. With little ambiguity it is concluded that Mercury, Venus, and Mars can not have a dynamo of tidal or precessional origin. The case for today's Earth is marginal. Here precessional strains (accidentally comparable to tidal strains) also are potential sources of inertial instabilities. The ancient Earth with its closer Moon, as well as all the giant planets, have tides well in excess of those needed to critically maintain dynamos. Hence the project proposed here proves to be successful only in part – an Earth in the distant future will not be able to sustain the geodynamo with its rotational energy. On the other hand, convect remains a possible dynamo energy source, with such a large number of ermined processes and parameters that it is unfairly easy to establish conditions for its inadequacy. A large literature explores its adequacy. A brief review of this literature, in both a "strong-field" and "weak-field" context, advances several cautionary restraints to be employed on that day when the limits of validity of a quantitative dynamo-convection theory are to be determined.

Vortex Dynamics in Zone–Belt Flows

P. S. Marcus and R. D. Van Buskirk

University of California at Berkeley

Department of Mechanical Engineering

October 27, 1992

We examine the dynamics of vortices superposed on zone–belt (uni–directional) flows with shears that changes sign as a function of location. Regions of the zone–belt flow where the shear is the same sign as a test vortex are defined to be prograde with respect to that vortex: otherwise, they are adverse. Steady vortices are surrounded by closed streamlines, but there is a last one beyond which the streamlines extend to infinity. Bifurcation diagrams of families of steady vortices show that as $\cdots$ furcation parameter increases, the ratio of the vortex area to the area enclosed by the $\cdots$ closed streamline goes to unity. There is a limiting vortex beyond which there are no solutions (Van Buskirk 1991). Limiting solutions are end points and not turning points in the bifurcation diagrams. Boundaries of limiting vortices lie in regions of adverse zone–belt flow and contain one or more stagnation points. Vortices with finite and infinite L_r behave differently. Those with infinite L_r have stable limit points while those with finite L_r have unstable limit points, and the onset of linear stability is clearly shown as a turning point in the bifurcation diagram before the limit point is reached. (Van Buskirk & Marcus 1993a, 1993b)

Using a spectral contour method (Van Buskirk & Marcus 1993c) to solve the Euler and

quasigeostrophic equations (with dissipation included by removing contours far from the center of vorticity) we compute time-dependent flows and plot their paths through energy-circulation ($\tilde{E}$-Γ') phase space. Usually there is no dissipation; it typically happens only when a vortex boundary runs into a stagnation point. Then, a thin tail forms which is swept away. The slope of the path in ($\tilde{E}$-Γ') phase space determines the ratio of dissipated circulation to energy, and at late times is proportional to the stream function at the stagnation point. Vortices with circulations initially larger than the limiting vortex shed circulation and are attracted to a point in ($\tilde{E}$-Γ') space near the limiting solution when L_r is infinite and near the turning point when L_r is finite. Vortices with smaller initial circulations are attracted to the line in ($\tilde{E}$-Γ') space corresponding to the family of linearly stable, steady vortices with the same strength vorticity as the initial vortex. Pairs of initially nearby vortices merge and entrain irrotational fluid, though flows with small L_r compared to the square root of the areas of the initial vortices entrain very little. The merged vortices are attracted to the small area in ($\tilde{E}$-Γ') space consisting of the locus of all steady, stable families with vorticity less than the value of the initial vortex pair.

Robust vortices always have their centers of vorticity within the prograde part of the zone-belt flow, but large vortices with finite L_r are different from those with infinite L_r in two important ways: With infinite L_r vortices grow in size until they overflow their own belt or zone into the surrounding zone or belt (with adverse shear). The maximal vortices have stagnation points on their boundaries. With finite L_r two things can happen that can prevent vortices from reaching their stagnation points. The first is that the vortex can overflow into the region of adverse shear and grow in size, but it becomes linearly unstable (ie. it reaches its turning point on the bifurcation diagram) before it reaches its stagnation (limit) point. A second thing that can happen is that the vortex can grow in size (in all

directions) until one part of its boundary moves in latitude into a region of its own belt or zone where the shear is still prograde but where it is much stronger than it is at the vortex center. Then as the vortex grows, its area increases, but the boundary of the vortex no longer changes latitude — only the longitudinal extent of the vortex increases. Thus the latitudinal extent of the vortex asymptotes to a finite value. We have computed numerically the value critical value of the shear where the boundary asymptotes as a function of L_r. For infinite L_r the critical shear is infinite.

We argue that these flows model the Jovian atmosphere and the long-lived Jovian vortices, such as the Great Red Spot (GRS) of Jupiter and White Ovals. In particular we argue that the GRS shows both finite L_r effects. On its northern side it overflows into a region of adverse shear until it reaches a point of linear instability. Thus the northernmost part of the GRS is located just south of the flow's stagnation point. The southern part of the GRS has grown in size until it lies in a region of large prograde shear. The strength of the shear at the southernmost part of the GRS is approximately the critical value; regions farther south of this location have even greater value of shear.

References

Van Buskirk, R. D. 1991 Quasigeostrophic vortices in zonal shear. Ph.D. thesis Harvard University.

Van Buskirk, R. D. & Marcus, P. S. 1993a Vortex dynamics in flows with non-uniform shear. Part I *J. Fluid Mech.* submitted.

Van Buskirk, R. D. & Marcus, P. S. 1993b Vortex dynamics in flows with non-uniform shear. Part II: finite Rossby deformation radius. *J. Fluid Mech.* submitted.

Van Buskirk, R. D. & Marcus, P. S. 1993c Spectrally Accurate Contour Dynamics for Vortices and Potential Vortices. *J. Comput. Phys.* submitted.

Uniform vortices in stratified flows.

Steve Meacham
Florida State University

A variety of known results for simple vortices in 2-D Euler flow have simple analogues in stratified quasigeostrophic flow (see Table 1.) The main reason for this analogy is the similarity between the vorticity/streamfunction relations for the two types of flow.

2-D Euler	Stratified QG
Circular patch of uniform vorticity	Spherical blob of uniform potential vorticity
Elliptical vortex	Ellipsoidal vortex
V–State	V–State
Elliptical vortex in uniform strain & shear	Ellipsoidal vortex in uniform strain & shear

Table 1. Simple 2-D Euler vortex flows and their 3-D analogues.

1 Potential vorticity/Streamfunction relation

In 2-D Euler flow, described by a streamfunction $\psi(x, y)$, the vertical component of vorticity ζ is related to ψ by an isotropic elliptic operator, the two-dimensional Laplacian,

$$\zeta = \nabla_2^2 \psi \tag{1}$$

and satisfies the conservation relation

$$\partial_t \zeta + J(\psi, \zeta) = 0. \tag{2}$$

Quasigeostrophic flow in a continuously stratified fluid with uniform buoyancy frequency, $N^2 = -\frac{g}{\rho}\frac{\partial \rho}{\partial z}$, is pseudo-two-dimensional. The horizontal velocity is again given by a stream-function

$$u_H = k \wedge \nabla \psi, \qquad\qquad \psi = \psi(x, y, z)$$

A potential vorticity (pv),

$$q = k.\nabla \wedge u_H + \partial_z \frac{f^2}{N^2} \partial_z \psi$$

$$= \nabla_2^2 \psi + \frac{f^2}{N^2} \partial_z^2 \psi$$

is conserved by the horizontal motion and satisfies

$$\partial_t q + J(\psi, q) = 0 \tag{3}$$

Rescaling the vertical coordinate by a uniform stretching factor N/f, transforms the operator in the pv/streamfunction relation to an isotropic elliptic operator:

$$q = \nabla_3^2 \psi \tag{4}$$

In two-dimensions when ζ is constant, $\psi =$ a quadratic + a harmonic function, while, when q is constant, we also have $\psi =$ a quadratic + a harmonic function. If ζ (q) is uniform in a singly connected area (volume) D bounded by a curve (surface) $S(\boldsymbol{x}, t) = 0$ and uniform but different outside this, then (2) or (3) imply that

$$\partial_t S + J(\psi, S) = 0 \tag{5}$$

If S and ψ are both quadratic in $\boldsymbol{x}$, then $\partial_t S$ and $J(\psi, S)$ are both quadratic in $\boldsymbol{x}$. Thus if one can show that $\psi = \nabla^{-2} \chi_D$ is quadratic on and next to S whenever S is quadratic, then one can infer that S will remain quadratic. A more detailed analysis shows that this is indeed the case when the flow domain is unbounded; eq. (5) then provides equations for the way in which the coefficients in the quadratic form S evolve in time. This result is a restatement of the central principle underlying the results of Kirchhoff (Lamb, 1932), Kida (1981), Zhmur and Pankratov (1989), Zhmur and Shchepetkin (1991), Meacham (1989, 1992), Meacham et al. (1992). This result suggests that blobs of uniform ζ and q bounded by a quadratic surface S may yield steadily rotating, isolated equilibria and time-dependent solutions for vortices embedded in a quadratic external ψ field.

Let us briefly review some of the known two-dimensional results for vortex patches in Euler flows on an unbounded plane.

   A. The simplest is perhaps the result that a circular patch of uniform vorticity and unit radius, embedded in a background of zero vorticity in which there is no imposed external flow at infinity, forms an azimuthally symmetric equilibrium. It possesses a countably infinite set of normal modes in which the perturbed boundary lies at $r = 1 + \eta(\theta, t)$ where $\eta \propto e^{im(\theta - \Omega t)}$. We can speak of these as having azimuthal symmetry m. The superposition of the circle and a single azimuthal mode is then a steadily rotating configuration of azimuthal symmetry m that departs infinitesimally from the circular state. We can introduce a measure of the departure from circular equilibrium by defining the length of the maximum radius of the distorted figure to be $1 + \rho$, $\rho > 0$. The normal modes represent a family of bifurcations from the spherical symmetry with bifurcation parameter ρ. As ρ increases beyond infinitesimal values, we obtain finite amplitude disturbances.

as the nonlinear continuation of the $m = 2$ mode. Kirchhoff showed that $m = 2$ equilibria existed for the entire range $0 < \rho < \infty$ and found their rotation rates, $\Omega(\rho)$.

C. Using numerical techniques, Deem and Zabusky (1978) showed that the $m > 2$ modes can also be continued to finite amplitude and called the resulting equilibria V-states. They conjectured, and Wu et al. (1984) later showed more clearly, that these solutions can only exist for a finite range of ρ, $0 < \rho < \rho_c(m)$. In the limit as $\rho \to \rho_c$, the V-states develop "points", discontinuities in boundary slope at their corners. It is believed that multiply-connected equilibria exist beyond this limit. Associated with the V-states are rotation rates, $\Omega(\rho, m)$.

D. Kida (1981) noted that even in the presence of a background flow described by a quadratic streamfunction, an initially elliptical uniform vortex will remain elliptical. A typical background streamfunction can be written

$$\psi = \frac{1}{4}(\omega + e)x^2 + \frac{1}{4}(\omega - e)y^2$$

In general, the aspect ratio (ratio of minor and major axes), λ, and orientation, ϕ, (figure 1d) of the ellipse will be time-dependent. These two variables are all that is required to describe the evolution of the vortex and they satisfy the following non-canonical, Hamiltonian equations

$$\dot\lambda = -e\lambda \sin 2\phi$$

$$\dot\phi = \Omega_K(\lambda) + \frac{1}{2}\omega + \frac{1}{2}e\frac{1 + \lambda^2}{1 - \lambda^2}\cos 2\phi$$

where

$$\Omega_K = \frac{\lambda}{(1 + \lambda)^2}$$

is the rotation rate for a free Kirchhoff vortex. Scaling time by ω^{-1}, setting $r = \omega^{-1}$, $p = e/\omega$, these equations become

$$\dot\lambda = -p\lambda \sin 2\phi$$

$$\dot\phi = r\Omega_K(\lambda) + \frac{1}{2} + \frac{1}{2}p\frac{1 + \lambda^2}{1 - \lambda^2}\cos 2\phi \qquad (6)$$

Since the system has only a two-dimensional phase space, the different possible behaviors of this system can be described by classifying the different possible phase portraits (see Meacham, Flierl and Send, 1989). The system depends on only two parameters (r, p). This parameter space can be divided into a small number of regions that have distinct types of phase portraits. These portraits contain three types of trajectory which we shall call tumbling, nutating and shearing. These are indicated in fig. 2. The first two types are periodic, while the third is not, representing instead a continual stretching of the vortex.
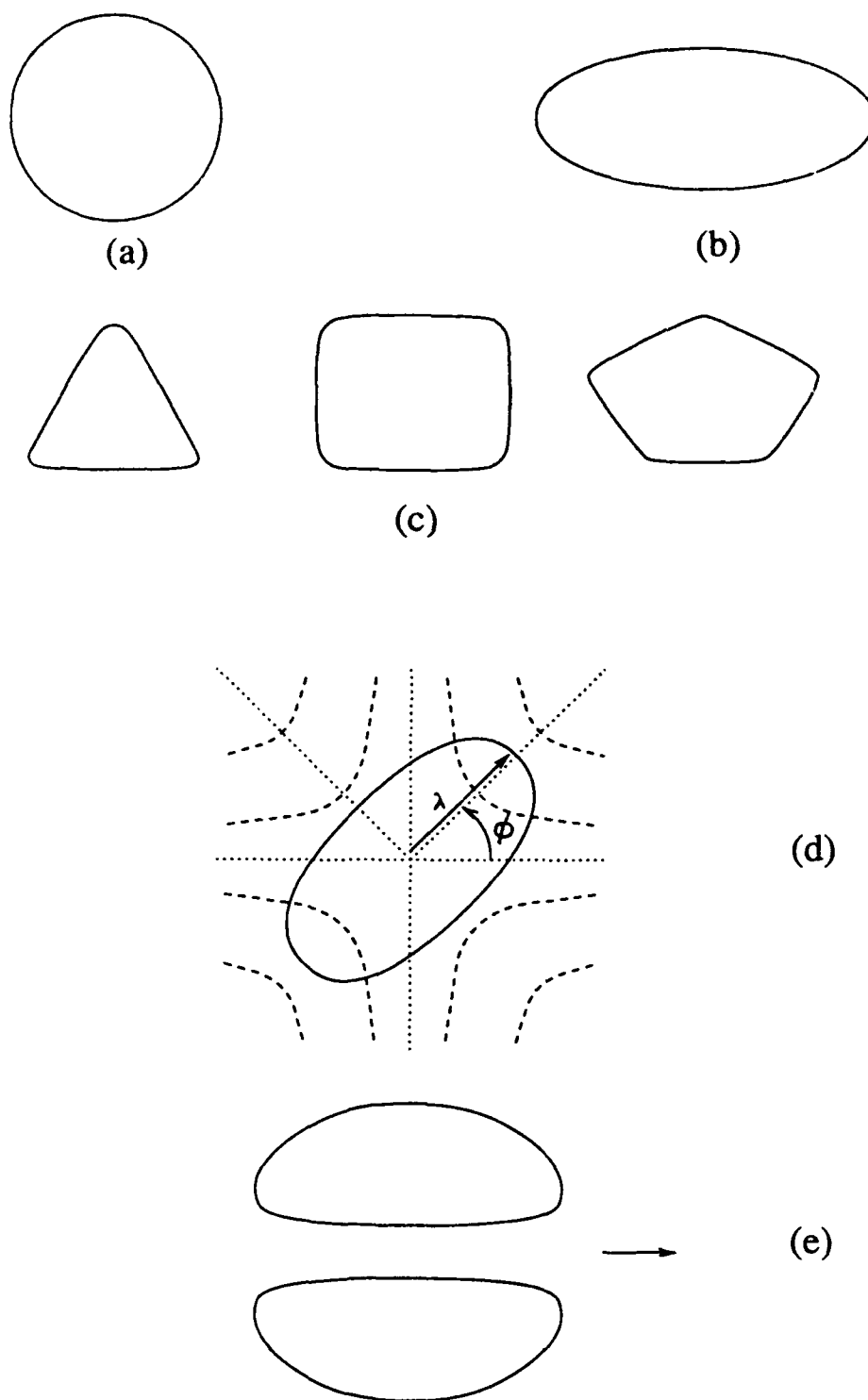
Figure 1. Examples of 2D equilibria. a) circular vortex patch, b) Kirchhoff ellipse, c) V-states, d) Kida vortex, e) dipole.
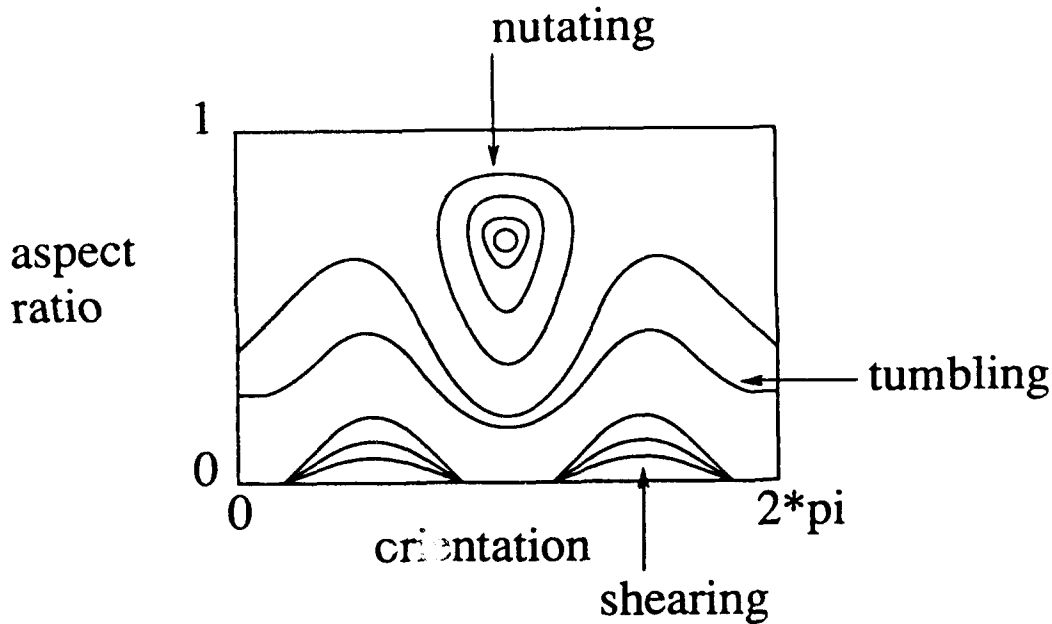
Figure 2. Sketch of the types of trajectory available to the Kida vortex

E. A last and distinct type of two-dimensional piecewise uniform vortex equilibrium is a steadily propagating dipole solution (fig. 1e), that can be obtained numerically and has been described by Pierrehumbert (1980).

2 Three dimensional quasigeostrophic uniform potential vorticity equilibria.

Turning now to quasigeostrophic vortices in 3D, we consider a continuously and uniformly stratified, resting fluid of infinite extent. This is disturbed by a blob of unit uniform anomalous potential vorticity of volume $\frac{4}{3}\pi$, with its centroid at the origin. We denote this blob by D. The basic equilibrium that we will consider is that of a spherical blob D of unit radius (in the vertically stretched coordinate system.) This is a steady equilibrium that possesses a set of steadily rotating normal modes with structure

$$(\phi_i, \phi_e, \eta) = (r^n, r^{-(n+1)}, (\Omega - \frac{1}{3})^{-1})e^{im(\phi-\Omega t)}L_n^{(m)}(\theta)$$

where ϕ_i and ϕ_e are the perturbation streamfunction within and outside the sphere, while η is the normal displacement of the surface of the sphere, $L_n^{(m)}$ is an associated Legendre function and $0 \leq n$, $0 \leq m \leq n$. The rotation rate Ω of the modes with non-trivial azimuthal structure is given by $\Omega = \{1/3 - 1/(2n + 1)\}$.

Each of these normal modes represents the beginning of a separate family of rotating equilibria that bifurcates directly from the spherical solution. Each family is characterised by a different azimuthal and vertical structure. In particular, for each n there is a collection of n modes that have different azimuthal structures but a common rotation rate Ω, and one stationary mode ($m = 0$). The stationary, $m = 0$ modes are azimuthally symmetric. The set of associated rotating equilibria is very extensive; we will discuss only a few here.

3 Ellipsoidal vortices

In a fashion similar to the Kirchhoff ellipse, an ellipsoidal blob of uniform potential vorticity anomaly (fig. 3) is an exact solution of the quasigeostrophic equations of motion. If one axis is aligned with the vertical, the vortex rotates steadily about this axis at a rate

$$\Omega_3(\alpha, \beta) = \frac{1}{2}\alpha\beta \int_0^\infty (s^2 + s)\left\{(\alpha^2 + s)(\beta^2 + s)(1 + s)\right\}^{-3/2} ds$$

This is a solution with $m = 2$ symmetry and is the natural extension of the $(n, m) = (2, 2)$ modes.

The linear stability of these solutions can be examined in a way similar to that used by Love in his analysis of the Kirchhoff ellipse (Meacham, 1992).
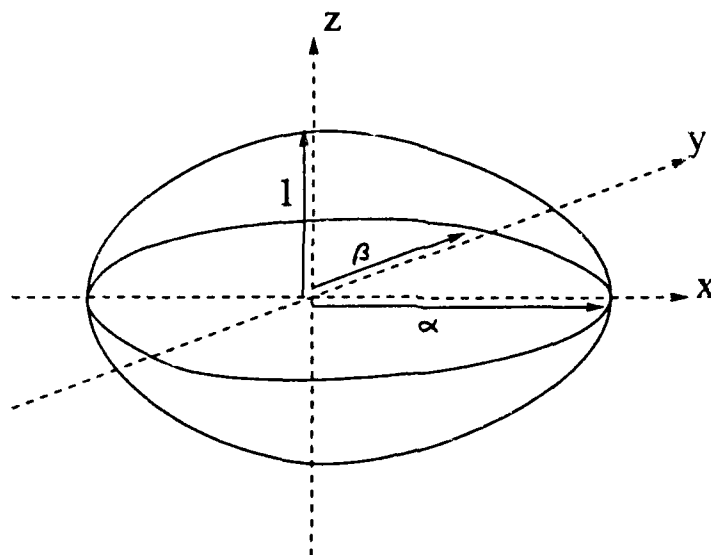
Figure 3. Sketch of ellipsoidal vortex

4 Three-dimensional V-states

As in the two-dimensional case, we can find steadily rotating equilibria with higher azimuthal symmetry ($m = 3, 4, 5, ...$) numerically. These 3D V-states form families of solutions. Under certain constraints (which include that the area of the mid-depth cross-section $= \pi$), a subset of the possible V-states are picked out. These can be viewed as forming a separate one parameter family for each choice of m. They are continuations of the $(n, m) = (3,3), (4,4), (5,5)$ etc. There are other types of solution with similar azimuthal symmetries but different vertical structures. For a given azimuthal symmetry, an appropriate parameter to choose is a bifurcation parameter similar to that used in the two-dimensional case. Here we define $1 + \rho$ to be the length of the maximum radius of the mid-depth section. The three-dimensional V-states

require an additional parameter, a vertical aspect ratio μ to complete their specification (see sketch, fig. 4).
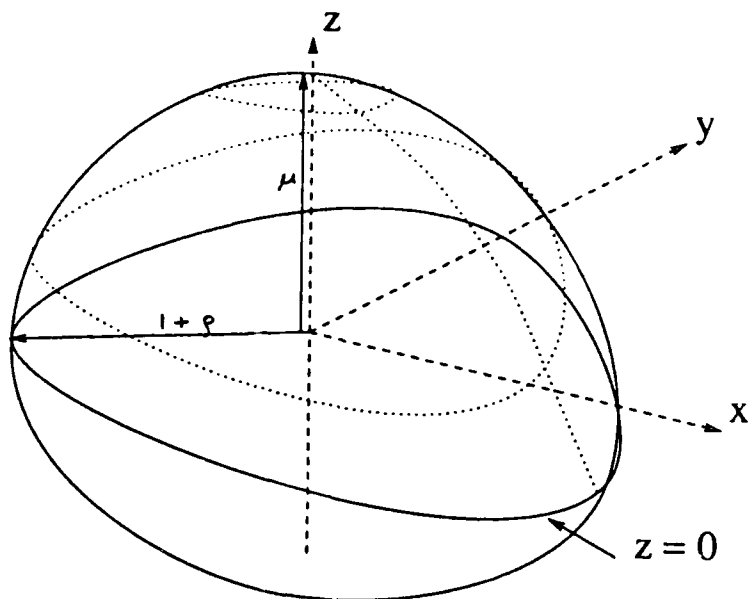
Figure 4. Sketch of a typical V-state

Examples of V-states can be seen in figure 5. As in the two-dimensional case, for $m > 2$, simple V-states only exist for a finite range of ρ, $0 < \rho < \rho_c(m)$. As ρ increases, corners become more pronounced until a weak singularity develops at $\rho < \rho_c(m)$.

Since numerical V-states are "exact" solutions, we can calculate dispersion relations for the normal modes of V-states.

$$\omega = \Omega(n', m'; \mu, \rho)$$

Here n' and m' are mode numbers analogous to those in the spherical normal mode problem. Over-simplifying a little, m' is analogous to an azimuthal wavenumber while n' contains information about the vertical structure of the mode. We have examind the case $\mu = 1$. In general, some of the low order modes (m' and n' small) are unstable if ρ is sufficiently large. The growth rates of modes that are unstable and have $n' < 5$ are sketched in figure 6. Those V-states with an even number of azimuthal lobes are unstable as soon as they bifurcate from the spherical state. In the case of the ellipsoidal ($m = 2$) V-state this instability corresponds to a tendency for the ellipsoid to tip over if its third axis is tilted slightly away from the vertical. When $\mu \neq 1$, there is a critical ρ that must be attained before this instability sets in. V-states with an odd number of azimuthal lobes enjoy a stability to low order modes until a threshold value of ρ is reached.
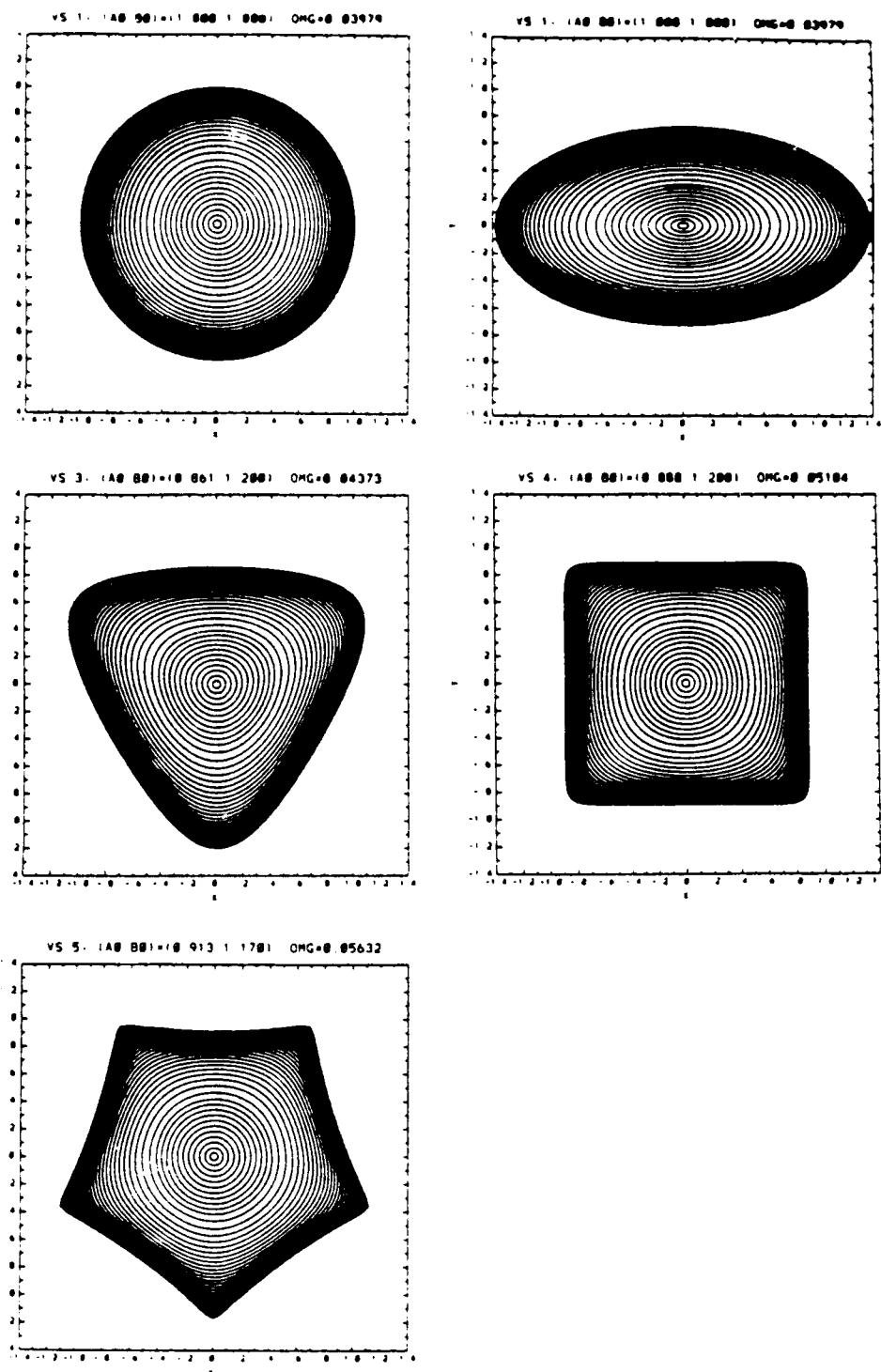
Figure 5. Examples of rotating equilibria with azimuthal symmetries of ∞,2,3,4 and 5. Contours are isolines of surface elevation as seen from above.

5 Ellipsoidal vortices in shear

A moderately general description of the behavior of ellipsoidal vortices in simple types of shear is given in Meacham, Pankratov, Shchepetkin and Zhmur (1992). Some results are briefly summarised here.
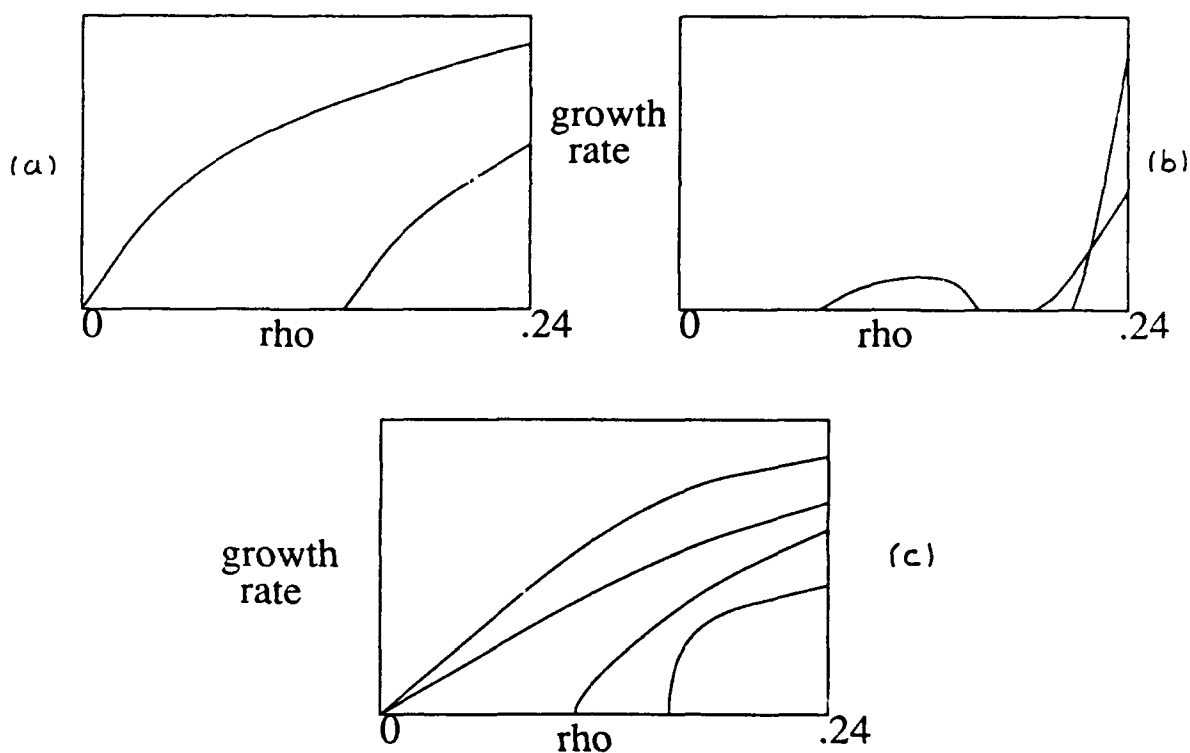
Figure 6. Sketch of growth rates of complex eigenmodes on rotating equilibria. a) ellipsoid, b) three-fold symmetric, c) four-fold symmetric.

For reasons analogous to those in the 2D Kida problem, an ellipsoidal vortex in a background flow with a quadratic streamfunction will remain ellipsoidal. For this problem, a general quadratic quasigeostrophic streamfunction can be written

$$\psi = \frac{1}{4}\omega(x^2 + y^2) + \frac{1}{4}e\{(x^2 - y^2)\cos 2\epsilon + 2xy\sin 2\epsilon\} + \tau z\{x\sin\chi - y\cos\chi\}$$

(Linear and constant terms do not affect the dynamics and can be removed by simple transformations.) This type of streamfunction embodies three distinct features: a background rotation at a rate $\omega/2$, a horizontal strain at a rate e with an orientation about the vertical axis of ϵ, and a vertical shear at a rate τ with orientation χ.

The geometry and orientation of the ellipsoid is specified by two aspect ratios, $\{\alpha(t), \beta(t)\}$ and three Euler angles, $\{\phi(t), \theta(t), \psi(t)\}$. The former are the lengths of the "horizontal" principle axes divided by the length of the third axis; the latter describe the transformation between a fixed coordinate frame, $Oxyz$, and a coordinate frame instantaneously aligned with the principle axes of the ellipsoid, $Ox_3y_3z_3$.

The evolution of the ellipsoid is described by the equations

$$\frac{\dot{\alpha}}{\alpha} = \frac{1}{2}e\left\{\cos\theta\sin 2\psi\cos 2(\phi-\epsilon) + \left[\cos 2\psi - \sin^2\theta(1+\cos^2\psi)\right]\sin 2(\phi-\epsilon)\right\}$$

$$+ \tau\sin\theta\left\{\frac{1}{2}\sin 2\psi\sin(\phi-\chi) - \cos\theta(1+\cos^2\psi)\cos(\phi-\chi)\right\}$$

$$\frac{\dot{\beta}}{\beta} = -\frac{1}{2}e\left\{\cos\theta\sin 2\psi\cos 2(\phi-\epsilon) + \left[\cos 2\psi + \sin^2\theta(1+\sin^2\psi)\right]\sin 2(\phi-\epsilon)\right\}$$

$$- \tau\sin\theta\left\{\frac{1}{2}\sin 2\psi\sin(\phi-\chi) + \cos\theta(1+\sin^2\psi)\cos(\phi-\chi)\right\}$$

$$\dot{\phi} = \frac{1}{2}(\Omega_1+\Omega_2) + \frac{1}{2}(\Omega_1-\Omega_2)\cos 2\psi + \frac{1}{2}\omega$$

$$- \frac{1}{2}e\left\{\left[\frac{\alpha^2+1}{\alpha^2-1}\sin^2\psi + \frac{\beta^2+1}{\beta^2-1}\cos^2\psi\right]\cos 2(\phi-\epsilon)\right.$$

$$\left. + \left(\frac{1}{\alpha^2-1} - \frac{1}{\beta^2-1}\right)\cos\theta\sin 2\psi\sin 2(\phi-\epsilon)\right\}$$

$$+ \frac{\tau}{\sin\theta}\left\{\cos\theta\left(\frac{\sin^2\psi}{\alpha^2-1} + \frac{\cos^2\psi}{\beta^2-1}\right)\sin(\phi-\chi)\right.$$

$$\left. - \frac{1}{2}\left(\frac{1}{\alpha^2-1} - \frac{1}{\beta^2-1}\right)\cos 2\theta\sin 2\psi\cos(\phi-\chi)\right\}$$

$$\dot{\theta} = \frac{1}{2}\sin\theta\sin 2\psi(\Omega_2-\Omega_1)$$

$$- \frac{1}{2}e\sin\theta\left\{\left[\frac{\alpha^2+1}{\alpha^2-1}\cos^2\psi + \frac{\beta^2+1}{\beta^2-1}\sin^2\psi\right]\cos\theta\sin 2(\phi-\epsilon)\right.$$

$$\left. + \left(\frac{1}{\alpha^2-1} - \frac{1}{\beta^2-1}\right)\sin 2\psi\cos 2(\phi-\epsilon)\right\}$$

$$+ \tau\left\{\left[\sin^2\theta - \cos 2\theta\left(\frac{\cos^2\psi}{\alpha^2-1} + \frac{\sin^2\psi}{\beta^2-1}\right)\right]\cos(\phi-\chi)\right.$$

$$\left. + \frac{1}{2}\left(\frac{1}{\alpha^2-1} - \frac{1}{\beta^2-1}\right)\cos\theta\sin 2\psi\sin(\phi-\chi)\right\}$$

$$\dot{\psi} = \cos\theta\left\{\Omega_3 - \frac{1}{2}(\Omega_1+\Omega_2) - \frac{1}{2}(\Omega_1-\Omega_2)\cos 2\psi\right\}$$

$$+ \frac{1}{2}e\left\{\cos\theta\left(\frac{\alpha^2+1}{\alpha^2-1}\sin^2\psi + \frac{\beta^2+1}{\beta^2-1}\cos^2\psi + \frac{\alpha^2+\beta^2}{\alpha^2-\beta^2}\cos 2\psi\right)\cos 2(\phi-\epsilon)\right.$$

$$\left. + \left[\left(\frac{1}{\alpha^2-1} - \frac{1}{\beta^2-1}\right)\cos^2\theta - \frac{1}{2}\frac{\alpha^2+\beta^2}{\alpha^2-\beta^2}(1+\cos^2\theta)\right]\sin 2\psi\sin 2(\phi-\epsilon)\right\}$$

$$- \frac{\tau}{\sin\theta}\left\{\left[\cos^2\theta\left(\frac{\sin^2\psi}{\alpha^2-1} + \frac{\cos^2\psi}{\beta^2-1}\right) - \sin^2\theta\frac{\alpha^2\cos^2\psi-\beta^2\sin^2\psi}{\alpha^2-\beta^2}\right]\sin(\phi-\chi)\right.$$

$$\left. - \frac{1}{2}\left[\left(\frac{1}{\alpha^2-1} - \frac{1}{\beta^2-1}\right)\cos\theta\cos 2\theta + \frac{1}{2}\frac{\alpha^2+\beta^2}{\alpha^2-\beta^2}\sin\theta\sin 2\theta\right]\sin 2\psi\cos(\phi-\chi)\right\}$$

Here, Ω_3 is defined as before while

$$\Omega_2 = \Omega_3(\beta^{-1}, \alpha\beta^{-1}) \qquad \Omega_1 = \Omega_3(\beta\alpha^{-1}, \alpha^{-1})$$

An alternative, Hamiltonian formulation of this system can also be given. While the equations above look fairly complicated, one can obtain a lot of information about the trajectories of the system.

We first note that there are three global invariants: volume, particle height (the z coordinate of a material fluid element) and excess energy. Volume conservation is implicit in our derivation. The remaining two invariants represent constraints on solutions of the above equations. The system, as represented above, has a five-dimensional phase space $\{\alpha, \beta, \phi, \psi, \theta\}$. Phase trajectories are confined to three-dimensional manifolds embedded within this and determined by the initial conditions. As we vary the initial conditions these manifolds fill out the five-dimensional space.

We can find a variety of simple time-dependent and steady equilibria that depend on the parameters that control the background flow.

5.1 Horizontal strain and rotation ($\tau = 0$)

When background vertical shear is absent and one axis of the vortex, say Oz_3, is initially vertical, it will remain so. The evolution of the vortex can then be described by only two independent variables and has a character that is very similar to that of the two-dimensional Kida problem. We can choose as our free variables, the horizontal aspect ratio, $\lambda = \alpha/\beta$, and the angle around the vertical axis, ϕ. Setting $r = \omega^{-1}$ and $p = e\omega^{-1}$, we obtain

$$\dot{\lambda} = -p\lambda \sin 2\phi$$
$$\dot{\phi} = r\Omega_3(\lambda; \mu) + \frac{1}{2} + \frac{1}{2}p\frac{1+\lambda^2}{1-\lambda^2}\cos 2\phi \tag{7}$$

The vertical aspect ratio, μ is conserved by the motion and so behaves as a constant parameter.

(7) is identical to the system for Kida's 2D problem, (6), except that $\Omega_K(\lambda)$ has been replaced by $\Omega_3(\lambda; \mu)$. To a good approximation,

$$\Omega_3(\lambda; \mu) = g(\mu)\Omega_K(\lambda)$$

where $g(\mu)$ is a monotonically decreasing function of μ with $g(\infty) = 1$ and $g(0) = 0$. Eq (7) becomes

$$\dot{\lambda} = -p\lambda \sin 2\phi$$
$$\dot{\phi} = r'\Omega_K(\lambda) + \frac{1}{2} + \frac{1}{2}p\frac{1+\lambda^2}{1-\lambda^2}\cos 2\phi$$

where $r' = rg(\mu) < r$ for $0 \le \mu < \infty$. Thus in the case ($\tau = 0, \theta = 0$), the motion of a 3D ellipsoid is similar to that of a 2D ellipse with reduced vorticity r'. Extrapolating from the

Kida problem, we see that when $|p| < 1$, ellipsoids will not be sheared out. When $|p| > 1$, some ellipsoids will be sheared out, depending on their initial shape and orientation. The fraction of the (λ, ϕ) phase space corresponding to initial conditions that will end up being sheared out increases as $|r/p|$ is reduced. When $|p| > 1$, an ellipsoid is more likely to be stretched out than the 2D ellipse of similar vorticity and initial aspect ratio, since $r' < r$. An important consequence of this is that tall vortices are less likely to shear out than shallower vortices since μ, and therefore $g(\mu)$, are larger for the taller vortices. Vertical shear has the opposite effect, tending to stretch out tall vortices more readily than short vortices. In the case of vortices drifting through a flow that contained both regions of horizontal strain and regions of vertical shear, one might expect to find a preference for vortices with $\mu \sim O(1)$.

The types of fixed points (steady ellipsoids) and periodic solutions (periodically oscillating ellipsoids) possible are just as in the Kida 2D case. The 3D problem also manifests a type of behavior that is not present in the Kida problem. When e is small and $\lambda^{1/2} < \mu < \lambda^{-1/2}$, the Kida-like solutions are unstable to disturbances that tilt the Oz_3 axis away from the vertical.

5.2 Vertical shear $(\omega = e = 0, \tau \neq 0)$

Going on to consider unidirectional flow that is parallel to the x-axis and contains a uniform vertical shear, one can show that there exist steady equilibria with $\phi = -\pi/2, \psi = \pi/2, \theta \neq 0$. These correspond to ellipsoids rotated through θ in the plane transverse to the flow. With this *anszatz*, the ellipsoidal variables satisfy,

$$\dot{\alpha} = 0 = \dot{\beta} = \dot{\theta}$$

$$\dot{\psi} = \cos\theta(\Omega_3 - \Omega_2) + \frac{\tau}{\sin\theta}\left\{\frac{\cos^2\theta}{\alpha^2 - 1} + \frac{\beta^2\sin^2\theta}{\alpha^2 - \beta^2}\right\}$$

$$\dot{\phi} = \Omega_2 - \frac{\tau}{\sin\theta}\frac{\cos\theta}{\alpha^2 - 1}$$

For steady equilibria, we must have $\dot{\psi} = 0$ & $\dot{\phi} = 0$ which together imply

$$(\alpha^2 - 1)\Omega_2 = \tau\cot\theta, \qquad (1 - \alpha^2/\beta^2)\Omega_3 = \tau\tan\theta$$

Given θ and τ, these determine α and β. The two relations can be combined to yield

$$\tau^2 = (\alpha^2 - 1)(\beta^2 - \alpha^2)\frac{1}{\beta^2}\Omega_2(\alpha,\beta)\Omega_3(\alpha,\beta) \equiv F(\alpha,\beta)$$

$F(\alpha,\beta)$ has two maxima of equal height with $F_{max} \approx 0.08$. This, at once, tells us that steady equilibria are not possible for $\tau > F_{max}^{1/2} \approx 0.28$. For values of τ that are less than this maximum shear rate, steady equilibria are possible for a range of θ: $0 > \theta > -\theta_0(\tau)$. $\theta_0 \to 0$ as $\tau \to F_{max}^{1/2}$ and is shown in figure 7.
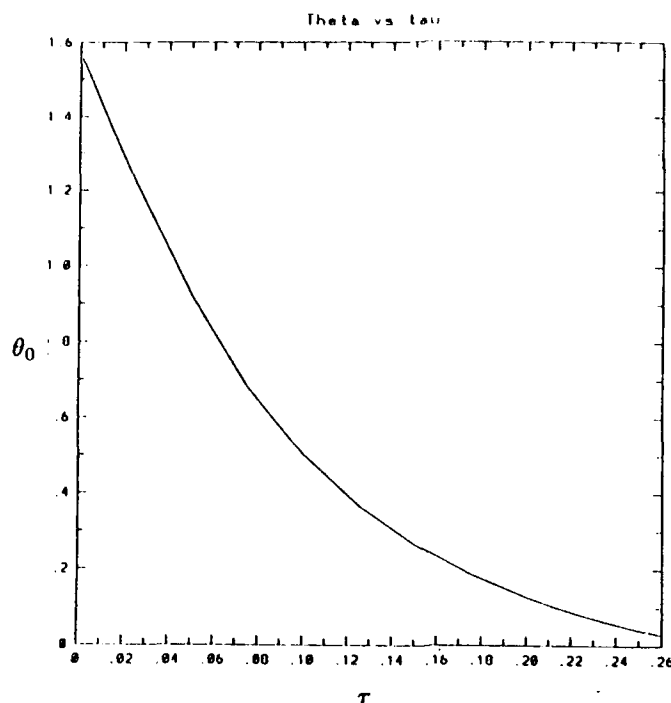
Figure 7. Width of range where equilibria are possible, θ_0, as a function of shear rate τ.

For each θ within the allowed range, there are two possible equilibria. Both have $\lambda < 1$ and so are elongated in the transverse direction. For moderate values of θ and τ, one solution has λ near 1 while the other has a λ near zero. It is straightforward to analyse the stability of these steady states to small perturbations in $\{\alpha, \beta, \theta, \psi, \& \ \dot\psi\}$ (perturbations which preserve the ellipsoidal character of the vortex). Solving the dispersion relation so obtained, we discover that the solutions along the branch that corresponds to the more elongated equilibria are unstable. Numerical integration of trajectories close to examples of these equilibria confirm this. In general, trajectories starting near the equilibria on the stable branch of solutions are quasiperiodic (figure 8).

5.3 Horizontal strain and vertical shear, ($\omega \neq 0, e \neq 0, \tau \neq 0$)

When both horizontal strain and vertical shear are included, things become a little more complicated. Steady equilibria are possible when ω, e, and τ are not too large. These again have $\phi = -\pi/2$, $\psi = \pi/2$, $\theta \neq 0$. For each value of θ, the values of α, β corresponding to equilibria are determined by

$$(\alpha^2 - 1)(\Omega_2(\alpha, \beta) + \frac{1}{2}\omega - \frac{1}{2}e) + e = \tau \cot\theta$$

$$(1 - \alpha^2/\beta^2)(\Omega_3(\alpha, \beta) + \frac{1}{2}\omega - \frac{1}{2}e) + e = \tau \tan\theta$$

Now there are three parameters and the behavior of the solution surfaces in parameter space is a bit too complicated to describe here. Instead an example is shown in figure 9.
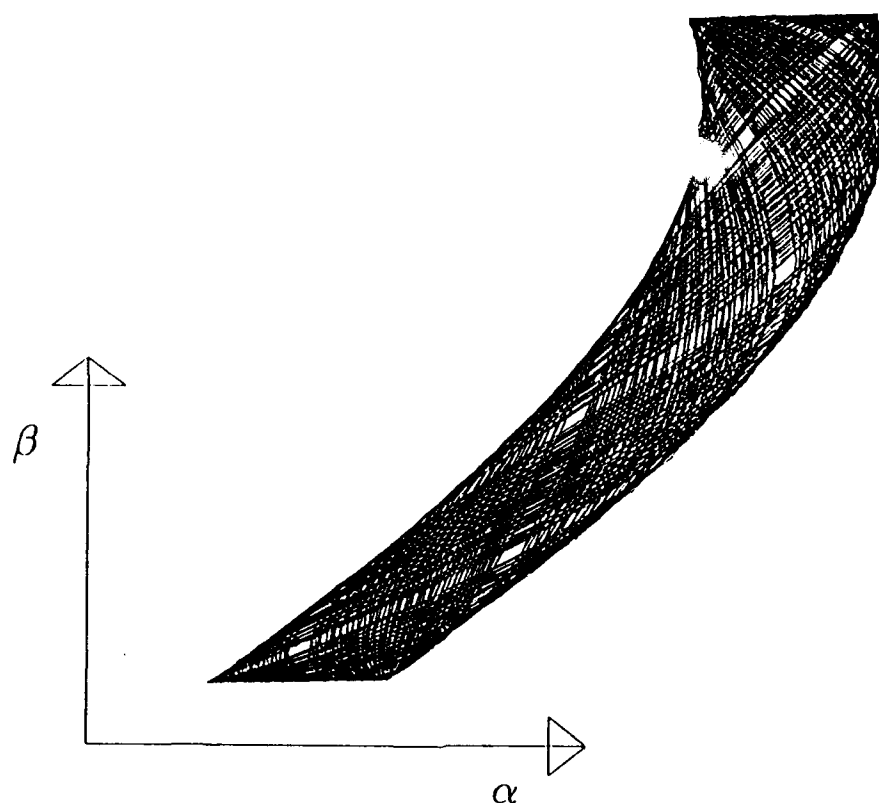
Figure 8. Quasiperiodic trajectory near a neutral equilibrium.

Figure 9. Loci of steady equilibria for the case: $\tau = 0.1$, $e = 0.1$.

6 Remarks

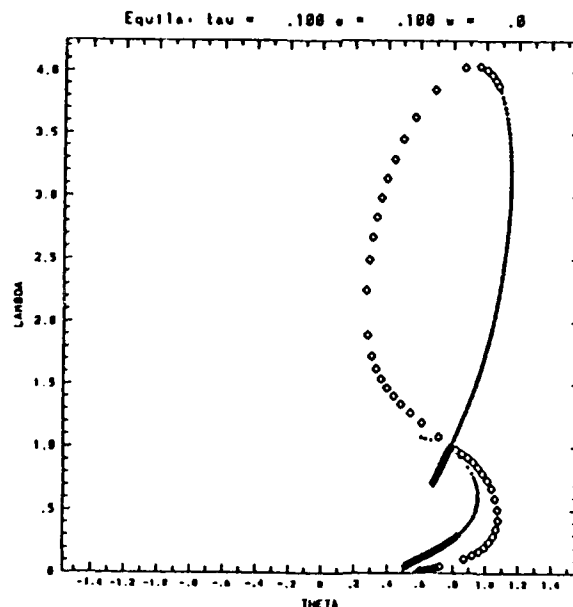There are some strong parallels between the behavior of 3D, quasigeostrophic, uniform blobs of potential vorticity and 2D patches of uniform potential vorticity. In the examples noted above there is a core of similarity while the addition of the third dimension enriches the

variety of possible solutions. When more than one vortex is considered, however, the three-dimensional case diverges from the two-dimensional case thanks to the inclusion of a process absent in two dimensions, the transfer of angular momentum vertically. Interactions between two-dimensional vortices are constrained by the two-dimensional conservation of angular momentum. This has a strong effect on the merger of pairs of identical vortex patches, necessitating horizontal transfers of angular momentum between the vortex cores and filamentary arms generated in the merger process. In the analagous three-dimensional problem for identic' vortices at the same depth, vortex merger involves angular momentum transfers in the vertical that allow the middle levels of the vortices to come together while the upper and lower levels of the two vortices are pushed apart. One consequence of this is that vortices that are initially far apart can ultimately merge, a result rather different to that in the two-dimensional problem.

References

Deem, G.S. and Zabusky, N.J. (1978) Vortex waves: Stationary V-states, interactions, recurrence and breaking. *Phys. Rev. Lett.*, **40**, 859–62.

Kida, S. (1981) Motion of an elliptic vortex in a uniform shear flow. *J. Phys. Soc. Japan*, **50**, 3517–3520.

Lamb, H. (1932) "Hydrodynamics". Cambridge University Press.

Meacham, S.P. (1989) Steadily rotating, quasigeostrophic vortices in a continuously stratified fluid. *In* Topological fluid mechanics: Proceedings of the IUTAM Symposium. Eds.H.K. Moffatt and A. Tsinober. Cambridge University Press, Cambridge, pp805.

Meacham, S.P. (1992) Quasigeostrophic, ellipsoidal vortices in a stratified fluid. *Dyn. Atmos. and Oc.*, **16** 189–223.

Meacham, S.P., Flierl, G.R. and Send, U. (1989) Vortices in shear. *Dyn. Atmos. and Oceans*, **14**, 333–386.

Meacham, S.P., Pankratov, K.K., Shchepetkin, A.S. and Zhmur, V.V., Ellipsoidal vortices in background shear and strain flows. *Dyn. Atmos. and Oc.* Submitted. (1992).

Pierrehumbert, R.T. (1980) A family of steady, translating vortex pairs with distributed vorticity. *J. Fluid Mech.* **99**, 129–144.

Wu, H.M., Overman, E.A. and Zabusky, N.J. (1984) Steady state solutions of the Euler equations in two dimensions. Rotating and translating V-states with limiting cases. 1. Numerical results. *J. Comp. Phys.*, **53**, 42-71.

Zhmur, V.V. and Pankratov, K.K. (1989) Dynamics of a semi-ellipsoidal subsurface vortex in a nonuniform flow. *Oceanology*, **29**, 205–211.

Zhm·r, V.V. and Shchepetkin, A.F. (1991) Evolution of an ellipsoidal vortex in a stratified ocean. Survivability of the vortex in a flow with vertical shear. *Fiz. Atmos. Okeana.*,**27**, 492–503 (in Rus.).

Hamiltonian contour dynamics*

P.J. Morrison

Department of Physics and Institute for Fusion Studies

The University of Texas at Austin, Austin, TX 78712

Abstract

The noncanonical Hamiltonian structure of the two-dimensional Euler equations for fluid flow and the quasigeostrophic equations for rotating fluid flow is derived from the Hamiltonian description of Kirchoff vortex dynamics. The resulting Hamiltonian structure is referred to as noncanonical because the Poisson bracket does not have the standard canonical form. Contour dynamics is reviewed and its reduced Hamiltonian structure is obtained from that of Euler's equations. This formalism is used to develop further approximations, in terms of finite degree-of-freedom Hamiltonian systems, based on amplitude expansions. Several applications are discussed. A single contour barotropic vortex is treated in detail. Low mode truncations are seen to compare very well with contour dynamics simulations. Similarly, a two contour barotropic simulation is considered and compared to contour dynamics simulation. Negative energy modes are defined and their association with nonlinear instability and subcritical bifurcations is described. Also, baroclinic and barotropic waves on a barotropic vortex are treated.

Wave and Vortex Dynamics on the Surface of a Sphere

Lorenzo M. Polvani
Department of Applied Physics
Columbia University, New York, NY 10027, USA

Motivated by the observed potential vorticity structure of the stratospheric polar vortex, we study the dynamics of linear and nonlinear waves on a zonal vorticity interface in a two-dimensional barotropic flow on the surface of a sphere [1]. After reviewing the linear problem, we determine, with the help of an iterative scheme, the shapes of steadily propagating nonlinear waves; a stability analysis reveals that they are (nonlinearly) stable up to very large amplitudes. We also consider multi-vortex equilibria on a sphere: we extend the results of Thompson (1883) and show that a (latitudinal) ring of point vortices is *more unstable* on the sphere than in the plane; notably, no more than three point vortices on the equator can be stable. We also determine the shapes of finite-area multi-vortex equilibria.

We discuss two specific applications to geophysical flows: for conditions similar to those of the wintertime terrestrial stratosphere, we show that perturbations to a polar vortex with azimuthal wavenumber 3 are close to being stationary, and hence are likely to be resonant with the tropospheric wave forcing. Secondly, we show that *the linear dispersion relation for waves on a vorticity* interface yields a good fit to the phase velocity of the waves observed on Saturn's "ribbon".

We also derive the conditions for the stability of strips or filaments of vorticity on the surface of a sphere [2]. We find that the spherical results are surprisingly different from the planar ones, owing to the nature of the spherical geometry. Strips of vorticity on the surface of a sphere show a *greater* tendency to roll-up into vortices than do strips on a planar surface. The implication for planetary atmospheres is that barotropic flows on the sphere have a more pronounced tendency to produce small, long- lived vortices, especially in equatorial and mid-latitude regions, than was previously anticipated from the theoretical results for planar flows. Essentially, the curvature of the sphere's surface weakens the interaction between different parts of the flow, enabling these parts to behave in relative isolation.

[1] L.M. Polvani and D.G. Dritschel, "Wave and vortex dynamics on the surface of the sphere", submitted to *J. Fluid Mech.* (1992)

[2] D.G. Dritschel and L.M. Polvani, "The roll-up of vorticity strips on the surface of a sphere", *J. Fluid Mech.*, **234**, 47-69 (1992)

What is potential vorticity?

by Rick Salmon
Scripps Institution of Oceanography

In this pedagogical lecture, we show that potential vorticity is just *ordinary vorticity measured in comoving coordinates*, that is, in coordinates whose coordinate-surfaces move with the flow. We then address the deeper question: Why does potential vorticity have such a special status in geophysical fluid dynamics?

Our starting point is the perfect-fluid equations,

$$\frac{D\mathbf{v}}{Dt} + 2\Omega \times \mathbf{v} = -\frac{1}{\rho}\nabla p - \nabla\Phi(\mathbf{x})$$

$$p = p(\rho, S)$$

$$\frac{D\rho}{Dt} + \rho\nabla \cdot \mathbf{v} = 0$$

$$\frac{DS}{Dt} = 0 \tag{1}$$

where Φ is the potential for external forces, S is the entropy, and the other symbols have their usual meanings. From (1) we obtain the vorticity equation

$$\frac{D\mathbf{w}}{Dt} - [\mathbf{w} \cdot \nabla]\mathbf{v} = \nabla p \times \nabla\frac{1}{\rho} \tag{2}$$

where

$$\mathbf{w} \equiv \frac{\omega}{\rho} \quad and \quad \omega \equiv \nabla \times \mathbf{v} + 2\Omega \tag{3}$$

is the absolute vorticity. If the entropy S is uniform, the pressure depends only on density, $p=p(\rho)$, and (2) reduces to

$$\frac{D\mathbf{w}}{Dt} - [\mathbf{w} \cdot \nabla]\mathbf{v} = 0 \tag{4}$$

which is equivalent to

$$\left[\frac{\partial}{\partial t} + L_v\right]\mathbf{w} = 0 \tag{5}$$

where

$$[L_v\mathbf{w}]^i \equiv v^j\frac{\partial w^i}{\partial x^j} - w^j\frac{\partial v^i}{\partial x^j} \tag{6}$$

is the Lie derivative of $\mathbf{w}$ with respect to $\mathbf{v}$. In (6), superscripts denote components, and the summation convention applies.

To explain the physical meaning of the Lie derivative, we note that (4) is analogous to the equation for the displacement $\delta\mathbf{r}(t)$ between two infinitesimally separated fluid particles at $\mathbf{r}(t)$ and $\mathbf{r}(t)+\delta\mathbf{r}(t)$, viz.,

$$\frac{d}{dt}\delta r^i - \frac{\partial v^i}{\partial x^j}\delta r^j = 0. \tag{7}$$

Noting that d/dt is equivalent to D/Dt (in this context), we see that (7) is the same as (4) with $\mathbf{w}$ replaced by $\delta\mathbf{r}$. This means that, in homentropic flow, the vector $\mathbf{w}$ is transported, tilted and stretched by the fluid in precisely the same way as the infinitesimal displacement vector between two fluid particles with the same initial location and orientation as the $\mathbf{w}$-vector being considered. In fluid mechanics, this analogy is often described by the statement that "the field of $\mathbf{w}$ is *frozen into the fluid*"; but the more mathematical statement that " $\mathbf{w}$ is *Lie-dragged by the flow* " seems more appropriate.

To obtain an equation for the potential vorticity in homentropic flow, we introduce a conserved scalar,

$$\frac{D\theta}{Dt} = 0 \tag{8}$$

and derive the equation

$$\frac{\partial \alpha_i}{\partial t} + v^j \frac{\partial \alpha_i}{\partial x^j} + \alpha_j \frac{\partial v^j}{\partial x^i} = 0 \tag{9}$$

for its gradient

$$\alpha_i \equiv \frac{\partial \theta}{\partial x^i}. \tag{10}$$

The scalar θ need not have any physical significance; it could be an arbitrarily defined tracer. But (5,6) and (9) combine immediately to give

$$\frac{\partial Q}{\partial t} + v^j \frac{\partial Q}{\partial x^j} \equiv \frac{DQ}{Dt} = 0 \tag{11}$$

where

$$Q \equiv \alpha_i w^i = \boldsymbol{\alpha} \cdot \mathbf{w} \tag{12}$$

is the potential vorticity. The potential vorticity equation (11) is simpler than its constituents (5) and (9) because tilting and stretching affect the vectors $\mathbf{w}$ and $\nabla\theta$ in compensating ways. In mathematical physics, this relationship is emphasized by writing (9) in the form

$$\left[\frac{\partial}{\partial t} + L_v\right]\boldsymbol{\alpha} = 0 \tag{13}$$

where the Lie derivative

$$[L_v\boldsymbol{\alpha}]_i \equiv v^j \frac{\partial \alpha_i}{\partial x^j} + \alpha_j \frac{\partial v^j}{\partial x^i} \tag{14}$$

of the *covariant vector* $\boldsymbol{\alpha}\equiv\nabla\theta$ is defined differently from the Lie derivative (6) of the *contravariant vector* $\mathbf{w}$. Their product is the scalar Q , whose Lie derivative is

$$L_v Q \equiv v^j \frac{\partial Q}{\partial x^j} \tag{15}$$

and (11) then follows from (5) and (13) by the Leibniz rule for Lie derivatives. The equations (7) and (8-10) illustrate the general concepts of Lie-dragging of vectors and covectors, respectively, and, in that sense, fluid mechanics illuminates geometry. But the converse is also true: from the standpoint of tensor analysis, the statement (4) that the vector $\mathbf{w}$ is Lie-dragged by $\mathbf{v}$, has been converted to the (simpler) statement (11) that the

scalar Q is Lie-dragged, by the standard trick of introducing a Lie-dragged covector α, the gradient of a conserved scalar being the simplest possible choice.

Has anything really been gained? *Without* the concept of potential vorticity conservation, the vorticity equation (4) for homentropic flow offers a way to step the three components of vorticity forward in time. At every time, the Biot-Savart law is needed to compute the velocity **v** from **w**. *With* the concept of potential vorticity, the *three* components of (4) are replaced by the *six* conservation equations:

$$\frac{D\theta_1}{Dt} = 0, \qquad \frac{D\theta_2}{Dt} = 0, \qquad \frac{D\theta_3}{Dt} = 0 \tag{16}$$

and

$$\frac{DQ_1}{Dt} = 0, \qquad \frac{DQ_2}{Dt} = 0, \qquad \frac{DQ_3}{Dt} = 0 \tag{17}$$

where

$$Q_1 = \mathbf{w} \cdot \nabla\theta_1, \qquad Q_2 = \mathbf{w} \cdot \nabla\theta_2, \qquad Q_3 = \mathbf{w} \cdot \nabla\theta_3 \tag{18}$$

To use these equations, we step the θ 's and Q 's, determine the three components of **w** from the definitions (18), and then use the Biot-Savart law as before. (Three independent θ 's are required to determine the three components of **w**.) The equations (16) and (17) seem simpler than (4), but this is at least partly an illusion; it is amusing to speculate than the human tendency to prefer (16,17) over (4) is rooted in our natural tendency, acquired early in infancy, to classify our environment into immutable objects that can be moved from place to place but not otherwise changed. It is likely that intelligent fish, who would appreciate the analogy between **w** and a stretchy piece of seaweed, would prefer the more condensed description offered by (4).

The formulation (16-18) of homentropic fluid dynamics invites the following interpretation of the three required potential vorticities: the three Q 's are simply the three components of **w** in *comoving coordinates* with curvilinear basis vectors $\nabla\theta_1$, $\nabla\theta_2$, $\nabla\theta_3$. Let $\mathbf{A} = (A_1, A_2, A_3)$ be the components of the velocity in this same comoving frame. That is, let

$$\mathbf{v} = A_1\nabla\theta_1 + A_2\nabla\theta_2 + A_3\nabla\theta_3 \tag{19}$$

It can then easily be shown that the conserved potential vorticities take the form

$$Q_i = \frac{\omega}{\rho} \cdot \nabla\theta_i = \frac{1}{\rho}\frac{\partial(\theta_1,\theta_2,\theta_3)}{\partial(x,y,z)}[\nabla_{\bullet} \times \mathbf{A}] \tag{20}$$

where

$$\nabla_{\bullet} = \left(\frac{\partial}{\partial\theta_1}, \frac{\partial}{\partial\theta_2}, \frac{\partial}{\partial\theta_3}\right) \tag{21}$$

is the gradient operator in comoving coordinates. If the conserved θ 's are initially assigned so that

$$d\theta_1\, d\theta_2\, d\theta_3 = d(mass) \tag{22}$$

(a comparatively weak restriction), then (20) reduces to

$$\mathbf{Q} = \nabla_{\bullet} \times \mathbf{A} \tag{23}$$

and the whole vorticity dynamics becomes

$$\frac{D}{Dt}[\nabla_\theta \times \mathbf{A}] = 0 \tag{24}$$

Since D/Dt is simply the local time derivative in comoving coordinates, (24) implies that the vorticity

$$\nabla_\theta \times \mathbf{A} = \mathbf{F}(\theta_1, \theta_2, \theta_3) \tag{25}$$

is simply a static field in the comoving reference frame. A translation of (25) into conventional notation leads to what has been called "Cauchy's solution of the vorticity equation."

In general non-homentropic flow, the torque term on the right-hand side of (2) destroys two of the three components of the conservation law (24). In that case, it may be convenient to take the entropy S as one of the comoving coordinates. Since the torque in (2) has no component in the direction of ∇S, we find that the S-component of (24) survives:

$$\frac{D}{Dt}[(\nabla_\theta \times \mathbf{A}) \cdot \nabla_\theta S] = 0 \tag{26}$$

The conserved quantity in (26) turns out to be the familiar Ertel potential vorticity. And, although (26) contains only one-third of the dynamical information in (24), it is — in strongly stratified flow — a much more useful equation. In unstratified ($\nabla S = 0$) flow, the θ-surfaces become very convoluted, and the simplicity of (24) is offset by the complexity of transforming back into physical coordinates. However, in strongly stratified flow, gravitational restoring forces resist the folding of isentropic surfaces, rendering the single equation (26) much more useful. Moreover, if the fluid is rotating ($\Omega \neq 0$), the single equation (26) corresponds to the *slow* part of the fluid motion, which is often of primary interest; we come back to this point below.

Hamilton's principle for a perfect fluid offers a much more direct and motivated derivation of the potential vorticity laws (24) and (26) (Salmon, 1988). The conservation law (24) corresponds to the symmetry property that the Hamiltonian for homentropic flow is unaffected by particle relabelings that do not affect the mass density. When entropy gradients are present, this symmetry is partly broken, and two components of (24) are "lost." In rotating flow, these two "lost" components of potential vorticity give rise to high-frequency inertia-gravity waves. This leads to what I call the "two-plus-one" view of geophysical fluid dynamics, a concept I will illustrate by the following description — and criticism — of the quasigeostrophic approximation.

Consider the primitive equations of motion, that is, the equations obtained by applying the Boussinesq, traditional, and hydrostatic approximations to (1). Choose a particular state of rest, and linearize the primitive equations about this rest state. Let R, G^+, and G^- be the amplitudes of the Rossby and gravity modes in a particular wavenumber $\mathbf{k}$. The plus and minus correspond to gravity waves propagating in the directions $\pm\mathbf{k}$. Now rewrite the fully nonlinear primitive equations in the modal variables R and G:

$$\frac{dR}{dt} + i\omega_R = \{R,R\} + \{R,G\} + \{G,G\}$$

$$\frac{dG^+}{dt} + i\omega_G = \{G,G\} + \{G,R\} + \{R,R\}$$

$$\frac{dG^-}{dt} - i\omega_G = \{G,G\} + \{G,R\} + \{R,R\}$$

$$(27)$$

where the brackets denote nonlinear terms, quadratic in the enclosed variables. Equation (27a) turns out to be the evolution equation for the linearized potential vorticity — the surviving component of the potential vorticity in non-homentropic flow. The gravity wave equations (27b) and (27c) correspond to the broken symmetries in the two non-entropy directions. As first recognized by Leith (1980), the conventional quasigeostrophic equations are equivalent to

$$\frac{dR}{dt} + i\omega_R = \{R,R\}$$

$$G^+ = 0$$

$$G^- = 0$$

$$(28)$$

Thus, the surviving symmetry becomes the whole dynamics, and the broken symmetries are replaced by balance conditions that filter out the unwanted high-frequency waves; equations (28b) and (28c) correspond to geostrophic balance in the two horizontal directions.

In their "two-plus-one" composition, with potential vorticity conservation being the "one" and the "two" balance conditions permitting the three-dimensional velocity to be calculated from the single component of potential vorticity, the quasigeostrophic equations (28) resemble other, more sophisticated, approximations to nearly geostrophic flow. But the quasigeostrophic equations are flawed in a way that makes them particularly unsuitable for large-scale oceanography. The result (28) depends on the particular choice of rest state, and the logic behind (28) disappears if the solution wanders far from this rest state. In the usual notation, the choice of rest state is reflected by the prescribed mean Vaisala frequency $N^2(z)$, and the quasigeostrophic approximation breaks down if deep isopycnals outcrop at the sea surface.

From the geometrical viewpoint, the approximation (28) to (27) corresponds to an ordinary projection of the initial conditions and the dynamics onto the R- axis in phase space. This amounts to the introduction of a *metric* for which R and G are the Cartesian coordinates. But phase space has no natural metric, and the *imposition* of a metric corresponding to an arbitary rest state is responsible for the flaws in the quasigeostrophic approximation noted above. Phase space does have a natural geometric structure, associated with a *symplectic tensor* or *antisymmetric metric* that does not correspond to a rest state, but comes from the underlying exact dynamics. When this symplectic tensor is used in place of the arbitrary metric, the equations corresponding to (28) are the *semigeostrophic equations*, which have none of the problems noted above. The best motivated development uses Dirac's theory of constrained Hamiltonian systems (Salmon, 1988a.)

References

Leith, C.E. 1980. Nonlinear normal mode initialization and quasigeostrophic theory. JAS 37:958-968.

Salmon, R. 1988. Hamiltonian fluid mechanics. Ann. Rev. Fluid Mech. 20:225-56.

Salmon, R. 1988a. Semigeostrophic theory as a Dirac-bracket projection. JFM 196:345-358.

On the Maintenance of the Westerlies

Theodore G. Shepherd

Department of Physics, University of Toronto, Toronto M5S 1A7 Canada

Observations suggest that the dominant forcing for the super-rotation (mean westerlies) in the Earth's atmosphere comes from meridional angular-momentum transport by eddies. It is natural to ask how one might understand, predict, or parameterize this transport. One possible approach is an appeal to mixing-length theory and eddy viscosity. But while this gives a rough estimate for the meridional eddy heat transport, it is hopeless for the momentum transport since the latter is up-gradient.

Another classical approach is an examination of the eddy fluxes associated with normal-mode baroclinic instability. Again, while this seems to give reasonable answers for heat transport, it fails miserably for the momentum transport which is observed to be maximal at much higher altitudes than expected from instability theory. Moreover, and more importantly, nonlinear numerical simulations of baroclinic instability under realistic conditions (Simmons & Hoskins 1978) demonstrate that the momentum transport occurs at a later stage in the life cycle of a baroclinic wave than the heat transport, when the wave has lost its normal-mode structure and is decaying barotropically.

In his classical monograph, Lorenz (1967) summarized the situation thus: "We regard the problem of explaining the pattern of the transport of angular momentum by the eddies as the most important problem in general-circulation theory among those for which we now lack a fairly adequate explanation". While the problem is far from being completely understood, there has been considerable progress over the last 15 years or so. It is the goal of this paper to review the salient points of this development.

The problem of eddy angular-momentum transport is ultimately one of wave, mean-flow interaction, for which we now have a comprehensive theoretical framework in the small-amplitude quasi-geostrophic limit (Andrews & McIntyre 1976):

$$\left(\frac{\partial^2}{\partial y^2} + \frac{1}{\rho_s} \frac{\partial}{\partial z} \frac{\rho_s}{S} \frac{\partial}{\partial z} \right) \frac{\partial \overline{u}}{\partial t} = \frac{\partial^2}{\partial y^2} (\boldsymbol{\nabla} \cdot \overline{\boldsymbol{F}}) = \frac{\partial^2}{\partial y^2} \left(\overline{\mathcal{D}} - \frac{\partial \overline{A}}{\partial t} \right).$$

The differential operator applied to the zonal-wind tendency $\partial \overline{u}/\partial t$ is elliptic and hence invertible; thus the above expression demonstrates how a combination of transient and non-conservative effects *on the eddies* can drive mean-flow changes. The second equality follows from the pseudomomentum (wave-activity) conservation relation

$$\frac{\partial \overline{A}}{\partial t} + \boldsymbol{\nabla} \cdot \overline{\boldsymbol{F}} = \overline{\mathcal{D}}.$$

In the above,

$$\overline{A} = \frac{\rho_s}{2} \frac{\overline{(q')^2}}{\overline{q}_y} \quad \text{and} \quad \overline{F} = -\rho_s \overline{u'v'} \, \hat{y} - \frac{\rho_s}{S} \overline{v'\psi'_z} \, \hat{z}$$

are respectively the "Eliassen-Palm" (E-P) wave activity and its flux, q is the quasi-geostrophic potential vorticity, and $\overline{\mathcal{D}}$ represents non-conservative effects on the eddies (also, in this context, ageostrophic and nonlinear effects). The notation is standard: see, for example, Andrews et al. (1987).

A more physical interpretation of the above control comes from the fact that

$$\nabla \cdot \overline{F} = \overline{v'q'} = \text{meridional flux of potential vorticity.}$$

This leads to an explicit demonstration of the *potential-vorticity invertibility principle*: there can be no mean-flow changes without mean potential-vorticity changes.

In baroclinic life cycles, $\displaystyle\int_0^\infty \frac{\partial \overline{A}}{\partial t} \, dt = 0$ so

$$\left(\frac{\partial^2}{\partial y^2} + \frac{1}{\rho_s} \frac{\partial}{\partial z} \frac{\rho_s}{S} \frac{\partial}{\partial z} \right) \frac{\partial \overline{u}}{\partial t} = \frac{\partial^2}{\partial y^2} (\nabla \cdot \overline{F}) = \frac{\partial^2 \overline{\mathcal{D}}}{\partial y^2};$$

thus irreversible mean-flow changes are controlled by non-conservative effects on eddies, and reflected in non-zero $\nabla \cdot \overline{F} = \overline{v'q'}$. The evidence from baroclinic life-cycle calculations (Edmon et al. 1980; Hoskins 1983; Held & Hoskins 1985) reveals that these non-conservative effects occur primarily at the surface (associated with occlusion and fronto-genesis) and on the flanks of the jet stream near the tropopause (associated with Rossby wave breaking and an enstrophy cascade to small scales).

These non-conservative effects are sometimes referred to as *irreversible mixing* (of potential vorticity). This is because

$$\nabla \cdot \overline{F} = \overline{v'q'} = \overline{\frac{D\eta}{Dt} \left(-\eta \overline{q}_y \right)} = -\frac{1}{2} \overline{q}_y \frac{d}{dt} (\overline{\eta^2})$$

where η is the meridional particle displacement (Rhines 1977). Hence non-zero $\nabla \cdot \overline{F}$ can be associated with irreversible growth in particle displacements. In the case of baroclinic life cycles this has been verified by Held & Hoskins (1985).

Idealized numerical experiments (Feldstein & Held 1989) show that the existence of a single life cycle involving irreversible potential-vorticity mixing depends on the existence of a critical layer. Without a critical layer, one finds baroclinic (normal-mode) vacillation and repeated life cycles: hence reversible decay. With a critical layer, on the other hand, one finds baroclinic (normal-mode) growth followed by barotropic (non-modal) decay, and a single life cycle: hence irreversible decay. The reason for this is that critical layers generate

small length scales and lead to mixing, whence irreversibility. More generally, though, one just needs *wave breaking*: namely the wrapping-up of potential-vorticity contours. (The point is that critical layers induce wave breaking.)

The implication of the above theory is that the problem of transient-eddy parameterization is essentially one of *Rossby wave drag parameterization*. In this view, developed over the past decade or so principally by McIntyre, Hoskins, and Held, the maintenance of the westerlies is associated with radiation of negative (westward) pseudomomentum out of the jet core region. Focusing on the Reynolds stress alone is a red herring, and leads to such non-sensical notions as "negative viscosity".

Indeed, within the framework of wave, mean-flow interaction theory, the westerly forcing of the mid-latitude jet is seen to come from $\nabla \cdot \bar{F}$ at the ground, and is associated with cyclone growth, occlusion and frontogenesis: this is, perhaps, a somewhat radical notion!

The above considerations suggest that the problem of eddy flux closure may be focused on the determination of the location and strength of the low-level and the upper-level potential-vorticity mixing. In the case of the low-level mixing, the location might be determined from linear baroclinic instability theory and the strength from nonlinear baroclinic-saturation theory (Shepherd 1989). In the case of the upper-level mixing, the location might be determined from linear ray-tracing theory and the strength from nonlinear saturation together with wave-activity conservation.

Now, linear theory predicts complete absorption of the E-P flux at a diffusive critical layer (Dickinson 1969); this would provide a logical basis for parameterization (Held & Hoskins 1985). This approach was shown to be viable for sufficiently small-amplitude eddies by Held & Phillips (1987), using numerical "barotropic decay" experiments. For atmospheric parameter values, however, nonlinear effects would appear to be crucial.

The possible connection between critical layers and wave-activity absorption was also addressed in an observational study by Randel & Held (1991). They found that while the basic notions of wave-activity propagation and barotropic decay where the intrinsic phase speed $(c - \bar{u})$ is small seem qualitatively correct, linear critical-layer absorption is *not* a good basis for eddy-flux closure.

On the other hand, critical-layer absorption is merely an idealized model, valid in a certain parameter limit, of the more general and robust phenomenon of nonlinear wave breaking and enstrophy cascades. This is the province of large-scale turbulence theory. Quantitative examination of irreversible mixing (of potential vorticity) is provided by the spectral transfer or cascade of (potential) enstrophy to small scales. In particular, there is a component of this transfer involving the down-scale transfer of transient enstrophy induced by the time-mean flow, which is associated with an up-scale transfer of energy from the transients to the mean: hence the observed "negative viscosity". This is precisely

the process described earlier within the context of wave, mean-flow interaction theory. Preliminary investigations along these lines have been made by Shepherd (1987a,b), but more work is required to bridge the gap between large-scale turbulence theory and wave, mean-flow interaction theory.

References

Andrews, D.G., Holton, J.R. & Leovy, C.B. 1987 *Middle Atmosphere Dynamics*. Academic Press.

Andrews, D.G. & McIntyre, M.E. 1976 Planetary waves in horizontal and vertical shear: The generalized Eliassen-Palm relation and the mean zonal acceleration. *J.Atmos.Sci.* **33**, 2031-2048.

Dickinson, R. 1969 Theory of planetary-wave zonal flow interaction. *J.Atmos.Sci.* **26**, 73-81.

Edmon, H.J., Hoskins, B.J. & McIntyre, M.E. 1980 Eliassen-Palm cross-sections for the troposphere. *J.Atmos.Sci.* **37**, 1600-1616 (see also Corrigendum, *J.Atmos.Sci.* **38**, 1115).

Feldstein, S. & Held, I.M. 1989 Barotropic decay of baroclinic waves in a two-layer beta-plane model. *J.Atmos.Sci.* **46**, 3416-3430.

Held, I.M. & Hoskins, B.J. 1985 Large-scale eddies and the general circulation of the troposphere. *Adv.Geophys.* **28A**, 3-31.

Held, I.M. & Phillips, P.J. 1987 Linear and nonlinear barotropic decay on the sphere. *J.Atmos.Sci.* **44**, 200-207.

Hoskins, B.J. 1983 Modelling of the transient eddies and their feedback on the mean flow. In *Large-Scale Dynamical Processes in the Atmosphere* (ed. B.J. Hoskins & R.P. Pearce), pp. 169-199. Academic Press.

Lorenz, E.N. 1967 *The Nature and Theory of the General Circulation of the Atmosphere*. World Meteorological Organization.

Randel, W.J. & Held, I.M. 1991 Phase speed spectra of transient eddy fluxes and critical layer absorption. *J.Atmos.Sci.* **48**, 688-697.

Rhines, P.B. 1977 The dynamics of unsteady currents. In *The Sea*, vol.6, pp. 189-318. Wiley.

Shepherd, T.G. 1987a Rossby waves and two-dimensional turbulence in a large-scale zonal jet. *J.Fluid Mech.* **183**, 467-509.

Shepherd, T.G. 1987b A spectral view of nonlinear fluxes and stationary-transient interaction in the atmosphere. *J.Atmos.Sci.* **44**, 1166-1178.

Shepherd, T.G. 1989 Nonlinear saturation of baroclinic instability. Part II: Continuously stratified fluid. *J.Atmos.Sci.* **46**, 888-907.

Simmons, A.J. & Hoskins, B.J. 1978 The life cycles of some nonlinear baroclinic waves. *J.Atmos.Sci.* **35**, 414-432.

Experimental studies of flows in a rotating annulus:
Barotropic instabilities and Hamiltonian transport

T. H. Solomon, M.S. Pervez and H.L. Swinney
Center for Nonlinear Dynamics,
University of Texas at Austin, Austin, TX 78712
and
D. del Castillo Negrete and P.J. Morrison
Institute for Fusion Studies,
University of Texas at Austin, Austin, TX 78712

Experiments are performed on azimuthal flows in a rotating annulus with barotropic (source-sink) forcing and a beta effect. These flows are of significant interest because of their close relationship with planetary flows (such as the Gulf Stream and the Antarctic Circumpolar Jet) and plasma flows (such as drift waves). Fundamentally, the rapid rotation results in a velocity field that is almost perfectly two-dimensional, as is expected by the Taylor-Proudman theorem. Because of this two-dimensionality, precise comparisons can be made between theoretical and numerical predictions of the dynamics and the experimental results. In addition, the tools of Hamiltonian mechanics can be applied to studies of transport and mixing in these flows. In particular, concepts of Lagrangian chaos (chaotic advection) and Kolmogorov-Arnold-Moser (KAM) invariant surfaces can be exploited to analyze trapping in and hopping between "islands" (or vortices) in the flow.

Studies of the dynamics concentrate primarily on the low Reynolds number (R) regimes. For small R, the flow is an axisymmetric jet bounded by strong shear layers. With increasing R, each of these shear layers independentally becomes unstable to the formation of vortex chains. The resulting state consists of two concentric chains of vortices, each with its own mode number and propagation speed. Near onset, the vortex chains have many properties typical of shear-induced instabilities. They are nevertheless influenced by the beta effect, which results in an asymmetry between co-rotating and counter-rotating flows. Most significant is the decrease in the propagation speed of co-rotating vortex chains for small Rossby number e. Increasing R above onset, the vortex chains grow, resulting in a decrease in e and in the propagation speed (for co-rotating flows). For large enough forcing, the vortex chains lock, having the same mode number and propagation speed. For co-rotating flows, the locked states have the properties of Rossby waves; specifically, the propagation speed of the states agrees with that predicted by a dispersion relation for Rossby waves. For counter-rotating flows, however, the locked states still retain the basic properties of a shear-induced instability. Experiments are currently under progress to study the behavior of Rossby waves at intermediate values of R, and, in particular, the bifurcations to a chaotic state.

Studies of the kinematics examine the transport and mixing properties of the flows. Hamiltonian models that describe the velocity field predict that transport can be chaotic if the velocity field has two or more modes. The phase space, which is real space for two-dimensional flows, is divided into ordered and chaotic regions, separated by KAM invariant surfaces that act as barriers to transport. These structures are seen experimentally if dye is injected into the annulus. The dye does not cross the KAM surfaces, leaving holes in

the concentration field. Particle- tracking techniques are being developed to quantify the transport and mixing in the system. Neutrally-buoyant particles suspended in the fluid are tracked with a rotating video camera and a computer with an image acquisition system. Trapping of particles in vortices is observed. In addition, particles in the chaotic regions "stick" temporarily in the vicinity of the vortices. Measurements are being made of the distribution of sticking times.

Chaos and Intermittency in the Solar Cycle

E.A. Spiegel, Columbia University

1. The Data. We look at the solar cycle coarsely and we see an aperiodic oscillation that may well be chaotic and that shows signs of intermittency. In modeling these data, we need to decide how much coarsening is desirable. The solar data are probably not extensive enough in time to decide such issues as whether the cycle is deterministic (in the sense of being a low order system), so the decision must be made by the modeler. In §2., the cycle is regarded as a relatively low order system and a dynamical model is proposed.

2. On/Off Intermittency. The dearth of spots that occured during the time of Newton may well be taken as a switching off of the solar cycle. The implied variation between states of high magnetic activity and virtual inactivity has been called *on/off intermittency* in work with N. Platt and C. Tresser. We attempt to understand this process by positing a subsystem of the solar process that is somewhat short of being overstable. This subsystem is coupled to a chaotic or turbulent subsystem in such a way that its effective growth rate is modified. When the the first subsystem is made effectively unstable, it performs oscillations for some time before settling back into inactivity. For suitable parameters, this temporal behavior resembles that of the solar cycle.

3. The Solar Tachocline. One way to produce the intermittent dynamical process of **2** is to have the two postulated subsystems in two spatially disparate regions. (This notion arose in discussion with D.W. Moore.) The actual cyclic process occurs in a layer just below the solar convection zone, which is the second subsystem. The tachocline has been detected by helioseismologists and an attempt to rationalize it made with J.-P. Zahn (stemming in part from unpublished work with F.P. Bretherton) has been made. This layer makes the transition between the strong differential rotation of the convection zone and the nearly rigid rotation of the solar deeps.

4. Waves of Solar Excitation. A closer look at the data shows that the solar variation takes place in space and time. The longitudinally averaged spacetime portrait of activity looks like a row of ragged butterflies flying along the time axis with their wings spread in latitude. This so-called butterfly diagram provides an empirical description of the temporal evolution of a Poincaré map of the solar magnetic field, with the sun's outer boundary as the surface of section. A simple dynamical system made with M.R.E. Proctor describes the world lines that define the centers of the butterfly wings in latitude. In this picture, these are the world lines of solitary waves formed in the shallow tachocline acting as a wave guide. If the tacjhocline is overstable, either because there is an $\alpha - \omega$ process in the tachocline, or because of an instability of magnetic buoyancy (as discussed with S. Childress), we can expect the envelope of the wave to satisfy a complex, time-dependent Ginzburg-Landau equation. We suggest that the parameters in this equation vary weakly with latitude. For simple models of this variation, we can obtain equations of motion for the activity waves that capture many qualitative features of the butterfly diagram.

5. Solar Maculation. A project with S.P. Meacham is focussed on the study of vortices in the tachocline. When the activity wave passes by, the toroidal field is wrapped up by the vortices. The field is expelled, but not into the ambient tachocline. Instead it is assumed to be buoyed inot the convection zone, there to wind upward to the solar surface to protrude as a spot.

The Role of Eddies in Gulf Stream Entrainment

Melvin E. Stern
Florida State University

A strong potential vorticity gradient in the upper layer of an oceanic jet inhibits *laminar* cross-stream flow (and entrainment) in an underlying isopycnal layer even if its potential vorticity gradient vanishes, as is shown in a two layer quasi-geostrophic model with piecewise uniform potential vorticity and with cross stream bottom topography. It is suggested that *eddies* at the edge of the Gulf Stream are necessary to overcome the constraint on entrainment, and to incorporate water from the adjacent "recirculating gyres," and to provide the observed downstream increase in stream transport. The entrainment produced by eddy-shear flow interaction is computed for a wide range of conditions in the limiting case of a very deep lower layer, this being necessary for comparison with (future) calculations using the full two layer model. Especially noteworthy is the pronounced tendency for cyclones (anti- cyclones) on the anti-cyclonic (cyclonic) shear side of a jet to move towards and across the axis of the jet, in agreement with observations of Bane et al (1989).

LARGE-SCALE WAVES AND VORTICES

George Sutyrin

P.P.Shirshov Institute of Oceanology
Russian Academy of Sciences
23 Krasikova Street, Moscow 117218
Russia

Emerging of large-scale vortex structures, remaining coherent during many turnaround times, has been recognized to be typical in planetary atmospheres and oceans. Strongly nonlinear coherent vortices have the ability of carrying particles over long distances. We consider how their transport properties are affected by the interaction with the highly dispersive Rossby waves generated by the beta-effect.

Two well-known types of two-dimensional coherent vortices are (i) the circularly symmetric monopole with swirling velocity of the same sign everywhere and (ii) the dipole, consisting of two closely packed counter-rotating vortices. Any monopolar vortex is stationary in the absence of the beta-effect, any background flow, forcing and dissipation. So the monopole cannot transport fluid by itself. On the other hand, coupling of dipolar partners provides an internal self-propelling mechanism, which causes the dipole to propagate in a direction depending on the relative intensity of two partners. Thus, without the beta effect, the dipole is able to transport particles trapped in its central part in any direction.

The dynamics of coherent vortices have been intensively studied during the last decades, both by analytical, numerical and laboratory methods. On the beta-plane the permanent form solutions were proved to exist only with zonal direction of their propagation. In the traditional quasigeostrophic approximation such steadily propagating solutions have a dipolar structure with zero net angular momentum (Flierl, 1987). Within the more general shallow water model a wide class of westward propagating anticyclonic monopoles of a size larger than the deformation radius can also steadily persist (Nycander, Sutyrin, 1992). Thus, meridional transport on the beta-plane can not be described in terms of steadily propagating structures.

An approximate theory for an initial evolution of the wavenumber-1 azimuthal perturbation, which accelerates a monopolar vortex both westward and meridionally, has been proposed by Sutyrin (1987). This approach was succesfully used for calculating the trajectory of the geostrophic point vortex and the propagation of a strong Gaussian vortex depending on the radius of deformation (Sutyrin, 1988). For a piece-wise constant potential vorticity distribution in the vortex core the effect of distortion in the vortex shape in the evolution of the wavenumber-1 perturbation has been elucidated recently by Sutyrin and Flierl (1992). To consider long-time evolution of a monopolar vortex it is necessary to take into account an appearance of higher azimuthal modes as well as the change in the vortex structure due to the meridional drift and Rossby wave radiation (Sutyrin ,1989).

The evolution of monopolar and dipolar vortices within the equivalent barotropic quasigeostrophic equation using a spectral numerical model has been investigated recently by Hesthaven, Lynov, Rasmussen and Sutyrin (1992). Lagrangian transport of trapped fluid particles was analysed considering closed isolines of the potential vorticity.

It has been shown that dynamical properties of localized monopolar and dipolar vortices on the beta-plane differ strongly from their properties on the f-plane without the beta-effect. A strong monopolar vortex, being stationary on the f-plane, provides effectively meridional transport on the beta-plane due to self- propelling by the wavenumber-1 perturbation in agreement with asymptotic theory (Sutyrin, 1987). Strong dipolar vortices, being most effective for transport on the f-plane, oscillate and propagate predominantly zonally without essential meridional transport.

An important new feature of the evolution of a strong monopolar vortex on the beta-plane is the emergence of a tripolar structure due to weak instability caused by meridional displacement of the vortex center. Rotation and oscillation of the tripole lead to increased mixing near the boundary of the vortex core and loss of some trapped particles. This intrincically inviscid mechanism may play an important role in the evolution of coherent vortices providing an exchange between the vortex core and the surronding flow.

The influence of the beta-effect on initially f-plane dipoles depends on their intensity and direction of propagation. Weak dipoles can survive without essential radiation only in the case of eastward direction on the beta-plane. The westward dipole accelerates while its partners move closer during an adjustment to the steadily propagating state. The eastward dipole deccelerates due to slight separation of its partners. The steadily propagating solutions on the beta-plane are thus attractors for initially f-plane dipoles only when they are strong enough.

References

Flierl, G.R.,1987: Isolated eddy models in geophysics. *Ann. Rev. Fluid Mech.*, 19, 493-530.

Hesthaven,J.S., J.P.Lynov, J.Juul Rasmussen and G.G.Sutyrin, 1992: Dynamical properties of vortical structures on the beta-plane. *J. Fluid Mech.* (submitted).

Nycander, J. and G.G. Sutyrin, 1992: Steadily translating anticyclones on the beta-plane. *Dyn. Atmos. Oceans*, 16 473-498.

Sutyrin, G.G., 1987. The beta-effect and the evolution of a localized vortex. *Sov. Phys. Dokl.*, 32, 791-793.

Sutyrin, G.G., 1988. Motion of an intense vortex on a rotating globe. *Fluid Dyn.*, 23, 215-223.

Sutyrin, G.G., 1989. Forecast of intense vortex motion with an azimuthal modes model. In *Mesoscale/Synoptic Coherent Structures in Geophysical Turbulence.* J C.J.Nihoul and B.M.Jamart, Eds., Elsevier Oceanography Series, 50, 771-782.

Sutyrin, G.G. and G.R. Flierl, 1992: Intense vortex motion on the beta-plane. Part 1. Development of the beta-gyres. *J. Atmos. Sci.*, submitted.

A simple convection model of planetary atmospheres

George Veronis, Yale University

When a two-dimensional layer of fluid is heated non-uniformly at the top surface, the downward diffusion of heat into the fluid leads to a horizontal pressure gradient which drives a circulation. Laboratory (Rossby, 1965) and numerical (Beardsley and Festa, 1972) studies of such a system reveal an asymmetric circulation in which a downward jet of fluid near the coldest point penetrates into the layer, spreads horizontally in the lower part of the layer, and pushes the isotherms up toward the top boundary. When the surface temperature difference, 0 to T_s, is large, the bulk of the fluid at depth acquires a temperature that is less than $0.3T_s$. A warm boundary layer is formed just under the cooler half of the top boundary and transports heat out of the layer and a cool boundary layer under the warm half of the top boundary conducts heat downward. The net heat flux vanishes.

The addition of an upward heat flux at the bottom of the layer raises the mean temperature of the fluid layer and expands the width and compresses the thickness of the warm boundary layer, thereby enabling the added heat to escape through the top boundary. There is a concomitant narrowing and weakening of the cold boundary layer near the top which decreases the incoming heat through the top.

To simulate conditions at the surface of planetary atmospheres, the fixed surface temperature at the top boundary was replaced by a heat flux law, $k\frac{\partial T}{\partial z} = \lambda(T_e - T_s)$, where k is the thermometric diffusivity, λ is a relaxation constant velocity, and T_e is a given external temperature. T_e was taken to be $\Delta T \sin \pi x/2L$, where L is the horizontal width of the layer. This form is a crude simulation of insolation of planetary atmospheres. When λ is large, the flux law reduces to the fixed surface temperature condition. For very small λ the range of T_s is small compared to ΔT and becomes relatively smaller as ΔT is increased. A warm boundary layer forms under the cool half of the surface and a cool boundary layer is generated below the warm half of the surface, just as in the fixed temperature case.

When an upward heat flux is introduced at the bottom of the layer, the entire fluid layer is heated and the surface temperature becomes more nearly isothermal. The warm boundary layer near the top spreads across the entire width. The overall temperature of the system becomes larger than ΔT and the fluid layer is nearly isothermal (very mildly stably stratified) except for thin boundary layers near the top and bottom . The associated time- averaged circulation is essentially symmetric about the midpoint of the layer.

The model suggests that the internal heat source of a giant planet leads to a nearly isothermal, thin, gravitationally unstable "weather layer", overlying a mildly stably stratified thick base. The nearly isothermal surface temperature is consistent with observations of the surface temperatures of the giant planets.

The system can easily be extended to include rotation. The width-to- depth ratio can be increased. These two additional features should lead to a more realistic basic model for planetary atmospheres.

References

Rossby, H.T.(1965) Deep-Sea Research, vol. 12, pp 9-16.

Beardsley, R.C. and J.F Festa (1972) Journal of Physical Oceanography, vol 2, pp 444-455.

Vapour flow through a hot porous rock

Andrew W. Woods

Institute of Theoretical Geophysics
DAMTP, Cambridge, England

In this presentation, the motion of compressible vapour through a hot porous rock was described using Darcy's Law and equations for the conservation of mass and enthalpy. In the limit of small porosity, the vapour rapidly attains the temperature of the host rock, and only over long time scales relative to that of the flow does the rock cool down. In this limit, it was shown that the vapour moves according to a non-linear diffusion equation, and several similarity solutions describing the motion of the vapour in an unbounded domain were presented.

We then extended the model to include a moving, vaporising liquid-vapour interface which may be produced when water is injected into the reservoir of hot rock. This interface propagates faster than the isotherms in the liquid and since the thermal diffusivity is relatively small compared to the vapour diffusivity, the liquid supplied to the interface is already at the temperature of the interface. Only a fraction of the liquid supplied to the interface actually vaporises, the remainder of the liquid causes the interface to advance; the mass fraction of the injected liquid which vaporises is determined by the amount of heat released as the rock is invaded by the water and cools.

We developed a similarity solution to describe the coupled problem of the injection of water from a line source into an unbounded domain. In this problem, a cylindrically symmetrical vaporising front spreads from the source. We found that as the rate of injection of liquid is increased, the pressure gradient ahead of the vaporising front also increases in order that the additional vapour produced can migrate ahead of the interface; as a result, the interface pressure increases. Therefore, the interface temperature increases according to the Clausius-Clapeyron equation and so the superheat available from the rock for vaporising the liquid decreases. Hence, the mass fraction of liquid which vaporises decreases. At very high flow rates, the mass fraction of the liquid which vaporises becomes very small; in contrast, at slow injection rates, the maximum mass fraction of liquid which may vaporise is approached - this maximum is given by the maximum thermal energy

which may be released by the rock as it is invaded by the liquid - this is a function of the rock superheat.

We next considered the same process of injection of liquid, but now into a bounded reservoir. The unbounded similarity solution applies until the vapour has migrated to the outer edge of the reservoir. However, over longer time-scales, the pressure and vapour content of the reservoir become nearly uniform except near the point of injection. Therefore, over longer time scales a very simple bulk model may be used to describe the increase in pressure and vapour content of the reservoir. This bulk model was successfully compared with the full solution of the diffusion equation. It was found that the pressure in the reservoir may increase until it has nearly reached the saturation pressure, after which point no more vapour may be produced, and the reservoir fills up with liquid.

The final problem we discussed was the simultaneous injection of water from a line source and extraction of vapour from a circular sink surrounding the source. After the initial similarity type transients have decayed, we found that a quasi-steady state is established in which the rate of injection and extraction are nearly equal, and the vapour which is extracted is derived from the vaporised input liquid rather than the original reservoir vapour. Owing to the non-linear diffusion coefficient, in this quasi-steady solution, th. pressure varies non-linearly across the reservoir. This quasi-steady state persists until the liquid front has advanced from the original point of injection to the point of extraction, at which stage the reservoir has become full of liquid. The simple bulk model of this process agrees well with the full numerical solution of the radial diffusion equation.

Further details are given in:

Woods, A.W. and Fitzgerald, S.D., 1992, The generation of vapour in a hot, porous rock through the injection of liquid, sub-judice, J. Fluid Mech.

Fitzgerald, S.D. and Woods, A.W., 1992, The production and extraction of vapour from a geothermal reservoir, sub-judice, Geothermics.

Linear Thermal Convectio in a Model Jupiter

by

Jun-Ichi Yano

A linear theory for thermal convection inside Jupiter has been proposed by Busse (1970, 1976, 1986). In this Summer School John Hart has talked about β-convection, which is a strongly nonlinear version of Busse's model. The purpose of my talk is to look at the justification for this kind of formulation. A general principle to derive a consistent formulation for nonlinear dynamical systems has been presented by Ed Spiegel in terms of central manifold theorem. The theorem namely says that in order to obtain the consistent derivation of a nonlinear dynamical system, we have to define a countable number of set of marginally unstable and stable modes. The first job for this purpose is to define the most unstable (preferred) mode on a complex growth–rate plane. I solely concentrate to this problem in my talk. It turns out that this problem is by itself tough to solve and also very interesting.

The system to be considered is under the Boussineq approximation, assuming a homogeneous heat distribution. We consider a rapidly rotating limit, or a low viscosity limit, which is considered as a limit of vanishing Ekman number, or a limit of infinite Taylor number, in terms of nondimensional parameters. The scales of the marginal modes are measured in terms of either of limiting nondimensional parameters. A WKBJ-type analysis in this asymptotic limit has been done by Roberts (1968) and Busse (1970). According to them, marginal convection is basically constrained by Taylor Proudman theorem, so that it takes a form of a row of Taylor columns aligned along a cylindrical surface coaxial to the axis of rotation. However the actual radial structure is left to be determined, because in their simple minded WKBJ-approach predicts a radial scale much larger the azimuthal scale (but still much shorter than the radius of the system, or the planet). Soward (1977) tried to solve a higher order modulation equation, which turns out to offer a spatially growing mode, such that cannot be consistent with the finite domain of the system. If we examine the operator derivatives which define the modulation equation, it is found that that the trouble maker is the spatial dispersion of the marginally unstable wave: whenever the marginal mode is described by a spatially dispersive wave we encounter the spatially growing mode.

At this point, it is worthwhile to remind what Brian Farrell talked about the temporal evolution of an unstable disturbance: Brian's point was, if we consider the instability problem as an initial value problem, the major contributing mode is coming from a point in a complex wavenumber space, where the complex frequency is non-dispersive against the complex wavenumber. In the present problem, the frequency does not only depend on the wavenumber, but also depend on the position (the distence from the axis of rotation). A simple extension of Brian's reasoning is that we require a vanishing of spatial dispersion on a complex distance plane. This is also equivalent to seek a complex radial distance where the Rayleigh number takes an extremum: this is a saddle point on a Rayleigh number topology.

Consequently, the asymptotically correct critical Rayleigh number takes a value by a finite factor larger than the value estimated from a simple minded WKBJ-approach. In

more physical term, a larger Rayleigh number is required than a simple minded WKBJ solution, because an exponentially decaying tail away from the center of the Taylor columns is 'maintained' by strong diffusivities there. In order to sustain the Taylor columns against these strong dissipations, a stronger buoyancy force is required than expected from a conventional WKBJ-type theory.

The diagnosis of the physical balances is also done by using full numerical solutions with help of Wolfram Hirsching. This diagnosis supports the results of this revised asymptotic theory well.

Basis for a Volatile Transport Model on Pluto

Abstract

GFD Summer Workshop, 1992

E.F. Young

NASA Ames Research Center

The recently completed set of mutual eclipses and occultations between Pluto and Charon have enabled several research teams [Young and Binzel, 1992, Buie et al., 1992, Burwitz et al., 1991] to construct albedo maps of Pluto's surface, as shown in Figure 1. These maps reveal several bright features on Pluto, including a south polar cap with normal reflectances of 0.8 - 1.0. The maps motivate an examination of frost transport on Pluto in hopes of explaining the high albedos and extreme contrast of surface features.

There are two systems that can serve as role models for frost transport on Pluto; these are Triton and Io. The Triton model is characterized by an atmosphere that is nearly uniform in temperature and pressure, despite the fact that regions of the planet may be in constant sunlight or darkness for years at a time. The governing agent that maintains the uniform conditions is the volatile N_2 frost present on most of the surface. The vapor pressure of N_2 is a very steep function of temperature. Any appreciable temperature gradient (e.g., a degree) translates into pressure gradients on the order of 50%. This pressure gradient cannot be sustained, so the temperature reaches a global equilibrium. The dark side is heated by frost forming on the surface, and the insolated side is cooled by sublimating frost. Thus there is a constant wind from the bright side to the dark side.

The global temperature is determined by balancing the total received power (insolation) and the total emitted power (thermal radiation), which we assume are equal in the steady state.

$$T = \left[\frac{L_{sun}(1 - A)}{16 \, \pi d^2 \epsilon \sigma} \right]^{1/4} \tag{1}$$

where T is the global surface temperature, L_{sun} is the luminosity of the sun, A is Pluto's average Bond albedo, d is Pluto's distance from the sun, σ is the Stefan-Boltzmann constant, and ϵ is the emissivity of nitrogen frost (assumed to be unity). In the steady state the insolation and thermal radiation balance each other globally but not locally. When there is a shortfall or overabundance of sunlight, mass loss from the surface has to make up the slack.

$$\dot{E}H = \frac{L_{sun}(\hat{n} \cdot \hat{p})(1 - A)}{4 \, \pi d^2} - \epsilon \sigma T^4 \tag{2}$$

Here H is the latent heat of sublimation, $\dot{E}$ is the sublimation rate, and $(\hat{n} \cdot \hat{p})$ is the projection factor, given by the dot product between vector normals to the local surface and

the subsolar point respectively. Eq. (2) demonstrates the simplicity with which local surface mass loss rate, $\dot{E}$, can be calculated using the Triton model.

The Triton model breaks down when the winds required to balance the incipient pressure imbalances are supersonic. The flux required to balance a given pressure imbalance will give rise to higher winds if the atmosphere is more rarified. On Io the surface pressure is so low that volatiles sublimating from the subsolar point basically expand into a vacuum. They cool and form supersonic winds directed to the back of the planet, but condense before they get there.

Does Pluto span both the Triton and Io regimes? Pluto's current atmosphere is certainly dense enough to support a globally uniform atmosphere. We expect Pluto's temperature to drop about 5.5 K over the next 50 years with a corresponding drop in column abundance of 97% (Fig. 2). The thinner atmosphere will require higher winds to balance the same pressure gradients. When will the maximum wind speed approach the speed of sound? The net volume of volatiles sublimating from the surface within a closed contour is equal to the volume of volatiles crossing that contour. In differential form this gives us the equation

$$\dot{E} = \nabla \cdot \left(\frac{P_s}{g} \, \mathbf{v} \right) \tag{3}$$

where P_s is the surface pressure, g is the acceleration due to gravity (about 64 cm/sec^2), and $\mathbf{v}$ is the velocity. Equation (3) is the result of vertically integrating the conservation of mass equation,

$$\frac{\partial \rho}{\partial t} = \nabla \cdot (\rho \, \mathbf{v}) \tag{4}$$

bearing in mind that the actual horizontal velocity will undoubtedly be a function of height. Ignoring effects like turbulence, surface friction or confinement to an Ekman boundary layer, we use Eq. (3) to get a preliminary expression for the maximum wind speeds on the planet. We combine Eq.'s (2) and (3), substituting for $\dot{E}$ and solving for $\mathbf{v}$, which points radially outward from the subsolar point. We find that $\mathbf{v}$ has a maximum 68° from the subsolar point with a v_{max} magnitude of

$$v_{max} = 0.29 \frac{g \, S_0 \, R}{H \, P_s} \tag{5}$$

where S_0 is the insolation at the subsolar point and R is Pluto's radius. Notice that v_{max} is inversely proportional to the column abundance, roughly equivalent to (P_s/g).

Because of the steep vapor pressure-temperature relation, a small uncertainty in Pluto's global temperature translates to large uncertainty in the time of onset of supersonic winds. Figure 3 shows the year of supersonic cross-over as a function of the planet's global temperature at perihelion. Notice that no cross-over occurs for perihelion temperatures as low as 36.7 K. While Pluto's temperature is not currently known, it seems unlikely that it is lower than nitrogen's α and β transition temperature of 35.6 K. Other factors that we have

not yet considered are thermal inertia of the surface and the potential energy available from phase transitions of the surface frost.
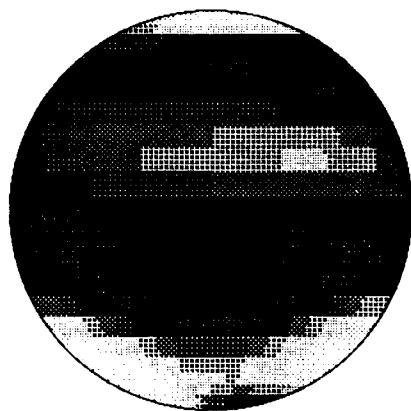

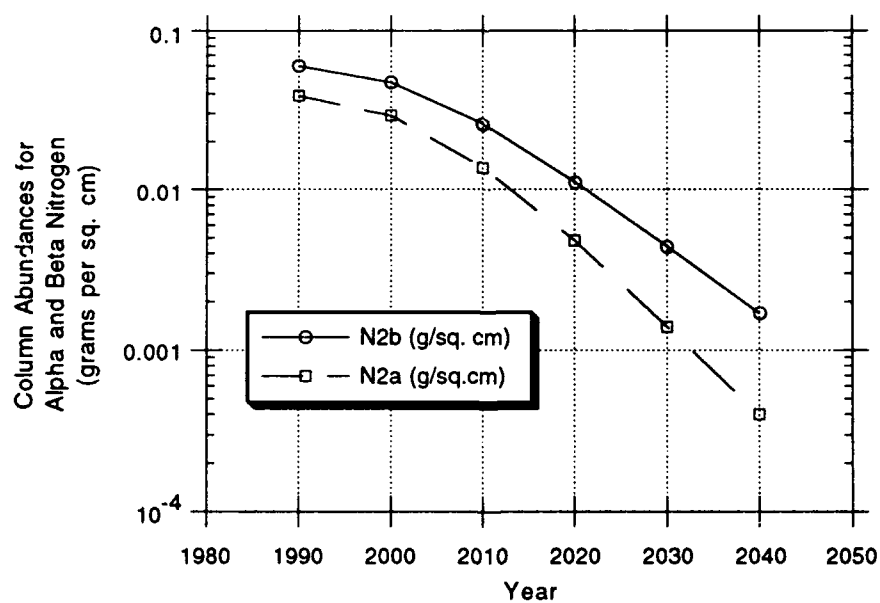Figure 1.   A map of the geometric albedos of Pluto's sub-Charon hemisphere.

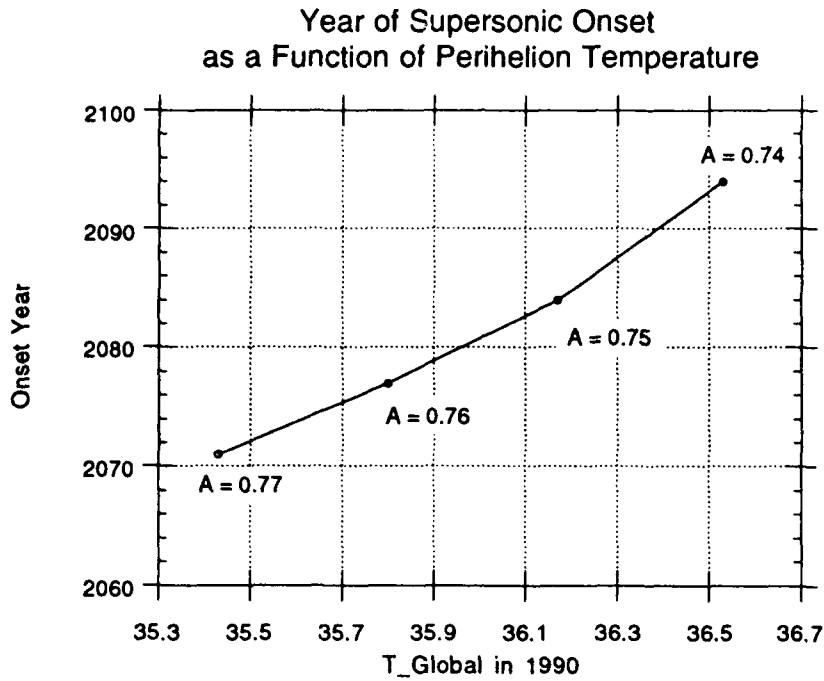Figure 2. α and β N_2 column abundances as a function of time.

Figure 3. The year of supersonic onset as a function of the temperature at perihelion. The A's are the Bond albedos corresponding to a given perihelion temperature. This model neglects the thermal inertia of the surface.

Generalized two-layer planetary geostrophic equations

Rupert Ford. *Department of Applied Mathematics and Theoretical Physics, Silver Street, Cambridge, CB3 9EW, UK.*

1 Introduction

This report is concerned with developing conceptually simple models of the large scale circulation of the ocean, in which the Rossby number is assumed to be so small that the effects of inertia can be completely neglected. We shall take as our starting point a three-dimensional continuously-stratified hydrostatic Boussinesq inertialess model - the so-called Planetary Geostrophic Equations:

$$f\boldsymbol{k} \wedge \boldsymbol{u} = -\nabla \phi \tag{1}$$

$$0 = -\phi_z + \theta \tag{2}$$

$$\nabla_3 . (\boldsymbol{u}, w) = 0 \tag{3}$$

$$\theta_t + (\boldsymbol{u}, w) . \nabla_3 \theta = 0 \tag{4}$$

where f is the Coriolis parameter, $\boldsymbol{k}$ is a unit vector in the z direction, $\boldsymbol{u} = (u, v)$ is the horizontal velocity, w is the vertical velocity, θ is the buoyancy, ϕ is the pressure, ∇ is the two-dimensional gradient operator, and ∇_3 is the three dimensional gradient operator.

We shall see how to reduce these equations to a two-layer system which possesses the standard two-layer system, with uniform density (potential temperature) in each layer, as a special case. The neglect of inertia makes it possible to obtain the general solution by reducing the equations to characteristic form. In this way we can generalize Salmon's (1992) Gulf Stream model to a set of equations in which the temperature is everywhere continuous in the vertical as well as horizontal directions.

We investigate the linear and nonlinear waves in the system where possible, with particular reference to linear Rossby waves propagating over large scale topography, where the basic state is the relevant generalization of that given by Salmon (*op. cit.*). We conclude with some suggestions for future work, both analytical and numerical.

2 Reduction to a two-layer system

We start by considering the equations (1-4) in isopycnal coordinates - where the vertical coordinate z is replaced by θ. Then (1-4) become

$$f\boldsymbol{k} \wedge \boldsymbol{u} = -\nabla B \tag{5}$$

$$z = -\frac{\partial B}{\partial \theta} \tag{6}$$

$$\frac{\partial}{\partial t}\left(\frac{\partial z}{\partial \theta}\right) + \frac{\partial}{\partial x}\left(u\frac{\partial z}{\partial \theta}\right) + \frac{\partial}{\partial y}\left(v\frac{\partial z}{\partial \theta}\right) = 0 \tag{7}$$

Equations (5-7) can be combined into the single equation

$$\frac{\partial}{\partial t}B_{\theta\theta} + \frac{\partial(B, f^{-1}B_{\theta\theta}, \theta)}{\partial(x, y, \theta)} = 0 \tag{8}$$

It follows immediately that the solution is steady in θ coordinates if

$$\frac{1}{f}B_{\theta\theta} = F(\theta) \tag{9}$$

for any function $F(\theta)$. Transforming back into physical space, this is equivalent to

$$f\frac{\partial \theta}{\partial z} = G(\theta) \tag{10}$$

for some function G which is related to F. The simplest case, and the only case which we shall consider in this report, is the case where G takes two distinct constant values, i.e.

$$G(\theta) = \begin{cases} Q_1 & \text{for } z > -h(x,y,t) \\ Q_2 & \text{for } z < -h(x,y,t) \end{cases} \tag{11}$$

Note that $f\theta_z$ is the potential vorticity for (1-4), so (11) can be regarded as a "uniform potential vorticity " approximation.

An evolution equation for the interface $h(x,y,t)$ can then be derived. It turns out that, although motivated by the case where $h(x,y,t)$ is a surface of constant θ, the evolution equations derived by this method are consistent for *any* interface, so that in general θ may vary along the interface on either side of it.

3   General equations for two layer dynamics

Starting from then general ansatz (10,11), we shall show how to derive a general set of "two layer" equations for (1- 4). To simplify the following algebra, without loss of generality, we take $f \equiv y$. We start by integrating (10) with respect to z, giving

$$\theta_i = Q_i\frac{z}{y} + T_i(x,y,t) \tag{12}$$

where the subscript i refers to the layers 1 and 2. Using the hydrostatic equation (2) gives

$$\phi_i = \frac{Q_i z^2}{2y} + T_i z + \Phi_i \tag{13}$$

for the pressures in the two layers. From here we can use (1) to give the horizontal velocities in the two layers. It remains to relate these equations to (3, 4) and hence to derive either prognostic or diagnostic equations for Φ_1, Φ_2, T_1, T_2. We start by eliminating Φ_1 and Φ_2 in favour of the interface depth h and the vertically integrated streamfunction ψ. The existence of ψ results from the fact that the upper and lower boundary conditions on the vertical velocity w:

$$\begin{aligned} w &= 0 \quad \text{at } z = 0 \\ w &= -\boldsymbol{u}.\nabla H \quad \text{at } z = -H \end{aligned} \tag{14}$$

are equivalent by (3) to the statement

$$\nabla . \int_{z=-H}^{z=0} (u,v)dz = 0 \tag{15}$$

and therefore there exists a flux streamfunction ψ such that

$$\int_{z=-H}^{z=0}(u,v)dz = (-\psi_y, \psi_x) \tag{16}$$

Continuity of pressure ϕ at the interface $z = -h$ implies a relationship between Φ_1 and Φ_2 in the form

$$\frac{1}{2}\frac{Q_1}{y}h^2 - T_1 h + \Phi_1 = \frac{1}{2}\frac{Q_2}{y}h^2 - T_2 h + \Phi_2 \tag{17}$$

An evolution equation for h is derived from the kinematic condition

$$\frac{D}{Dt}(h+z) = 0 \qquad \text{at } z = -h \tag{18}$$

We should note that if the upper boundary $z = 0$ is allowed to move, we no longer have a vertically integrated streamfunction for the flow. However, we could assume that the atmosphere is essentially a zero pressure interface, and hence obtain a relationship between Φ_1 and the surface elevation. An additional evolution equation derived from the kinematic condition for the free surface would replace the diagnostic equation for ψ.

We should note that, with a rigid lid present, we could still use surface pressure Φ_1 in preference to ψ, using the condition (15) to derive a diagnostic equation for Φ_1. However, note that if we define E by

$$E \equiv -\int_{-H}^{0} z\theta \tag{19}$$

then

$$J(\psi, f/H) = J(E, 1/H) \tag{20}$$

Thus the equation for ψ is an equation involving just two Jacobians, whereas the corresponding equation for Φ_1 typically seems to involve three or more Jacobians. As we shall see later, the possibility to write the streamfunction equation with just two Jacobian terms can lead to great simplification in the search for general solutions of the equations. We should also note that the equation (20) is a hyperbolic equation for ψ. This means that we cannot in general impose boundary conditions that ψ be zero on all boundaries. It turns out that introducing Rayleigh damping in the geostrophic equation introduces a Laplacian term in (20) which makes it elliptic, and so in a sense the dynamics becomes well posed only in the presence of at least some sort of damping. For the present report, we have not retained frictional terms in our analysis, and we assume that any difficulties at boundaries can be corrected with thin frictional boundary layers over which ψ is adjusted to zero.

We turn now to deriving the evolution equations for T_1, T_2 and h. To derive evolution equations for T_1 and T_2, we substitute from (12,13) and (1) into (4). w must be obtained by using (14) and integrating (3) with respect to z, It turns out that the z-dependent terms cancel exactly. The resulting equations involve derivatives of Φ_1 and Φ_2 with respect to x and y, which are replaced with ψ derivatives using (16) and (17). The details are lengthy and will not be given here. The result is

$$\frac{\partial T_1}{\partial t} + \frac{1}{H}J(\psi, T_1)$$
$$- \frac{1}{6yH}\left[Q_2(H-h)^2(H+2h) + Q_1 h^2(3H-2h)\right]J\left(\frac{1}{y}, T_1\right)$$

$$+ \frac{(H-h)^2}{2yH}J(T_2,T_1) - \frac{H-h}{yH}\left((Q_1-Q_2)\frac{h}{y}-(T_1-T_2)\right)J(h,T_1) = 0 \qquad (21)$$

$$\frac{\partial T_2}{\partial t} + \frac{1}{H}J(\psi,T_2) - \frac{1}{6yH}(Q_2(H-h)^2(H+2h)-2Q_1h^3)J\left(\frac{1}{y},T_2\right)$$

$$- \frac{Q_2h^2}{2y}J\left(\frac{1}{y},T_1\right) + \frac{h}{yH}\left[\frac{h}{y}(Q_1-Q_2)-(T_1-T_2)\right]J(h,T_2)$$

$$+ \frac{Q_2h}{y}\left[\frac{h}{y}(Q_1-Q_2)-(T_1-T_2)\right]J\left(\frac{1}{y},h\right) - \frac{H^2}{2yH}J(T_1,T_2) = 0 \qquad (22)$$

Since the kinematic condition for h is applied specifically at $z = -h$, it is clear that it gives rise to an equation without z dependence. Φ_1 and Φ_2 must be substituted for as in the derivation of the T equations, and the resulting equation for the evolution of the interface is

$$\frac{\partial h}{\partial t} + J\left(\psi,\frac{h}{H}\right) - \frac{h^2}{2yH}J(T_1,h) + \frac{(H-h)^2}{2yH}J(T_2,h)$$

$$+ \left[(T_1-T_2)\frac{h}{H}(H-h) + \frac{Q_1h^2}{3yH}(2h-3H) + \frac{Q_2}{6yH}(H^3+3Hh^2-4h^3)\right]J\left(h,\frac{1}{y}\right)$$

$$+ \frac{h^2}{2}\left(1-\frac{h}{H}\right)J\left(T_1,\frac{1}{y}\right) + \frac{h}{2H}(H-h)^2J\left(T_2,\frac{1}{y}\right)$$

$$+ \frac{h^2}{yH^2}\left[(T_1-T_2)-\frac{h}{y}(Q_1-Q_2)\right]J(h,H)$$

$$- \left[\frac{(Q_1-Q_2)h^4}{3yH^2}+Q_2\frac{hH}{3y}\right]J\left(\frac{1}{y},H\right)$$

$$+ \frac{h^3}{2yH^2}J(T_1,H) + \frac{h}{2y}\left(1-\frac{h^2}{H^2}\right)J(T_2,H) = 0 \qquad (23)$$

As we have already discussed, the equation for ψ can always be written in terms of just two Jacobians. Writing it explicitly gives

$$J\left(\psi,\frac{y}{H}\right) = J\left(\frac{Q_2-Q_1}{3}\frac{h^3}{y}-\frac{Q_2H^3}{3y}+\frac{T_1-T_2}{2}h^2+\frac{T_2H^2}{2},\frac{1}{H}\right) \qquad (24)$$

The immense complexity of the equations (21-24), with high order nonlinearity and coupling between upper and lower layer temperature fields and with the interface depth should be contrasted with the more conventional two-layer model - a specialization of the above system, in which $Q_1 = Q_2 = 0$ and T_1 and T_2 are assumed to be (distinct) constants. Only h then depends on x, y and t, and its evolution equation is greatly simplified, since all Jacobians with T_1 and T_2 are zero. The resulting equations are

$$\frac{\partial h}{\partial t} + J\left(\psi,\frac{h}{H}\right) + J\left(g'\frac{h^2}{2},\frac{1}{y}\left(1-\frac{h}{H}\right)\right) = 0 \qquad (25)$$

$$J\left(\psi,\frac{y}{H}\right) = J\left(g'\frac{h^2}{2},\frac{1}{H}\right) \qquad (26)$$

Although the above presentation of these general two-layer equations is almost certainly not the simplest way in which they can be written, concerted efforts to combine Jacobian terms met with only limited success. To make progress, therefore, we sought a specialization which could nonetheless be thought to capture the essential character of the thermal structure of the ocean.

4   Restriction to the special case $Q_2 = T_2 = 0$

Typically, oceanographic charts show an "upper" layer with a rich thermal structure lying above a deep lower layer in which the temperature is almost uniform. We therefore specialize at once to the case where the lower layer temperature θ is a constant, which may be zero without loss of generality. This is equivalent to taking $Q_2 = T_2 = 0$ in our model. The equations as written simplify somewhat, but it turns out that the form of conserved quantities suggests a way to write this reduced system in such a way that only two Jacobians appear with the time derivative in each of the evolution equations.

We begin by noting that, if the surface pressure formulation is used instead of the streamfunction formulation, the equation for T_1 takes the very simple form

$$\frac{\partial T_1}{\partial t} + \frac{1}{y}J(\Phi_1, T_1) = 0 \tag{27}$$

It therefore follows that

$$\frac{d}{dt} \int \int y F(T_1) dx dy = 0 \tag{28}$$

for any function $F(T_1)$. We also recall that since θ is conserved on fluid particles,

$$\frac{d}{dt} \int \int dx dy \int_{-H}^{0} dz\, G'(\theta) = 0 \tag{29}$$

for any function G. Performing the z integration explicitly with our chosen form of θ gives

$$\frac{d}{dt} \int \int dx dy \frac{y}{Q}[G(T) - G(T - Qh/y)] = 0 \tag{30}$$

Note that $T - Qh/y$ is the temperature just above the deep cold lower layer. It follows that

$$\frac{d}{dt} \int \int dx dy\, y G(T - Qh/y) = 0 \tag{31}$$

and this motivates us to prove the following result:

$$\frac{d}{dt} \int \int dx dy\, y F(\theta(x, y, h(x, y, t), t)) = 0 \tag{32}$$

for any F and any $h(x, y, t)$ such that

$$\frac{D}{Dt}(z - h) = 0 \qquad \text{at } z = h \tag{33}$$

The proof proceeds as follows. We regard $\Theta(x, y, t)$ a function of x, y and t such that $\Theta(x, y, t) \equiv \theta(x, y, z, t)$ on $z = h(x, y, t)$. Then

$$\frac{\partial \Theta}{\partial t} = \frac{\partial \theta}{\partial t} + \frac{\partial \theta}{\partial z}\frac{\partial h}{\partial t} \tag{34}$$

$$\frac{\partial \Theta}{\partial x} = \frac{\partial \theta}{\partial x} + \frac{\partial \theta}{\partial z}\frac{\partial h}{\partial x} \tag{35}$$

$$\frac{\partial \Theta}{\partial y} = \frac{\partial \theta}{\partial y} + \frac{\partial \theta}{\partial z}\frac{\partial h}{\partial y} \tag{36}$$

Then

$$\frac{d}{dt} \int \int y F(\Theta(x,y,t)) dx dy \tag{37}$$

$$= \int \int y F'(\Theta) \frac{\partial \theta}{\partial t} \tag{38}$$

$$= -\int \int y F'(\Theta)(u\theta_x + v\theta_y + w\theta_z) \tag{39}$$

$$= -\int \int y F'(\Theta) \left[u(\Theta_x - \theta_z h_x) + v(\Theta_y - \theta_z h_y) + w\theta_z - \theta_z \frac{\partial h}{\partial t} \right] \tag{40}$$

$$= -\int \int F'(\Theta)(yu\Theta_x + yv\Theta_y) + y\theta_z F'(\Theta) \frac{D}{Dt}(z - h) \tag{41}$$

$$= +\int \int \Theta F'(\Theta)\nabla.(yu) - \nabla.(\Theta F'(\Theta)yu) \tag{42}$$

$$= -\int \int \nabla.(\Theta F'(\Theta)yu) \tag{43}$$

We assume that boundary terms are unimportant, and so this remaining integral can be set to zero by converting it into a boundary integral by the divergence theorem. This completes our proof.

It now seems natural to work not with T and h, but instead to work with T and $T - Qh/y$, since by the above argument, if either is initially zero then it remains zero for all time. We now rewrite (21-24) with $T_2 = Q_2 = 0$, and using $T_s \equiv T$ and $T_+ \equiv T - Qh/y$ and ψ as the three remaining dependent variables. We choose the notation T_s to represent the temperature at the surface, and T_+ to represent the temperature just above the thermocline, $z = -h+$. Then, after some algebra, one obtains

$$\frac{\partial T_s}{\partial t} + \frac{1}{H} J(\psi, T_s) + \frac{1}{y} J\left(\frac{T_s^2 - T_+^2}{2Q} y, T_s \right) = \frac{1}{yH} J(E, T_s) \tag{44}$$

$$\frac{\partial T_+}{\partial t} + \frac{1}{H} J(\psi, T_+) = \frac{1}{yH} J(E, T_+) \tag{45}$$

$$J(\psi, y/H) = J(E, 1/H) \tag{46}$$

where E is the energy density, given by

$$E = -\int_{-H}^0 z\theta dz = \frac{y^2(T_s - T_+)^2}{Q^2} \left(\frac{T_s}{6} + \frac{T_+}{3} \right) \tag{47}$$

It is clear from the form of these equations that if either T_s or T_+ is initially constant, then it remains constant for all time. Moreover, as we shall see, in the simplest steady solutions, in which T_s, T_+ and ψ are arbitrary functions of y, and H is constant, there must be gradients of both T_s and T_+ in the basic states if linear disturbances on these states are to be unstable.

4.1 Linear stability of zonal flows

To gain some insight into the stability of steady solutions, we consider the case where the bottom topography is flat (H constant), and the basic states T_s and T_+ are arbitrary functions of y only. We consider disturbances of the form $e^{ik(x-ct)}$. Linearizing (46) immediately implies $\psi' = 0$. We generally regard k as a fixed real wavenumber and c as a possibly complex growth rate. However, as we shall see, the stability criterion does not depend on k, so we may, if we prefer, regard kc, the frequency, as real, and deduce a downstream growth rate $\Im k$. Linearizing gives

$$-cT'_\bullet - \frac{1}{H}\psi_y T'_\bullet = \frac{1}{yH}(E'(T_\bullet)_y - T'_\bullet E_y)$$

$$+ \frac{1}{y}\left(\frac{y}{Q}(T_+ T'_+ - T_\bullet T'_\bullet)(T_\bullet)_y - \left(\frac{T_+^2 - T_\bullet^2}{2Q}y\right)_y T'_\bullet\right) \quad (48)$$

$$-cT'_+ - \frac{1}{H}\psi_y T'_+ = \frac{1}{yH}(E'(T_+)_y - T'_+ E_y) \quad (49)$$

For convenience, we write

$$E' = \alpha T'_\bullet + \beta T'_+ \quad (50)$$

where

$$\alpha = \frac{y^2}{2Q^2}(T_\bullet^2 - T_+^2); \qquad \beta = -\frac{y^2}{Q^2}T_+(T_\bullet - T_+) \quad (51)$$

By considering (48,49) as an eigenvalue problem for c, we see that it is straightforward to derive a condition for which c is complex. Since eigenvalues for a system of linear equations with real coefficients must come in complex conjugate pairs, this implies a growing disturbance for the system.

We remark that this is an eigenvalue calculation for each latitude y separately. Disturbances may grow at some latitudes and oscillate at others. The behaviour at one latitude does not influence the behaviour at another, and we should think of disturbances of the form

$$T_\bullet, T_+ \sim F(y)e^{ik(x-c(y)t)} \quad (52)$$

These are not really "modes" for the system. True eigenmodes, in whic c takes only one value, would in general require that F be a δ-function of y.

Proceeding to calculate the instability condition, we obtain

$$\left(\frac{1}{yH}(\beta(T_+)_y - \alpha(T_\bullet)_y) - \frac{T_+(T_+)_y}{Q} + \frac{T_\bullet^2 - T_+^2}{2Qy}\right)^2 +$$

$$4\frac{\alpha}{yH}\left(\frac{T_+}{Q} + \frac{\beta}{yH}\right)(T_\bullet)_y(T_+)_y < 0 \quad (53)$$

The full stability condition is perhaps difficult to interpret. However, it is clear that a necessary, though not sufficient condition, is that

$$\frac{\alpha}{yH}\left(\frac{T_+}{Q} + \frac{\beta}{yH}\right)(T_\bullet)_y(T_+)_y < 0 \quad (54)$$

If we assume that the ocean is stably stratified, so that $T_\bullet > T_+ > 0$, then $\alpha > 0$. Moreover,

$$\frac{T_+}{Q} + \frac{\beta}{yH} = \frac{T_+}{Q}\left(1 - \frac{y}{QH}(T_\bullet - T_+)\right) \quad (55)$$

Now $T_\bullet - T_+ = Qh/y < QH/y$ and hence we have a necessary condition for baroclinic instability:

$$(T_\bullet)_y(T_+)_y < 0 \quad (56)$$

This condition is similar to more familiar baroclinic instability criteria, in which one typically requires oppositely signed potential vorticity gradients in different vertical layers for instability. A more complete physical understanding of this instability condition has not been attempted.

However, if we recall that $T_\bullet$ and/or T_+ being constant are symmetries of the system, we can see at once that there is no *linear* symmetry breaking instability - the instabilty criterion (56) cannot be met if either $T_\bullet$ or T_+ is constant.

4.2 Nonlinear stability

The non-existence of linear symmetry breaking instabilities does not, of course, mean that there might not be nonlinear instability mechanisms which can act to destroy the basic flow.

As we have mentioned previously, standard two-layer models have a constant temperature jump across the thermocline. In the case where that jump is zero, their effective "reduced gravity" becomes zero, and all that remains of the dynamics is an essentially instantaneous response to wind forcing. In our model, however, setting the thermocline temperature jump T_+ to zero is merely one case of a whole class of symmetries in which T_+ is constant everywhere. We have been particularly interested in the case $T_+ = 0$, since a jump in the stratification at the thermocline -i.e. θ_z discontinuous - seems closer to observations than a jump in the temperature at the thermocline - i.e. $T_+ \neq 0$.

Now, assuming that the *basic state* is given by $T_+ = 0$, we may suppose that small disturbances might develop on the interface for which $T_+ \neq 0$. If these were unstable, we would have found a *symmetry breaking instability* for the symmetry $T_+ = 0$. To see that no such symmetry breaking instability exists, we return to the general result given by (32,33), which states that

$$\frac{d}{dt} \int \int dx dy \, y F(\theta) = 0 \tag{57}$$

on a material surface for any function F. Choosing the material surface to be a surface just above the thermocline, where $\theta = T_+$, and choosing $F(\theta) = \theta^2$, we obtain

$$\frac{d}{dt} \int \int dx dy \, y T_+^2 = 0 \tag{58}$$

Now, we assume that T_+ is small, since its basic state value is zero, so it is comprised only of disturbance quantities. Then, in the above norm, which is similar in spirit to the enstrophy norm for two dimensional vortex dynamics, the flow is nonlinearly stable, provided we restrict ourselves to a domain in which y is single-signed. In that case, it is clear that if T_+ is to become large, it must do so in only a very localized way, which would presumably be prevented by the reintroduction of some form of Rayleigh damping in the horizontal momentum equation (1), or diffusion in the temperature equation (4). We therefore conclude that no symmetry breaking instability exists for the symmetry $T_+ = 0$. Of course, the argument does not apply to the case T_+ constant but non-zero, since then yT_+^2 is an order-one quantity. However, we feel that there is no *a priori* reason why a *uniform* temperature jump should be natural for large scale ocean dynamics, and we concentrate hereafter on the case $T_+ = 0$, safe in the knowledge that the symmetry cannot be broken by instabilities which may be present in a more general two-layer model of the type we have been developing.

5   Restriction to the case $T_s = Qh/y$

Having already obtained evolution equations for our reduced two layer system in terms of T_+ and T_s, one might be tempted to think that the simplification $T_+ = 0$ could not simplify the equations any further than simply setting $T_+ = 0$ in (44-46). However, since we have effectively reduced the dynamics to a single evolution equation for T_s, we are prompted to compare our system with the more conventional one given by (25,26). To do this, we convert (44) in the case $T_+ = 0$ into an equation for the thermocline depth h. We recall that, with $T_+ = 0$, h is given by $T_s = Qh/y$. After some algebra, one obtains

$$\frac{\partial h}{\partial t} + J\left(\psi, \frac{h}{H}\right) + J\left(\frac{Qh^3}{6y}, \frac{1}{y}\left(1 - \frac{h}{H}\right)\right) = 0 \tag{59}$$

$$J\left(\psi, \frac{y}{H}\right) = J\left(\frac{Qh^3}{6y}, \frac{1}{H}\right) \tag{60}$$

Note that these equations are *apparently* identical to (25, 26) under the replacement

$$\frac{g'h^2}{2} \leftrightarrow \frac{Qh^3}{6y} \tag{61}$$

which is really a rule for replacing g' with $Qh/3y$ in the first argument of the Jocobians in (25,26). However, it is sensitive to the way in which (25) is written. For example, in place of

$$J\left(\frac{g'h^2}{2}, \frac{1}{y}\left(1 - \frac{h}{H}\right)\right) \tag{62}$$

we could have written

$$J\left(g'h, \frac{h}{y}\left(1 - \frac{h}{H}\right)\right) \tag{63}$$

In this form, the substitution (61) into (25) would *not* recover (59).

The remainder of this report will be concerned with the equations (59,60), with a view to contrasting their behaviour with (25,26).

We shall start by considering the general solutions to these equations, and then go on to consider waves propagating on certain steady solutions.

6 Steady state solutions of the reduced equations

The aim of this section is to classify the solutions of

$$J\left(\psi, \frac{h}{H}\right) + J\left(\frac{Qh^3}{6y}, \frac{1}{y}\left(1 - \frac{h}{H}\right)\right) = 0 \tag{64}$$

$$J\left(\psi, \frac{y}{H}\right) = J\left(\frac{Qh^3}{6y}, \frac{1}{H}\right) \tag{65}$$

In solving a set of equations such as (64,65), one strategy is to find some transformation of the independent variables which reduces the equations to semi-linear form. The method of characteristics can then be used to integrate the equations along characteristics. If Riemann invariants exist, it is frequently then preferable to return to the original equations, using the Riemann invariants as the independent variables. Special cases arise in the case of simple waves, when one or other of the Riemann invariants is uniform over a region of space, and the form of the solution appears more natural.

One can see at once that the equations (64,65) can be put into semi-linear form through the choice of independent variables α and β defined by

$$\alpha = \frac{Qh^3}{6y}; \qquad \beta = \psi \tag{66}$$

It turns out that the Riemann invariants are

$$q_1 = \frac{h}{y}; \qquad q_2 = \frac{H - h}{y} \tag{67}$$

214

and the characteristic equations are

$$q_1 \text{ constant on } \frac{d\beta}{d\alpha} = \frac{hH}{3 - 2h/H} \tag{68}$$

$$q_2 \text{ constant on } \frac{d\beta}{d\alpha} = \frac{3\alpha}{Qh^3}\left(2 - 3\frac{H}{h}\right) \tag{69}$$

Then, rewriting (64,65) in terms of q_1, q_2 and $\eta \equiv h^2/y$, we obtain

$$J\left(\psi, \frac{q_1}{q_1 + q_2}\right) + J\left(\frac{Q\eta^2}{6q_1}, \frac{q_1^2}{\eta}\frac{q_2}{q_1 + q_2}\right) = 0 \tag{70}$$

$$J\left(\psi, \frac{1}{q_1 + q_2}\right) = J\left(\frac{Q\eta^2}{6q_1}, \frac{q_1^2}{\eta(q_1 + q_2)}\right) \tag{71}$$

The aim now is to write these equations in such a form that we obtain two equations, where q_1 appears as the second argument of the Jacobians in one equation, and q_2 appears as the second argument of the Jacobians in the other equation. A little manipulation shows that

$$J(\psi, q_1) + \frac{Q(q_1 + 3q_2)}{6}J(\eta, q_1) = 0 \tag{72}$$

$$J(\psi, q_2) - \frac{Qq_1^2}{6\eta}J\left(\frac{\eta^2}{q_1}, q_2\right) = 0 \tag{73}$$

Now, in the case where $J(q_1, q_2) \neq 0$, we can take q_1 and Q_2 as independent variables, and we may take the Jacobians with respect to q_1 and q_2. The result is

$$\frac{\partial \psi}{\partial q_1} - \frac{Qq_1^2}{6\eta}\frac{\partial}{\partial q_1}\left(\frac{\eta^2}{q_1}\right) = 0 \tag{74}$$

$$\frac{\partial \psi}{\partial q_2} + \frac{Q(q_1 + 3q_2)}{6}\frac{\partial \eta}{\partial q_2} = 0 \tag{75}$$

Differentiating (74) with respect to q_2 and (75) with respect to q_1 and adding gives

$$\frac{Q}{2}(q_1 + q_2)\frac{\partial^2 \eta}{\partial q_1 \partial q_2} = 0 \tag{76}$$

Then, since $q_1 + q_2 = H/y \neq 0$, we can write

$$h = \frac{F'(q_1)}{q_1} + \frac{G'(q_2)}{q_1} \tag{77}$$

for arbitrary functions F and G. Substituting back into (74) and (75) readily gives

$$\psi = \frac{Q}{6}(2q_1 F'(q_1) - 3F(q_1) - q_1 G'(q_2) - 3q_2 G'(q_2) + 3G(q_2)) \tag{78}$$

In the case where $J(q_1, q_2) = 0$, we let H and $\alpha \equiv H/y$ be the independent variables, and define $\Phi \equiv h/H$. Then (73) becomes

$$J\left(\psi, \frac{1}{\alpha}\right) = J\left(\frac{Q}{6}\Phi^3 H^2\alpha, \frac{1}{H}\right) \tag{79}$$

which gives

$$\frac{\partial\psi}{\partial H} = -\frac{Q}{6}\alpha^2\frac{\partial}{\partial\alpha}(\Phi^3\alpha) \tag{80}$$

Moreover, since $J(q_1, q_2) = 0$, we have

$$\frac{h}{y} = E\left(\frac{H}{y}\right) \tag{81}$$

for some function E. Therefore

$$\frac{h}{H} = \frac{y}{H}\frac{h}{y} = \frac{E(\alpha)}{\alpha} \tag{82}$$

$$\Rightarrow \frac{\partial\Phi}{\partial H} = 0 \tag{83}$$

and hence (80) can be integrated once with respect to H to give

$$\psi = R(\alpha) - \frac{Q}{6}\alpha^2 H\frac{d}{d\alpha}(\Phi^3\alpha) \tag{84}$$

Then substituting into (72) gives

$$J(\psi, \Phi) + J\left(\frac{Q}{6}\Phi^3 H^2\alpha, \frac{\alpha}{H}(1 - \Phi)\right) = 0 \tag{85}$$

Expanding and factorizing gives

$$\left(\frac{d}{d\alpha}(\Phi^3\alpha) + 2\Phi^3\right)\left(\frac{d}{d\alpha}(\alpha(1 - \Phi))\right) = 0 \tag{86}$$

and hence

$$\Phi = \frac{\text{const}}{\alpha} \quad \text{or} \quad \Phi = 1 + \frac{\text{const}}{\alpha} \tag{87}$$

i.e., either

$$q_1 = \text{constant} \quad \text{or} \quad q_2 = \text{constant} \tag{88}$$

Substituting for ψ gives

$$q_1 \text{ constant}, \quad \psi = R\left(\frac{H}{y}\right) + \frac{Q}{3}q_1^3 y \tag{89}$$

or

$$q_2 \text{ constant}, \quad \psi = R\left(\frac{H}{y}\right) - \frac{QH^3}{6y^2}\left(1 - \frac{q_2 y}{H}\right)^2\left(1 + \frac{2q_2 y}{H}\right) \tag{90}$$

The situation we have now arrived at is very similar to the one arrived at by Salmon for the general solution of (25,26). However, the appearance of the corresponding physical system, particularly in the

thermal layer above the thermocline, is quite different, and the temperature is continuous across the thermocline.

As Salmon remarks, it is difficult to see how to use (77, 78) to construct exact steady solutions of (59,60). However, by judicious choice of the special solutions, in which q_1 or q_2 was constant, he was able to construct a model of the Gulf Stream with a Southward return flow in an internal boundary layer required to resolve a discontinuity in ψ between the regions q_1 constant and q_2 constant. The procedure is not a rational one, since there is no obvious reason to expect the forced dissipative system to evolve into a state in which one or other of the q_i are constant, with an internal boundary layer between them. However, for the purpose of the present report, we are interested in comparing the systems (59,60) and (25,26), and so we shall now proceed to compute the corresponding Gulf Stream solution for (59,60).

7 Reconstruction of the Gulf Stream solution

Following Salmon (1992), we consider the ocean to consist of three regions:

(1) A Southern Region, in which q_1 is constant, $h \propto y$, and the thermocline is at finite depth;

(2) A Gulf Stream region, in which q_2 is constant, $(H - h) \propto y$, and the thermocline outcrops ($h = 0$) along a line of constant H/y;

(3) A Northern Region, in which the upper thermal layer is completely absent, the temperature is zero, and the streamfunction ψ is an arbitrary function of H/y.

To be more precise, we have the three regions

$$1 \quad : \quad \frac{H_0}{y_2} > \frac{H}{y} \tag{91}$$

$$2 \quad : \quad \frac{H_0}{y_2} > \frac{H}{y} > \frac{H_0}{y_1} \tag{92}$$

$$3 \quad : \quad \frac{H}{y} > \frac{H_0}{y_2} \tag{93}$$

7.1 Region 1

In region 3, h is zero, and the streamfunction is allowed to be an arbitrary function of H/y, i.e.

$$\psi = \psi_0 \left(\frac{H}{y} \right) \tag{94}$$

7.2 Region 2

To match the solution (94) onto region 2, we impose continuity of h across the boundary. Since $h = 0$ in region 3, and q_2 is constant in region 2, the boundary must be a line of constant H/y. It follows that $q_2 = 1/y_1$. It turns out that we can use the arbitrary function available to us in the solution for ψ to impose that $\psi = \psi_0$ in the deep ocean where H is a constant, which we shall here set equal to 1. Thus

$$h = H - \frac{y}{y_1} \tag{95}$$

$$\psi = \psi_0 \left(\frac{H}{y} \right) - \frac{Q}{6} \frac{H^2(H - H_0)}{y^2} \left(1 - \frac{y}{y_1 H} \right)^2 \left(1 + \frac{2y}{y_1 H} \right) \tag{96}$$

7.3 Region 3

It follows from elementary considerations that a boundary between regions of constant q_1 and constant q_2 must also be a line of constant H/y. Then, by continuity of h across the boundary, we have $q_1 = (y_1 - y_2)/y_1 y_2$. Again, we can use the available arbitrary function of H/y in the streamfunction to impose that $\psi = \psi_0$ in the deep ocean. Then

$$h = \frac{y_1 - y_2}{y_1 y_2} y \tag{97}$$

$$\psi = \psi_0 \left(\frac{H}{y} \right) + \frac{Q H_0^3}{3} \left(\frac{y_1 - y_2}{y_1 y_2} \right)^3 \left(\frac{H - H_0}{H} \right) y \tag{98}$$

7.4 Southward return current

The key new component about Salmon's Gulf Stream model was the prediction of a Southward return current concentrated at the internal boundary between regions one and two as a result of a discontinuity of ψ there. As one might have expected, this same feature is present in this model. The jump in ψ is given by

$$\Delta \psi = \frac{Q}{2} \frac{H_0^3}{(y_1 y_2)^3} y_1 (y_1 - y_2)^2 (y_2 - y) \tag{99}$$

This takes the same form as the jump found by Salmon for the conventional two-layer model:

$$\Delta \psi = g' H_0^2 \frac{y_1 - y_2}{y_1^2 y_2} (y_2 - y) \tag{100}$$

and is identical if Q and g' are related by

$$Q = \frac{2 g' y_2^2}{H_0 (y_1 - y_2)} \tag{101}$$

We have not attempted to compare (99) with observations. It would be interesting to see whether (99) or (100) could be regarded as in any sence the more realistic model.

8 Linear waves over mid-ocean topography

We have now shown that it is possible to reconstruct Salmon's Gulf Stream solution using our reduced set of equations (59,60). However, the solution is not entirely rational. The choice of the "separation latitudes" y_1 and y_2 is arbitrary. Moreover, there is no obvious reason why one should choose the special solutions, rather than try to use some combination of the general solutions, if only one could be sufficiently ingenious. Perhaps the internal boundary layer and the associated Southward return current could be avoided by suitable choices of F and G in (77,78).

One way to try to address these questions is to study the time dependent dynamics of (59,60), rather than rely on the steady states found in §6.

The general problem is that, with three independent variables x, y and t, the method of characteristics is no longer available as a method of general solution. In the absence of topography, of course, ψ is an arbitrary function of y, and the remaining equation in (59,60) is a nonlinear wave equation corresponding to (nondispersive) Rossby waves.

Of course, the nonlinear wave equation can develop shocks, and in general some form of diffusion is needed to resolve these difficulties. There is high-order nonlinearity in the system, and one might suppose that travelling wave solutions could possess multiple shocks, which can completely change the nature of the solution at large time (Lee-Bapty & Crighton, 1987). However, it turns out that, for $0 < h < H$, there is only one value of h for a given travelling wave speed, and so the more conventional Taylor shock analysis is appropriate in this case.

The original motivation for using a set of equations such as (59,60) was to include topography at leading order in the dynamics, and one is tempted to ask whether it might be possible to derive some form of jump condition for nonlinear waves propagating over a rapid jump in bottom depth H.

To gain some insight into this problem, we have considered the case of *linear* waves propagating over an arbitrary bottom topography. We could have chosen to linearize about the state $h = 0$. However, we are really more interested in perturbations about our supposed Gulf Stream solution, so we have chosen instead to linearize about the states q_1 constant and q_2 constant.

8.1 Linearization about q_1 constant

In this section, we consider linear waves propagating on the basic state given by

$$h = ay \tag{102}$$

$$\psi = \frac{Qa^3}{3}\left(1 - \frac{H_0}{H}\right)y \tag{103}$$

where a and H_0 are constants. a corresponds to q_1, and H_0 should be thought of as some reference depth. Recall that we may add to ψ any arbitrary function of H/y. We have chosen not to do so here for simplicity - technically there would not seem to be any difficulty in doing so. To fix our ideas, let us consider a topography of the form

$$H(x) = \begin{cases} H_0 & \text{for } x > x_0 \\ \mathcal{H}(x) & \text{for } x_1 < x < x_0 \\ H_1 & \text{for } x < x_1 \end{cases} \tag{104}$$

In the regions where H is constant H_0 or H_1, ψ' is an arbitrary function of y, which we shall tentatively set to zero. h' then satisfies the linear wave equation

$$\frac{\partial h'}{\partial t} + \left(-\frac{Qa^2}{2y} + \frac{Qa^3}{3H}\right)\frac{\partial h'}{\partial x} = 0 \tag{105}$$

Recalling the $H > h = ay$, it straightforward to see that this corresponds to westward wave propagation, consistent with our ideas about Rossby waves. Notice that h' can have arbitrary y dependence - y essentially behaves as parameter in (105).

Given that, in the absence of strong adverse ψ', Rossby waves propagate westward in this model, we shall set $\psi' = 0$ in the eastern "basin" where $H = H_0$, and concentrate our attention on the behaviour of linear wave   they encounter the region where H is an arbitrary function of x.

The full linear wave equations are

$$\frac{\partial h'}{\partial t} + J\left(\overline{\psi}, \frac{h'}{H}\right) + J\left(\psi', \frac{\overline{h}}{H}\right)$$

$$+ J\left(\frac{Q\overline{h}^2 h'}{2y}, \frac{1}{y}\left(1 - \frac{\overline{h}}{H}\right)\right) + J\left(\frac{Q\overline{h}^3}{6y}, -\frac{h'}{yH}\right) = 0 \qquad (106)$$

$$J\left(\psi', \frac{y}{H}\right) = J\left(\frac{Q\overline{h}^2 h'}{2y}, \frac{1}{H}\right) \qquad (107)$$

In the region with non-trivial topography, it is convenient to define new independent variables

$$\alpha \equiv \frac{1}{H}; \qquad \beta \equiv \frac{y}{H} \qquad (108)$$

Then from (107) we have

$$\frac{\partial \psi'}{\partial \alpha} + \frac{\partial}{\partial \beta}\left(\frac{Qa^2 y}{2} h^i\right) = 0 \qquad (109)$$

We can integrate this at once by introducing a variable Φ such that

$$\frac{Qa^2 y}{2} h' = \frac{\partial \Phi}{\partial \alpha}; \qquad \psi' = -\frac{\partial \Phi}{\partial \beta} \qquad (110)$$

If we now let

$$\frac{\partial}{\partial t} \to -i\omega; \qquad \frac{\partial(\alpha, \beta)}{\partial(x, y)} = \mathcal{J}^{-1} \qquad (111)$$

then, substituting into (106) and collecting terms we obtain

$$\left(\frac{\alpha}{\beta^2} - \frac{2\alpha^2 a H_0}{3\beta}\right)\frac{\partial^2 \Phi}{\partial \alpha^2} + \frac{1}{\beta}\frac{\partial^2 \Phi}{\partial \alpha \partial \beta} + \left(\frac{2i\omega\alpha}{Qa^2\beta}\mathcal{J} - \frac{4\alpha a H_0}{3\beta}\right)\frac{\partial \Phi}{\partial \alpha} = 0 \qquad (112)$$

We note that, since $1/\beta \equiv H/y \neq 0$, (112) is always a hyperbolic system. Moreover, since the equations for the characteristics depend only on the coefficients of the highest derivatives, in the $\alpha - \beta$ coordinate system they are independent of of the frequency of the waves ω, and of the details of the topography, represented by $\mathcal{J}$.

The characteristics for (112) are given by lines of constant φ, where φ satisfies the equation

$$\left(\frac{\alpha}{\beta^2} - \frac{2\alpha^2 a H_0}{3\beta}\right)\varphi_\alpha \varphi_\alpha + \frac{1}{\beta}\varphi_\alpha \varphi_\beta = 0 \qquad (113)$$

One branch of the solution of (113) is simply $\varphi_\alpha = 0$, which corresponds to characteristic lines of constant $\beta \equiv y/H$. For the other family of characteristics, we obtain φ constant on lines given by

$$\frac{d\alpha}{d\beta} = \frac{\alpha}{\beta} - \frac{2}{3}aH_0\alpha^2 \qquad (114)$$

Inetgrating this gives

$$\frac{\beta}{\alpha} - \frac{aH_0\beta^2}{3} = \text{constant} \qquad (115)$$

We therefore take as the characteristic variables

$$\xi = \frac{\beta}{\alpha} - \frac{1}{3} a H_0 \beta^2; \qquad \eta = \beta \tag{116}$$

Rewriting (112) in terms of ξ and η gives

$$\Phi_{\xi\eta} + \left(\frac{2i\omega\alpha}{Qa^2} \mathcal{J} - \frac{1}{\xi} \right) \Phi_\xi = 0 \tag{117}$$

where α and $\mathcal{J}$ are to be regarded as functions of ξ and η.

Recall that we were initially interested in the limit of a steep slope. Now, if H depends only on x, we have that

$$\mathcal{J}^{-1} = \frac{\partial(\alpha, \beta)}{\partial(x, y)} = -\frac{1}{H^3} \frac{dH}{dx} \tag{118}$$

which is large if the slope is steep. Therefore, in the limit of steep slope, we can neglect the $\mathcal{J}$ term in (117). This is clearly equivalent to the limit of small ω, since high frequency waves will have many wavelengths over the slope, whereas low frequency waves will essentially not be expected to oscillate appreciably over the slope if the slope is sufficiently steep.

To avoid a lengthy study of the effects of different types of topography, we have chosen to concentrate on the limit $\mathcal{J} \to 0$. Then we can integrate (117) once to obtain Φ_ξ and, interpreting this in terms of the original equations, we obtain

$$h' = F(\xi) y \tag{119}$$

for some arbitrary function $F(\xi)$. In principle F is chosen from boundary data at the eastern edge of the slope, since it should be forced by westward proagating Rossby waves incident on the topography.

Since we have effectively scaled time dependence out of our problem for the slope region, we note that we could have obtained the result (119) directly from the general solution of the steady problem (77, 78). To see this, first rewrite (77) in the form

$$q_1 = F'^{-1}(hq_1 - G'(q_2)) \tag{120}$$

and let $F'^{-1}(x) = a$, constant, so that $h = ay$. Now since F' takes all values between $-\infty$ and ∞, we can regard it as the limit of straight line passing through the point $(a, 0)$ with gradient becoming infinitely steep. Therefore it is consistant to take $F(q_1) = 0$ for $q_1 = a$. Hence

$$\psi = \frac{Q}{6} (2a^3 y - 3(a + q_2) G'(q_2) + 3G(q_2)) \tag{121}$$

To obtain ψ in the form (103), we must take

$$G'(q_2) = \frac{1}{3} a^3 H_0 (q_2 + a)^{-2} \tag{122}$$

We now suppose that F^{-1} and G are allowed to have small perturbations of order ϵ to their functional forms given above. Then

$$q_1 = a + \epsilon F_1 (a^2 y - G'(q_2)) \tag{123}$$

where F_1 is an arbitrary function, from which we obtain the perturbation h' in the form

$$h' = F(\xi)y \tag{124}$$

for an arbitrary function F, and for

$$\xi = y - \frac{1}{3}aH_0\left(\frac{y}{H}\right)^2 \equiv \frac{\beta}{\alpha} - \frac{1}{3}aH_0\beta^2 \tag{125}$$

as before.

We are now in a position to describe the effect of a rapid change in depth with x on a Rossby wave propagating on a basic state with q_1 constant. We imagine that the wave is characterized by a disturbance height field h' over some latitude range along the Eastern boundary of the topography. Then the disturbance is transmitted across the ridge by keeping h'/y constant on lines of constant ξ. In the limit investigated here, the transmission processes is effectively instantaneous.

To get some idea of how this might effect propagating Rossby waves in practise, we examine lines of constant ξ .or cases of possible oceanographic interest.

Typical characteristics of constant ξ are shown in figure 1. In all cases, $a = 1$, y runs from 0 at the foot (South) of the diagrams to 1 at the top (North). The bottom depth is 1 at the left (West) side, increasing linearly to a constant value $H_0 > 1$ (see figure captions) on the right (East). The basic state and topography are thus arranged so that the thermocline touches the floor of the ocean in the North-West corner of the domains shown in figure 1. We have chosen the depth of the ocean is decreasing from East to West, so the waves can be thought of as incident on a ridge, such as the mid-Atlantic ridge.

Notice that, sufficiently far South, the characteristics cross the ridge, but that in Northern lattitudes the characteristics turn and head North along the ridge. Eventually these characteristics would re-emerge from the ridge on the Eastward side, but not before the thermocline depth h had exceeded H. In our solutions, we have in mind that the characteristics would encounter the internal boundary layer where the transition from constant q_1 to constant q_2 occurs as they head North.

The equivalent characteristics for the standard model are shown in figure 2. In general, although the characteristics are deflected slightly more in the standard model, we feel that the two models are give remarkably similar results in all cases considered.

8.2 Linearization about the basic state q_2 constant

Having completed the analysis for Rossby waves propagating over topography in the case of constant q_1, there is nothing to prevent us from repeating the entire analysis in the case of constant q_2. However, since we have restricted our investigation to the rapid jump limit, it is sufficient, as we have arued above, to derive steady perturbations from the general solution of the steady equations (64,65).

This time, we rewrite (77) as

$$q_2 = G'^{-1}(q_1h - F'(q_1)) \tag{126}$$

An entirely analogous set of calculations to those presented above gives $q_2 = a$, constant, and

$$F'(q_1) = \frac{1}{3}H_0\left(2(q_1 + a) - \frac{a^3}{(q_1 + a)^2}\right) \tag{127}$$

from which it follows that

$$q_2 = G'^{-1}\left(hq_1 - \frac{1}{3}H_0\left(2\frac{H}{y} + a^3\left(\frac{y}{H}\right)^2\right)\right) \tag{128}$$

Repeating arguments given above, we find

$$h' = G(\zeta)y \tag{129}$$

for an arbitrary function G, where ζ is the equivalent characteristic variable for the case of constant q_2, and is given by

$$\zeta = y\left(\frac{H}{y} - q_2\right)^2 - \frac{1}{3}H_0\left(2\frac{H}{y} + q_2^3\left(\frac{y}{H}\right)^2\right) \tag{130}$$

It remains to check the direction of Rossby wave propagation for this basic state when H is constant. After some manipulation, we can obtain the equation for linear waves propagating on the basic state q_2 constant, $\overline{\psi} = 0$ in the form

$$\frac{\partial h'}{\partial t} - \frac{(H + 2yq_2)}{yH}\frac{(H - q_2 y)^2}{6y^2}\frac{\partial h'}{\partial x} = 0 \tag{131}$$

from which one can easily verify that linearized disturbances are westward progating.

Typical characteristics of constant ζ are shown in figure 3. We use the same topography as for figures 1 & 2. Here $q_2 = 1$, so the thermocline outcrops at in the North-West corner of the domain in each case, and otherwise $h > 0$.

Note the stark constrast with figure 1. For the case q_2 constant, characteristics in the Southmost part of the domain do not cross the ridge for small jumps in height. As the jump in height is increased, increasingly fewer characteristics cross the ridge, until eventually none does. Thic complete inability of characteristics to cross a topographic obstacle has not been observed in the case of constant q_1.

The corresponding characteristics for the standard model in this case are shown in figure 4. Again, we remark that they are very similar to those in figure 3.

9   Remarks

Our original goal for this report was to understand the behaviour of the planetary geostrophic equations (1 - 4) when a layer structure of form (11) was imposed.

We have concluded that the general two-layer equations seemed too complex for analytical progress, and we found it convenient to reduce to the case where the lower layer stratification and temperature were zero.

The resulting system was observed to possess baroclinic instability for certain arrangements of the surface and thermocline temperatures T_s and T_+, but was shown to be nonlinearly stable when T_+ was initially small. This justified our subsequent restriction to the case $T_+ = 0$.

We were then able to reconstruct a Gulf Stream solution in much the same way as Salmon (1992). The essential point of Salmon's Gulf Stream - the Southward counter current concentrated in an internal boundary layer - survived. Indeed, it was possible to express our upper layer potential vorticity Q in terms of his reduced gravity g' in such a way that the return current was identical, although that relationship depended on the "separation latitudes" y_1 and y_2, which are not set mechanistically in Salmon's model.

To investigate the dynamics of the system, we have considered linear waves propagating on the basic states required by the Gulf Stream solutions. We have seen that, as Westward propagating Rossby waves approach a mid-ocean ridge, waves propagating in the region q_1 constant are deflected Northwards. Sufficiently far South, the waves will propagate across the ridge and emerge on the other

side, whereas further North the deflection is greater and eventually the waves are deflected along the ridge into the internal boundary layer between the two regions of constant q_i.

Waves approaching the ridge in the region q_2 constant, however, are all deflected South along the ridge towards the internal boundary layer. It is possible that none are transmitted across the ridge, a situation which is impossible in the case q_1 constant. In view of this, we might suppose that the basic states described by this arrangement of the thermocline might experience considerable disruption if a significant quantity of Rossby waves are generated in the Eastern ocean, particularly in the region of constant q_2, as waves seem to be focussed into the internal boundary layer.

The existance of considerable regions where the waves cannot cross the ridge suggests that a general jump condition for nonlinear waves propagating on the thermocline crossing a ridge is unlikely to exist. In addition, the fact that many waves travel a large distance along the ridge must call into question the steep jump approximation. Time has not permitted a complete investigation of the dependence of the ξ and ζ characteristics on $\mathcal{J}$.

10   Acknowledgements

11   References

Lee-Bapty I.P. & Crighton D.G. (1987) Nonlinear wave motion governed by the Modified Burgers Equation. *Phil. Trans. Roy. Soc. Lond.* **A323** 173-209

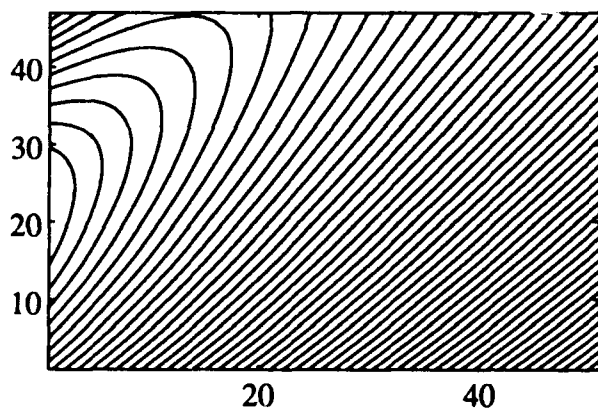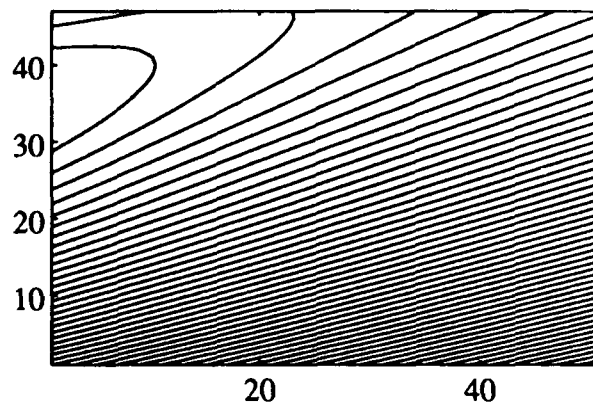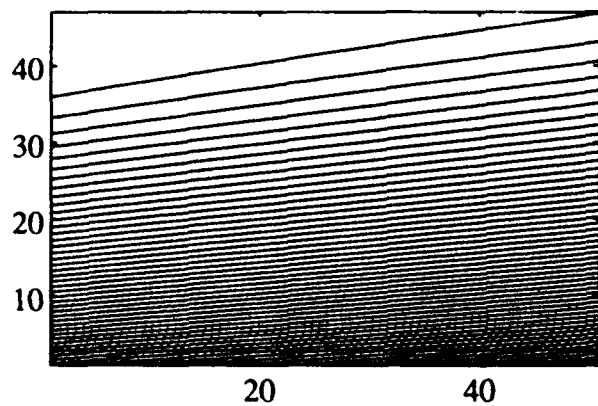Salmon R. (1992) A two-layer Gulf Stream over a continental slope. *J. Mar. Res.* To appear.

12 Figure Captions

- Figure 1 Characteristics of constant ξ, for $H_0 = 1.1$ (a), 1.3 (b), and 2 (c). For explanation, see text.

- Figure 2 As figure 1, but for standard model

- Figure 3 Characteristics of constant ζ, for $H_0 = 1.1$ (a), 1.3 (b), and 2 (c).

- Figure 4 As figure 3, but for standard model
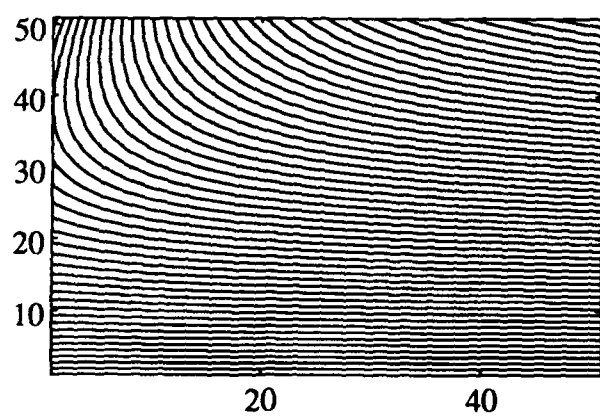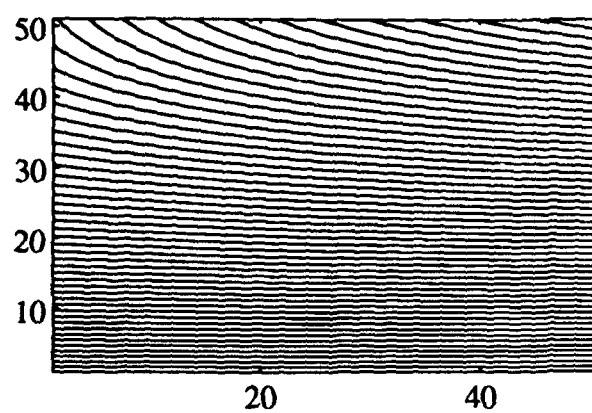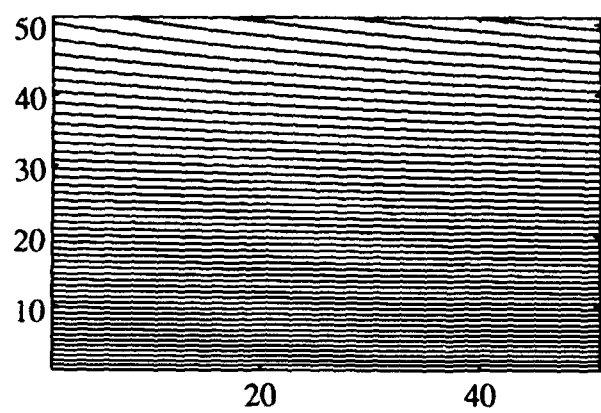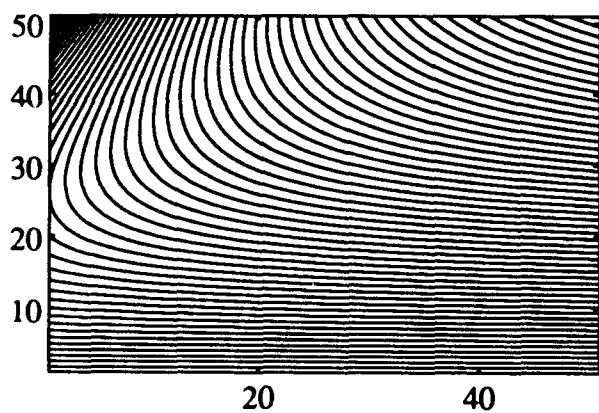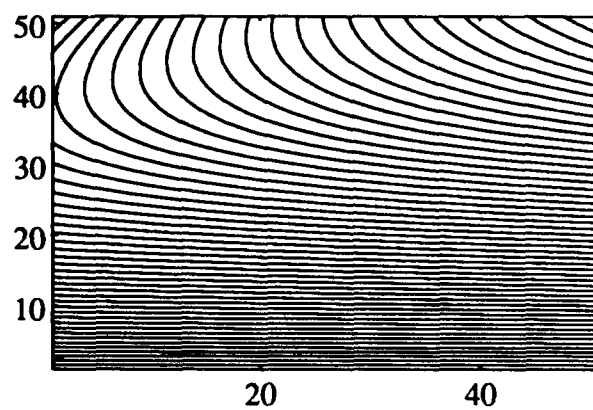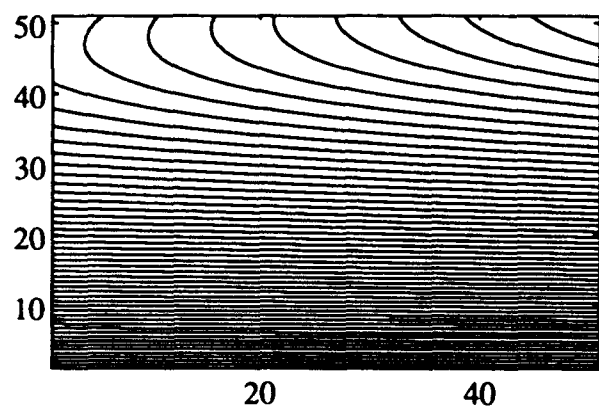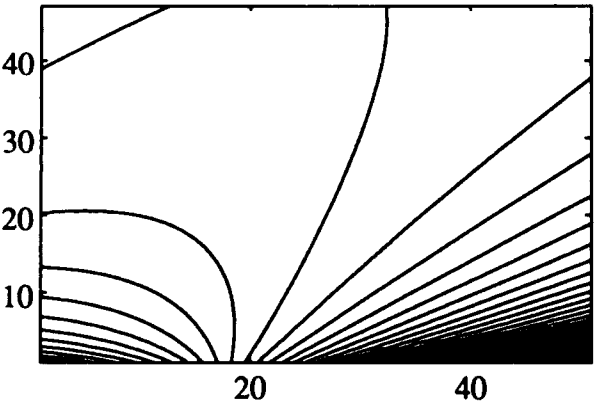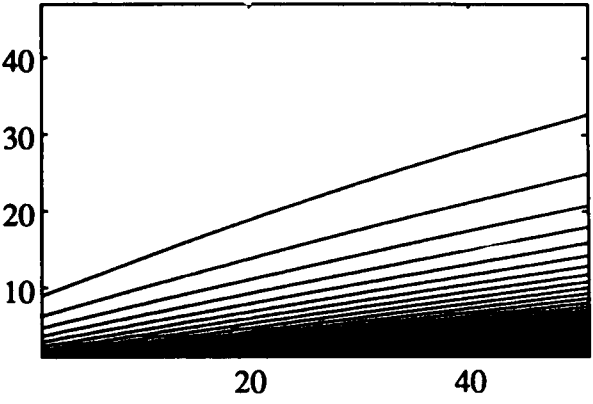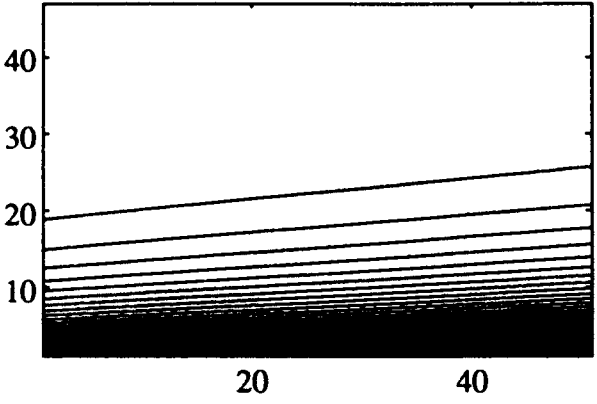
Baroclinic instability in a quasigeostrophic planetary interior

By Richard Holme, Harvard University.

1   Introduction

The surface temperature distributions of the outer planets form some of the most unexpected and puzzling data obtained by the Voyager spacecraft. The surface temperatures of Jupiter and Saturn are almost uniform, despite a dominant contribution to their heat budget from solar insolation, which would suggest a decrease in temperature with latitude as seen on the Earth. Uranus is actually hotter on the face currently shielded from the sun. The simplest explanation for these observations is that there is a very efficient mechanism for heat transfer. There are conflicting views on how this is achieved. Williams (1979) has suggested that the observations can be explained by thermal transfer within the surface weather layer of the planets, while Ingersoll and Porco (1978) prefer convection within the planets deep interior. Here we suggest an alternative - that the planets are internally stably stratified, and that heat is transported by sloping convection driven by a baroclinic instability.

Our approach is as follows. Firstly we derive a quasigeostrophic formulation for motions within a cylindrical shell bounded by the spherical planetary surface, and demonstrate that this formalism is self-consistent by deriving an energy conservation relation. We then examine the stability of a basic state of purely zonal flow, both analytically by deriving a Rayleigh stability criterion, and also numerically. Finally, we draw conclusions as to what extent our results help to explain the observations.

2 Deep Quasigeostrophy for Jovian planets

We model the basic state of a Jovian planet as stably stratified and barotropic with spherical symmetry. Surfaces of constant basic state entropy (S_0), temperature (T_0), density (ρ) and gravitational potential (Φ) coincide and are functions only of spherical radius R. We assume that the interiors of the planets are homogeneous and so neglect the effect of phase changes and discontinuous chemical differentiation. We extend the anelastic formulation of Ingersoll and Pollard (1982) to allow for a non-adiabatic basic state. The governing equations for the system are then continuity,

$$\nabla.(\rho_0 \mathbf{v}) = 0, \tag{1}$$

conservation of momentum,

$$\frac{d\mathbf{v}}{dt} + 2\mathbf{\Omega} \wedge \mathbf{v} = -\nabla M - \delta s \nabla T_0, \tag{2}$$

and conservation of energy,

$$\frac{d\delta s}{dt} + \mathbf{v}.\nabla T_0 = 0, \tag{3}$$

where

$$M = E + \Phi - T_0 \delta s - \int T_0 dS_0. \tag{4}$$

Here E is enthalpy, Ω is the rotation of the planet, and δs is the departure of entropy from the basic state.

We wish to simplify these equations, and so consider motions within a planet of radius R_0, which are confined to a cylindrical shell, central radius r_0, internal and external radii r_1 and r_2. This is shown schematically in Figure 1. We adopt a right handed coordinate system (θ, r, z), where θ is a westward longitude, with corresponding velocities (u, v, w). This is shown in Figure 2. We consider variations on the basic state which may vary rapidly in the $\hat{r}$ direction, but slowly in the $\hat{\theta}$ and $\hat{z}$ directions. For perturbation variables $\mathbf{v}$, M and δs,

$$\frac{\partial}{\partial r} \sim \frac{1}{L}, \quad \frac{\partial}{\partial z} \sim \frac{1}{R_0}, \quad \frac{1}{r}\frac{\partial}{\partial \theta} \sim \frac{1}{R_0}, \tag{5}$$
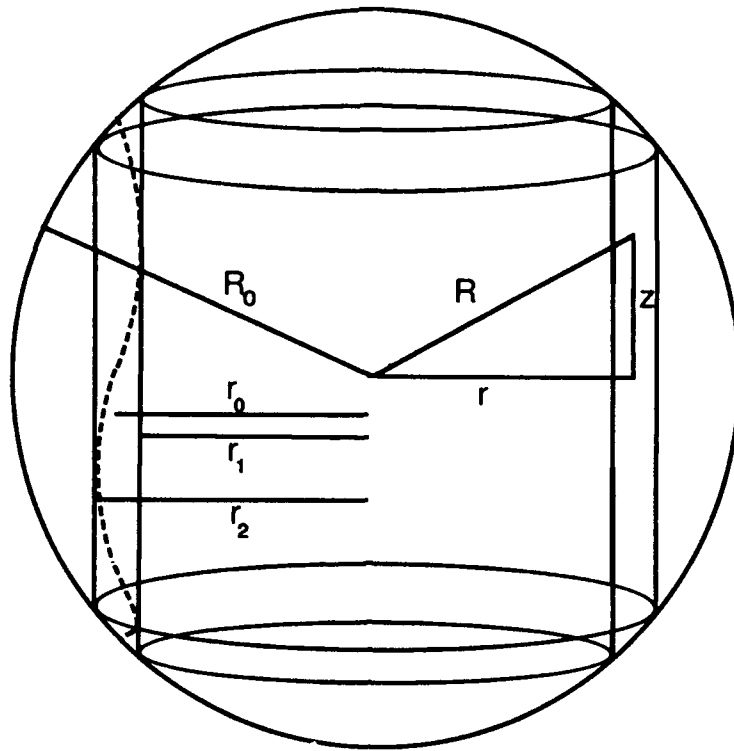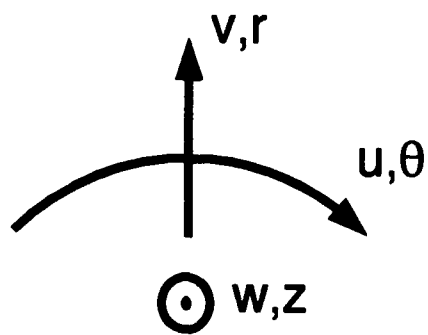
Figure 1: Cylindrical zone containing motion

Figure 2: Coordinate system

with $L << R_0$, but for base state variables,

$$\frac{\partial}{\partial r} \sim \frac{1}{R_0}.$$ (6)

The continuity equation suggests velocity scalings

$$u \sim U, \quad v \sim \frac{L}{R_0}U.$$ (7)

A surface boundary condition of no normal velocity requires a scaling

$$w \sim v \sim \frac{L}{R_0}U.$$ (8)

We assume a quasigeostrophic formulation,

$$\frac{L}{R_0} \sim \frac{U}{2\Omega L} \ll 1.$$ (9)

To satisfy the continuity equation, we define a stream function ψ, such that

$$u = -\frac{\partial \psi}{\partial r}, \quad v = \frac{1}{r}\frac{\partial \psi}{\partial \theta}, \quad \psi = \frac{M}{2\Omega}, \quad \zeta = \frac{1}{r}\frac{\partial}{\partial r}\left(r\frac{\partial \psi}{\partial r}\right) \approx \frac{\partial^2 \psi}{\partial r^2}$$ (10)

where ζ is the vorticity. Using this, the anelastic equations may be written

$$2\Omega\frac{\partial \psi}{\partial z} + \delta s\frac{z}{R}\frac{dT_0}{dR} = 0,$$ (11)

$$\frac{d\zeta}{dt} - \frac{2\Omega}{\rho}\left(\frac{1}{R}\frac{\partial \psi}{\partial \theta}\frac{d\rho}{dR} + \frac{\partial}{\partial z}(\rho w)\right) = -\frac{1}{R}\frac{\partial \delta s}{\partial \theta}\frac{dT_0}{dR},$$ (12)

$$\frac{d\delta s}{dt} + \frac{1}{R}\left(\frac{\partial \psi}{\partial \theta} + zw\right)\frac{dS_0}{dR} = 0.$$ (13)

To further simplify these equations, we adopt a new, non-orthogonal coordinate system, based upon r, the cylindrical radius, and R, the spherical radius. This would normally complicate things a good deal: for example, differentiation by r and R is not commutative. However, to first order the problems are not encountered here, as the additional cross terms may be neglected by the scaling we have adopted. We define a radial velocity

$$\dot{R} = \frac{r}{R}v + \frac{z}{R}w.$$ (14)

In this coordinate system, the equations of motion are written

$$2\Omega \frac{\partial \psi}{\partial R} + \delta s \frac{dT_0}{dR} = 0, \tag{15}$$

$$\frac{d\zeta}{dt} + 2\Omega \left(\frac{z}{R}\right) \left(\frac{\partial}{\partial R}\left(\frac{1}{z}\frac{\partial \psi}{\partial \theta}\right) - \frac{1}{\rho}\frac{\partial}{\partial R}\left(\rho \dot{R}\frac{R}{z}\right)\right) = -\frac{1}{R}\frac{\partial \delta s}{\partial \theta}\frac{dT_0}{dR}, \tag{16}$$

$$\frac{d\delta s}{dt} + \dot{R}\frac{dS_0}{dR} = 0. \tag{17}$$

Substituting for δs from equation (15) into equations (16) and (17) we obtain a vorticity equation

$$z^2\frac{d\zeta}{dt} - 2\Omega \left(\frac{\partial \psi}{\partial \theta} + \frac{z^3}{R\rho}\frac{\partial}{\partial R}\left(\rho \dot{R}\frac{R}{z}\right)\right) = 0, \tag{18}$$

and a heat equation

$$\frac{d}{dt}\left(\frac{\partial \psi}{\partial R}\right) + \frac{N^2}{2\Omega}\dot{R} = 0, \tag{19}$$

where N is the Brunt-Vaisala frequency, defined

$$N^2 = -\frac{dS_0}{dR}\frac{dT_0}{dR}. \tag{20}$$

N^2 is greater than 0 because of stable stratification. Eliminating $\dot{R}$, we obtain

$$z^2\frac{dq}{dt} = 0, \tag{21}$$

where we define the potential vorticity q as

$$q = \zeta - \Omega\frac{r^2}{z^2} + \frac{z}{R\rho}\frac{\partial}{\partial R}\left(\frac{4\Omega^2\rho R}{N^2 z}\frac{\partial \psi}{\partial R}\right). \tag{22}$$

We may express several relevant boundary conditions very naturally in this formulation. Firstly, we require no normal velocity at the surface of the planet. Using equation (19) gives the condition

$$\dot{R} = 0 \Rightarrow \frac{d}{dt}\left(\frac{\partial \psi}{\partial R}\right) = 0 \tag{23}$$

at $R = R_0$. We note also that in the equatorial plane, the $\hat{r}$ and $\hat{R}$ vectors are identical. Thus we require the components of velocity in these directions to be identical also. At $z = 0$, this requires

$$\dot{R} = \frac{1}{r}\frac{\partial \psi}{\partial \theta} = -\frac{2\Omega}{N^2}\frac{d}{dt}\left(\frac{\partial \psi}{\partial R}\right). \tag{24}$$

3 Energy considerations

As with conventional quasigeostrophy, we may derive a global energy conservation relation for our motion. We consider the cylindrical shell bounded by the planet's surface, the equatorial plane, and solid walls at r_1 and r_2, such that there is no normal velocity through the cylindrical surfaces. This may seem unrealistic, but similar approaches are used successfully in meteorology and oceanography. The requirement could also be satisfied by the amplitude of the motion tending to zero towards the boundaries. Hence, in addition to the boundary conditions (23) and (24), we have

$$r = r_1, r_2 \Rightarrow \frac{1}{r}\frac{\partial \psi}{\partial \theta} = 0. \tag{25}$$

One further boundary condition is required. This is obtained by integrating the $\hat{\theta}$ component of the momentum equation (2) along a closed circular contour, radius $r = r_1$ or r_2. The term in ∇M vanishes by Stoke's theorem, while T_0 is a function of R only, and so ∇T_0 has no azimuthal component. The remaining terms require

$$\oint \left(\frac{\partial u}{\partial t} + v\frac{\partial u}{\partial r} - \frac{u}{r}\frac{\partial u}{\partial \theta} + \frac{uv}{r} + w\frac{\partial u}{\partial z} - \Omega v\right) d\theta = 0. \tag{26}$$

At r_1 and r_2, $v = 0$, and the z-derivative term is of low order. Further

$$\frac{u}{r}\frac{\partial u}{\partial \theta} = \frac{1}{2r}\frac{\partial u^2}{\partial \theta}, \tag{27}$$

which, as θ is a periodic coordinate, integrates to 0. Thus

$$\oint \left(\frac{\partial u}{\partial t}\right) d\theta = -2\pi\frac{\partial^2 \psi}{\partial t \partial r} = 0. \tag{28}$$

To obtain an energy equation, we multiply the equation of conservation of potential vorticity (21) by $\rho\psi/z^2$ and then integrate over the cylindrical shell. Thus

$$\int \rho\psi \frac{dq}{dt} r \frac{R}{z} dr d\theta dR =$$

$$\int \rho\psi \left(\frac{\partial q}{\partial t} + \frac{1}{r} \left(\frac{\partial \psi}{\partial \theta} \frac{\partial q}{\partial r} - \frac{\partial \psi}{\partial r} \frac{\partial q}{\partial \theta} \right) \right) r \frac{R}{z} dr d\theta dR = 0. \quad (29)$$

First consider the spatial derivatives. These may be written

$$\int \rho\psi \left(\frac{\partial \psi}{\partial \theta} \frac{\partial q}{\partial r} - \frac{\partial \psi}{\partial r} \frac{\partial q}{\partial \theta} \right) \frac{R}{z} dr d\theta dR$$

$$= \int \rho \frac{1}{2} \left(\frac{\partial(\psi)^2}{\partial \theta} \frac{\partial q}{\partial r} - \frac{\partial(\psi)^2}{\partial r} \frac{\partial q}{\partial \theta} \right) \frac{R}{z} dr d\theta dR$$

$$= \int \rho \frac{1}{2} \left(\frac{\partial}{\partial r} \left(\frac{\partial(\psi)^2}{\partial \theta} q \right) - \frac{\partial}{\partial \theta} \left(\frac{\partial(\psi)^2}{\partial r} q \right) \right) \frac{R}{z} dr d\theta dR \quad (30)$$

The second term in equation (30) integrates to zero as θ is a periodic coordinate, while the first term integrates in r to give

$$\left[\int \rho \frac{1}{2} \frac{\partial(\psi)^2}{\partial \theta} q \frac{R}{z} d\theta dR \right]_{r_1}^{r_2} = \left[\int \rho\psi \frac{\partial \psi}{\partial \theta} q \frac{R}{z} d\theta dR \right]_{r_1}^{r_2}. \quad (31)$$

But at r_1 and r_2, radial velocity is zero, so $\frac{\partial \psi}{\partial \theta} = 0$. Therefore, the spatial derivative (Jacobian) terms in equation (29) make no contribution to the integral.

Substituting for the potential vorticity, the time derivative terms are

$$\int \rho\psi \frac{\partial q}{\partial t} r \frac{R}{z} dr d\theta dR =$$

$$\int \rho\psi \left(\frac{1}{r} \frac{\partial}{\partial r} \left(r \frac{\partial^2 \psi}{\partial r \partial t} \right) + \frac{z}{R\rho} \frac{\partial}{\partial R} \left(\frac{4\Omega^2 \rho R}{N^2 z} \frac{\partial^2 \psi}{\partial R \partial t} \right) \right) r \frac{R}{z} dr d\theta dR. \quad (32)$$

The first term in equation (32) integrates by parts to

$$\left[\int \rho\psi r \frac{\partial^2 \psi}{\partial r \partial t} \frac{R}{z} dr d\theta dR \right]_{r_1}^{r_2} - \int \rho r \frac{\partial \psi}{\partial r} \frac{\partial^2 \psi}{\partial r \partial t} \frac{R}{z} dr d\theta dR. \quad (33)$$

The boundary terms are zero from equation (28), while the remaining integral can be written

$$-\int \rho \frac{1}{2}\frac{\partial}{\partial t}\left(\frac{\partial\psi}{\partial r}\right)^2 r\frac{R}{z}drd\theta dR \tag{34}$$

The second term in equation (32) also integrates by parts to give

$$\left[\int \psi\frac{4\Omega^2\rho R}{N^2 z}\frac{\partial^2\psi}{\partial R\partial t}rdrd\theta\right]_{z=0}^{R_0} + \int \frac{4\Omega^2\rho R}{N^2 z}\frac{\partial\psi}{\partial R}\frac{\partial^2\psi}{\partial R\partial t}rdrd\theta dR \tag{35}$$

To evaluate the boundary terms, we write

$$\frac{\partial^2\psi}{\partial R\partial t} = \frac{d}{dt}\frac{\partial\psi}{\partial R} - \frac{1}{r}\left(\frac{\partial\psi}{\partial\theta}\frac{\partial q}{\partial r} - \frac{\partial\psi}{\partial r}\frac{\partial q}{\partial\theta}\right) \tag{36}$$

The spatial derivatives integrate to zero by the same manipulations used in equations (30) and (31), leaving the boundary terms to be

$$\left[\int \psi\frac{4\Omega^2\rho R}{N^2 z}\frac{d}{dt}\frac{\partial\psi}{\partial R}rdrd\theta\right]_{z=0}^{R_0}. \tag{37}$$

The upper limit is zero from equation (23), while from equation (24), the lower limit becomes

$$\int \psi\frac{4\Omega^2\rho R}{N^2 z}\frac{N^2}{2\Omega}\frac{1}{r}\frac{\partial\psi}{\partial\theta}rdrd\theta\bigg|_{z=0} = \int \frac{\partial(\psi)^2}{\partial\theta}\frac{\rho R\Omega}{z}drd\theta\bigg|_{z=0} = 0, \tag{38}$$

again because θ is a periodic coordinate. The remaining integral in equation (35) can be written

$$-\int \frac{4\Omega^2\rho R}{N^2 z}\frac{\partial\psi}{\partial R}\frac{\partial^2\psi}{\partial R\partial t}rdrd\theta dR = -\int \frac{1}{2}\rho\frac{4\Omega^2}{N^2}\frac{\partial}{\partial t}\left(\frac{\partial\psi}{\partial R}\right)^2 r\frac{R}{z}drd\theta dR \tag{39}$$

Thus the total energy relation has become

$$\frac{d}{dt}\int_V \left(\frac{\rho}{2}\left(\frac{\partial\psi}{\partial r}\right)^2 + \frac{\rho}{2}\frac{4\Omega^2}{N^2}\left(\frac{\partial\psi}{\partial R}\right)^2\right)dV = 0. \tag{40}$$

We may identify these terms as follows. $\frac{\partial \psi}{\partial r} = -u$, so the first term in the expression is equal to the dominant, zonal, contribution to the kinetic energy. Using equations (15) and (20), the second term can be written

$$-\frac{\rho}{2}\frac{dT_0}{dS_0}(\delta s)^2,\tag{41}$$

which is identifiable as the available potential energy. Thus equation (40) states that the total rate of change of the sum of the kinetic and available potential energies is zero, or, more simply, that the total energy within the cylindrical shell is conserved.

4 Derivation of a Rayleigh Stability criterion

We are interested in the linear stability of a basic state of entirely zonal flow $\overline{u}(R)$. Consider a perturbation with streamfunction

$$\psi' = \psi(r, R)\exp[ik(r\theta - ct)]\tag{42}$$

We anticipate a complex phase speed under certain conditions, and so write

$$c = c_R + ic_I\tag{43}$$

For unstable behaviour, we require $c_I > 0$.

Conservation of potential vorticity can be written

$$\frac{d}{dt}(\overline{q} + q') = 0\tag{44}$$

Using the relationships

$$\frac{1}{r}\frac{\partial}{\partial\theta} \to ik, \qquad \frac{\partial}{\partial t} \to -ikc, \qquad \frac{d}{dt} = \frac{\partial}{\partial t} + \frac{1}{r}\left(\frac{\partial\psi}{\partial\theta}\frac{\partial}{\partial r} - \frac{\partial\psi}{\partial r}\frac{\partial}{\partial\theta}\right)\tag{45}$$

we obtain

$$q' + \frac{\psi'}{(\overline{u} - c)}\frac{\partial\overline{q}}{\partial r} = 0.\tag{46}$$

238

We now multiply this expression by $\rho\psi'^*$ and integrate over the volume of the cylindrical shell:

$$\int \rho\psi'^* \left(q' + \frac{\psi'}{(\overline{u}-c)}\frac{\partial\overline{q}}{\partial r} \right) r\frac{R}{z}drd\theta dR = 0. \tag{47}$$

The boundary conditions are defined in equations (23), (24) and (25). With the assumed form of the streamfunction, these are written

$$v = \frac{1}{r}\frac{\partial\psi'}{\partial\theta} = ik\psi' = 0 \tag{48}$$

at $r = r_1$ and $r = r_2$,

$$\frac{\partial\psi'}{\partial R} = \frac{\psi'}{\overline{u}-c}\overline{u}_R \tag{49}$$

at $R = R_0$, and

$$\frac{\partial\psi'}{\partial R} = \frac{\psi'}{\overline{u}-c}\left(\overline{u}_R - \frac{N^2}{2\Omega}\right) \tag{50}$$

at $R = r$ $(z = 0)$.

Evaluating the integral using the boundary conditions, and taking the imaginary part, gives

$$c_I \left(\left[\int \frac{|\psi'|^2}{|\overline{u}-c|^2}\frac{4\Omega^2\rho R}{N^2 z}\left(\overline{u}_R - \frac{N^2}{2\Omega}\right) rdrd\theta \right]_{z=0}^{R=R_0} \right.$$

$$\left. + \int \frac{|\psi'|^2}{|\overline{u}-c|^2}\frac{\rho R}{z}\frac{\partial\overline{q}}{\partial r}rdrd\theta dR \right) = 0 \tag{51}$$

For an unstable solution, $c_I \neq 0$, so that the sum of the integrals must be zero. Evaluating the limits of the surface integral, we assume $\rho(R_0) = 0$, so the upper boundary term is 0. The remaining expression can be simplified using the Dirac delta function (Bretherton, 1965) to read

$$\int \left(\left(2\Omega - \frac{4\Omega^2\overline{u}_R}{N^2} \right) \delta(R-r) - \frac{2r\Omega}{z^2} - \frac{z}{R\rho}\frac{\partial}{\partial R}\left(\frac{4\Omega^2\rho R}{N^2 z}\overline{u}_R \right) \right)$$

$$\times \frac{|\psi'|^2}{|\overline{u}-c|^2}\rho r\frac{R}{z}drd\theta dR = 0 \tag{52}$$

The terms outside the brackets are non-negative definite. Thus, a necessary (but not sufficient) condition for instability is that the quantity

$$\left(2\Omega - \frac{4\Omega^2 \bar{u}_R}{N^2}\right)\delta(R-r) - \frac{2r\Omega}{z^2} - \frac{z}{R\rho}\frac{\partial}{\partial R}\left(\frac{4\Omega^2 \rho R}{N^2 z}\bar{u}_R\right) \qquad (53)$$

change sign within the region of integration. Simple algebraic manipulation allows us to rewrite this

$$\left(2\Omega - \frac{r}{R}\frac{4\Omega^2 \bar{u}_R}{N^2}\right)\left(\delta(R-r) - \frac{r}{z^2}\right) - \frac{1}{\rho}\frac{\partial}{\partial R}\left(\frac{4\Omega^2 \rho}{N^2}\bar{u}_R\right). \qquad (54)$$

It can be shown by integrating by parts that the δ-function part of equation (54) exactly balances the singular nature of the $\frac{1}{z^2}$ term at $R = r$. Furthermore, we note from equation (21) that the formalism we have developed is not strictly valid at $R = r$. Based on this rather tenuous logic, we will assume that the delta function does not cause a change of sign at $R = r$, and so will neglect it. This approach will be partially vindicated by its success.

In order to obtain more insight from this relationship, we nondimensionalise it. All lengths are scaled by R_0, the radius of the planet. The scaling of the base state velocity is defined by equation (9), so we write

$$u = \tilde{u}\frac{2\Omega L^2}{R_0}, \qquad (55)$$

where $\tilde{u}$ is the nondimensional velocity. Dropping the tildes, the simplified sufficient condition for stability is that

$$K = \frac{r}{z^2} + \frac{z}{R\rho}\frac{\partial}{\partial R}\left(\frac{\rho R}{Bz}\bar{u}_R\right) \qquad (56)$$

is of definite sign. This condition is the deep quasigeostrophic analogue of the *Rayleigh stability criterion*. Here

$$B = \left(\frac{NR_0}{2\Omega L}\right)^2 \qquad (57)$$

is the Burger number for the problem. This can be shown to be $O(1)$, and can depend on R if N^2 does.

This can be examined for some interesting special cases.

1. $\overline{u}_R = 0$. In this case, $K > 0$ throughout the volume, so the basic flow is stable to small perturbations. Thus, solid body rotation is Rayleigh stable.

2. $\overline{u}_R = $ a negative constant. As both ρ and (R/z) are decreasing functions of radius, provided that the Burger number (or rather the Brunt-Vaisala frequency) is constant or an increasing function with radius, again $K > 0$ throughout the volume. Hence linear super-rotation is Rayleigh stable.

3. $\overline{u}_R = $ a positive constant. In this case, the two terms of K are of different signs, so stability is not guaranteed for all parameter ranges.

5   Numerical investigations

5.1   Nondimensional equations

We examine numerically the stability of various basic states. The equations which we wish to solve are derived from the heat and vorticity equations using the perturbation formalism of section 4, with the additional ansatz that the radial form of the streamfunction is $\cos l(r - r_0)$, where l is such that

$$\cos l(r - r_0) = 0 \quad \text{at} \quad r = r_1, r_2. \tag{58}$$

This satisfies the boundary condition equation (25). Defining a new variable

$$\phi' = -iR\dot{R}\rho/k \tag{59}$$

and applying (45), equations (18) and (19) reduce to

$$\frac{\partial \psi}{\partial R} = \frac{1}{\overline{u} - c} \left(\overline{u}_R \psi - \frac{N^2}{2\Omega \rho R} \phi \right) \tag{60}$$

$$\frac{\partial \phi}{\partial R} = -\rho R \left(\frac{r}{z^2} + (\overline{u} - c)\frac{l^2}{2\Omega} \right) \psi + \frac{R}{z^2} \phi. \tag{61}$$

Here, ψ, ϕ and c are considered complex, while all other quantities are real. Taking the complex conjugate of these two equations demonstrates that if

c is a valid eigenvalue for the system, so is c^*, so complex eigenvalues will occur in complex conjugate pairs.

We non-dimensionalise these equations, identifying the radial length scale $L \sim 1/l$. The scaling of ϕ is determined by equation (24), the boundary condition at $z = 0$. This requires

$$\dot{R} = ik\psi' = ik\phi'/(\rho R) \tag{62}$$

so if

$$\psi' = \psi_0' \tilde{\psi} \tag{63}$$

then

$$\phi' = \psi_0' \rho_0 R_0 \tilde{\phi} \tag{64}$$

Dropping the tildes, the equations are written

$$\frac{\partial \psi}{\partial R} = \frac{1}{\bar{u} - c}\left(\bar{u}_R \psi - \frac{B}{\rho R}\phi\right), \tag{65}$$

$$\frac{\partial \phi}{\partial R} = -\rho R\left(\frac{r_0}{z^2} + (\bar{u} - c)\right)\psi + \frac{R}{z^2}\phi. \tag{66}$$

Again,

$$B = \left(\frac{N R_0 l}{2\Omega}\right)^2 \tag{67}$$

is the Burger number, here for a particular wavenumber l, $O(1)$. Boundary conditions (23) and (24) reduce to

$$R = R_0 \quad \Rightarrow \quad \phi = 0 \tag{68}$$

$$R = r_0 \quad \Rightarrow \quad \phi = \rho r \psi. \tag{69}$$

5.2 Numerical procedure

We adopt the following physical parameters. We treat the Brunt-Vaisala frequency as a constant within the planet, so that the Burger number is also constant. We choose as a density profile the solution of the Lane-Emden equations (Chandrasekhar, 1958) for a polytropic planet with equation of state $p = K\rho^2$, which is

$$\rho = \frac{\sin \pi R}{\pi R}. \tag{70}$$

242

This is a smoothly decreasing function which tends to zero at $R = 1$, and is considered to be a good first order relation for the outer planets, providing a good fit to the observed gravimetric data. Away from the centre of the planet, this density structure is well approximated by a linear relationship

$$\rho = \frac{5}{4}(1 - R) \tag{71}$$

which will prove useful in analytic calculations.

We integrate this system of equations numerically by a shooting technique using a 4th order Runge-Kutta method with constant step size. For a given value of c, we treat the system as an initial value problem defined by equation (69), and integrate to $R = R_0$. To determine valid eigenvalues c, we construct contour plots of $|\phi|$ at R_0, and look for zeros, which are improved by an iterative Newton-Raphson method. The solution is then continued in B.

As we would expect from the analysis of the Rayleigh stability criterion of section 4, we find no unstable solutions to the problem for the special cases 1 and 2. Indeed, as a generalisation of case 2, we find no unstable solution for any monotonically decreasing velocity profile. We concentrate our attention on case 3. We use a velocity profile

$$\bar{u} = \frac{R - r_0}{1 - r_0}. \tag{72}$$

This is linear with R, and varies between 0 and 1. For most of our calculations, we take the value of r_0 to be 0.7. This is probably consistent with the assumption of no phase changes within the cylindrical region for the outer planets.

Figure 3 shows contour plots of the $|\phi|$ plane for different values of B. There is little change in behaviour until $B > 1$ is reached, as shown by the upper plots. Below this, there are two valid eigenvalues, both on the negative real axis, and hence both stable. However, at higher Burger numbers, more valid solutions appear, as shown in the lower left plot, including some with non-zero imaginary part, as shown in the lower right plot.

Figure 4 shows the values of c_I against Burger number for unstable solutions. Several points are worth noting. Unstable solutions appear only for Burger number greater than about 3, and there is only one unstable solution for any given Burger number. In order to understand this behaviour, we examine the phase plane of the real and imaginary components of c for all
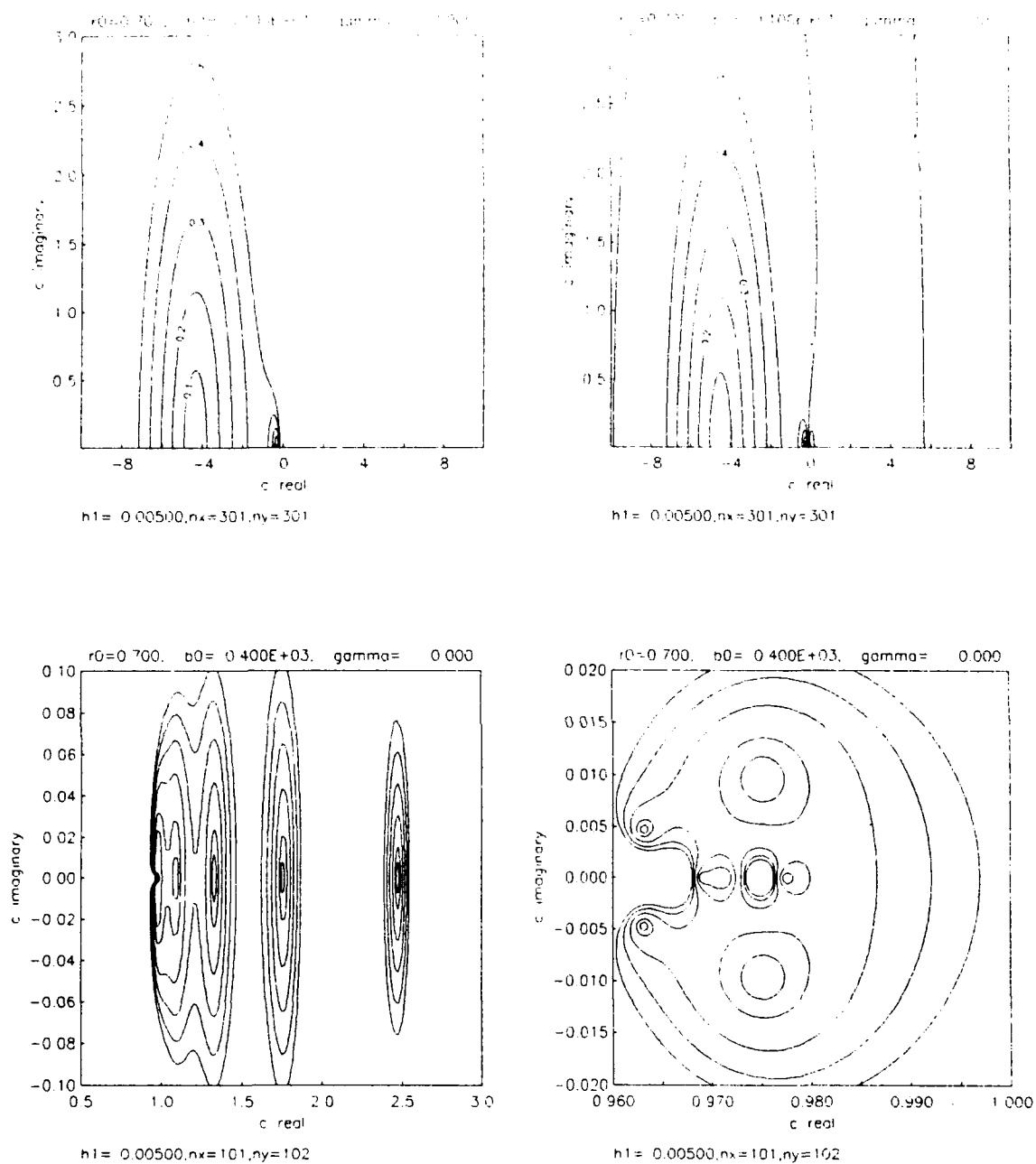
Figure 3: Contour plots for $|\phi|$ for varying Burger number. Valid eigenvalues are located in contour minima. On axis solutions in the bottom right plot are probably numerical noise.

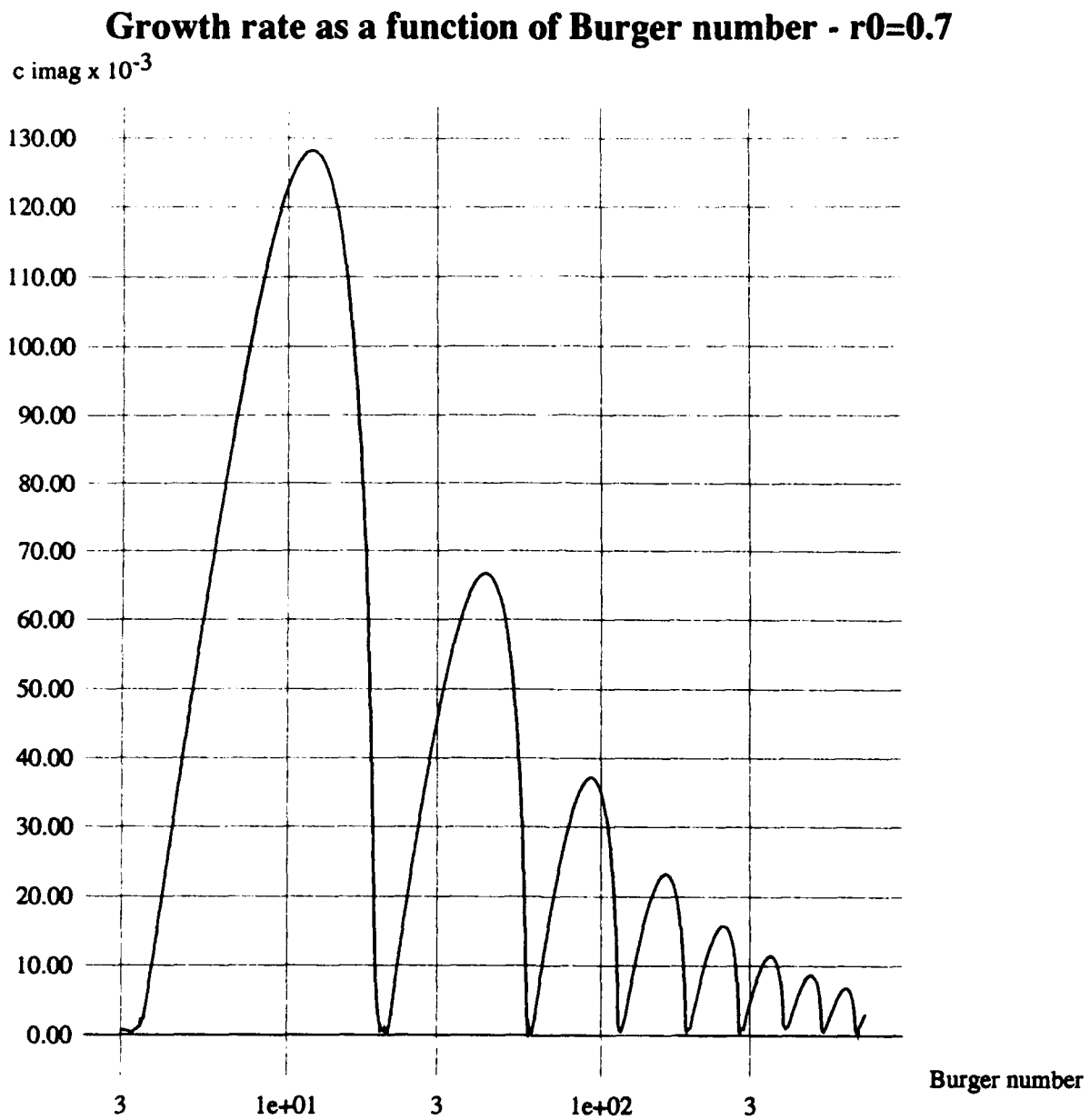| Upper left: | $B = 0.01$ |
| Upper right: | $B = 1.0$ |
| Lower left and right: | $B = 400$ |

Growth rate as a function of Burger number - r0=0.7

c imag x 10^{-3}

Figure 4: Unstable modes as a function of Burger number.
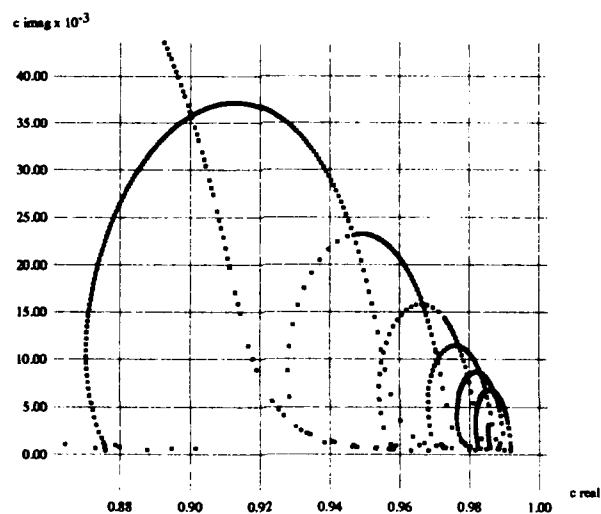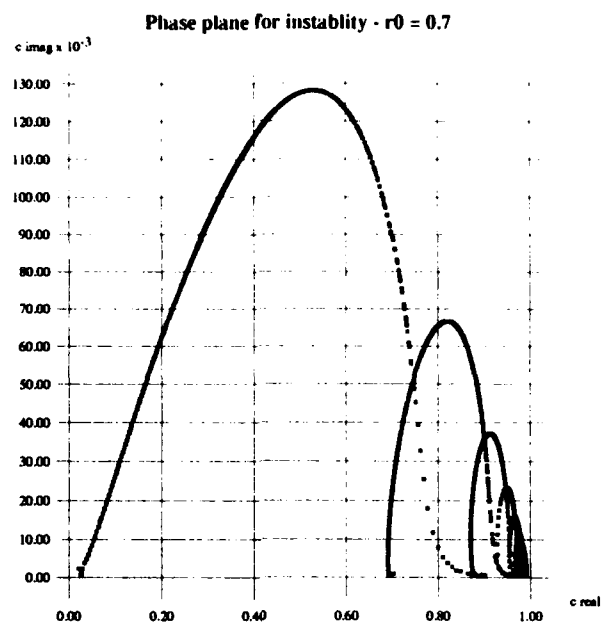
Figure 5: Phase plane of eigenvalues for all unstable solutions. Lower diagram is an enlargement of the region near $c_R = 1$.

Burger numbers and all unstable solutions. This is shown in Figure 5. As Burger number is increased from 1, one of the two solutions on the negative axis becomes more negative and remains on the axis. The other moves through the origin, and then at Burger number a little greater than 3 becomes unstable and follows the largest curve in the phase plane. When this returns to the real axis, as Burger number is further increased it stays on the the real axis with c_R increasing. At the value for B at which this mode becomes stable, a new unstable mode appears, and follows the second largest curve. Again, as Burger number increases, this returns to the real axis and becomes stable, when a third unstable mode develops. Thus at higher Burger numbers, there are multiple stable solutions on the real axis, and one unstable solution just off it, as seen in the lower contour plots in Figure 3.

It is instructive to look at the form of the eigenfunctions ψ and ϕ for these different modes, shown in Figure 6. The mode numbers in the figure refer to the "hump" number on Figure 4. Thus the first unstable mode is monotonic for both eigenfunctions, while higher orders have increasing numbers of turning points.

5.3 B=0 limit

To aid in understanding the behaviour of the system at low Burger number, we note that in the limit of $B \to 0$, the equations have a closed form analytical solution. Equation (65) integrates directly to give

$$\psi = A(\overline{u} - c) \tag{73}$$

where the amplitude A is arbitrary and undeterminable. Substituting this in equation (66) and collecting terms gives

$$\frac{\partial(\phi/z)}{\partial R} = -\frac{A\rho R}{z} \left(\frac{r_0}{z^2} + (\overline{u} - c) \right) (\overline{u} - c), \tag{74}$$

a closed form solution that can be integrated numerically for any arbitrary density or velocity profile. We specialise here to the parameters we have used for our numerical calculation, with the simplified linear density profile given by equation (71), and obtain a function that can be integrated analytically. The full solution is somewhat messy, and provides little insight, but examining the boundary conditions is more helpful.
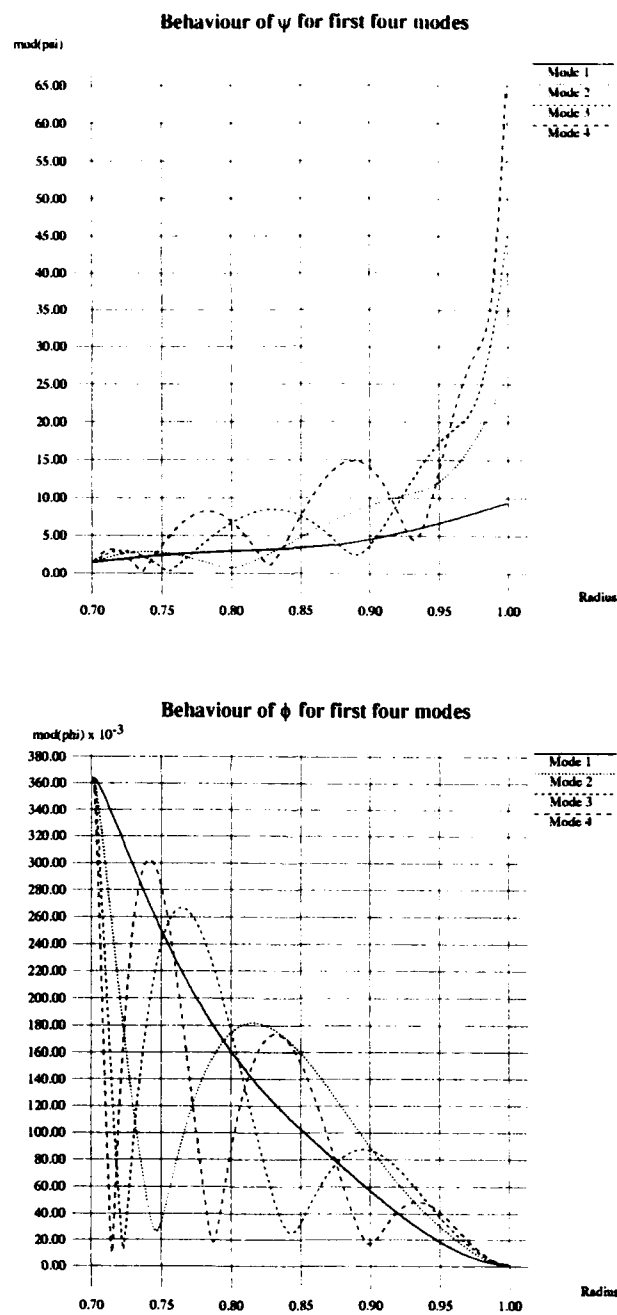
Figure 6: Eigenfunctions characteristic of different branches of unstable solutions

Equation (69) requires that $\psi = \phi/(\rho r_0)$ at $R = r_0$. To achieve this, we examine Taylor expansions in z of the two functions about $z = 0$. These are

$$\psi = -Ac + \frac{A}{2r_0(1 - r_0)}z^2 + O(z^4) \tag{75}$$

and

$$\phi/(\rho r_0) = -Ac + \left[A\ln(r_0)\left(\frac{r_0}{2(1 - r_0)}c^2 + \frac{(r_0^2 + 2r_0 - 1)}{(r_0 - 1)^2}c \right.\right.$$
$$\left.\left. + \frac{(\frac{7}{8}r_0^3 + 2r_0^2 - 1)}{(1 - r_0)^3}\right) + \Gamma\frac{4}{5r_0(1 - r_0)}\right] z + O(z^2), \tag{76}$$

where Γ is the constant of integration. Note that the lowest order terms are automatically equal, so the matching condition is the requirement that the $O(z)$ term in the second expression is identically zero. This is also required for ϕ to be analytic at $R = r_0$. Equation (68) requires that ϕ be zero at $R = 1$. This produces another quadratic equation in c:

$$\frac{96\Gamma}{5A} + 12c^2(r_0^2\ln(1+z_0) - z_0) + \frac{8c}{1 - r_0}(3\ln(1+z_0)r_0(r_0^2 + 2r_0 - 1) + z_0(1 + r_0)(1 - 4r_0))$$
$$+ \frac{1}{(1 - r_0)^2}(3\ln(1 + z_0)r_0(r_0 + 2)(7r_0^2 + 2r_0 - 4) - z_0(32r_0^3 + 19r_0^2 - 8r_0 + 2)) = 0 \tag{77}$$

where $z_0^2 = 1 - r_0^2$. Eliminating Γ between equations (76) and (77) yields an eigenvalue relation, which for $r_0 = 0.7$ has solutions

$$c = -3.667, -0.461. \tag{78}$$

These are qualitatively the same as for the simulation shown (see Figure 3 for comparison). Much better agreement can be obtained by using a different constant for the linear density profile, while complete agreement is achieved when the numerical simulation is run with the exact linear profile used here.

Interestingly, this method also predicts instability for values of r_0 below about 0.4, a result confirmed by numerics. This is less physically applicable than instability previously discussed, as at these depths in the real planets phase changes will have occurred to invalidate the basic assumptions we have been using.

Thus, this analytic result gives a good understanding and confirmation of the behaviour of the system at low Burger number, and in an asymptotic sense is a good approximation to $B \sim 1$. For insight into the behaviour at higher B, we must turn to other techniques.

6 The Rayleigh criterion and the onset of instability

We wish to see whether the simplified Rayleigh stability criterion (equation (56)) derived earlier can provide insight as to why the system becomes unstable. In particular, we might hope to recover a lower bound for B at which instability can occur. Consider a generalised linear density profile

$$\rho \sim (1 - R), \tag{79}$$

with the linear velocity profile (72). The Rayleigh criterion (equation (56)) is then that

$$K = \frac{r_0}{z^2} + \frac{z}{R(1 - R)} \frac{\partial}{\partial R} \left(\frac{R(1 - R)}{Bz(1 - r_0)} \right) \tag{80}$$

must change sign for some value of R. Assuming constant Burger number, this is the same as requiring

$$K' = BKz^2 = Br_0 - \frac{z^2}{(1 - R)(1 - r_0)} - \frac{r_0^2}{R(1 - r_0)} \tag{81}$$

to change sign. It is easy to show that this function is monotonically decreasing with R in the range $[r_0, 1]$. We look for the value of B at which $K' = 0$ at $R = r_0, z = 0$. Hence

$$B_{\text{crit}} = \frac{1}{1 - r_0} \tag{82}$$

is the minimum value for possible intability. Thus, when $r_0 = 0.7$, $B_{\text{crit}} = 3\frac{1}{3}$. This is very close to the critical value found numerically, as can be seen from Figure 7.

The Rayleigh criterion provides only a necessary condition for instability. However, in this case the condition seems to be sufficient. This can be understood from the nature of the integral kernal K. For values of B below $3\frac{1}{3}$ this is negative througi.out the region. When the sign change occurs, it is at $z = 0$, where the kernal is highly singular. Thus a small region of positive contribution here can provide a very large net positive effect, allowing the whole integral to be zero.
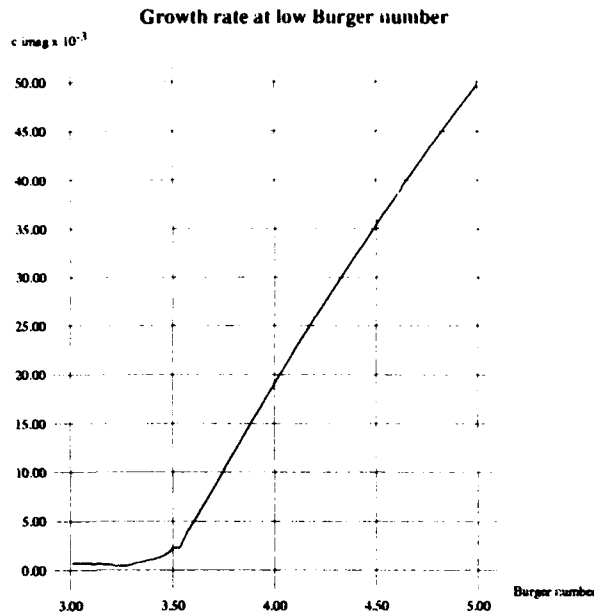
Figure 7: Onset of instability

7 Application to the solar system

We have found that baroclinic instability can occur for subrotating basic velocity states, but that superrotating states are stable. If we differentiate equation (15) with respect to r, we obtain

$$2\Omega\frac{\partial u}{\partial R} = \frac{\partial \delta s}{\partial r}\frac{dT_0}{dR} \tag{83}$$

Remembering that temperature decreases with planetary radius, this means that a superrotating state corresponds to greater incident heat at the equator than the poles, whereas a subrotating state corresponds to the reverse. The winds of Jupiter and Saturn are dominantly prograde (superrotating), and there is an excess of heat at the equator, which is consistent with our formulation. Unfortunately, this also precludes the instability we require for heat transport. Uranus, however, has dominant heat input at the poles, while Neptune's winds are observed to be retrograde, so the baroclinic instability we have discovered may be important in these planets. We have also ignored the possible influence of an inpenetrable core which may provide instability even for Jupiter and Saturn.

Future work must also consider the effect of more rapid zonal variations, as without these influences the growth rate is unbounded with increase in wavenumber k. However, such considerations are unlikely to affect the existence of the instability.

References

Bretherton, F. P. Critical layer instability in baroclinic flows. *Quart. J. Roy. Meteor. Soc.*, 92(393):325–334, 1965.

Chandrasekhar, S. *An introduction to the study of stellar structure.* Dover (New York), 1958.

Ingersoll, A. P. and D. Pollard. Motion in the interiors and atmospheres of Jupiter and Saturn: Scale analysis, anelastic equations, barotropic stability criterion. *Icarus*, 52:62–80, 1982.

Ingersoll, A. P. and C. C. Porco. Solar heating and internal heat flow on Jupiter. *Icarus*, 35:27–43, 1978.

Williams, G. P. Planetary circulations 2: The Jovian quasi-geostrophic regime. *J. Atmos. Sci.*, 36:932–968, 1979.

Acknowledgements

Stochastic forcing of boundary layer turbulence

Petros J. Ioannou

M.I.T

1. Introduction.

Transition to turbulence typically occurs in shear flow experiments at $R \approx 1000$ where R is the flow Reynolds number[1]. Careful control of the intensity of background disturbances results in persistence of laminar flow to much higher Reynolds numbers which for pipe Poiseuille flow[2] can reach as high as $R = 10^5$. The dynamics of such small perturbations as are associated with high R transition can at least initially be described with accuracy by the Navier-Stokes equations linearized about the background mean flow. Assuming that the background noise is stochastic it is of interest to address, making use of linearized perturbation theory, the level of variance sustained in the mean by this stochastic forcing.

The familiar problem of the damped harmonic oscillator excited by random and un-correlated impulses exemplifies the physical processes operating in most familiar dynamical systems. It can be shown that the ensemble average variance of the displacement, x, of the oscillator is given by

$$< \mid x \mid^2 > = \frac{\pi \mid \epsilon \mid^2}{\gamma \omega^2} , \qquad (1.1)$$

where $\mid \epsilon \mid^2$ is the amplitude of the random forcing, ω the natural frequency of the oscillator, and γ the damping coefficient[3]. When $\omega = 0$ there is no restoring force and we obtain

Brownian motion for which there is no stationary state. When $\gamma = 0$ there is no damping and random driving again leads to nonstationary statistics, while for nonvanishing restoring force and nonvanishing damping the variance reaches a finite statistically stationary amplitude such that the input of energy from the driving balances the dissipation and a variance level inversely proportional to the damping coefficient results. This behavior is characteristic of all dynamical systems with self-adjoint dynamical operators. The total variance in such systems is the sum of the variance of each of the normal modes taken separately, the same as if each mode were independently excited by stochastic forcing.

Consider now a fluid with a background flow field having nonvanishing rate of strain but with sufficient dissipation so that all small perturbations impressed on the flow eventually decay. Linearization of this dynamical system about its background flow results in a non-self-adjoint dynamical operator and an associated set of modes that are not mutually orthogonal either in the inner product associated with the L_2 or the energy norm. This lack of orthogonality corresponds to the potential for extraction of energy by the perturbations from the background flow, irrespectively of the existence of exponential instabilities. The energy balance in such a system is between the stochastic forcing together with the induced extraction of energy from the background flow, on the one hand, and the dissipation on the other. Without stochastic forcing the perturbation field would vanish. With stochastic forcing an enhanced level of variance can be maintained by the stochastically induced transfer of background flow energy to the perturbation field which exceeds that arising simply by accumulation of energy from the forcing. In this respect stochastically forced

non-self-adjoint dynamical systems differ fundamentally from the classical stochastically forced harmonic oscillator.

These considerations led Farrell and Ioannou[4] to investigate the maintained variance in 2D unbounded constant shear and deformation flows. It was found that the variance in pure deformation flows increases without bound under stochastic excitation for any value of the viscosity. In contrast, in shear flow the variance is stationary and is limited to an increase of a factor of three over that arising from the same forcing of the unsheared fluid.

The importance of treating the stochastic forcing of 3D channel flows was further motivated by the calculations of Butler and Farrell[5] and Farrell and Ioannou[6] in which it was found that the maximal growth of perturbations in 3D channel flows far exceeds the growth of their 2D counterparts and is simultaneously more persistent. While unbounded constant shear flow has the convenient property, exploited in the aforementioned works, of a closed form solution both in 2D and in 3D, this is not true for bounded flows. In this work a general method is presented which is valid, in principle, for calculating the response of any bounded flow to stochastic forcing.

2. Stochastic forcing of linear dynamical systems.

Consider the linear autonomous dynamical system :

$$\frac{d}{dt}x_i = \mathcal{A}_{ij}x_j + \mathcal{F}_{ij}\epsilon_j. \tag{2.1}$$

The linear dynamical operator, $\mathcal{A}$, which controls the deterministic evolution of the system is in general non-normal (*i.e.* $\mathcal{A}'\mathcal{A} \neq \mathcal{A}\mathcal{A}'$, where ($'$) denotes the Hermitian transpose). The stochastic nature of the dynamical system stems from the random nature of the

forcing, ϵ. This forcing is assumed to be a δ-correlated Gaussian white-noise process with zero mean: $< \epsilon_i > = 0$, $< \epsilon_i(t)\epsilon_j^*(t') > = \delta_{ij}\delta(t - t')$ [1], which excites with equal probability and independently each forcing function, specified by the columns $f^{(j)}$ of the matrix $\mathcal{F}_{ij}$. The norm will be assumed to be generated by the inner product defined by $(\phi, \mathcal{M}\psi)$, where $\mathcal{M}$ is a positive definite hermitian operator. We will employ the energy norm $< E > = \lim_{t->\infty} < x_i'(t)\mathcal{M}_{ij}x_j(t)) >$, with $\mathcal{M}$ to be determined in sequel, rather than the L_2 norm for which $\mathcal{M}$ would be equal to the identity matrix, recognizing that we want to measure the ensemble average velocity variance which is related by a constant factor to the energy.

When $\mathcal{A}$ is stable (*i.e.* all the eigenvalues of $\mathcal{A}$ have negative real parts), the dynamical system reaches a statistically steady state, the statistics of which we wish to determine. The solution of (2.1) for $t \geq 0$, with initial condition x_o is given by

$$x = e^{\mathcal{A}t}x_o + \int_0^t \mathcal{G}(t - s)\mathcal{F}\epsilon ds, \qquad (2.2)$$

where $\mathcal{G}(t - s) = e^{\mathcal{A}(t-s)}$. The random response, x, is linearly dependent on ϵ and consequently is also Gaussian distributed. The first moment, given by $< x > = e^{\mathcal{A}t}x_o$, vanishes for large times because of the assumed stability of $\mathcal{A}$ thus making the system independent of its initial conditions. The total variance is given by:

$$< E^t > = < (\mathcal{M}^{1/2}x(t))_i' (\mathcal{M}^{1/2}x(t))_i >$$

$$= \mathcal{F}'_{lb} \left(\int_0^t \mathcal{G}'_{ba}(t - s) \mathcal{M}_{ac} \mathcal{G}_{cd}(t - s) \, ds \right) \mathcal{F}_{dl} \qquad (2.3)$$

$$= \sum_l f'^{(l)}_b \mathcal{B}^t_{ba} f^{(l)}_a .$$

---

[1] Notation: $< >$ denotes ensemble averaging, and $*$ complex conjugation. We will freely use the summation convention.

256

We have defined $\mathcal{B}^t \equiv \int_0^t \mathcal{G}'(t-s) \, \mathcal{M} \, \mathcal{G}(t-s) \, ds$, and $f_a^{(b)} \equiv \mathcal{F}_{ab}$. Recall that $f_a^{(b)}$ represents the a-th coordinate of the b-th forcing function.

The stability of $\mathcal{A}$ ensures the existence of $\lim_{t\to\infty} \mathcal{B}^t = \mathcal{B}^\infty$ and it can be shown, under this same condition, that $\mathcal{B}^\infty$ satisfies the Liapunov equation:

$$\mathcal{A}'\mathcal{B}^\infty + \mathcal{B}^\infty\mathcal{A} = -\mathcal{M}, \tag{2.4}$$

which can be solved by standard methods [7]. Alternatively, $\mathcal{B}^\infty$ may be obtained by direct integration noting that $\mathcal{A}$ can be diagonalized by a similarity transformation using the matrix, $\mathcal{P}$, of the eigenvectors of $\mathcal{A}$ arranged in columns so that $\mathcal{A} = \mathcal{P}\mathcal{S}\mathcal{P}^{-1}$ with $\mathcal{S}_{ij} = \sigma^{(i)}\delta_{ij}$, where σ^i is the i-th eigenvalue of $\mathcal{A}$, and $\mathrm{Re}(\sigma^{(i)}) < 0$ by the assumption of stability of $\mathcal{A}$. Consequently:

$$\mathcal{B}_{ij}^\infty = -\mathcal{P}'^{-1}_{ia} \left(\frac{\mathcal{P}'_{ab}\mathcal{M}_{bc}\mathcal{P}_{cd}}{\sigma^{*(a)} + \sigma^{(d)}} \right) \mathcal{P}_{dj}^{-1}. \tag{2.5}$$

Returning to the calculation of variance we first show that $< E^t >$, given by (2.3), does not depend on the forcing distribution, assuming only that the forcing is properly normalized. To this end we call two sets of forcing distributions $\mathcal{F}_1, \mathcal{F}_2$ equivalent if there is a non-singular linear transformation $\mathcal{F}_2 = \mathcal{T}\mathcal{F}_1$ which preserves the $\mathcal{M}$-norm. Such a transformation can be expressed in the form $\mathcal{T} = \mathcal{M}^{-1/2}\mathcal{U}\mathcal{M}^{1/2}$, where $\mathcal{U}$ is a unitary transformation, and it satisfies: $\mathcal{T}' = \mathcal{M}\mathcal{T}^{-1}\mathcal{M}^{-1}$. Note that $\mathcal{F}'\mathcal{M}\mathcal{F} = I$ implies $\mathcal{F}\mathcal{F}'\mathcal{M} = I$ and consequently two equivalent forcing distributions $\mathcal{F}_1, \mathcal{F}_2$ have the property:

$$\mathcal{F}_1\mathcal{F}'_1 = \mathcal{F}_2\mathcal{F}'_2. \tag{2.6}$$

Using the identity Trace $(\mathcal{ABC})$ = Trace $(\mathcal{CAB})$, it immediately follows from (2.6) that two equivalent sets of forcing produce equal variance. Consequently, we are at liberty to select any $\mathcal{M}$-normalized forcing $\mathcal{F}_{ij}$ in (2.1) so long as it is of full rank.

We select the forcing set, $\mathcal{F}$, whose columns f render the functional

$$I[f] = \frac{f'\mathcal{B}^\infty f}{f'\mathcal{M}f} \tag{2.7}$$

stationary (note that $\mathcal{B}^\infty$ is hermitian). These stationary forcing distributions are found by solving the eigenvalue problem:

$$\left(\mathcal{M}^{-1/2}\mathcal{B}^\infty\mathcal{M}^{-1/2}\right)\mathcal{M}^{1/2}f = \lambda\mathcal{M}^{1/2}f. \tag{2.8}$$

The eigenfunctions $\phi^i \equiv \mathcal{M}^{-1/2}f^i$ are orthogonal in the inner product associated with the L_2 norm, while the corresponding f^i are orthogonal in the inner product associated with the energy norm, and can be scaled to be orthonormal. The non-singularity of $\mathcal{M}^{-1/2}$ ensures that the forcing distributions f^i, derived from ϕ^i, also form a spanning set and the normalized f^i provide unit forcing of (2.1) if we set $\mathcal{F}_{ab} \equiv f^{(b)}$

The forcings obtained from solution of the eigenvalue   em (2.8) can be ordered according to their relative contribution to the stochastically maintained variance. In sequel we will contrast these ordered forcings with the responses ordered according to their contribution to the induced variance.

258

The x resulting from (2.2) is Gaussian with zero mean. Its full specification is obtained from the correlation matrix:

$$
\begin{aligned}
C_{ij}(t) &= < (\mathcal{M}^{1/2}x(t))_i\, (\mathcal{M}^{1/2}x(t))_j^* > \\
&= \left\langle \mathcal{M}_{ia}^{1/2} \int_0^t ds \int_0^t ds'\; \mathcal{G}_{ab}(t-s)\, \mathcal{F}_{bc}\epsilon_c(s)\mathcal{G}_{de}^*(t-s')\, \mathcal{F}_{eg}^*\epsilon_g^*(s')\mathcal{M}_{jd}^{1/2} \right\rangle \\
&= \mathcal{M}_{ia}^{1/2} \int_0^t ds\; \mathcal{G}_{ab}(t-s)\, \mathcal{F}_{bc}\mathcal{F}_{ec}^*\mathcal{G}_{de}^*(t-s)\; \mathcal{M}_{jd}^{1/2} \\
&= \mathcal{M}_{ia}^{1/2} \left(\int_0^t ds\; \mathcal{G}_{ab}(t-s)\, \mathcal{F}_{bc}\mathcal{F'}_{ce}\mathcal{G'}_{ed}(t-s) \right).\mathcal{M}_{dj}^{1/2}\, ,
\end{aligned}
\tag{2.9}
$$

or in matrix form

$$
C(t) = \mathcal{M}^{1/2}\mathcal{K}^t\mathcal{M}^{1/2} \tag{2.10}
$$

where

$$
\mathcal{K}^t = \int_0^t \mathcal{G}(t-s)\,\mathcal{H}\mathcal{G}'(t-s)\, ds\, , \tag{2.11}
$$

and $\mathcal{H} = \mathcal{F}\mathcal{F}'$. The correlation matrix depends on the metric $\mathcal{M}$, the dynamical operator $\mathcal{A}$, and the forcing distribution $\mathcal{F}$. It is clear from (2.6), that equivalent forcings result in the same $\mathcal{H}$ and therefore in the same correlation matrix.

It can be readily verified from (2.9) that $C(0) = 0$ and that $\lim_{t->\infty} C(t) = C^\infty$ is a well defined stationary limit, given asymptotic stability of $\mathcal{A}$. The equation governing the temporal evolution of $C(t)$ follows from differentiation of $\mathcal{K}^t$ with respect to time to obtain:

$$
\frac{d}{dt}\mathcal{K}^t = \mathcal{H} + \mathcal{A}\mathcal{K} + \mathcal{K}\mathcal{A}'. \tag{2.12}
$$

The solution to (2.12) is:

$$
\mathcal{K}^t = \mathcal{K}^\infty - e^{\mathcal{A}t}\mathcal{K}^\infty e^{\mathcal{A}'t}\, , \tag{2.13}
$$

and the asymptotic stationary correlation matrix is obtained from the solution of the Liapunov equation:

$$\mathcal{A}\mathcal{K}^\infty + \mathcal{K}^\infty \mathcal{A}' = -\mathcal{H}, \tag{2.14}$$

upon taking the limit of (2.10) which gives $\mathcal{C}^\infty = \mathcal{M}^{1/2}\mathcal{K}^\infty \mathcal{M}^{1/2}$. The variance maintained by the stochastic forcing is then $< E > = \text{Trace}(\mathcal{C}^\infty)$. As expected, this value of the variance is the same as that obtained from (2.3) by means of which the principle forcings were found. This can be seen from the following:

$$
\begin{aligned}
\text{Trace } (\mathcal{F}'\mathcal{B}^\infty \mathcal{F}) &= \mathcal{F}'_{jb} \int_0^\infty ds\, \mathcal{G}'_{ba}(t-s)\mathcal{M}_{ad}\mathcal{G}_{ds}(t-s)\mathcal{F}_{sj} \\
&= \int_0^\infty ds\, \mathcal{G}'_{ba}(t-s)\mathcal{M}_{ad}^{1/2}\mathcal{M}_{de}^{1/2}\mathcal{G}_{es}(t-s)\mathcal{H}_{sb} \\
&= \text{Trace } \left(\mathcal{M}^{1/2} \int_0^\infty ds\, \mathcal{G}(t-s)\mathcal{H}\mathcal{G}'(t-s)\, \mathcal{M}^{1/2} \right),
\end{aligned}
$$

upon identifying the integral with $\mathcal{K}^\infty$ in (2.11).

The correlation matrix is a positive definite Hermitian operator by construction, and therefore it has positive real eigenvalues associated with mutually orthogonal eigenvectors. Each eigenvalue equals the variance accounted for by the pattern of its corresponding eigenvector and the pattern that corresponds to the largest eigenvalue contributes most to the variance. The decomposition of the correlation matrix into its orthogonal components is called the Karhunen-Loeve decomposition[8] (referred to as K-L in sequel). This decomposition has been widely used in analysis of synoptic meteorological data[9] and has been applied recently in turbulence research[10]. To determine the K-L decomposition in the $\mathcal{M}$-norm we solve the eigenvalue problem:

$$\mathcal{C}^\infty u^{(i)} = \lambda^{(i)} u^{(i)}. \tag{2.15}$$

In the energy norm the K-L functions in (2.15) determine the $\mathcal{M}$-orthogonal set of velocity correlations; the corresponding streamfunctions are given by $\psi^{(i)} = \mathcal{M}^{-1/2}u^{(i)}$. Note that these streamfunctions, unlike the $u^{(i)}$, are not in general themselves $\mathcal{M}$-orthogonal.

We have determined two sets of orthogonal functions: using (2.8) we ordered the forcing functions according to their contribution to the variance, and using (2.15) we ordered the response functions according to their contribution to the steady state correlation matrix. If the dynamical operator $\mathcal{A}$ is self-adjoint in the $\mathcal{M}$-inner product, the two sets of orthogonal functions reduce to the eigenfunctions of $\mathcal{A}$. This is easily seen in the L_2 norm because in that case if $\mathcal{A}$ is self adjoint $\mathcal{A}$, $\mathcal{B}^t$, and $C(t)$ commute and therefore they are simultaneously diagonalized by the same eigenvectors. For a self-adjoint operator the K-L patterns have special dynamical significance: they correspond to the normal modes of the dynamical system and also to the forcings that excite the normal modes and produce the independent modal contributions to the variance. This is not true when $\mathcal{A}$ is non-selfadjoint as is usually the case for fluid dynamical applications. North[11] realized that when the operator $\mathcal{A}$ is not self-adjoint the K-L decomposition of the correlation matrix does not identify the normal modes of $\mathcal{A}$. Identification of the forcings that account for the variance of the statistical steady state for non-selfadjoint dynamical systems is an important theoretical question. We have shown that these forcings can be obtained by solving the back Liapunov equation (2.4), and we call them the back K-L decomposition. It may be argued that spanning the forcing functions found from the back K-L decomposition is at least as necessary in dynamical investigation of the system as spanning the response functions found from the K-L decomposition, as suggested by Lumley[10].

3. Stochastic forcing of channel flows.

The linearized Navier-Stokes equations governing evolution of disturbances in steady mean flow with x velocity $U(y)$ are:

$$\left(\frac{\partial}{\partial t} + U\frac{\partial}{\partial x}\right)u + U_y v = -\frac{\partial}{\partial x}p + \frac{1}{R}\Delta u , \qquad (3.1.a)$$

$$\left(\frac{\partial}{\partial t} + U\frac{\partial}{\partial x}\right)v = -\frac{\partial}{\partial y}p + \frac{1}{R}\Delta v , \qquad (3.1.b)$$

$$\left(\frac{\partial}{\partial t} + U\frac{\partial}{\partial x}\right)w = -\frac{\partial}{\partial z}p + \frac{1}{R}\Delta w , \qquad (3.1.c)$$

$$\frac{\partial}{\partial x}u + \frac{\partial}{\partial y}v + \frac{\partial}{\partial z}w = 0 , \qquad (3.1.d)$$

where (u, v, w) denote perturbation velocities in the x, y, z directions respectively, $\Delta \equiv \frac{\partial^2}{\partial x^2} + \frac{\partial^2}{\partial y^2} + \frac{\partial^2}{\partial z^2}$ is the Laplacian operator, and $R \equiv \frac{U_o L}{\nu}$ is the Reynolds number, U_o is the maximum velocity in a channel of half width L, and ν is the kinematic viscosity. We impose no slip boundary conditions at $y = \pm 1$. Couette flow has mean flow $U = y$, and Poiseuille flow has $U = 1 - y^2$.

It is useful to eliminate u, p, w in favor of the normal velocity v and normal vorticity $\omega \equiv \frac{\partial}{\partial z}u - \frac{\partial}{\partial x}w$. The reduced equations take the form:

$$\left(\frac{\partial}{\partial t} + U\frac{\partial}{\partial x}\right)\Delta v - U_{yy}\frac{\partial}{\partial x}v = \frac{1}{R}\Delta\Delta v , \qquad (3.2.a)$$

$$\left(\frac{\partial}{\partial t} + U\frac{\partial}{\partial x}\right)\omega = \frac{1}{R}\Delta\omega - U_y\frac{\partial}{\partial z}v , \qquad (3.2.b)$$

with equivalent boundary conditions $v = \frac{\partial}{\partial y}v = \omega = 0$ at $y = \pm 1$.

Consider a single Fourier component:

$$v = \hat{v}\exp(ikx + ilz) , \qquad (3.3.a)$$

$$\omega = \hat{\omega}\exp(ikx + ilz) , \qquad (3.3.b)$$

physical variables being identified with the real part of these complex forms. The field equations can be written in the compact form:

$$\frac{\partial}{\partial t} \begin{bmatrix} \hat{v} \\ \hat{\omega} \end{bmatrix} = \begin{bmatrix} \mathcal{L} & 0 \\ \mathcal{C} & \mathcal{S} \end{bmatrix} \begin{bmatrix} \hat{v} \\ \hat{\omega} \end{bmatrix} , \tag{3.4}$$

in which the Orr-Sommerfeld operator $\mathcal{L}$, the Squire operator $\mathcal{S}$, and the coupling operator $\mathcal{C}$ are defined as:

$$\mathcal{L} = \Delta^{-1}(-ikU\Delta + ikU_{yy} + \Delta\Delta/R) , \tag{3.5.a}$$

$$\mathcal{S} = -ikU + \Delta/R , \tag{3.5.b}$$

$$\mathcal{C} = -ilU_y , \tag{3.5.c}$$

with $\alpha^2 \equiv k^2 + l^2$, and $\Delta = \frac{d^2}{dy^2} - \alpha^2$.

We define the perturbation energy density, in the usual manner, as:

$$E(k,l) = \frac{kl}{16\pi^2} \int_{-1}^{1} dy \int_{0}^{2\pi/k} dx \int_{0}^{2\pi/l} dz \, (u^2 + v^2 + w^2) \tag{3.6.a}$$

$$= \frac{1}{8} \int_{-1}^{1} dy \left(\hat{v}^*\hat{v} + \frac{1}{\alpha^2}\frac{d}{dy}\hat{v}^*\frac{d}{dy}\hat{v} + \frac{1}{\alpha^2}\hat{\omega}^*\hat{\omega} \right) \tag{3.6.b}$$

$$= \frac{1}{8} \int_{-1}^{1} dy \, \psi' . \mathcal{M}\psi , \tag{3.6.c}$$

with $\psi \equiv \begin{bmatrix} \hat{v} \\ \hat{\omega} \end{bmatrix}$. The energy metric, $\mathcal{M}$, is given by:

$$\mathcal{M} = \begin{bmatrix} -\Delta & 0 \\ 0 & I \end{bmatrix} , \tag{3.7}$$

where I is the identity matrix. In deriving (3.6.b) we made use of:

$$\hat{u} = -\frac{i}{\alpha^2} \left(l\hat{\omega} - k\frac{d}{dy}\hat{v} \right) , \tag{3.8a}$$

$$\hat{w} = \frac{i}{\alpha^2} \left(k\hat{\omega} + l\frac{d}{dy}\hat{v} \right) . \tag{3.8b}$$

In deriving (3.6.c) we integrated by parts and made use of the boundary conditions.

Consider now the discrete equivalent of (3.4). The state vector for an N level discretization is,

$$
\psi = \begin{bmatrix} \hat{v}_1 \\ \cdot \\ \cdot \\ \hat{v}_i \\ \cdot \\ \cdot \\ \hat{v}_N \\ \hat{\omega}_1 \\ \cdot \\ \cdot \\ \hat{\omega}_i \\ \cdot \\ \cdot \\ \hat{\omega}_N \end{bmatrix} , \tag{3.9}
$$

and the initial value problem (3.4) assumes the discretized form:

$$
\frac{d}{dt}\psi = \mathcal{A}\psi , \tag{3.10}
$$

in which the linear dynamical operator, $\mathcal{A}$, is the discretized form of $\begin{bmatrix} \mathcal{L} & 0 \\ \mathcal{C} & \mathcal{S} \end{bmatrix}$. According to Lax's equivalence theorem, if the discretization is consistent and stable integrations based on the discretized operator converge to those of the continuous operator[12]. In sequel stability has been tested by doubling the number discretization levels.

The stochastic dynamical system associated with (3.10) is:

$$
\frac{d}{dt}\psi = \mathcal{A}\psi + \mathcal{F}\epsilon , \tag{3.11}
$$

in which ϵ is a random Gaussian white noise process, and $\mathcal{F}$ a forcing distribution initially assumed to provide unit energy density driving to each of the N functions f^i that form the columns of $\mathcal{F}$. The analysis presented in section 2 applies with the metric $\mathcal{M}$ given by (3.7).

Alternatively, we could have forced, for instance, with unit enstrophy by appropriately modifying the metric. In the energy metric the maintained variance corresponds to the ensemble average energy density, $< E >$, of the statistical steady state. Note that the operator $\mathcal{A}$ is stable, $i.e$ has a spectrum with negative real parts, for all R in the case of the Couette flow, while for the Poiseuille flow $\mathcal{A}$ is stable for $R < 5772.22$ [13,14]. We will limit our investigation to $R \leq 5000$, so that it may be anticipated that both the Couette and the Poiseuille flow will reach a statistical steady state.

Consider first the Fourier component with $k = 1$. The ensemble average energy density as a function of R for a variety of channel flows is shown in Fig. 3.1. First consider the 2D case with $l = 0$ and no flow (curve 5), and the 3D case with $l = 2$ and no flow (curve 3). Note the linear growth of $< E >$ with R as would be expected for a self-adjoint dynamical system. The increased variance (nearly double) in the 3D flow as compared to the 2D flow can be attributed to the larger number of forcing modes in the former. In the case of no flow $\mathcal{A}$ is self-adjoint and consequently the K-L decomposition of the variance to obtain the response functions yields the same structures as the back K-L decomposition to obtain the forcing function. The $< E >$ maintained in 2D Couette flow with unit shear,$S = 1$, is shown in curve 4, from which it is apparent that the the non-selfadjointness of the operator leads to increased $< E >$. Comparison can be made with the perturbation variance sustained in unbounded 2D Couette flow[4]. In the unbounded 2D flow $< E >$ was found to asymptote as $S- > \infty$ to three times the variance at zero shear. In the bounded 2D flow for $k = 1$ and $R = 750$ the variance reaches an asymptotic value nearly twice that sustained when there is no flow which is consistent with the previous result. The sustained

variance when the full 3D effects are allowed is shown for the Couette and the Poiseuille flow as a function of R in Fig. 3.1 curves (1) and (2) respectively. Note the remarkable increase of variance with Reynolds number ($< E > \approx R^{3/2}$).

We have obtained the ensemble average energy density under the assumption that each degree of freedom receives unit input of forcing. As the number of degrees of freedom increase the total variance converges, because the principal contribution to the variance is made by a few structures. If we want to address the question of amplification of background disturbances we have of necessity to make assumptions about the spectral energy distribution of the background noise. The simplest calculation, which also turns out to be also indicative, is to assume that the noise energy is distributed equally in $R^{1/2}$ modes. Then the noise amplification is the total variance, shown in Fig. 3.1, divided by $R^{1/2}$. The resulting amplification is shown in Fig. 3.2. Observe that the amplification is larger for Couette flow, reaching a 100 fold at $R \approx 750$, while for Poiseuille flow this level is reached only at $R \approx 1300$. Also note the small amplification of the 2D flow. To relate the level of maintained variance to the amplification of background noise needed to instigate transition to turbulence, recall that the fluctuation energy which is typical of a turbulent state is approximately 1% of the energy of the mean flow[15]. Consequently, background fluctuations of 1% rms in the velocity field require a 100 fold amplification for the variance of the flow to attain an amplitude characteristic of turbulence. If the amplification for the $k = 1, l = 2$ component is typical, our analysis predicts that transition for the 3D Couette occurs at $R \approx 750$ and for the 3D Poiseuille at $R \approx 1300$, while for the 2D Couette transition does not occur. These transition values are remarkably consistent with observations.

5. Conclusions

We have shown that stochastic excitation of viscous shear flow produces high levels of variance if the Reynolds number of the flow is sufficiently large. This variance arises primarily from excitation of a restricted subset of favorably configured forcing functions which can be found as the solutions of a Liapunov equation. In a similar manner, the response functions that form the primary structures of the maintained variance can be identified with solutions of a related Liapunov equation. The primary forcing functions determine a low dimensional subspace which must be spanned by a basis for the stochastic dynamics while the primary response functions similarly determine a subspace which must also be spanned by the dynamical basis. The distinction between the forcing and response functions is a consequence of the non-selfadjointness of the linear dynamical operator and no such distinction arises in unsheared flow, simple convection, or other dynamical systems characterized by self-adjoint operators.

Observations of transition from laminar to turbulent flow have consistently shown, since the experiments of Reynolds[16], that transition is highly sensitive to background disturbances. The reason for this sensitivity can be understood from this work to arise from the existence of a subset of forcings which produce high levels of variance even though these canonical problems typically are asymptotically stable at the Reynolds numbers for which transition is found to occur. Unless the background disturbance field is contrived to have a null projection on the primary forcing functions these will amplify to produce the level of variance observed in turbulent flows when forcing typical of ambient background variance in experiments is imposed.

The fact that stochastic forcing has been shown to produce high levels of variance and the fact that transition is observed to depend on free stream turbulence levels taken together lead to the theoretical explanation for transition advanced in this work.

Acknowledgements

References

[1] S. J. Davies and C. M. White, "An experimental study of the flow of water in pipes of rectangular section," *Proc. Roy. Soc. A* 119 , 92 (1928).

[2] W. Pfenninger, "Boundary layer suction experiments with laminar flow at high Reynolds numbers in the inlet length of a tube by various suction methods" in *"Boundary Layer and Flow Control"*, edited by G. V. Lachmann (Pergamon, Oxford, 1961), p. 970.

[3] R. Kubo, M. Toda, and N. Hashitsume, *Statistical Physics II* (Springer-Verlag, New York, 1983).

[4] B. F. Farrell and P. J. Ioannou, "Stochastic Forcing of Perturbation Variance in Unbounded Shear and Deformation Flows," *J. Atmos. Sci.* , in print.

[5] K. M. Butler and B. F. Farrell, "Three-dimensional optimal perturbations in viscous shear flow," *Phys. Fluids A* 4, 1637 (1992).

[6] B. F. Farrell and P. J. Ioannou, "Optimal Excitation of 3D Perturbations in Viscous Constant Shear Flow," *Phys. Fluids A*, submitted.

[7] S. Lefschetz, *Differential Equations: Geometric Theory* (Dover Publications, New York,

268

1963).

[8] M. Loeve, *Probability Theory, Vol. II* (Springer-Verlag, New York, 1978).

[9] E. N. Lorentz, "Empirical orthogonal functions and statistical weather prediction," Rep. 1, Statist. Forecasting Project, MIT, (1956).

[10] J. L. Lumley, "The structure of inhomogeneous turbulent flows" in *"Atmospheric Turbulence and Radio Wave Propagation"*, edited by A. M. Yaglom and V. I. Tatarsky (Nauka, Moscow, 1967), p. 166.

[11] G. R. North, "Empirical orthogonal Functions and Normal Modes," *J. Atmos. Sci.* 41, 879 (1984).

[12] R. D. Richtmeyer and K. W. Morton, *Difference Methods for Initial Value Problems* (Interscience Publishers, New York, 1967).

[13] W. Heisenberg, "Über Stabilität und Turbulenz von Flussingkeitsströmen," *Ann. Phys.*, *Lpz.(4)* 74 (1924).

[14] S. A. Orszag, "Accurate solution of the Orr-Sommerfeld stability equation," *J. Fluid Mech.*50, 689 (1971).

[15] A. A. Townsend, *The Structure of Turbulent Shear Flow* (Cambridge University Press, Cambridge, 1976).

[16] O. Reynolds, "An experimental investigation of the circumstances which determine whether the motion of water shall be direct or sinuous, and the law of resistance in parallel channels," *Phil. Trans.*, 51 (1883).

Fig. 3.2. Variance maintained by various flows as a function of R for unit forcing with

$k = 1, l = 2$. The forcings are assumed to excite $R^{1/2}$ modes. The curves shown are for

3D Couette flow, 3D Poiseuille flow, and 2D Couette flow.

$$k = 1 \ l = 2$$
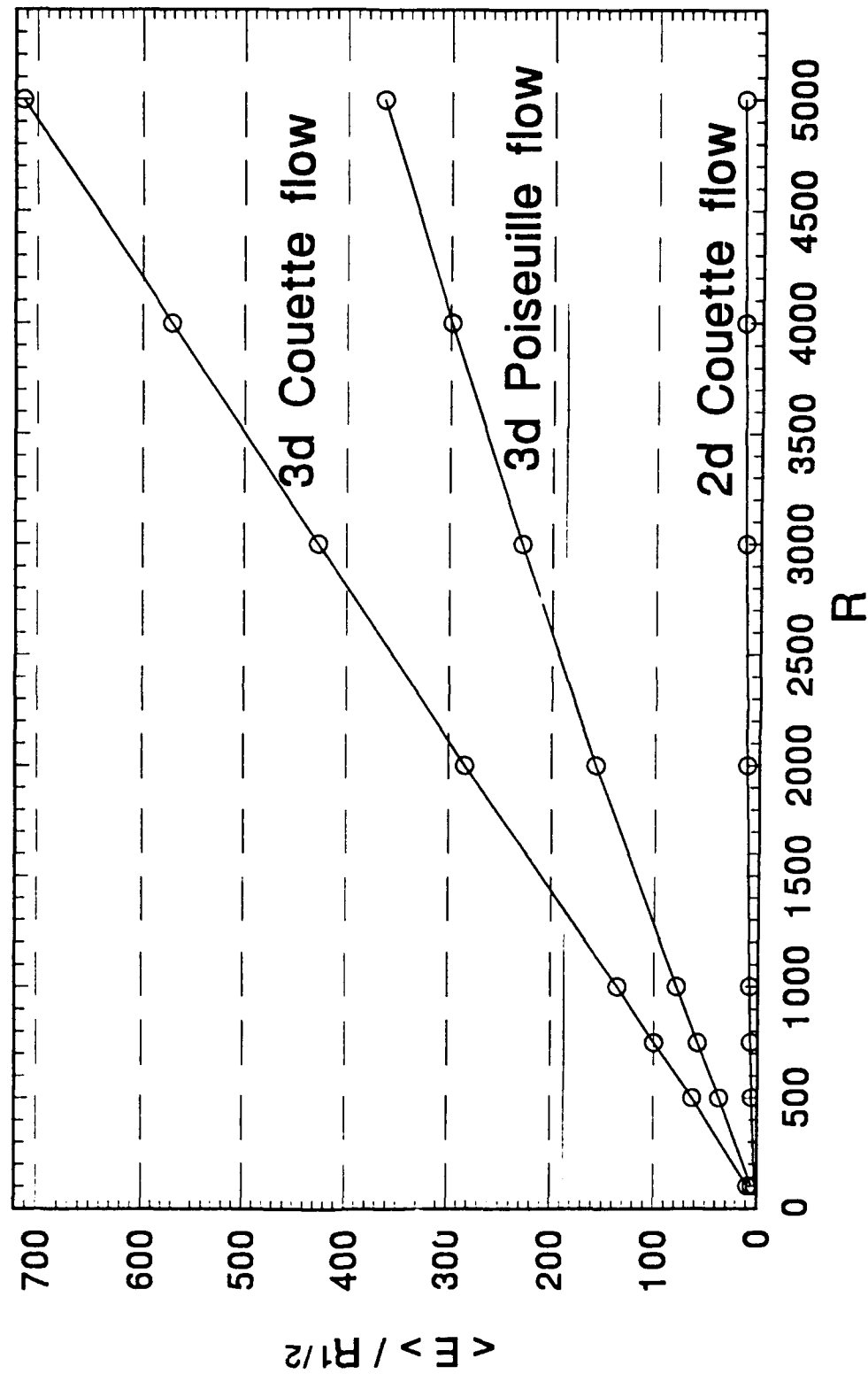
Fig. 3.1. The ensemble average energy density, $< E >$, for various channel flows as a function of Reynolds number, R. Curve 1 is for 3D Couette flow with $k = 1, l = 2$. Curve 2 is for 3D Poiseuille flow with $k = 1, l = 2$. Curve 3 is for a 3D channel with $U = 0$ and $k = 1, l = 2$. Curve 4 is for 2D Couette flow and $k = 1$. Curve 5 is for a 2D channel with $U = 0$ and $k = 1$. Curves 3 and 5 are linear in R while in curves 1 and 2 $< E >\approx R^{3/2}$.

1 : 3d Couette flow , k = 1 l = 2
2 : 3d Poiseuille flow, k = 1 l = 2
3 : 3d with U = 0, k = 1 l = 2
4 : 2d Couette flow , k = 1
5 : 2d with U = 0, k = 1
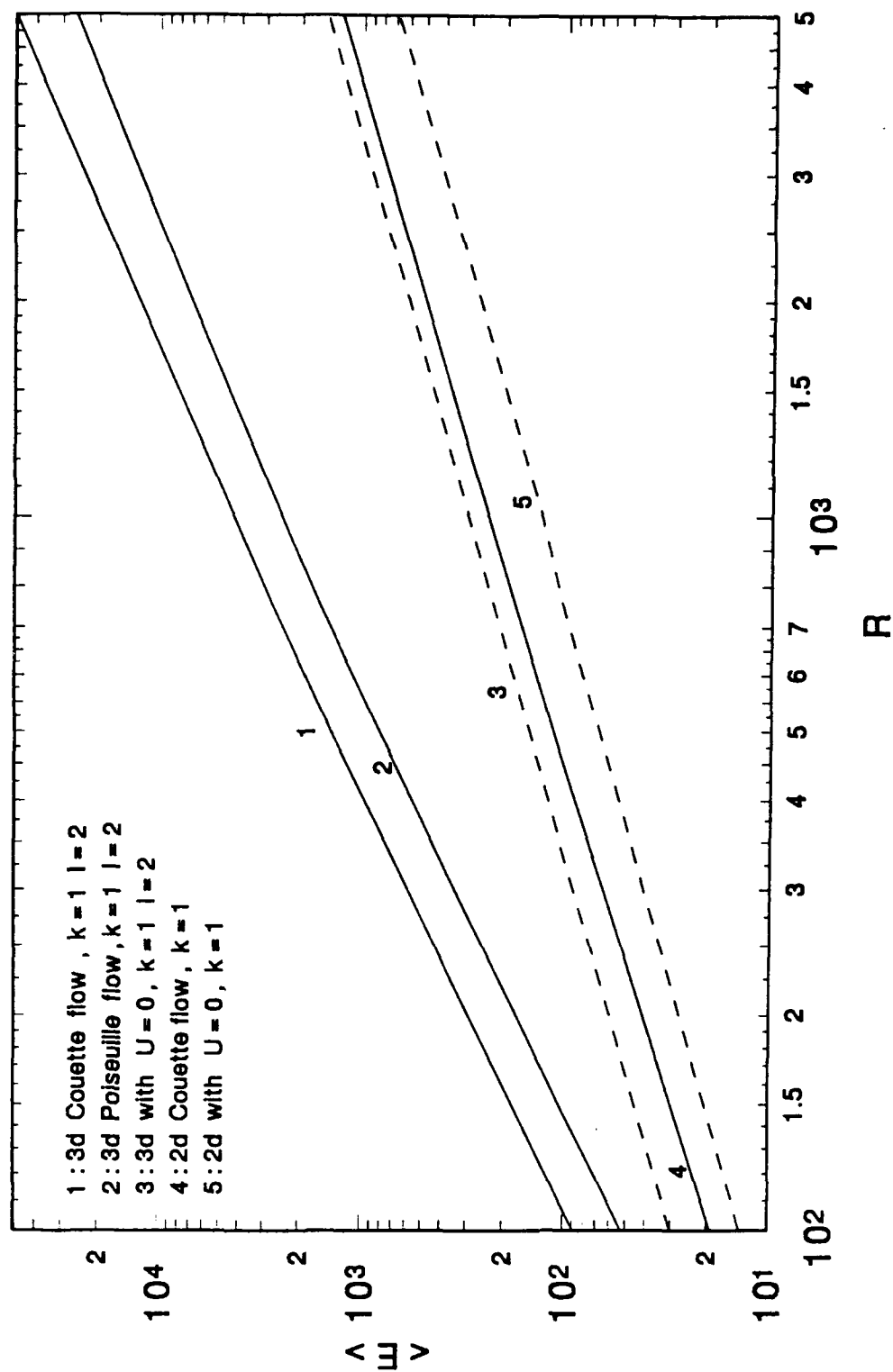
A Nightside Atmosphere of Io?

Raymond P. LeBeau, Jr.

Several models of the atmosphere of Io have indicated that there may exist a high velocity/supersonic flow of material away from the subsolar point towards the nightside of Io (Ingersoll et al., 1985; Ingersoll, 1989; Moreno et al., 1990). Despite this large mass flux to the nightside of the moon, the rapid condensation of sulfur dioxide to the surface in these cold regions probably would result in a negligible SO_2 atmosphere on the darkside of Io. However, photodissociation of the sulfur dioxide into other chemical constituents (sulfur, oxygen, sulfur monoxide) on the dayside would result in a flux of non-condensing constituents to the nightside which could yield a significant atmosphere. This study numerically models such a process in a sublimation-driven atmosphere, determining the chemical composition the nightside atmosphere over a variety of subsolar and darkside temperatures. The results indicate that a non-SO_2 atmosphere on the nightside may reach pressures on the order of 10^{-8} bar, significantly above that needed to explain the Pioneer 10 occultation data. Therefore, non-sulfur dioxide constituents of the atmosphere may provide a explanation for excess pressure detected by Pionner 10 at the Ionian terminator.

I Overview

The Io-Jupiter system is one of the most active and complicated in the solar system. On the moon's surface volcanic vents driven by tidal forces spew gas hundreds of kilometers above the frost-covered ground. Surrounding the orbit of Io, a large torus consisting of neutral and ionized sulfur and oxygen is continuously maintained by material from the moon. The ions of the torus are swept up in the strong, rotating magnetic field of Jupiter, striking Io at relative velocities greater than 50 km/s. These collisions create a self-supplying mechanism for the torus, sputtering particles into the Ionian corona.

In the midst of this complex system, there likely exists a tenuous, yet relatively substantial atmosphere, covering a portion of the moon in sulfur dioxide gas sublimated from the surface frost or outgassed from the vents. Since the detection of an ionosphere during the Pioneer 10 occultations in 1975, there have been a series of observational and computational efforts that have begun to define the nature of this atmosphere; however, the atmosphere is still not well understood, in part because it has proven difficult to observe directly. Yet, numerous observations of the Io-Juptier system do provide guidelines to understanding the movement, distribution, and composition of the Ionian atmosphere.

While observations of post-eclipse brightening had suggested that Io might possess an atmosphere, the Pioneer 10 occultations provided the first strong indication that an atmosphere of some sort existed on Io (Kilore et al., 1975). The occultation geometry (fig 1.1) allowed electron density profiles of an ionosphere at 81.5 and 94.4 degrees colatitude (relative to the subsolar point) to be measured. Based on the profiles, the surface pressure of the atmosphere can be inferred to be on the order of 5×10^{-10} bars in the vicinity of the terminator (90 degrees colatitude).

Another important observation was the detection of sulfur dioxide surface frost on Io. The reflectance spectrum of Io shows a strong 4.05 μm absorption band that corresponds to

a sulfur dioxide feature which best fits surface frost as opposed to atmospheric gas (Fanale et al., 1979; Howell et al., 1984). The depth of the absorption band implies that around 80% of the surface is covered with optically thick frost, providing a potential source for a sulfur dioxide atmosphere.

The direct detection of sulfur dioxide gas in the atmosphere was made by the Voyager IRIS observation of a 7.4 μm absorption in the thermal radiation spectrum of the hot spot Loki. The depth of this absoption indicates that the surface pressure of the gas was about 10^{-7} bars, consistent with the vapor pressure of sulfur dioxide at 130 K which would be a typical frost temperature at the time of this observation. Other observations, notably the disk-averaged IUE spectrum from 0.20-0.32 μm (Butterworth et al., 1980) imply subsolar frost temperatures in the vicinity of 125 K, but even at these temperatures the vapor equilibrium of SO_2 would yield a substantial atmosphere.

A ready interpetation of this collection of observations is that Io possesses a locally-buffered sulfur dioxide atmosphere that reaches significant pressures on the warmer dayside of the moon. However, the vapor pressure of SO_2 for surface frost temperatures that can be reasonably expected near the terminator is considerably less than the pressures derived from the Pioneer 10 occultation. For example, at 105 K the vapor pressure of sulfur dioxide is only 3×10^{-11} bar. Therefore, while this simple model seems to be a good starting point, the actual atmosphere must involve some other physical mechanisms.

Two possible mechanisms that have been suggested are local hot spot activity and atmospheric constituents other than sulfur dioxide. The first approach explains the Pionner 10 occultation as having looked through an atmospheric 'bubble' resulting from volcanic venting in the immediate vicinity. The second method relies on the atmosphere of Io being dominated by a gas with a higher vapor pressure than sulfur dioxide (such as O_2) in the region about the terminator. It is the feasability of this second mechanism that is discussed in this paper.

II Dayside Atmosphere

The general form of a sulfur dioxide atmosphere in approximate vapor equilibrium with a frost surface is shown in fig. 2.1. The atmosphere is thickest (surface pressure of roughly 10^{-7} to 10^{-8} bars) in the vicinity of the subsolar point. The surface pressure decreases towards the terminator until the nightside, where the atmosphere of SO_2 is exospheric in nature. Ingersoll et al. (1985, hereafter referred to as ISS85) demonstrated that these large pressure gradients would induce supersonic winds flowing outward from the subsolar region towards the terminator. However, local buffering rapidly absorbs excess outflowing material, such that the surface pressure is always within a few percent of vapor pressure and therefore cannot account for the higher pressure values at the terminator given by the Pionner 10 observations

While the pure sulfur dioxide atmosphere models result in exospheric surface pressures at the terminator, photodissociation of SO_2 could produce significant quanities of non-condensing gases (notably O, O_2, and SO), yielding a substantial, non-sulfur dioxide atmosphere at the terminator and on the nightside of the moon. A schematic of such an atmospheric model is shown in figure 2.2. In the vicinity of the subsolar point, the atmosphere is predominantly sulfur dioxide, with the photodissociaton of SO_2 dominating

the chemistry. Gradually, the condensing of sulfur dioxide onto the surface reduces its partial pressure to levels comparable and then possibly much below that of the other consituent gases. The chemistry would likewise change, with different reactions and possibly the condensation of sulfur governing the chemical composition.

2.1 Methodology

In order to more readily model such an atmosphere, certain simplifications are made to the physical system. First, the surface of Io is treated as uniformly covered with SO_2 frost whose temperature is governed by thermal equilibrium with incoming radiation. A correlative assumption is that the atmosphere is treated as optically thin with regard to photodisocciation. Based on the results of ISS85, frictional interaction with the surface is treated as negligible. A final simplification is to ignore the rotation of the moon.

With these modifications, the atmosphere can be treated as symmetric about the subsolar-antisolar axis. To reduce the problem to one-dimension, the atmosphere will be treated as a series of hydrostatic, vertically adiabatic columns of ideal gas with a constant horizontal velocity with repsect to altitude. As demonstrated in ISS85, with these assumptions the equations of fluid motion are vertically integrable, yielding three equations that govern the variation of pressure, temperature, and horizontal velocity with repsect to co-latitude. The resulting equations (from ISS85) are:

$$\frac{1}{r \sin \theta} \frac{d}{d\theta} (\frac{p}{g} v \sin \theta) = E \tag{2.1}$$

$$\frac{1}{r \sin \theta} \frac{d}{d\theta} (\frac{p}{g} v^2 \sin \theta) = -\frac{1}{r} \frac{d}{d\theta} (\beta C_p' T p) + \tau \tag{2.2}$$

$$\frac{1}{r \sin \theta} \frac{d}{d\theta} (\frac{p}{g} v (\frac{v^2}{2} + C_p T)) = Q \tag{2.3}$$

where p, v, and T stand for atmospheric pressure, velocity, and temperature at the surface (distinct from the surface frost temperature), θ is colatitude measured from the subsolar point, β is a parameter defined by $R/(R + C_p)$ (R is the ideal gas constant), and E, τ, and Q represent the flux of mass, momentum, and energy from external sources respectively.

For this model, the only external mass flux considered is the sublimation/condensation of material with the surface. This flux is defined by:

$$E = \alpha \sqrt{\frac{1}{2\pi R T_f}} (p_v - p) \tag{2.4}$$

with α, the sticking coefficient, treated as unity for sulfur dioxide. The vapor pressure of the surface frost (p_v) is a function of the frost temperature (T_f) (Wagman, 1979):

$$p_v = 1.516 x 10^{13} (Pa) exp(-4510(K)/T_f) \tag{2.5}$$

and frost temperature is determined from:

$$T_f = (Tss - Tas) \cos^{\frac{1}{4}} \theta + Tas \tag{2.6}$$

274

with subsolar (Tss) and nightside (Tas) temperature as model parameters.

With regard to chemistry, the flux of the individual chemical constituents, in terms of column densities (N), is governed by:

$$\frac{1}{r \sin \theta} \frac{d}{d\theta} (N_x v \sin \theta) = (P_x - L_x) \tag{2.7}$$

where x represents S, O, O_2, and SO. Production and loss of the constituents due to chemical reactions, photodissociation, and condensation onto the surface are represented by P_x and L_x. In regions where sulfur dioxide is not treated as dominant, its column density is found from:

$$\frac{p}{m_{avg} g} - N_s - N_o - N_{o_2} - N_{so} = N_{so_2} \tag{2.8}$$

These five chemical flux equations in conjuction with the three flow equations define the fluid motions in the atmospheric model.

The important photodissociation and chemical reactions for this atmosphere are listed in Table 2.1. The various dissociation (J) and reaction (k') rates are from Summers (1985), which studied the potential vertical composition of a static dayside atmosphere. In this study, the chemistry was based on local number density, so it is necessary to convert the given reaction coefficients to a form applicable to column densities. Assuming that the atmosphere is optically thin, adiabatic, and well-mixed (such that the mixing ratios of the constituents are constant with respect to altitude), the reaction equations may be integrated over a column to yield the following form:

$$\dot{N} = k N_1 N_2 ... N_{n+1} \tag{2.9a}$$

where N represents the column densities of the various reactants and catalysts. The relation between the number density (k') and column density (k) coefficients is:

$$k = k'(\frac{\gamma}{\gamma + n})(\frac{1}{H})^n \quad where \quad \gamma = \frac{C'_p}{C'_v}, \quad H = \frac{RT}{g} \tag{2.9b}$$

for an (n+1)-body reaction. This conversion treats the k's as constant with respect to the integration in altitude. In this study, the mass-average temperature of the column was used for the temperature dependence in the k' terms (but not in the conversion calculation itself, which is based on surface temperature). The photodissociation coefficients are not modified by the integration process but for this study did decrease as $\cos \theta$ due to the spherical geometry of the model. By combining these photodissociation and reaction equations, the formulas for P_x and L_x are constructed, forming the right-hand side of the chemical flux equations.

To solve the model equations, different approaches are used depending on whether sulfur dioxide is or is not the dominant constituent of the atmosphere. In regions where SO_2 is dominant, the flow equations have an approximate analytical solution developed by Ingersoll (1989). By setting the atmospheric surface pressure equal to the vapor pressure

of the frost, the flow equations can be solved to give the following equations for velocity and surface temperature:

$$v = \sqrt{\frac{2\beta C'_p T_o}{3-\beta}(\frac{p_o - p}{p})} \qquad (2.10)$$

$$T = T_o - \frac{v^2}{2C'_p} \qquad (2.11)$$

In the chemistry equations, the pressure and column densities of sulfur dioxide are considered equal to the total atmospheric pressure and column density respectively. The column densities of the remaining constituents are found by solving the flux equations for each constituent numerically using a fourth-order Runge-Kutta scheme.

When sulfur dioxide is not dominant it is necessary to solve both the flow and the flux equations numerically. As detailed in ISS85, equation 2.2 can be written as:

$$\frac{1}{r \sin\theta}\frac{d}{d\theta}(\frac{p}{g}(v^2 + \beta C'_p T)\sin\theta) = \frac{1}{gr\tan\theta}\beta C'_p T p + \tau \qquad (2.2a)$$

When written in finite-difference form, the three conservation equations have the form:

$$[pv]_{k+1} = [pv]_k + G_1 = g_1 \qquad (2.12)$$

$$[p(v^2 + \beta C'_p T)]_{k+1} = [p(v^2 + \beta C'_p T)]_k + G_2 = g_2 \qquad (2.13)$$

$$[pv(\frac{v^2}{2} + C'_p T)]_{k+1} = [pv(\frac{v^2}{2} + C'_p T)]_k + G_3 = g_3 \qquad (2.14)$$

where G_1, G_2, and G_3 are functions of the right-hand sides of equations 2.1, 2.2a, and 2.3 such as those used in Runge-Kutta schemes, k indicates the values at a given value of theta, and k+1 indicates the values at $\theta + \Delta\theta$. Therefore, the flux equations are solved by applying the fourth-order Runge-Kutta scheme to these equations and thereby deriving values for g_1, g_2, and g_3. Equations 2.12-2.14 are then solved algebraically to yield new values for p, v, and T as necessary. Simultaneously, the constituent flux equations are solved as in the sulfur dioxide dominant region, with the column density of SO_2 determined from equation 2.8. Additionally, 'constants' that are dependent on atmospheric chemical composition (such as C'_p) are updated as the composition changes in this numerical approach.

As demonstrated in ISS85, eliminating p and T from equations 2.12-2.14 results in a quadratic equation in velocity, which leaves the following solution for v:

$$v = \frac{g_2 \pm \sqrt{g_2^2 - 2\beta(2-\beta)g_1 g_3}}{g_1(2-\beta)} \qquad (2.15)$$

This equation defines the supersonic and subsonic regimes, with the negative radical solution for velocity corresponding to the subsonic case and the positive solution to the supersonic one.

The boundary between the sulfur-dioxide dominant and mixed composition regimes is chosen to be the colatitude where sublimation ends and condensation begins as derived

from the approximate analytical solution. This boundary is convenient for several reasons, foremost being that the flow is always supersonic beyond this point, eliminating the need to make a numerical extrapolation across the mach one boundary. Another advantage is that where E=0, the vapor pressure does equal the atmospheric surface pressure, allowing a smoother transition between the two domains. Finally, as the results show, this point is well within the region were sulfur dioxide dominates the atmosphere.

Therefore, the numerical model first calculates the atmospheric pressure, velocity, temperature, and composition from the subsolar point to the E=0 boundary using the sulfur dioxide dominant approach, and then continues to terminator using the second method. At the subsolar point, the initial values for the flow variables are the local vapor pressure, local frost temperature, and zero velocity. Initial column densities of the non-sulfur dioxide constituents are derived by approximately balancing equation 2.7, with the outflow velocity determined from a Taylor expansion about the subsolar point. Setting the change in the number density of the given constituent (x) to zero from $\theta = 0$ to $\theta = \Delta\theta$, the initial concentrations may be found from:

$$c_{x,o} N_{so2,o} \frac{2}{R} [\frac{\partial v}{\partial \theta}]_o + L_{x,o} = P_{i,o} \tag{2.16}$$

where c is the concentration and the zero subscript indicates the given quantity evaluated at $\theta = 0$. The velocity derivative is determined from the analytic solution (eqn. 2.10):

$$[\frac{\partial v}{\partial \theta}]_o = \sqrt{(\frac{2\beta C_p T_o}{(3 - \beta)})\frac{B(Tss - Tas)}{8T_o^2}} \tag{2.17}$$

where B=4510 K (from eqn. 2.5). The values of τ and Q are taken from IN89:

$$E > 0 : \quad \tau = 0, \quad Q = C_p T_f E$$
$$E < 0 : \quad \tau = vE, \quad Q = (\frac{v^2}{2} + C_p T)E \tag{2.18}$$

These values are already incorporated into equations 2.10-2.11, and so are only explicitly needed in the non-sulfur dioxide dominant region.

2.2 Results

In order to account for a range of reasonable subsolar and nightside temperatures, results from several atmospheric models are presented. The range of temperature values studied varies from 120-130 K for Tss, and 50-80 K for Tas. For all cases studied, the assumption of SO_2 dominance in the sublimating region proved valid, with the sum of the partial pressures of S, O, O_2, and SO consistently less than 3% of the total pressure at the E=0 boundary.

In general, all cases result in atmospheres that roughly correspond to the model of figure 2.2. As illustrated in figure 2.3a, the flow variables follow expected trends, with the temperature and pressure decreasing and velocity increasing with increasing subsolar colatitude. These variations in the flow variables are nearly indistinguishable from the pure sulfur dioxide models (see ISS85) until beyond 70 degrees colatitude. At this point, sulfur dioxide begins to lose dominance (fig. 2.3b), with sulfur monoxide and atomic oxygen becoming the important atmospheric constituents Thus, the overall atmospheric pressure does not collapse to exospheric values, as in the case of the pure SO_2 atmosphere, but rather levels off at about 4×10^{-10} bars. Therefore, while the region in which the non-sulfur dioxide constituents are significant is relatively small, the model indicates that they will dominate in the vicinity of the terminator with total pressures comparable to that observed by Pioneer 10.

However, the important chemistry actually occurs in the region about the subsolar point, as is illustrated in figure 2.4. This plot of the chemical mass flux (essentially the left-hand side of equation 2.7) shows that the production of non-SO_2 constituents is primarily through the photodissociation of sulfur dioxide in the thicker region of the atmosphere. In fact, except for the minor constituent of molecular oxygen (O_2), the magnitude and mixing ratios of the non-sulfur dioxide atmosphere are essentially established by a short distance into the condensing region. Physically, this is the result of less photodissociation due to decreasing sulfur dioxide and of higher flow velocities which reduce the effective time in which the chemical reactions occur relative to horizontal distance as the terminator approaches. Therefore, the dayside models indicate that the non-sulfur dioxide atmosphere is formed primarily by photodissociation within 45 degrees of the subsolar point, beyond which it is relatively constant except for geometric expansion. The eventual dominance of SO and O near the terminator is not a result of local chemistry, but the rapid condensing of sulfur dioxide onto the surface revealing a previously formed, non-SO_2 atmosphere.

Qualtitatively, the other four cases presented are similar to case 1: the non-sulfur dioxide atmosphere is the result of photodissociation about the subsolar point and becomes dominant near the terminator as the sulfur dioxide condenses out to very low surface pressures (fig. 2.5-2.8). In general, the variation of subsolar temperature changes the overall pressure of the atmosphere (cases 2. 5), decreasing from 4×10^{-10} bars at the terminator for Tss = 130 K to 2×10^{-11} bars for Tss = 120 K. The primary effect of decreasing the nightside temperature (cases 3. 4) is to increase the angular size of the region where sulfur dioxide is the dominant constituent of the atmosphere. In the end, the models are really more similar than different—the atmospheric pressure at the terminator is 0.2 - 0.4% of the subsolar pressure and the mixing ratios of O, SO, and S are likewise relatively invariant

278

for all the cases studied–with the most important parameter effect being the reduction of overall pressure with lower subsolar temperatures.

III Nightside Atmosphere

The results of the dayside model show that a substantial flux of sulfur, oxygen, and sulfur monoxide could flow across the terminator to the nightside of the planet. While this material would mostly be reincorporated into the surface frost as sulfur and sulfur dioxide, this process is limited to the rate at which the oxygen is recombined into SO_2, which is relatively slow at the lower nightside temperatures. The implication is that the non-SO_2 flux could supply a significant darkside atmosphere.

3.1 Methodology

As suggested by ISS85, this nightside atmosphere would probably be relatively stagnant with a near-uniform temperature with respect to latitude. The drastic drop in velocity from dayside to nightside would be in large part due to a hydraulic jump (or low temperature shock) that would occur when the supersonic flow runs against a near-static atmosphere. At this jump, the flow would abruptly move from the supersonic to the subsonic regime, with a correlative increase in pressure and temperature. A schematic of a simple model of such a nightside atmosphere is illustrated in fig. 3.1, in which the dark side atmosphere is treated as having a uniform surface temperature and pressure with no velocity field. The jump location is determined by where the backside pressure equals the post-jump (subsonic) pressure of the dayside flow.

Given this atmospheric model, the nightside atmosphere does not require solving the flow equations once a temperature is selected. Rather, the problem is to solve modified versions of the chemistry equations such that the influx of material at the shock is balanced by an outflux of material in the form of condensing sulfur dioxide. Assuming that excess sulfur dioxide condenses instantaneously, the chemistry equations take the form:

$$F_x + P_x - L_x = 0 \tag{3.1}$$

where P_x and L_x have the same form as before without the photodissociation terms (no sunlight on the nightside) for a given constituent (S, O, O_2, SO). F_x is the external flux term for the given constituent and is defined by:

$$F_x = \frac{(N_x v)_{jump} \sin \theta_{jump}}{R_{Io}(1 + \cos \theta_{jump})} \tag{3.2}$$

noting that N_x and v should be post-jump values. A similar equation also exists for SO_2 which technically gives five algebraic equations that can be solved for the nightside column densities of each consituent. However, only three of the equations are independent as the system is constrained by stochiometry, requiring that number of sulfur atoms and oxygen atoms be conserved:

$$N_{so2} = N_s + N_{so} \tag{3.3a}$$

$$2N_{so2} = N_{so} + N_o + 2N_{o2} \tag{3.3b}$$

Considering sulfur dioxide to be in vapor pressure equilibrium with the surface provides a fourth equation. The fifth equation comes from the fact that SO_2 acts as the source/sink for the other constituents. Therefore, the ratio of two oxygen atoms to each sulfur atom must be maintained in the non-SO_2 atmosphere, yielding:

$$N_o - N_{so} = 2(N_s - N_{o_2})$$

(3.4)

closing the algebraic system. Since the vapor equilibrium equation is independent of the other constituent concentrations, the problem is actually to find the nightside column densities of S, O, O_2, and SO by solving the four remaining equations.

The hydraulic jump values for the dayside atmosphere are found by taking the values of the flow variables at a given colatitude and solving for the negative branch of equation 2.15. Since the jump is relatively cold, it is reasonable to assume that there is no chemistry in the shock so that the mixing ratios of the constituents remain constant. Since for a given dayside atmosphere the flux is solely a function of colatitude, the iterative problem is to find the θ_{jump} that yields a post-jump pressure equal to that of the nightside atmosphere.

3.2 Results

Nightside atmospheres were calculated for each of the dayside cases at several nightside atmospheric temperatures. The temperatures chosen were bounded on the low end by the value of the antisolar frost temperature and at the high end by when sulfur became a major constituent of the atmosphere. High sulfur atmospheres cannot be realistically modeled by the given approach since significant amounts of sulfur would be expected to condense out of the atmosphere rapidly at the low frost temperatures of the nightside, an effect not accounted for in this model.

Figures 3.2 and 3.3 show the results for case 1 (Tss=130K, Tas=50K). The first figure illustrates the partial pressures of the various constituents at various nightside surface temperatures, noting both the temperature and the colatitude of the jump for each case. The second figure gives the actual total pressure jumps as a function of theta for each temperature case. A notable feature of the jump region is that the location of the jump (and therefore, the total pressure of the nightside atmosphere) is relatively insensitive to the nightside temperature. However, the chemical reaction rates are temperature sensitive. Therefore, the nightside temperature does play a significant role in determining the chemical composition of the nightside atmosphere, with the sulfur and monatomic oxygen concentration increasing and the diatomic oxygen concentration decreasing with increasing temperature. Overall, the darkside atmosphere is considerable, with surface pressures on the order of a hundred times larger than the terminator pressure of the dayside model and around 45% of the subsolar pressure.

The four other cases evidence the same trends shown in the case 1 models with regard to nightside temperature (fig. 3.4-3.7). The colder atmospheres are primarily sulfur monoxide, with some diatomic and monatomic oxygen, and the warmer ones consist of sulfur, monoatomic oxygen, and sulfur monoxide. In all cases variations in the nightside atmospheric temperature did not cause large variations in the backside pressure or the jump location, nor did changes in the nightside frost temperature have much effect on the overall nature of the atmosphere except for minor changes in jump location. Decreases in

subsolar temperature did lower the overall pressure of the nightside atmosphere (down to about 6.5×10^{-9} bars in case 2) as well as shifting the jump location closer to the subsolar point to where the flow would never become supersonic in the lower subsolar temperature cases. Yet, in all cases the terminator pressure is well above that needed to produce the Pioneer 10 data, implying that a non-sulfur dioxide atmosphere is a possible explanation of these observations.

3.3 Improvements to the Atmospheric Model

However, the zero-order nightside model has several problems which need to be addressed, primarily as a result of these 'nightside' atmospheres extending well onto the dayside. A model more consistent with an actual atmosphere (fig. 3.8) would treat three distinct regions: an accelerating dayside regime, a decelerating, post-jump dayside regime, and a static, nightside atmosphere. The post-jump dayside region would be modeled in the same manner as the supersonic region except that the subsonic solution to equation 2.15 would be applied. The nightside would be the same as before, except that its domain would be limited to just the dark hemisphere. The model would be solved iteratively by shifting the jump location until the pressures of the post-jump dayside and nightside regions matched at the terminator.

A second correction that must be made to the model is a more realistic treatment of sulfur. While it is reasonable to expect the oxygen and sulfur monoxide gas not to condense in this temperature and pressure regime, the vapor pressure of sulfur is probably less than that of sulfur dioxide and is likely to have considerable condensation rates. This rate will vary between a slow, diffusion dependent process when sulfur is a minor constituent to the faster, pure condensation of gas if sulfur becomes a dominant component of the atmosphere. This latter regime can be treated in the same manner as sulfur dioxide condensation (eqn. 2.8), but the former situation is a far more complex problem which has not been well-studied for the gases concerned. However, the known data as well as kinetic theory of gases may provide a reasonable approach to this regime as well.

With these modifications, a first-order model would reasonably be able to look at the possible nature of a sulfur dioxide sublimation-driven atmosphere on Io, within the context of a one-dimensional system. Further investigations could include the effect of different chemical reaction rates (notably those of Kumar (1982)), more complete interaction with the surface (catalytic reactions and conductive heat fluxes), and interaction with the torus (mass and plasma flux).

IV Conclusions

The models presented indicate that the photodissociation of sulfur dioxide in the region near the subsolar point could lead to a significant, non-SO_2 atmosphere both on the nightside and in the vicinity of the terminator. The surface pressure of this nightside atmosphere is primarily dependent on the pressure of the sulfur dioxide atmosphere at the subsolar point, while the chemical composition of the nightside atmosphere varies with the nightside atmospheric temperature. At cooler temperatures (60 K) the nightside atmosphere is predominantly sulfur monoxide and diatomic oxygen, while at warmer temperatures (100 K) it is a mixture of sulfur, monoatomic oxygen, and sulfur monoxide. In all cases the pressure at the terminator is at least sufficient to support the electron density profiles of the Pioneer 10 occultation.

However, while these results show the qualitative possiblities of a non-sulfur dioxide atmosphere, improvements must be made to the post-jump/nightside model to increase the quantitative accuracy. The first is that the post-jump region on the dayside of the moon needs to be approached in the same manner as the rest of the dayside, assuming a subsonic solution. The second is to include the deposition of sulfur onto the surface in some reasonable manner, as this would probably significantly reduce the nightside pressures. Yet, even with these modifications it is expected that a non-sulfur dioxide atmosphere in the vicinity of the terminator can be found with sufficiently high pressures to support the Pioneer 10 observations.

Acknowledgements

References

Butterworth, P. S., J. Caldwell, V. Moore, T. Owen, A. R. Rivola, and A. L. Lane (1980). An upper limit to the global SO_2 abundance on Io. *Nature* **285**, 308-309.

Fanale, F. P., R. Hamilton Brown, D. P. Cruikshank, and R. N. Clark (1979). Significance of absorption features in Io's IR reflectance spectrum. *Nature* **280**, 761-763.

Howell, R. R., D. P. Cruikshank, and F. P. Fanale (1984). Sulfur dioxide on Io: Spatial distribution and phsyical state. *Icarus* **57**, 83-92.

Kilore, A. J., G. Fjeldbo, B. L. Seidel, D. N. Sweetnam, T. T. Sesplaukis, P. M. Woiceshyn, and S. I. Rasool (1975). Atmosphere of Io from Pioneer 10 radio occultation measurements. *Icarus* **61**, 101-123.

Kumar, S. (1982). Photochemistry of SO_2 in the atmosphere of Io and implications on atmospheric escape. *J. Geophys. Res.*, **87**, 1677-1684.

Ingersoll, A. P., M. E. Summers, and S. G. Schlipf (1985). Supersonic Meteorology of Io: Sublimation-Driven Flow of SO_2. *Icarus* **64**, 375-390.

282

Ingersoll, A. P. (1989). Io Meteorology: How Atmospheric Pressure is Controlled Locally by Volcanos and Surface Frosts. *Icarus* **81**, 298-313.

Summers, M. E. (1985) *Theoretical Studies of Io's Atmosphere* Ph.D. thesis, Calfornia Institute of Technology.

Wagman, D. D. (1979). *Sublimation Pressure and Enthalpy of SO_2*. Chem. Thermodynamics Data Center, Nat. Bureau of Standards, Washington, D.C.
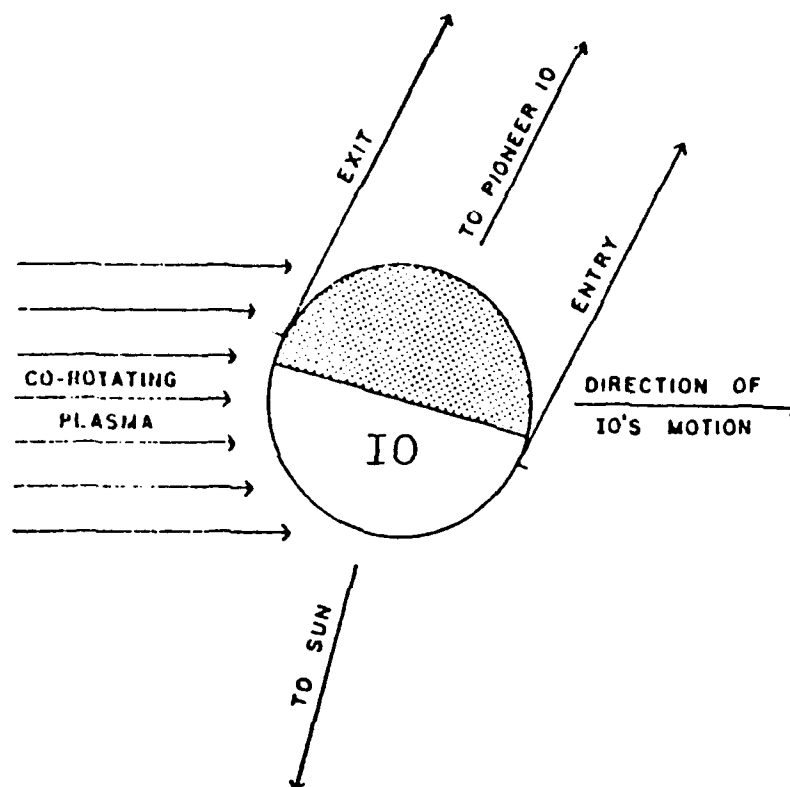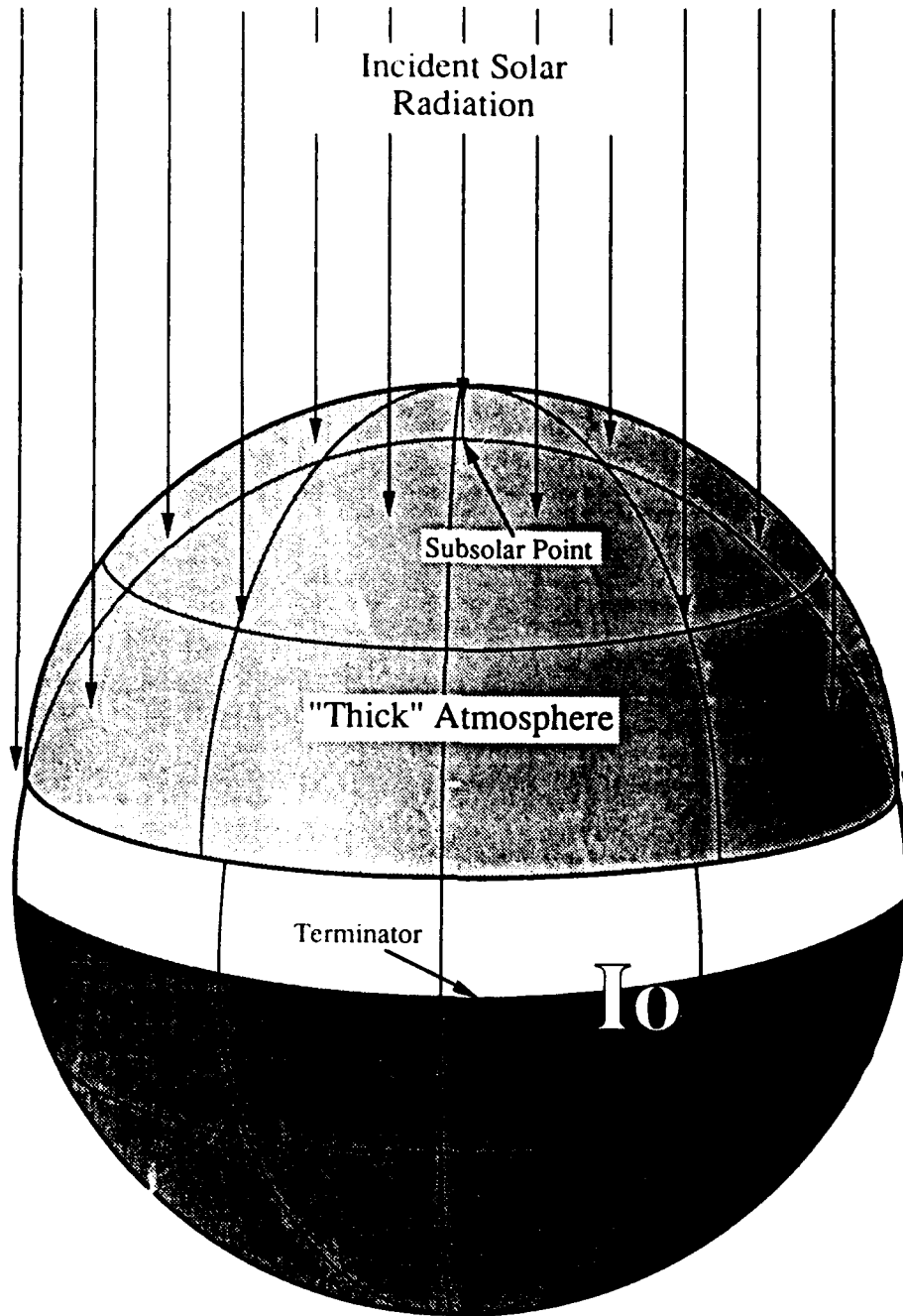
Figure 1.1: Pionner 10 Occultation Geometry

(from Summers, 1985)

Figure 2.1: Vapor Equilibrium Atmosphere
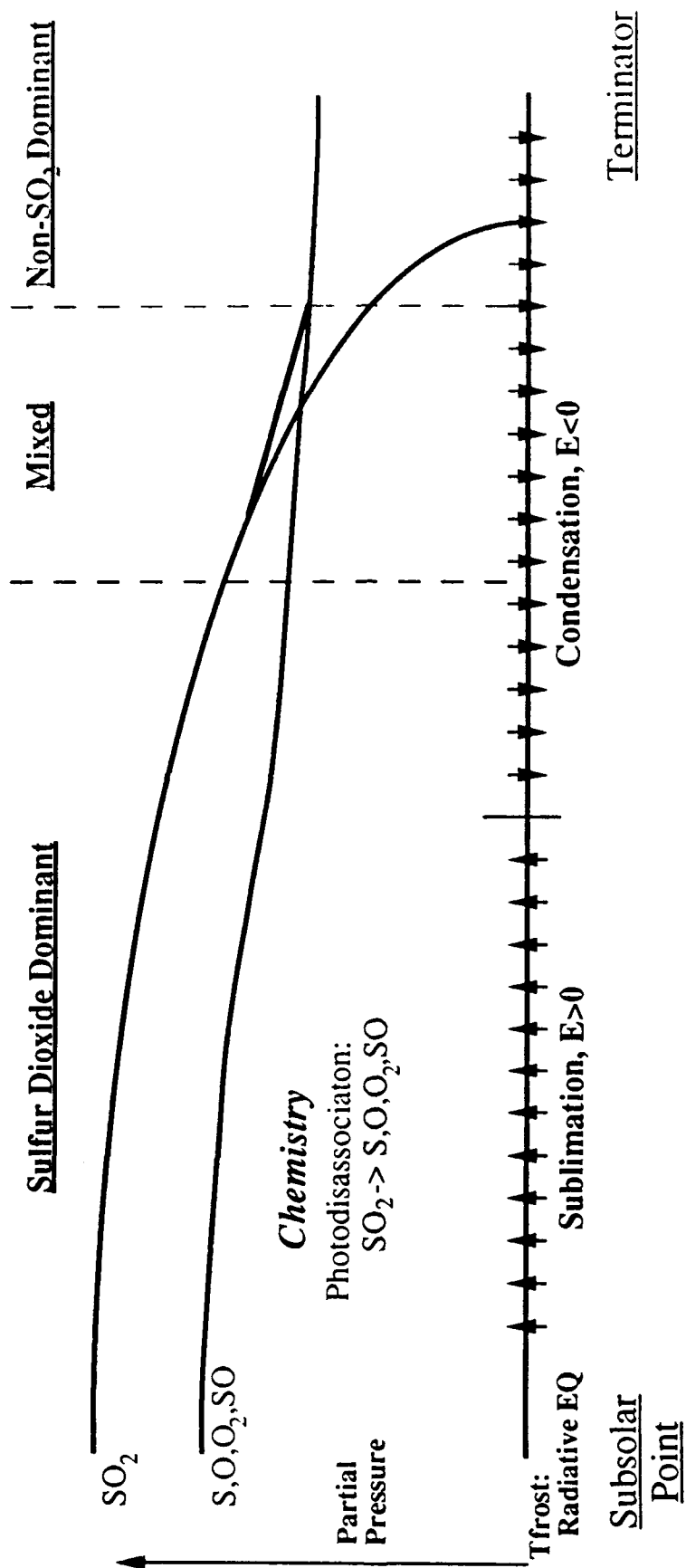
Figure 2.2: Model Dayside Atmosphere

Photodissociation:

$$O_2 + h\nu \rightarrow O + O \qquad\qquad J_1 = 9.1e\text{-}8$$
$$SO + h\nu \rightarrow S + O \qquad\qquad J_2 = 1.1e\text{-}5$$
$$SO_2 + h\nu \rightarrow SO + O \qquad\qquad J_3 = 2.8e\text{-}6$$
$$SO_2 + h\nu \rightarrow S + O_2 \qquad\qquad J_4 = 1.0e\text{-}6$$

Two-Body Reactions:

$$S + O_2 \rightarrow SO + O \qquad\qquad k_6' = 2.3e\text{-}18$$
$$SO + O_2 \rightarrow SO_2 + O \qquad\qquad k_7' = 2.4e\text{-}19 \exp(-2370/T)$$
$$SO + SO \rightarrow SO_2 + S \qquad\qquad k_8' = 5.8e\text{-}18 \exp(-1760/T)$$

Three-Body Reactions:

$$O + O + M \rightarrow O_2 + M \qquad\qquad k_{13}' = 8.6e\text{-}40/(T*T)$$
$$SO + O + M \rightarrow SO_2 + M \qquad\qquad k_{16}' = 6.0e\text{-}43$$
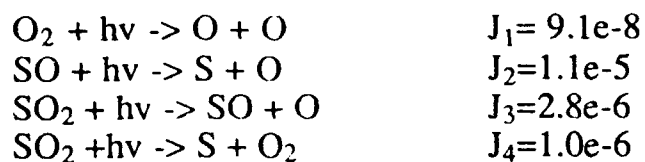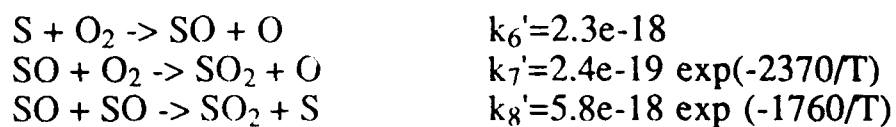
Table 2.1: Chemistry Coefficients (from Summers, 1985)

Figure 2.3a: Flow Variables, Case 1 (Tss = 130 K, Tas = 50 K)
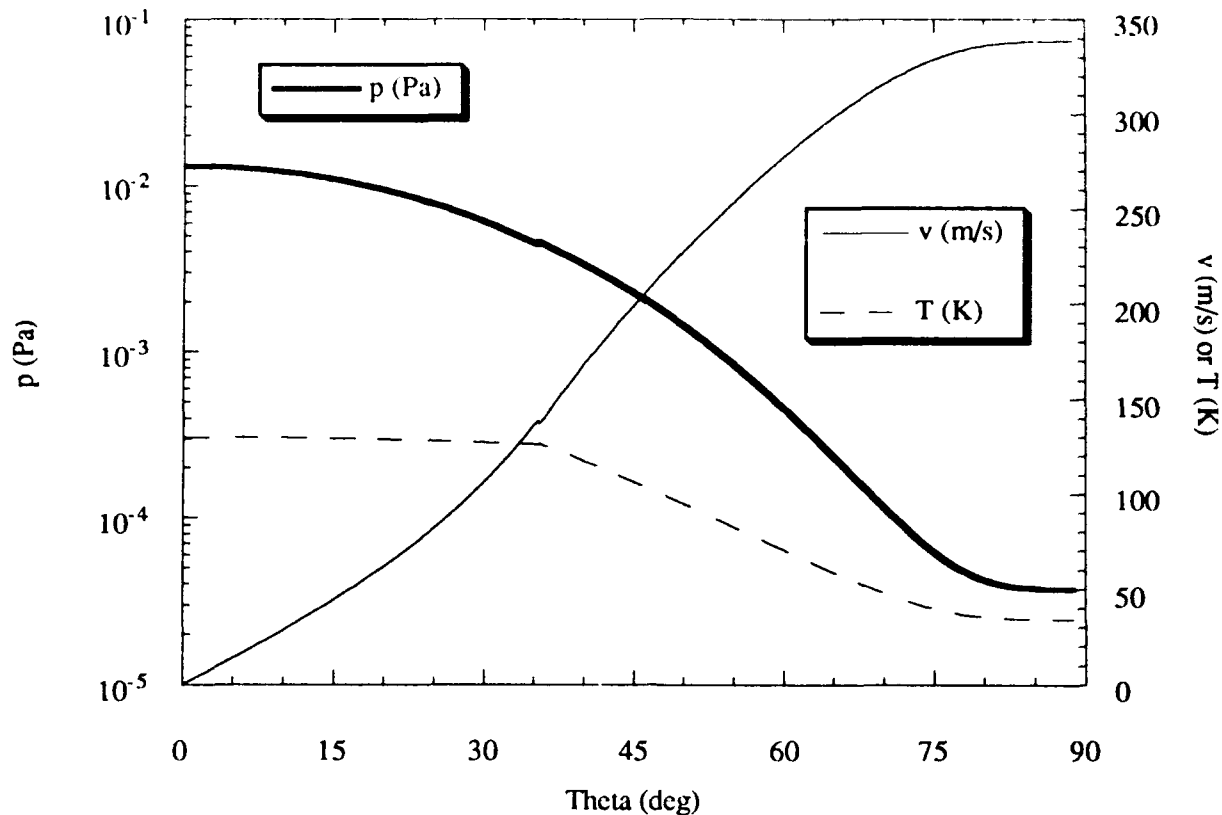
Figure 2.3b: Partial Pressures, Case 1
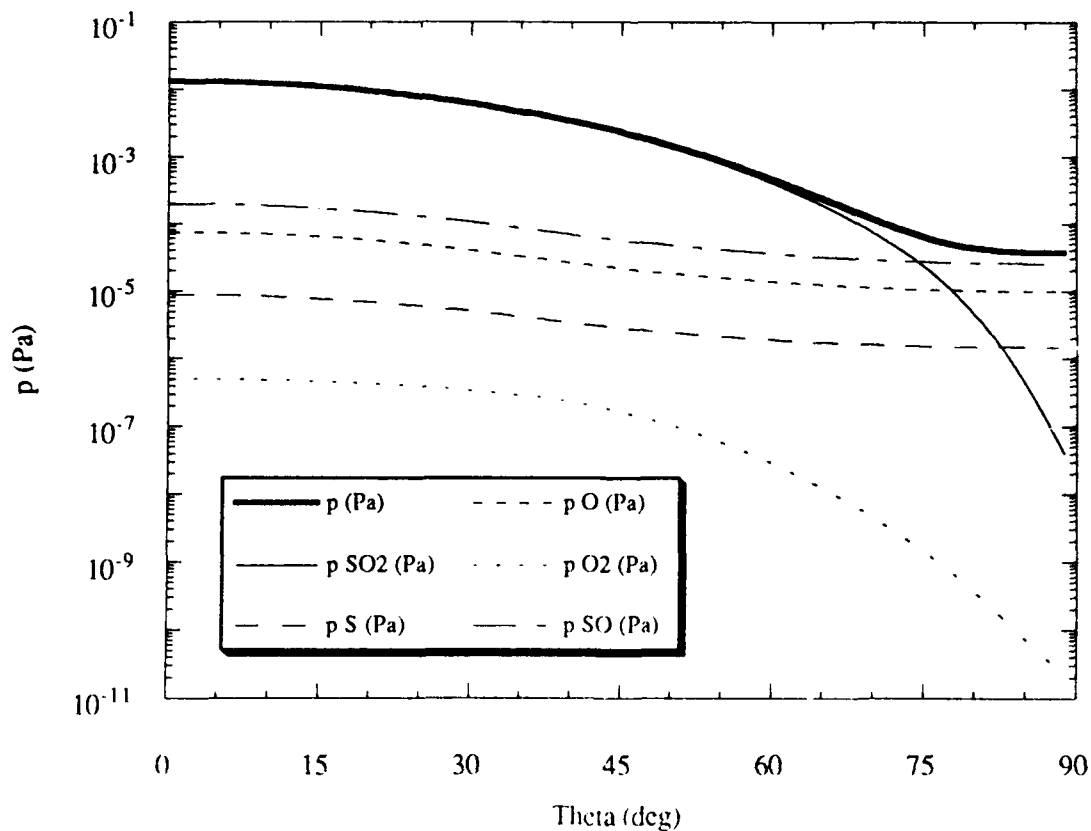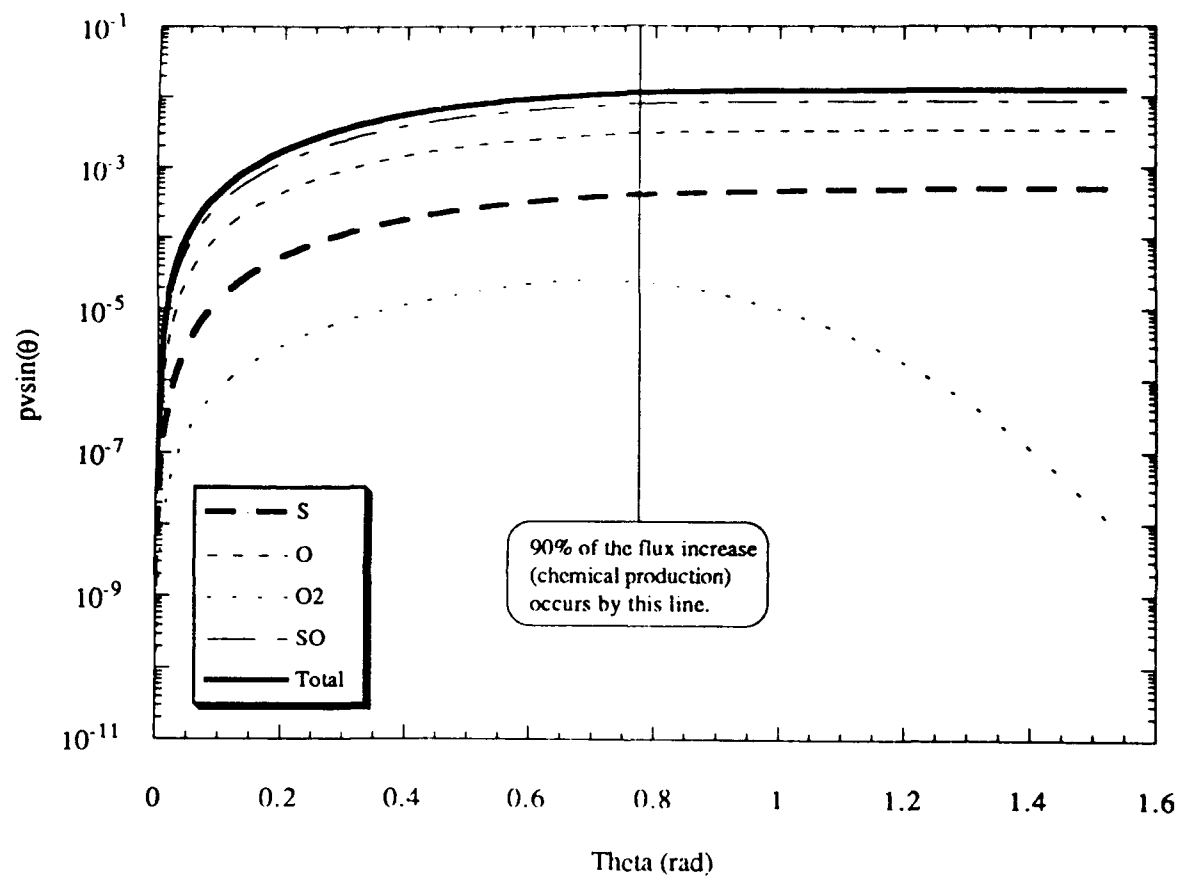
Figure 2.4: Chemical Mass Flux, Case 1

Figure 2.5a: Flow Variables
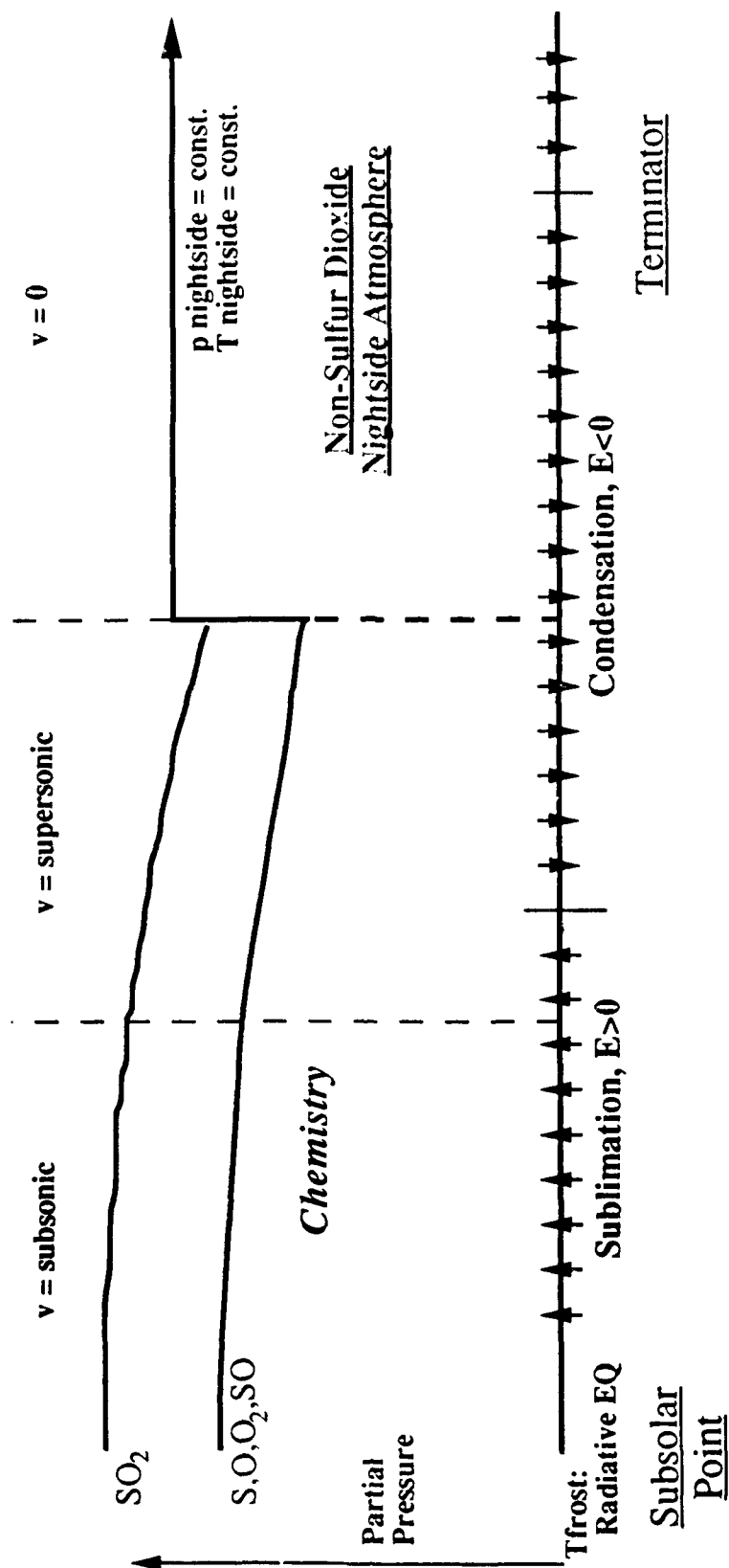Case 2 (Tss = 120K, Tas = 50 K)
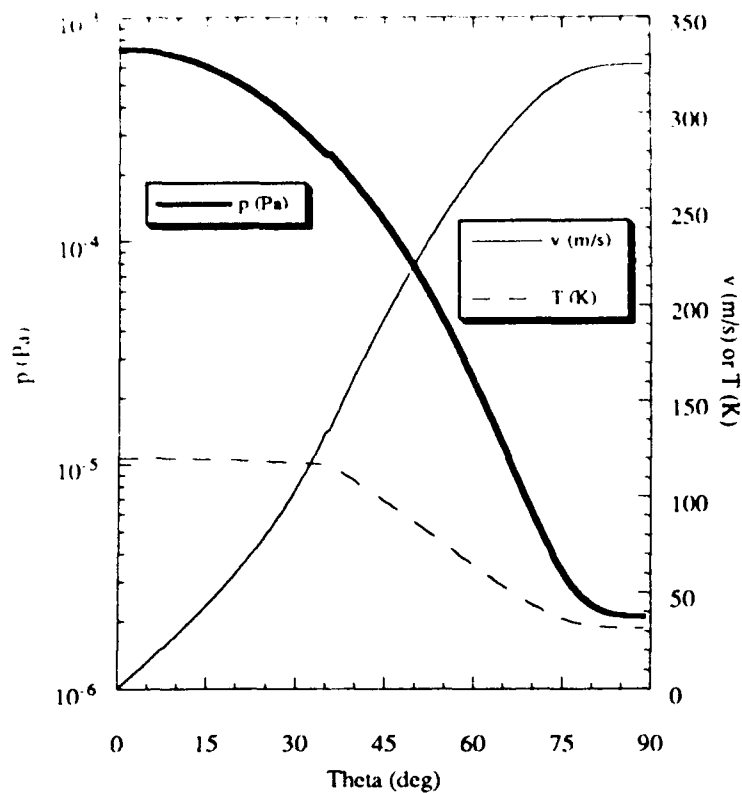
Figure 2.5b: Partial Pressures, Case 2
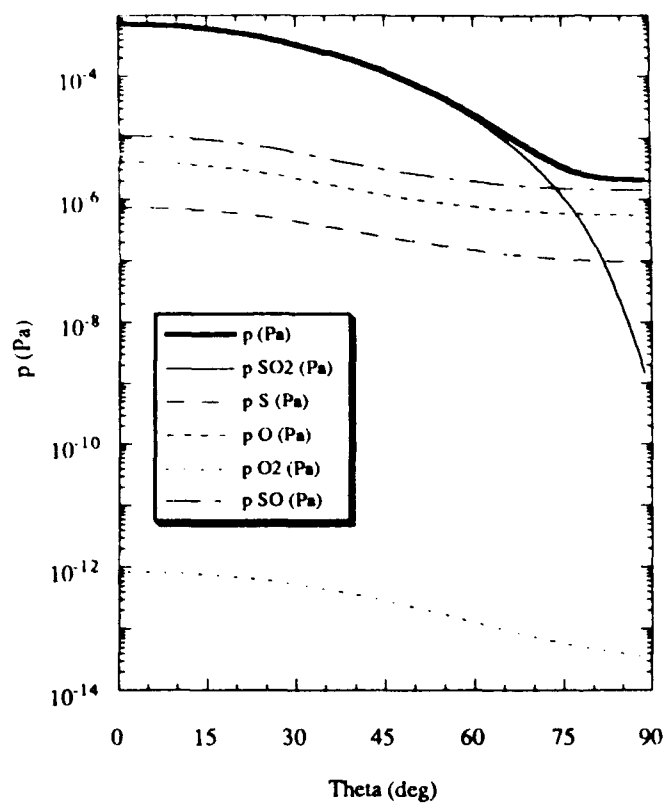
Figure 2.6a: Flow Variables
Case 3 (Tss = 130 K, Tas = 80 K)
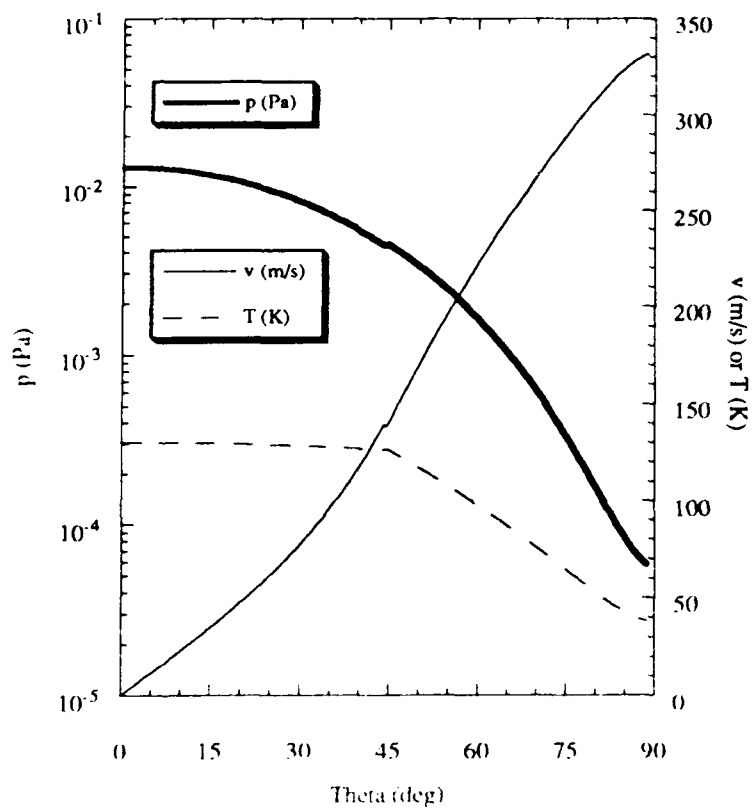
Figure 2.6b: Partial Pressures, Case 3

290
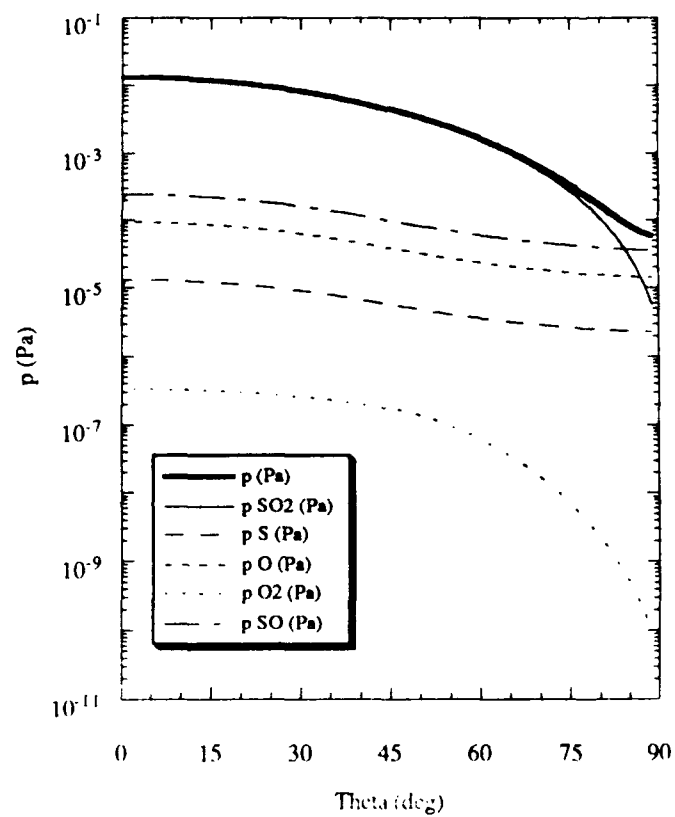
Figure 2.7a: Flow Variables
Case 4 (Tss =130 K, Tas = 65 K)
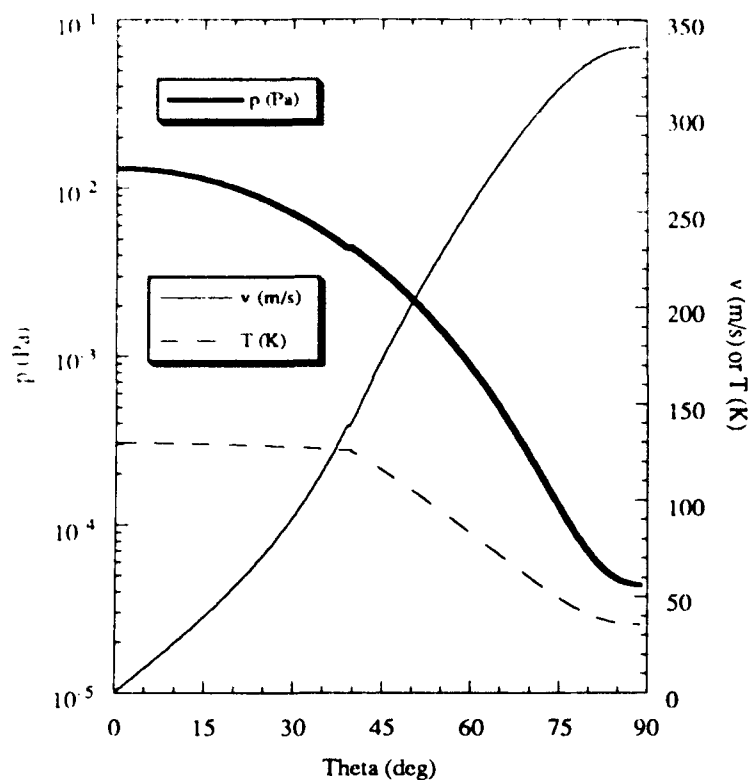
Figure 2.7b: Partial Pressures, Case 4
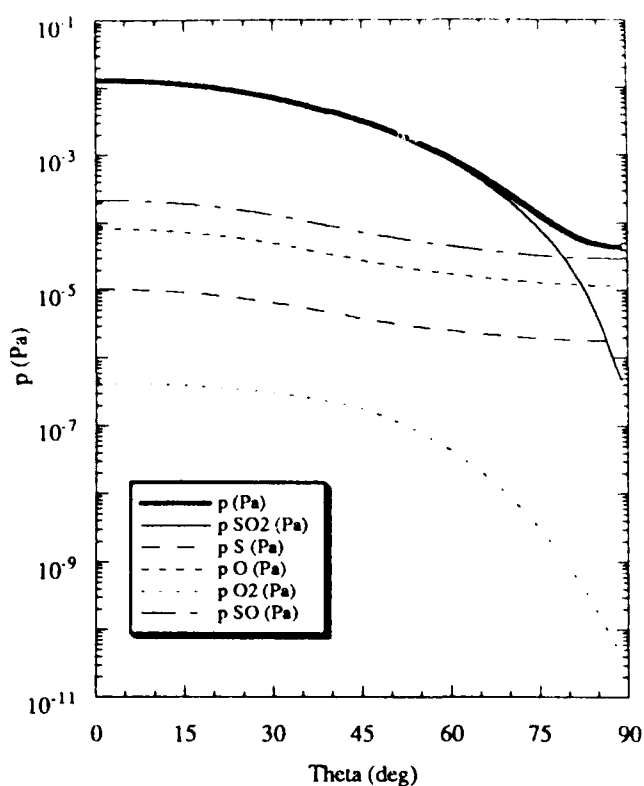
Figure 2.8a: Flow Variables
Case 5 (Tss = 125 K, Tas = 50 K)
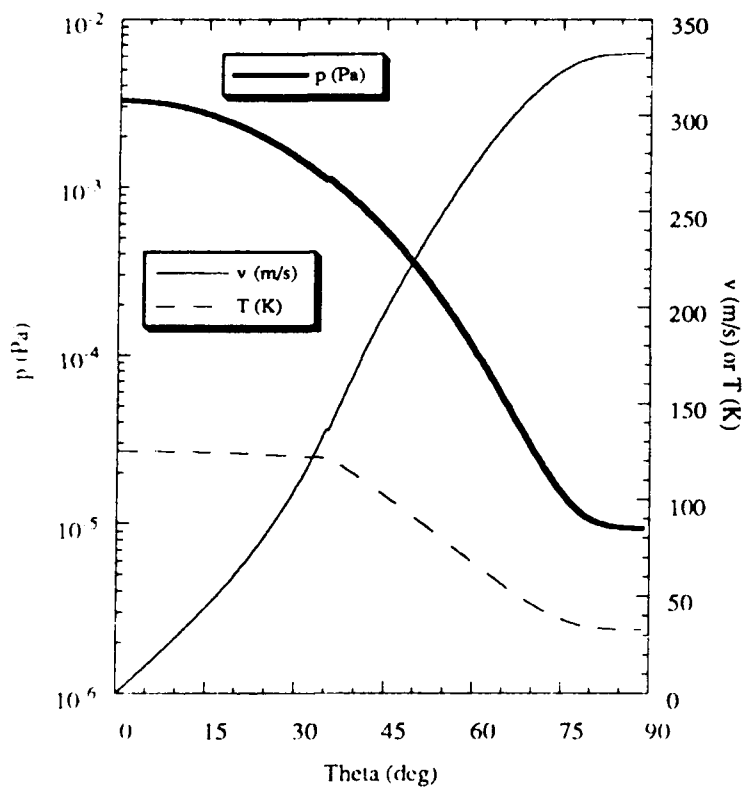
Figure 2.8b: Partial Pressures, Case 5

$v = 0$

$v = \text{subsonic}$

$v = \text{supersonic}$

p nightside = const.
T nightside = const.

Non-Sulfur Dioxide
Nightside Atmosphere

SO_2

S,O,O_2,SO

Chemistry

Partial
Pressure

Tfrost:
Radiative EQ

Subsolar
Point

Sublimation, E>0

Condensation, E<0

Terminator
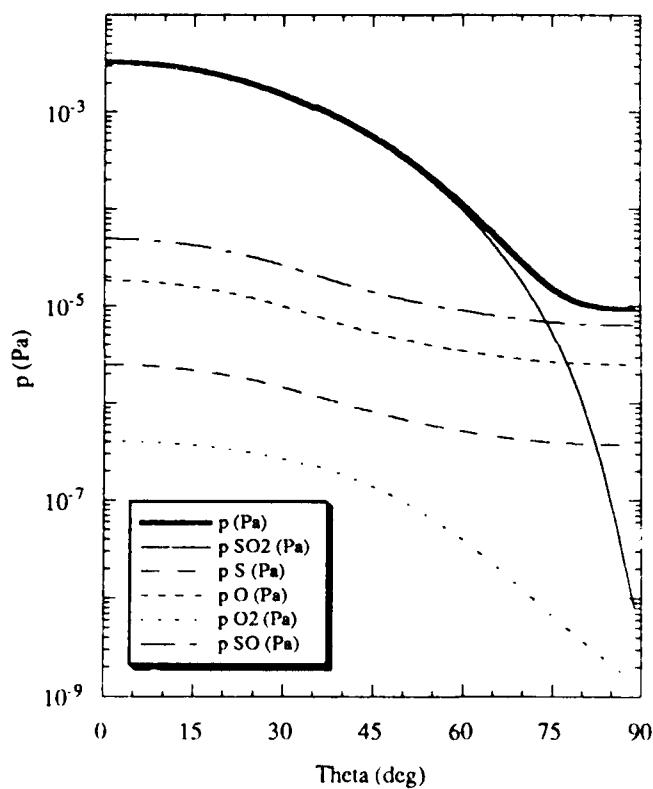
Figure 3.1: Zero-Order Model, Dayside/Nightside Atmosphere

Figure 3.2: Nightside Atmosphere
Case 1 (Tss = 130 K, Tas = 50K)

T Night (K) and Theta of Jump (deg)
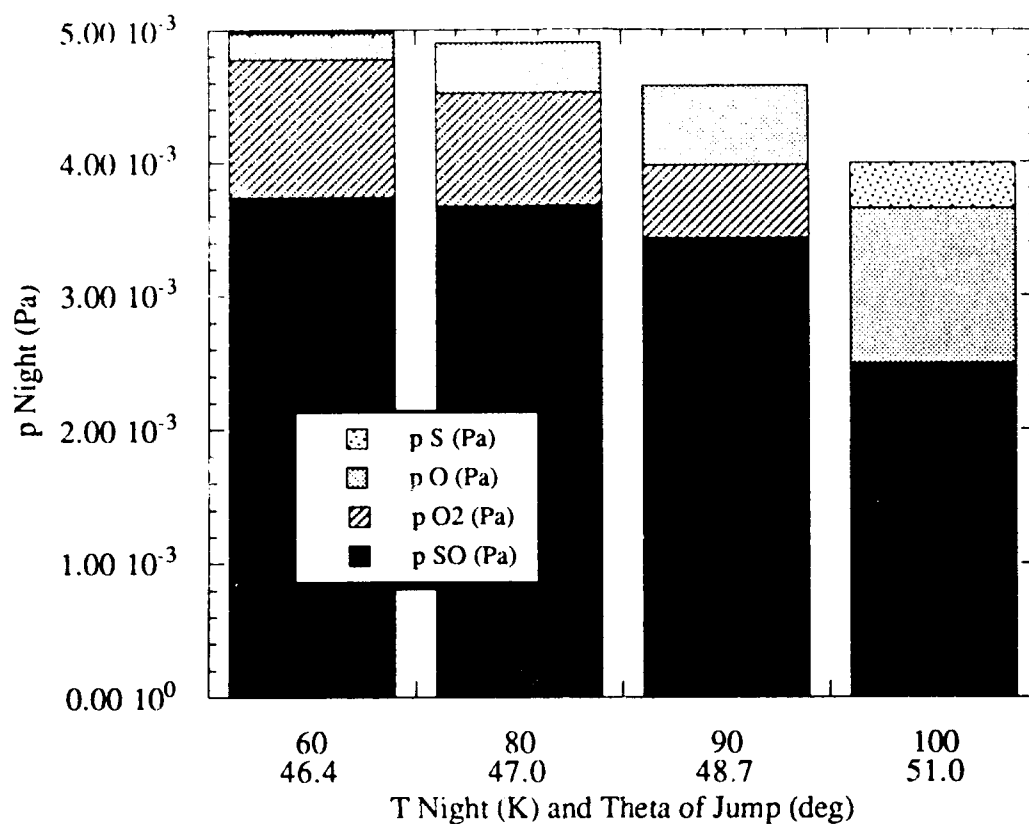
Figure 3.3: Pressure Variations at Shock, Case 1

Theta (deg)
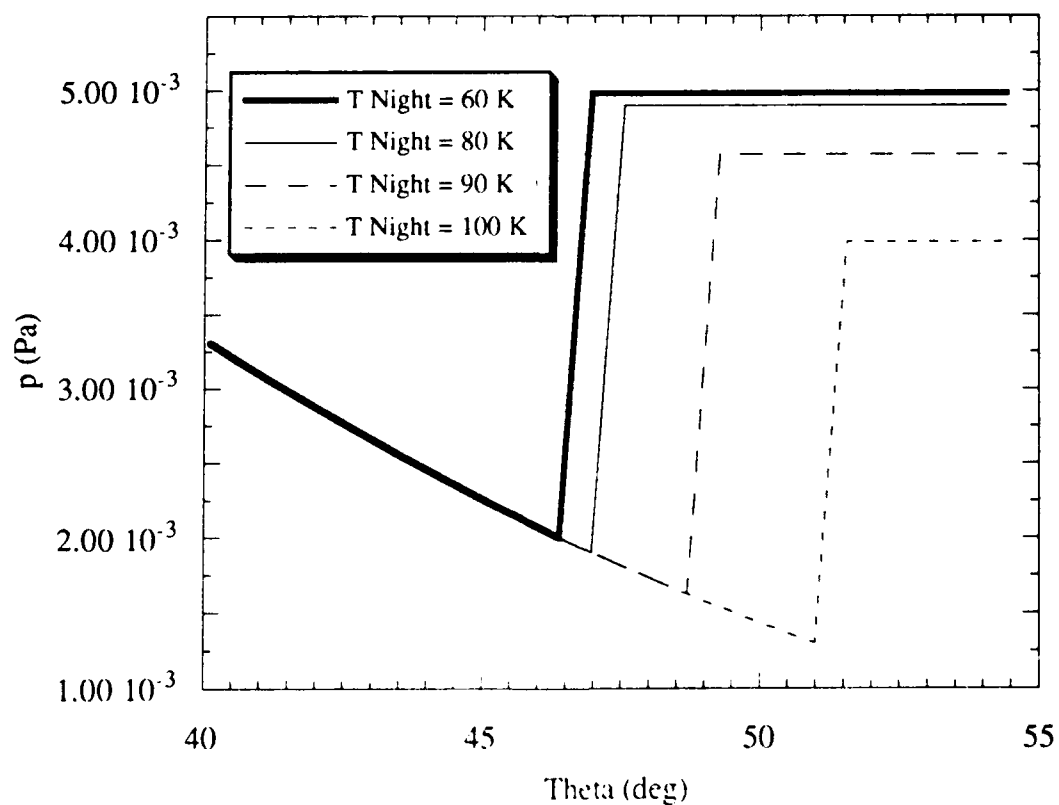
**Figure 3.4: Nightside Atmosphere
Case 2 (Tss = 120 K, Tas = 50K)**

p Night (Pa)

$8.0\ 10^{-4}$
$7.0\ 10^{-4}$
$6.0\ 10^{-4}$
$5.0\ 10^{-4}$
$4.0\ 10^{-4}$
$3.0\ 10^{-4}$
$2.0\ 10^{-4}$
$1.0\ 10^{-4}$
$0.0\ 10^{0}$

- ⊡ p S (Pa)
- ▣ p O (Pa)
- ▨ p O2 (Pa)
- ■ p SO (Pa)

80
5.2

100
8.6

T Night (K) and Theta of Jump (deg)
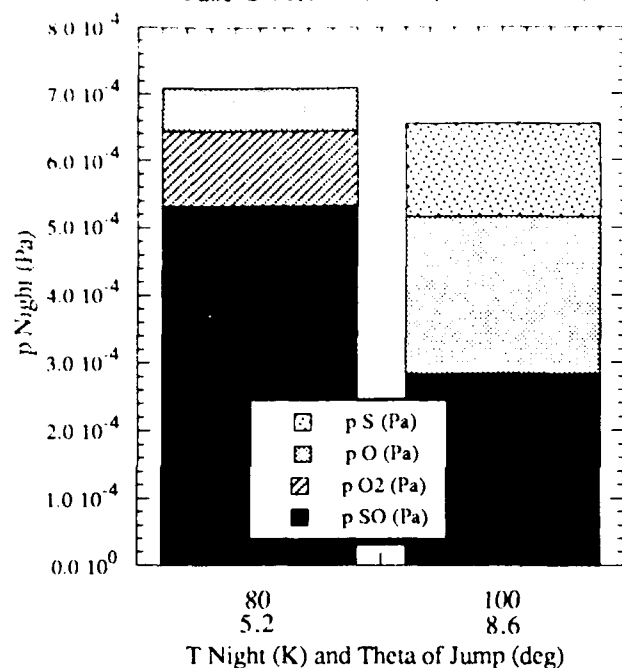
**Figure 3.6: Nightside Atmosphere
Case 4 (Tss = 130K, Tas = 65 K)**

p Night (Pa)

$6.0\ 10^{-3}$
$5.0\ 10^{-3}$
$4.0\ 10^{-3}$
$3.0\ 10^{-3}$
$2.0\ 10^{-3}$
$1.0\ 10^{-3}$
$0.0\ 10^{0}$

- ⊡ p S (Pa)
- ▣ p O (Pa)
- ▨ p O2 (Pa)
- ■ p SO (Pa)

60
49.8

80
49.8

100
53.9

110
51.0

T Night (K) and Theta of Jump (deg)
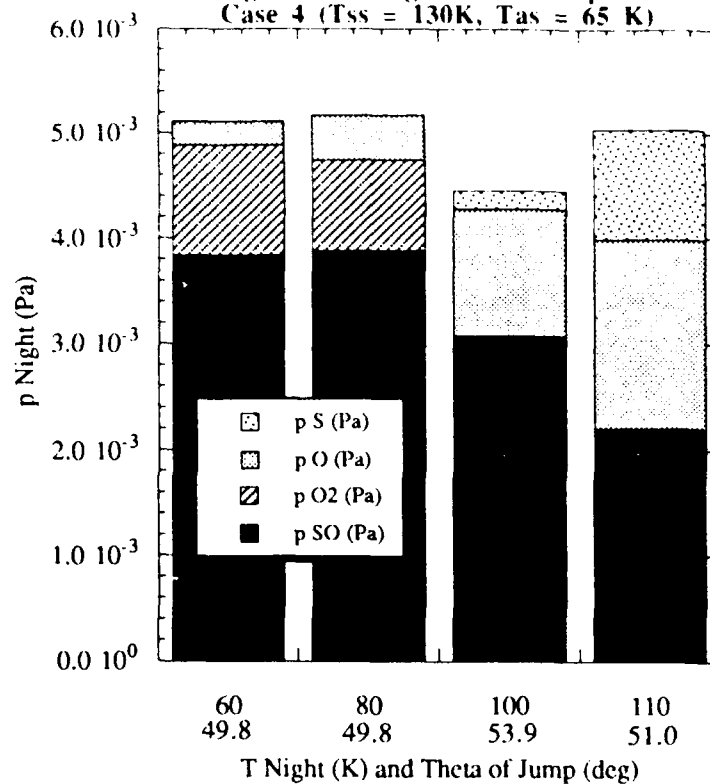
**Figure 3.5: Nightside Atmosphere
Case 3 (Tss = 130 K, Tas = 80 K)**

p Night (Pa)

$6.0\ 10^{-3}$
$5.0\ 10^{-3}$
$4.0\ 10^{-3}$
$3.0\ 10^{-3}$
$2.0\ 10^{-3}$
$1.0\ 10^{-3}$
$0.0\ 10^{0}$

- ⊡ p S (Pa)
- ▣ p O (Pa)
- ▨ p O2 (Pa)
- ■ p SO (Pa)

80
54.4

100
58.4

110
53.9

T Night (K) and Theta of Jump (deg)
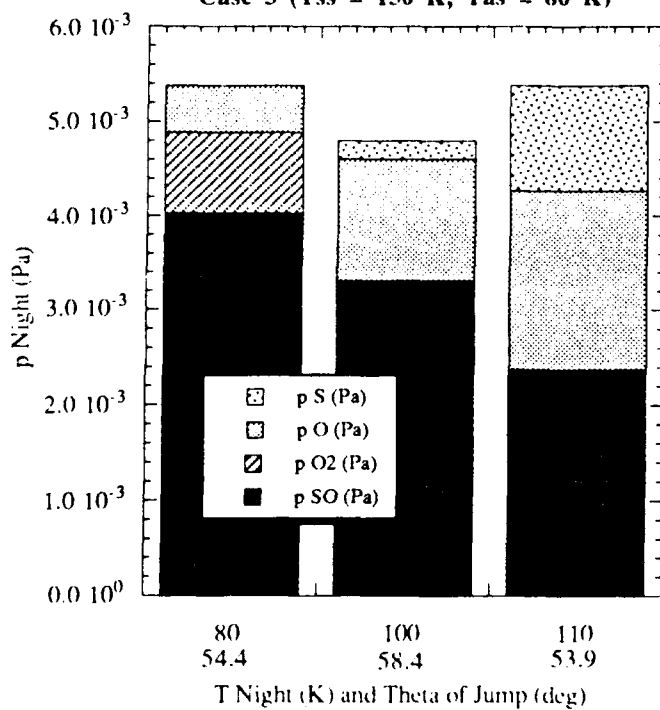
**Figure 3.7: Nightside Atmosphere
Case 5 (Tss = 125 K, Tas = 50 K)**

p Night (Pa)

$2.5\ 10^{-3}$
$2.0\ 10^{-3}$
$1.5\ 10^{-3}$
$1.0\ 10^{-3}$
$5.0\ 10^{-4}$
$0.0\ 10^{0}$

- ⊡ p S (Pa)
- ▣ p O (Pa)
- ▨ p O2 (Pa)
- ■ p SO (Pa)

60
20.1

80
20.1

100
24.1

T Night (K) and Theta of Jump (deg)
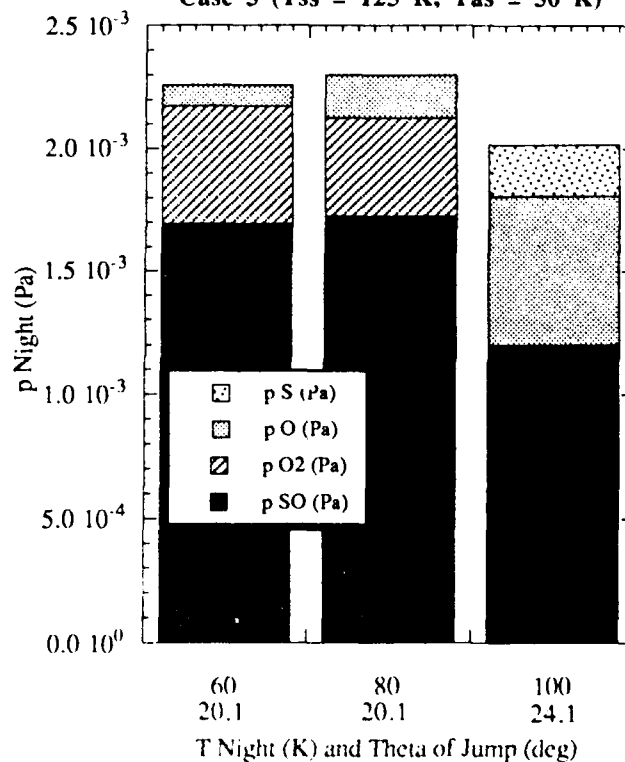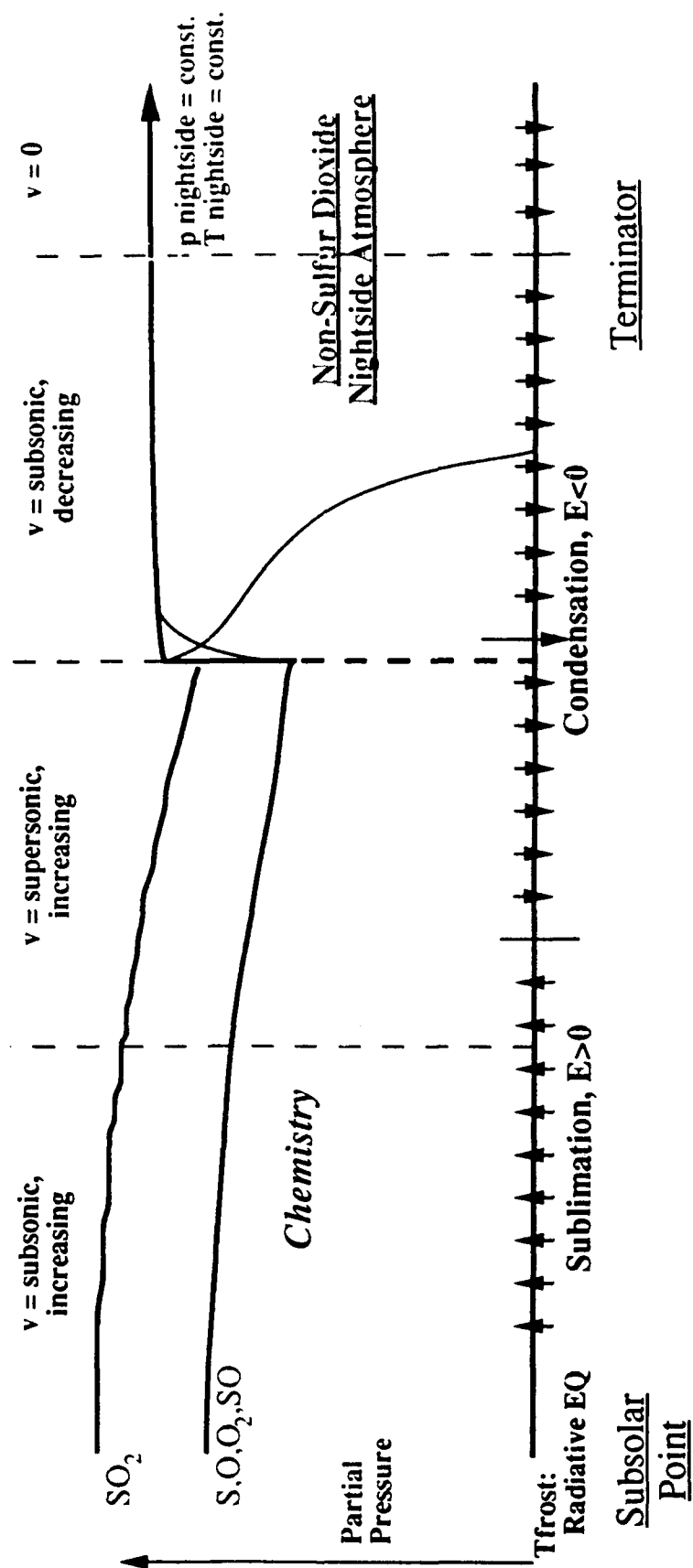
Figure 3.8: First-Order Model, Dayside/Nightside Atmosphere

Dynamical Aspects of Jovian Vortex Structure.

Douglas Parker

May 10, 1993

1 Abstract.

Recent data of Jupiter's cloud-top winds have given much insight into the structure of the zonal jets and persistent eddies, in particular the Great Red Spot (GRS) and White Ovals. It is here attempted to provide physical insights into the details of the vortex structures, by modelling with a $1\frac{1}{2}$ layer quasigeostrophic system. Idealised vortices of piecewise constant potential vorticity (pv) anomalies reveal how the shape and pv distribution of the vortex is determined by the nature of the shear flow within which it resides; this work follows that of Yano and Flierl (1992). Similar models of 'modon' formulation, an approximation that appears to be well suited to these Jovian systems, are constructed and exhibit a much greater degree of boundary 'stiffness' in the presence of mean-flow shear than the piecewise constant cases.

Speculation is also made as to the implications of the non-trivial structure in these large vortices, especially the possibility of geostrophically forced vertical motion and 'moist' convective processes.

2 Introduction.

Recent photographs of the cloud-tops of Jupiter taken by the Voyager II spacecraft have provided data of unprecedented accuracy. Various theories for the planetary dynamics have been inferred from these data; in particular

Dowling and Ingersoll (1989) (DI89) have deduced streamfunction profiles, pv profiles and equivalent bottom topography for the zonal flows and some of the persistent vortices on Jupiter. Figure 1 illustrates these deductions. The strongly anticyclonic GRS has a maximum of pv (negative in southern hemisphere) to the edge of the inner, less active layer (this peak would qualitatively occur as the result of taking the Laplacian of a Gaussian streamfunction to obtain relative vorticity). The anticyclonic shear of the zonal flow is shown; the inferred deep winds are of similar form but of slightly different phase and different amplitude. It is interesting to note that the less active centre of the spot appears to be shifted poleward within its envelope of more rapid flow. Other observations are that the GRS is expected to weaken with height due to its temperature profile (warm core system) and oscillates in latitude and longitude with a period of roughly 90 days. The external velocity profile appears to be relatively quiescent.

Figure 2 shows DI's graph of pv versus Bernoulli function, B, in the region of the GRS. Since B is similar to a streamfunction for the flow, a linear approximation to the relationship between pv and streamfunction, as used in the formulation of modons (Flierl et al, 1980) immediately seems reasonable. This approach will be discussed in section 4.

The persistence of vortices on the giant planets against the inevitable processes of dissipation (in the case of the GRS, for over 300 years) is one of their most remarkable aspects. Essentially there must be a steady flux of energy and vorticity into these systems to maintain them. It has been hypothesised that this occurs by merger with smaller vortices. The Voyager images show a vividly turbulent wake to the northwest of the GRS, possibly involving strongly baroclinic instabilities and diabatic effects. Eddies from this region, however, tend not to merge with the GRS; rather, small vortices from the East may be observed travelling around and through the outer ring of the GRS and being absorbed into the centre. This process must bear strongly on the theory of the Earth's 'blocking highs' in which it is the baroclinic eddies from the storm track regions which are thought to maintain long-lived high-pressure systems. Haines and Marshall (1987) have attempted to model such a system using modon ideas. The energy source for the jets on Jupiter is widely believed to derive from deep winds, in turn driven by the strong interior heating of the planet. It is possible that the forced weather layer jets and lower flow may have a direct dynamical influence on the GRS, for example by the nature of Rossby wave propagation, or through diabatic processes.

In this work, analytical approaches to modelling the dynamics of large vortices will be made. A '$1\frac{1}{2}$ layer' quasi geostrophic model, in which the ratio of upper to lower layer depths is approximated to be zero, is used throughout and it is assumed that the deep lower layer flows are unaffected by the existence of the vortex; that is, the vortex is shallow (Yano, 1987a). In section 3, $1\frac{1}{2}$ layer baroclinic vortices of piecewise constant pv will be constructed, with boundaries perturbed from the circular in order to balance a weak basic flow. In section 4, perturbed circular modon solutions will be derived for shear flows on a β plane. The 5th section discusses qualitative implications of the vortex asymmetries observed and modelled here. Speculation is made as to significance of vertical motion and latent heating. All solutions will be derived for the Northern hemisphere.

3 Basic Concepts.

Some aspects of the structure of Jupiter's GRS and White Ovals may be interpreted immediately. Fig. 3 shows a cortoon of the influence of a planetary vorticity gradient on a vortex in which pv is conserved. The relative vorticity of the fluid must change as it moves meridionally and the Coriolis parameter changes, so the streamlines deform in the sense illustrated, as is seen for the GRS. Since there is no finite pv structure for the vortex, little infomation is gained about deformation of the boundaries of such a pv patch in shear flow.

The point vortex lies at a level of zero relative zonal flow, since it is simply advected. Information about the general phase speed of larger vortices can be obtained from the integral theorem of Flierl, Stern and Whitehead (1983), that for a strongly compacting primitive system,

$$\int \int \int \rho \psi d^3 r = 0, \tag{1}$$

where $\psi' \equiv \psi - \overline{\psi}$. For the $1\frac{1}{2}$ layer problem, in which,

$$Q = (\nabla^2 - F)\psi + F\psi_2 + \beta y, \tag{2}$$

this gives,

$$(\beta + Fc)\int \int \psi' dx dy - F \int \int \overline{u}_2 \psi' dx dy = 0, \tag{3}$$

In the case of $\overline{u}_2 = 0$ for a monopolar vortex it is required that $c = -\frac{\beta}{F}$; westward and fixed. If $\overline{u}_2$ varies slowly over the region of the vortex (if the scale of the lower layer flow is large) the approximation may be made, to first order, that,

$$(\beta + Fc) - F\overline{u}_2(0) = 0 \tag{4}$$

If this is substituted into (2) for the far field, using the modon formulation, $Q = \Lambda(\psi + cy)$ to give,

$$(\nabla^2 - (F + \Lambda))(\overline{u} - c) + F(\overline{u}_2 - \overline{u}_2(0)) = 0 \tag{5}$$

simple arguments will demand that $F + \Lambda = 0$.

The quantity $\nu^2 \equiv F + \Lambda$ is related to the 'refractive index', n, for the flow (Flierl, 1987), where $n = i\nu$. For regions of $\nu^2 > 0$ solutions are evanescent with distance, while they are wavelike in regions of $\nu^2 < 0$. A motivation behind seeking modon solutions is to find ones which are essentially non-radiating. The idea that $\nu^2 = 0$ in the basic flow on Jupiter implies a 'neutrality' in the modon formulation. It is interesting to observe that this condition is equivalent to the limit beyond which Arnol'd's second theorem guarantees stability in the QG form; $\frac{\partial Q}{\partial \psi} = -\frac{1}{L_d^2}$.

4   Piecewise Constant Anomaly Models.

The basic formulation is illustrated in figure 4. Here the quasi geostrophic potential vorticity equation (QGPVE) will be used to decompose the solution into that of a weak zonal flow and a stronger azimuthal flow due to the pv anomalies q_1 and q_a. The assumption of weak zonal flow is required in order that a linearisation be made on the boundaries of the pv patches, in terms of the boundary perturbations, η and τ from the circular. This assumption is not justified by the observations from Jupiter, but the model serves to illuminate certain dynamical effects and may be seen as a modon with $\Lambda = 0$ except at the boundaries between pv patches, in the notation of the previous section.

The method for steady vortices follows the approach of Flierl (1988) for instability problems; the QGPVE is decomposed into three parts so that, for a single patch of anomalous pv,

$$(\nabla^2 - F)\overline{\psi} + \beta y = q_\infty(y) - F\psi_2(y),$$

$$\begin{aligned}(\nabla^2 - F)\psi_0 &= qH(1-r)\\(\nabla^2 - F)\psi' &= q\eta\delta(1-r),\end{aligned}\qquad(6)$$

and $\psi + cy$ is required to be constant and continuous at $r = 1 + \eta$ for the propagating vortex. The linearisation occurs in writing $\psi(1+\eta) = \psi(1)+\eta\psi_r$ and regarding far field and asymmetric parts to be of small order. ψ' is related to the Green's function for the operator and arises as the 'source' perturbation η induces a non-axisymmetric component to the flow, required to balance the basic flow, $\bar{u}$.

$$\begin{aligned}\psi' = &-q\Sigma\eta_k K_k(\mu)I_k(\mu r)\sin k\theta,\\&-q\Sigma\eta_k I_k(\mu)K_k(\mu r)\sin k\theta,\end{aligned}\qquad(7)$$

for the interior and exterior respectively, where $\mu^2 = F$ ($\mu^2 = \nu^2$ in the modon notation) η_k is the k Fourier component of η and I_k, K_k are Bessel functions ψ_0 may be found as,

$$\begin{aligned}\psi_0 = &\tfrac{q}{\mu}K_1(\mu)I_0(\mu r) - \tfrac{q}{F},\\&-\tfrac{q}{\mu}I_1(\mu)K_0(\mu r),\end{aligned}\qquad(8)$$

for the interior and exterior. For uniform basic flow, $\bar{\psi} = -\bar{u}$, the boundary condition is degenerate in η and it is required that $-\bar{u} + c = 0$, a non-propagating vortex. This arises because the form of the basic flow corresponds, in η, to a uniform shift of the vortex in y. More general basic flows will yield more interesting results and may allow propagation relative to the flow at $y = 0$. For instance, simple shear $\bar{u} = \gamma y$, gives the $\cos 2\theta$ component of boundary perturbation as,

$$\eta_2 = \frac{1}{4}\frac{\gamma}{q(I_2 K_2 - I_0 K_0)}\qquad(9)$$

This behaves as μ^3 for $\mu \gg 1$.

In an attempt to allow more structure to the vortex, assume two pv steps q_1 and q_a at $r = 1, a$ respectively with perturbation boundaries of η and τ, so that,

$$\begin{aligned}(\nabla^2 - \mu^2)\psi_0 &= q_1 H(1-r) + q_a H(a-r),\\(\nabla^2 - \mu^2)\psi' &= q_1\eta\delta(1-r) + q_a\tau\delta(a-r).\end{aligned}\qquad(10)$$

From these, obtain,

$$
\begin{aligned}
V_0(1) &= q_1 I_1(\mu)K_1(\mu) + q_a a I_1(\mu)K_1(\mu a), \\
V_0(a) &= q_1 I_1(\mu)K_1(\mu a) + q_a a I_1(\mu a)K_1(\mu a), \\
\psi'_m(1) &= -q_1 \eta_m I_m(\mu)K_m(\mu) - q_a a \tau_m I_m(\mu)K_m(\mu a), \\
\psi'_m(a) &= -q_1 \eta_m I_m(\mu)K_m(\mu a) - q_a a \tau_m Im(\mu a)K_m(\mu a), \qquad (11)
\end{aligned}
$$

where $V_0 \equiv \frac{\partial \psi_0}{\partial r}$. Now, in uniform basic flow, $\bar{u}$, the boundary conditions at $r = 1 + \eta$ and $r = a + \tau$ yield,

$$
\begin{aligned}
\bar{u} - c &= -a q_a I_1(\mu)K_1(\mu a)(\tau_1 - \eta_1), \\
(\bar{u} - c)a &= q_1 I_1(\mu)K_1(\mu a)(\tau_1 - \eta_1). \qquad (12)
\end{aligned}
$$

For non-zero $\bar{u} - c$, the pv steps are related by $q_a = -\frac{q_1}{a^2}$ and the relative shift in boundaries, $\Delta_1 \equiv \tau_1 - \eta_1 = \frac{c - \bar{u}}{q_a a I_1(\mu)K_1(\mu a)}$. These forms are sketched in figure 5. The outer band of the (anticyclonic) system is relatively cyclonic so that the shift of the boundaries admits a dipolar component to balance the basic flow. However, this form of radial pv structure is dynamically unstable, as can be seen from contour dynamics routines, and is not of physical interest. For a system with sheared basic flow $\bar{u} - c$ may be zero and q_1 and q_a may be varied freely. The $cos2\theta$ terms must be matched and give,

$$
\begin{aligned}
\eta_2(q_1(I_1 K_1 - I_2 K_2) + a q_a I_1 K_1(\mu a)) & \\
-\tau_2 a q_a I_2 K_2(\mu a) + \frac{1}{4}\gamma &= 0, \\
\tau_2(q_1 I_1 K_1(\mu a) + a q_a(I_1(\mu a)K_1(\mu a) - I_2(\mu a)K_2(\mu a))) & \\
-\eta_2 a q_a I_2(\mu a)K_2(\mu a) + \frac{1}{4}\gamma a^2 &= 0, \qquad (13)
\end{aligned}
$$

where the arguments of the Bessel functions are μ unless given otherwise. This is a linear pair of equations for (η_2, τ_2), given q_1, q_a, a and γ. To investigate these, fix $q_1 + q_a, a$ and γ so as to create a vortex of fixed inner pv and varying outer structure. The curves η_2 and τ_2 are shown in figure 6, for different values of outer radius, a=1.25 and 2. When a = 1.25 the boundaries are sufficiently close to interact (recalling that the Rossby radius of deformation, L_D, is 0.1 here, when F=10) whereas in the a=2 case they behave independently. This is reflected in eqns (13), since the $I_\nu(\mu)K_\nu(\mu a)$ terms will become very small as $a \gg 1$, so the solutions reduce to those of a single boundary.

5 Modons in Weak Basic Flows.

The QG theory follows,

$$[\frac{\partial}{\partial t} + J(\psi, .)]Q = 0. \tag{14}$$

For steady, propagating solutions, write $\frac{\partial}{\partial t} = -c\frac{\partial}{\partial x}$ and obtain,

$$J(\tilde{\psi}, Q) = 0, \tilde{\psi} = \psi - cy, \tag{15}$$

so that $Q = Q(\tilde{\psi})$. Then,

$$Q(\tilde{\psi}) \approx Q_0 + \tilde{\psi}\frac{dQ}{d\tilde{\psi}} + \frac{1}{2}\tilde{\psi}^2\frac{d^2Q}{d\tilde{\psi}^2} + O(\tilde{\psi}^3) \tag{16}$$

which gives,

$$[\nabla^2 - (F + \Lambda)]\tilde{\psi} - \frac{1}{2}\Lambda'\tilde{\psi}^2 = (Fc - \beta)y - F\psi_2 + Q_0, \tag{17}$$

where $\Lambda = dQ/d\tilde{\psi}$.

The 'modon' formulation is that in which it is taken that $Q = \Lambda\tilde{\psi}$ in the above, where Λ is piecewise constant (Flierl et al, 1980), so that (17) becomes,

$$[\nabla^2 - (F + \Lambda)]\tilde{\psi} = (Fc - \beta)y - F\psi_2 + Q_0. \tag{18}$$

In the comments of section N the quantity $\nu^2 = F + \Lambda$ was defined to describe the nature of solutions. When ν^2 is a positive constant, free solutions of (18) are of the form,

$$\tilde{\psi} = (a_n I_n(\nu r) + b_n K_n(\nu r))e^{in\theta}, \tag{19}$$

and when ν^2 is a negative constant,

$$\tilde{\psi} = (c_n J_n(\nu r) + d_n Y_n(\nu r))e^{in\theta}, \tag{20}$$

where I_n, K_n, J_n and Y_n are Bessel functions and (r, θ) are polar coordinates.

A combination of the modon and piecewise constant solutions may be made in which a linear (Q, ψ) relationship is applied, both within and outside a perturbed circular boundary. The motivation is to produce an improvement on the piecewise system while perturbing the boundary in order to add n-pole

solutions to the basic monopolar modon, to balance the non-uniform external pv. The linear relationship may be chosen to match the observations of DI89, from which the graph in figure 7 is plotted. Effectively this shows $F+\Lambda$, where Λ is the constant of proportionality, through the GRS (actually calculated for the 'generalised geostrophic' form). Of note is the strongly 'evanescent' interior flanked by alternating bands of slightly wavelike or evanescent nature. In particular, far from the vortex the observations of Dowling (1992) indicate a relationship $\overline{Q} = -F\overline{\psi}$, or 'neutrality' in this formulation. The departure from neutral to the North of the GRS (fig 7) is likely to relate to the fact that this region of the flow is not steady, and involves travelling disturbances.

An alternative far-field approximation would be that of Ingersoll and Cuong (1981) for which $\overline{\psi} \equiv \psi_2$. This will not be pursued here; in the exterior it will be taken that Q is a linear function of $\tilde{\psi} \equiv \psi + cy$, where the constant of proportionality is taken to be -F.

The basic system will be,

$$Q = \begin{array}{l} Q_0 + \Lambda\tilde{\psi} \\ -F\tilde{\psi}, \end{array} \tag{21}$$

for the interior and exterior, with $\partial\mathcal{D} = \{r = 1 + \Sigma\eta_k sink\theta\}$. It is required that $\tilde{\psi}$ be constant and $\tilde{\psi}_r$ be continuous on $\partial\mathcal{D}$: wlog set $\tilde{\psi} = 0$ on $\partial\mathcal{D}$. Thus the jump in pv across $\partial\mathcal{D}$ will be $-Q_0$. For an anticyclone a negative value of Q_0 corresponds to the limit of a narrow band of large negative $\frac{dQ}{d\psi}$ i.e. a 'wavelike' band of $F+\Lambda = -k^2$. The equations become, for the exterior with $c = 0$,

$$\begin{array}{ll} (\nabla^2 - F)\overline{\psi} + F\psi_2 + \beta y & = -F\overline{\psi} \\ \nabla^2\psi' & = 0, \end{array} \tag{22}$$

where $\psi = \overline{\psi} + \psi'$, and for the interior,

$$(\nabla^2 - (F + \Lambda))\psi' = (F + \Lambda)\overline{\psi} + Q_0, \tag{23}$$

where $F + \Lambda$ will be taken to be positive to match the structure deduced from DI89 (figure 7). Since ψ_2 is not specified the choice of $\overline{\psi}$ is arbitrary; $\overline{\psi}$ will be specified a priori and ψ_2 will be defined to satisfy (22). This function ψ_2 will be assumed independent of the vortex and continued into the interior region. For the case of simple shear in the basic flow, take

$$\overline{\psi} = -\frac{1}{2}\gamma y^2, \tag{24}$$

where γ is a small parameter (positive for northern hemisphere anticyclonic shear), and expand ψ' as $\psi' = \psi_0 + \gamma\psi_1 + O(\gamma^2)$ so that,

$$
\begin{aligned}
\nabla^2\psi' &= 0 \\
(\nabla^2 - \mu^2)\psi_0 &= Q_0, \\
(\nabla^2 - \mu^2)\psi_1 &= -\mu^2 y^2
\end{aligned}
\tag{25}
$$

for the exterior and interior respectively, with $\psi = 0$ on $\partial\mathcal{D}$ and continuous normal derivatives. Note that although in this case the terms βy and $F\psi_2$ in the QGPV cancel, the far field pv, $\overline{Q}$, is not uniform. Rather, $\overline{Q} = \frac{1}{2}F\gamma y^2$, so Rossby wave radiation is not excluded. However, there is a clear symmetry to the pv field and the perturbations can not have the north-south asymmetry of figure 3.

The matching conditions for (25) yield, for the zero order vortex,

$$
\begin{aligned}
\psi_0 = \ &\frac{Q_0}{\mu^2}\left(\frac{I_0(\mu r)}{I_0(\mu)} - 1\right) \\
&\frac{Q_0}{\mu^2}\frac{I_1(\mu)}{I_0(\mu)}\log r,
\end{aligned}
\tag{26}
$$

for the interior and exterior. The forms are plotted in figure 8, for various values of Λ for the interior, to move the system slightly away from the constant interior pv scenario. There are a broad range of axisymmetric forms that may be evaluated within this format.

Solving for ψ_1 yields for the perturbation terms,

$$
\begin{aligned}
\overline{\psi} + \psi_1 = \ &\frac{\gamma}{\mu^2}\left(1 - \frac{I_0(\mu r)}{I_0(\mu)}\right) + a_2 I_2(\mu r)\cos 2\theta, \\
&C\ln r + \frac{\gamma}{4}(1 - r^2) + \left(\frac{d}{r^2} + \frac{\gamma}{4}(r^2 - \frac{1}{r^2})\right)\cos 2\theta,
\end{aligned}
\tag{27}
$$

in which $d = -\eta_2\frac{d\psi_0}{dr}$, $a_2 = -\frac{\eta_2}{I_2(\mu)}\frac{d\psi_0}{dr}$, $C = \frac{\gamma}{2} - \frac{\gamma I_1(\mu)}{\mu I_0(\mu)}$ and,

$$
\eta_2 = \frac{\gamma}{Q_0}\frac{I_0(\mu)I_2(\mu)}{I_0(\mu)I_2(\mu) - I_1(\mu)^2}.
\tag{28}
$$

For $\gamma > 0$ and $Q_0 < 0$ (anticyclonic vortex in anticyclonic shear) $\eta_2 > 0$ - the vortex's y dimension is reduced as in the case of the Moore-Saffman ellipse when the vorticity of the flow has the same sign as that of the vortex. A, B and a_1 are linear functions of η_1 which is arbitrary: any uniform component of far field flow may be admitted by appropriate choice of boundary perturbation. The Flierl-Stern-Whitehead integral theorem will remain satisfied because of the balance between ψ_2 and $\overline{\psi}$ in the basic flow equation.

It is now important to compare the magnitude of the boundary deformation η_2 in this case with that of the piecewise constant case. Fig 9 shows the curves of η_2 against μ. The modon form is dramatically less perturbed at the boundary: in essence it seems that the modon is much 'stiffer' and is deformed much less than the piecewise constant case, for a given external flow. This may be illuminated by considering the equations for the external perturbation streamfunctions in each case:

$$\nabla^2 \psi' = 0, \tag{29}$$

for the modon, and

$$(\nabla^2 - F)\psi' = 0, \tag{30}$$

when the pv is piecewise uniform. The modon perturbation is solved in an effectively barotropic form, with a wide radius of influence. The perturbation exterior streamfunction for the modon feels itself to be in the limit of small μ for the piecewise solution.

Plots of the streamfunction with various values of Froude number, μ^2, and basic shear, γ, are shown in figure 10. For large μ^2 and γ there are clear problems in the linearisation of the boundary condition but for lower $\gamma = 0.05$ (a factor of 10. greater than the typical shears for the piecewise constant vortices of Yano and Flierl (1992)) the match seems good. For lower Froude number, very large shears can be accomodated. There is a clear motivation here to numerically locate an exact boundary which will allow the inner and outer fields to balance. Another useful extension would be to study a case with an annulus of $\nu^2 < 0$ ('wavelike') in order to match more closely the observed structure of figure 7, from DI89.

6   The Role of Vortex Asymmetry.

The asymmetry of the GRS may be crucial to its dynamics in other ways, apart from allowing it to reside in a far field pv gradient. From the expansion of the shallow water equations in small Rossby number it is possible to deduce, at first order, a diagnostic equation for the vertical velocity in terms of geostrophic quantities. This is usually written in the form of an 'ω-equation' in which the Laplacian of the pressure tendency ($\omega \equiv \frac{Dp}{Dt}$) is forced by the divergence of a 'Q-vector' (Gill, 1983) which represents a balance between

terms involving advection of entropy and vorticity:

$$\nabla^2 \omega = \nabla . Q. \qquad (31)$$

Q is defined as $Q = -(\nabla_g).\nabla S$, where S is the entropy and is proportional to $\hat{k} \wedge \frac{\partial}{\partial s}$ where ds is the path along isentropes. In polar coordinates Q is given by,

$$Q = \left(\frac{\partial u_r}{\partial r} \frac{\partial S}{\partial r} + \frac{1}{r^2} \left(\frac{\partial u_r}{\partial \theta} - u_\theta \right) \frac{\partial S}{\partial \theta}, \frac{\partial u_\theta}{\partial r} \frac{\partial S}{\partial r} + \frac{1}{r^2} \left(\frac{\partial u_\theta}{\partial \theta} + u_r \right) \frac{\partial S}{\partial \theta} \right), \qquad (32)$$

and it may be shown that its divergence for a circularly symmetric system is identically zero. Given suitable boundary conditions, ω must be zero. However, asymmetries may allow vertical motions within the vortex.

Speculation as to the consequences of vertical motion within the GRS is difficult owing the great lack of understanding of the composition and physical behaviour of its clouds and condensate matter. Certainly it has been suggested in the past that the GRS is a form of tropical cyclone (vorticity increasing downwards) with internal diabatic heating maintaining the circulation over long time periods. If it is held that the vortex must be weak in magnitude below the weather layer then the warm core would require that the upper level flow be anticyclonic. It is observed that around $\frac{9}{10}$ of Jupiter's vortices are anticyclonic - a tentative explanation could be that the longest-lived vortices are tropical cyclones with latent heating at the core and weak low level circulation due to the relationship between the weather layer and deep winds. It has also been observed that the cloud top temperatures within the central region of the GRS are lower than those on the periphery, possibly indicating diabatic convective processes. Problems with the idea of diabatic forcing of Jovian vortices include the fact that the observed horizontal scale of the core is not small, as it would be expected to be for Earth's moist systems: this could be a consequence of the microphysics involved. Also, Yano (1987b) has argued that the influence of latent heating must be small.

Remaining with the problem of circularly symmetric/asymmetric systems, it is known for tropical cyclones that for their angular momentum to increase, the system must not be symmetric. This, in the context of the GRS could be a allowed intermittently by vortex merger, but appears in practice to be an overall feature of the system.

7   Summary.

Many of the features of the dynamical structure of large Jovian vortices can be immediately understood in qualitative terms. For example the equatorward shift of the outer region of faster flow may be explained by the existence of a β-effect, probably modified by the existence of a deep streamfunction (section 2). In more specific terms, it has been possible to model the pv structure of these vortices using one or two perturbed circular boundaries. Regions of piecewise constant pv illuminate how the boundary of a spot will deform in order to exist in a far-field flow and, in the two-contour case, how the width of the intermediate region may change. More sophistication has been used in this formulation by including a modon formulation within the near-circular boundaries. This is strongly motivated by the observational data and, for the one contour case, produces much more robust vortices than those of piecewise constant pv.

There are several directions in which this work may be fruitfully extended. Firstly, numerical computations of the exact, steady boundaries in all the modelled cases above would be useful, in examining the success of the linearisation. Also, stabilities of these solutions should be tested; this is probably also amenable to numerical work. Beyond the results given here, it would be worthwhile to repeat the analyses for cases in which $\beta y + F\psi_2$ has a nontrivial y-dependence, in which case there may be N-S asymmetries in the perturbation to the vortex: the obvious next case would be that of a basic flow cubic in y. Finally, it should be straightforward, if algebraically tricky, to construct modonlike solutions with an annulus of $\nu^2 = -k^2 > 0$ (wavelike) in order to gain a closer look at the behaviour of the sharp gradient of Q with ψ near the edge of the vortices.

It would be relatively simple for all these cases to evaluate the Q-vector structure of their interiors. This could be performed for the observational data, provided assumptions about the thermal field are made. There is very little understood about the thermodynamics of Jovian vortices and this could be a revealing starting-point for their investigation.

8   Acknowledgements.

I have to thank, for their truly invaluable help, Jun-Ichi Yano and Glenn Flierl. Glenn, of course, deserves special thanks for his directorship of the Summer Program this year - we have all found it a most stimulating and unique experience. Other people who have given advice and assistance are Steve Meacham, Tim Dowling, Andy Ingersoll and George Veronis (on the softball field). Last but not least, thanks to Niel Balmforth for his moral guidance, Andrew Stamp for the midnight density current experiment and all the barn fellows for some marvellous times.

9   References.

Dowling, T.E. and Ingersoll, A.P., 1989, 'Jupiter's Great Spot as a shallow water system.', J. Atmos. Sci., 46, 3256-3278.

Dowling, T.E.,1992, Not yet published, J. Atmos. Sci.

Gill,A.E., 1983, 'Atmosphere-Ocean Dynamics.', Wiley.

Flierl,G.R., Stern,M.E. and Whitehead,J.A.Jr., 1983, 'The physical significance of modons: laboratory models and general integral constraints.' Dyn. Atmos. Oceans, 7, 233-263.

Flierl, G.R., 1987,'Isolated eddy models in geophysics', Ann. Rev. Fluid Mech., 19, 493-530.

Flierl, G.R., Larichev,V.D., McWilliams, J.C. and Reznik, G.M., 1980, 'The dynamics of baroclinic and barotropic solitary eddies.', Dyn, Atmos. Oceans, 5, 1-41.

Haines, K. and Marshall, J.C., 1987, 'Eddy forced coherent structures as a prototype of atmospheric blocking.', Q.J.Roy.Met.Soc., 113, 681-704.

Ingersoll, A.P. and Cuong, P.G., 1981, 'Numerical model of long-lived Jovian vortices.' J. Atmos. Sci.,38, 2067-2076.

Yano, J.I., 1987a, 'Rudimentary considerations of the dynamics of Jovian atmospheres. Part I: The depth of motions and energetics.', J.Meteor. Soc. Japan, 65, 313-327.

Yano, J.I., 1987b, 'Rudimentary considerations of the dynamics of Jovian atmospheres. Part II: Dynamics of the atmospheric layer.', J.Meteor. Soc. Japan, 65, 329-340.

Yano, J-I. and Flierl, G.R., 1992, 'Isolated potential vorticity patches in quasi geostrophic zonal shear flows.' Dyn, Atmos. Oceans, 16, 439-472.

10 Figure Captions.

1. Cross-sectional structure of the Great Red Spot, White Ovals and zonal flows of Jupiter, from Dowling and Ingersoll (1989).

2. Relatonship between Bernoulli function, B, and potential voricity, q, for the Great Red Spot and White Ovals, from Dowling and Ingersoll (1989).

3. Cartoon of streamlines for a point vortex on a Northern Hemisphere β-plane. Flow moving from South to North becomes more anticyclonic (its relative vorticity decreases) due to the β effect, and vice versa. This helps to explain the form of the streamlines of the GRS and White Ovals.

4. The basic formulation for the piecewise continuous models. Boundaries $r = 1 + \eta$ and $r = a + \tau$ at which there are pv steps of q_1 and q_a respectively, enclose regions of constant potential vorticity anomaly.

5. The steadily propagating solution in the piecewise continuous case. The deformation of the boundaries allows a dipole perturbation streamfunction. This solution will not be stable.

6. Graphs of the boundary perturbations η and τ for the piecewise continuous system, with $\mu \equiv \frac{L}{L_D} = 3$, that is, $L_D = 0.1$, and a=1.25 or a=2, against structure, q_a. The central pv is fixed to be -1; the structure with varying q_a is sketched. When the boundaries are close, their perturbations are coupled; when a is larger the perturbations become independent.

7. Graph of $k^2 \equiv -\nu^2$ against latitude through the Great Red Spot. $n = i\nu$ is a 'refractive index' for the flow and determines whether solutions will be wavelike or evanescent. The departure from 'neutral' to the North is probably due to the unsteadiness of the flow in this region. Plotted by Tim Dowling, from DI89 data.

8. Basic state pv and streamfunction profiles with radius through the vortex, for varying Q, ψ relationship. (a),(b) $\Lambda = 0$ so interior pv is constant, (c) *Lambda* = 10, (d) *Lambda* = 1.

9. Graphs of boundary perturbation η with $\mu \equiv \frac{L}{L_D}$, for the piecewise continuous case and the modon form, each with single boundaries and a pv step of -1. The basic flow is simple shear with $\overline{\psi} = -\gamma y^2$, symmetric about $y = 0$. The modon form seems much more 'robust', being deformed

considerably less for given shear (γ) and μ.

10. Streamfunction contours in the (x,y) plane. (a) Basic state, ψ_0, with $F = 10$ and $\Lambda = 1$ (small departure from constant interior pv), (b) total streamfunction for this case when shear, $\gamma = .05$, so that boundary perturbation, $\eta_2 = .12$, (c) total streamfunction for $F = 1$, $\gamma = 0.2$ so that $\eta_2 = .23$.

b

u_2 [m/s]

latitude

1b
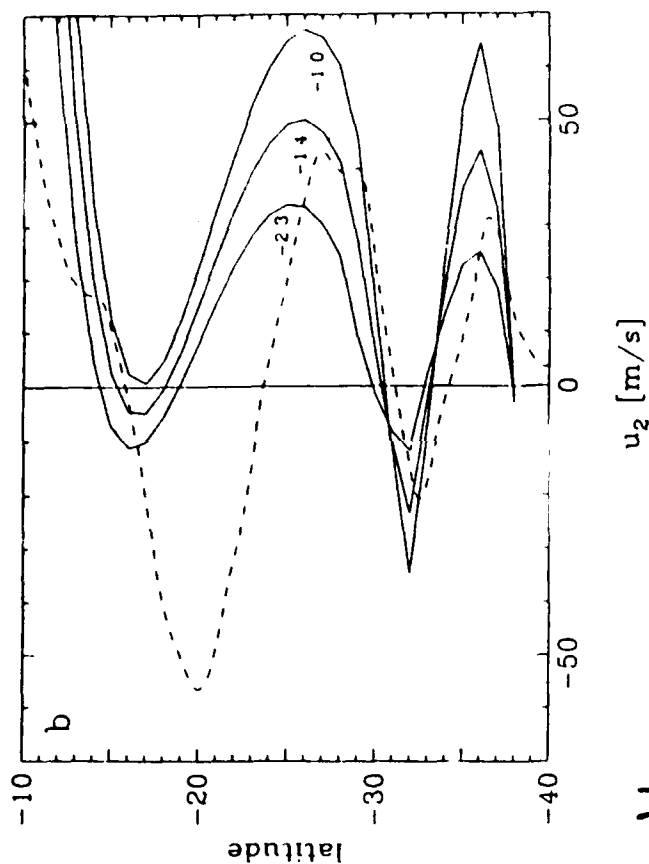
FIG. 4. Bottom topography gh_2 and deep-layer velocity u_2, in the System III reference frame. (a) The dashed curve shows the far-field free-surface height $g(\bar{h} + h_2)$ calculated from the cloud-top zonal wind profile of Limaye (1986). The solid curves show different solutions for the bottom topography gh_2 inferred from the data. See the text for a description of the data inversion method. The error bars indicate the variation of the data about each model fit, and are two standard deviations in total length. The curves are labeled by the parameter q_0 in units of 10^{-9} s m^{-2}. The bottom topographies under the GRS and Oval BC are assumed to be quartics in latitude, and are spliced together by fitting a parabola to the points in the interval $-30.5 \pm 2°$. The results are presented in the System III reference frame, with the zero of the ordinate defined to be the minimum of the curve $g(\bar{h} + h_2)$. (b) The dashed curve shows the cloud-top wind profile of Limaye. The solid curves show different solutions for the deep-layer velocity u_2, corresponding to the gh_2 presented in (a).

latitude

q [10⁻⁹ s/m²]

1a
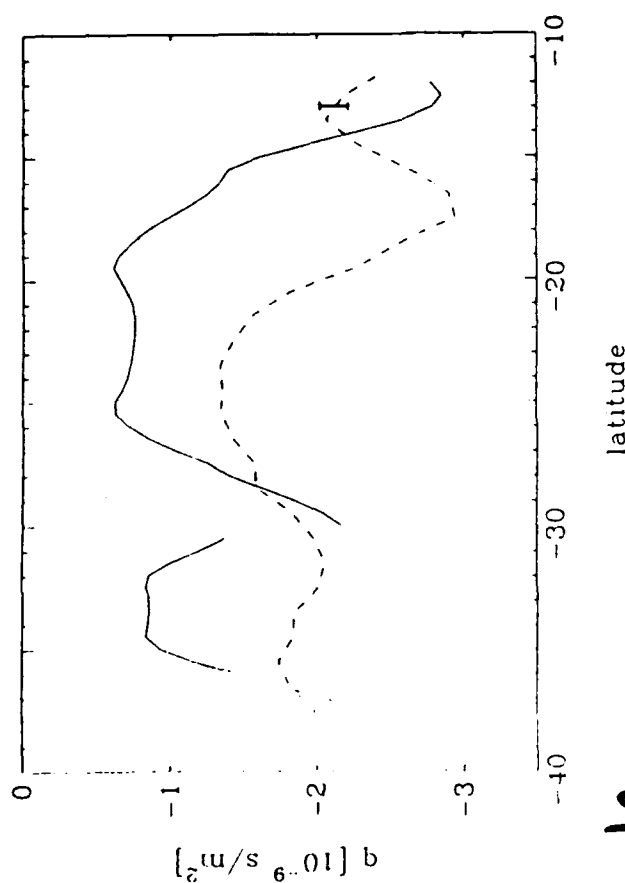
FIG. 5. Potential vorticity q versus latitude λ. The dashed curve shows the far-field potential vorticity $\bar{q}$, calculated from the cloud-top zonal winds and inferred bottom topography (Fig. 4). The case presented has $q_0 = -1.40 \times 10^{-9}$ s m^{-2} for the GRS. The error bar indicates the variation of the data about the model fit, and is two standard deviations in total length. Instability of the flow is possible where $\bar{q}$ is a local extremum. The solid curves show profiles of q versus λ through the centers of the GRS (right curve) and Oval BC (left curve). These are computed using the calculated functions $B(\phi, \lambda)$ and $q(B)$ shown in Figs. 2 and 3, respectively.

Dowling & Ingersoll, 1987

2
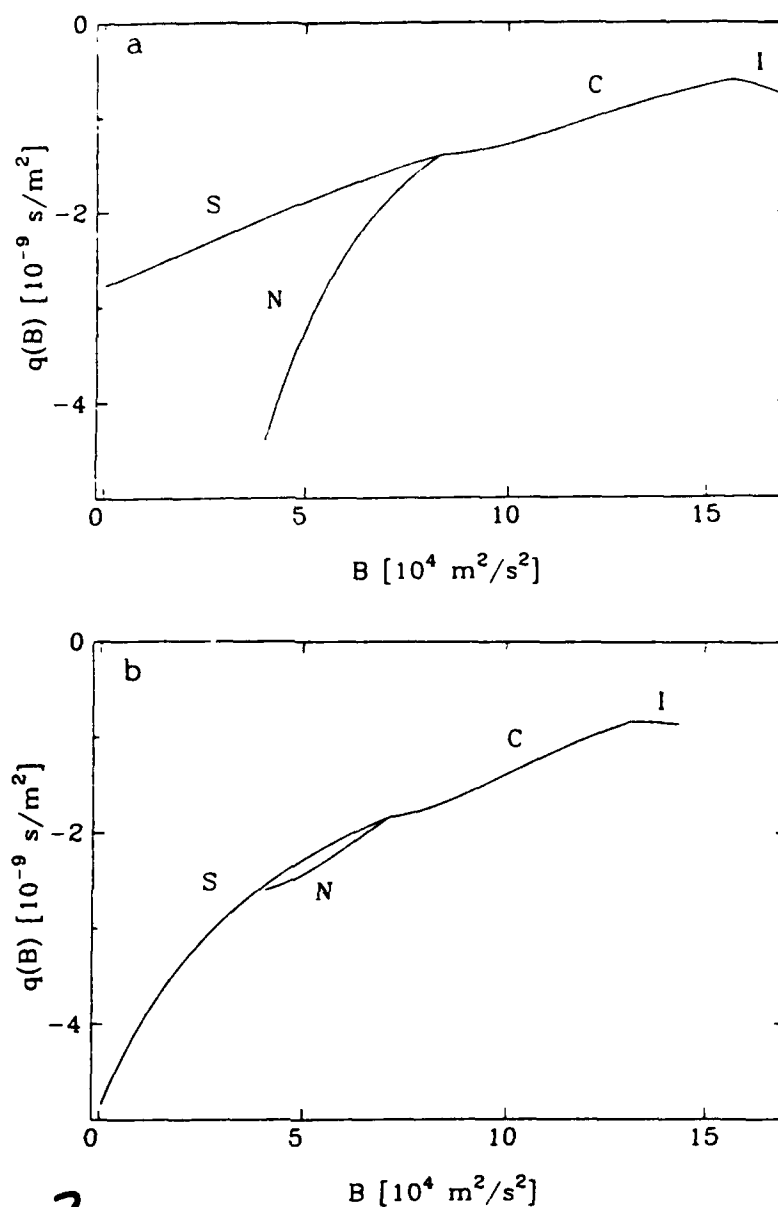
Fig. 3. Potential vorticity q versus Bernoulli function B. (a) Model results for the GRS. Different functions $q(B)$ are allowed for the northern and southern open streamline regions, denoted by N and S, respectively. The central closed streamline region is split into two pieces, denoted by C and I. The inner region I is defined by $B > 15.6 \times 10^4 \ m^2 \ s^{-2}$, the region C is defined by $15.6 \geqslant B > 8.3 \times 10^4 \ m^2 \ s^{-2}$, and the regions N and S are defined by $B \leqslant 8.3 \times 10^4 \ m^2 \ s^{-2}$ with latitude greater or less than $-23°$, respectively. Refer to Fig. 2a for a map of B. The function $1/q(B)$ is assumed to be piecewise quadratic in each region. The constant term $1/q_0$ is specified and equals $1/(-1.40 \times 10^{-9} \ s \ m^{-2})$ in this figure. (b) Same as (a) but for the Oval BC. The region I is defined by $B > 13.1 \times 10^4 \ m^2 \ s^{-2}$, the region C is defined by $13.1 \geqslant B > 7.1 \times 10^4 \ m^2 \ s^{-2}$, and the regions N and S are defined by $B \leqslant 7.1 \times 10^4 \ m^2 \ s^{-2}$, with latitude greater or less than $-34.5°$, respectively. The specified parameter $1/q_0$ equals $1/(-1.84 \times 10^{-9} \ s \ m^{-2})$.

312

③

$$f > 0$$
$$\beta > 0$$

④

$$q = q_\infty(y) + q_a$$

$$q = q_\infty(y) + q_a + q_1$$

$$r = 1 + \eta(\theta)$$

$$q = q_\infty(y)$$

$$r = a + \tau(\theta)$$

Figure 3

$$y$$
$$x$$

$$f > 0$$
$$\beta > 0$$

Figure 4

$$r$$
$$\theta$$

$$q = q_\infty(y)$$
$$+ q_1 + q_a$$

$$r = 1 + \eta(\theta)$$

$$q = q_\infty(y) + q_a$$

$$r = a + \tau(\theta)$$

$$q = q_\infty(y)$$

Figure 5

$$q$$
$$r$$

eta2, tau2 for $a = 2$, $\mu = 3$

$a = 2$

$\frac{\eta_2}{\gamma}$, $\frac{\tau_2}{\gamma}$

eta2, tao2 for $a = 1.25$, $\mu = 3$

$\frac{\eta_2}{\gamma}$, $\frac{\tau_2}{\gamma}$

Figure 6

GRS

$\left(q_0 = -1.4 \times 10^{-9} \, Sm^{-2} \right)$

k^2
$[10^{-13} m^2]$

3 — S | C | I | C | N

(neutral)

(wave)

(evan)

(wave)

(evan)

(wave)

(evan)

(wave)

-30   -25   -20   -15

latitude [°]

66.

$$k^2 \equiv -gh\left\{ q^2 + q \, gh \, \frac{d\alpha}{d\beta} \right\} = -gh\left\{ q^2 + \frac{dq}{d\psi} \right\} \quad [-\psi_y = u]$$

GRS

latitude

-15

-25

Ⓝ Ⓒ

Ⓘ

Ⓢ

120°   (110°)   100°

longitude

(I haven't estimated error bars)

Figure 7.
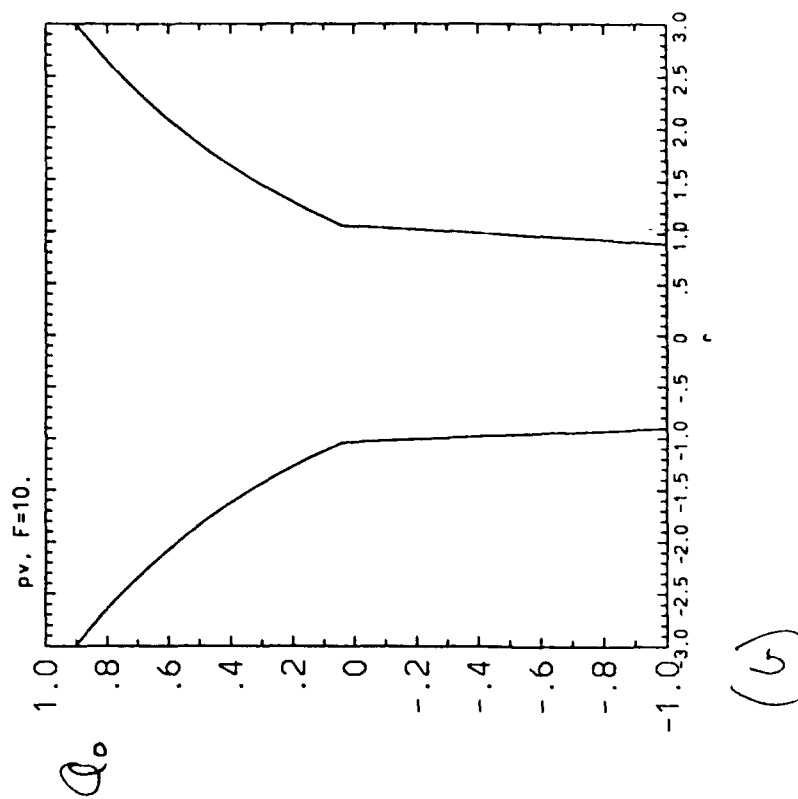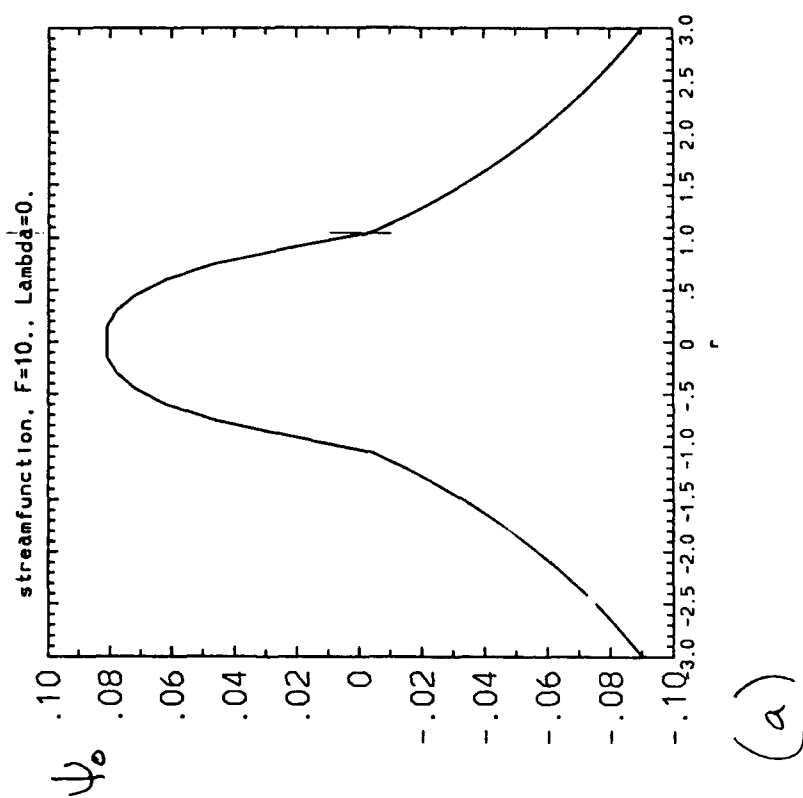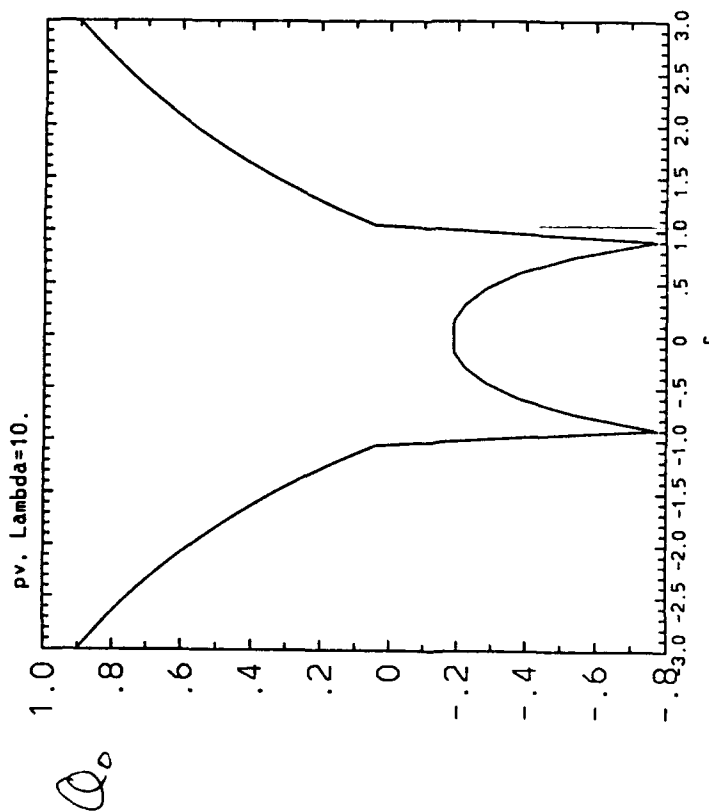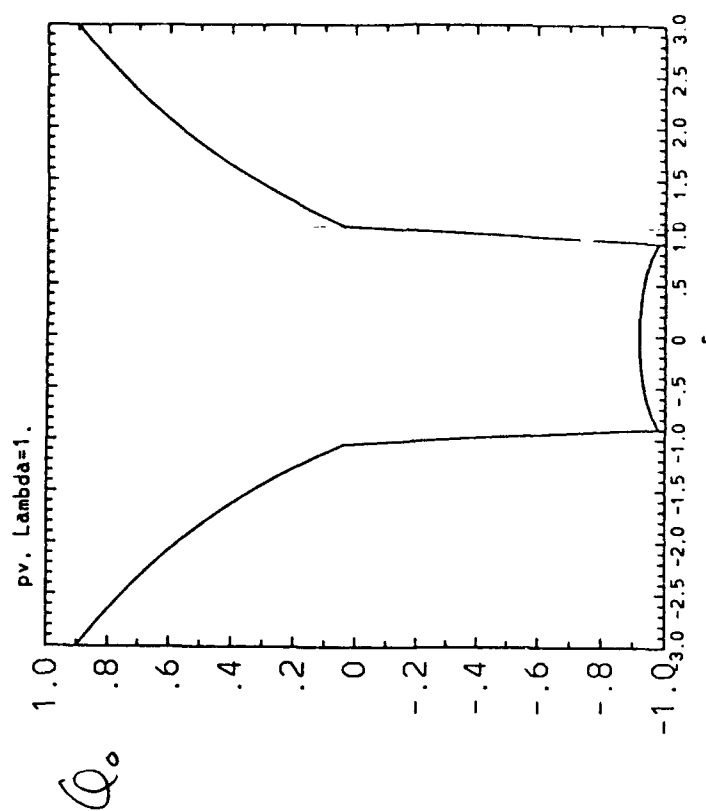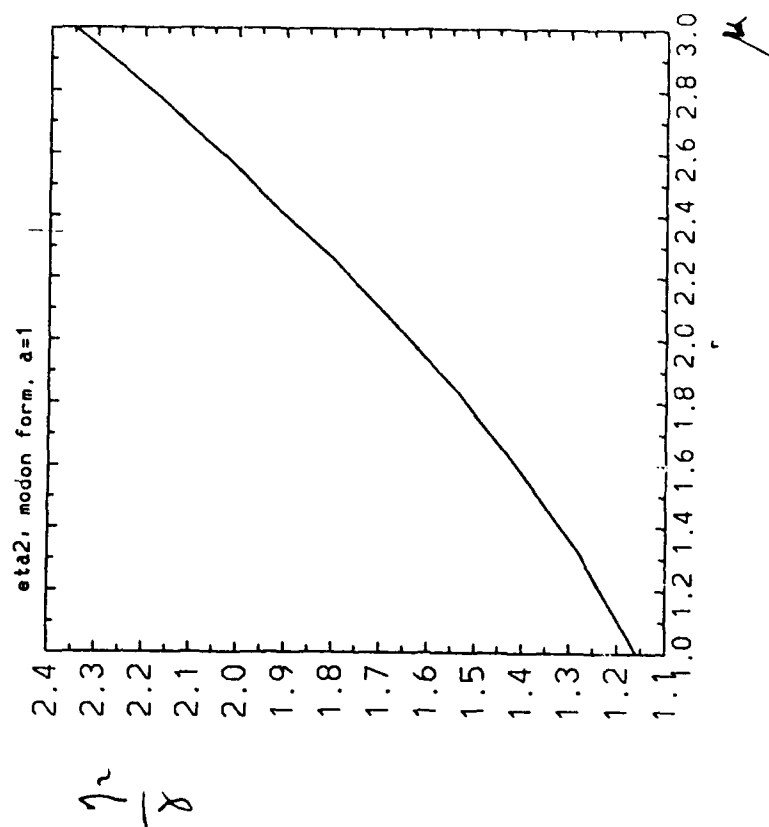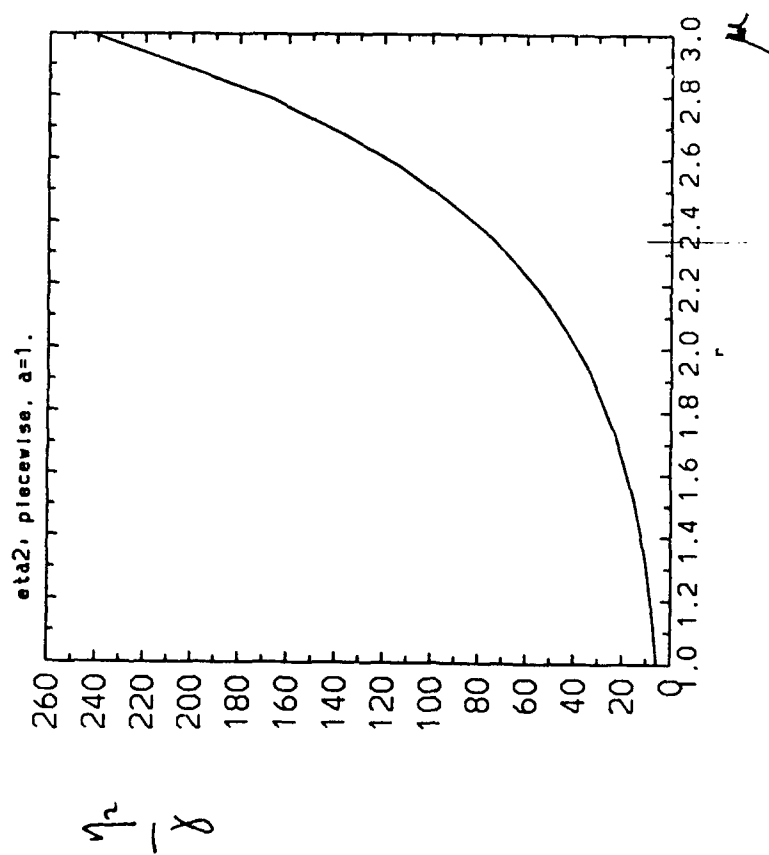
pv, F=10.

$\mathcal{Q}_o$

(b)

streamfunction, F=10., Lambda=0.

ψ_o

(a)

Figure 8

pv. Lambda=1.

Q_o

r

(α)

pv. Lambda=10.

Q_o

r

(c)

Figure 8

318

Figure 8

$\dot{\gamma} = 0.05$
$F = 10$
$\eta_2 = 0.12$

(b)

(a)

Figure 10.

(c)

$\gamma = c \cdot 2$
$\eta = c \cdot 23$
$(z = 1)$
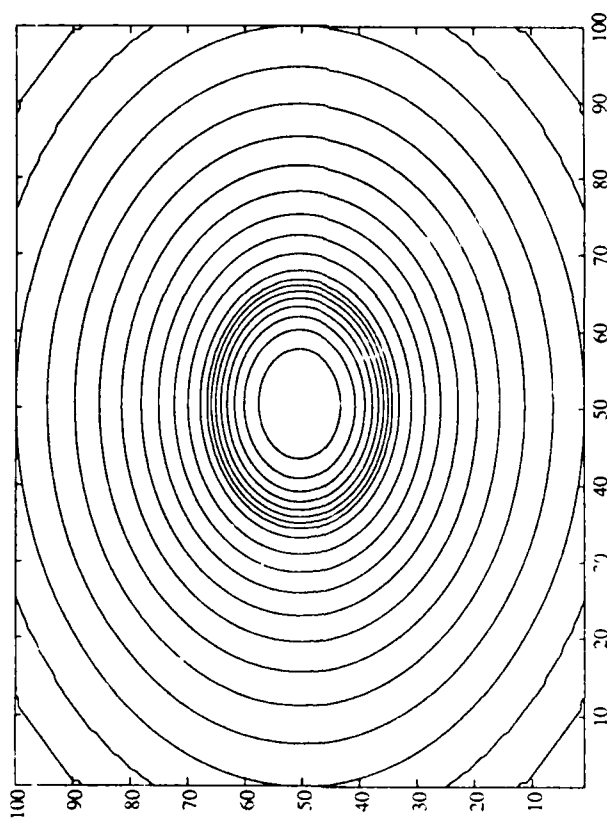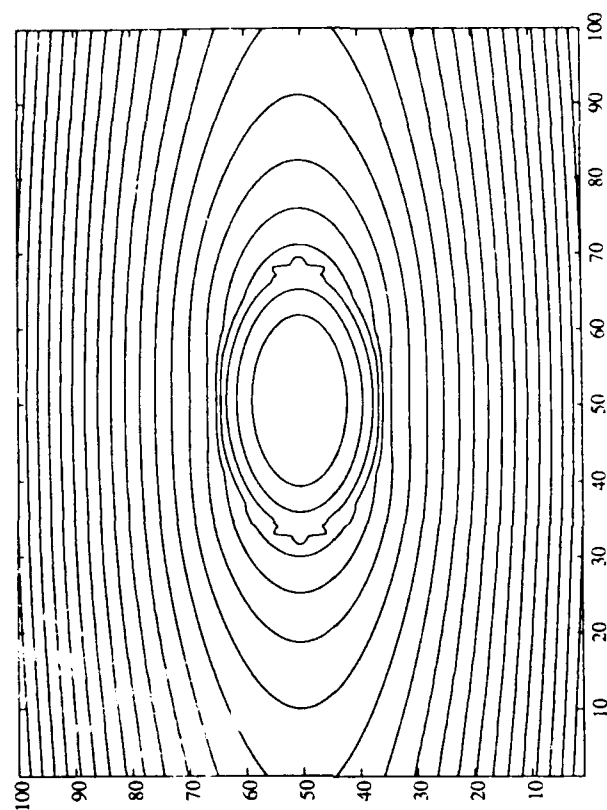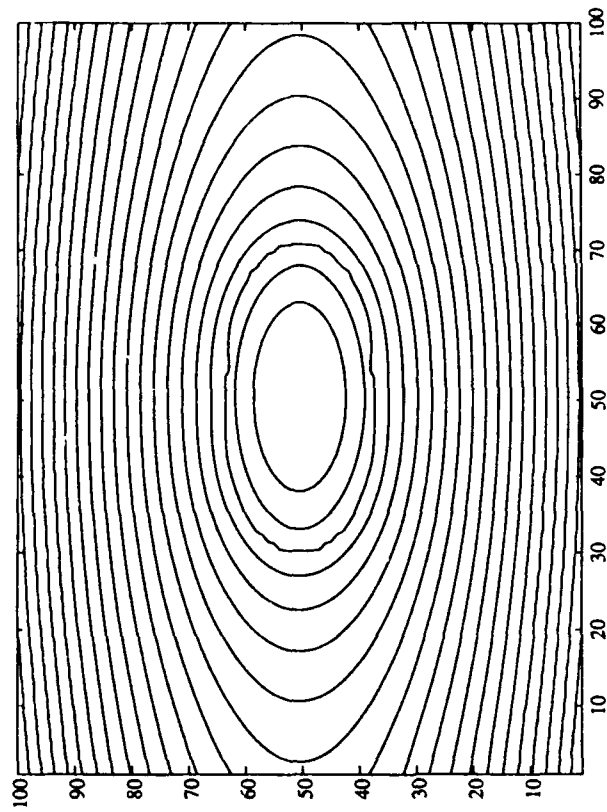
Figure 10.

The Stability of Jupiter's Zonal Winds

Andrew Stamp
Research School of Earth Sciences
The Australian National University

August 1992

1   Introduction

The wealth of data obtained by the Voyager spacecraft encounters with Jupiter, Saturn, Uranus and Neptune has sparked interest in the dynamics of the atmospheres of the giant planets. Of particular interest are the long-lived vortices, the alternating jet streams, and the slowly moving waves. We would like to understand what gives rise to these features, and what maintains them. Some pieces of the puzzle have fallen into place, for example it has been demonstrated numerically that Jupiter's zonal winds give rise to the Great Red Spot through a shear instability mechanism (Dowling & Ingersoll 1989). But if the zonal winds beget the vortices, then what begets the zonal winds?

Before we try to understand the larger problem of the origin of Jupiter's zonal winds, the first step is to analyze the high-quality Voyager data and determine the basic-state winds, both the cloud-top winds and the underlying deep winds. The next step is to investigate the stability properties of the basic-state winds. It is known that Jupiter's cloud-top zonal winds strongly violate the Rayleigh-Kuo stability criterion. However, the zonal winds determined from Voyager images taken in 1979 precisely match the zonal winds determined from Hubble Space Telescope images taken in 1991 (Huber *et al.* 1992), and it is hard to understand how a complicated wind profile like Jupiter's could be unstable and yet not vary at all in 12 years. We will take as our starting point the hypothesis that Jupiter's cloud-top zonal winds are *neutrally stable* with respect to Arnol'd's 2nd stabilty theorem (Dowling 1992), and investigate numerically the growth rates and phase speeds of zonal-wind configurations that are close to this neutral configuration. Since stability theorems are more completely developed for the quasi-geostrophic equations than for the primitive equations, we will study both cases in order to gain insight into the differences and similarites.

1.1   Review of wave observations

Wave phase speeds are an important diagnostic of an atmosphere's basic-state configuration. Several observers have recently reported evidence of slowly moving Rossby waves in Jupiter's atmosphere. The waves are notable for having about 10 wavelengths in the zonal direction and for having motions that are slow in comparision to the local zonal wind speed, as measured in the planet's magnetic-field reference frame. The first observations of slowly moving waves on Jupiter were reported by Magalhães *et al.* (1989) from an analysis of the Voyager infrared (4-55 μm) IRIS data. They found

a mode 9 wave located in the lower stratosphere between 5-15° N, moving with a phase speed of $c = 10.5 \pm 12.4\,\mathrm{ms}^{-1}$. Soon thereafter, Deming *et al.* (1989) reported similar waves at deeper levels from an analysis of ground-based infrared $(8 - 13\,\mu\mathrm{m})$ observations. Two mode 10 waves, one at the equator and other at 20° N, were found with the latter having a phase speed of $c = 25 \pm 33\,\mathrm{ms}^{-1}$. Figure (1) shows the temperature structure of the wave at 20° N on two successive days and the cross-correlation function used to determine the phase velocity.

There is apparently little correlation between these stratospheric waves and the underlying features in the cloud tops. In contrast, Saturn displays two prominant waves in its cloud tops. Sromovsky *et al.* (1983) carried out a detailed analysis of the *Ribbon*, a narrow, dark, wavy line in the clouds at 42° N, which is centered on a strong eastward jet. The dispersion relation for the Ribbon, shown in Figure (2), is noisy but does indicate that the phase speeds are bounded between zero and the peak jet speed. Godfrey (1988) discovered Saturn's *Polar Hexagon*, a mode 6 wave at 76° N that is moving with a phase speed of only $c = 0.8 \pm 1.1\,\mathrm{ms}^{-1}$. The Hexagon is centered in a jet that has a peak speed of just over $100\,\mathrm{ms}^{-1}$. Voyager images of the Hexagon reveal the existence of an isolated vortex on one of its six sides, and the most likely explanation is that the vortex is forcing a standing, mode 6 Rossby wave. We will return to these observations of slowly moving waves on Jupiter and Saturn when we examine the Rossby-wave dispersion relations for the basic-state zonal wind profiles considered in this paper.

1.2   1-1/2 Layer Model

In attempting to qualitatively reproduce the phenomena seen in Jupiter's atmosphere, numerical modelers have represented the continuously stratified atmosphere with simple 2-layer *shallow-water* models. The models consist of a thin "weather layer" of constant density ρ that lies above a deep layer of constant density $\rho_2 > \rho$. All deep layer variables will be distinguished with a subscript "2." In such models the lower layer represents the convectively adjusted, neutrally stratified deep atmosphere. The constant-density assumption is not as unrealistic as it first appears to be, because when entropy is used as the vertical coordinate in the full equations they are mathematically similar to the shallow-water equations.

A common simplifying assumption is that the lower-layer motions are zonal, steady and unaffected by the time-dependent motions in the upper layer. Such a model is called a "1-1/2 layer" model, rather than a 2-layer model, because the deep layer is not free to evolve. As shown in Figure (4) the 1-1/2 layer model is equivalent to a 1-layer model with bottom topography because the deep-layer motions give rise to horizontal variations in the deep-layer pressure field that appear to the upper layer as variations in a lower boundary.

The 1-1/2 layer model has been applied to Jupiter by many groups and a number of different assumptions about the deep layer motions have been made; see for example Ingersoll & Cuong (1981), Williams & Yamagata (1984) and Marcus (1988). However, Dowling & Ingersoll (1989) inferred the deep layer motions to within a free parameter by applying a vortex-tube stretching analysis to the Voyager data. More recently Dowling (1992) sought to determine an empirical relationship between the upper layer's zonal velocity, $\overline{u}(y)$, and the meridional gradient of potential vorticity, $\overline{q}_y(y)$, from the Jupiter data. (An overbar will hereafter denote a zonal average.) It was found that the data satisfy:

$$\overline{u} = \frac{\overline{q}_y}{\overline{q}^2} = -\left(\frac{1}{\overline{q}}\right)_y \,, \tag{1}$$

where

$$\overline{q} = \frac{f - \overline{u}_y}{g\overline{h}} \ , \quad \overline{q}_y = \frac{1}{g\overline{h}}(\beta - \overline{u}_{yy} + f\overline{q}(\overline{u} - \overline{u}_2)) \ , \tag{2}$$

f is the Coriolis parameter, $\beta = f_y$, $\overline{u}_2(y)$ is the deep-layer zonal wind, g is the reduced gravity and $\overline{h}(y)$ is the upper layer thickness. This relationship is shown graphically in Figure (5).

1.3 Current research

In this paper we investigate the stability of the empirical basic state (1). The structure of the paper is as follows. A review of the various analytical stability criteria that are relevant to the problem is presented in § 2. Since most stability theorems provide necessary rather than sufficient conditions for instability, and since such theorems do not provide estimates of growth rates in the case of instability, we proceed with a numerical linear analysis that will address these questions. In § 3 and § 4 we examine the quasi-geostrophic and primitive shallow-water cases, respectively, and in §5 we draw conclusions and point to future work.

2 Review of Stability Theorems

The ubiquitous nature of zonal shear flows has resulted in considerable efforts to determine the stability properties of such flows. An instability occurs when an interaction between waves draws energy from the zonal winds and causes the waves to grow to large amplitudes. Stability theorems specify conditions that guarantee that there will be no such destabilizing interactions. The restoring force for Rossby waves, the large, slowly moving waves that control the meteorology, is proportional to changes in the background potential vorticity, so most stability theorems specify there conditions in terms of the potential-vorticity gradient. But the faster moving gravity waves can have a destabilizing influence as well. At present, stability properties are better understood for the quasi-geostrophic equations, which filter out the gravity waves, than for the primitive shallow-water equations.

In the quasi-geostrophic limit the potential vorticity gradient (2) takes the form:

$$\overline{Q}_y = \beta - \overline{u}_{yy} + L_d^{-2}(\overline{u} - \overline{u}_2) \ , \tag{3}$$

where $L_d^2 = g\overline{h}/f^2$ is the square of the (first baroclinic) deformation radius. The most commonly cited stability theorem is the Rayleigh-Kuo theorem, which states that if for all y:

$$\overline{Q}_y \geq 0 \quad \text{or} \quad \overline{Q}_y \leq 0 \ , \tag{4}$$

then the flow is stable. The *barotropic* stabilty criterion refers to the special case $\overline{u} = \overline{u}_2$. It has been known since the Voyager encounters in 1979 that the strong positive curvature in Jupiter's westward jets is enough to overcome β, which is positive-definite, and make $\overline{Q}_y$ negative. Estimates of the term involving $\overline{u} - \overline{u}_2$ only add to the conclusion that Jupiter's winds violate the Rayleigh-Kuo stability criterion.

However, there are at least two known ways to violate the Rayleigh-Kuo stability criterion and still have a stable flow. For example, if in some reference frame:

$$-\infty < \frac{\overline{Q}_y}{\overline{u}} < 0 \ , \tag{5}$$

for all y, then the flow is stable. This stability criterion is known as Fjørtoft's (1950) theorem, or in the case of large-amplitude perturbations as Arnol'd's (1966) 1st stability theorem. Ripa (1983) extended this theorem for small-amplitude perturbations to the 1-layer shallow-water equations, for both the local cartesian (beta-plane) geometry and the spherical geometry. The added condition $\overline{u}^2 < gh$ is needed to insure that gravity waves do not destabilize the flow. In addition to his 1st theorem, Arnol'd also showed that if in some reference frame:

$$0 < \frac{\overline{Q}_y}{\overline{u}} < \frac{1}{L_d^2} , \tag{6}$$

for all y, then the flow is stable. We have written (6) in its linear-stability form and for the special case when the deformation radius is much smaller than the planet's radius, as it is on Jupiter; for a complete discussion of Arnol'd's stability theorems see McIntyre and Shepherd (1987). Arnol'd's 2nd stability theorem has not yet been extended to the primitive shallow-water equations. Our numerical experiments below will explore this area.

3 Quasi-geostrophic Model

In the quasi-geostrophic limit Jupiter's empirical basic state (1) becomes:

$$\overline{u} = \overline{Q}_y \, L_d^2 . \tag{7}$$

This relationship between the zonal wind and the potential vorticity gradient violates both the Rayleigh-Kuo and Fjørtoft-Arnol'd stability criteria. However, it is evident that it is on the margin of stability with respect to Arnol'd's 2nd stability theorem (6). Arnol'd's stability criteria are sufficient conditions and their violation does not imply instability. However, we will now show numerically that violation of Arnol'd's 2nd stability theorem is in fact sufficient for instability for the $\overline{u} = \cos(y)$ basic state.

3.1 Preliminary analysis

The shallow-water equations consist of two equations that describe the conservation of momentum and one that describes the conservation of mass. The quasigeostrophic approximation introduces a streamfunction ψ such that:

$$u = -\psi_y , \quad v = +\psi_x , \tag{8}$$

and combines the three shallow-water equations into a single equation that describes the conservation of potential vorticity:

$$Q_t + uQ_x + vQ_y = 0 , \tag{9}$$

where

$$Q = f_0 + \beta y + \psi_{xx} + \psi_{yy} - L_d^{-2}(\psi - \psi_2) . \tag{10}$$

We now write u, v, and Q as the sum of a basic state plus a small perturbation:

$$u(x,y,t) = \overline{u}(y) + u'(x,y,t) , \tag{11a}$$

$$v(x,y,t) = v'(x,y,t) , \tag{11b}$$

$$Q(x, y, t) = \overline{Q}(y) + Q'(x, y, t) \,. \tag{11c}$$

All basic-state quantities will be distinguished by an overbar since they are assumed to be zonal, while all perturbation quantities will be distinguished by primes. By substitution in (9) the linear perturbation equation is found to be:

$$Q'_t + \overline{u}Q'_x + v'\overline{Q}_y = 0 \,. \tag{12}$$

To investigate Jupiter's empirically determined basic state (7) we introduce a one-parameter family of basic states:

$$\overline{u} = A\,\overline{Q}_y\,L_d^2 \,. \tag{13}$$

For a given zonal wind profile $\overline{u}(y)$ the parameter A determines the strength of the potential vorticity gradient $\overline{Q}_y$ and thus the restoring force driving the destabilizing Rossby waves. Application of Arnol'd's 2nd stability theorem to (13) shows that the case $A > 1$ is stable. The case $A \leq 1$ will be investigated here. If we define a perturbation streamfunction ψ' such that:

$$u' = -\psi'_y \,, \quad v' = +\psi'_x \,, \tag{14}$$

then by substitution (12) becomes:

$$Q'_t + \overline{u}\frac{\partial}{\partial x}\left(Q' + A^{-1}L_d^{-2}\psi'\right) = 0 \,. \tag{15}$$

To solve (15) note from (10) that the perturbation potential vorticity and streamfunction are related by

$$Q' = \left[\frac{\partial^2}{\partial x^2} + \frac{\partial^2}{\partial y^2} - L_d^{-2}\right]\psi' \,. \tag{16}$$

Next, we Fourier decompose the perturbation streamfunction in x and t:

$$\psi' = \hat{\psi}(y)\exp[ik(x - ct)] \,, \tag{17}$$

and rewrite (15) in the form:

$$(\overline{u} - c)\left[\frac{\partial^2}{\partial y^2} - (k^2 + L_d^{-2})\right]\hat{\psi} + A^{-1}L_d^{-2}\overline{u}\hat{\psi} = 0 \,. \tag{18}$$

To facilitate comparision of numerical solutions with observations it is necessary to nondimensionalize (18). In anticipation of approximating Jupiter's basic state zonal flow (Figure (5)) by a cosine profile

$$\overline{u}(y) = u_0 \cos(\frac{2\pi y}{L}) \tag{19}$$

we nondimensionalize all velocities by the maximum zonal jet velocity u_0 and all lengths by $L/2\pi$ where L is the meridional zonal jet wavelength. For Jupiter $u_0 \approx 50$ ms^{-1} and $L \approx 15,000$ km. Finally, for convenience the notation L_d is used to refer to the nondimensional deformation radius $2\pi L_d/L$ hereafter. The resulting nondimensional perturbation equation has the form (18) with all variables being nondimensional and of the same order.

3.2 Application of Arnol'd's stability theorems

The energy associated with the linear perturbations may be calculated by multiplying (15) by $\rho\psi'$ and integrating over the area of the domain, which yields:

$$\frac{\partial E}{\partial t} = -\rho \int\int \overline{u}\psi'Q' \, dx \, dy \,, \quad \text{where} \quad E = \frac{\rho}{2}\int\int |\psi'_x|^2 + |\psi'_y|^2 + L_d^{-2}|\psi'|^2 \, dx \, dy \,. \quad (20)$$

Similarly, the enstrophy associated with the linear perturbations may be calculated by multiplying (15) by $\rho Q'$ and integrating, which yields:

$$\frac{\partial Z}{\partial t} = -\rho A^{-1}L_d^{-2}\int\int \overline{u}\psi'Q' \, dx \, dy \,, \quad \text{where} \quad Z = \frac{\rho}{2}\int\int |Q'|^2 \, dx \, dy \,. \quad (21)$$

From   two equations it is seen that

$$\frac{\partial}{\partial t}\left(E - AL_d^2 Z\right) = 0 \,. \quad (22)$$

Assuming that the system is periodic in y, as is the case for the basic state $\overline{u} = \cos(y)$, then the perturbation streamfunction may be expressed as:

$$\psi' = \exp[ik(x - ct)] \sum_{l=-\infty}^{\infty} \psi_l \exp(ily) \,, \quad (23)$$

where $c = c_r + ic_i$. Subsequently the energy-enstrophy conservation equation (22) may be reduced to the form:

$$c_i \left[\sum_{n=-\infty}^{\infty} \left\{ (k^2 + l^2 + L_d^{-2})(\psi_l)_i^2 \left[1 - AL_d^2\left(k^2 + l^2 + L_d^{-2}\right)\right] \right\} \right] = 0 \,. \quad (24)$$

We note that if every term $[1 - AL_d^2(k^2 + l^2 + L_d^{-2})]$ in the sum is either positive definite or negative definite then $c_i \equiv 0$ and the flow must be stable. The positive-definite case yields the Fjørtoft-Arnol'd stability criterion:

$$1 - AL_d^2(k^2 + l^2 + L_d^{-2}) > 0 \quad \Rightarrow \quad A < 0 \,, \quad (25)$$

and the negative-definite case yields Arnol'd's 2nd stability criterion:

$$1 - AL_d^2(k^2 + l^2 + L_d^{-2}) < 0 \quad \Rightarrow \quad A > 1 \,. \quad (26)$$

These results are for small-amplitude perturbations, but Arnol'd's original work was for the more general case of large-amplitude perturbations. See McIntyre & Shepherd (1987) for more details on the subject of nonlinear stability.

3.3 Stationary neutral stability

The special case of stationary neutral stability, $c = c_r + ic_i = 0$, yields simple analytic solutions to perturbation equation (18) that are useful for checking numerical code and for providing points about which to derive asymptotic solutions.

When $c = 0$ the perturbation equation (18) reduces to

$$\left[\frac{\partial^2}{\partial y^2} - \left[k^2 + L_d^{-2}\left(1 - \frac{1}{A}\right)\right]\right]\hat{\psi} = 0 .$$ (27)

Again we decompose $\hat{\psi}(y)$ into a summation of exponential functions

$$\hat{\psi}(y) = \sum_{l=-\infty}^{\infty} \psi_l \exp(ily) ,$$ (28)

and by substitution find that stationary neutral stability occurs at the discrete set of wavenumbers given by

$$k^2 = L_d^{-2}\left(\frac{1}{A} - 1\right) - l^2 .$$ (29)

Figure (6) shows how the number of cases of stationary neutral stability varies with L_d and A. Neither L_d nor A is known for Jupiter, but we anticipate that the most appropriate nondimensional parameter range is:

$$0.7 \leq A , \quad L_d \leq 1.2 .$$ (30)

In this parameter range (29) implies that there is only one k for which $c = 0$. We will have more to say on this subject later in connection with the slowly moving waves on Jupiter.

3.4 Galerkin formulation

Numerical solutions of the perturbation equation (18) are achieved by employing the Galerkin method. In this method the dependent variables are expanded in terms of orthogonal functions, each of which satisfy the boundary conditions; here

$$\hat{\psi}(y) = \sum_{n=-(N-1)/2}^{(N-1)/2} \psi_n \phi_n(y) .$$ (31)

The basis functions are presumed to satisfy

$$< \phi_n(y)\phi_m(y) > = \delta_{nm} ,$$ (32)

where the inner product represents an integration in y over the domain. This produces a matrix equation

$$< \gamma_n \phi_n \phi_m > \psi_n = c\psi_n ,$$ (33)

where γ_n is independent of y. That is, for each k there is an $N \times N$ matrix eigenvalue system of the form (33). The N eigenvalues are the complex phase speeds, $c = c_r + ic_i$, and the N modes are given by the eigenvectors, $\hat{\psi} = \psi_n$ in (31). We note that if $c_i > 0$ for a given mode then this mode is unstable and growing exponentially at the rate kc_i.

In order to complete the calculations the basic zonal flow was chosen to be $\overline{u} = \cos(y)$ as this approximates Jupiter rather well and is amenable to numerical solution. Since this basic state is periodic in y we use complex exponentials as the Galerkin expansion functions, $\phi_n(y)$. This simple case yields a Galerkin matrix that is tridiagonal, with zeros on the diagonal:

$$M\hat{\psi} = c\hat{\psi}; \quad M = \frac{1}{2}\left[1 - \frac{1}{AL_d^2(k^2 + L_d^{-2} + n^2)}\right](\delta_{n-m,1} + \delta_{n-m,-1})$$ (34)

This matrix eigenvalue system was solved for different values of the stability parameter, A, and deformation radius, L_d. For each parameter pair a range of wavenumbers k were considered and the growth rate and phase speed of the most unstable mode were recorded.

3.5 Results

The results of the numerical calculations are now presented and it is noted that because the most unstable modes were always stationary $c_r = 0$ it is not necessary to show plots of c_r vs. k. Figures (7a,b) show the growth rate kc_i vs. k for the most unstable mode, for two parameter regimes. For the Jupiter-like case of $L_d = 1.0$ and $A = 0.8$ there is a single wavenumber, given by $k = 0.5$, at which $c = 0$. Conversely, for the less Jupiter-like parameters $L_d = 0.2$ and $A = 0.8$ stationary neutral stability occurs at three wavenumbers given by $k = 1.50$, 2.29 and 2.50. Both of these results are predicted theoretically by (29). It is important to note that in both cases there is a large k (small wavelength) cutoff which, because all of the instabilities are stationary, is given by (29) with $n = 0$. Furthermore, in the Jupiter-like case the instability curve is smooth with a single maximum indicating that it is the same mode that is the most unstable at all wavenumbers. In Figure (9a) the eigenfunction of the most unstable mode is plotted and it is seen that at $y = \pm\pi/2$, or when $\bar{u}(y) = 0$, the Reynolds stress $\overline{u'v'}$ is in the opposite direction to the shear of the zonal velocity $\bar{u}_y$, thus causing the instability.

To investigate the necessary and sufficient nature of Arnol'd's 2nd stability theorem two other plots were made. The growth rate is plotted against wavenumber for different values of A but with $L_d = 1.0$ in Figure (10). It is evident that the growth rates decrease as $A \to 1$. This is because the potential vorticity gradient $\overline{Q}_y$, which provides the restoring mechanism for the destabilizing Rossby waves, decreases in this limit. In Figure (11) the maximum growth rate is plotted against A for $L_d = 0.8, 1.0, 1.2$. The obvious implication of this plot is that in all cases the point $A = 1$ defines neutral stability and thus violation of Arnol'd's 2nd stability theorem is sufficient for instability for the $\bar{u} = \cos(y)$ basic state. It is also seen that for any given A the growth rate increases with decreasing L_d.

Finally, it is useful to compare the numerical results with the observations of slowly moving waves discussed in §1.1. For the Jupiter-like parameter regime $L_d = 1.0$ and $A = 0.75$ the most unstable mode occurs at $k = 0.36$. If we consider a Rossby wave on Jupiter at 20°N then the planetary mode number is

$$71,400 \text{ km} \times \cos(20°) \times 0.36 \times \left(\frac{2\pi}{15,000 \text{ km}}\right) = 10 , \tag{35}$$

where $71,400$ km is the radius of Jupiter. This is consistent with the slowly moving waves of Magalhães et al. (1989) and Deming et al. (1989). Furthermore, the positioning of the instability at latitudes where $\bar{u}(y) = 0$ as, shown in the eigenfunction for this case (Figure (9a)), is also consistent with numerical simulations. Of course, as shown in Figure (10), changing L_d and A alters the wavenumber of the most unstable mode; for $L_d = 1.0$ the range $0.8 \leq A \leq 0.9$ corresponds to $0.2 \leq k \leq 0.3$. However, the predicted planetary wavenumbers remain consistent with the observations.

An analysis of Saturn's Ribbon was also conducted. Stable, narrow eigenfunctions centered on the eastward jet ($y = 0$, $\bar{u} = 1$) were found that resemble the Ribbon. These turnedstward jet ($y = 0$, $\bar{u} = 1$) were found out to be nondispersive continuum modes, whereas the c_r vs. k found by

Sromovsky *et al.* (1989) (Figure (2b)) appears to be dispersive. Sromovsky modeled the dispersion relation assuming an infinite deformation radius and neglecting the contribution of the zonal wind curvature to the potential vorticity gradient:

$$c = \overline{u} - \frac{\beta - \overline{u}_{yy} + L_d^{-2}(\overline{u} - \overline{u}_2)}{k^2 + l^2 + L_d^{-2}} \approx \overline{u} - \frac{\beta}{k^2 + l^2} \ . \tag{36}$$

As Dowling (1992) showed that β contributes only approximately 20% to the potential vorticity gradient for Jupiter and Saturn the accuracy of this dispersion relation may be limited. Re-evaluating the dispersion relation in light of the error bars the Ribbon could be nondispersive as suggested by our numerical calculations. Alternatively, the dispersion relation may be valid and our analysis unable to reproduce its behavior. This could result from several reasons. First, although the basic state (7) is appropriate for Jupiter it may not be so for Saturn. Second, this basic state may have been appropriate but representing the basic state zonal wind by a cosine profile inappropriate. Third, the correct parameter ranges in L_d, A or ϵ may not have been explored. However, we favor the explanation that the Ribbon is fundamentally a nonlinear phenomenon.

4 Shallow-water Model

4.1 Preliminary analysis

In the shallow-water system there are three governing equations; conservation of eastward and northward momentum and conservation of mass. In order to make the periodic assumption discussed in § 3.4 it is necessary to restrict the analysis to the $f-$plane (*i.e.* $f_y = \beta = 0$). This restriction is not compromising because β contributes only approximately 20% to the potential vorticity gradient $\overline{q}_y$ on Jupiter (Dowling 1992). The resulting conservation equations are

$$u_t - (\zeta + f_0)v + g(h + h_2)_x + uu_x + vv_x = 0 \ , \tag{37a}$$

$$v_t + (\zeta + f_0)u + g(h + h_2)_y + uu_y + vv_y = 0 \ , \tag{37b}$$

$$gh_t + \nabla.(gh\vec{v}) = 0 \ , \tag{37c}$$

where $\zeta = -u_x + v_y$ is the relative vorticity. As Jupiter's empirical basic state (1) is most simply expressed in terms of $\overline{q}^{-1}$, it is convenient to define the *potential height*

$$\eta \equiv q^{-1} = \frac{gh}{\zeta + f_0} \ . \tag{38}$$

Using η instead of gh, the shallow-water equations become

$$u_t - (\zeta + f_0)(v - \eta_x) + (gh_2)_x + uu_x + vv_x + (-u_{yx} + v_{xx})\eta = 0 \ , \tag{39a}$$

$$v_t + (\zeta + f_0)(u + \eta_y) + (gh_2)_y + uu_y + vv_y + (-u_{yy} + v_{xy})\eta = 0 \ , \tag{39b}$$

$$\eta_t + u\eta_x + v\eta_y = 0 \ . \tag{39c}$$

As for the quasi-geostrophic case we investigate stability by decomposing the fields into two portions; a basic state and a small perturbation

$$u(x, y, t) = \overline{u}(y) + u'(x, y, t) \ , \tag{40a}$$

$$v(x, y, t) = v'(x, y, t) , \tag{40b}$$

$$\eta(x, y, t) = \overline{\eta}(y) + \eta'(x, y, t) . \tag{40c}$$

We find that prescribing this basic state requires that the lower layer topography have the form

$$(gh_2)_y = -\overline{u}\,\overline{u}_y + \overline{u}_{yy}\overline{\eta} - (-\overline{u}_y + f_0)(\overline{u} + \overline{\eta}_y) , \tag{41}$$

and Figure (4) shows the form of the free surface and bottom topography for a cosine basic state zonal flow used in this study. By substitution the linear perturbation equations are found to be

$$u'_t - (-\overline{u}_y + f_0)(v' - \eta'_x) + \overline{u}u'_x + (-u'_{xy} + v'_{xx})\overline{\eta} = 0 , \tag{42a}$$

$$v'_t + (-\overline{u}_y + f_0)(u' + \eta'_y) + (-u'_y + v'_x)(\overline{u} + \overline{\eta}_y) + \overline{u}u'_y + u'\overline{u}_y - \overline{u}_{yy}\eta' + \overline{\eta}(-u'_{yy} + v'_{xy}) = 0 , \tag{42b}$$

$$\eta'_t + \overline{u}\eta'_x + v'\overline{\eta}_y = 0 . \tag{42c}$$

To investigate Jupiter's empirical basic state (1) we write

$$\overline{u} = A\frac{\overline{q}_y}{\overline{q}^2} , \tag{43}$$

where A is the same stability parameter as in the quasi-geostrophic case. Furthermore it is convenient to introduce a basic state streamfunction $\overline{\psi}$ which allows us to write

$$\overline{q} = \frac{A}{(\overline{\psi} + \overline{\psi}_0)} \quad \text{or} \quad \eta = \frac{(\overline{\psi} + \overline{\psi}_0)}{A} , \tag{44}$$

where $\overline{\psi}_0$ is a constant of integration. The resulting linear perturbation equations are

$$u'_t - (\overline{\psi}_{yy} + f_0)(v' - \eta'_x) - \overline{\psi}_y u'_x + A^{-1}(-u'_{xy} + v'_{xx})(\overline{\psi} + \overline{\psi}_0) = 0 , \tag{45a}$$

$$v'_t + (\overline{\psi}_{yy} + f_0)(u' + \eta'_y) + (A^{-1} - 1)\overline{\psi}_y(-u'_y + v'_x) - (\overline{\psi}_y u')_y + \overline{\psi}_{yyy}\eta' + A^{-1}(-u'_{yy} + v'_{xy})(\overline{\psi} + \overline{\psi}_0) = 0 , \tag{45b}$$

$$\eta'_t - \overline{\psi}_y\eta'_x + A^{-1}v'\overline{\psi}_y = 0 . \tag{45c}$$

As for the quasi-geostrophic system we Fourier decompose the perturbation fields in x and t:

$$\begin{bmatrix} u' \\ v' \\ \eta' \end{bmatrix}(x, y, t) = \begin{bmatrix} \hat{u} \\ \hat{v} \\ \hat{\eta} \end{bmatrix}(y)\exp[ik(x - ct)] , \tag{46}$$

and rewrite system (45) in the form:

$$-\left[A^{-1}(\overline{\psi} + \overline{\psi}_0)\frac{\partial}{\partial y} + \overline{\psi}_y\right]\hat{u} - \left[f_0 + \overline{\psi}_{yy} + k^2 A^{-1}(\overline{\psi} + \overline{\psi}_0)\right]\hat{v} + \left[f_0 + \overline{\psi}_{yy}\right]\hat{\eta} = c\hat{u} , \tag{47a}$$

$$\frac{1}{k^2}\left[A^{-1}(\overline{\psi} + \overline{\psi}_0)\frac{\partial^2}{\partial y^2} + A^{-1}\overline{\psi}_y\frac{\partial}{\partial y} - f_0\right]\hat{u} + \left[A^{-1}(\overline{\psi} + \overline{\psi}_0)\frac{\partial}{\partial y} + (A^{-1} - 1)\overline{\psi}_y\right]\hat{v} - \cdots$$

$$\cdots \frac{1}{k^2}\left[(\overline{\psi}_{yy} + f_0)\frac{\partial}{\partial y} + \overline{\psi}_{yyy}\right]\hat{\eta} = c\hat{v} , \tag{47b}$$

$$A^{-1}\overline{\psi}_y \hat{v} - \overline{\psi}_y \hat{\eta} = c\hat{\eta} \ . \tag{47c}$$

The nondimensionalization proceeds in the manner described for the quasi-geostrophic system. The perturbation system remains the same with all variables being nondimensional and order $O(1)$ with the exception of the Coriolis parameter f_0 which is scaled by the Rossby number:

$$f_0 \to \frac{1}{\varepsilon} \quad \text{where} \quad \varepsilon = \frac{2\pi u_0}{f_0 L} \ . \tag{48}$$

This system of shallow-water perturbation equations was solved numerically using the Galerkin method discussed in §3.4. This was achieved by expanding $\hat{u}$, $\hat{v}$ and $\hat{\eta}$ in terms of orthogonal functions as in (31), again complex exponentials were used here. Then each of the perturbation equations were written in matrix form; for (47a) the matrix equation has the form

$$< \gamma_u(y)\phi_n(y)\phi_m(y) > u_n + < \gamma_v(y)\phi_n(y)\phi_m(y) > v_n + < \gamma_\eta(y)\phi_n(y)\phi_m(y) > \eta_n = cu_n \ , \tag{49}$$

where $\gamma_u(y)$, $\gamma_v(y)$ and $\gamma_\eta(y)$ are functions determined from the original equation. Collecting all the coefficients into a single vector and combining all the $N \times N$ submatrices like $< \gamma_v(y)\phi_n(y)\phi_m(y) >$ into a single $3N \times 3N$ matrix reduces the system to a simple matrix eigenvalue system similar to that derived for the quasi-geostrophic case. It is interesting to note that replacing the potential vorticity q with potential height η reduces each of the $N \times N$ submatrices to tridiagonal form.

4.2 Results

As noted in §2 the shallow-water system supports gravity waves in addition to the Rossby waves inherent in the quasi-geostrophic system. Figure (8a) shows the phase speed of all the shallow-water modes plotted against wavenumber for the Jupiter-like case of $L_d = 1.0$, $A = 0.8$ and $\varepsilon = -0.2$. Examination of this plot indicates that there are indeed two types of waves present; those with phase speeds bounded by the zonal jet speed $0 \leq | c_r | \leq 1$ and those with very large phase speeds $\sqrt{gh} \leq c_r \leq \infty$. The first class of waves are the Rossby waves found in the quasi-geostrophic limit. The second class of waves are Poincaré or gravity waves.

Poincaré waves generally have a dispersion relationship of the form (Gill 1982)

$$c_r^2 = \frac{f_0^2 + (k^2 + l^2)gh}{(k^2 + l^2)} \ , \tag{50}$$

In the large wavelength limit

$$k^2 + l^2 \to 0 \ , \quad c^2 \to \frac{f_0^2}{(k^2 + l^2)} \ , \tag{51}$$

and the resulting waves are known as *inertial waves*. Conversely, in the short wavelength limit

$$k^2 + l^2 \to \infty \ , \quad c^2 \to gh \ , \tag{52}$$

and the waves the are nondispersive shallow-water gravity waves that exist in the absence of rotation. These two limits are observed in Figure (8a). In this study it was found that the the Poincaré waves were always stable. However, their presence weakly destabilized Rossby waves that had been stable in the quasi-geostrophic limit.

Figure (7a) shows the growth rate plotted against wavenumber for two different values of the Rossby number; for $L_d = 1.0$ and $A = 0.8$. The agreement of the $\varepsilon = 0.01$ shallow-water case with the quasi-geostrophic calculations for the same L_d and A is quite good. For the Jupiter-like case of $\varepsilon = -0.2$ it is seen that at small k (large wavelengths) the most unstable modes are the quasi-geostrophic stationary Rossby waves. However, at large k, where the quasi-geostrophic system is stable, the shallow-water system is unstable to travelling Rossby waves, presumably as a result of the presence of the gravity waves. The phase speed is plotted against wavenumber for this case in Figure (8b) and is observed to approach the maximum zonal jet speed with increasing wavenumber. Finally, the eigenfunction for the most unstable mode is plotted in Figure (9b)

In Figure (10) the growth rate is plotted against the wavenumber for different values of A, but with $L_d = 1.0$ and $\varepsilon = -0.2$. Again the maximum growth rate decreases as A increases, but unlike in the quasi-geostrophic case, the flow remains unstable when $A > 1$. Figure (11) shows the maximum growth rate plotted against A for the same case and again it is clear that the flow remains unstable for $A > 1$. Thus, *there is no simple extension* of Arnol'd's 2nd stability theorem to the shallow-water system. However, the unstable growth rates are quite small for $A \geq 1$ and in nonlinear numerical simulations virtually no growth of instability is observed (Dowling 1992).

Finally, the conclusions drawn from the quasi-geostrophic limit regarding the slowly moving waves observed on Jupiter (§3.5) remain valid in the shallow-water case. This, is because for the Jupiter-like parameters the most unstable mode is a quasi-geostrophic stationary Rossby wave.

5 Conclusions

Recently Dowling (1992) presented an empirical relationship between Jupiter's basic state zonal wind and meridional gradient of potential vorticity. In this study the linear stability of this basic state was investigated numerically for a cosine zonal wind profile. In the quasi-geostrophic limit the basic state was found to be neutrally stable with respect to Arnol'd's 2nd stability theorem with the violation of this theorem being sufficient for instability. The most unstable waves were always found to be stationary and centered at latitudes at which the basic zonal flow changed sign.

For the more general shallow-water case it was found that gravity waves were always stable, but that their presence weakly destabilized Rossby waves that had been stable in the quasi-geostrophic system. As a result the basic state was found to be always unstable and thus there appears to be no simple extension of Arnol'd's 2nd theorem to the shallow-water equations. However, in the parameter regime at which the quasi-geostrophic system was stable the shallow-water growth rates were weak. Finally, it was found that the numerical results were consistent with the observations of slowly moving waves on Jupiter.

There remain several areas of further research on this topic. First, in the quasi-geostrophic limit a perturbation expansion about the stationary cutoff wavenumber could be used to prove that this wavenumber is in fact a general cutoff criterion. Second, a proof that the most unstable quasi-geostrophic modes are stationary could be done. Finally, the complete analysis could be done for a more realistic basic state zonal wind profile.

and organising the Summer Program. I would also to thank the Senior Fellows and Program for rekindling my interest in fluid dynamics and showing me how science should be really be done. Finally, may I be so bold as to acknowledge the friendship all the barn fellows, Sam Adams and the Lee Side.

References

Arnol'd, V. I., 1966 On an a priori estimate in the theory of hydrodynamic stability. *Izv. Vyssh. Uchebn. Zaved. Matematika* **54**(5) 3. (English transl. American Math. Soc. transl., Series 2 **79**, 267 (1969).

Deming, D., Mumma, M. J., Espenak, F., Jennings, D. E. & Kostiuk, T., 1989 A search for p-mode oscillations of Jupiter: Serendipitous observations of nonacoustic thermal wave structure. *Ap. J.* **343**, 456.

Dowling, T. E., 1992 A relationship between potential vorticity and zonal wind on Jupiter. *J. Atmos. Sci.*, in press.

Dowling, T. E. & Ingersoll, A. P., 1989 Jupiter's Great Red Spot as a shallow water system. *J. Atmos. Sci.* **46**, 3256.

Fjørtof, R., 1950 Application of integral theorems in deriving criteria of stability for laminar flows and the baroclinic circular vortex. *Geofys. Publr* **17**, no. 6, 52.

Gill, A. E., 1982 Atmosphere-ocean dynamics. *Academic Press.*

Godfrey, D. A., 1988 A hexagonal feature around Saturn's North Pole. *Icarus* **76**, 335.

Huber, L. F., Beebe, R. F., and Westphal, J. A., 1992 A preliminary wind profile of Jupiter from Hubble Space Telescope data. *J. Geophys. Res.; Variable Phenomena in Jovian Planetary Systems* special issue, in press.

Ingersoll, A. P. & Cuong, P. G., 1981 Numerical model of long lived vortices. *J. Atmos. Sci.* **38**, 2067.

Magalhães, J. A., Weir, A. L., Conrath, B. J., Gierasch, P. J., & Leroy, S. S., 1989 Slowly moving thermal features on Jupiter. *Nature* **337**, 444.

Marcus, P. S., 1988 A numerical simulation of the Great Red Spot of Jupiter. *Nature* **331**, 693.

McIntyre, M.E. & Shepherd, T.G., 1987 An exact local conservation theorem for finite-amplitude disturbances to non-parallel shear flows, with remarks on Hamiltonian structure and on Arnol'd's stability theorems. *J. Fluid Mech.* **181**, 527.

Ripa, P. 1983 General stability conditions for zonal flows in a one-layer model on the β-plane or the sphere. *J. Fluid Mech.* **126**, 463.

334

Sromovsky, L. A., Revercomb, H. E., Krauss, R. J., and Suomi, V. E. 1983 Voyager 2 observations of Saturn's northern mid-latitude cloud features: morphology, motions, and evolution. *J. Geophys. Res.* **88**, 8650.

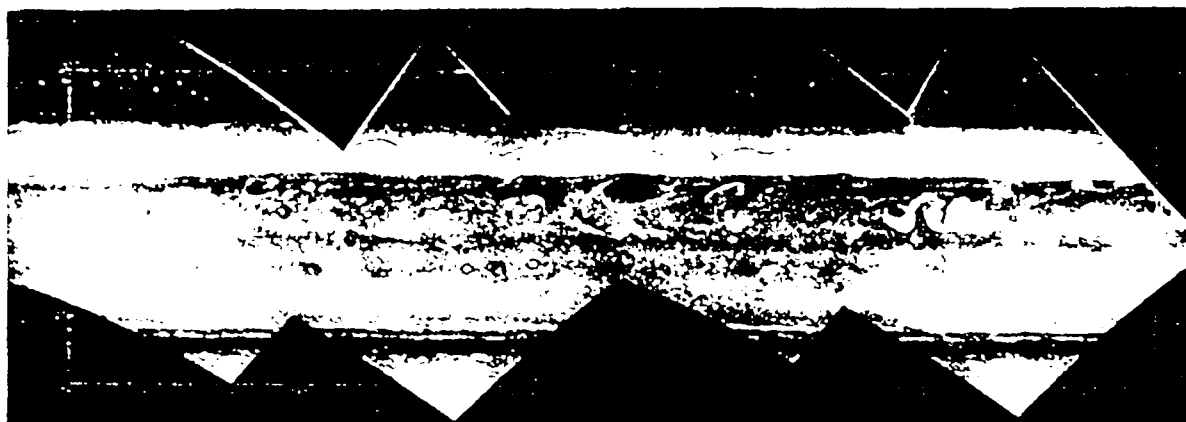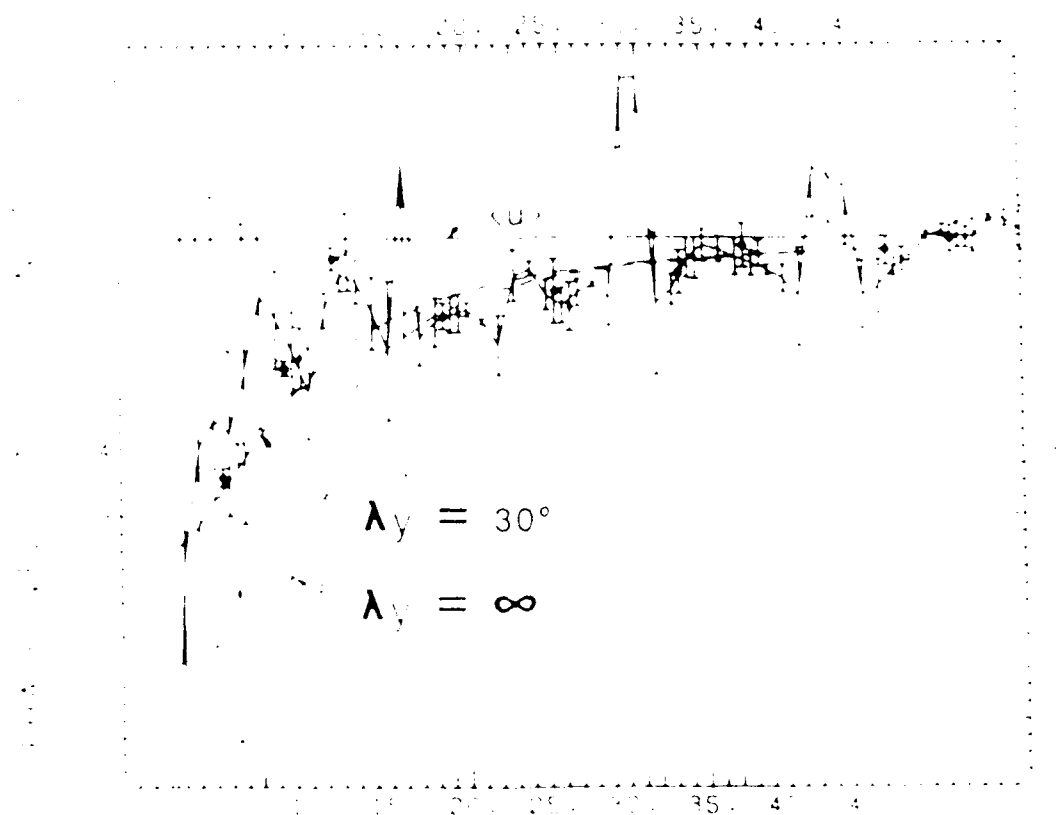Williams, G. P. & Wilson, R. J., 1988 The stability and gensis of Rossby vortices. *J. Atmos. Sci.* **45**, 207.
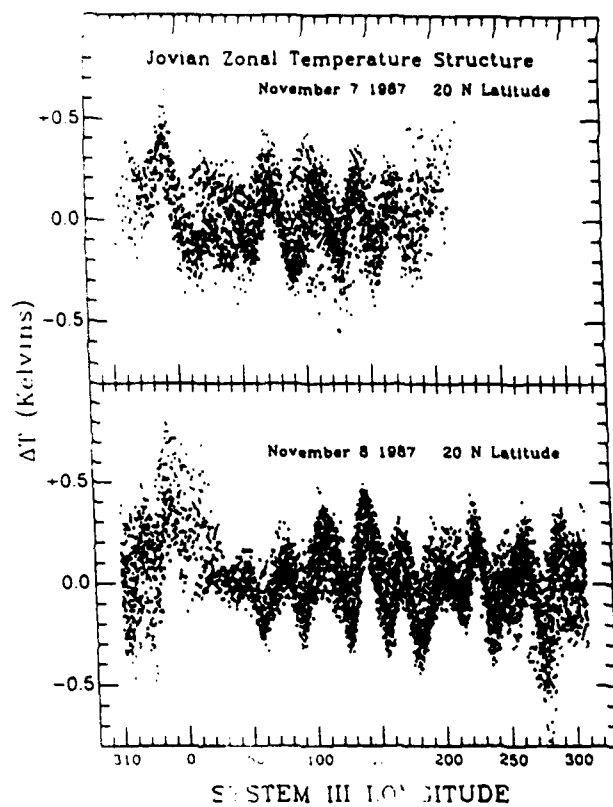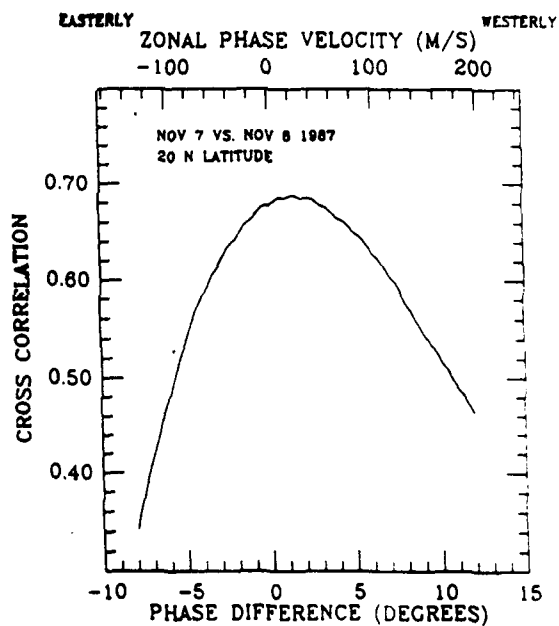
Figure 1: Slowly moving mode 10 Rossby wave observed on Jupiter at 20° N by Deming *et al.* (1989). (a) Temperature structure on two successive days. (b) Cross-correlation function used to determine the phase velocity $c = 25 \pm 33\,\mathrm{ms}^{-1}$.

$\lambda_y = 30°$

$\lambda_y = \infty$

WAVENUMBER

(b)

A narrow dark wavy line in the clouds at 42° N centered on a polar projection mosaic of Saturn's northern mid-latitudes as seen by Voyager seen at the top of the picture. (b) Phase velocities vs. planetary wavenumber plotted by Sromovsky et al. (1983).
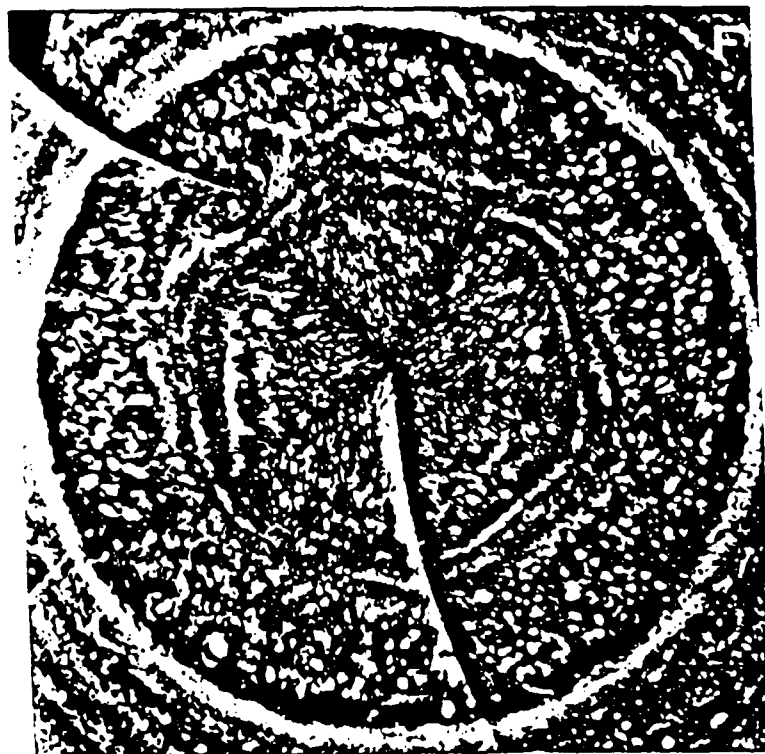
Figure 3: Photograph of Saturn's Hexagon from Godrey (1988). The Hexagon is centered in a jet with peak speed just over $100\,\mathrm{ms}^{-1}$. The images of the Hexagon also reveal the existence of an isolated vortex on one of its six sides, and the most likely explanation is that the vortex is forcing a standing, mode 6 Rossby wave.

free surface

weather layer: $\rho,\ \bar{u}(y)$

$\Longleftrightarrow$

lower layer: $\rho_2,\ \bar{u}_2(y)$
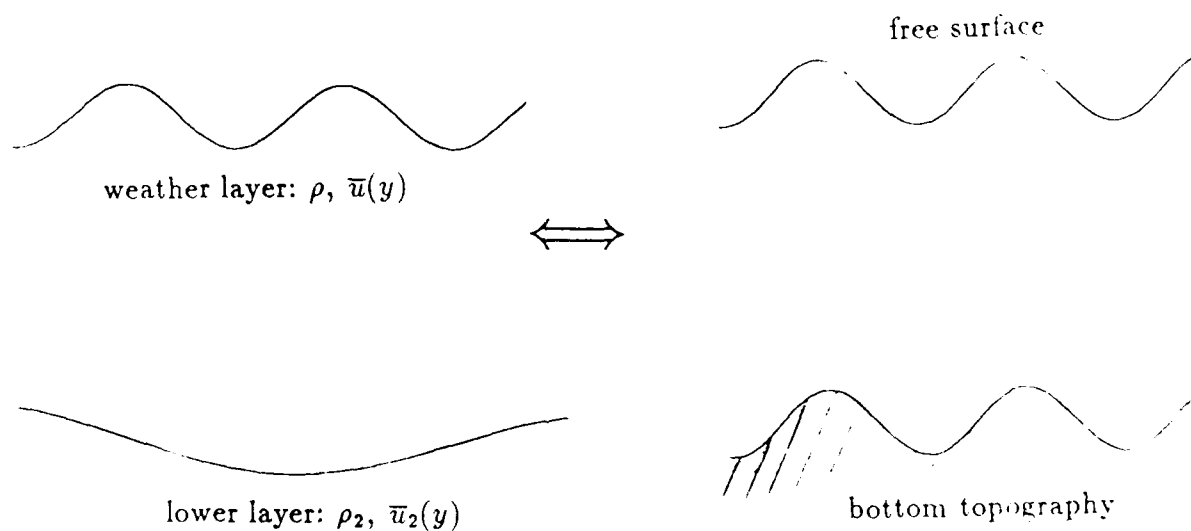
bottom topography

Figure 4: Sketch showing the equivalence of the "$1\frac{1}{2}$-layer" model and the 1-layer model with solid bottom topography. The 1-layer model also shows the meridional variation of the free surface and bottom topography with the cosine basic state profile used in this study.

338
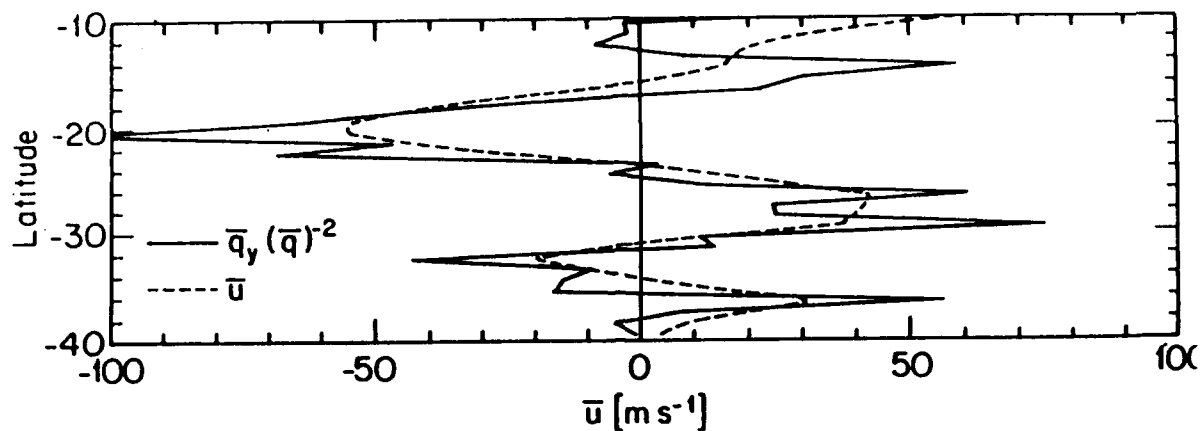
Figure 5: Empirical relationship between Jupiter's zonal velocity $\overline{u}(y)$ and $\overline{q}_y/\overline{q}^2$ inferred from the Voyager data by Dowling (1992).
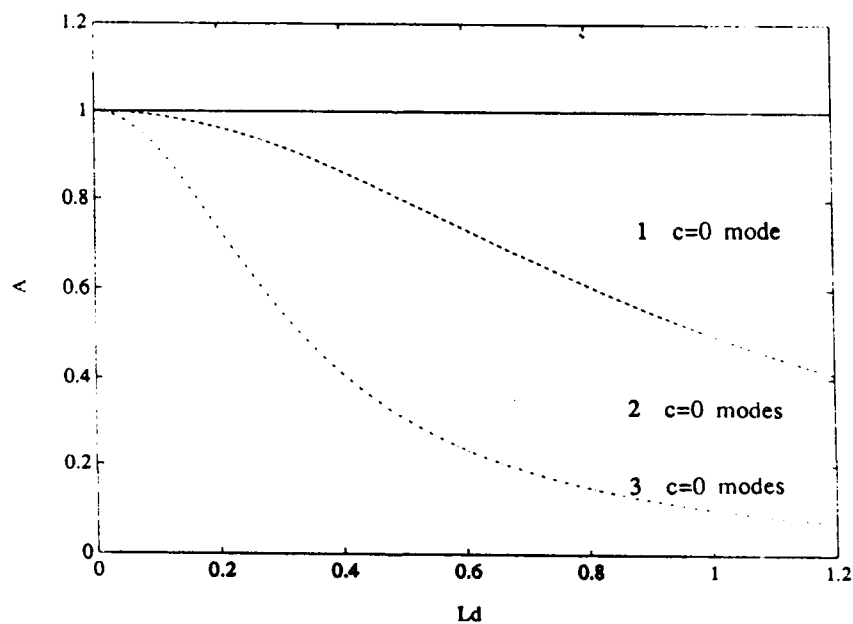
Figure 6: Number of cases of stationary neutral stability vary with A and L_d

(a)

(b)
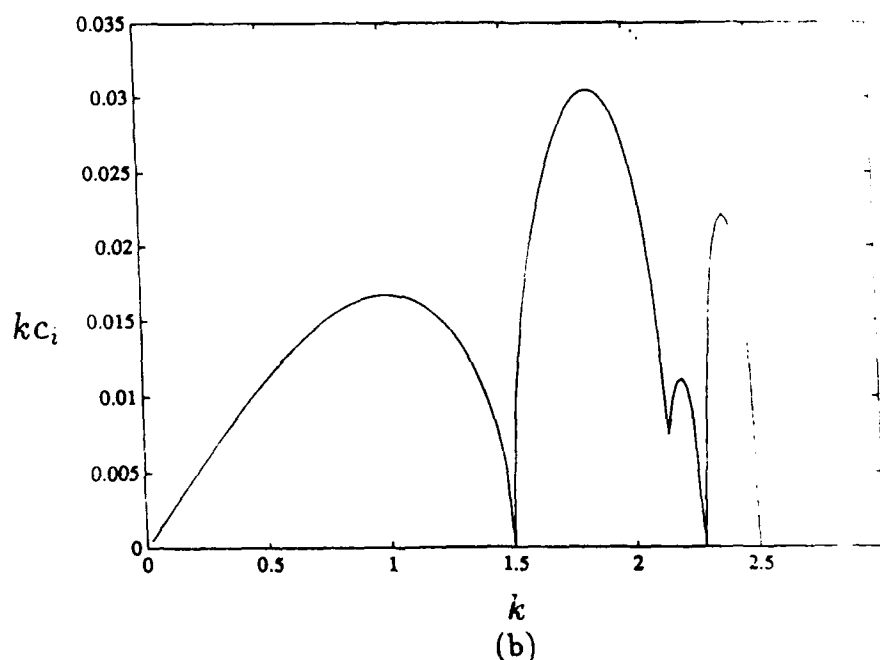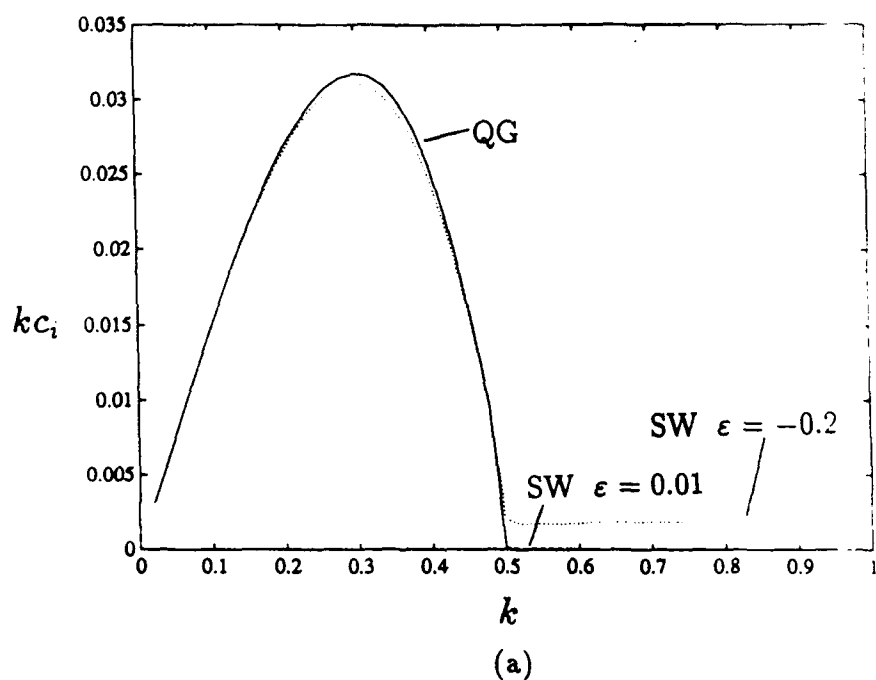
Figure 7: Growth rate kc_i vs. wavenumber k for two different parameter regimes. (a) Quasi-geostrophic and shallow-water solutions for $L_d = 1.0$ and $A = 0.8$. Note that in the quasi-geostrophic limit $c = 0$ at a single wavenumber given by $k = 0.5$ as predicted theoretically. Furthermore, both shallow-water solutions exhibit quasi-geostrophic behaviour with stationary instability at small k (large wavelengths). However, in the $\varepsilon = -0.2$ case there is no large k (small wavelength) cutoff as the presence of gravity waves acts to destabilize Rossby waves stable in the quasi-geostrophic limit. (b) Quasi-geostrophic solution for the non Jupiter-like parameters $L_d = 0.2$ and $A = 0.8$ has $c = 0$ at a three wavenumbers given by $k = 1.50$, 2.29 and 2.50 as predicted theoretically.

(a)

(b)
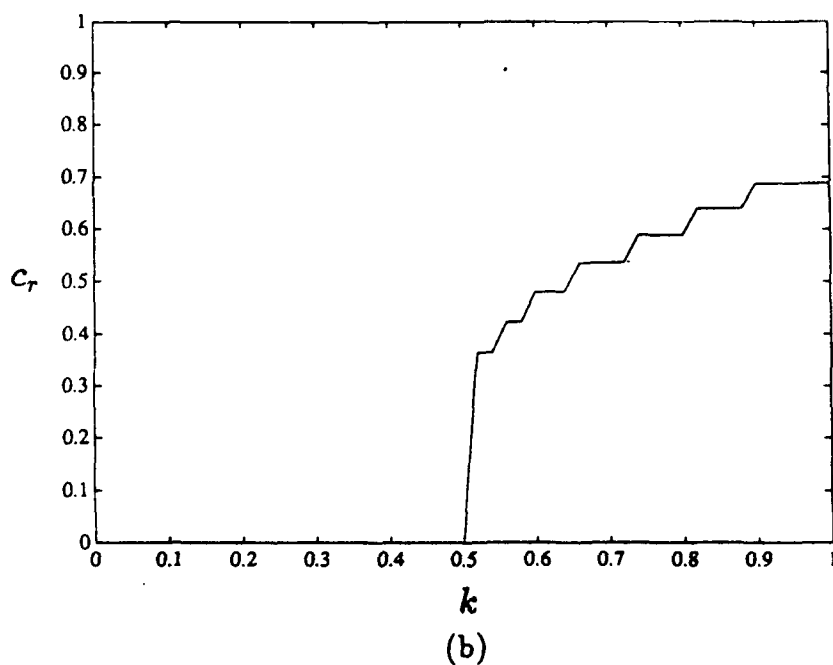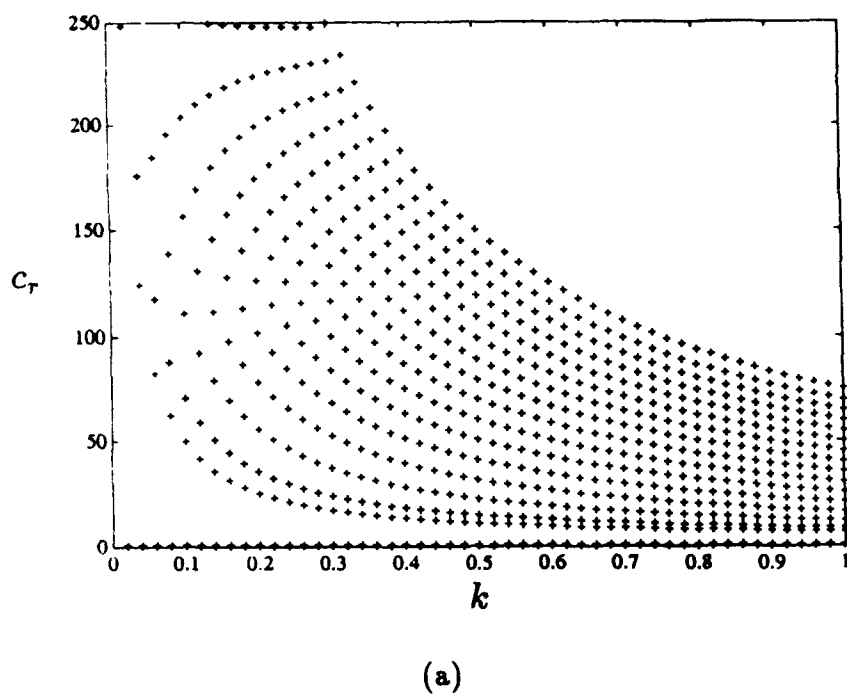
Figure 8: Phase speed c_r against wavenumber k for the shallow-water system with $L_d = 1.0$, $A = 0.8$ and $\varepsilon = -0.2$. In (a) the phase speeds of all modes are plotted with the $c_r \approx f_0/k$ behaviour of the gravity waves at small k being evident. (b) Shows the phase speed of the most unstable mode.
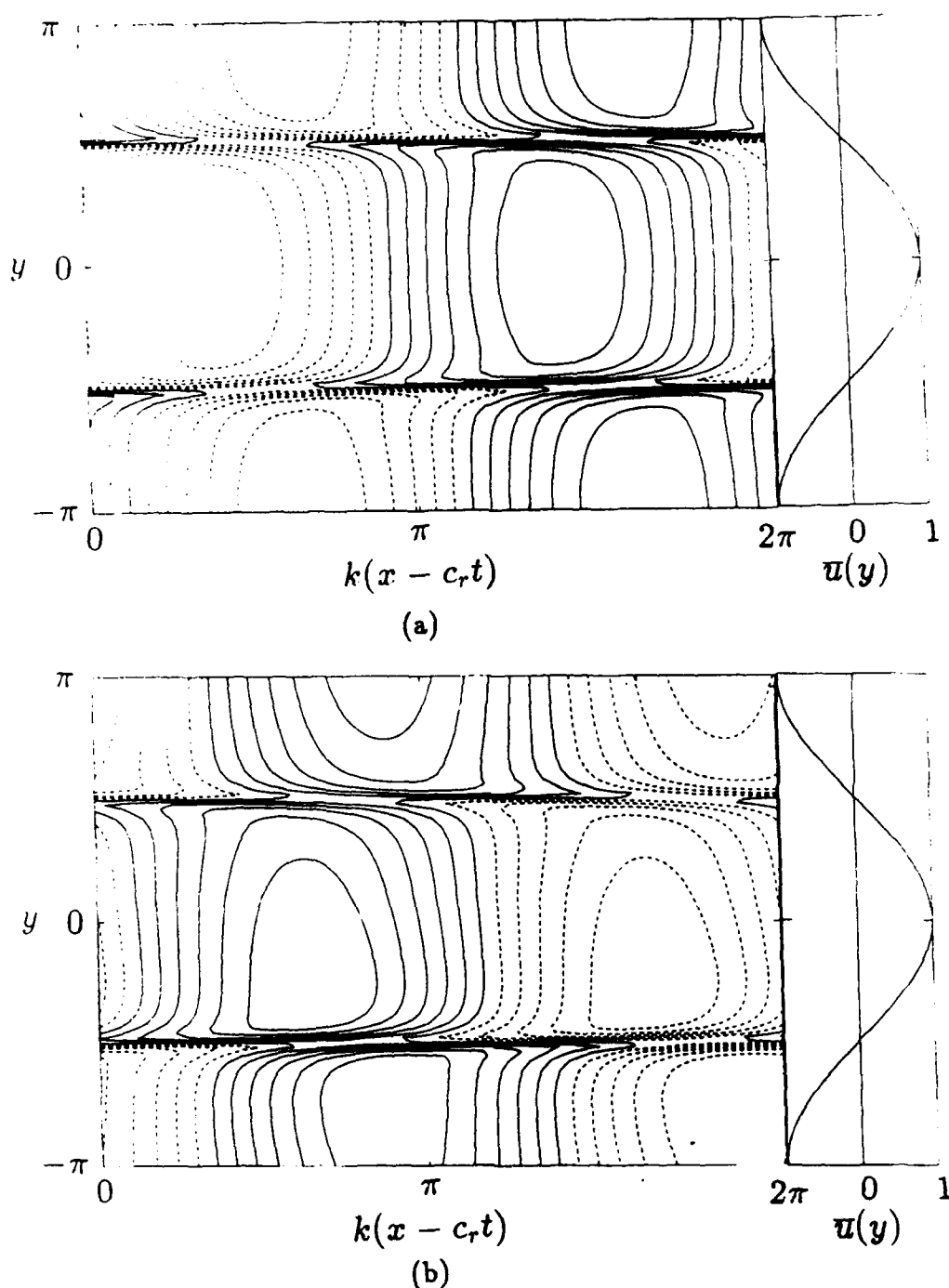
Figure 9: Contours of the eigenfunctions corresponding to the most unstable mode for the parameters $L_d = 1.0$ and $A = 0.8$. In both plots the solid and dashed lines correspond to positive and negative values, respectively. There are 10 equally spaced contour intervals and the basic zonal flow is shown on the right of each contour plot. (a) Quasi-geostrophic solution for the perturbation potential vorticity Q'. Note that at $y = \pm \pi/2$ the Reynolds stress term $\overline{u'v'}$ is in the opposite direction to the shear of the zonal velocity $\overline{u}_y$ thus causing the instability. (b) Shallow-water solution for $\varepsilon = -0.20$ for the perturbation potential height $\eta' \approx -q'/\overline{q}^2$.

342

(a)

(b)
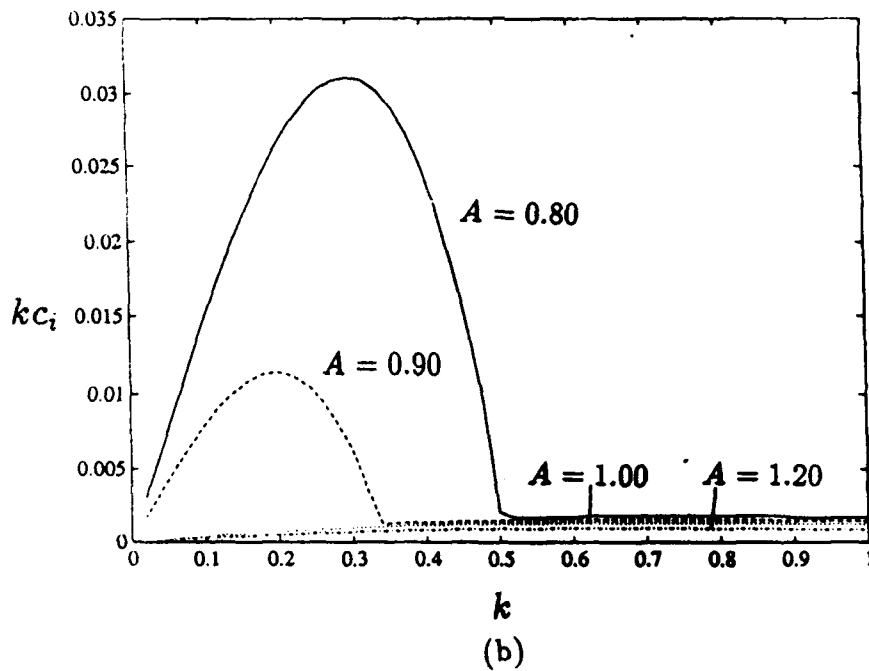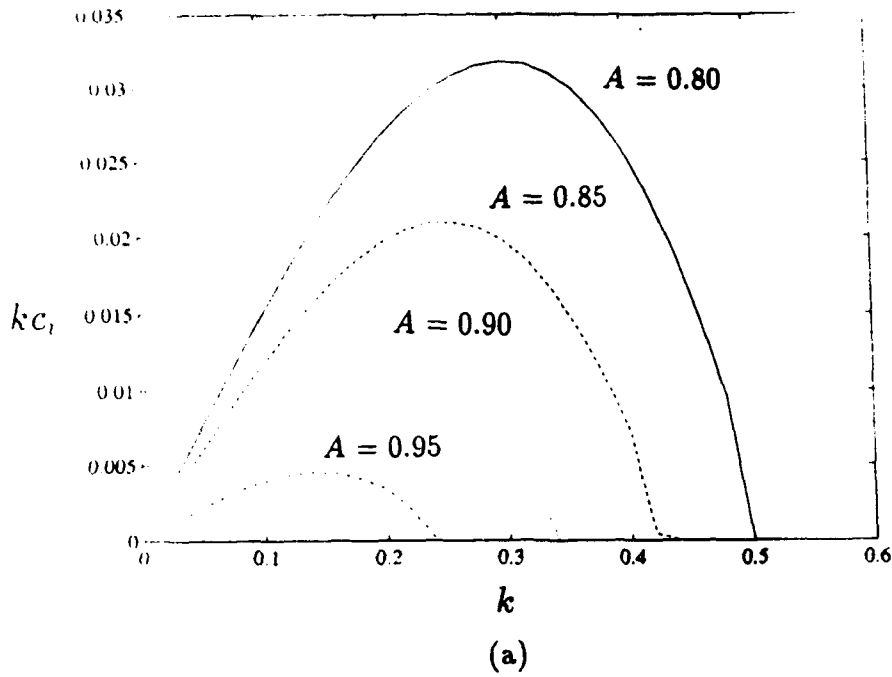
Figure 10: Plots of the growth rate kc_i vs. wavenumber k for different values of A with $L_d = 1.0$. (a) Quasi-geostrophic solutions. Note that the growth rates decrease as $A \to 1$ at which point the flow remains stable. (b) Shallow-water solutions for $\varepsilon = -0.2$. Unlike in the quasi-geostophic system the flow is unstable when $A > 1$, however it is observed that the maximum growth rate is small and decreases with increasing A.
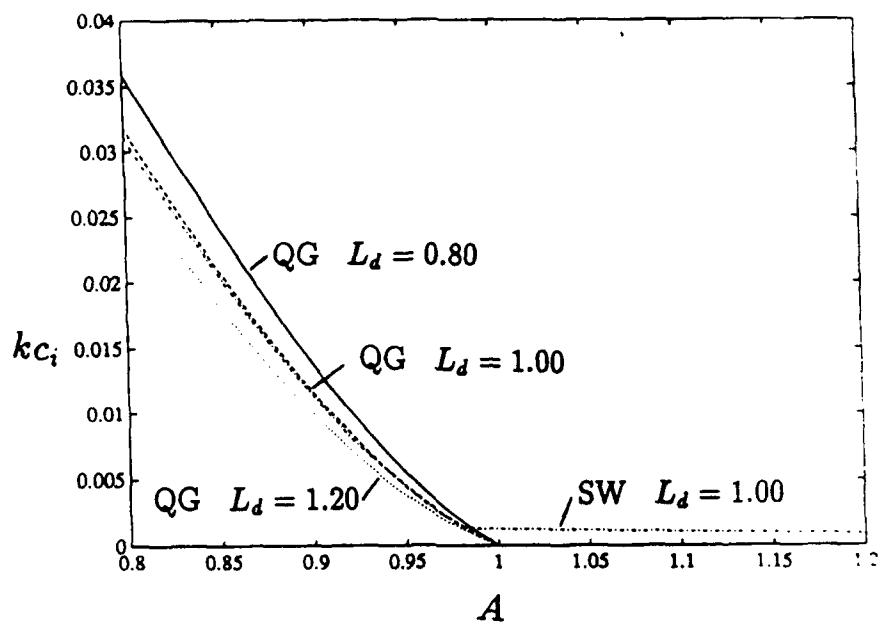
Figure 11: Plot of the quasi-geostrophic and shallow-water growth rates kc_i vs. stability parameter A for different values of L_d. The shallow-water calculations are for a Rossby number $\varepsilon = -0.20$. It is seen that for all values of L_d the point $A = 1$ defines neutral stability in the quasi-geostrophic limit and thus violation of Arnol'd's 2nd stability theorem is in fact a sufficient condition for instability for the cosine profile. However, in the shallow-water case the flow is only weakly unstable when $A > 1$.

A Solitary Summer

by Louis Tao

Introduction

Solitons and coherent structures appear in many flows. During the GFD program of 1981, Christopher Bretherton examined the roll waves in two dimensional Boussinesq thermalhaline convection and discovered that unstable roll waves near the Hopf bifurcation point have amplitudes that are governed by the complex Ginzburg–Landau equation. He then showed that a soliton in this system would eventually evolve to a particular soliton, i. e., it converges to a fixed point in the amplitude–velocity phase plane. So a train of solitons eventually turns into a uniform train of modulations. Typically, we can describe waves and solitary objects in unstable situations by amplitude equations and these dynamical systems are what Spiegel (*Long Buoyancy Waves*, 1981) called the metaphorical minds of solitons. Here we demonstrate the existence of solitons whose *minds* contain strange attractors.

1. Brief on Solitons

Equations which admit soliton solutions are ubiquitous in mathematical physics. They have led to an industry of mathematicians classifying second order ordinary differential equations (Painlevé and others) and of physicists looking for integrable models. The equations that we are interested arise in shallow water theory (Korteweg-de Vries equation), in thermalhaline convection (complex Ginzburg–Landau equation—see Bretherton, 1981), in dynamics of vortex filaments in three dimensions (the nonlinear Schrodinger equation—see Hasimoto, 1976) among other places. The particular equation we chose for our studies this summer—the sine–Gordon equation—is a special case of the nonlinear Klein–Gordon equation, which also can be derived for certain cases of thermalhaline convection (Bretherton, 1981). And the principal aim of this summer project is to show that chaotic solitons can exist in fairly generic dynamical circumstances.

So what is a soliton? It is a stable solitary travelling wave solution to the relevant equations. Typically, the forms of such solitary waves persist under perturbation. However, what distinguishes solitons from mere solitary waves is that during collisions of two such objects, solitary waves interact and dissipate, whereas two solitons interact and then go along their own merry way.

(For references on solitons, see Ablowitz and Segur, 1981, Lamb, 1980, and Newell, 1985.)

2. Karpman's Results

Using the inverse scattering transform, Karpman (see the myriad of articles by Karpman and his collaborators, Maslov and Solov'ev) derives the following formulas for a perturbed sine–Gordon soliton described by the perturbed equation[1]:

$$\partial_{xt}^2 u + \sin u = \epsilon R[u]$$
$$\partial_{xt}^2 u^{(0)} + \sin u^{(0)} = 0 \tag{2.1}$$

where $u^{(0)}$ is the kink solution to the sine–Gordon equation,

$$u^{(0)} = 2\sigma \sin^{-1} \tanh z + \gamma \pi \tag{2.2}$$

where $z = 2\nu\theta = 2\nu[x - \xi(t)]$, $\sigma = \pm 1$, $\gamma = \pm 1$, and $\xi(t) = t/4\nu^2 + \xi_0$.

$$\frac{d\nu}{dt} = \sigma \frac{\epsilon}{4} \int_{-\infty}^{\infty} R[u]\mathrm{sech}z\,dz$$
$$\frac{d\xi}{dt} = \frac{1}{4\nu^2} + \sigma \frac{\epsilon}{8\nu^2} \int_{-\infty}^{\infty} R[u]z\,\mathrm{sech}z\,dz \tag{2.3}$$

where ν and ξ are the slope and position of the kink, respectively.

Here we use a locally known method—two–timing perturbation techniques—to derive the above formulas.

Essentially, one writes out a perturbative expansion and finds corrections to the soliton solution at each order; the successive corrections each satisfy a linear equation. We allow parameters of the soliton to depend (slowly) on time to remove resonances. The time dependence is determined by a solvability condition. Though the linear equations are second order, only one of the needed null vectors can be found readily, and this gives us the amplitude equation for one of the parameters. Then in order to evaluate the other amplitude equations, we have to evaluate conservation laws (see Ablowitz and Segur, 1981). We illustrate the utility of this technique by applying it to the perturbed sine–Gordon equation (2.1).

Expanding u in increasing orders of ϵ,

$$u = u^{(0)} + \epsilon u^{(1)} + \epsilon^2 u^{(2)} + \ldots \tag{2.4}$$

(where $u^{(0)}$ is the kink soliton solution to the unperturbed equation (2.2)) introducing the slow time variable $T = \epsilon t$, and substituting into the perturbed sine–Gordon equation, we get, to first order in ϵ

---

[1] These are actually the equations in characteristic coordinates. The sine–Gordon equation in laboratory coordinates takes the form

$$\partial_t^2 u - c^2 \partial_x^2 u = \sin u + \epsilon R[u]$$

346

$$\partial_{xt}^2(u^{(0)} + \epsilon u^{(1)}) + \sin(u^{(0)} + \epsilon u^{(1)}) = \epsilon R[u^{(0)} + \epsilon u^{(1)}] \tag{2.5}$$

$$\partial_{xt}^2 u^{(0)} + \epsilon \partial_{xT}^2 u^{(0)} + \epsilon \partial_{xt}^2 u^{(1)} + \sin u^{(0)} + \epsilon u^{(1)} \cos u^{(0)} = \epsilon R[u^{(0)}] \tag{2.6}$$

or rewriting in the variable θ,

$$\frac{1}{4\nu^2} u_{\theta\theta} + \sin u = \epsilon R[u] - \epsilon u_{\theta T} \tag{2.7}$$

At o(ϵ), we separate into linear and nonlinear parts,

$$\mathbf{L}u^{(1)} = \frac{1}{4\nu^2} u_{\theta\theta}^{(1)} + u^{(1)} \cos u^{(0)} = \mathbf{F}^{(1)} \tag{2.8}$$

where $\mathbf{F}^{(1)}$ is given by

$$\mathbf{F}^{(1)} = R[u^{(0)}] - u_{\theta T}^{(0)} \tag{2.9}$$

By inspection from equation, we see that sech $2\nu\theta$ is a proper solution of the adjoint problem[2] $\mathbf{L}u = 0$, i.e.,

$$\mathbf{L}^\dagger \text{sech} 2\nu\theta = 0 \tag{2.10}$$

where

$$\mathbf{L}^\dagger = \frac{1}{4\nu^2}\partial_{\theta\theta}^2 + \cos u^{(0)} \tag{2.11}$$

is the adjoint.

Then the solvability condition gives us the amplitude equation for ν:

---

[2] In order to define an adjoint operator, we need to situate our functions in an inner product space and define an inner product:

$$< \phi, \mathbf{L}\psi > = < \mathbf{L}^\dagger \phi, \psi >$$

where $< \phi, \psi >$ is the inner product between vectors ϕ and ψ. For instance, in our case, our space has as inner product integration over all space:

$$< \phi, \psi > = \int_{-\infty}^{\infty} \phi(x)\psi(x)dx$$

And knowing the null vectors of the adjoint problem immediately gives us the solvability conditions:

$$< v, \mathbf{L}u^{(1)} > = < \mathbf{L}^\dagger v, u^{(1)} > = 0$$

if v is the null vector of the adjoint problem, i. e., $\mathbf{L}^\dagger v = 0$.

$$\int_{-\infty}^{\infty} \mathbf{F}^{(1)} \mathrm{sech} z \, \mathrm{d}z = \int_{-\infty}^{\infty} \mathrm{sech} z (\mathbf{L} u^{(1)}) \mathrm{d}z$$

$$= \int_{-\infty}^{\infty} (\mathbf{L}^{\dagger} \mathrm{sech} z) u^{(1)} \mathrm{d}z = 0 \tag{2.12}$$

substituting for $\mathbf{F}^{(1)}$

$$\int_{-\infty}^{\infty} R[u^{(0)}] \mathrm{sech} z \, \mathrm{d}z = \int_{-\infty}^{\infty} u_{\theta T}^{(0)} \mathrm{sech} z \, \mathrm{d}z$$

$$= 2\sigma\nu_T \int_{-\infty}^{\infty} \mathrm{sech} z \, \mathrm{d}z$$

$$= 4\sigma\nu_T$$

and rearranging

$$\frac{d\nu}{dT} = \frac{\sigma}{4} \int_{-\infty}^{\infty} R[u^{(0)}] \mathrm{sech} z \, \mathrm{d}z \tag{2.13}$$

which is exactly what Karpman (1977,1979,1981) obtained.

To get the other amplitude equation requires more work. We have to use the energy conservation equation (obtained by multiplying the sine–Gordon equation in characteristic form by u_x—as Bretherton (1981) did for the Ginzburg–Landau equation). Then expanding, we get a relation between the first order correction to u (i.e., $u^{(1)}$) and $\dot{\xi}$, which gives us the relevant amplitude equation for ξ.

We see that Karpman's formulas can only describe the following two component system:

$$\dot{\nu} = \mathrm{F}(\nu, \dot{\xi})$$
$$\dot{\xi} = \mathrm{G}(\nu, \dot{\xi}) \tag{2.14a}$$

which we can rewrite as

$$\dot{\nu} = \bar{\mathrm{F}}(\nu) = \mathrm{F}(\nu, \bar{\mathrm{G}}(\nu))$$
$$\dot{\xi} = \bar{\mathrm{G}}(\nu) \tag{2.14b}$$

after explicitly solving for $\dot{\xi}$ in terms of ν.

The reason for this is the form of the kink solution:

$$u^{(0)} = 2\sigma \sin^{-1} \tanh z + \gamma\pi \tag{2.2}$$

where $z = 2\nu\theta = 2\nu[x - \xi(t)]$, $\sigma = \pm 1$, $\gamma = \pm 1$, and $\xi(t) = t/4\nu^2 + \xi_0$.

We see that differentiating with respect to the x–coordinate gives us

$$u_x^{(0)} = 4\sigma\nu \mathrm{sech} z \tag{2.15}$$

and brings out an overall factor of ν. Differentiating with respect to the t-coordinate brings out an overall factor of $\nu\xi$. There is no way of obtaining a factor of ξ because of the way ξ is buried in the argument of the kink function.

As a result of this, we see immediately that using these perturbative formulas, we have only a system of co-dimension one in which the slope of the kink, ν evolves on the slow time scale, and the speed of the kink, ξ, passively evolves with its slope. *Karpman's formulas can only describe a dynamical system of co-dimension one!* From numerical results we expect that in the perturbed soliton system (without coupling to another soliton or an external field) to be of co-dimension two. So how do we show that there is a dynamical system of co-dimension two in the perturbed sine–Gordon equation? We shall use the approach of Bogoliubov et al, from normal form theory. This method is a general one. We shall first start from rudimentary normal form theory.

3a. Normal Form Theory

When we study the time development of instabilities in fluid dynamical systems, typically, we can put the system in the following form:

$$\partial_t \mathbf{U} = M\mathbf{U} + \mathbf{N}(\mathbf{U}) \tag{3.1}$$

where $\mathbf{U}$ denotes the variables of the system (e. g., velocity, density, temperature, salinity), M is a linear *operator* and $\mathbf{N}$ is strictly nonlinear. Usually, we make appropriate transformation so that $\mathbf{U} = 0$ is a solution of (3.1) (i. e., we are interested in the time development of instabilities so we subtract out the steady state behavior.)

We now study the linearized problem:

$$\partial_t \mathbf{U} = M\mathbf{U} \tag{3.2}$$

with solution of the form[3]

$$\begin{aligned} \mathbf{U}(\mathbf{x}, t) &= e^{st}\Phi(\mathbf{x}) \\ M\Phi &= s\Phi \end{aligned} \tag{3.3}$$

where s's are the eigenvalues of M.

We can classify the eigenmodes of the linear problem by the real part of the eigenvalues, s, typically functions of the parameters of the system. And the number of parameters we need to tune to get the values of these s's close to zero (i. e., close to the instabilities we are trying to study) is the *co-dimension* of the system. Letting $s = \eta + i\omega$. Eigenmodes with small $|\eta|$ are called *slow* modes, while modes with large $|\eta|$ are called *fast* modes. We will assume not only that there are no unstable fast modes, i. e., no modes with large positive η, but also that there is a separation of scale between the fast and slow modes. When we have a discrete spectrum of eigenmodes, we can expand

---

[3] Typically, we can do this if M does not depend on t and ∂_t.

$$\mathbf{U}(\mathbf{x}, t) = \sum_{i=1}^{n} \alpha_i(t)\phi_i(\mathbf{x}) + \sum_{i=1}^{n} \beta_i(t)\psi_i(\mathbf{x}) \tag{3.4}$$

where ϕ_i are the slow modes and ψ_i are the fast modes.

When we substitute (3.4) into (3.1), we obtain the following system of coupled ordinary differential equations

$$\dot{\alpha} = M\alpha + \mathbf{F}(\alpha, \beta)$$
$$\dot{\beta} = N\beta + \mathbf{G}(\alpha, \beta) \tag{3.5}$$

where α and β stand for all the α_i's and β_i's, M and N are the linear operator that operate on the slow and the fast modes, and $\mathbf{F}$ and $\mathbf{G}$ are the strictly nonlinear terms. Since the eigenvalues of K have large negative real parts (they are, by definition, fast stable modes), we can solve for β

$$\beta = K^{-1}\left[\dot{\beta} - \mathbf{G}(\alpha, \beta)\right] \tag{3.6}$$

by successive iterations (starting with $\dot{\beta} = 0$).

Typically, the amplitude equations we derive from physical systems in this manner take the form

$$\dot{\mathbf{a}} = M\mathbf{a} + \mathbf{\Gamma}(\mathbf{a}) \tag{3.7}$$

where M is the matrix representation of a linear operator, $\mathbf{\Gamma}$ is some complicated strictly nonlinear function of $\mathbf{a}$, and the $\mathbf{a}$'s include only the slow modes. The question now confronts us is how to obtain a good coordinate system to describe the slow modes, i. e., to rewrite our amplitude equation as

$$\dot{\mathbf{A}} = M\mathbf{A} + \mathbf{g}(\mathbf{A}) \tag{3.8}$$

where M is the same matrix as before (we want to preserve the linear theory), and $\mathbf{g}(\mathbf{A})$ is of some standard form.

We make the nonlinear transformation

$$\mathbf{a} = \mathbf{A} + \psi(\mathbf{A}) \tag{3.9}$$

By substituting the last two equations into our original amplitude equation, we get

$$\dot{\mathbf{A}} + \dot{\mathbf{A}}\frac{\partial\psi}{\partial\mathbf{A}} = M(\mathbf{A} + \psi(\mathbf{A})) + (\mathbf{\Gamma}(\mathbf{A} + \psi(\mathbf{A}))) \tag{3.10}$$

subtracting $M\mathbf{A}$ from both sides,

$$\mathbf{g}(\mathbf{A}) + M\mathbf{A} + \mathbf{g}(\mathbf{A})\frac{\partial\psi}{\partial A} = M\psi(\mathbf{A}) + (\mathbf{\Gamma}(\mathbf{A} + \psi(\mathbf{A}))) \tag{3.11}$$

and separating into linear and nonlinear parts in ψ

$$L\psi = \Gamma(\mathbf{A} + \psi(\mathbf{A})) - \mathbf{g}\partial_{\mathbf{A}}\psi - \mathbf{g} \qquad (3.12)$$

where the linear operator L in component form is given by

$$L_{ij} = M_{kl}A_l\partial_{A_k}\delta_{ij} - M_{ij} \qquad (3.13)$$

To find our normal form, we expand ψ and $\mathbf{g}$ in Taylor series in the components of $\mathbf{A}$. At a quick glance, it may seem as if we have only one equation for two unknowns, ψ and $\mathbf{g}$. However, we only have one unknown (and that is ψ); we want to pick a possible form of $\mathbf{g}$. What happens is that the above equation does not give us a regular solution for every possible $\mathbf{g}$. We have to place constraints on the possible forms of $\mathbf{g}$ by solving for the null vectors of the adjoint problem. This may seem a little abstract right now, but we hope the theory will become apparent after the worked example below. To illustrate the power of normal form theory, we use it to solve for the generic amplitude equation for

$$M = \begin{pmatrix} 0 & 1 \\ 0 & 0 \end{pmatrix}$$

which will give us the canonical co–dimension two behavior.[4] (See Spiegel, 1985.) Then we show that this approach will allow us to identify the co–dimension two behavior in our perturbed soliton system.

3b. Amplitude Equations of Co–dimension Two: A Worked Example

Following Spiegel (*Cosmic Arrhythmias*, 1985), we rewrite equation (3.6)

$$L\psi = \mathbf{T} - \mathbf{g} \qquad (3.14)$$

where

$$\mathbf{T} = \Gamma(\mathbf{A} + \psi(\mathbf{A})) - \mathbf{g}\partial_{\mathbf{A}}\psi \qquad (3.15)$$

We expand in a Taylor series in homogeneous polynomials of components of $\mathbf{A}$ that are of the same degree. For instance, writing out the two components of $\mathbf{A}$ as A and B, and letting $|\mathrm{J}, \mathrm{M}\rangle$[5] be the monomial

$$|\mathrm{J}, \mathrm{M}\rangle = N \mathrm{A}^{\mathrm{J}-\mathrm{M}} \mathrm{B}^{\mathrm{J}+\mathrm{M}} \qquad (3.16)$$

where the normalization is $N = [(\mathrm{J} + \mathrm{M})!(\mathrm{J} - \mathrm{M})!]^{-1/2}$

And we introduce the Taylor series

---

[4] or, more generally, in Arnold normal form $M = \begin{pmatrix} 0 & 1 \\ \alpha & \beta \end{pmatrix}$

[5] We put this in Dirac bracket notation to suggest that the calculations to follow are similiar to quantum mechanical calculations.

$$\psi = \sum_{J=0}^{\infty} \psi_J \quad = \sum_{J=0}^{\infty} \sum_{M=-J}^{J} \psi_{JM}|J,M\rangle$$

$$\mathbf{T} = \sum_{J=0}^{\infty} \mathbf{T}_J \quad = \sum_{J=0}^{\infty} \sum_{M=-J}^{J} \mathbf{T}_{JM}|J,M\rangle \tag{3.17}$$

$$\mathbf{g} = \sum_{J=0}^{\infty} \mathbf{g}_J \quad = \sum_{J=0}^{\infty} \sum_{M=-J}^{J} \mathbf{g}_{JM}|J,M\rangle$$

So we have at each order J in the expansion

$$L\psi_J = \mathbf{T}_J - \mathbf{g}_J \tag{3.18}$$

And for our particular choice of M,

$$L_{ij} = M_{kl}A_l\partial_{A_k}\delta_{ij} - M_{ij} \tag{3.7}$$

$$L = B\partial_A \begin{pmatrix} 1 & 0 \\ 0 & 1 \end{pmatrix} - \begin{pmatrix} 0 & 1 \\ 0 & 0 \end{pmatrix} \tag{3.19a}$$

$$L^{\dagger} = A\partial_B \begin{pmatrix} 1 & 0 \\ 0 & 1 \end{pmatrix} - \begin{pmatrix} 0 & 0 \\ 1 & 0 \end{pmatrix} \tag{3.19b}$$

A little algebra shows us that

$$L^{\dagger}\left[A^{2J}\begin{pmatrix} 0 \\ 1 \end{pmatrix} \right] = 0 \tag{3.20a}$$

$$L^{\dagger}\left[A^{2J}\begin{pmatrix} 1 \\ 0 \end{pmatrix} + BA^{2J}\begin{pmatrix} 0 \\ 1 \end{pmatrix} \right] = 0 \tag{3.20b}$$

At each order J, $L^{\dagger}$ has two null vectors and $2J - 1$ generalized null vectors. The constraint on $\mathbf{g}_J$ is that it is not orthogonal to any of the null vectors so we can expand $\mathbf{g}_J$ in terms of the null vectors. However, only the coefficients of the two null vectors can be determined by solvability conditions; we set the other coefficients to zero. Therefore the amplitude equation for **A** can be written as

$$\dot{\mathbf{A}} = \mathbf{B} + \sum_{J=1}^{\infty} \alpha_J A^{2J}$$

$$\tag{3.21}$$

$$\dot{\mathbf{B}} = \sum_{J=1}^{\infty} \beta_J A^{2J} + \sum_{J=1}^{\infty} \alpha_J BA^{2J-1}$$

where the α_J's and the β_J's are determined by the solvability conditions at each order J.

We now show that using essentially the same approach we can write out the appropriate amplitude equations for our co–dimension two perturbed sine–Gordon soliton.

4. The Co–dimension Two Soliton: Theory

We rewrite the perturbed sine–Gordon equation in two component form, separating the linear and nonlinear terms:

$$\partial_t \Psi = \mathbf{L}\Psi + \mathbf{N}(\Psi) \tag{4.1}$$

where

$$\Psi = \begin{pmatrix} u_x \\ u \end{pmatrix} \tag{4.2}$$

i. e.,

$$
\begin{aligned}
\partial_t \begin{pmatrix} u_x \\ u \end{pmatrix} &= \begin{pmatrix} \sin u + \epsilon R[u] \\ \int (\sin u + \epsilon R[u]) dx \end{pmatrix} \\
&= \begin{pmatrix} u \\ 0 \end{pmatrix} + \begin{pmatrix} \sin u - u + \epsilon R[u] \\ \int (\sin u + \epsilon R[u]) dx \end{pmatrix} \\
&= \begin{pmatrix} 0 & 1 \\ 0 & 0 \end{pmatrix} \begin{pmatrix} u_x \\ u \end{pmatrix} + \begin{pmatrix} \sin u - u + \epsilon R[u] \\ \int \sin u + \epsilon R[u] dx \end{pmatrix}
\end{aligned} \tag{4.3}
$$

We make the ansatz

$$u(x,t) = v(x, \mathbf{A}(t)) \tag{4.4}$$

knowing that from Karpman's analysis

$$\frac{d\nu}{dt} = \sigma \frac{\epsilon}{4} \int_{-\infty}^{\infty} R[u] \mathrm{sech} z \, dz$$

$$\frac{d\xi}{dt} = \frac{1}{4\nu^2} + \sigma \frac{\epsilon}{8\nu^2} \int_{-\infty}^{\infty} R[u] z \mathrm{sech} z \, dz$$

Rewriting $\alpha = 1/4\nu^2$, we can recast the two equations above into

$$\dot{\mathbf{a}} = \begin{pmatrix} \xi \\ \alpha \end{pmatrix} = \begin{pmatrix} 0 & 1 \\ 0 & 0 \end{pmatrix} \begin{pmatrix} \xi \\ \alpha \end{pmatrix} + \Gamma(\xi, \alpha) = \mathbf{M}\mathbf{a} + \Gamma(\mathbf{a}) \tag{4.5}$$

where the form of Γ is determined by the perturbation. Right away, we know from normal form theory that we can rewrite the amplitude equation in the form

$$\dot{\mathbf{A}} = M\mathbf{A} + \mathbf{g}(\mathbf{A}) \tag{3.9}$$

where $\mathbf{A}$ is given by the nonlinear transformation

$$\mathbf{a} = \mathbf{A} + \psi(\mathbf{A}) \tag{3.10}$$

and $\mathbf{g}(\mathbf{A})$ is of some standard form (e.g. our worked example above).

To show explicitly that we have the generic co–dimension two behavior in our perturbed soliton system, we combine equation (4.2) and the ansatz (4.3):

$$\Psi = \begin{pmatrix} u_x \\ u \end{pmatrix} = \Phi = \begin{pmatrix} v_x \\ v \end{pmatrix} \tag{4.6}$$

$$
\begin{aligned}
\partial_t \Psi &= \partial_t \Phi \\
&= \dot{\mathbf{A}} \partial_\mathbf{A} \Phi \\
&= (M\mathbf{A} + \mathbf{g}(\mathbf{A})) \partial_A \Phi \\
&= \mathbf{L}\Phi + \mathbf{N}(\Phi) \\
&= \mathbf{L}\Psi + \mathbf{N}(\Psi)
\end{aligned} \tag{4.7}
$$

or rewriting

$$
\begin{aligned}
(M\mathbf{A} + \mathbf{g}(\mathbf{A})) \partial_\mathbf{A} \Phi &= \mathbf{L}\Phi + \mathbf{N}(\Phi) \\
(M\mathbf{A}\partial_\mathbf{A} - \mathbf{L})\Phi &= \mathbf{N}(\Phi) - \mathbf{g}(\mathbf{A})\partial_\mathbf{A} \Phi
\end{aligned} \tag{4.8}
$$

Since here the matrix representation of our linear $\mathbf{L}$ is exactly our linear normal form matrix M, we see that this equation is exactly the equation we get for our nonlinear transformation ψ in normal form theory (i.e., the transformation to find the correct basis in our space of slow modes). The equivalence of solving the two problems tells us that we can constrain the nonlinear terms of our amplitude equations by knowing the linear terms. Therefore, we know there exists amplitudes $\mathbf{A}$ related to our $\mathbf{a} = \begin{pmatrix} \xi \\ \alpha = 1/4\nu^2 \end{pmatrix}$ by (3.9) and that the form of the amplitude equations is that of (3.21) with the α_J's and the β_J's functionals of ϵ and $R[u]$.

5. The Co–dimension Two Soliton: Nume   Results

Now armed with the assurance that there is a co–dimension two soliton, we try to construct one numerically. We utilize the numerical method used in Ablowitz, Kruskal and Ladik, 1979—a centered, second order leap–frog scheme.

Physically, we need to put in a perturbation that includes both dissipative terms and driving terms. We tried a variety of perturbations,[6] and, generally, we can accelerate the velocity of the kink solution. See Figures 1 and 2. This behavior is well described by Karpman's result as velocity of the kink is passively evolved as a function of the slope of the kink. However, with other perturbations,[7] we obtain relaxation oscillation solutions (see Figure 3). And this cannot be described by Karpman's formulas. Hence, the numerical result substantiates our theoretical analysis.

---

[6] e. g., $R[u] = u_x$, $R[u] = u_{xx}$, $R[u] = u_t$

[7] e. g., $R[u] = \alpha u_x + \beta u_{xx}$

6. Attempts at a Chaotic Soliton

To derive a chaotic soliton system of the perturbed equations, we have to work out a co–dimension three system. Because the kink soliton only has two parameters (ν and ξ), this is impossible unless we include a second soliton (see Kaupman and Solov'ev, 1981, and Newell, 1977) or a field that couples itself to the soliton. Theoretically, we know such a chaotic soliton exists in both cases. In the two soliton case, we get a co–dimension four system, and the linear part of our normal form is of the form

$$M = \begin{pmatrix} 0 & 1 & 0 & 0 \\ 0 & 0 & 0 & 0 \\ 0 & 0 & 0 & 1 \\ 0 & 0 & 0 & 0 \end{pmatrix}$$

which is just the direct sum of two co–dimension two matrices.

In the coupled field case, we get a co–dimension three system,

$$M = \begin{pmatrix} 0 & 1 & 0 \\ 0 & 0 & 0 \\ 0 & 0 & 0 \end{pmatrix}$$

which is simply a co–dimension two system coupled to a slowly changing field.

It can be shown that the latter is the linear part of the third order Lorenz equations (Spiegel, 1985):

$$\begin{aligned} \dot{X} &= Y \\ \dot{Y} &= -X^3 + ZY - \beta\gamma Y \\ \dot{Z} &= -\beta\left[Z + \alpha(X^2 + 1)\right] \end{aligned} \tag{6.1}$$

which for a wide range of parameters α, β, and γ exhibit chaotic behavior.

We chose to attack the third order problem, and tried to couple the soliton to an external field as follows:

$$\begin{aligned} \partial_{xt}\psi &= \sin\psi + \epsilon R[\psi, \phi] \\ \partial_t\phi &= \epsilon S[\psi, \phi] \end{aligned} \tag{6.2}$$

where ψ is our perturbed solitary kink and $\phi = \phi(x, t)$ is the external field. We had many ideas that we tried briefly during the last week of the summer. One possible idea that since we can accelerate and decelerate the kink so that it changes directions (see Figure 2), and the sign of the acceleration comes from the sign of our perturbation, we can couple the perturbation with the external field in the following manner:

$$R[u] = \psi_x \phi \tag{6.3}$$

so that whenever ϕ changed sign, the kink acceleration would change sign. Numerically, we observe that singularities tend to develop when we solve the second PDE in (6.2). We

did not have time to understand this fact. Most of the perturbations we tried did not work in the way we wanted them to work.[8]

What we ended up doing was to couple the soliton to an ordinary differential equation instead of a partial differential equation. A similiar system was studied by Pedlosky (1980), who obtained the Lorenz equations while studying the finite amplitude evolution of baroclinic waves in a two layer quasi–geostrophic model. Pedlosky derived the ODE that couples to the potential vorticity equation by the usual asymptotic analysis of the unstable baroclinic wave in QG. His uncoupled system does not admit a soliton solution; however, we may imagine a similiar system in two–dimension thermalhaline convection. The main point here is that we can show that we can make a soliton chaotic.

So our perturbed equations are as follows:

$$\partial_t \psi = \sin\psi + \epsilon R[\psi, \phi]$$
$$\dot\phi = \epsilon S[\psi, \phi] \tag{6.4}$$

where ϕ now depends only on time. From numerical results, we know the forms of perturbation we need to obtain a co–dimension two system; here we can explicitly concoct the Lorenz system by demanding our ODE to be the third equation in the Lorenz system. For instance, one possible system of equations (in laboratory coordinates) is:

$$\partial_t^2 \psi - \partial_x^2 \psi = \sin\psi + \epsilon(\partial_x\psi + \gamma\partial_t\psi)\phi$$
$$\dot\phi = \epsilon\beta\left[\phi - \alpha(I^2 - 1)\right] \tag{6.5}$$

where I is given by

$$I = \int_\infty^\infty (\psi_x)^3 dx$$

And we show the world line of this system in Figure 4 (the space time diagram is shown in Figure 5). The idea, once again, is to couple the external field in the manner of (6.3). And if ϕ changes sign aperiodically, we obtain a chaotic soliton. It is too early to tell if this particular kink is chaotic or not; however, we know from our theoretical analysis above that the underlying attractor is chaotic (in some region of parameter space). Further numerical work needs to be done to show explicitly the chaotic behavior, while future theoretical analysis will be focused on obtaining such a system in some physical circumstances.

---

[8] Steve Meacham suggested that we try the following system:

$$\partial_{xt}\psi = \sin\psi + \epsilon R[\psi, \phi]$$
$$\partial_{xt}\phi = \sin\phi - \epsilon R[\psi, \phi]$$

which is almost a two soliton system. It bears some philosophical resemblance to Andy Ingersoll's two Red Spots idea—that there is another vortex underneath the Great Red Spot of Jupiter and that the second vortex is resposible for the overall dynamics.

356

Acknowledgement.

References.

Ablowitz, M. J., Kruskal, M. D., and Ladik, J. F. *Solitary Wave Collisions. SIAM J. Appl. Math.*, **36**, 428, 1979.

Ablowitz, M. J. and Segur, H. *Solitons and the Inverse Scattering Transform.* SIAM, 1981.

Arneodo, A., Coullet, P. H., Spiegel, E. A., and Tresser, C. *Asymptotic Chaos, Physica* **14D**, 327, 1985.

Bretherton, C. S. GFD notes, 1981

Bretherton, C. S. and Spiegel, E. A. *Intermittency through Modulational Instability. Phys. Lett.*, **96A**, 152, 1983.

Coullet, P. H. and Spiegel, E. A. *Amplitude Equations for Systems with Competing Instabilities. SIAM J. Appl. Math.*, **43**, 776, 1983.

Hasimoto, R. *A Soliton on a Vortex Filament. J. Fluid Mech.*, **51**, 477, 1972.

Karpman, V. I. *Soliton Evolution in the Presence of Perturbation. Phys. Scripta*, **20**, 462, 1979.

Karpman, V. I. and Maslov, E. M. *Inverse Problem Method for the Perturbed Nonlinear Schrodinger Equation. Phys. Lett.*, **61A**, 355, 1977.

Karpman, V. I. and Maslov, E. M. *A Perturbation Theory for the Korteweg–de Vries Equation. Phys. Lett.*, **60A**, 307, 1977.

Karpman, V. I. and Maslov, E. M. *Perturbation Theory for Solitons. Sov. Phys. JETP*, **46**, 281, 1977.

Karpman, V. I. and Solov'ev, V. V. *A Perturbational Approach to the Two–Soliton Systems. Physica*, **3D**, 487, 1981.

Lamb, G. L. *Elements of Soliton ˆˇeory.* Wiley, 1980.

Moore, D. W. and Spiegel, E. A. *A Thermally Excited Non–Linear Oscillator. Ap. J.*, **143**, 871, 1966.

Newell, A. C. *Solitons in Mathematics and Physics*. SIAM, 1985.

Newell, A. C. *Synchronized Solitons*. *J. Math. Phys.*, **18**, 922, 1977.

Pedlosky, J. and Frenzen, C. *Chaotic and Periodic Behavior of Finite-Amplitude Baroclinic Waves*. *J. Atm. Sci*, **37**, 1177, 1980.
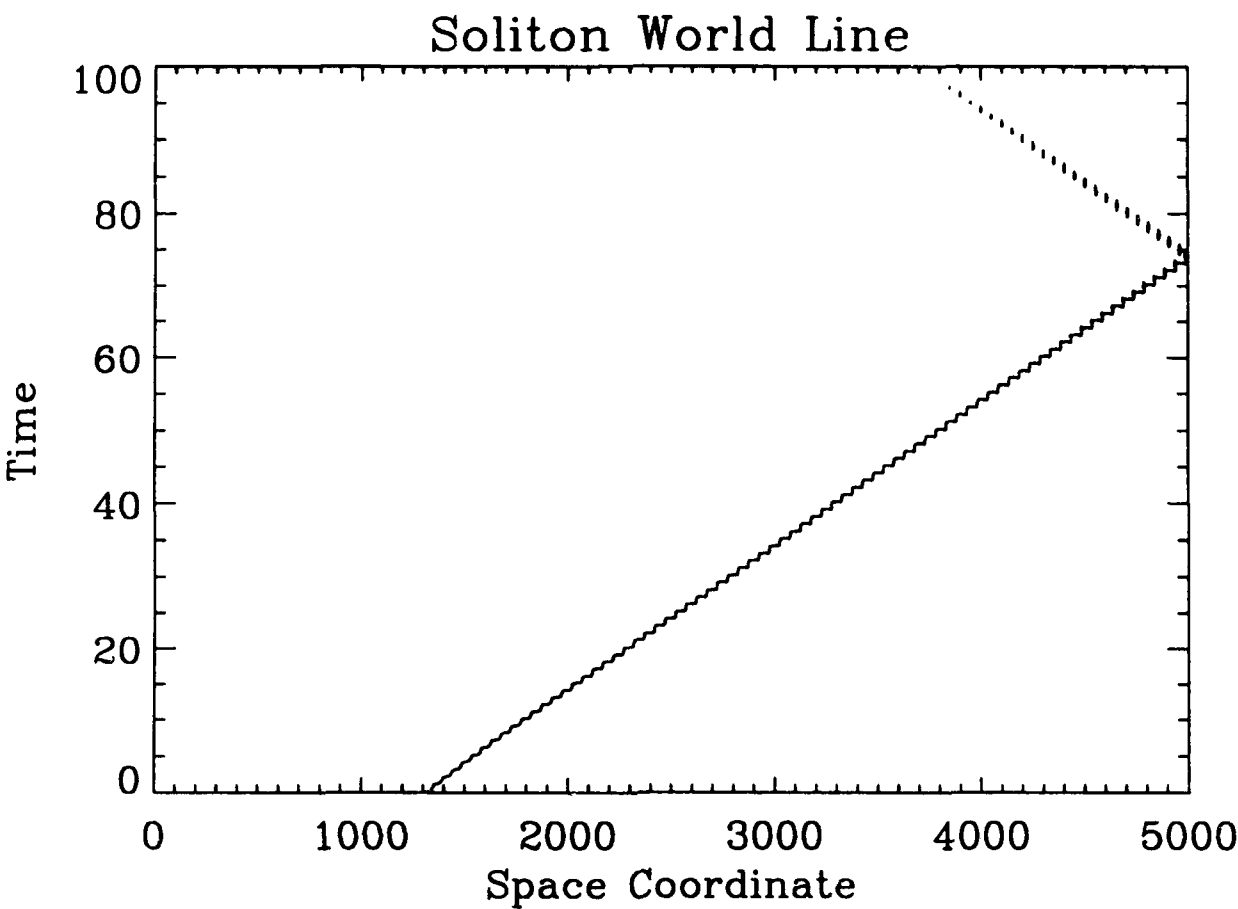
Spiegel, E. A. *Cosmic Arrythmias* from *Chaos in Astrophysics*, 91–135, 1985 (edited by J. R. Buchler *et al.*).
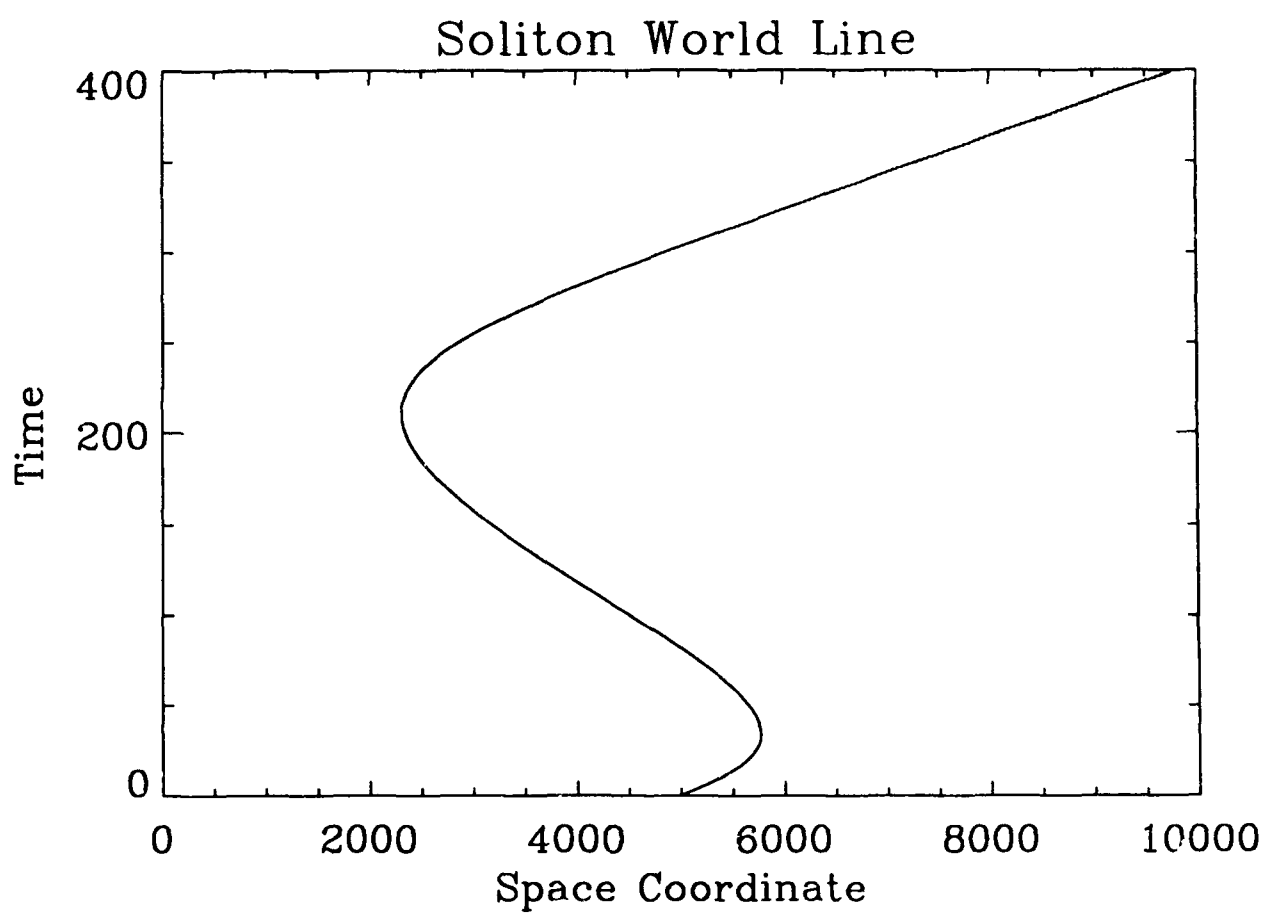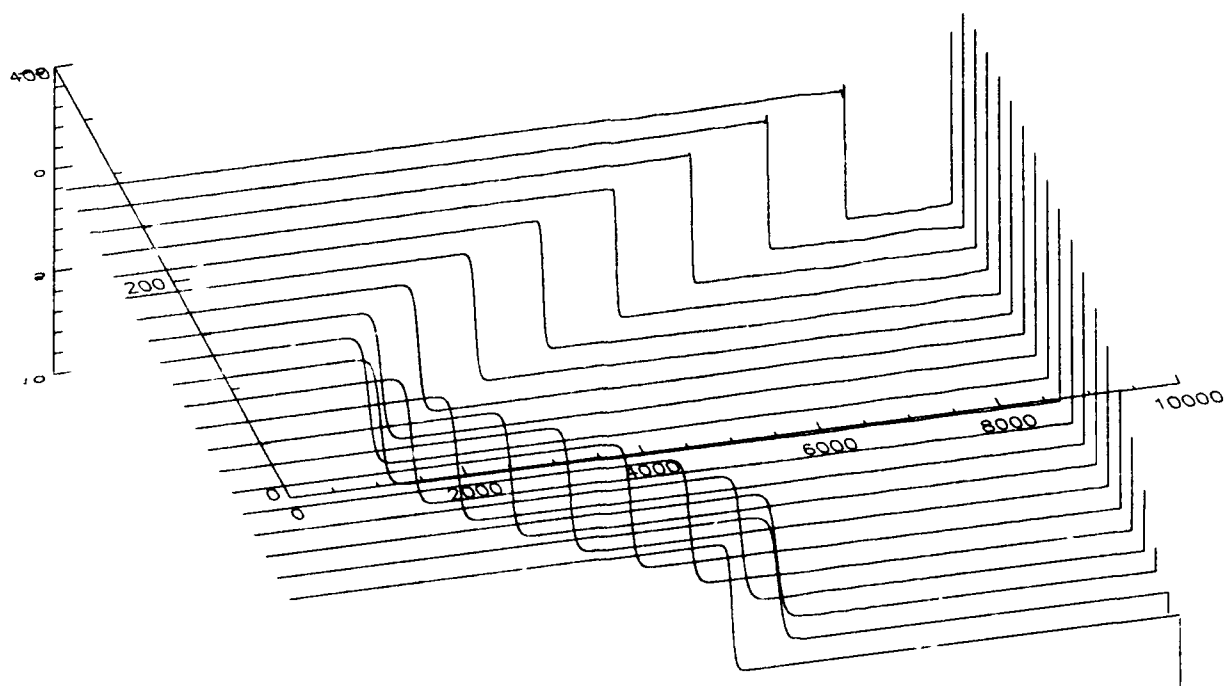
Spiegel, E. A. *Double Convection*. GFD notes, 1981.

Spiegel, E. A. *Long Buoyancy Waves and Solar Variability; a Geometrical View of Dynamical Systems*. GFD notes, 1981.

Soliton World Line

Soliton World Line

Soliton World Line

Soliton World Line

362
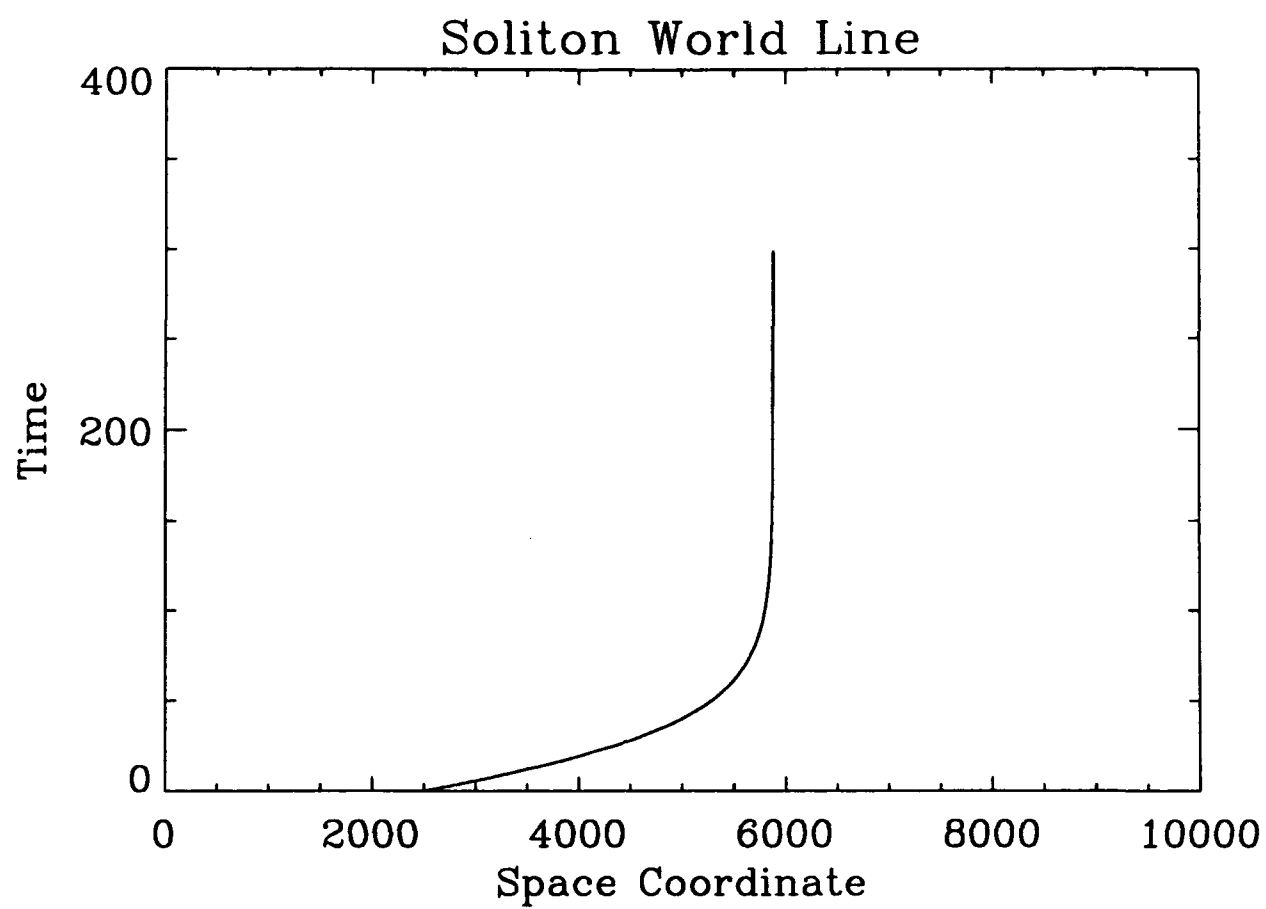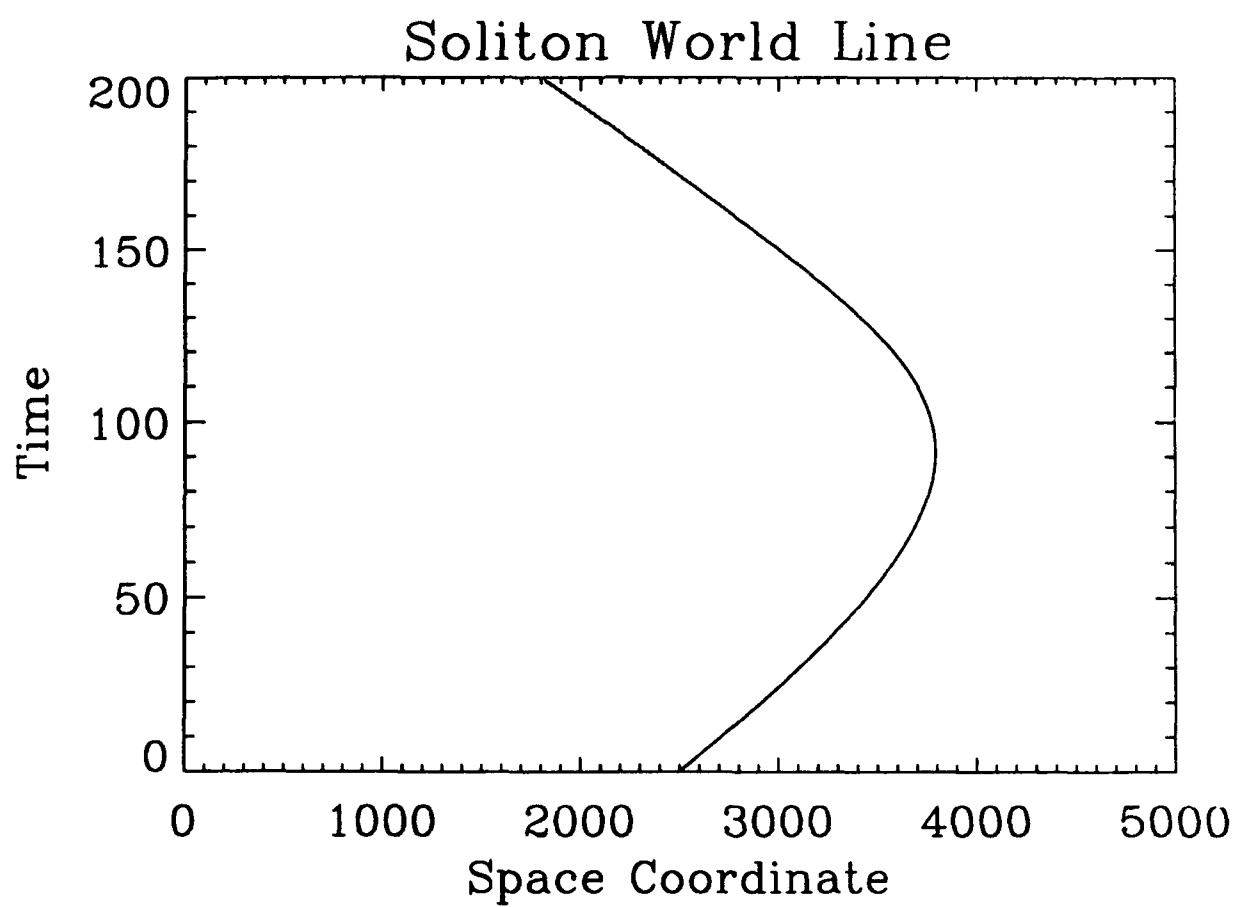
Disks: Just the Place for a Spot!

Phillip Yecko

Abstract

The equations governing a thin accretion disk orbiting a central object are reduced to a shallow water system. The integrals of motion of this system are used to find conditions necessary for the formal stability of azimuthal basic states. Linear perturbation theory is used to show that one of the conditions of stability (that the velocities be sub-gravity-wave speed) is easily violated, but that associated growth rates of gravity wave instabilities may be small. Numerical experiments are performed to investigate the stability of basic states (axisymmetric equilibria) and basic states with superimposed vortices. It is found that the near-Keplerian shear of a thin disk is hostile to vortices, but also that superposition of a vortex is destablizing to the basic state of the disk. Possibilites for a balanced basic state that incorporates a large vortex are investigated analytically and numerically.

1. Introduction

The astrophysical disk is ubiquitous: most galaxies have a disk component; the central engines of active galactic nuclei are thought to be powered by matter falling onto a massive black hole via an accretion disk or torus; many binary star systems evolve through a mass exchange phase that produces an accretion disk; and, finally, star formation (including the formation of our solar system) is believed to nucleate at the center of a so-called proto-stellar accretion disk in the process of gravitational collapse. We can think of the disk as an astro-fluid-dynamical phenomenon responsible for the redistribution of matter and angular momentum in the universe - concentrating the matter at its center and dispersing the angular momentum as far from the center as possible. The redistribution of angular momentum this way in an orbital "flow" depends, of course, on there being anisotropic internal stresses (viscosity) within the disk (Shakura & Sunyayev 1973). Molecular viscosity, turbulent viscosity and wave interaction provide such stress in a fluid, though molecular viscosity is negligible for most length scales of the disk. Even in a many-particle disk system, such as a planetary ring, anisotropic stress can be effected by collisional processes that extract energy from the orbits. So understanding the fluid dynamics of a disk is essential to understanding how it may oscillate, whether it is unstable, or possibly turbulent, and what its turbulent structure would be. By analogy to Jovian systems (MacLow & Ingersoll 1986), laboratory experiments with rotating fluids (Sommeria et al 1988) and extensive numerical simulations of

364

vortices in reduced systems (Dowling & Ingersoll 1989; McWilliams 1984), we conjecture that the complementary processes of small scale turbulence generation and vortex merger may produce long lived coherent structures, like the Jovian "spots," in disks.

2. Shallow-Water Disks

We distinguish those disks which have a dominantly massive central object (accretion disks in binary star systems) from those in which self gravity is important (galactic disks), and concentrate on the former. In fact, we assume that the mass within the disk is small enough in comparison to that of the central object that self gravity can be neglected entirely, and the central object is included as an external gravitational potential.

The equations governing the conservation of mass and momentum for an inviscid disk are:

$$\frac{\partial \rho}{\partial t} + \nabla \cdot (\rho \mathbf{v}) = 0 \,, \tag{2.1}$$

$$\frac{\partial \mathbf{v}}{\partial t} + \mathbf{v} \cdot \nabla \mathbf{v} = -\frac{\nabla p}{\rho} - \nabla \Phi_g \,, \tag{2.2}$$

where

$$\Phi_g := -\frac{GM_o}{R} \,,$$

represents the gravitational potential of a point mass M_0 at $R = 0$ and the fluid is assumed to be barotropic:

$$p = p(\rho).$$

This description is valid as long as any ionization effects can be included in the barotropic equation of state and the fluid velocities are non-relativistic.

The outer surface of the disk is defined by its thickness $h(r, \phi, t)$ where we have now adopted cylindrical polar coordinates (r, ϕ, z) as shown in figure 1. We immediately make a distinction between vertical and horizontal lengthscales (H and L), and define their ratio: $\varepsilon := \frac{H}{L}$. In a thin disk, ε is a small parameter.

The equations (2.1) and (2.2) should be nondimensionalized if we hope to bring out the dominant balances. The nondimensionalization of (2.1) shows that the vertical and horizontal velocity scales (W and U) are related by: $W = \varepsilon U$. The dimensionless equations for the velocity components (u, v, w) are:

$$\frac{\partial \rho}{\partial t} + \frac{\partial}{\partial r}(\rho u) + \frac{1}{r}\frac{\partial}{\partial \phi}(\rho v) + \frac{\partial}{\partial z}(\rho w) = 0 \,, \tag{2.3}$$

$$\frac{\partial u}{\partial t} + u\frac{\partial u}{\partial r} + \frac{v}{r}\frac{\partial u}{\partial \phi} + w\frac{\partial u}{\partial z} - \frac{v^2}{r} = -\frac{\alpha}{\rho}\frac{\partial p}{\partial r} - \beta\frac{\partial \Phi_g}{\partial r} \,, \tag{2.4}$$

$$\frac{\partial v}{\partial t} + u\frac{\partial v}{\partial r} + \frac{v}{r}\frac{\partial v}{\partial \phi} + w\frac{\partial v}{\partial z} + \frac{uv}{r} = -\frac{\alpha}{\rho r}\frac{\partial p}{\partial \phi} - \frac{\beta}{r}\frac{\partial \Phi_g}{\partial \phi} . \tag{2.5}$$

The scale separation is more apparent in the vertical momentum equation, which reduces to hydrostatic balance to $O(\varepsilon^2)$; neglecting small terms it is:

$$\frac{\alpha}{\rho}\frac{\partial p}{\partial z} + \beta\frac{\partial \Phi_g}{\partial z} = 0 . \tag{2.6}$$

The momentum equations now contain the dimensionless parameters:

$$\alpha = \frac{p_*}{\rho_* U^2} = \frac{c_g^2}{U^2} ,$$

where c_g is the characteristic speed of divergent waves (usually sound, but in shallow water theory, these are the surface gravity waves); and:

$$\beta = \frac{GM_o}{LU^2} .$$

But the choice of $\beta = 1$ just corresponds to scaling the horizontal velocity by its Keplerian value at $r = L$, so we adopt that. It would clearly be fortuitous to introduce the enthalpy:

$$\nabla E = \frac{\alpha}{\rho}\nabla p ,$$

where we are free to incorporate the parameter α in the definition. So the vertical momentum equation can be rewritten:

$$\frac{\partial \mathcal{F}}{\partial z} = 0 , \tag{2.6'}$$

where $\mathcal{F}$ is therefore the z-independent "combined potential" defined by:

$$\mathcal{F} := E + \Phi_g .$$

Since the pressure, and therefore the enthalpy, must go to zero on the surfaces of the disk, $\mathcal{F}$ can be found immediately by integrating (2.6') and applying that boundary condition:

$$\mathcal{F} = \Phi_g[r, h(r,\phi,t), t] = -\frac{1}{(r^2 + h^2)^{\frac{1}{2}}} .$$

Since $\frac{h}{r}$ is small, $\mathcal{F}$ can be separated into two terms: a purely radial term representing the gravitational potential on the $z = 0$ midplane Φ; and another term representing the *midplane enthalpy* e associated with the pressure produced by the local vertical gravity acting on the local total thickness.

$$\mathcal{F} = \frac{h^2}{2r^3} - \frac{1}{r} = e + \Phi$$

Since $\mathcal{F}$ is independent of the vertical coordinate z, the horizontal components of the momentum equation therefore have no vertically dependent accelerations. Disks, because of their thinness, are

therefore describable by a variation of the standard *shallow water* approximation (Pedlosky 1987). Following that derivation, we assume that since no vertical variations of velocity can be induced, there will be none if none were pre-existing. Unlike standard shallow-water theory, the fluid in the disk is compressible, but if we introduce the vertically integrated surface density:

$$\sigma := \int_{-h}^{h} \rho \, dz \; ,$$

then the momentum and continuity equations can be vertically integrated to give:

$$\frac{\partial \sigma}{\partial t} + \frac{\partial}{\partial r}(\sigma u) + \frac{1}{r}\frac{\partial}{\partial \phi}(\sigma v) = 0 \; , \qquad (2.7)$$

$$\frac{\partial u}{\partial t} + u\frac{\partial u}{\partial r} + \frac{v}{r}\frac{\partial u}{\partial \phi} - \frac{v^2}{r} = -\frac{\partial \mathcal{F}}{\partial r} \; , \qquad (2.8)$$

$$\frac{\partial v}{\partial t} + u\frac{\partial v}{\partial r} + \frac{v}{r}\frac{\partial v}{\partial \phi} + \frac{uv}{r} = -\frac{1}{r}\frac{\partial \mathcal{F}}{\partial \phi} \; . \qquad (2.9)$$

This description is incomplete until we relate σ, h and e. Midplane enthalpy e has already been identified with $\frac{h^2}{2r^3}$, so if we specify the polytropic function $p = K\rho^\gamma$, the definition of σ can be directly integrated to give the relationship:

$$\sigma = \mathcal{N}h^l r^{-\frac{3l}{\gamma+1}} \; , \qquad (2.10)$$

and therefore:

$$\sigma = \mathcal{N}(2e)^{\frac{l}{2}} r^{\frac{3}{2}} \; , \qquad (2.11)$$

with the ersatzen: $l := \frac{\gamma+1}{\gamma-1}$ and

$$\mathcal{N} := \left[\frac{\gamma-1}{2\gamma}\right]^{\frac{1}{\gamma-1}} \int_0^1 (1 - x^2)^{\frac{1}{\gamma-1}} \, dx \; ,$$

introduced for convenience.

In what we call *basic state*, we assume that the disk has only an azimuthal circulation. This may seem strange, since we stressed that disks are important because they have a radial flow to carry material to their centers, but this flow is substantially smaller than the angular velocity. The radial is commonly thought of as a secondary flow induced by (and therefore proportional to) the viscous stress, although what created that flow is not specified, and we have been treating the inviscid case so far. The equilibrium structure of an accretion disk describes a balance among the central accretion, injection of external material and energy dissipation. A quick analytic calculation will show that turbulent stress associated with the azimuthal basic state does indeed produce negligible radial infall and this is further verified by the evolution of the numerical models, so we neglect u.

A basic state (quantities endowed with overbars) which is time independent, non-radial and azimuthally symmetric is then:

$$\bar{v} = \left(r\frac{\partial \bar{e}}{\partial r} + \frac{1}{r} \right)^{\frac{1}{2}} . \tag{2.12}$$

This is simply a relationship between $\bar{v}$ and $\bar{e}$ such that one is determined, but the other is free to be specified. Because a disk is just a big azimuthally circulating flow, we can think of it as a particular vortex whose velocity profile satisfies (2.12); in oceanic terms, it is a self-contained vortical layer which outcrops at the outer edges of the disk, if such edges are specified. We find that the (vertical) vorticity of the disk is:

$$\zeta = \hat{z} \cdot \nabla \times \mathbf{v} = \frac{1}{r}\left(\frac{\partial}{\partial r}(rv) - \frac{\partial u}{\partial \phi} \right) , \tag{2.13}$$

which obeys the conservation law:

$$\frac{\partial \zeta}{\partial t} + \nabla \cdot (\zeta \mathbf{v}) = 0 ; \tag{2.14}$$

(2.14) is combined with (2.7) to express the conservation of disk potential vorticity q:

$$\frac{dq}{dt} = \frac{d}{dt}\left(\frac{\zeta}{\sigma} \right) = 0 . \tag{2.15}$$

As in the shallow water equations, we can identify the energy that is conserved by the system by forming $\frac{1}{2}[u \cdot (2.8) + v \cdot (2.9)]$. This construct reduces to:

$$\frac{\partial}{\partial t}\left(\sigma \left[\frac{1}{2}(u^2 + v^2) + \frac{l}{l+2}e + \Phi_g \right] \right) + \nabla \cdot \left(\mathbf{v}\sigma \left[\frac{1}{2}(u^2 + v^2) + e + \Phi \right] \right) = 0 . \tag{2.16}$$

The form of (2.16) defines a *global* integral of motion E for any disk with no net momentum flux through its edges (by virtue of the vanishing divergence upon integration over the area of a disk with no flux through its surfaces):

$$E := \int \int \mathcal{E} \, d\Sigma = constant. \tag{2.17}$$

The quantity $\mathcal{E}$, appearing after $\frac{\partial}{\partial t}$ in (2.16), is therefore the energy per unit area of the disk, and it is seen to contain the kinetic energy, the energy of the total potential $\mathcal{F}$ and the work done by the internal stress accociated with e. This is made explicit by rewriting it:

$$\mathcal{E} := \sigma \left[\frac{1}{2}(u^2 + v^2) + \mathcal{F} - \frac{2}{l+2}e \right] . \tag{2.18}$$

3. Formal Stability

Since the prescription of time independent basic states simply involves a relation between $\bar{v}$ and $\bar{e}$, we are concerned that many choices of $(\bar{v}, \bar{e})$ may not be stable. To follow the variational method of formal stability analysis used by Arnol'd (1965), we first adopt the idea that stable states lie at local minima of the surfaces (in the Banach space of the field variables) of the integrals of motion of the system. Stability is therefore ensured by the condition of a local minumum of an integral of motion S and a minimum is identified when all variations from it are positive:

$$\Delta S > 0 . \tag{3.1}$$

By expressing S as:

$$S := E + \lambda J , \tag{3.2}$$

we can include in the variation the constraint that some function J of potential vorticity is also conserved. (Since J is still unspecified, there is really no need for the multiplier λ, but we have included it anyway.) Alternatively, S can be thought of as some analog of action for a fluid that conserves total potential vorticity; S itself is an integral of motion since its parts are. We need to be more specific about the integral of motion associated with the potential vorticity. Potential vorticity conservation is inherently Lagrangian; it is a material invariant (conserved moving along with fluid particles). So its integral of motion is given by:

$$\lambda J := \int \int \mathcal{J}\left[q(\mathbf{l})\right] d^3\mathbf{l} = constant, \tag{3.3}$$

where $\mathbf{l}$ is the Lagrangian fluid label variable. We would like to express this integral in Eulerian form, since we work and think in physical space; so we need to change coordinates from Largrangian labels to Eulerian variables. The Jacobian of this coordinate change, which can be shown to simply be σ (Abarbanel and Holm 1985), is therefore introduced into the integrand:

$$\lambda J := \int \int \sigma \mathcal{J}\left[q(\mathbf{r})\right] d\Sigma = constant. \tag{3.3'}$$

$\mathcal{E}$ is rewritten by inverting (2.11) to eliminate the variable e:

$$\mathcal{E} = \sigma \left[\frac{1}{2}\mathbf{v} \cdot \mathbf{v} + \mathcal{F}(\sigma) - \frac{2}{l+2} \frac{\sigma^{\frac{7}{2}}}{2\mathcal{N}^{\frac{7}{2}} r^{\frac{7}{2}}} \right] = \sigma \left[\frac{1}{2}\mathbf{v} \cdot \mathbf{v} + \mathcal{F} + \mathcal{H} \right] ,$$

which defines $\mathcal{H}$. Now we replace the variation by the sum of the first two terms, one linear in the variation, the other quadratic, of its functional Taylor series expansion:

$$\Delta S = \delta S + \delta^2 S + \ldots \tag{3.1'}$$

The condition for minima and subsequent guarantee of stability then requires that the linear variation term *must* be identically zero. If δS were positive for some variation $(\delta\bar{\mathbf{v}}, \delta\bar{\sigma})$ then it would be negative for the inverse variation $(-\delta\bar{\mathbf{v}}, -\delta\bar{\sigma})$ and indicate a saddle point rather than an extremum in S at $(\bar{\mathbf{v}}, \bar{\sigma})$. Remember that although we have let $\mathcal{J}(q)$ be arbitrary, it cannot be *so* arbitrary that λJ won't serve as a Lyapunov functional of the system. So the requirement that δS vanish just provides information about $\mathcal{J}$ such that it can be used in (3.1) and (3.2). The first variation then, must satisfy:

$$\delta(E + \lambda J) = 0 \,,$$

or

$$\int\int d\Sigma \left[\frac{1}{2}\bar{\mathbf{v}}\cdot\bar{\mathbf{v}} + \frac{d}{d\bar{\sigma}}(\mathcal{F} + \mathcal{H}) + \mathcal{J} - \bar{q}\frac{d\mathcal{J}}{d\bar{q}}\right]\delta\sigma + \int\int d\Sigma\delta\mathbf{v}\cdot\left[\bar{\sigma}\bar{\mathbf{v}} - \frac{d^2\mathcal{J}}{d\bar{q}^2}\nabla\times(\bar{q}\hat{\mathbf{z}})\right] = 0 \,, \quad (3.4)$$

where we have used the definition of potential vorticity to relate variations in q to variations in $(\mathbf{v}, \sigma)$:

$$\delta q := \frac{\nabla\times\delta\mathbf{v} - \bar{q}\delta\sigma}{\bar{\sigma}} \,,$$

and integrated the $\nabla\times\delta\mathbf{v}$ term by parts to get $\nabla\times\bar{q}\hat{\mathbf{z}}$. For each of the integrands to separately vanish we must have:

$$\bar{q}\frac{d\mathcal{J}}{dq} - \frac{d}{d\bar{\sigma}}(\mathcal{F} + \mathcal{H}) = \mathcal{J} + \frac{1}{2}\bar{\mathbf{v}}\cdot\bar{\mathbf{v}} = \mathcal{B}(\bar{\mathbf{v}}, \bar{\sigma}) \,, \quad (3.5)$$

and

$$\frac{d^2\mathcal{J}}{d\bar{q}^2}\frac{d\bar{q}}{dr} = \bar{\sigma}\bar{v} \,, \quad (3.6)$$

since the basic state has no $\bar{u}$. Any steady basic state also satisfies:

$$\nabla\cdot(\bar{\sigma}\bar{\mathbf{v}}) = 0 \,,$$

so we can introduce a vector potential for the flux $\bar{\sigma}\bar{\mathbf{v}}$, whose only component is the vertical one representing the flux streamfunction Ψ:

$$\bar{\sigma}\bar{\mathbf{v}} = \nabla\times\mathbf{A} = \nabla\times(0, 0, \Psi) \,.$$

The Bernoulli function $\mathcal{B}$ that appears in equation (3.5) is known to be a function of Ψ only for steady barotropic flow, but the other terms of equation (3.5) are functions $\mathcal{J}(\bar{q}) = \mathcal{J}[\bar{q}(r)]$. Therefore, $\mathcal{J}$ and $\bar{q}$ are also functions of Ψ. So equation (3.6) can be given as:

$$\frac{d^2\mathcal{J}}{d\bar{q}^2} = -\frac{d\Psi}{d\bar{q}} \,,$$

which implies:

$$\frac{d\mathcal{J}}{d\bar{q}} = -\Psi \,. \quad (3.7)$$

Now we look at the conditions for the positivity of the second variation of S:

$$\delta^2 S = \delta^2(E + \lambda J) > 0 ,$$

which can be directly expressed as:

$$\delta^2(E + \lambda J) = \int \int d\Sigma \left[\frac{1}{2}\bar{\sigma}(\delta\mathbf{v})^2 + \bar{\mathbf{v}} \cdot \delta\mathbf{v}\delta\sigma + \frac{d}{d\bar{\sigma}}(\mathcal{F} + \mathcal{H})(\delta\sigma)^2 + \frac{1}{2}\frac{d^2 J}{d\bar{q}^2}\bar{\sigma}(\delta\sigma)^2 \right] > 0 . \quad (3.8)$$

The first three terms in the integrand can be rewritten (Ripa 1991):

$$\bar{\sigma}\left(\delta u + \frac{\bar{u}\delta\sigma}{\bar{\sigma}}\right)^2 + \bar{\sigma}\left(\delta v + \frac{\bar{v}\delta\sigma}{\bar{\sigma}}\right)^2 + \frac{(\delta\sigma)^2}{\bar{\sigma}}\left[\frac{d}{d\bar{\sigma}}(\mathcal{F} + \mathcal{H}) - (\bar{u}^2 + \bar{v}^2)\right] ,$$

so that the positive definity of the integrals is ensured by the conditions:

$$\left[\frac{d}{d\bar{\sigma}}(\mathcal{F} + \mathcal{H}) - (\bar{u}^2 + \bar{v}^2)\right] > 0 ,$$

and

$$\frac{d^2 J}{d\bar{q}^2} > 0 ,$$

which can be simplified to:

$$\bar{v} < \left[\frac{d}{d\bar{\sigma}}(\mathcal{F} + \mathcal{H})\right]^{\frac{1}{2}} , \quad (3.9)$$

and

$$\frac{\bar{v}}{d\bar{q}/dr} > 0 . \quad (3.10)$$

The first condition (3.9) requires that the basic state flow velocities not exceed the RHS of the inequality, which can be identified with the speed of gravity waves in the disk. The second condition requires that the potential vorticity gradient of the basic state not change sign except where the velocity profile itself changes sign, a generalization of Fjortoft's condition for shear flow. These conditions ensure (they are sufficient for) formal, but not nonlinear stability. Stronger conditions can be obtained from convexity estimates of S, but that problem is difficult (possibly impossible) to pose in shallow water.

The stability conditions also indicate that there are two mechanisms that may destablize the disk: violation of the second condition, which is corresponds to an unstable distribution of angular momentum in the disk; and violation of the first condition, which suggests the over-reflection of gravity waves in the disk (Narayan et al 1987). One way to interpret (3.9) then, is that it ensures that a critical layer is contained in the disk for some part of the gravity wave spectrum. It is a *necessary* condition for instability because it guarantees the presence of the appropriate wave geometry for over-reflection (Lindzen 1986), but insufficient since it says nothing about the resonant nature of any of the modes. So we look next at the behavior of linear perturbations to try to better understand the propagation and instability of gravity waves in disks.

4. Linear Theory

It is essential to understanding the behavior of wavelike disturbances, including the propagation and possible unstable growth of waves, to study the problem of linearized disturbances to some conjectured basic state. If we decompose the fields described by equations (2.7) – (2.9) into a time-independent basic state plus a linearized perturbation $\chi_n := \bar{\chi}_n(r) + \chi_n'$, then we get the following equations for the perturbations:

$$\left(\frac{\partial \sigma'}{\partial t} + \frac{\bar{v}}{r}\frac{\partial \sigma'}{\partial \phi}\right) + \frac{\partial}{\partial r}(\bar{\sigma} u') + \frac{\bar{\sigma}}{r}\frac{\partial v'}{\partial \phi} = 0 \,, \tag{4.1}$$

$$\left(\frac{\partial u'}{\partial t} + \frac{\bar{v}}{r}\frac{\partial u'}{\partial \phi}\right) - \frac{2\bar{v}v'}{r} + \frac{\partial \epsilon'}{\partial r} = 0 \,, \tag{4.2}$$

$$\left(\frac{\partial v'}{\partial t} + \frac{\bar{v}}{r}\frac{\partial v'}{\partial \phi}\right) + \left(\frac{\bar{v}}{r} + \frac{\partial \bar{v}}{\partial r}\right)u' + \frac{1}{r}\frac{\partial \epsilon'}{\partial \phi} = 0 \,, \tag{4.3}$$

while from (2.11) we can write:

$$\sigma' = I(r)e' \,,$$

where the function $I(r)$ is used to represent $\frac{d\bar{\sigma}}{d\epsilon}$. Notice that the coefficient of u' in (4.3) is just the vorticity of the basic state:

$$B(r) = \frac{\bar{v}}{r} + \frac{\partial \bar{v}}{\partial r} = \frac{1}{r}\frac{\partial}{\partial r}(r^2 \bar{\Omega}) \,,$$

where $\bar{\Omega} := \frac{\bar{v}}{r}$ is the basic state angular velocity. Since the basic state, and therefore the coefficients of (4.1) – (4.3) are functions of r only, we can consider normal mode perturbations obtained from the ϕ, t transform:

$$\chi_n' := \chi_n(r)e^{i(m\phi - \omega t)} \,,$$

where the unprimed variable label has been recycled for use as the r-dependent part of the perturbation, or the so-called perturbation amplitude. With the useful definitions:

$$\nu := m\bar{\Omega} - \omega \,,$$

and

$$\kappa^2 := \nu^2 - 2\bar{\Omega}B \,,$$

we can obtain a single 2nd order ODE for ϵ:

$$\frac{d}{dr}\left(\frac{\bar{\sigma}}{\kappa^2}\frac{d\epsilon}{dr}\right) + \left(\frac{2m}{\nu}\frac{d}{dr}\left[\frac{\bar{\sigma}\bar{\Omega}}{\kappa^2 r}\right] + I(r) - \frac{\bar{\sigma}m^2}{\kappa^2 r^2}\right)e = 0 \,. \tag{4.4}$$

We expect to recover the Rossby type oscillations in the disk from the low-frequency limit of this equation, and indeed that limit retains the vorticity gradient terms present in (4.4) (first

term in the coefficient of ϵ). The instability problem in this case is analogous to the standard two-dimensional barotropic instability problem, since we have removed the gravity waves in the low-frequency limit. In the high-frequency limit, we expect to filter the Rossby modes and recover a variation of the stratified shear instability problem; the stratification in this case is contained entirely in the variations in the radial variations of surface density:

$$\frac{d^2\epsilon}{dr^2} + \left(\kappa^2\frac{l(r)}{\sigma} - \frac{m^2}{r^2}\right)\epsilon \sim 0 .$$

(4.5)

Taking a local and high frequency limit, we can also look at (4.5) over radial scales small enough that we can approximate:

$$\chi_n \approx constant \quad \& \quad \frac{d\chi_n}{dr} \approx 0.$$

In this case, we can find the local dispersion relation, and therefore local phase speed for gravity waves in the disk:

$$c_g = \bar{v} \pm \left(\frac{\epsilon}{l}\right)^{\frac{1}{2}} .$$

Thus wave speeds are comparable to the mean azimuthal velocity, and the necessary instability condition (3.9) is likely to be violated.

This variety of instability problem has been physically interpreted as the radial over-reflection of an internal gravity-wave normal mode across its critical layer (Lindzen 1986; Takehiro and Hayashi 1992). A WKBJ analysis of the modes of this genericized instability problem by Knessel and Keller(1992) finds the dispersion relation for the gravity waves and further analysis (Balmforth *private communication*) shows that the growth rate associated with an over-reflecting normal mode will be small.

5. Numerical Models and Turbulence

The model equations that we would like to evolve are just a variation of those of shallow water. The numerical history of shallow water algorithms is deep, but there is one guiding selection criterion relevant to modelling disks: the finite extent of the disk means that the code will have to accomadate a vanishing layer thickness. A similar problem arises in layer models of the ocean: the dynamics often forces layer interfaces to intersect horizontal boundaries, or even pinch off a layer, producing what is called an outcropping. There has been much progress recently in numerical models that effectively treat the boundaries of outcropped layers (Sun, Bleck and Chassignet 1992), so we have adapted this code to treat a disk exactly as if it were a solitary outcropped layer. The code is based on an energy and enstrophy conserving finite difference algorithm with high order

flux calculations applied to the outcropping regions (in this case, the edges of the disk) to correct for overly diffusive fluxes calculated there by standard shallow water code.

It is common in astrophysical problems to assume that flows are turbulent simply because typical Reynolds numbers are immense, or because a single theoretical model often neglects a host of processes that are known or believed to catalyze flow instability (magnetic fields, radiat on, material infall, etc). The standard assumption for (turbulent) disks is that the associated eddy viscosity will dominate molecular viscosity by many orders of magnitude and become the quintessential source of tangential stress and therefore govern the nature of the mass infall and angular momentum transport. Disk theory further assumes that the disk thickness provides an upper bound for the scale of action by turbulent viscous stress(Shakura & Sunyayev 1973), saying, in effect, that disk turbulence is globally three dimensional in nature. But we know that vertical motions are effectively quenched in a thin disk (hence the applicability of shallow water theory), suggesting that the fluid dynamics of disks is dominantly two-dimensional. Even outside the shallow regime, two dimensionality is strongly induced by rotation, and accretion disks are rotational objects by their very nature. So the flow of a disk ought to be dominantly two-dimensional. This tells us a lot, since we know something about two-dimensional turbulence. First, that the turbulent stucture in the plane of the disk is independent of its vertical structure. But also, that as the turbulence evolves, energy will cascade to larger spatial scales as enstrophy cascades to smaller scales, eventually falling victim to dissipation by molecular viscosity. This is the nature of two-dimensional and quasi-two-dimensional turbulence. There is more to the turbulence problem than the cascade process, though; within the equilibration cascade it is common to see unpredictable phenomena. Foremost among these is the emergence of coherent structures: typically a small number of isolated vortices.

Ideally, a simulation would be able to resolve flow at most length- and time-scales so that we could numerically evolve an unstable disk, follow the growth of instability and transition to turbulence and only then follow the turbulent equilibration to its natural end state. Ultimately, we hope to perform this experiment with full exploit of computational resources. But understanding of the Jovian planets (also described by the shallow rapidly rotating regime) indicates that similar processes produced the phenomena that we observe there, and therefore that large vortices in the shallow rotating fluid regime are expected. For this reason, we investigate the proclivity of a disk to contain an embedded vortex stably, in the same way that Jupiter and Neptune are host to "great spots."

6. Disks as a Site for Vortices

When such large vortices come into being as the end result of vortex mergers, we must pay

374

particular attention to the background flow in which the vortices sit. The same is true when the vortex is thought to persist for long times: merger of vortex pairs and the stability and axisymmetrization of isolated vortices has been shown to be a sensitive function of the background flow. The oval shapes characteristic of many large Jovian vortices are probably the result of the sizes and strengths of the shear zones in which they sit.

In the steady basic state of a disk, velocity is purely azimuthal and determined by Keplerian flow, modified by the presence of pressure in the form of the enthalpy gradient. Even when this gradient is large, it will scale with the enthalpy itself, which cannot become too large before we violate the small $\frac{H}{L}$ scaling. Thin disks, then, are nearly Keplerian. A sharp discontinuity in the enthalpy can still produce a large gradient, but in that case, only over a very small physical extent. So we expect that no thin disks will have regions (in radial extent) of flow that are known to nurture large vortices, simply because Keplerian flow has strong gradients in velocity ar ~orticity everywhere. Nowhere does a disk seem to have a flow that isn't hostile to the stab" v ⸱' large vortex. Solid body rotation, for example, would require of (2.12) a very large enth ⸱⸱ gradient acting over a large region; clearly such a disk will become "too thick" for the shallow water model derived here, since it implies large enthalpy gradients over large extent. Alternatively, we could solve for an enthalpy distribution that produces solid body rotation according to (2.12). In this case, we get a functional form of $\bar{e}(r)$ with three arbitrary constants. One must be chosen to ensure a thin disk; the second can be chosen to represent the outer edge of the disk, ensuring that it is finite. The form of $\bar{e}(r)$ then demands that the disk thickness again go to zero at some radius (the inner edge) which turns out to closely approach the outer edge. So a thin disk must actually become a narrow ring to have solid body rotation, and a narrow ring naturally precludes large vortices. So we adopt a straightforward initial enthalpy that gives a well defined torus:

$$\bar{e} := e_0 \left[(r - r_i)(r_o - r) \right]^{\frac{3}{2}} \ . \tag{5.1}$$

The vorticity of the disk (viewed from inertial space) is cyclonic:

$$\bar{\zeta} = \frac{1}{r} \frac{\partial}{\partial r} \left(r^3 \frac{\partial \bar{e}}{\partial r} + r \right)^{\frac{1}{2}} \ .$$

Such a disk is mathematically pleasing, but there is nothing to say about its physical likelihood. Indeed, we find that a slightly unbalanced disk of this type rapidly evolves to something quite different (figure 2) with a less tapered outer edge. So long as this disk is balanced, though, it remains stable (always looking like the first frame of figure 2) indefinitely. [In this and all susequent figures, a disk is shown from the point of view of a rotating coordinate system fixed with the rotation of the disk at $r = 1$ (approximately half-way through the disk) after 0,5 and 10 rotation preiods. The contours are of constant surface density.]

7. Vortices in Disks

Following the spirit of the stability condition (3.10) locally (but addressing vorticity rather than potential vorticity to simplify matters), we anticipate that there can be stable anticyclones in the disk as long as the total vorticity doesn't change sign:

$$\bar{\zeta} + \zeta_{vortex} > 0 \; .$$

The vortex is introduced by superposition onto the balanced basic state (5.1). Two different types of balanced vortex were used: the two-dimensional vortex patch; and the exponential hump. The two-dimensional patch is also know as the Rankine solution; it is simply the streamfunction inside and outside a patch of a given vorticity which has a matched solution at the vortex boundary.

$$e_{vortex} = \frac{\mu}{2}(\rho_0^2 - \rho^2) \; ,$$

$$e_{external} = -\mu \, \rho_0^2 \, ln\left(\frac{\rho}{\rho_0}\right) \; ,$$

$$v_i = \frac{\partial e_i}{\partial \rho} \; ,$$

then describes a vortex patch with radius ρ_0, vorticity μ and circulation velocity v_i.

A series of numerical experiments were run for a wide range of vortex strengths, sizes and positions using the two-dimensional vortex streamfunction to serve as its enthalpy field in the disk. Since enthalpy plays the role of pressure, this produces geostrophically balanced vortices. The unfortunate conclusion is that the strong far-field properties (the external solution) of the two-dimensional vortex produce a finite amplitude deviation from the basic state that we superimposed the vortex onto. The initial states then, are significantly unbalanced and strong instability develops, initially at the outer edge of the disk where the deviations introduced by the vortex are most in excess. Figure 3 shows the evolution of such a disk.

At the same time that the disk instability begins to grow, the vortex becomes strongly sheared by the basic state, and eventually separated into two tilted vorticity tongues (visible in the last frame). Closer examination of these tongues reveals that the vorticity of the initial vortex has been squeezed from a patch into a ring, although the ring has also been sheared in two. Ring-like vortices are known to arise as solutions of the two-dimensional vortex patch problem in the case of small Rossby deformation radius- fast rotation in other words. Keplerian shear is probably better characterized by the scale of its vorticity *gradients* than the scale of the vorticity itself. Still, the deformation radii are small everywhere, so the vortex ring may be the preferred large scale structure on disks. We intend to investigate this in future numerical experiments.

To minimize the far-field contribution of a superimposed vortex, the Rankine solution was replaced by a simple exponential "hump":

$$e_{vortex} = \rho_0 v_0 e^{-\frac{\rho}{\rho_0}}.$$

The outer edge instability incited by the Rankine patch in the previous case is clearly absent now, and the vortex shearing is more evident (figures 4 and 5).

Strong vortices are sheared into pieces that can be followed, and appear to be more robust than their progenitor. If there is an upper limit to the size of a stable vortex in near-Keplerian shear, perhaps we are seeing this scale-selection process at work. Longer model runs are needed to test this. Weaker vortices are more effectively sheared away, but in the process transient spiral mode oscillations are excited within the disk (figure 6).

8. Discussion

The shallow water disk equations are shown to have axisymmetric basic state solutions that have nearly Keplerian velocity profiles. The superposition of large coherent vortices on these basic states in a numerical mode has verifed that the basic state velocity profile is hostile to such Jovianesq "spots" because of the rapid radial variation of the background shear. The evolution of the models shows exactly how vortices are sheared, stretched and bent by the basic states and suggests that smaller vortices, perhaps more ring-like, may persist. But we do not know to what extent these specific cases can be used to generalize, so we cannot say with certainty that a vortex patch will be sheared into something that approximates a maximum-extent steady vortex in near-Keplerian shear and curvature. It is also verified that vortex superposition is an inherently destablizing technique for finding a stable disk with a spot. As we are actually looking for a vortex embedded within another (albeit special) vortex, any steady solution ought to reflect this vortical bi-polarity. The model was also run as a semi-relaxation code in which the material of the disk was allowed to redistribute itself to match the combined flow around both the central object and a nearby large vortex, and in fact, produced just such an asymmetrical disk (figure 7).

The asymmetric equilibration in this case is further indication that a disk-vortex system is too distant a departure from a symmetric basic state. The problem that bears further investigation, then, is the the time-independent basic state solution of a disk with a vortex, perhaps related to the steady solutions of vortex dipoles and modons. In this case, a steady dipolar disk would have approximately Keplerian flow around the central object coupled to opposite flow around a large vortex. The companion vortex must be counter-circulating (anti-cyclonic) if it is to coexist rather than merge with the central object vortex.

Acknowledgments

References

Abarbanel, H.D.I. & Holm, D.D. 1987. **Phys. Fluids 30**, 3369-3382.

Abramowicz, M.A., Lanza, A., Spiegel, E.A. & Szuszkiewicz, E. 1992. **Nature 356**, 41-43.

Arnold, V.I. 1965. **Dokl. Akad. Nauk. SSSR 162**, 975-978.

Dowling, T.E. & Ingersoll, A.P. 1989. **J. Atm. Sci. 46**, 3256-3278.

Dowling, T.E. & Spiegel, E.A. 1991. **Ann. NY Acad. Sci. 617**, 190-216.

Knessel, C. & Keller, J. 1992. to be published in **J. Fluid Mech.**

Lindzen, R.S. & Barker, J.W. 1986. **J. Fluid Mech. 151**, 189-217.

MacLow, M.M. & Ingersoll, A.P. 1986. **Icarus 65**, 353-369.

McWilliams, J.C. 1984. **J. Fluid Mech. 146**, 21-43.

Narayan, R., Goldreich, P. & Goodman, J. 1987. **Mon. Not. R. Astr. Soc. 228**, 1-41.

Pedlosky, J. 1987. **Geophysical Fluid Dynamics**.

Ripa, P. 1991. **J. Fluid Mech. 222**, 119-137.

Shakura, N.I. & Sunyayev, R.A. 1973. **Astron. Astrophys. 24**, 337-

Sommeria, J., Meyers, S.D. & Swinney, H.L. 1988. *Nature* **331**, 689-693.

Sun, S., Bleck, R., & Chassignet, E. 1992. *Preprint*

Takehiro, S.-I. & Hayashi, Y.-Y. 1992. *J. Fluid Mech. 236*, **259-279**.

378
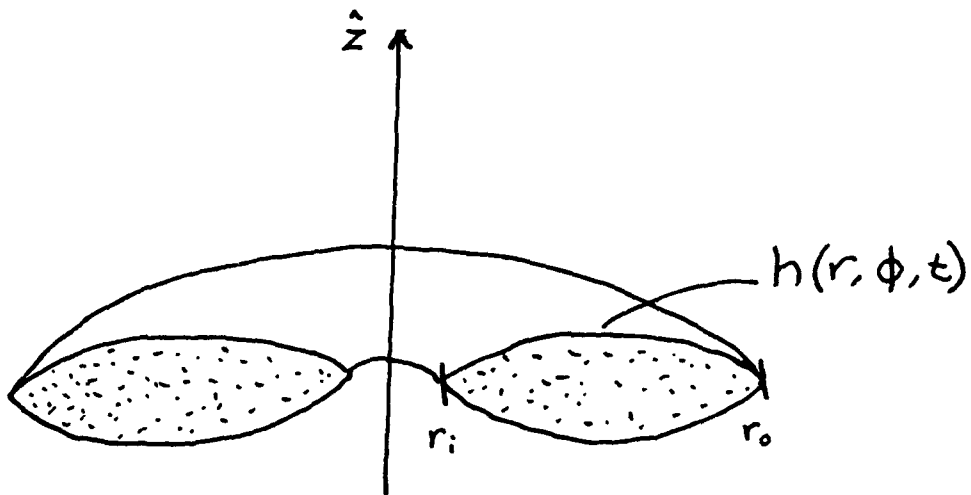
figure 1
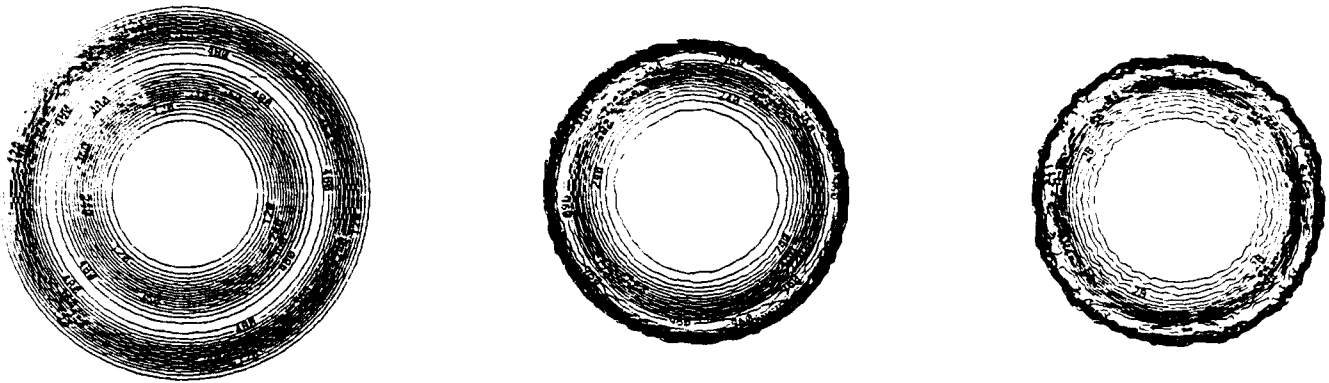schematic of a disk with surfaces $z = h(r, \phi, t)$ and inner and outer edges r_i and r_o

figure 2
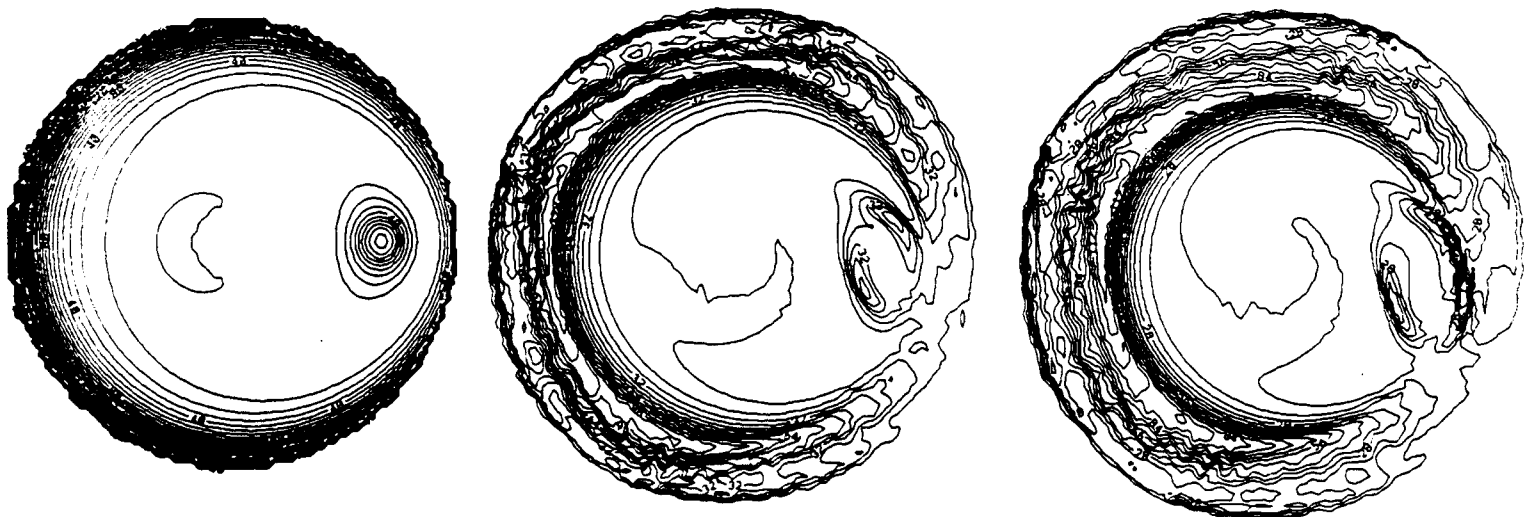equilibration of an unbalanced disk
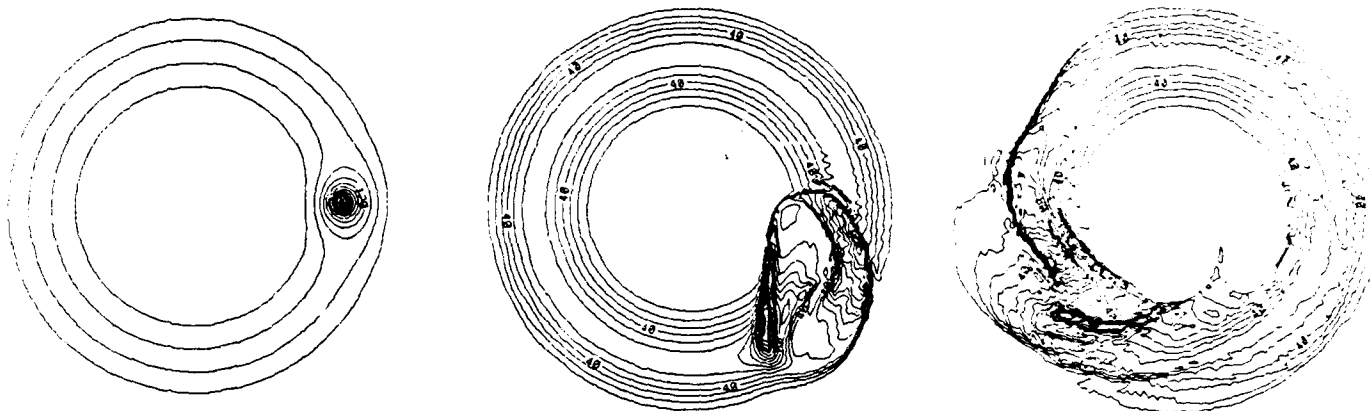

figure 3
evolution of a Rankine patch

figure 4
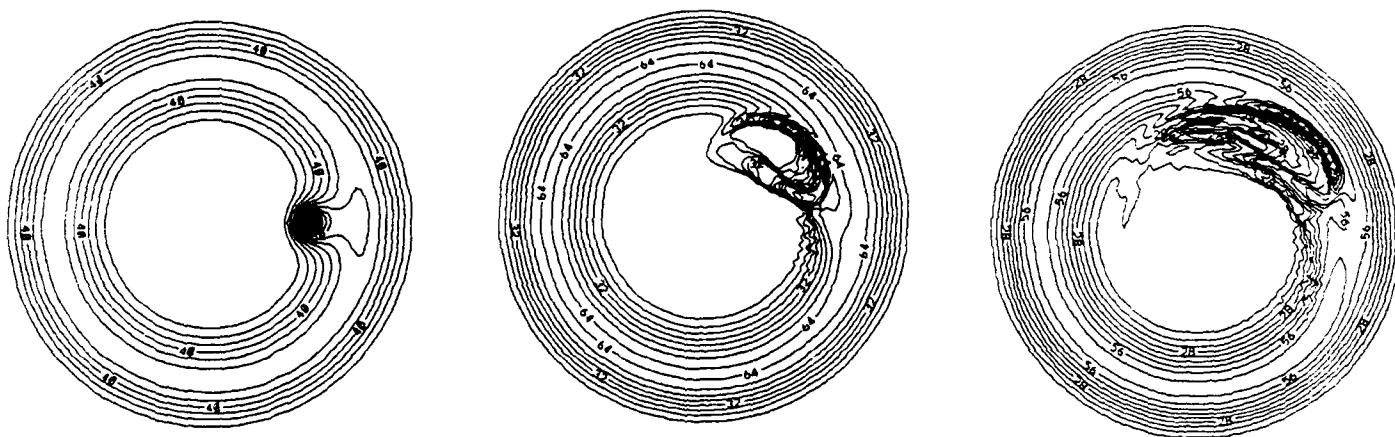exponential vortex at $r = 1\,25$
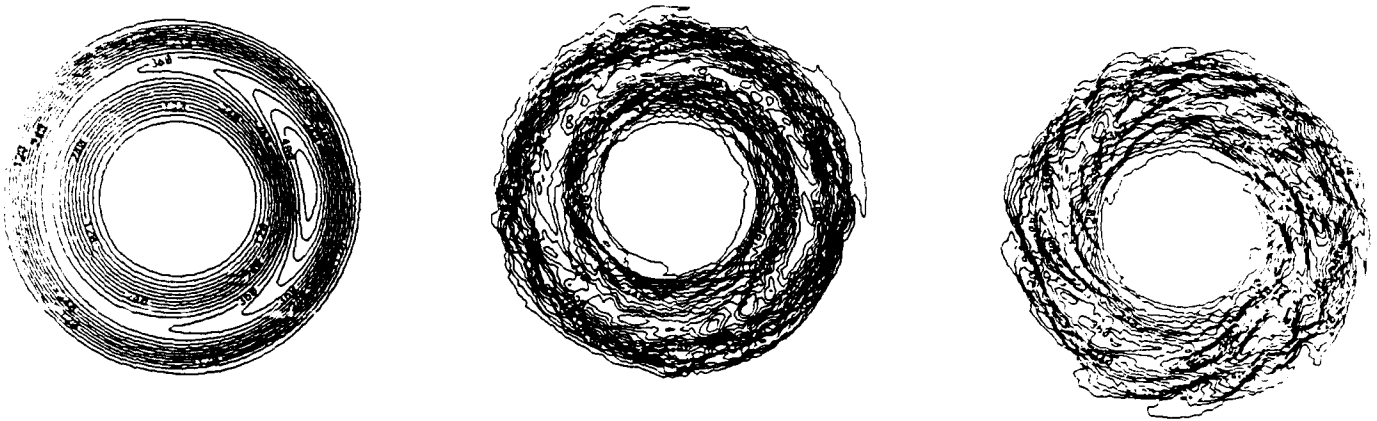

figure 5
exponential vortex at $r = 0.5$

figure 6
weak expoential vortex at $r = 1$

figure 7
material relaxation dipole

Shear Flow Instability Near Froude Number One
-Theory and Experiment

Qingping Zou

Scripps Institute of Oceanography, La Jolla, CA 92093.

"When the stream is narrow the waves which diverge from the opposite banks meet and cross in the middle , where the resulting , stationary mounds of water are sometimes higher than either component, even at the place of origin by the bank."
From oceanwaves by V. Cornish (1934)

Abstract

The linear parallel shear flow instabilty in water of finite depth is addressed theoretically and experimentally. Following Howard (1964), the semi-circle theorem is rederived for this problem. To obtain an explicit dispersion formula, we introduce the matched asymptotic expansion method (MAEM). As an essential supplement to Satomura (1981), the neutral curve F_r vs k is obtained numerically by the Newton-Raphson-Kavantochi method for intermediate k and extended to $k \ll 1$ and $k \gg 1$ analytically by MAEM, and it is shown that $F_r \gg 1$ and $F_r \gg 2$ are the sufficient conditions for instabilty in Satomura's case I and case II. The vertical structure enters the problem in the second-order equations. From the solvability condition of these equations, we derive the second-order correction to the phase speed . This might explain the existence of the stationary unstable mode in the experiment. The case of single wall is simulated by a two layer flow in a rotating cylindrical tank. The experimental results show that the critical Froude number is located within 0.75 ± 0.25 and suggest that the shallow water theory is not applicable here.

1   Introduction

Problems of large Froude number have been of limited interest for oceanographers and geophysicists. However, it has been found that this Froude number can be rather large in some stratified geophysical fluids.In addition, the shear flow instability due to velocity divergence could be essential to understand the atmosphere of the earth as well as the outer planets (Matsuda, 1980). To separate the inflection point instability from the divergence one, Satomura examined the linear shear flow instability in shallow water. His results were further interpreted by Shin-ichi and Hayashi (1992) in regard to the over–reflection effect. In 1984, Narajan applied Satomura's theory to differentially rotating systems such as disc galaxies, etc.; moreover , he defined a conserved action that has opposite signs on the two sides of the "co-rotation radius", where wave is stationary relative to the local fluid. Lindzen and Barker pointed out that the wave over–reflection is necessary in order to obtain normal mode instability in a plane parallel shear flow and that over–reflection is the essential mechanism for both inviscid and viscous problems.

Nevertheless, all these theories are based on the shallow water theory which is not necessarily valid in our case. Actually, the shallow water theory results in the semi-circle theory prohibiting the stationary unstable modes , moreover, the vertical shear may interact with the gravity waves and destabilize them. To derive the first order correction from this effect, we assumed small aspect ratio $\delta = \frac{H}{L} \ll 1$ and then asymptotically expanded the equations and boundary conditions about δ^2. The second-order correction to the phase speed is derived from the solvability condition of the second order equations.

In § 2, the experimental setup and method are discussed and the results are compared with the theory. In § 3, we derive the eigenvalue equation of the along stream velocity u, the MAEM solutions and finally we extend the theory by including small vertical variations.

2   Experiment

2.1   Gutter Wave in a Sloping Channel

In 1934, V.Cornish described in his book *oceanwaves* about the stationary wave in the middle of a narrow stream. During a rainy day, one who's as observant as Melvin Stern may also see these stationary waves in a narrow inclined gutter. If one looks further down stream, he will probably find roll waves travelling forward.

The gutter wave experiment was conducted in an inclined channel shown in Figure 1. The upper end of the channel was connected to a reservoir and the lower end to a sink. We kept the free surface of the reservoir about 1 cm above the bottom of the channel by controlling the flow entering it. After that, we observed waves diverging diagonally from the walls , interfering in the middle and forming herring-bone like stationary patterns that covered most of the channel. These regular stationary patterns extended all the way down stream to the sink. The typical water depth was about 6 mm, the wavelength was estimated at about 4 mm and the velocity at about 40 cm/s. Therefore, the Froude number F_r was about 5 to 7. One may argue that these are just ship waves. Nevertheless, if one dips his finger into the running water, he will find the ship waves fade away within a couple centimeters, in addition, there was no distkurbing source on the wall. Even there was one, it could not have generated the very regular pattern we saw. So what is the mechanism producing these stationary waves? Maybe the shear flow instability .

One may note that some other factors such as the capillary effect and the bottom viscous effect also entered the problem and complicated the physics. Besides, this experiment made it hard to obtain small Froude number which is important to find the critical Froude number for instability. To avoid these disadvantages, we designed another experiment described in the following section.

2.2   Gutter Waves in a Rotating Cylindrical Tank

2.2.1   Experiment Method

The second experiment was carried out in a cylindrical tank of 22 cm in radius and 40 cm in depth (c.f. Fig 2) on a turntable. The tank was filled with salt water up to 20 to 30 cm. The intrusive fresh water was very gently introduced through a sponge inserted in a block of foam floating on the surface of the salt water. We used the shadowgraph technique in our measurements: a beam of parallel light shone down on the tank. Video records of the shadows of the interfacial waves at the bottom were taken with a 35 mm video camera mounted about 30 cm above the edge of

384

the tank. The waves of interest were produced on the interface between layers as the tank spun up from rest. The rate of rotation was measured by counting the time interval for 5 cycles. Data were obtained by reviewing the videotape : the wavelength λ, the oblique angle of the wave crest relative to the wall θ, the extent of the wave pattern in the radial direction W and the lasting time of the regular stationary pattern T_l. The length measurement was calibrated by comparison with a 6 cm tapes near the bottom of the tank. The measurement data are estimated to be within ± 15 percent.

After each run, the top layer of fresh water was siphoned out. Some salt was added to the maintain the density of the salt water and the new mixture was stirred throughly before introducing a new layer of fresh water..

2.2.2 Results and Dicussions

The summary of the wave characteristics and the results from 23 experiments are given in table 1 through 4 where H_1 is the upper layer depth, H_2 the lower layer depth, $H_e = \frac{H_1 H_2}{H_1 + H_2}$ the effective depth, ρ_s the density of the salt water, V the rotating velocity. Fig 3a to Fig 3e show the sequence of snapshots of the wave behaviour in the experiment 8 in table1. Fig 4 illustrates the relation between T_l, λ, W and F_r of Table1 to Table4. From Fig 4b, we can derive the empirical relation of $\frac{\lambda}{H}$ vs F_r from the least square fit as:

$$\frac{\lambda}{H} = 2.1 F_r ,$$

therefore,

$$F_r \propto k^{-1}$$

which is analogous to the theoretical results (c.f equation (49) in §.3.4).

From both Table1 to 4 and Fig 4, we observe that the measured data not only depend on the F_r but also on the effective depth H_e. This result strongly suggests that shallow water theory is not valid here. Following Table 3, we can estimate the critical Froude number for the instability at 0.75 ± 0.25. It is also worthwhile to mention that the wave appeared about 0.5 s to 1 s after the turntable started. According to E. H. Wedemeyer (1964), the spin-up time is

$$T_s = \frac{R_e^{\frac{1}{2}} T}{0.443 \left(\frac{2R}{h}\right) 2\pi}$$

where T, R, h, and R_e are the rotating period, the radius of the tank, the depth of the water and the Reynolds number respectively. The typical value of T_s in our experiment was about 40 s. Therefore for the first 10 s, we can neglect the rotating effect as well as the Kelvin-Helmhotz instability caused by the vertical shear. As shown in Fig 3, waves formed near the wall with crests almost perpendicular to it, extended rapidly toward the centre , the wave crests became oblique relative to the wall. As the patterns developed further, it became distorted and turbulent motion grew outward from the wall, coexisting with the regular wave patterns in the middle of the tank; finally the radial wave re-appeared and the fluid went back to regular motion.

For large Froude number, we observed intermittent behaviour of the wave pattern, namely, it appeared, was replaced by the turbulent motion , and then reappeared again for a short time and so on. One of the most spectcular characteristics of the wave we observed is its stationariness with the wall. This was conflict with what the semi-circle theorem predicts As a matter of fact,

the wavelengths in the experiments were the same order as the depth, moreover, the thickness of the shear layer next to the wall was about a couple millimeters, which was much smaller than the depth and the wavelength. Besides, the variation structure within the shear layer will decrease the estimated $R_e \sim 200$ to $R_e \sim 50$ or so. Accordingly, the viscous effect was more important than we expected. Also, the thickness of the thermocline h_T between the two layer varied at each run. That might cause the real Froude number to be larger than the one we calculated.

3 Theoretical background

3.1 Shallow Water Theory

We consider the stability of a parallel plane flow $\overline{u(y)}$ along the x-axis in shallow water. It is advantageous to use dimensionless variables. The scales are

$$(x, y) \;\longrightarrow\; (x, y)/L, \qquad t \;\longrightarrow\; tU_o/L,$$

$$\overline{u} \;\longrightarrow\; \overline{u}/U_o, \qquad (u, v) \;\longrightarrow\; (u, v)/U_o, \qquad (1)$$

$$h \;\longrightarrow\; h/H,$$

where (u, v) is the infinitesimal disturbance in the (x, y) directions, h the free surface displacement, L the horizontal variation length scale for the mean flow, U_o, the velocity scale of the mean flow and H, the depth of the water. The normalized linear equations in the ideal shallow water are

$$\left(\frac{\partial}{\partial t} + \overline{u}\frac{\partial}{\partial x}\right)u + v\frac{d\overline{u}}{dy} \;=\; -\frac{1}{F_r^2}\frac{\partial h}{\partial x}, \qquad (2)$$

$$\left(\frac{\partial}{\partial t} + \overline{u}\frac{\partial}{\partial x}\right)v \;=\; -\frac{1}{F_r^2}\frac{\partial h}{\partial y}, \qquad (3)$$

$$\left(\frac{\partial}{\partial t} + \overline{u}\frac{\partial}{\partial x}\right)h + \frac{\partial u}{\partial x} + \frac{\partial v}{\partial y} \;=\; 0, \qquad (4)$$

where $F_r = \frac{U_0}{\sqrt{gH}}$ is the Froude number. We assume the variables in the above equations take the form of an infinitesimal wave along the x-axis:

$$\begin{pmatrix} u \\ v \\ h \end{pmatrix} = \begin{pmatrix} u(y) \\ v(y) \\ h(y) \end{pmatrix} e^{i(kx - ct)}. \qquad (5)$$

The corresponding reduction of (2) and (4) yields

$$ik(\overline{u} - c)u + v\frac{d\overline{u}}{dy} \;=\; \frac{-1}{F_r^2}ikh, \qquad (6)$$

$$ik(\overline{u} - c)v \;=\; \frac{-1}{F_r^2}h_y, \qquad (7)$$

$$ik(\overline{u} - c)h + iku + v_y \;=\; 0. \qquad (8)$$

The combination of the equations (6) to (8) gives us the potential vorticity conservation equation:

$$u_y - ikv - \frac{d\bar{u}}{dy}h = 0.$$ (9)

By manipulating the equations (6), (7) and (9), we derive the eigenvalue equation for u:

$$\frac{d^2}{dy^2}u + k^2[F_r^2(\bar{u} - c)^2 - 1]u = 0.$$ (10)

Assuming the B.C at $y = a$ and $y = b$ are

$$u = \begin{cases} C_a\, u_y & (y = a), \\ C_b\, u_y & (y = b), \end{cases}$$ (11)

where C_a and C_b are constants, C_a, $C_b = 0$ corresponds to no-slip condition, and $C_a = \frac{-1}{F_r^2(a-c)}$, $C_b = \frac{-1}{F_r^2(b-c)}$ no normal flow at the boundary. For linear shear flow where $\bar{u} = y$, the equation (10) can be transformed into a parabolic cylindrical equation which has solutions in expansion forms. Nevertheless, we will use the MAEM in § 3.2 to derive the explicit dispersion equations.N

Following Howard (1964), we multiply the above equation with u^*, the conjugate of u, and intrgrate from boundary $y = a$ to $y = b$, then we have

$$-\int |u_y|^2 dy + k^2 \left\{ F_r^2 \left[\bar{u}^2 - 2c_r\bar{u} + c_r^2 - c_i^2 \right] - 1 \right\} \int |u|^2\, dy = 0,$$ (12)

$$c_i \int (\bar{u} - c_r)\,|u|^2\, dy = 0,$$ (13)

where c_r and c_i are the real and imaginary part of c. Making use of the (12) and (13), we have

$$0 \geq \int (\bar{u} - \bar{u}_{min})(\bar{u} - \bar{u}_{max})\,|u|^2\, dy$$ (14)

$$= \int \bar{u}^2\,|u|^2\, dy - (\bar{u}_{min} + \bar{u}_{max}) \int \bar{u}\,|u|^2\, dy + \bar{u}_{min}\bar{u}_{max} \int |u|^2 dy$$

$$= [2c_r - (\bar{u}_{min} + \bar{u}_{max})] \int \bar{u}\,|u|^2\, dy + (-c_r^2 + c_i^2 - \bar{u}_{min}\bar{u}_{max}) \int |u|^2 dy$$

$$= \left[\left(c_r - \frac{\bar{u}_{max} + \bar{u}_{min}}{2} \right)^2 + c_i^2 - \left(\frac{\bar{u}_{max} - \bar{u}_{min}}{2} \right)^2 \right] \int |u|^2 dy + \frac{1}{k^2 F_r^2} \int |u_y|^2 dy,$$

Accordingly,

$$\left(c_r - \frac{\bar{u}_{max} + \bar{u}_{min}}{2} \right)^2 + c_i^2 \leq \left(\frac{\bar{u}_{max} - \bar{u}_{min}}{2} \right)^2.$$ (15)

Thus, the complex phase speed c of the unstable mode must lie within the semi-circle in the upper half-plane which has the range of the mean velocity as the diameter. Stationary unstable modes are therefore impossible.

3.2 Matched Asymptotic Expansion Method (MAEM)

We consider the following equation

$$\frac{d^2u}{dy^2} - \kappa(y)u = 0. \qquad (16)$$

Suppose that $\kappa(y)$ has zeros at $y = y_-$ and $y = y_+$ with a maximum in between and

$$|\kappa'(y)| << |\kappa(y)|^{\frac{1}{2}}$$

holds everywhere except in the neighbourhood of the turning points. By MAEM, the solutions to this equation can be written as

(1) $y << y_-$

$$u(y) = 2\alpha\,(-\kappa(y))^{-\frac{1}{4}}\cos(\int_y^{y_-}(-\kappa(y))^{\frac{1}{2}}dy - \frac{\pi}{4}) + \beta\tau\,(-\kappa(y))^{-\frac{1}{4}}\cos(\int_y^{y_-}(-\kappa(y))^{\frac{1}{2}}dy + \frac{\pi}{4}), \qquad (17)$$

(2) $|y - y_-| << |\kappa'(y_-)|^{-\frac{1}{3}}$

$$u(y) = 2\alpha\sqrt{\pi}\kappa'(y_-)^{-\frac{1}{6}}A_i\left[\kappa'(y_-)^{\frac{1}{3}}(y - y_-)\right] + \beta\tau\sqrt{\pi}\kappa'(y_-)^{-\frac{1}{6}}B_i\left[\kappa'(y_-)^{\frac{1}{3}}(y - y_-)\right], \qquad (18)$$

(3) $y_- << y << y_+$

$$u(y) = \alpha\,(\kappa(y))^{-\frac{1}{4}}e^{-\int_{y_-}^y(\kappa(y))^{\frac{1}{2}}dy} + \beta\,(\kappa(y))^{-\frac{1}{4}}e^{-\int_y^{y_+}(\kappa(y))^{\frac{1}{2}}dy}, \qquad (19)$$

(4) $|y - y_+| << |\kappa'(y_+)|^{-\frac{1}{3}}$

$$u(y) = \alpha\tau\sqrt{\pi}\,(-\kappa'(y_+))^{-\frac{1}{6}}B_i\left[\kappa'(y_+)^{\frac{1}{3}}(y - y_+)\right] + 2\beta\sqrt{\pi}\,(-\kappa'(y_+))^{-\frac{1}{6}}A_i\left[\kappa'(y_+)^{\frac{1}{3}}(y - y_+)\right], \qquad (20)$$

(5) $y >> y_+$

$$u(y) = \alpha\tau\,(-\kappa(y))^{-\frac{1}{4}}\cos(\int_{y_+}^y(-\kappa(y))^{\frac{1}{2}}dy + \frac{\pi}{4}) + 2\beta\,(-\kappa(y))^{-\frac{1}{4}}\cos(\int_{y_+}^y(-\kappa(y))^{\frac{1}{2}}dy - \frac{\pi}{4}), \qquad (21)$$

where

$$\tau = e^{\int_{y_-}^{y_+}(\kappa(y))^{\frac{1}{2}}dy}.$$

In the following sections, we will apply these solutions to some specific problems.

388

3.3 Case I Two Walls (c.f Fig. 5a)

The boundary conditions in this case correspond to no normal flow at the walls:

$$u_y + F_r^2 (y - c) u = 0 \begin{cases} y = 1 \\ y = -1 \end{cases} \tag{22}$$

Let's go back to our original equation (10). The corresponding $\kappa(y)$, y_+ and y_- are:

$$\kappa(y) = -k^2 \left[F_r^2 (y - c)^2 - 1 \right], \tag{23}$$

$$y_+ = c + \frac{1}{F_r}, \tag{24}$$

$$y_- = c - \frac{1}{F_r}. \tag{25}$$

The condition for valid MAEM becomes

$$k \gg \frac{2F_r^2(y - c)}{[F_r^2(y - c)^2]^{\frac{3}{2}}} \propto O(\frac{1}{F_r})$$

Also, we have

$$\kappa'(y_-) = -\kappa'(y_+) = 2k^2 F_r$$

We note that the equation (10) and B.C (22) are symmetric under the transformation $(c, y) \rightarrow (-c, -y)$, therefore, the eigenvalue is symmetric about $c = 0$, that is

$$k^2(\delta c, F_r) = k^2(-\delta c, F_r)$$

Let's expand the L.H.S and R.H.S of the above equation around $c = 0$:

$$k^2(\delta c, F_r) = k^2(0, F_r) + \left. \frac{\partial (k^2)}{\partial c} \right|_{c=0} \delta c + \left. \frac{\partial^2 (k^2)}{\partial^2 c} \right|_{c=0} \delta c^2 + \cdots \tag{26}$$

$$k^2(-\delta c, F_r) = k^2(0, F_r) - \left. \frac{\partial (k^2)}{\partial c} \right|_{c=0} \delta c + \left. \frac{\partial^2 (k^2)}{\partial^2 c} \right|_{c=0} \delta c^2 + \cdots \tag{27}$$

as $\delta c \rightarrow 0$, the R.H.S of the above two equations equal each other, which gives us

$$\left. \frac{\partial (k^2)}{\partial c} \right|_{c=0} = 0. \tag{28}$$

It follows from (28) that

$$\delta c = \left[\frac{k^2(-\delta c, F_r) - k^2(0, F_r)}{\left. \frac{\partial^2 (k^2)}{\partial c^2} \right|_{c=0}} \right]^{\frac{1}{2}}. \tag{29}$$

The $\left. \frac{\partial^2 (k^2)}{\partial c^2} \right|_{c=0}$ has fixed sign, therefore , the bracketed part has opposite sign,while c is either imaginary or real number, on the either side of the neutral curve $k^2(0, F_r)$. On the other hand, for $c = 0$, $u(-y) = u(y)$, hence,

$$u(0) = 0 \tag{30}$$

From (24) and (25), we have,

$$y_+ = -y_- = \frac{1}{F_r} \tag{31}$$

Plugging (19) into (30) provides $\alpha = \beta$.

Case a) $F_r \approx 1$

According to (31),

$$y = 1 \rightarrow y_+$$

holds here. we can apply (20) to the B.C (22) at $y = 1$. By further assumption $\tau \ll 1$, we get

$$A_i'(z)\kappa'(y_+)^{\frac{1}{3}} + F_r^2 A_i(z) = 0, \tag{32}$$

where

$$z = \kappa'(y_+)^{\frac{1}{3}}(y - y_+). \tag{33}$$

The above equation can be rewritten as

$$A_i'(z) = -\frac{F_r^2}{(2k^2 F_r)^{\frac{1}{3}}} A_i(z) = O(k^{-\frac{2}{3}}) \approx 0 \tag{34}$$

Therefore

$$z = -1 \qquad at \ y = 1 \tag{35}$$

which compared with (33), we find

$$F_r = 1 + \left(2k^2\right)^{-\frac{1}{3}} \tag{36}$$

Case b) $F_r \gg 1$

Because $y = 1 \gg y_+$ here, the combination of the (21) and (22) gives

$$\tan\left\{ \int_{y_+}^{1} (-\kappa(y))^{\frac{1}{2}} \, dy - \frac{\pi}{4} \right\} = \frac{\frac{1}{4}(-\kappa(1))^{-1} \kappa'(1) + F_r^2}{(-\kappa(1))^{\frac{1}{2}}} = O(F_r^2) \gg 1, \tag{37}$$

therefore

$$\int_{y_+}^{1} (-\kappa(y))^{\frac{1}{2}} \, dy - \frac{\pi}{4} = (2n + 1)\frac{\pi}{2} \qquad (n = 0, 1, 2, 3 \cdots). \tag{38}$$

We combine the above equation with

$$\int_{y_+}^{1} (-\kappa(y))^{\frac{1}{2}} \, dy = \int_{\frac{1}{F_r}}^{1} k \left[F_r^2 y^2 - 1 \right]^{\frac{1}{2}} dy \approx \frac{kF_r}{2}(1 - \frac{1}{F_r^2}) \approx \frac{kF_r}{2} \tag{39}$$

and obtain

$$F_r = (2n + \frac{3}{2})\pi k^{-1} \tag{40}$$

390

For the first mode $n = 0$, we have

$$F_r = \frac{3}{2}\pi k^{-1} \tag{41}$$

Please refer to Appendix A for Case c) $c \neq o$. By Newton-Raphson-Kavantochi method, the neutral curve F_r vs k is also calculated numerically from the original equation (10) and the boundary condition (22). Fig 6 illustrates the comparison of this result with the analytical asymptotical bahaviour by (36), (41) and Satomura's. We can see that they coincide with each other very well.

3.4 Case II Single wall (c.f Fig. 5b)

In region $y \leq 0$, the equation changes to

$$u_{yy} + k^2 \left(F_r^2 c^2 - 1 \right) u = 0 \tag{42}$$

Physically as $y \to -\infty$, u should be finite and the wave can only propagate in the opposite y-axis direction, in other words

$$u = const \cdot e^{\tilde{\kappa} y}, \tag{43}$$

where

$$\tilde{\kappa} = \kappa(0) = \begin{cases} -ik\sqrt{F_r^2 c^2 - 1} & c \geq \frac{1}{F_r} \\ k\sqrt{1 - F_r^2 c^2} & c \leq \frac{1}{F_r} \end{cases} \tag{44}$$

The variables v and h should be continuous across the interface $y = 0$ of the rest fluid and the shear flow. Therefore, we have

$$u(0^+) = u(0^-), \tag{45}$$

$$u_y(0^+) = u_y(0^-). \tag{46}$$

From (43), we get

$$u_y(0^-) = \begin{cases} -ik\sqrt{F_r^2 c^2 - 1}\,u(0^-) & c \geq \frac{1}{F_r} \\ k\sqrt{1 - F_r^2 c^2}\,u(0^-) & c \leq \frac{1}{F_r} \end{cases} \tag{47}$$

Combining (47) with (45) and (46), we have

$$u_y(0^+) = \begin{cases} -ik\sqrt{F_r^2 c^2 - 1}\,u(0^+) & c \geq \frac{1}{F_r} \\ k\sqrt{1 - F_r^2 c^2}\,u(0^+) & c \leq \frac{1}{F_r} \end{cases} \tag{48}$$

Please see Appendix B for further details.

According to (113), the imaginary part of the phase speed is nonzero for $c \leq \frac{1}{F_r}$, therefore by using similiar approximation to case a) and case b) in the last subsection, we derive the following asymtotic behaviour of the neutral curve:

$$F_r = \frac{3}{2}\pi k^{-1} \qquad \text{for } F_r \gg 1 \tag{49}$$

$$F_r = 2 + \left(\frac{2}{k^2} \right)^{\frac{1}{3}} \qquad \text{for } F_r \approx 1 \tag{50}$$

Similiar to the last subsection (3.3), the neutral curve F_r vs k is also calculated numerically from the original equation (10) and the boundary condition (45) and (46). Fig 7 shows the comparison of this result with the analytical asymptotical bahaviour by (49)and (50) and with Satomura's result. We note that they coincide with each other very well.

3.5 "Deeper" Water Theory

The general equations for the incompressible nonviscous flow of finite depth is

$$\frac{\partial u}{\partial t} + u\frac{\partial u}{\partial x} + v\frac{\partial u}{\partial y} + w\frac{\partial u}{\partial z} = -p_x, \tag{51}$$

$$\frac{\partial v}{\partial t} + u\frac{\partial v}{\partial x} + v\frac{\partial v}{\partial y} + w\frac{\partial v}{\partial z} = -p_y, \tag{52}$$

$$\frac{\partial w}{\partial t} + u\frac{\partial w}{\partial x} + v\frac{\partial w}{\partial y} + w\frac{\partial w}{\partial z} = -p_z, \tag{53}$$

$$u_x + v_y + w_z = 0. \tag{54}$$

The corresponding boundary conditions at the surface and at the bottom are

$$\left. \begin{array}{rcl} w & = & \frac{\partial h}{\partial t} + u\frac{\partial h}{\partial x} + v\frac{\partial h}{\partial y} \\ p & = & gh \end{array} \right\} z = 1 \tag{55}$$

$$w = 0 \qquad\qquad z = 0 \tag{56}$$

Nondimensionizing the above formula with the following scaling and linearizing it

$$(x, y) \;\longrightarrow\; (Lx, Ly), \quad t \;\longrightarrow\; \frac{L}{U}t,$$

$$h \;\longrightarrow\; hH, \quad z \;\longrightarrow\; zH, \tag{57}$$

$$p \;\longrightarrow\; gHp$$

we have

$$\left(\frac{\partial}{\partial t} + \bar{u}\frac{\partial}{\partial x}\right) u + v\frac{d\bar{u}}{dy} = -\frac{1}{F_r^2}p_x, \tag{58}$$

$$\left(\frac{\partial}{\partial t} + \bar{u}\frac{\partial}{\partial x}\right) v + \bar{u}\frac{\partial v}{\partial x} = -\frac{1}{F_r^2}p_y, \tag{59}$$

$$\delta^2 \left(\frac{\partial}{\partial t} + \bar{u}\frac{\partial}{\partial x}\right) w = -\frac{1}{F_r^2}p_z, \tag{60}$$

and the boundary conditions

$$\left. \begin{array}{rcl} w & = & \left(\frac{\partial}{\partial t} + \bar{u}\frac{\partial}{\partial x}\right) h \\ p & = & h \end{array} \right\} z = 1, \tag{61}$$

$$w = 0 \qquad\qquad z = 0, \tag{62}$$

where the Froude number $F_r = \frac{U}{\sqrt{gh}}$ and aspect ratio $\delta = \frac{H}{L}$. We assume that the variables in the above equation can be written as

$$q(x, y, z, t) = q(y, z)e^{i(kx - ct)}$$

except

$$h(x, y, t) = h(y)e^{i(kx - ct)}$$

and both the amplitude $q(y, z)$ and the phase speed c can be further expanded in the following series:

$$q(y, z) = q^{(o)}(y, z) + \delta^2 q^{(2)}(y, z) + \cdots, \tag{63}$$

$$c = c^{(0)} + \delta^2 c^{(2)} + \cdots. \tag{64}$$

Plugging the above formula back into the equations, linearizing them and separating by the powers of δ^2, at $O(\delta^{(0)})$, we have

$$ik \left(\bar{u} - c^{(0)} \right) u^{(0)} + v^{(0)} \frac{d\bar{u}}{dy} = -\frac{1}{F_r^2} ik p^{(0)}, \tag{65}$$

$$ik \left(\bar{u} - c^{(0)} \right) v^{(0)} = -\frac{1}{F_r^2} p_y^{(0)}, \tag{66}$$

$$p_z^{(0)} = 0, \tag{67}$$

$$iku^{(0)} + v_y^{(0)} + w_z^{(0)} = 0, \tag{68}$$

and B.C

$$\left. \begin{array}{rcl} w^{(0)} & = & (\bar{u} - c^{(0)})ikh^{(0)} \\ p^{(0)} & = & h^{(0)} \end{array} \right\} z = 1, \tag{69}$$

$$w^{(0)} = 0 \qquad z = 0. \tag{70}$$

at $\delta^{(2)}$, we have

$$ik \left(\bar{u} - c^{(0)} \right) u^{(2)} + v^{(2)} \frac{d\bar{u}}{dy} = -\frac{1}{F_r^2} ik p^{(2)} + c^{(2)} iku^{(0)}, \tag{71}$$

$$ik \left(\bar{u} - c^{(0)} \right) v^{(2)} = -\frac{1}{F_r^2} p_y^{(2)} + c^{(2)} ikv^{(0)}, \tag{72}$$

$$ik \left(\bar{u} - c^{(0)} \right) w^{(0)} = -\frac{1}{F_r^2} p_z^{(2)}, \tag{73}$$

$$iku^{(2)} + v_y^{(2)} + w_z^{(2)} = 0, \tag{74}$$

and the B.C

$$\left. \begin{array}{rcl} w^{(2)} & = & (\bar{u} - c^{(0)})ikh^{(2)} - c^{(2)}ikh^{(0)} \\ p^{(2)} & = & h^{(2)} \end{array} \right\} z = 1, \tag{75}$$

$$w^{(2)} = 0 \qquad z = 0. \tag{76}$$

Integrating the (70) from 0 to 1 and using B.C (75) and (76), we derive

$$w^{(0)} = \left(iku^{(0)} + v_y^{(0)} \right) z \tag{77}$$

$$p^{(2)}(z) = h^{(2)} + ikF_r^2 \left(\bar{u} - c^{(0)} \right) \left(iku^{(0)} + v_y^{(0)} \right) \frac{1 - z^2}{2} \tag{78}$$

Integrating equations (71) to (74) from 0 to 1, we get

$$\left(\bar{u} - c^{(0)}\right) ik\tilde{u}^{(2)} + \tilde{v}^{(2)}\frac{du}{dy} = \frac{-ik}{F_r^2}\tilde{p}^{(2)} + c^{(2)}iku^{(0)}, \tag{79}$$

$$\left(\bar{u} - c^{(0)}\right) ik\tilde{v}^{(2)} = \frac{1}{F_r^2}\tilde{p}_y^{(2)} + c^{(2)}ikv^{(0)}, \tag{80}$$

$$ik\tilde{u}^{(2)} + \tilde{v}_y^{(2)} + \left(\bar{u} - c^{(0)}\right) ikh^{(2)} = c^{(2)}ikh^{(0)}. \tag{81}$$

The variables with a tilde denote the vertical integral of that variables. for convenience, we drop the tilde in the context. Consider the mean velocity profile $\bar{u} = y$, The combination of equations (79) to (81) gives us the potential vorticity conservation equation

$$u_y^{(2)} - ikv^{(2)} - h^{(2)} = 0. \tag{82}$$

Compared with (77) to (78), the equations (79) to (80) can be rewritten as

$$\left(\bar{u} - c^{(0)}\right) u^{(2)} + \frac{v^{(2)}}{ik} = \frac{-1}{F_r^2}h^{(2)} + (g^{(0)} + c^{(2)}u^{(0)}), \tag{83}$$

$$\left(\bar{u} - c^{(0)}\right) v^{(2)} = \frac{-1}{F_r^2}h_y^{(2)} + (g_y^{(0)} + c^{(2)}ikv^{(0)}), \tag{84}$$

where

$$g^{(0)} = \frac{-ik}{3}\left(\bar{u} - c^{(0)}\right)\left(iku^{(0)} + v_y^{(0)}\right). \tag{85}$$

Using similiar method to that in the shallow water case, we eliminate the $v^{(2)}$ and $h^{(2)}$ from the above equation and obtain the following ODE for $u^{(2)}$

$$u_{yy}^{(2)} + k^2\left[F_r^2\left(\bar{u} - c^{(0)}\right)^2 - 1\right]u^{(2)} \tag{86}$$

$$= F_r^2\left[k^2\left(\bar{u} - c^{(0)}\right)g^{(0)} + g_y^{(0)}\right] + c^{(2)}\left[F_r^2 k^2\left(\bar{u} - c^{(0)}\right)u^{(0)} + \left(k^2 + F_r^2\right)ikv^{(0)} - k^2 u_y^{(0)}\right].$$

Multiplying the above equation with $u^{(0)}$ and integrating it from boundary $y = a$ to $y = b$, we have

$$\left[u^{(0)}u_y^{(2)} - u_y^{(0)}u^{(2)}\right]_a^b + u^{(2)}\Re u^{(0)} = \int_a^b\left[G_1^{(0)} + c^{(2)}G_2^{(0)}\right]u^{(0)}dy, \tag{87}$$

where

$$\Re = \frac{d^2}{dy^2} + k^2\left[F_r^2\left(\bar{u} - c^{(0)}\right)^2 - 1\right], \tag{88}$$

and

$$G_1^{(0)} = F_r^2\left[k^2\left(\bar{u} - c^{(0)}\right)g^{(0)} + g_y^{(0)}\right], \tag{89}$$

$$G_2^{(0)} = F_r^2 k^2\left(\bar{u} - c^{(0)}\right)u^{(0)} + \left(k^2 + F_r^2\right)ikv^{(0)} - k^2 u_y^{(0)}. \tag{90}$$

The L.H.S of the above equation is zero, hence,

$$c^{(2)} = -\frac{\int\limits_{a}^{b} G_1^{\prime(0)} u^{(0)} dy}{\int\limits_{a}^{b} G_2^{\prime(0)} u^{(0)} dy}. \tag{91}$$

According to the above second order correction of the phase speed, we conclude that semi-circle theorem is not valid here. Therefore, stationary unstable modes may exist in "deeper water".

Appendix A

Case c) $c \neq 0$

Fig 2 indicates that for small Froude number, k is larger, therefore, WKB is good approximation here. We apply (17) and (21) to B.C (22) respectively, which results in

$$\alpha\tau\cos(\theta_+ - \theta_{o1} + \frac{\pi}{4}) + 2\beta\sin(\theta_+ - \theta_{o1} - \frac{\pi}{4}) = 0, \tag{92}$$

$$2\alpha\cos(\theta_- - \theta_{o2} - \frac{\pi}{4}) + \beta\tau\sin(\theta_- - \theta_{o2} + \frac{\pi}{4}) = 0, \tag{93}$$

where

$$\theta_+ = kX^+(y_+(c),c), \tag{94}$$

$$X^+(y_+(c),c) = \int_{y_+}^{1} \sqrt{F_r^2(y-c)^2 - 1}\,dy$$

$$= \frac{F_r}{2}\left[(1-c)\sqrt{(1-c)^2 - \frac{1}{F_r^2}} + \frac{1}{F_r^2}\log\frac{(1-c) + \sqrt{(1-c)^2 - \frac{1}{F_r^2}}}{\frac{1}{F_r}}\right],$$

$$\theta_- = kX^-(y_-(c),c), \tag{95}$$

$$X^-(y_-(c),c) = \int_{-1}^{y_-} \sqrt{F_r^2(y-c)^2 - 1}\,dy \tag{96}$$

$$= \frac{F_r}{2}\left[(1+c)\sqrt{(1+c)^2 - \frac{1}{F_r^2}} + \frac{1}{F_r^2}\log\frac{(1+c) + \sqrt{(1+c)^2 - \frac{1}{F_r^2}}}{\frac{1}{F_r}}\right], \tag{97}$$

$$\tag{98}$$

$$\theta_{o1} = \arctan\left[\frac{k\left(F_r^2(1-c)^2 - 1\right)^{\frac{3}{2}}}{F_r^2(1-c)\left[-\frac{3}{2} + F_r^2(1-c)^2\right]}\right], \tag{99}$$

$$\theta_{o2} = \arctan\left[\frac{k\left(F_r^2(1+c)^2 - 1\right)^{\frac{3}{2}}}{F_r^2(1+c)\left[-\frac{3}{2} + F_r^2(1+c)^2\right]}\right]. \tag{100}$$

To obtain nonzero α and β, the following equation has to be valid

$$\cos(\theta_+ - \theta_{o1} - \frac{\pi}{4})\cos(\theta_- - \theta_{o2} - \frac{\pi}{4}) = \frac{1}{4}\tau^2 sin(\theta_+ - \theta_{o1} - \frac{\pi}{4})sin(\theta_- - \theta_{o2} - \frac{\pi}{4}) \tag{101}$$

Further assuming that $\tau \ll 1$, we derive

$$k_m = \frac{(m + \frac{3}{4})\pi + \theta_{o1}}{X^+(y_+(c),c)} \quad (m = 0, 1, 2, 3, \cdots), \tag{102}$$

$$k_n = \frac{(n + \frac{3}{4})\pi + \theta_{o2}}{X^-(y_-(c),c)} \quad (n = 0, 1, 2, 3, \cdots). \tag{103}$$

We note that according to (99) as $c \to \frac{1}{F_r}$, the denominator of (103) $X^-(y_-(c), c) \to 0$, therefore, $k_n \to \infty$ and from (102), as $c \to 1 - \frac{1}{F_r}$, $X^+(y_+(c), c) \to 0$, hence, $k_m \to \infty$.

The intersections of these two branches of curves are

$$k_{mn} = \frac{\left(m + \frac{3}{4}\right)\pi + \theta_{o1}}{X^+(y_+(c), c)} = \frac{\left(n + \frac{3}{4}\right)\pi + \theta_{o2}}{X^-(y_-(c), c)} \tag{104}$$

Following C.Knessl & J.Keller (1992), we assume

$$k - k_{mn} = \frac{\epsilon}{X^-(y_-(c), c)}, \tag{105}$$

$$c - c_{mn} = \delta \tag{106}$$

Substitution of the above formula into equation (101) leads to

$$\frac{X'^+}{X^-}\frac{X'^-}{X^-}\left[\varepsilon + \frac{k_{mn}X^-}{X'^-}X_c^-\delta\right]\left[\varepsilon + \frac{k_{mn}X^-}{X'^+}X_c^+\delta\right] \tag{107}$$

$$= \frac{1}{4}\exp\{-2k_{mn}X\},$$

$$c - c_{mn} = -\left[\frac{X'^+}{X_c'^+} + \frac{X'^-}{X_c'^-}\right]\frac{\varepsilon}{2k_{mn}X^-} \tag{108}$$

$$\pm\frac{1}{2k_{mn}X^-}\left\{\left(\frac{X'^+}{X_c'^+} + \frac{X'^-}{X_c'^-}\right)^2\varepsilon^2 + \frac{X^+X^-}{X_c'^+X_c'^-}\frac{X^-}{X^+}\exp[-2k_{mn}X]\right\}^{\frac{1}{2}}.$$

where

$$X'^+ = X^+ + \frac{\partial\theta_{o1}}{\partial k}, \tag{109}$$

$$X'^- = X^- + \frac{\partial\theta_{o2}}{\partial k},$$

$$X_c'^+ = X_c^+ + \frac{1}{k}\frac{\partial\theta_{o1}}{\partial c},$$

$$X_c'^- = X_c^- + \frac{1}{k}\frac{\partial\theta_{o2}}{\partial c}.$$

$$X = \int_{y^-}^{y_+}\sqrt{F_r^2(y - c)^2 - 1}\,dy$$

The critical value of k where c becomes complex is the k where the last term of the above formula vanishes, namely,

$$k - k_{mn} = \frac{\pm 1}{X^-}\left|\frac{X'^+}{X_c'^+} + \frac{X'^-}{X_c'^-}\right|^{-1}\left[-\frac{X^+X^-}{X_c'^+X_c'^-}\frac{X^-}{X^+}\right]^{\frac{1}{2}} \tag{110}$$

$$\exp\{-k_{mn}X\}$$

The maximum growth rate occurs at $\epsilon = 0$:

$$c_{imn} = \frac{1}{2k_{mn}} \left\{ \frac{1}{X_c'^+ X_c'^-} \exp\left[-2k_{mn}X\right] \right\}^{\frac{1}{2}} \tag{111}$$

Fig 8 shows the caculated dispersion curves from (102), they are symmetric about the line $c_r = 0$ as we expected from the symmetry of the model.

Appendix B

Case a) $\quad c \geq \frac{1}{F_r}$

We assume that $y = 0 \ll y_-$ and $y = 1 \gg y_+$ holds here and substitute (17) into B.C (48), which leads to

$$2\alpha \left\{ \left[\frac{1}{4} (-\kappa(0))^{-1} \kappa'(0) + ik\sqrt{F_r^2 c^2 - 1} \right] \cos\left(\theta_o - \frac{\pi}{4} \right) + (-\kappa(0))^{\frac{1}{2}} \sin\left(\theta_o - \frac{\pi}{4} \right) \right\} \quad (112)$$

$$+\beta\tau \left\{ \left[\frac{1}{4} (-\kappa(0))^{-1} \kappa'(0) + ik\sqrt{F_r^2 c^2 - 1} \right] \cos\left(\theta_o + \frac{\pi}{4} \right) + (-\kappa(0))^{\frac{1}{2}} \sin\left(\theta_o + \frac{\pi}{4} \right) \right\} = 0$$

Equation (92) is still valid here. Combination of these two equations gives us

$$\cos(\theta_+ - \theta_{o1} - \frac{\pi}{4}) \left\{ \cos(\theta_o - \theta' - \frac{\pi}{4}) + ik\sqrt{F_r^2 c^2 - 1} \cos(\theta_o - \frac{\pi}{4}) \right\} \quad (113)$$

$$= \frac{1}{4}\tau^2 \sin\left(\theta_+ - \theta_{o1} - \frac{\pi}{4} \right) \sin\left(\theta_o - \theta' - \frac{\pi}{4} \right)$$

where

$$\theta' = \arctan\left[\frac{4(-\kappa(0))^{-\frac{1}{2}}}{(-\kappa(0))^{-1} \kappa'(0)} \right] \quad (114)$$

$$\theta_o = k \int_0^{y_-} \sqrt{F_r^2(y - c)^2 - 1}\, dy \quad (115)$$

Case b) $\quad c \leq \frac{1}{F_+}$

In this case ,we assume that $y_- \ll y = 0 \ll y_+$ and substitute (19) into the B.C (48), we get

$$\left(\frac{\kappa'(0)\kappa(0)^{-\frac{3}{2}}}{4} + 2 \right) \alpha + \frac{\kappa'(0)\kappa(0)^{-\frac{3}{2}}}{4}\beta\tau e^{2\theta} = 0 \quad (116)$$

where

$$\theta = \int_{y_-}^0 (\kappa(y))^{\frac{1}{2}}\, dy \quad (117)$$

From (116) and (92), we obtain

$$\kappa'(0)\kappa(0)^{-\frac{3}{2}}\tau^2 e^{2\theta} \cos\left(\theta_+(1) - \theta_o + \frac{\pi}{4} \right) = \quad (118)$$

$$2\left(\kappa'(0)\kappa(0)^{-\frac{3}{2}} + 8 \right) \cos\left(\theta_+(1) - \theta_o - \frac{\pi}{4} \right)$$

By ommitting the L.H.S of the above formula, we get

$$\theta_+(1) - \theta_o + \frac{\pi}{4} = \frac{2n + 1}{2}\pi \quad (119)$$

Acknowledgement

References

Howard, L. N., 1961. Note on a paper of John W. Miles, *J. Fluid Mech.*, **10**, 509–512.

Knessl, C. and Keller, J., 1992. Stability of rotating shear flows in shallow water. *J. Fluid Mech.*, in press.

Lindzen, R. S. and Barker, J. W. 1985. Instability and wave over-reflection in stably stratified shear flow. *J. Fluid Mech.*, **151**, 189–217.

Matsuda, Y., 1980. Dynamics of the four-day circulation in the Venus atmosphere. *J. Meteor. Soc. Japan*, **58**, 443–470.

Narayan, R., Goldreich, P and Goodman, J. 1987. Physics of modes in a differentially rotating system-analysis of the shearing sheet. *Mon. Not. R. Astr. Soc.*, **228**, 1–41.

Satomura T., 1981. An investigation of shear instability in a shallow water. *J. Met. Soc. Japan*, **59**, 148–167.

Takehiro, S. and Hayashi, Y., 1992. Over-reflection and shear instability in a shallow-water model. *J. Fluid Mech.*, **236**, 259–279.

Wedemeyer, E.H, 1964. The unsteady flow within a spinning cylinder. *J. Fluid Mech*, **20**, 383–399.
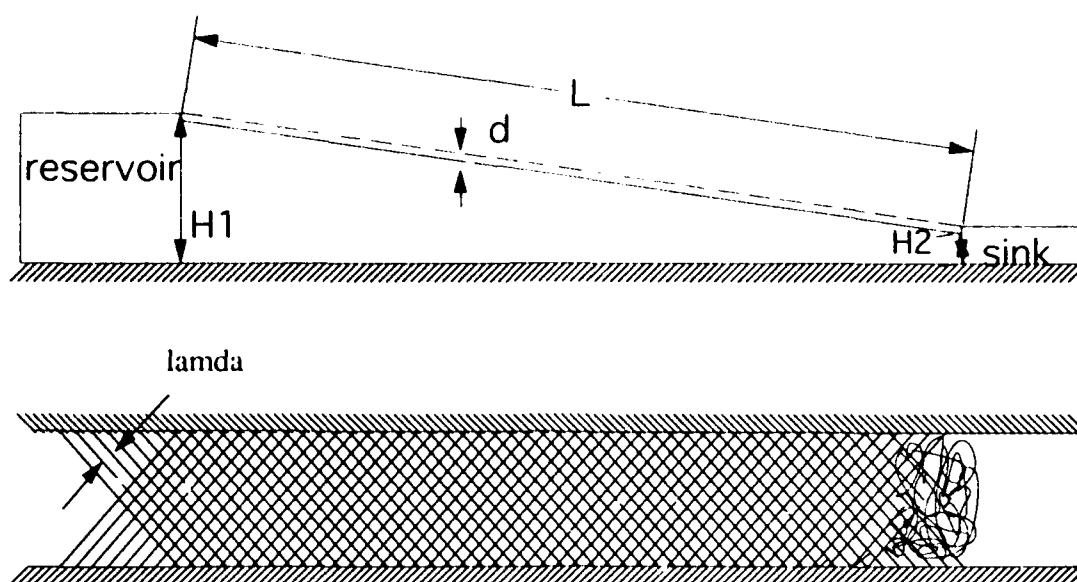
Fig.1 Experimental set-up of gutter wave in a sloping channel.
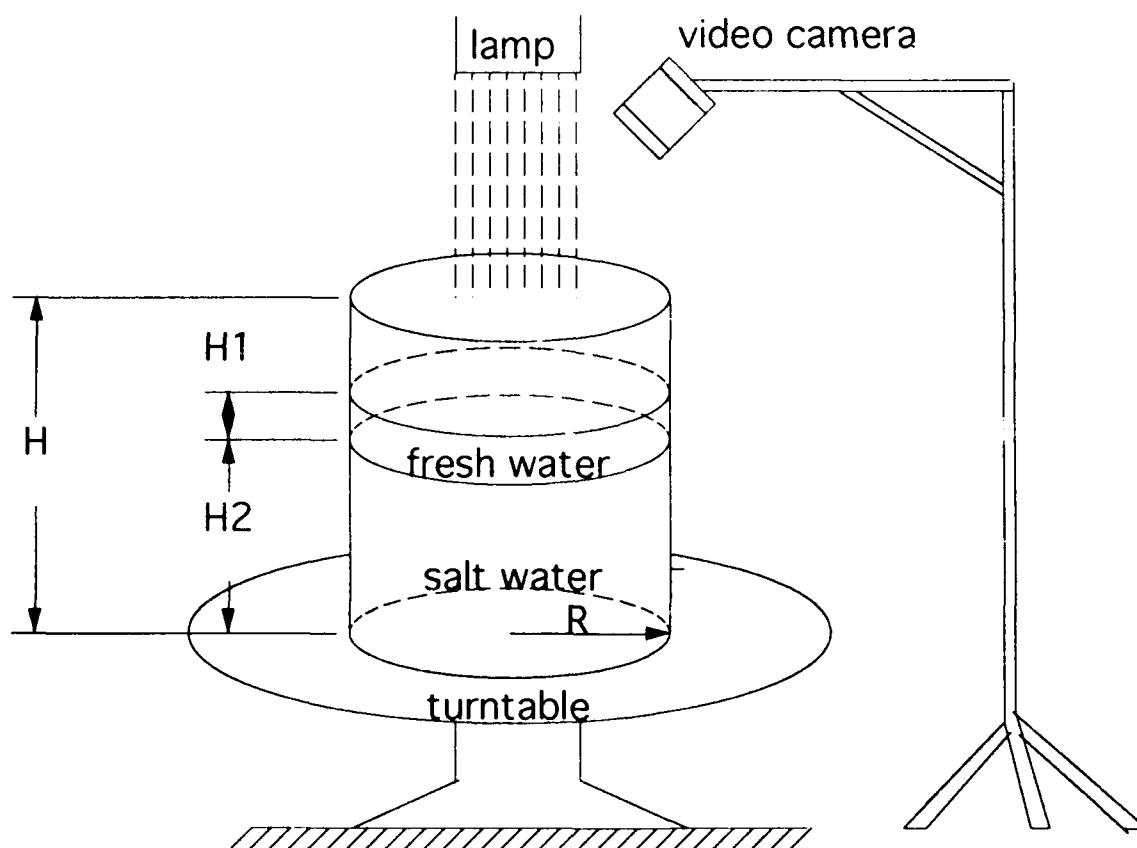
Fig.2 Experimental set-up of gutter wave in a rotating cylindrical tank.
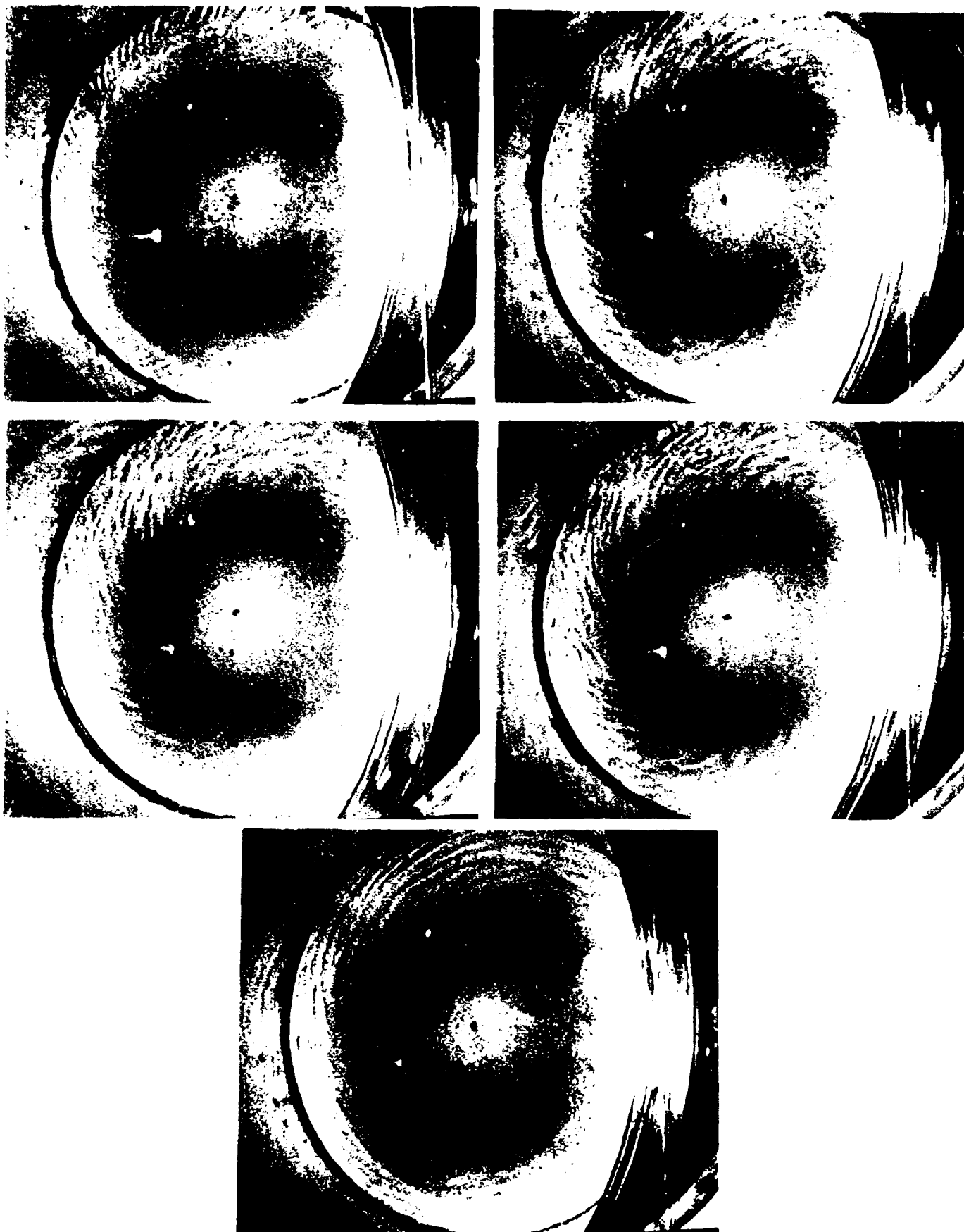
Figure 3. Exps in the Table 1 (a) t = 1 (s); (b) t = 3 (s); (c) t = 9 (s); (d) t = 10 (s); (e) t = 23 (s).

Table1 The experimental results for $H_1 = 1.5$ (cm)

EXP	H_1	H_2	H_e	ρ_s	V	F_r	T_l	λ	θ	W
	cm	cm	cm	g/cm^3	cm/s		s	cm	°	cm
1	1.5	24.0	1.4	1.085	20.49	1.9	1	0.75		6.0
2	1.5	23.7	1.4	1.094	27.24	2.36	1.5	0.86	50	6.9
3	1.5	24.0	1.4	1.089	27.24	2.4	2.5	0.86	48	9.0
4	1.5	24.1	1.4	1.106	31.09	2.5	6.0		46	11.4
5	1.5	22.6	1.4	1.120	39.27	3.0	8.0	1.0	42	12.0
6	1.5	21.1	1.4	1.128	45.56	3.4	6.0	1.2	35	13.5
7	1.5	19.6	1.4	1.139	57.4	4.1	7.0	1.3	30	15.0
8	1.5	24.3	1.4	1.068	54.35	5.5	8.0	1.75	35	11.7

Table2 The experimental results for $H_1 \approx 3.0$ (cm)

EXP	H_1	H_2	H_e	ρ_s	V	F_r	T_l	λ	θ	W
	cm	cm	cm	cm	cm/s		s	cm	°	cm
1	3.0	27.0	2.7	1.172	19.9	0.9	1.0		75	7.8
2	3.0	27.5	2.7	1.173	29.1	1.3	1.5	1.0	3	8.1
3	3.0	28.0	2.7	1.170	35.4	1.6	8.0	1.2	46	10.8
4	3.5	29.0	3.1	1.160	41.6	2.3	10.0	1.2	36	12.0
5	3.1	28.0	2.8	1.165	48.4	1.8	11.0	1.3	30	11.1

Table3 The experimental results for $H_1 \approx 6.0$ (cm)

EXP	H_1	H_2	H_e	ρ_s	V	F_r	T_l	λ	θ	W
	cm	cm	cm	cm	cm/s		s	cm	°	cm
1	6.6	27.0	5.3	1.172	16.3	0.54	N	N	N	N
2	6.2	27.5	5.0	1.177	18.73	0.63	Y	Y	Y	Y
3	6.5	27.6	5.3	1.176	22.86	0.75	0.8		82	7.8
4	5.0	21.0	4.0	1.150	18.53	0.76	N	N	N	N
5	6.1	27.4	5.0	1.173	25.24	0.84	3.0		70	8.4
6	6.5	19.5	4.9	1.180	26.38	0.89	1.5	0.86	65	6.6
7	6.0	20.0	4.6	1.180	28.94	1.0	2.0	0.86	55	7.5

Table4 The experimental results for other H_1

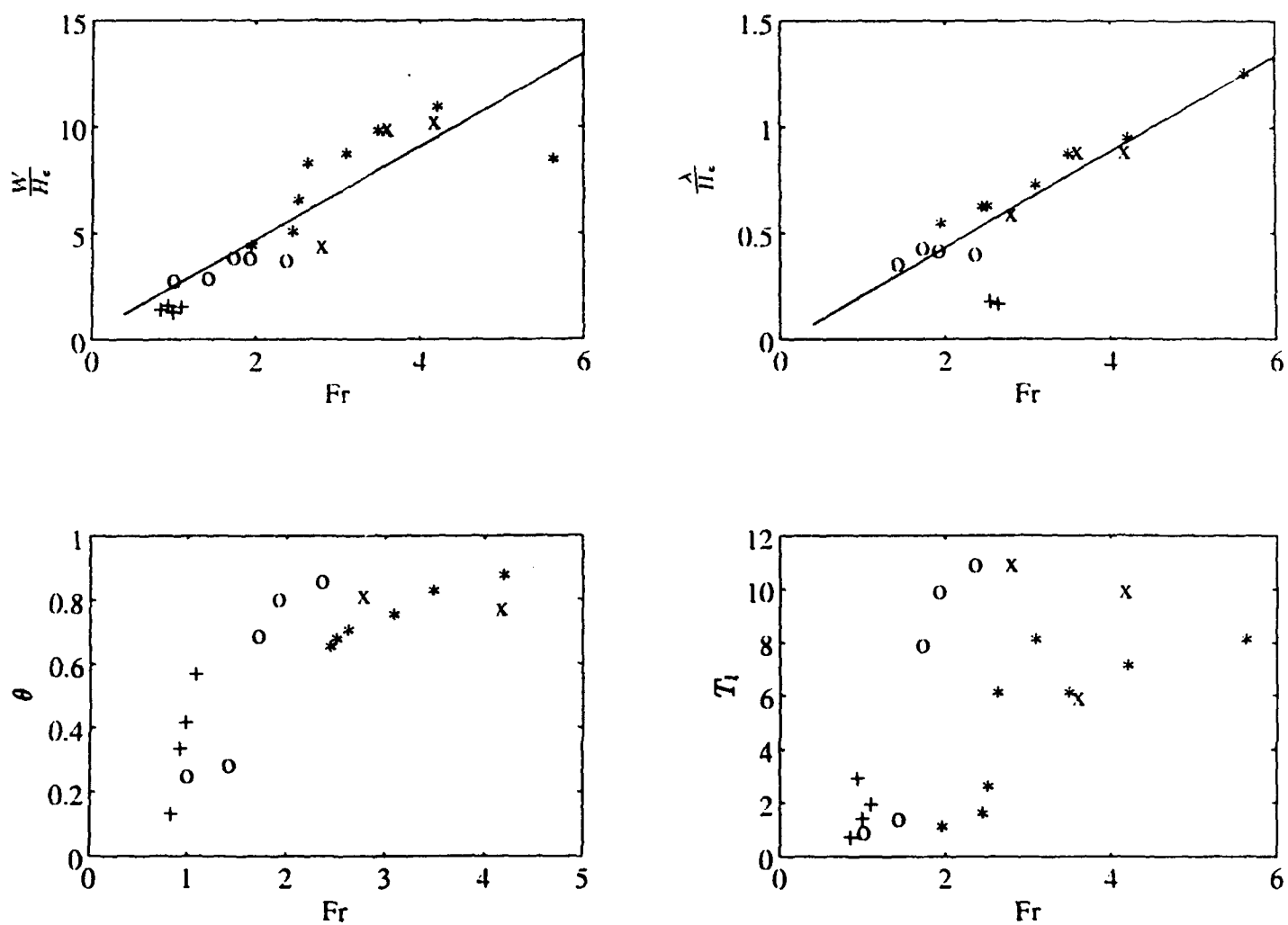| EXP	H_1	H_2	H_e	ρ_s	V	F_r	T_l	λ	θ	W
	cm	cm	cm	cm	cm/s		s	cm	°	cm
1	4.0	20.3	3.3	1.083	45.3	2.7	11.0	2.0	35	15.0
2	1.0	24.1	0.96	1.1	34.5	3.5	6.0	0.857		9.6
3	1.0	24.1	0.96	1.096	39.23	4.1	10	0.857	39	9.9

404

Fig.4 Experimental results from Table 1 to 4 and the corresponding least square fits.
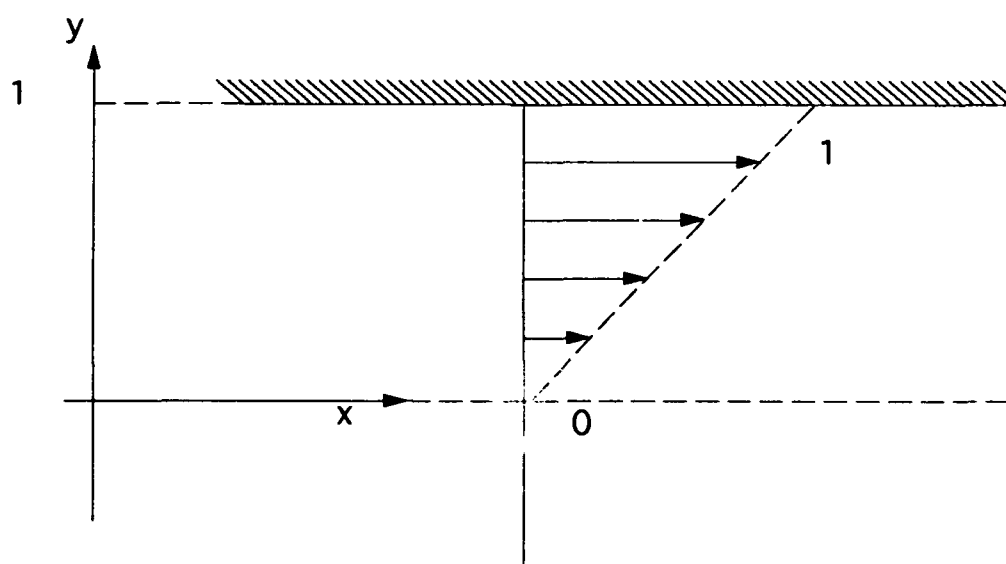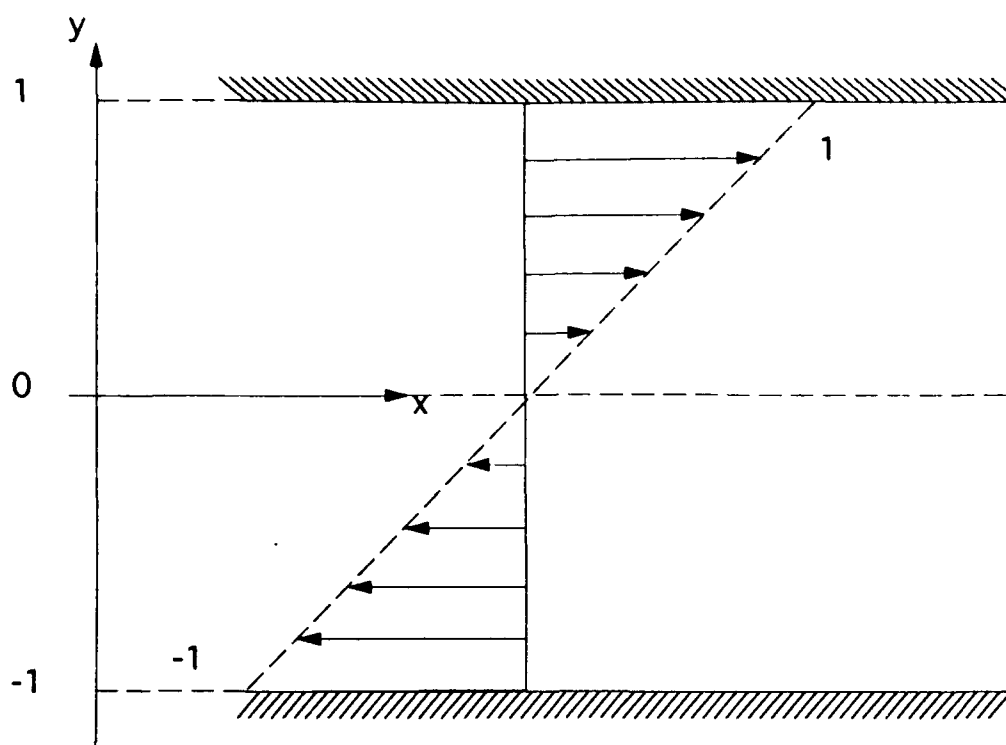
Fig.5 (a) Two wall: Mean flow profile $u(y) = y$ (b) Single wall: Mean flow profile $u(y) = y$ *for* $y \geq 0$ *and* $u(y) = 0$ *for* $y \leq 0$.
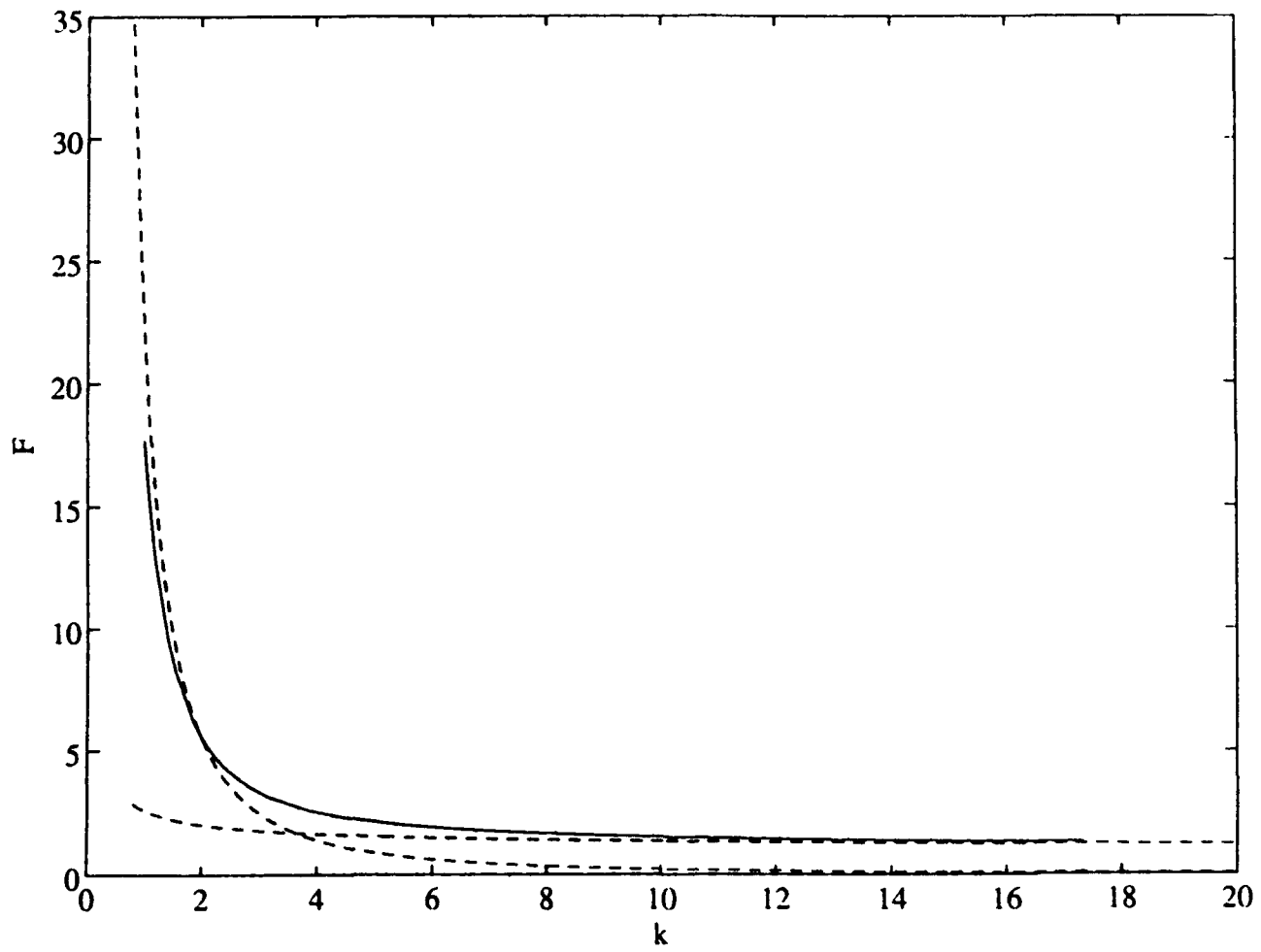
Fig.6 Neutral curve for case I where $F = F_r^2$. Solid line indicates the numerical resultes. Dash line represents the asymptotic behaviours by (36) and (41).
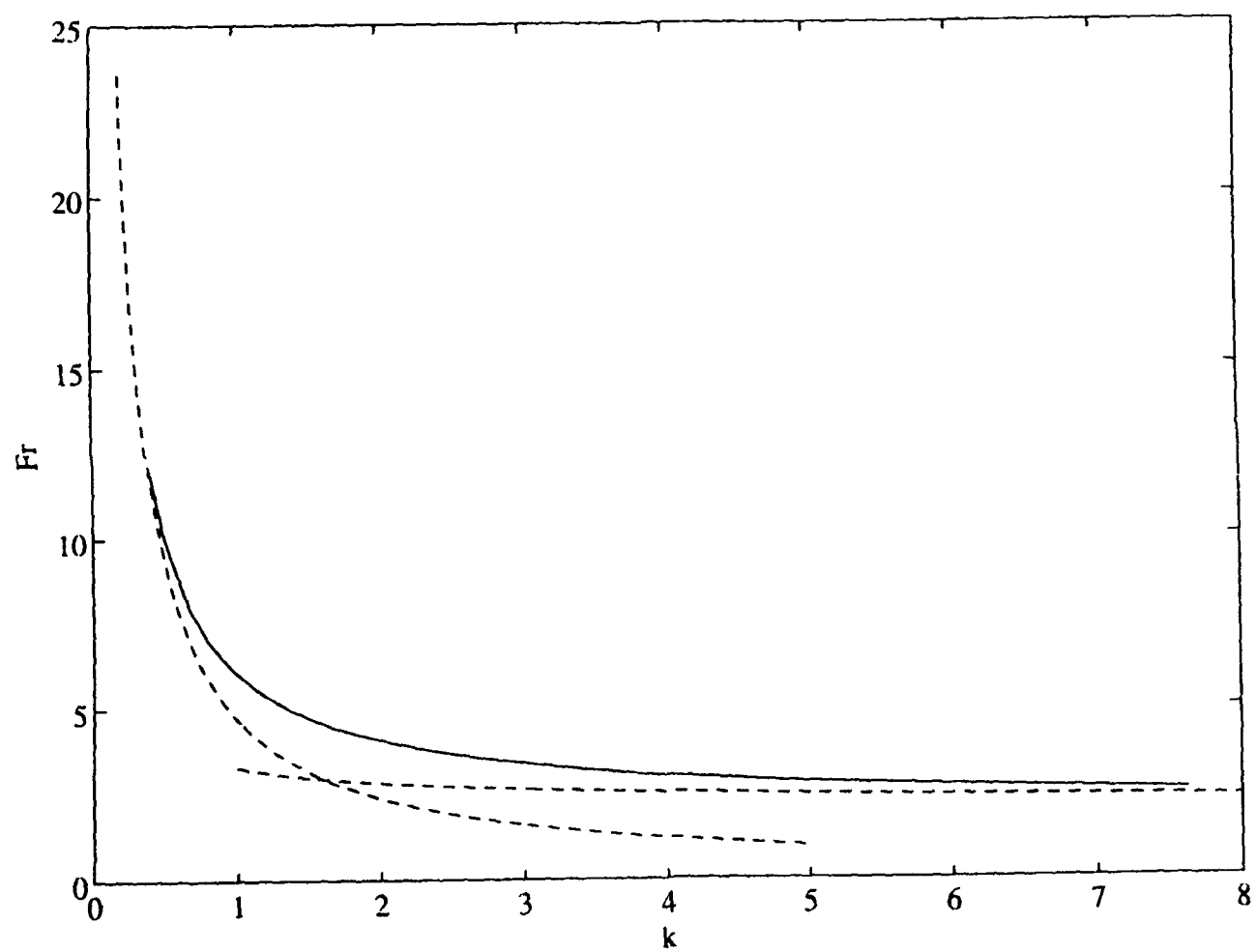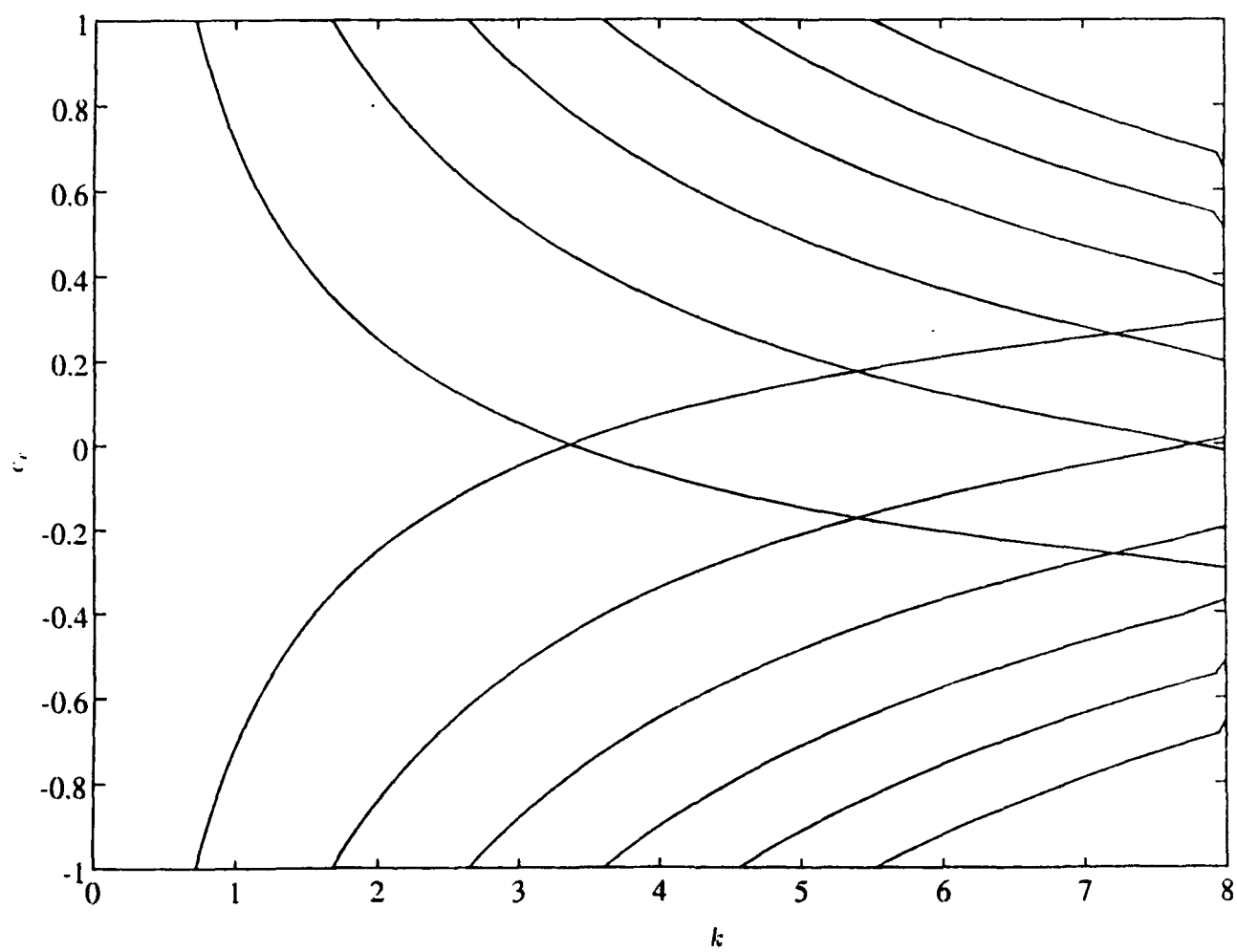
Fig.7 Neutral curve for case II. Solid line indicates the numerical resultes. Dash line represents the asymptotic behaviours by (49) and (50).

Fig.8 the dispersion curve c_r vs k for $F_r = 7$ by MAEM

50272-101

REPORT DOCUMENTATION PAGE	1. REPORT NO. WHOI-93-24	2.	3. Recipient's Accession No.

4. Title and Subtitle

Dynamics of the Outer Planets

5. Report Date

Summer 1992

6.

7. Author(s) Glenn Flierl, Andrew Ingersoll, Jun-Ichi Yano

8. Performing Organization Rept. No.

WHOI-93-24

9. Performing Organization Name and Address

Woods Hole Oceanographic Institution
Woods Hole, Massachusetts 02543

10. Project/Task/Work Unit No.

11. Contract(C) or Grant(G) No.

(C) OCE8901012

(G)

12. Sponsoring Organization Name and Address

National Science Foundation

13. Type of Report & Period Covered

Technical Report

14.

15. Supplementary Notes

This report should be cited as: Woods Hole Oceanog. Inst. Tech. Rept., WHOI-93-24.

16. Abstract (Limit: 200 words)

The topic this summer was "The Dynamics of the Outer Planets." Andrew Ingersoll gave an excellent review of the current understanding of the structure of the atmospheres of Jupiter, Neptune, Saturn, and Uranus. He presented the flow structures inferred from the information gathered by the Voyager probes and other observations. The models of the circulations of the interior and of the weather layer – the jets and vortices that we see in the images – were discussed. Jun-Ichi Yano gave further discussions on vortex dynamics in the lab, analytical, and numerical models as applied to the outer planets. Finally, Andy returned with a discussion of thin atmospheres (some so thin that they disappear at night) and new approaches to the dynamics of the interiors. These lectures provided a thorough background in both the data and the theory.

As usual, we had talks (or what are sometimes called interactive seminars!) from many visitors during the summer, some directly related to the main topic and others covering other new research in geophysical fluid dynamics. From these, the fellows and staff found new areas for collaborative research and new ideas which they may explore after the summer.

Finally, the summer was completed with talks from the fellows on their individual research during the summer. These reports reflect the thought and energy that went into learning new topics and formulating new problems. We look forward to seeing fuller versions of these in journal articles.

We gratefully acknowledge the support of the National Science Foundation and the Office of Naval Research. The assistance of Jake Peirson and Barbara Ewing-DeRemer, made the summer, once again, pleasant and easy for all.

17. Document Analysis   a. Descriptors

geophysical fluid dynamics
planetary circulations
vortex dynamics

b. Identifiers/Open-Ended Terms

c. COSATI Field/Group

18. Availability Statement	19. Security Class (This Report) UNCLASSIFIED	21. No. of Pages 422
Approved for public release; distribution unlimited.	20. Security Class (This Page)	22. Price

(See ANSI-Z39.18)   *See Instructions on Reverse*   OPTIONAL FORM 272 (4-77)
(Formerly NTIS-35)
Department of Commerce